POLITECNICO DI TORINO
Repository ISTITUZIONALE

Evaluation of Deep Learning models applied to remotely sensed imagery for object detection and segmentation tasks in territorial monitoring.

Original
Evaluation of Deep Learning models applied to remotely sensed imagery for object detection and segmentation tasks in territorial monitoring / Demartis, A., Giulio Tonolo, F. (TRENDS IN EARTH OBSERVATION). - In: Smart Earth Observation for a Sustainable Future / Rossi P.. - ELETTRONICO. - Firenze : Associazione Italiana di Telerilevamento, 2026. - ISBN 978-88-944687-3-1. - pp. 163-166 [10.978.88944687/31]

Availability:
This version is available at: 11583/3013810 since: 2026-07-31T13:01:03Z

Publisher:
Associazione Italiana di Telerilevamento

Published
DOI:10.978.88944687/31

Terms of use:

This article is made available under terms and conditions as specified in the corresponding bibliographic description in the repository

Publisher copyright

(Article begins on next page)

26 August 2026

AIT Series

Trends in earth observation

Volume 4

Smart Earth Observation for a Sustainable Future

Edited by

Associazione Italiana di Telerilevamento (AIT)

Smart Earth Observation for a Sustainable Future

Edited by

Associazione Italiana di Telerilevamento (AIT)

AIT Series: Trends in earth observation

The guest editors of this volume are:

Enrico Borgogno Mondino (AIT President)
Mirco Boschetti
Claudia Giardino
Lucia Maria Laurenza

All contributions published in the Volume Smart Earth Observation for a Sustainable Future were subject to blind peer review by independent reviewers. The revision of the contributions was meticulously carried out by the guest editors and the following researchers, to whom we extend our sincere gratitude

Claudia Arcidiacono
Anna Balenzano
Cristiana Bassani
Piero Boccardo
Luigi Boschetti
Mariano Bresciani
Sandro Brivio
Elena Candigliota
Francesco Casu
Gherardo Chirici
Roberto Colombo
Giacomo De Carolis
Maria Antonietta Dessena
Biagio Di Mauro
Francesco Fava
Federico Filipponi
Giacomo Fontanelli
Paolo Gamba
Marco Gianinetto
Fabio Giulio-Tonolo
Antonino Maltese
Maria Teresa Melis
Giuseppe Modica
Fernando Monterroso
Simonetta Paloscia
Monica Pepe
Pietro Picuno
Monica Pinardi
Serena Sapio
Giuseppe Satalino
Pasquale Striano
Daniela Stroppiana
Paolo Tagliolato
Deodato Tapete
Emiliana Valentini
Paolo Villa
Maria Virelli
Cristina Vittucci

The volume editing and typsetting was carried out by Patrizia Rossi.

Volume 4 - Published in June 2026
Edited by Associazione Italiana di Telerilevamento (AIT)
Published on behalf of the Associazione Italiana di Telerilevamento (AIT)
Via Lucca 50
50142 Firenze, Italy

ISSN 2612-7911
ISBN 978-88-944687-3-1
DOI: 10.978.88944687/31

AIT Series “Trends in earth Observation” is indexed in Scopus and Web of Science

All contributions published in the Volume “Smart Earth Observation for a Sustainable Future” were subject to blind peer review from independent reviewers.
Publication Ethics and Publication Malpractice Statement
Editors, Reviewers and Authors agreed with Publication Ethics and Publication Malpractice Statement

© 2026 by the authors; licensee Italian Society of Remote Sensing (AIT).
This Volume is an open access volume distributed under the terms and conditions of the Creative Commons Attribution license (http://creativecommons.org/licenses/by/4.0/).

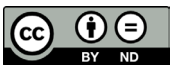

Preface

Earth Observation is a new and effective way to mean image-based remote sensing. Something has drastically changed since the first Landsat missions, and now we are experiencing a new era, where the ordinary satellite missions are sharing the space and the market with the various LEO (Low Earth Orbit), aerial and drone platforms. This new situation would require a significant reinforcement of users' skills and, consequently, a higher level of data and data processing consciousness. This reasonable expectation has been paradoxically disattended, and a new type of users seems to be, now, on. They appear to be well skilled in using tools, but poorly conscious about the inner meaning of data where the information they are looking for, comes from. The main responsible of this unexpected effect has been the huge technological advance, especially in the ICT context (computational power has enormously increased in the last decades), that has made possible the development of processing tools that can be applied globally, providing the users ready-to-use products and services accepted as they come. Scientific community has therefore to recover a central role, not only in proposing applications for those products/services, but also, once they have been eventually found, defining guidelines and rules for a proper use of data/methods/tools.

AIT strongly believe that the greatest and most urgent new challenge is a proper reverse engineering of the tools, products and services that are continuously exposed on the web. This must be intended for (i) recognizing the level of explainability of the processing chain, (ii) making explicit (if present) the calibration/validation metrics associated to the products/services in terms of both meaning and recurrency, (iii) eventually proposing (if lacking) guidelines and operational standards. Legal actions should be ignited to support this process, aiming at recognizing accredited controllers able to ensure an adequate level of **officiality** to data, products and services, to guarantee robustness and comparability of deductions. This need is, for example, at the basis of making deductions from EO data to be assumed as probatory within legal concerns (e.g. environmental crimes). This is furtherly true today, when we are experiencing the introduction of AI in many of Geomatics-related topics. Robustness and reliability of deductions from EO products/services, beyond whatever commercial exploitation, has still to be demonstrated and supported. **Each new map provided** (and EO is continuously producing maps wherever around the world) should undergo an adequate, recognized and official **validation procedure certified by accredited subjects**. This is not, now. Whatever standard procedure (for calibration and validation) requires the adoption of well-defined criteria and tools/procedures aimed at testing their satisfaction, that, once defined, should remain steady for a reasonable time. Such requirement, if considered in the framework of the present technology transfer, suggest to change the paradigm: one must stop running behind the latest new tool/algorithm and embrace slowness of science as the only reasonable way to

reliability. Technological advance cannot, obviously, be stopped. Its application, differently, can. Proper time steps, consistent with the definition and application of standards for products/services utilizations by final users, have to be defined and respected (e.g. standards refer to the state-of-the-art of time t and are updated every 3-5 years). In the meantime, the scientific community has to monitor, and possibly drive, the ongoing technological advance preparing new standards/procedures for the next updating step. It is AIT conviction that scientific associations can be the place where this process can be ignited and eventually managed, having no direct political or commercial involvements in the technology transfer process. And academy (Bachelor, Master and PhD) the place where a new generation of experts should be properly shaped.

It is within this vision that we have filled this volume, longing for a mosaic of works showing different points of views (from scientists, institutions, service providers, professionals, etc.), that could make it profitable for the future advance of Earth Observation.

AIT President (2023-2026)
Enrico Borgogno Mondino

Contents

Introduction ..... **viii**

Urban application **1**

1. Semi-automatic training and test sample selection using urban Spatial indices in random forest based LCZ mapping: a Milan case Study 2
A. Moazzam, X. Guo, J. Jiang, M.A. Brovelli
2. Geospatial analysis of local climate zones and urban heat islands in Italy and Vietnam 6
Matej Žgela, Srojish Sabareesh Nivas Manikandan, Alberto Vavassori, Giovanna Venuti, Deodato Tapete, Patrizia Sacco, José Antonio Gámez García, Pham Thi Mai Thy, Lam Dao Nguyen, Maria Antonia Brovelli
3. A prototype earth observation-based framework for simulating urban intervention effects on land surface temperature..... 10
D. Oxoli, A. Vavassori, M.A. Brovelli
4. Simplified estimation of land surface temperature using surface energy balance model..... 14
N. Naila, G. Tognon, J. Vivian, M. De Carli
5. A geospatial decision-support framework for urban and suburban photovoltaic deployment..... 19
M. Moretti, E. Tricomi, M. Koren, M. Gianinetto

Environment, climate risk..... 23

6. Map of land cover partial agreement: a probabilistic fusion 24
Qiongjie Xu and Maria Antonia Brovelli
7. A standalone software for post-fire erosion susceptibility assessment during the emergency phase 28
C. Pala, M.T. Melis, M.T. Brunetti C. Collu, R. Sarro, P.V. Miranda Garcia, J.P. Galve Arnedo, A. Millares
8. Integration of bioindication and remote sensing: UAV and stratospheric platforms for environmental monitoring 33
M. Gargiulo, C. Savarese, S. Parrilli, F. Tufano, M. De Mizio
9. Monitoring glacier snow cover of alpine glaciers with the TeNDIS index 37
N. Genzano, R. Zinelli, M. Scaioni
10. Monitoring the drying dynamics of the Sal'e Porcus salt pond using Sentinel-1 time series: a preliminary study for climate-driven surface evolution 42
C. Collu, M. Casu, I. Nobile, C. Nieddu, M. Musacchio, K. Onačillov, J. Šašak, Michal Galley, M.T. Melis
11. Heat wave and heat stress space-time patterns assessment in Lombardy using climate reanalysis data and in situ measurements..... 46
A. Vavassori, M. Žgela, F. Bissi, M.A. Brovelli
12. Long term "X" preservation and long time series generation for climate change..... 50
M.Albani , R.Biasutti, I. Maggio, S.Folco
13. Integrated GNSS and INSAR datasets for the monitoring of land subsidence in the Po river delta.... 54
A. Danti, M. Fabris, C. Masetto, U. Trivelloni

14. Synthetic aperture RADAr based flood extent mapping in complex land cover areas: a case study of tana river delta, Kenya 58
D.M. Muriithi, F. Mutwiri, A. Vitti
15. A Fast Bayesian inference for flood detection using gpu-accelerated statistical analysis of multi-temporal SAR stacks 63
R. Paudice, F. P. Lovergine, A. Refice

Agriculture & forestry 67

16. Estimating Agronomic Variables in Paddy Rice with Field and Spaceborne Hyperspectral Spectroscopy 68
R. Ceriani, F. Fava, F. Nutini, G. Candiani, M. Pepe, A. Crema, L. Parigi, S. Ambrosini, M. Boschetti
17. Assessing machine learning regression algorithms for wheat grain protein content (GPC) estimation exploiting ground spectral data and crop traits 73
L. Miazzo, M. Boschetti, M. Marshall, M. Belgiu, L. Parigi, G. Candiani
18. Mapping Tillage and Crop Residue presence Using Planet and Sentinel-2 Imagery 77
G. Tellina, M. Boschetti, M. Pepe1 A. Ferrarini, F. Filipponi, F. Zucca, F. Nutini
19. Investigating crop residues presence and persistence from Sentinel-2 time series 81
C. Bossio, E. Spirito, F. Filipponi, F. Nutini, G. Tellina, A. Ferrarini, F. Zucca, M. Boschetti, M. Pepe
20. Wheat yield estimation from sequences of hyperspectral images: preliminary investigation of spectral temporal information with Neural Network..... 85
L. Parigi, L. Miazzo, F. Nutini, G. Candiani, M. Marshall, M. Belgiu, M. Borschetti
21. Multi-source earth observation data integration for precision agriculture: a corn crop monitoring case study 89
Cicala, M. Gargiulo, C. Savarese, S. Parrilli, C.V. Angelino, F. Tufano, M. De Mizio
22. Exploring vineyard phenological variability through Unsupervised bi-temporal analysis of UAV multispectral and thermal data..... 93
A. Capolupo and E. Tarantino
23. Integration of MODIS NDVI data into Tuscany meteorological fire risk bulletin 97
R. Mari, G. Bartolini, G. Betti, L. Bottai, M. Chiesi, L. Fibbi, F. Maselli, F. Pasi, B. Gozzini
24. Leveraging Geospatial Techniques to Monitor Restoration Efforts and Assess Associated Forest Ecosystem Services in Kenya: Case Study of Maasai Mau Forest in Kenya 101
F.K. Mutwiri, D.M. Muriithi, A. Vitti
25. Monitor post-fire vegetation dynamics in forest ecosystems using Sentinel-2 and PlanetScope time series..... 105
F. Filipponi, E. D'Andrea, F. Zucca

Evapotranspiration, soil moisture and irrigation 109

26. Bayesian-Optimized LSTM Fusion of SAOCOM L-Band, Sentinel-1 C-Band, Sentinel-2 NDVI, nd Meteorological Forcings for High-Resolution Soil Moisture Retrieval in No-Till Croplands..... 110
J. O. Ondieki, M. Marsella, G. Laneve, M. Collins
27. Integrated analysis of evapotranspiration in the plant-nursery district of Pistoia 115
B. Rapi, P. Battista, M. Chiesi, L. Fibbi, F. Sabatini, L. Incrocci, M. Pieri, F. Maselli
28. Early estimation of irrigation needs of processing tomatoes at district scale: field identification and phenology 119
M. Rinaldi, P. Garofalo, F. Ciavarella, G. Satalino, F. Mattia, A. Balenzano, L. Nardella, N. Noviello R. Guarini, D., Tapete, S. Ruggieri

29. Modeling and mapping Kc dynamics from NDVI time series using a double logistic function..... 124
Ronco E, De Petris S., Ghilardi F., Borgogno Mondino E.
30. Towards a regional agricultural drought monitoring system based on evapotranspiration MODIS products: first issues 128
E. Ronco, M. Balin, S. De Petris, S. Tuand, M. Gianinetto, E. Borgogno Mondino
31. Advancing High-Resolution Retrieval of Soil and Vegetation Water Content from C- and L-band SAR Observations: the SARWATER Project 132
R. Eskandari, M. Scaioni, Z. Wang
32. Advanced satellite technologies and systems for environmental monitoring and sustainability in agriculture 136
L. Servadei

Algorithm, tool and new mission 141

33. The joint ASI-NASA/JPL surface biology and geology thermal infrared (SBG-TIR)mission..... 142
S. Venafra, S. Zoffoli, F. Longo, T. Scopa, R. Votta, G. Viavattene, F. Tataranni, A. Andrisani, D.K. Pallotti 1, V., Martucci, M. Orefice, R. Pellegrini, E. Ciocci, M.F. Buongiorno, M. Silvestri, G.L. Liberti, R. Colombo, S. Pignatti, C. Notarnicola, G. Laneve, V. Della Corte, A. Francioni, F. Antonacci, R. Basilio, S. Hook, K.C. Nicholson, S. Hunyadi-Lay, M. Larson, L. White, P. Xaypraseuth, S. Islas
34. Towards FLEX for water: analysis of ground and airborne observations in lake Garda 146
L. Panizza, M. Bresciani, C. Giardino, M. Pinardi, M. Austoni, R. Colombo, L. Caccetta, E. Canuti, B. Siegmann, P. Rademske, U. Rascher, K. Sakowska, L. Genesio, L. Vescovo and S. Cogliati
35. The EarthCARE mission: an overview of science objectives, data processing chain and products visualization 150
A. Piro, B. Abis, L. Di Ciolo, T. Hummel, B. Frommknecht, F. Capatano, V. Tzallas
36. PRISTAR-GEOSPEC: PRISMA tools for analysis in R for geocoding and Spectral refinement..... 154
E. Spirito, F. Filipponi, G. De Luca, L. Parigi, R. Ceriani, M. Boschetti, M. Pepe
37. A GeoAI approach to land cover change prediction using Multilayer Perceptrons and Copernicus EO data to support future territorial planning in Aosta valley (NW Italy)..... 158
T. Orusa, D. Cammareri, A. Viani
38. Evaluation of Deep Learning models applied to remotely sensed imagery for object detection and segmentation tasks in territorial monitoring..... 163
A. Demartis and F. Giulio Tonolo

Introduction

Smart Earth Observation for a Sustainable Future

The IV volume of the TEO collection presents a curated selection of studies originally presented at the XII AIT International Conference, held in Milan from November 12 to 14, 2025.

While the conference brought together the Earth Observation (EO) community to discuss how innovation in remote sensing, data science, and environmental monitoring can contribute to sustainability and societal resilience, this specific volume includes **38 peer-reviewed papers organized into 5 dedicated thematic sections**:

- Urban Applications: Focuses on urban monitoring, exploring Local Climate Zones , Urban Heat Islands, surface temperature simulations, and solar energy deployment.
- Environment, Climate Risk: Addresses hazards and climate indicators, including post-fire erosion, multi-temporal SAR flood mapping, glacier dynamics and regional heat stress.
- Agriculture & Forestry: demonstrates multi-source EO applications for precision farming, crop traits/yield estimation, tillage mapping and post-fire forest recovery
- Evapotranspiration, Soil Moisture, and Irrigation: Advances high-resolution soil water content retrieval via multi-band SAR, evapotranspiration modelling and Deep Learning for agricultural drought monitoring and irrigation management.
- Algorithm, Tool, and New Mission: showcases new space programs (SBG-TIR, FLEX, EarthCARE) alongside innovations in PRISMA pre-processing tools and GeoAI deep learning frameworks for territorial monitoring.

The central theme of this volume, “Smart Earth Observation for a Sustainable Future,” reflects the growing importance of advanced remote sensing technologies in addressing environmental and societal challenges. The scientific contributions collected in this volume demonstrate significant progress in the integration of multi-sensor data, emerging spaceborne EO missions, and advanced computational methodologies - particularly GeoAI - to enhance environmental monitoring and risk mitigation.

We warmly thank all authors and reviewers for their high-quality contributions, making this TEO volume a valuable document to share ideas, build collaborations, and advance the role of Earth Observation in supporting a more sustainable future.

Urban application

SEMI-AUTOMATIC TRAINING AND TEST SAMPLE SELECTION USING URBAN SPATIAL INDICES IN RANDOM FOREST BASED LCZ MAPPING: A MILAN CASE STUDY

A. Moazzam [1] *, X. Guo [2], J. Jiang [2], M.A. Brovelli [1]

[1] Department of Civil and Environmental Engineering, Politecnico di Milano, Milan, Italy - (afshin.moazzam, maria.brovelli)@polimi.it
[2] Beijing University of Civil Engineering and Architecture, Beijing, China - (guoxian, jiangjie)@bucea.edu.cn

KEY WORDS: Urban Heat Island (UHI), Local Climate Zone (LCZ), Urban Spatial Indices (USI), Spectral Indices, Classification, PRISMA

ABSTRACT:

Local Climate Zone (LCZ) mapping is essential for understanding urban heat island (UHI) effects but traditionally relies on time-consuming manual sample labeling prone to subjectivity. This study proposes a semi-automatic pipeline integrating urban spatial indices (BCR, CI, ABH) and remote sensing spectral indices (NDVI, BSI, MNDWI) to generate representative training and test polygons for LCZ classification via Random Forest classification methodology in Milan, Italy by using building height data from Milan's geotopographic database and PRISMA hyperspectral acquisition. Validation against a reference LCZ map revealed high agreement for some LCZ classes, with built-up classes outperforming natural types. Random Forest classification using generated samples achieved 56% overall accuracy on test data. While the workflow substantially reduced computation time and manual effort—particularly for complex urban morphologies—vegetation classes and soil-paved distinctions suffered from spectral overlap and weak thresholding, limiting comprehensive applicability. This method offers a scalable foundation for LCZ mapping but requires refined spectral strategies and machine learning integration for natural classes. Future work should leverage multi-temporal data and deep learning for robust, reproducible UHI analysis across cities.

1. INTRODUCTION

The urban heat island (UHI) effect represents one of the most critical environmental challenges facing contemporary cities, characterized by significantly elevated temperatures in urban areas compared to their rural surroundings (Dimitrov, 2024) (Yang, 2024). Rapid urbanization, increasing impervious surfaces, and declining vegetation coverage have intensified UHI effects worldwide, exacerbating heat stress, energy consumption, and public health risks during extreme temperature events (Chen, 2023) (Li, 2020) (Yu, 2025).

Local Climate Zones (LCZ) are a standardized classification system that divides urban and rural landscapes into 17 distinct classes based on physical surface properties like building height, density, and material cover. The primary purpose of the LCZ framework is to replace vague urban vs. rural descriptions with a universal, culture-neutral method that improves the accuracy and comparability of UHI studies globally. By defining zones through measurable parameters such as sky view factor and impervious surface fraction, researchers can consistently link specific urban forms to their thermal impacts across different cities (Stewart, 2012).

Based on the methodology described in (Vavassori, 2024), creating a LCZ map using Random Forest involves a combined Remote Sensing and GIS approach that integrates spectral data with morphological indicators. However, manual sample creation is typically labour-intensive and subjective, which may introduce inconsistencies across interpreters, particularly in large or heterogeneous urban areas where distinguishing between similar LCZ classes requires extensive local knowledge and subjective judgment.

These challenges can limit the scalability and reproducibility of LCZ mapping efforts across different cities and regions. Therefore, in this work we propose a semi-automatic method that leverages Earth observation data to systematically identify and generate training and test samples, reducing manual effort while improving consistency and objectivity in the sample selection process.

2. METHODOLOGY

The core design of the proposed pipeline is to decouple built-up and natural LCZ classes and exploit their distinct morphological and spectral signatures for semi-automatic sample generation. To automatically obtain representative polygons for all classes defined by the LCZ classification system, we propose a pipeline that integrates satellite imagery and geotopographic data to delineate each class group (Figure 1).

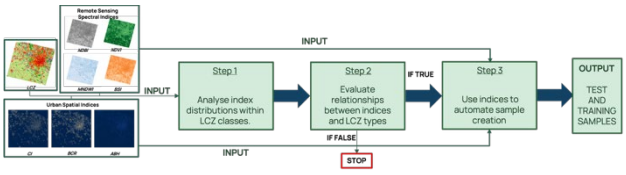

Figure 1. The flowchart of the proposed methodology.

It is also essential to ensure that the extracted samples maintain regular shapes, appropriate aspect ratios, and a balanced spatial

* Corresponding author

distribution across the study area. In this work, we selected Milan (Italy) and the surrounding areas as the case study because LCZ maps are for this area already available under the same methodological framework that we intend to follow. This allows us to compare the results of our semi-automatic sample generation approach with manually created samples and to evaluate the overall performance of the proposed method.

The LCZ classes can be broadly categorized into two subgroups: built-up classes and natural classes. For the built-up classes, we propose the use of Urban Spatial Indices (USI) that describe urban morphology. These indicators have been shown to correlate with the UHI effect and can help identify areas sharing similar characteristics to those defined in the LCZ classification system (Liu, 2023). The urban morphological parameters considered in this study include the Building Coverage Ratio (BCR), Compactness Index (CI), and Average Building Height (ABH). The BCR quantifies the proportion of the built-up area within a given grid cell, reflecting the extent of building coverage. The CI represents the spatial density of buildings within the grid, indicating whether the built environment is compact and closely spaced or more dispersed. Finally, the ABH captures the mean height of buildings in each grid cell, allowing differentiation among high-rise, mid-rise, and low-rise urban structures.

For the natural classes, conventional remote sensing indices—including the Normalized Difference Vegetation Index (NDVI), Normalized Difference Built-up Index (NDBI), Bare Soil Index (BSI), and Modified Normalized Difference Water Index (MNDWI)—are employed in this study to distinguish between different land cover types. NDVI highlights vegetation cover and health based on the spectral contrast between near-infrared and red reflectance. NDBI identifies built-up areas by exploiting the difference between shortwave infrared and near-infrared reflectance. BSI detects bare soil surfaces by integrating information from visible and infrared bands. Finally, MNDWI enhances the identification of water bodies by contrasting green and shortwave infrared reflectance.

The morphological parameters used in this study were derived from building footprint and building height data. The vector file containing building height information, with a spatial resolution of 1 m, was obtained from the geotopographic database of Milan. This vector dataset was subsequently converted into raster format. Using a raster calculator, cells with available building height values were assigned a value of one, indicating the presence of a building, while cells without building height information were assigned a value of zero, representing non-built areas. The resulting raster layer therefore represents the building footprint. Finally, the raster datasets were resampled to a 5 m resolution to prevent overfitting and to reduce computational time during the calculation of urban spatial indices. For the natural class indices, a PRISMA acquisition over Milan, dated 8 August 2023, was utilized. The image was processed to correct for registration errors using the closest Sentinel-2 acquisition in terms of acquisition date.

Once the morphological parameters and spectral indices were derived, they were aggregated to a spatial resolution of 30 m to align with the resolution of the reference LCZ map of Milan produced through manual delineation. This step ensured direct comparability between the manually derived classes and the semi-automatic products generated in this study. Both sets of indices—urban spatial and natural—were examined to assess their relationships with the reference LCZ classes. Upon validation of their relevance and discriminative capability, these indices were incorporated into a threshold-based classification workflow. Specifically, the built-up classes were characterized using BCR, CI, ABH, and NDVI, which were jointly used to distinguish between different structural typologies. For the natural classes, BCR, NDVI, BSI, and MNDWI were integrated to separate vegetation, bare soil, and water-related categories. The NDBI index was excluded from the final model due to its limited discriminatory performance, as it introduced confusion between soil- and concrete-covered areas when combined with BSI. Class assignments were performed by applying statistical thresholds to each index combination, thereby generating masks that labelled each 30 m grid cell with its corresponding LCZ class.

In the subsequent step, the building footprint raster was used to refine the boundaries of built-up areas within each 30 m grid cell, ensuring spatial consistency between the classified class and urban physical structures. For the natural classes, additional refinement was achieved using the Global Canopy Height dataset from ETH Zurich to separate vegetation classes based on canopy height and the road network data from the DBGT database of Milan to differentiate soil- from concrete-covered surfaces.

Finally, to ensure the quality and representativeness of the samples, all polygons were constrained to have an area between 0.04 and 0.05 km², an aspect ratio below 3, and a balanced spatial distribution across the study region. For each LCZ class, a maximum of 100 polygons were selected, of which 80% were assigned as training samples and the remaining 20% were reserved for testing. The derived polygons were subsequently used as input in the LCZ classification workflow, following the methodology proposed by (Vavassori, 2024), to generate the final LCZ map for Milan.

3. RESULTS

The agreement between the semi-automatically generated LCZ training and test samples and the reference LCZ map varies substantially across classes. The comparison is summarized in Table 1.

Class	Total Pixels	Matched Pixels	%
Compact-midrise (2)	158058	137755	87.2
Compact-lowrise (3)	93003	25708	27.6
Open-midrise (5)	80289	45774	57
Open-lowrise (6)	133328	87064	65.3
Large-lowrise (8)	486012	451713	92.9
Dense trees (101)	316804	5098	1.6
Scattered trees (102)	499396	152813	30.6
Low plants (104)	385911	224378	58.1
Bare rock or paved (105)	408619	157134	38.5
Bare soil or sand (106)	1886501	833689	44.2
Water (107)	57708	56614	98.1

Table1. LCZ samples agreement with the reference LCZ map.

Large Lowrise (LCZ 8) and Water (LCZ 107) exhibit very high correspondence, with more than 90% of pixels matching the reference LCZ labels, indicating that the proposed index-based strategy delineates these types very reliably. Built-up Compact Midrise (LCZ 2), Open Midrise (LCZ 5), and Open Lowrise (LCZ 6) also achieve moderate to high agreement, with match percentages between about 57% and 87%, suggesting that the urban spatial indices capture their morphological characteristics reasonably well. In contrast, classes Compact-lowrise (LCZ 3), Scattered trees (LCZ 102), Bare rock or paved (LCZ 105), and especially Dense Trees (LCZ 101) show relatively low overlap,

with this class reaching only 1.6% agreement, highlighting difficulties in distinguishing these types using the current threshold configuration. The large extent and intermediate match rate of Bare soil or sand (LCZ 106) (44.2%) further indicate that some broad natural or mixed classes remain partly confused with neighbouring types.

The LCZ classification obtained using the generated training samples (Figure 2) shows heterogeneous performance across classes. Among the built-up classes, LCZ 5 exhibits the strongest correspondence with the reference map, achieving a match percentage of 81.7%, demonstrating the effectiveness of the selected morphological and spectral indices in characterizing these urban forms. LCZ 6 follows with solid agreement at 62.3%, while LCZ 2 attains a moderate 49.4%, indicating reasonable but less consistent delineation for more densely structured environments. Built-up classes LCZ 3 and LCZ 8 show 39.9% and 88.2% agreement, respectively, with the high performance of LCZ 8 suggesting robust discrimination for extensive low-rise development patterns.

For the natural classes, LCZ 107 achieves excellent performance at 94.7%, confirming the effectiveness of MNDWI and related indices for water surface delineation. LCZ 104 performs well at 86.7%, while LCZ 105 reaches 29.9%, highlighting variable success in distinguishing impervious surfaces from other sparse covers. LCZ 101 shows very low agreement at 4.6%, LCZ 102 at 22.8%, and LCZ 106 at 49.9%, indicating persistent challenges in separating vegetation density gradients and bare ground types that spectrally overlap with adjacent classes.

When the classification workflow was repeated using the independent test samples (20% holdout), an overall accuracy of 56% was achieved, demonstrating reasonable generalization capability of the semi-automatic sample generation approach despite class-specific variability. Overall, the semi-automatic approach delivers superior results (>80%) for well-contrasted built and water classes, while vegetation and sparse surface types would benefit from refined thresholds or additional structural data.

It should be noted that the primary objective of this study is not to maximize classification accuracy, but to evaluate the reliability of semi-automatically generated samples for LCZ mapping.

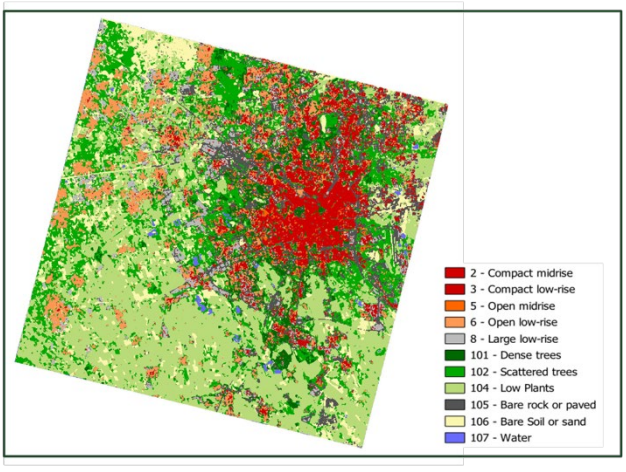

Figure 2. LCZ map generated with semi-automatic samples creation workflow.

4. CONCLUSION AND FUTURE WORKS

The proposed semi-automatic pipeline represents a promising step toward automating LCZ sample generation for Random Forest classification, successfully reducing manual labelling effort while achieving high correspondence (>90%) with the reference Milan LCZ map for well-defined classes such as large lowrise and water. Built-up classes demonstrated superior performance compared to natural classes which is a notable outcome given the complexity and criticality of urban morphology delineation where manual interpretation is most error prone. The workflow also delivered substantial computational efficiency gains, fulfilling a primary objective by enabling rapid, spatially balanced sample creation across large metropolitan areas.

Nevertheless, limitations persist for vegetation and bare-surface classes, where spectral overlap and threshold-based separation constrain classification reliability. Methodological refinement must prioritize overcoming the identified weaknesses through data-driven threshold optimization via supervised clustering or probabilistic models, replacing current heuristic separations for vegetation density and soil-paved distinctions. Integration of multi-temporal hyperspectral imagery and advanced canopy height models beyond ETH Global Canopy data could strengthen natural class discrimination, while city-scale LiDAR validation would test hypothesis robustness across diverse urban contexts.

To achieve operational scalability, deep learning frameworks (e.g., U-Net architectures) trained on expanded multi-city LCZ datasets could replace the threshold-based workflow, though this demands significantly larger, higher-quality training samples than currently available. Quantitative benchmarking against manual workflows—measuring time savings, reproducibility, and error reduction—across additional European cities will be essential.

ACKNOWLEDGEMENTS

This study was carried out within the Space It Up! project funded by the Italian Space Agency, ASI, and the Ministry of University and Research, MUR, under contract n. 2024-5-E.0 - CUP n. I53D24000060005.

REFERENCES

Chen, K. B. (2023). A multiscale analysis of heatwaves and urban heat islands in the western US during the summer of 2021. *Scientific Reports, 13(1)*, 9570.

Dimitrov, S. I. (2024). A Methodological Framework for High-Resolution Surface Urban Heat Island Mapping: Integration of UAS Remote Sensing, GIS, and the Local Climate Zoning Concept. *Remote Sensing, 16(21)*, 4007.

Li, Y. S. (2020). On the influence of density and morphology on the Urban Heat Island intensity. *Nature communications, 11(1)*, 2647.

Liu, B. G. (2023). How urban morphology relates to the urban heat island effect: A multi-indicator study. *Sustainability, 15(14)*, 10787.

Stewart, I. a. (2012). Local climate zones for urban temperature studies. *Bulletin of the American Meteorological Society, 93(12)*, 1879-1900.

Vavassori, A. O. (2024). A combined Remote Sensing and GIS-based method for Local Climate Zone mapping using PRISMA and Sentinel-2 imagery. *International*

Journal of Applied Earth Observation and Geoinformation, 131, 103944.

Yang, L. L. (2024). Different explanations for surface and canopy urban heat island effects in relation to background climate. *Iscience, 27(3)*.

Yu, H. Y. (2025). How does urbanization process affect urban heat island effect? Interpretation of 31 cities in China based on local climate zones. *Environmental Research Letters, 20(11)*, 114013.

This work is licensed under a Creative Commons Attribution-No Derivatives 4.0 International License.

GEOSPATIAL ANALYSIS OF LOCAL CLIMATE ZONES AND URBAN HEAT ISLANDS IN ITALY AND VIETNAM

Matej Žgela[1], Srojish Sabareesh Nivas Manikandan[1], Alberto Vavassori[1], Giovanna Venuti[1], Deodato Tapete[2], Patrizia Sacco[2], José Antonio Gámez García[2], Pham Thi Mai Thy[3], Lam Dao Nguyen[3], Maria Antonia Brovelli[1*]

[1] Department of Civil and Environmental Engineering, Politecnico di Milano, Milano, Italy
(matej.zgela, srojish.sabareesh, alberto.vavassori, giovanna.venuti, maria.brovelli)@polimi.it

[2] Italian Space Agency (ASI), Rome, Italy
(deodato.tapete, patrizia.sacco)@asi.it; jose.gamez@est.asi.it

[3] Vietnam National Space Center (VNSC), Ho Chi Minh City, Vietnam
(ldnguyen, ptmthy)@vnsc.org.vn

KEY WORDS: Local Climate Zones (LCZ), Urban Heat Island (UHI), Machine Learning, PRISMA Hyperspectral satellite, Urban Environments

ABSTRACT:

Urban areas are increasingly affected by global climate change and the Urban Heat Island (UHI) effect, which raises temperatures and intensifies heat stress. To analyse and mitigate these impacts, this study examines how Earth Observation (EO) and geospatial data can be integrated to characterise urban thermal environments by classifying cities into Local Climate Zones (LCZs) and interpolating near-surface air temperatures (AT) at high spatial resolution. It focuses on Rome, Milan, Hanoi, and Ho Chi Minh City to improve understanding of UHI dynamics across temperate and tropical regions. High-resolution LCZ maps were produced using a combined remote sensing–GIS method that integrates hyperspectral PRISMA data with detailed Urban Canopy Parameters (UCPs). These maps help reveal how urban morphology influences local temperatures. A fine-scale AT interpolation was performed for Milan during the 2022 heatwaves (HWs) using machine learning regression. It combines observations from official and crowdsourced stations with EO- and GIS-derived environmental predictors and examines specific diurnal phases to capture heating and cooling dynamics. Results show strong diurnal and seasonal variations, with urban areas consistently warmer, especially at night, due to delayed heat release from built surfaces. The study demonstrates the importance of detailed LCZ mapping and high-resolution temperature modelling for understanding spatial heat variability and supporting targeted strategies to reduce heat-related risks in cities.

1. INTRODUCTION

Over the last decades, the rapid expansion of cities and anthropogenic settlements in response to population growth and densification has led to a substantial increase in impervious surfaces, higher buildings, and more compact urban fabric, thus changing urban morphology (e.g., Akbari and Kolokotsa, 2016). This process is accelerating the Urban Heat Island (UHI) effect, i.e., an increase in local surface temperatures in densely populated cities compared to temperatures measured in rural/natural surroundings (Oke et al., 2017). Dense construction materials retain daytime heat and fail to dissipate such heat overnight (e.g., Oke, 1982; Kim et al., 2022). At the same time, the lack of green infrastructure diminishes the benefits of the vegetation cooling effect, especially through daytime evapotranspiration (e.g., Morabito et al., 2021). It can be concluded that there is a strict relationship between changes in land use/land cover (LULC), materials and morphology of buildings, on one side, and the urban microclimate, on the other, with the former factors strongly influencing the latter.

Given that this process is happening across cities and continents, and thus represents a global challenge, a systematic framework is required to investigate and correlate thermal variations caused by changes in urban morphology, LULC transitions and building construction (Yang et al., 2025). Numerous urban classification schemes were developed to study urban climate and contributed to advancing this research field. However, a unified classification system applicable to global cities was still missing (Huang et al., 2023). In this respect, the Local Climate Zones (LCZs) classification system formalised by Stewart and Oke (2012) was revolutionary and proved to be an effective climate-based generic framework for urban climate research. Based on a categorisation of urban and land cover types according to uniform surface cover characteristics that account for materials, morphology and LULC, LCZs enable differentiation not only between urban and rural areas, but more importantly across neighbourhoods within the same city and are capable of revealing the impact of urban planning and construction over time.

Methods for LCZ mapping fall into three main categories, depending on whether they are based on either remote sensing (RS) or Geographic Information System (GIS) techniques or a combination of the two (Huang et al., 2023). The latter has been increasingly explored in recent years to combine the advantages of RS and GIS, thereby improving LCZ mapping performance. In this respect, Earth Observation (EO) data are increasingly exploited, with optical multispectral and Synthetic Aperture Radar (SAR) data being mostly used. Hyperspectral data are used less frequently but increasingly indicate that higher accuracy can be achieved compared to multispectral data (e.g. Liang et al., 2023; Vavassori et al., 2023, 2024). LCZ classification is currently among the main application fields in urban remote sensing relying on hyperspectral satellite data (Gámez García et al., 2025).

Increasing temperatures imply greater heat stress affecting population thermal comfort and liveability in cities. In addition to increasing Land Surface Temperature (LST) and thus Surface UHI (SUHI), UHI also encompasses the so-called canopy-layer UHI (CUHI), which is instead related to spatial and temporal variations in near-surface air temperature (AT). AT exhibits strong diurnal and seasonal contrasts, which can vary significantly across the urban footprint. As such, AT is a critical variable to evaluate CUHI and infer heat stress. From a measurement point, gridded, high-resolution AT temporal data

are needed (Žgela et al., 2025), although it is not always trivial to access continuous or regularly collected sensor network data. Open and/or crowd-sourced data are therefore an asset that should always be valued when available.

In the above scientific and application-oriented contexts, the international project "Analysis of Local Climate Zones and the Urban Heat Island through Geomatic Techniques" (LCZ-UHI-GEO), undertaken as a collaboration between Politecnico of Milan (POLIMI), Italian Space Agency (ASI) and Vietnam National Space Center (VNSC), and jointly funded by the Italian Ministry of Foreign Affairs and International Cooperation (MAECI) and Vietnam's Ministry of Science and Technology (MST), aims to promote and replicate most advanced LCZ and AT mapping methodologies in major cities of Italy and Vietnam. In particular, the LCZ-UHI-GEO project is pursuing two primary research objectives. Firstly, generating LCZ maps based on hyperspectral satellite imagery from ASI's PRISMA mission and GIS data in Milan and Rome in Italy, Ho Chi Minh City and Hanoi in Vietnam. Secondly, developing high-resolution AT maps in Milan, selected as a case study.

2. LOCAL CLIMATE ZONES MAPPING

In this study, LCZs are classified using a combined RS and GIS-based method proposed by Vavassori et al. (2024). The approach relies on supervised classification of PRISMA (*Precursore IperSpettrale della Missione Applicativa*) hyperspectral imagery using the Random Forest machine learning algorithm. PRISMA, managed by the Italian Space Agency (ASI), provides high spectral resolution with 239 bands and a spatial resolution of 30 m within an image footprint of 30 km × 30 km. In coordination with ASI's PRISMA Mission Management, hyperspectral satellite imagery was tasked for collection over the four cities investigated in the LCZ-UHI-GEO project, beginning in July 2024 and continuing through 2025. Suitable data take opportunities (DTOs) were identified based on the ASI's PRISMA pre-feasibility tool (https://prismaprefeasibility.asi.it/). Orders were placed and authorised with the maximum priority for collection in all the DTOs that were not in conflict with other orders. Figure 1 shows the total number of PRISMA requests that were submitted for each city. After filtering by cloud coverage and effective usability, a total of 15 images were found to be cloud-free and usable for generating LCZ maps: Rome (9), Milan (3), Hanoi (2), and Ho Chi Minh City (1). These numbers highlight the challenge of collecting cloud-free imagery over Vietnam due to the typical weather conditions, as well as in European cities such as Milan, where more frequent adverse weather compared to previous years may occasionally reduce the number of usable satellite images.

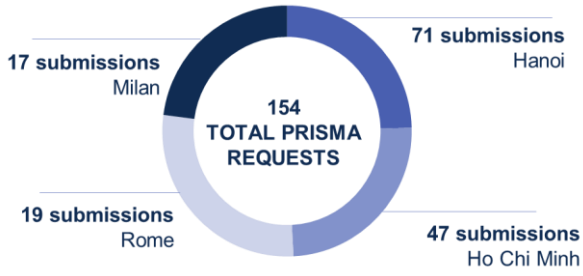

Figure 1. Number of submitted PRISMA data tasking requests between July 2024 and December 2025

Following the successful PRISMA acquisition, the imagery is integrated with relevant urban canopy parameters (UCPs) within the classification framework. The selected UCPs are included due to their ability to represent key urban morphological characteristics of the study areas. In Italy, high-quality local datasets are employed, whereas in Vietnam, the method relies on openly available global datasets, which have been validated and shown to provide reliable accuracy in urban environments. The UCPs considered include Building Height, Building Surface Fraction, Impervious Surface Fraction, Canopy Height, and Sky View Factor. PRISMA imagery is coregistered with close-in-time Sentinel-2 data, and its dimensionality is then reduced using Principal Component Analysis (PCA), a widely used technique in hyperspectral RS. Ten PCs were retained, accounting for 100% of the variance in the original 239 PRISMA bands, reducing dataset size while preserving all spectral information.

The resulting LCZ maps provide spatially explicit information on the local distribution of urban and natural climate zones, which is directly relevant for microclimate and urban climate applications. LCZs offer a standardised framework for describing surface structure and land cover properties that influence local thermal behaviour, enabling consistent assessment of urban climate processes across different geographic contexts. An example of LCZ maps for two cities, Rome and Ho Chi Minh City, is shown in Figure 2.

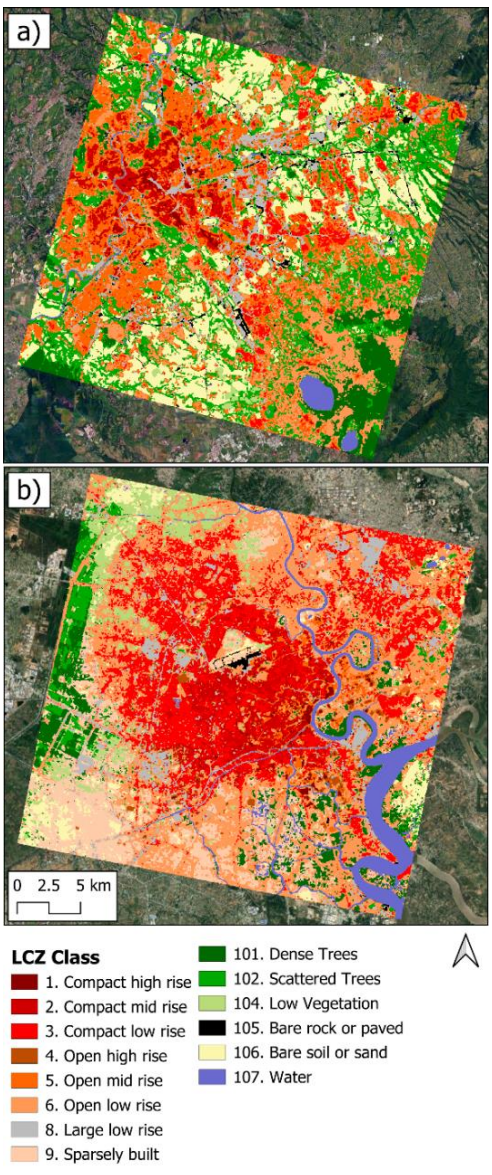

Figure 2. LCZ maps of (a) Rome on 12 August 2024 and (b) Ho Chi Minh City on 19 March 2025

Overall accuracy (OA) varies among cities but remains within comparable ranges for Milan, Hanoi, and Rome, mainly between 85% and 90%. For Ho Chi Minh City, OA is slightly lower at 79%, likely due to the high complexity and heterogeneity of the urban fabric in this megacity, which can increase class confusion and reduce classification performance. These OA values are in line with results reported in the literature for hyperspectral-based LCZ mapping. Vavassori et al. (2024), applying the same method to Milan using PRISMA at 30 m, reported OA above 85%. Similarly, Liang et al. (2023) reached OA as high as 87% for Beijing using Zhuhai-1 hyperspectral imagery at 10 m resolution with a Random Forest classifier, confirming that the accuracy range achieved here is consistent with the state of the art for hyperspectral LCZ mapping.

Per-class accuracy statistics confirm that natural classes (LCZ 101–107) are generally classified more accurately due to their greater land cover homogeneity, whereas urban classes (LCZ 1–10) exhibit higher internal variability and are therefore more challenging to distinguish. Nevertheless, the model successfully delineates the overall urban extent and captures the mixture of urban classes with varying building heights and compactness (Figure 2). This information is particularly relevant from an energy perspective, as these parameters strongly influence heat storage, heat fluxes, and heat trapping, and consequently affect thermal comfort at street level.

3. AIR TEMPERATURE MAPPING

The UHI phenomenon in Milan has gained increasing scientific relevance in recent years as a result of rising temperatures, rapid urbanisation, and the escalation of extreme heat events. Milan's geographic location in the Po Valley, a broad, low-lying basin with limited atmospheric ventilation, plays a central role in intensifying heat accumulation. This characteristic geographical constraint, described in detail by Žgela et al. (2025), reduces wind-driven cooling and contributes to the persistence of elevated temperatures, particularly during stable, anticyclonic conditions. In the case of Milan, UHI is amplified by extensive impervious surfaces, limited green infrastructure and a concentration of anthropogenic heat emissions, especially within the historical centre.

To quantify the spatial and temporal dynamics of UHI under real conditions, a combined dataset of 97 meteorological stations was used, integrating authoritative ARPA Lombardia measurements with crowdsourced observations from the Centro Meteorologico Lombardo (CML) network. The inclusion of crowdsourced data is consistent with emerging research demonstrating that citizen-operated weather stations can significantly enhance the spatial density of urban climate monitoring (Meier et al., 2017). However, their use requires systematic quality control. Following methodologies proposed by Napoly et al. (2018) and Puche et al. (2023), the CML data underwent multi-stage filtering to remove climatological outliers, harmonise sampling intervals, and correct for elevation differences.

This cleaned dataset served as the basis for a Random Forest regression framework capable of predicting AT at a spatial resolution of 20 meters. Random Forest was selected for its capacity to capture nonlinear relationships and complex feature interactions in urban climate modelling. A relevant set of predictors was selected based on their physical relevance and effect on AT, including vegetation, terrain, and spectral indices, some of which were derived from Sentinel-2 imagery.

Performance assessment demonstrated a clear dependence on time of day. The model showed its highest accuracy during late afternoon, evening, and nighttime periods, i.e. phases characterised by more stable atmospheric layering and stronger horizontal temperature gradients. During these periods, the coefficient of determination (R^2) ranged from 0.33 to 0.50 across different HW events. In contrast, morning heating phases exhibited substantially lower accuracy. These findings are consistent with results reported in the literature. Venter et al. (2020) reported an average R^2 of 0.33 for daily minimum AT in Oslo, and Ho et al. (2014) reported a similar value of 0.34 for maximum AT predictions. Overall, these results reflect modest but reasonable performance, consistent with the challenges of high-resolution urban AT modelling reported in the literature.

The resulting AT maps depict a well-defined nocturnal UHI structure. Central districts of Milan repeatedly emerged as the warmest areas, particularly during the Maximum UHI (MUHI) phase (2 h before sunrise), registering temperature anomalies of 3–5 °C relative to the vegetated and agricultural periphery (Figure 3). The persistence of elevated nighttime temperatures also has important public-health implications. As Ballester et al. (2023) observed, tropical nights, when the minimum daily AT remains above 20 °C, significantly contribute to excess mortality during HWs. Milan's modelled fields show that large portions of the city experienced such conditions repeatedly during summer 2022. Green areas displayed measurable cooling effects. Urban parks such as Parco Sempione and Parco Indro Montanelli, despite their limited size relative to the metropolitan area, exhibited temperature reductions of 1–2 °C compared with adjacent densely built-up districts (see zoom on Figure 3). This cooling magnitude confirms the role of vegetation in attenuating urban heat stress even when distributed in small patches.

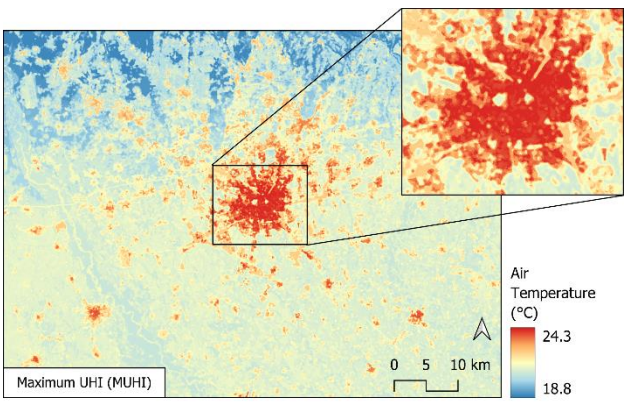

Figure 3. Predicted AT during the MUHI phase in June 2022

4. CONCLUSIONS

The results achieved in the LCZ-UHI-GEO project are proving the effectiveness of advanced geospatial techniques in mapping LCZs and AT across cities located in different geographic locations and characterised by different urban settings and historical development. Some constraints were found in the attempt to replicate the LCZ mapping methodology on the Vietnamese cities, which was developed and tested on the Italian cities, i.e. the technical challenge of successfully collecting cloud-free hyperspectral data in a predominantly tropical-climate country and sourcing urban geospatial data of comparable quality and suitable to derive UCPs. Overall, hyperspectral imagery offers new capabilities for LCZ mapping. In future work, comparisons with multispectral products will be conducted to quantify potential accuracy improvements.

AT prediction in Milan advances scientific understanding of urban thermal behaviour by combining dense meteorological networks, remote-sensing indicators, and machine learning modelling. The high-resolution temperature fields produced for

the 2022 HWs represent an important dataset for evaluating climate-adaptation strategies, informing urban planning, and supporting heat-health systems in the metropolitan area. Prediction accuracy can be improved, particularly during daytime conditions, when increased atmospheric instability in urban areas challenges reliable prediction. The methodological approach developed for Milan can be considered as a replicable model for other Italian and European cities suffering similar climatic pressures.

These results are relevant from an urban climate perspective. In the Italian context, the country has one of the oldest populations globally. With the strengthening of climate change and the UHI effect, urban microclimate information is increasingly important for understanding impacts on vulnerable population groups. In Vietnam, rapid urbanisation has intensified climate challenges, indicating the need for broader urban climate research.

ACKNOWLEDGEMENTS

This study is part of the LCZ-UHI-GEO project, funded by the Italian Ministry of Foreign Affairs and International Cooperation (MAECI) and Vietnam's Ministry of Science and Technology (MST) under the grant numbers: PGR12284 and NĐT/ITA/24/08. The LCZ products presented in the article were generated by the authors under a license from ASI Original PRISMA Product - © Italian Space Agency (ASI) - (2024, 2025).

REFERENCES

Akbari, H., Kolokotsa, D., 2016. Three decades of urban heat islands and mitigation technologies research. *Energy and Buildings*, 133, pp. 834–842. https://doi.org/10.1016/j.enbuild.2016.09.067

Ballester, J., Quijal-Zamorano, M., Méndez Turrubiates, R.F., Pegenaute, F., Herrmann, F.R., Robine, J.M., Basagaña, X., Tonne, C., Antó, J.M. and Achebak, H., 2023. Heat-related mortality in Europe during the summer of 2022. *Nature medicine*, 29(7), 1857-1866. https://doi.org/10.1038/s41591-023-02419-z

Gámez García, J.A., Lazzeri, G., Tapete, D., 2025. Airborne and Spaceborne Hyperspectral Remote Sensing in Urban Areas: Methods, Applications, and Trends. *Remote Sensing*, 17(17), 3126. https://doi.org/10.3390/rs17173126

Ho, H.C., Knudby, A., Sirovyak, P., Xu, Y., Hodul, M. and Henderson, S.B., 2014. Mapping maximum urban air temperature on hot summer days. *Remote sensing of environment*. https://doi.org/10.1016/j.rse.2014.08.012

Huang, F., Jiang, S., Zhan, W., Bechtel, B., Liu, Z., Demuzere, M., Huang, Y., Xu, Y., Ma, L., Xia, W., 2023. Mapping local climate zones for cities: A large review. *Remote Sensing of Environment*, 292, 113573. https://doi.org/10.1016/j.rse.2023.113573

Kim, J., Lee, D.-K., Brown, R.D., Kim, S., Kim, J.-H., Sung, S., 2022. The effect of extremely low sky view factor on land surface temperatures in urban residential areas. *Sustainable Cities and Society*, 80, 103799. https://doi.org/10.1016/j.scs.2022.103799

Liang, Y., Song, W., Cao, S., Du, M., 2023. Local Climate Zone Classification Using Daytime Zhuhai-1 Hyperspectral Imagery and Nighttime Light Data. *Remote Sensing*, 15(13), 3351. https://doi.org/10.3390/rs15133351

Meier, F., Fenner, D., Grassmann, T., Otto, M. and Scherer, D., 2017. Crowdsourcing air temperature from citizen weather stations for urban climate research. *Urban Climate*, 19, 170-191. https://doi.org/10.1016/j.uclim.2017.01.006

Morabito, M., Crisci, A., Guerri, G., Messeri, A., Congedo, L., Munafò, M., 2021. Surface urban heat islands in Italian metropolitan cities: Tree cover and impervious surface influences. *Science of the Total Environment*, 751, 142334. https://doi.org/10.1016/j.scitotenv.2020.142334

Napoly, A., Grassmann, T., Meier, F. and Fenner, D., 2018. Development and application of a statistically-based quality control for crowdsourced air temperature data. *Frontiers in Earth Science*, *6*, 118. https://doi.org/10.3389/feart.2018.00118

Oke, T.R., 1982. The energetic basis of the urban heat island. *Quarterly journal of the royal meteorological society*, *108*(455), 1-24. https://doi/10.1002/qj.49710845502

Oke, T.R., Mills, G., Christen, A., Voogt, J.A., 2017. Urban Climates. Cambridge University Press: Cambridge, UK.

Puche, M., Vavassori, A. and Brovelli, M.A., 2023. Insights into the Effect of Urban Morphology and land cover on Land Surface and Air Temperatures in the Metropolitan City of Milan (Italy) using Satellite Imagery and in situ measurements. *Remote Sensing*, *15*(3), 733. http://dx.doi.org/10.3390/rs15030733

Stewart, I.D., Oke, T.R., 2012. Local climate zones for urban temperature studies. *Bulletin of the American Meteorological Society*, 93(12), pp. 1879–1900. https://doi.org/10.1175/BAMS-D-11-00019.1

Vavassori, A., Giuliani, G., Brovelli, M.A., 2023. Mapping Local Climate Zones in Lausanne (Switzerland) with Sentinel-2 and PRISMA imagery: comparison of classification performance using different band combinations and building height data. *International Journal of Digital Earth*, 16(2), pp. 4790–4810. https://doi.org/10.1080/17538947.2023.2283485

Vavassori, A., Oxoli, D., Venuti, G., Brovelli, M.A., de Cumis, M.S., Sacco, P. and Tapete, D., 2024. A combined Remote Sensing and GIS-based method for Local Climate Zone mapping using PRISMA and Sentinel-2 imagery. *International Journal of Applied Earth Observation and Geoinformation*, *131*, p.103944. https://doi.org/10.1016/j.jag.2024.103944

Venter, Z.S., Chakraborty, T. and Lee, X., 2021. Crowdsourced air temperatures contrast satellite measures of the urban heat island and its mechanisms. *Science Advances*, *7*(22). https://doi.org/10.1126/sciadv.abb9569

Yang, X., Yang, L., Huang, D., Chen, L., Yang, Y., Luo, Y., Liu, Y., Na, J., Ding, H., 2025. Revealing the Impact of Urban Morphology Evolution on the Urban Heat Island Effect in the Main Urban Area of Guangzhou: Insights from Local Climate Zones. *Remote Sensing*, *17(17)*, 2959. https://doi.org/10.3390/rs17172959

Žgela, M., Vavassori, A. and Brovelli, M.A., 2025. Predicting Air Temperature Patterns in Milan Using Crowdsourced Measurements and Earth Observation Data. *Remote Sensing*, *17*(21), 3520. https://doi.org/10.3390/rs17213520

This work is licensed under a Creative Commons Attribution-No Derivatives 4.0 International License.

A PROTOTYPE EARTH OBSERVATION-BASED FRAMEWORK FOR SIMULATING URBAN INTERVENTION EFFECTS ON LAND SURFACE TEMPERATURE

Daniele Oxoli *, Alberto Vavassori, Maria Antonia Brovelli

Department of Civil and Environmental Engineering, Politecnico di Milano, P.zza Leonardo da Vinci 32, 20133, Milan, Italy - (daniele.oxoli, alberto.vavassori, maria.brovelli)@polimi.it

KEY WORDS: Surface Urban Heat Island, Land Surface Temperature, Urban Digital Twin, Random Forest Regression, What-if Simulations

ABSTRACT:

The surface urban heat island phenomenon poses critical challenges for climate-resilient urban planning, due to its well-known negative impact on thermal comfort and increased health risks during heatwave events. This work presents a prototype Earth Observation-based framework for the simulation of Land Surface Temperature (LST) to support scenario-driven assessment of urban transformations. The framework integrates Landsat 8/9 LST observations from 2015 to 2024 with Sentinel-2 reflectance data, used to derive surface material fractions through spectral unmixing, together with a set of Urban Canopy Parameters including sky view factor, building height, tree canopy height and soil imperviousness. These inputs form a comprehensive set of predictor layers that describe urban morphology and surface materials, and which can be modified in typical urban planning or retrofitting interventions. Random Forest regression models are trained to predict seasonal average LST from the predictor variables. The Metropolitan City of Milan is used as a case study. A Python module is designed to allow users to delineate intervention areas and adjust predictor layers to generate what-if scenarios that mimic real urban interventions. The summer model achieves the best performance, with a mean absolute error lower than 2 K, and the accuracy assessment shows good agreement with Landsat observations ($R^2 > 0.74$) and moderate agreement with ECOSTRESS data ($R^2 > 0.63$). An example application illustrates the potential of the framework for the analysis of urban heat mitigation strategies and its future integration into operational urban digital twin systems.

1. INTRODUCTION

The Surface Urban Heat Island (SUHI) phenomenon describes how urban areas often record substantially higher Land Surface Temperature (LST) than their rural surroundings. This temperature increase can affect thermal comfort and exacerbate health risks, particularly during heatwaves, by amplifying heat stress exposure for urban dwellers and city users (Ebi et al., 2021). Unlike the Urban Heat Island (UHI), which refers to the near-surface air temperature difference between urban and rural areas and is strongly influenced by local meteorological factors, SUHI patterns primarily emerge as a direct result of urbanisation, which alters both morphological characteristics and surface material properties, thereby changing heat accumulation in cities (Shao et al., 2023). Although the correlation between LST and surface air temperature (one of the most common thermal comfort indicators) is not always linear, LST remains a reasonable proxy for capturing spatial and seasonal variations in air temperature (Muse et al., 2024). Moreover, LST can be systematically observed through widely available Earth Observation (EO) thermal imagery, such as Landsat, enabling consistent and spatially extensive monitoring of urban thermal patterns at the city scale. By contrast, air temperature data rely on ground sensor networks, which typically have scattered spatial coverage, limiting the ability to monitor UHI dynamics across entire metropolitan areas. With this in mind, this work aims to develop a prototype urban digital twin application for the analysis and simulation of urban thermal dynamics, driven by surface material characteristics and urban morphological features.

The proposed simulation framework integrates thermal EO data and surface material fractions (from the spectral unmixing of multispectral imagery) with Urban Canopy Parameters (UCP), such as sky view factor, building height, soil imperviousness, and tree canopy height, to train a machine-learning model predicting how urban transformations (e.g., new construction, retrofitting, or greening) may affect LST (Li et al., 2020). The selected predictors layers represent a comprehensive set of urban features associated with the SUHI effect, for which LST variation is a direct physical observable (Mokarram et al., 2024). The workflow includes a dedicated module for the preparation of simulation layers, where the user is allowed to delineate planned intervention areas and specify the type of change to be applied. This allows for the generation of "what-if" urban transformation scenarios and the analysis of triggered impacts on LST patterns. The framework is designed for integration into urban digital twin platforms, supporting scenario-based urban planning through EO-driven simulations.

The activities have been carried out within the project Smart Urban Resilience Enhancement (SURE), funded by the European Space Agency (ESA) and led by the e-GEOS company (https://www.e-geos.it). The prototype's requirements were defined through continuous dialogue with key public and private stakeholders, including the Metropolitan City of Milan (Northern Italy), which serves as the case study for the development and testing of the proposed LST simulation model. The accuracy of the predicted LST maps, generated using actual predictor layer values, was evaluated against both ECOSTRESS thermal data (https://ecostress.jpl.nasa.gov) and air temperature sensor observations. Finally, examples of LST simulated maps, produced by altering predictor values to explore hypothetical what-if scenarios, are presented and discussed.

2. MATERIALS AND METHODS

The development of the LST simulation model considered multi-source geospatial datasets spanning 10 years (2015–2024) for the

* Corresponding author

Metropolitan City of Milan. LST from Landsat 8/9 (https://www.usgs.gov/landsat-missions/landsat-collection-2-surface-temperature) was derived from 76 cloud-free daytime acquisitions. Surface material fractions were derived from Sentinel-2 imagery (30 acquisitions within ±3 days of Landsat LST dates) through regression-based spectral unmixing (Okujeni et al., 2016). The resulting fractions represent the proportional abundance of key urban surface materials within each pixel, including: asphalt/concrete, shingle, metal, bare soil/sand, low vegetation/grass, tall vegetation, and water. UCP layers, considered instead as time-invariant in the model development, were derived from the Milan digital surface model and building geodatabase, as well as from global tree canopy height and soil imperviousness maps (Vavassori et al., 2024). UCP layer values were normalised to [0–1] range to match the scale of surface material fractions for model training.

The LST simulation model is based on a Random Forest regression (see Figure 1). Training data combine time-invariant layers with time-variant LST and surface material fraction observations, aggregated over three seasonal periods: summer (June-September), winter (December-March), and intermediate. Sampling was restricted to stable areas identified using multitemporal soil consumption maps (https://www.isprambiente.gov.it/en/databases/data-base-collection/soil-and-territory/use-of-soil) to exclude zones affected by relevant changes between the years 2015 and 2024.

A stratified sampling scheme, based on seasonal Local Climate Zone (LCZ) maps (Stewart & Oke, 2012; Xi et al., 2024), derived from Sentinel-2 imagery following a procedure previously published by the authors (Vavassori et al., 2024), was applied to ensure balanced coverage and representation of different urban textures in the model training phase.

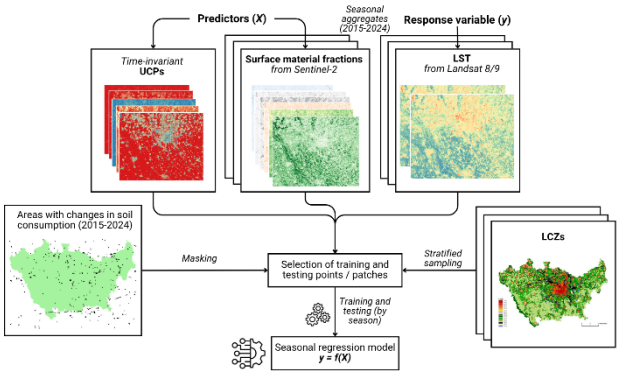

Figure 1. Schematic of the LST model implementation workflow

The trained seasonal LST models are used to simulate LST responses by varying input predictor layers to represent planned or hypothetical urban transformations. The workflow includes a simulation module (Python notebook) that modifies input raster layers using user-defined vector masks to outline transformation areas and specify changes to predictor layers. Two main approaches are supported: value replacement masking and percentage adjustment masking, allowing for exploratory what-if scenarios testing. Additional details on this module are reported in Section 4.

The draft Python source code used to implement the entire simulation framework is openly available on GitHub (https://github.com/gisgeolab/SURE).

3. RESULTS AND MODEL ASSESSMENT

The LST simulation model was optimised and validated through a series of tuning and accuracy assessments combining cross-validation, grid search, and independent comparisons. Model accuracy was evaluated using approximately 1,000 randomly sampled points located outside the training areas. Considered accuracy metrics included the Pearson's correlation coefficient (r), the coefficient of determination (R^2), the Mean Absolute Error (MAE), the Root Mean Square Error (RMSE) and the Mean Bias Error (MBE). The final seasonal models achieved satisfactory accuracy, with the summer model performing best against LST Landsat observations used for testing (r = 0.86, R^2 = 0.74, MAE = 1.67 K, RMSE = 2.18 K, MBE ~ 0). Validation against ECOSTRESS observations revealed instead a moderate agreement (r = 0.80, R^2 = 0.64), with higher errors (MAE = 3.03 K; RMSE = 3.59 K) and a negative bias (MBE = −2.89 K), suggesting that ECOSTRESS LST values are systematically lower than the simulated ones (see Figure 2).

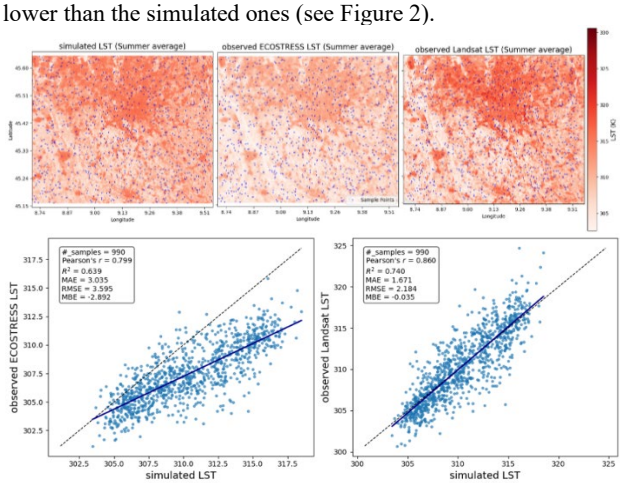

Figure 2. Summary of agreement statistics between simulated and observed LST values. Upper panels: Spatial distributions of average summer LST [K] for simulated data, ECOSTRESS and Landsat observations with random sampling locations shown as blue dots. Lower panels: Scatterplots comparing the sampled simulated LST with ECOSTRESS and Landsat observations, including regression lines (dark blue), 1:1 reference lines (black dashed) and agreement metrics

The comparatively lower agreement observed with ECOSTRESS observations may be associated with differences in temporal representativeness, given the shorter period available to derive ECOSTRESS-based reference LST (2019–2024), as well as with systematically different acquisition times relative to Landsat observations. In particular, Landsat acquires around 10:00 AM GMT over the Milan area, whereas ECOSTRESS observations are collected at variable times of day due to its non-sun-synchronous orbit. To mitigate the impact of these temporal discrepancies, only ECOSTRESS acquisitions falling within a central daytime window (09:00–12:00 GMT) were considered in the analysis.

Finally, regression analyses against ground-based air temperature (averaging period: 2015-2024), retrieved from the local regional environmental protection agency (ARPA) network, confirmed physically plausible relationships, with higher LST values corresponding to higher air temperatures in compact and mid-rise building areas, and cooler conditions in vegetated or open areas (see Figure 3). While a positive relationship is observed, LST values tend to be consistently higher than air temperature, especially in compact built LCZ classes. This behaviour reflects

the different physical nature of the two variables: LST responds directly to radiative forcing and surface material properties, while air temperature also responds to local atmospheric processes. Consistent with previous studies, these differences are amplified during warm conditions and in built environments, where the LST–air temperature discrepancy is typically larger and associated with a higher spatial variability (Naserikia et al., 2024). This comparison should nevertheless be interpreted with caution, given the limited number of available ground stations in the study area. Despite these residual ambiguities, the LST model effectively captures overall urban thermal variability and shows promising potential for scenario-based simulations.

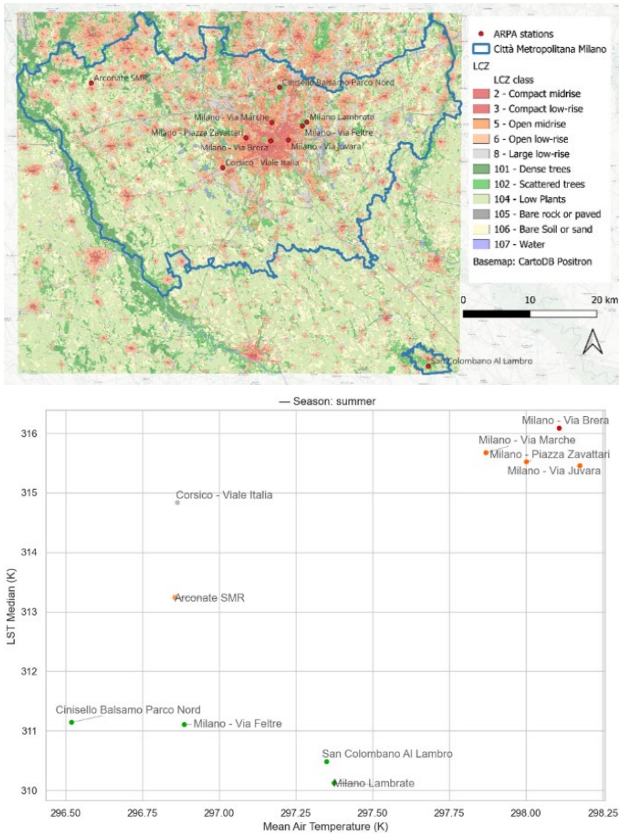

Figure 3. Comparison between simulated LST and ground-based air temperature observations for the Metropolitan City of Milan. Upper panel: Spatial distribution of air temperature monitoring stations over the LCZ map of Milan. Lower panel: Scatter plot of observed mean air temperature at ARPA station locations versus median simulated LST computed within a 200 m buffer from each station; point colours indicate the dominant LCZ class within the buffer

4. DEMONSTRATIVE FRAMEWORK APPLICATION

As a demonstrative application of the proposed framework, a what-if simulation was prepared considering an urban park in Milan to assess the potential cooling effect induced by a hypothetical urban forestation intervention. The experiment simulates an increase in tall vegetation fraction and tree canopy height, combined with a proportional reduction of grass and bare soil fractions (see Figure 4).

The simulation was implemented using the input layer simulator module, which enables controlled modification of input predictor layers through raster algebra operations driven by polygonal vector masks. Within the selected area of intervention, predictor values can be altered either by percentage-based adjustments or by direct value replacement, allowing the emulation of planned or hypothetical changes in urban texture.

The resulting simulated predictor layers were subsequently used as input to the trained LST model to generate a scenario-based LST map, which was compared against the baseline condition. The results show a reduction in LST within the intervention area, consistent with the expected cooling effect of increased tree canopy cover and, in turn, suggest the capability of the model to provide physically consistent outcomes.

The source code and test data used in this example are available in a dedicated branch of the GitHub project repository (https://github.com/gisgeolab/SURE/tree/layers_simulator). The modular structure and rule-based layer manipulation make the approach particularly suitable for integration within urban digital twin environments, where alternative planning scenarios can be rapidly tested and evaluated under consistent modelling assumptions.

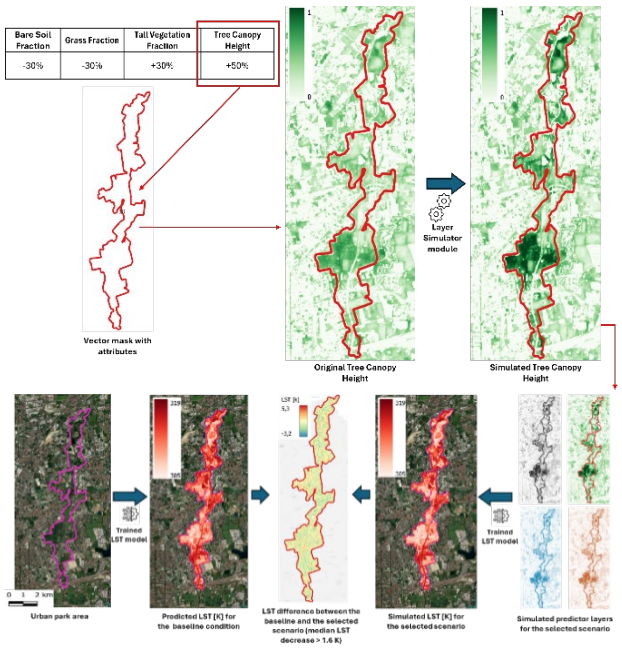

Figure 4. Schematic of what-if simulation workflow for an urban park in Milan. Upper panels: Modification of input predictor layers using the layer simulator module to increase tall vegetation fraction and tree canopy height while reducing grass and bare soil fractions. Lower panels: Baseline and scenario-based LST maps generated using the trained LST model, together with the corresponding LST difference, illustrating the cooling effect of the hypothetical urban forestation intervention

5. CONCLUSIONS AND OUTLOOK

The proposed framework demonstrates how EO-based modelling can support urban heat risk analysis through LST simulation, by empowering urban planners to assess the impact of greening, material, and morphological interventions on LST without requiring advanced technical expertise. As most of the considered input predictors and LST satellite observations are widely available globally, the approach is readily transferable across different urban contexts worldwide.

Despite these advantages, several limitations currently constrain full operational deployment. In particular, the simplified representation of urban thermal processes, driven mainly by surface properties and urban morphology, lacks an explicit treatment of meteorological forcing. This choice reflects the necessary trade-off between model complexity and usability that is required to support urban digital twin applications by non-expert users, but it also limits very accurate simulations of fine-scale and short-term thermal dynamics. In addition, the reliance on medium-resolution, multi-source Earth Observation datasets with heterogeneous spatial and temporal characteristics may introduce spatial aggregation artefacts and limit robust validation and uncertainty quantification. Implementation and validation on additional real-world scenario testing are foreseen in subsequent phases of this work.

Future developments will consider the integration of higher-resolution thermal observations from upcoming missions such as the Copernicus Land Surface Temperature Monitoring (LSTM), alongside high-resolution multispectral and hyperspectral optical data from missions such as PRISMA and the Italian IRIDE constellation. The combined availability of spatially and temporally resolved thermal and optical data is expected to support the extension of the framework toward finer-scale urban applications. The availability of such data is key to modelling intra-urban thermal variability and short-term heat dynamics in heterogeneous urban environments. From a modelling perspective, while the framework builds on established EO workflows, further advances are needed to improve simulation capabilities and to strengthen the linkage between LST modelling and urban heat-risk assessments. In this context, recent advances in artificial intelligence modelling provide opportunities to extend the relatively simple regression-based approach adopted in this prototype toward more advanced predictive models. However, their application to urban heat modelling will require careful validation and interpretability to ensure suitability for decision-support applications.

Ultimately, the framework can serve as a prototype component for future urban digital twins, where its modular, EO-driven architecture could be embedded within broader digital ecosystems to enable near-real-time urban heat monitoring, data assimilation, and dynamic scenario testing. Beyond data and modelling developments, future work will also address the design and integration of user-friendly dashboards and interfaces that will allow a broader range of users, including planners and decision-makers, to effectively access, interpret, and interact with simulation outputs.

ACKNOWLEDGEMENTS

This work was supported by the Smart Urban Resilience Enhancement (SURE) project 2024-2025, funded by the European Space Agency (Programme: *ESA-DTE-B-02 Early DTCS Development Actions*, Contract No. *400014627212411-KE*, Principal Investigator: e-GEOS, https://www.e-geos.it).

REFERENCES

Ebi, K.L., Capon, A., Berry, P., Broderick, C., de Dear, R., Havenith, G., Honda, Y., Kovats, R.S., Ma, W., Malik, A., et al., 2021. Hot weather and heat extremes: health risks. *The Lancet*, 398(10301), pp. 698–708.

Li, Y., Schubert, S., Kropp, J.P., Rybski, D., 2020. On the influence of density and morphology on the Urban Heat Island intensity. *Nature Communications*, 11(1), 2647.

Mokarram, M., Taripanah, F., Pham, T., 2024. SUHI intensity in relation to land use changes in urban areas using neural networks and remote sensing. *International Journal of Environmental Science and Technology*, 21(13), pp. 8417–8430.

Muse, N., Clement, A., Mach, K.J., 2024. Daytime land surface temperature and its limits as a proxy for surface air temperature in a subtropical, seasonally wet region. *PLOS Climate*, 3(10), e0000278.

Naserikia, M., Hart, M.A., Nazarian, N., Bechtel, B., Lipson, M., Nice, K.A., 2024. Land surface and air temperature dynamics: The role of urban form and seasonality. *Science of The Total Environment*, *905*, 167306.

Okujeni, A., van der Linden, S., Suess, S., Hostert, P., 2016. Ensemble learning from synthetically mixed training data for quantifying urban land cover with support vector regression. *IEEE Journal of Selected Topics in Applied Earth Observation and Remote Sensing*, 10(4), pp. 1640–1650.

Shao, L., Liao, W., Li, P., Luo, M., Xiong, X., Liu, X., 2023. Drivers of global surface urban heat islands: Surface property, climate background, and 2D/3D urban morphologies. *Building and Environment*, 242, 110581.

Stewart, I.D., Oke, T.R., 2012. Local climate zones for urban temperature studies. *Bulletin of the American Meteorological Society*, 93(12), 1879–1900.

Vavassori, A., Oxoli, D., Venuti, G., Brovelli, M.A., de Cumis, M.S., Sacco, P., Tapete, D., 2024. A combined remote sensing and GIS-based method for Local Climate Zone mapping using PRISMA and Sentinel-2 imagery. *International Journal of Applied Earth Observation and Geoinformation*, 131, 103944.

Xi, Y., Wang, S., Zou, Y., Zhou, X., Zhang, Y., 2024. Seasonal surface urban heat island analysis based on local climate zones. *Ecological Indicators*, 159, 111669.

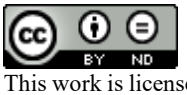

This work is licensed under a Creative Commons Attribution-No Derivatives 4.0 International License.

SIMPLIFIED ESTIMATION OF LAND SURFACE TEMPERATURE USING SURFACE ENERGY BALANCE MODEL

N. Naila [1,2]*, G. Tognon [1,2], J. Vivian [2], M. De Carli [2]

[1] Centre of Studies and Activities for Space "G. Colombo" (CISAS), University of Padua, Italy - naila@phd.unipd.it, giacomo.tognon@unipd.it
[2] Department of Industrial Engineering (DII), University of Padua, Italy
(jacopo.vivian, michele.decarli)@unipd.it

KEY WORDS: Surface temperature, Surface energy balance, Physics-inspired modelling, Remote sensing, Urban climate modelling

ABSTRACT

Due to the presence of diverse land cover types, surface materials, and morphology, urban areas experience significant spatial variations in land surface temperature. This research aims to understand the thermal heterogeneity of urban areas using a simplified energy balance approach. The methodology involves using high-resolution satellite imagery (Landsat 8/9) to estimate solar absorptance and emissivity of urban surfaces from albedo and vegetation index, while the incident solar radiation and ambient air temperature are retrieved from local meteorological stations. The proposed simplified dynamic surface energy balance model uses these parameters to calculate the land surface temperature for the key urban surface types. The proposed method was tested in a 10×10 km area, including the centre and the surrounding areas of the municipality of Legnaro (Italy). The model accuracy was verified against satellite-observed land surface temperature data for sixteen clear days spanning across 2024. Results show that the proposed physics-inspired approach can capture the main patterns in the temporal and spatial distribution of land surface temperatures, with vegetated areas exhibiting lower surface temperatures compared to industrial and highly cemented neighbourhoods. However, the model shows 1.3°C spatial mean deviations from the observations. These discrepancies are likely due to some missing heat fluxes and coarse surface classification, making the model unable to accurately represent the detailed dynamic thermal behaviour of urban environments. Despite the limitations, this research highlights the potential of using remote sensing integrated with simplified physical modelling to explore the impact of various surface types on urban microclimates.

1. INTRODUCTION

Cities are complex and heterogeneous systems in which natural and built elements interact across multiple spatial and temporal scales. Variations in land cover, surface materials, vegetation density, and urban morphology produce pronounced spatial contrasts in land surface temperature (LST). This thermal heterogeneity is a key driver of urban and suburban microclimates, with direct implications on buildings' energy demand, outdoor thermal comfort, and the representativeness of climate boundary conditions used in building- and district-scale energy simulations (Salvati and Kolokotroni, 2023). Capturing urban surface hot or cool spots is therefore central to evaluate urban climate impacts and design proper mitigation strategies.

Satellite thermal infrared observations have become a widely used source of spatially distributed LST information, offering consistent coverage over large areas. However, satellite-driven LST remains challenging to use as a standalone input for urban-scale simulation studies. First, thermal products face a spatial–temporal resolution trade-off: higher spatial resolution observations are infrequent (e.g., Landsat), whereas more frequent missions typically provide LST at kilometre-scale resolution that is too coarse for neighbourhood-scale applications. Second, cloud cover limits data availability and can introduce irregular temporal sampling. Third, satellite LST snapshots provide limited insights into the physical drivers of the observed patterns, and they do not directly support continuous, hourly assessments required for many applications in building performance, urban microclimate modelling, and heat-risk evaluation (Nogueira et al., 2022; Mei et al., 2025).

To address these limitations, a broad literature has proposed techniques to increase the apparent spatial detail of thermal imagery or to infer fine-scale LST fields from auxiliary information. LST downscaling methods are commonly grouped into thermal sharpening and temperature unmixing approaches (Zhan et al., 2013). The former increases the spatial resolution of coarse thermal imagery using environmental variables statistically correlated with LST at local scales, while the latter seeks to estimate the temperatures of sub-pixel surface components (e.g., vegetation, soil, built-up areas) using additional spatial, temporal, angular, or spectral information. Beyond this high-level split, downscaling approaches have been implemented through multiple modelling strategies, including regression and machine-learning models, physical and classification-based methods, geostatistical techniques, and multi-resolution fusion schemes. Despite their effectiveness in producing visually detailed LST maps, these methods often lack physical interpretability and fail to generate continuous diurnal temperature patterns needed for urban-scale simulations.

At the other end of the spectrum, physics-based urban canopy and land surface models explicitly represent surface energy exchanges, including heat transfer phenomena, heat storage, and moisture balance. They can reproduce diurnal dynamics, yet they typically require detailed and often uncertain information about geometry, material properties, and anthropogenic heat and water fluxes, and may be computationally intensive when applied at high spatial resolution across urban areas. As a result, there is a practical need for approaches that are simultaneously computationally efficient and physically interpretable, while capturing the dominant processes governing urban surface temperatures (Hu et al., 2023).

In this context, the aim of this study is to develop and evaluate a simplified, surface energy balance (SEB) inspired model capable of generating spatially continuous surface temperature patterns at neighbourhood scale using a minimal set of inputs derived from remote sensing and local meteorological data. The proposed framework represents the dominant surface heat fluxes while

* Corresponding author

avoiding the heavy parameter requirements of more complex urban canopy models. The model is applied to Legnaro, a town in the northeast of Italy. The estimated surface temperature patterns are compared against clear-sky LST observations from Landsat 8 and 9, for sixteen days spanning winter to summer in 2024. By combining satellite-derived surface properties with simplified physics, the framework aims to provide spatially continuous thermal boundary conditions that can support urban-scale building energy simulations, microclimate assessment, and urban heat island mitigation studies under restrained computational resources.

1.1 Study Area and Data

The proposed physics-inspired approach is applied to Legnaro, a suburban town in the Padua metropolitan area (Italy), and its surrounding agricultural landscape, covering approximately 10×10 km. The landcover of the study area mostly includes urban core (comprising roads and buildings, etc.) and rural mosaics (i.e. trees, farmlands, brown crop fields, bare-soil areas), as illustrated by the ESA Worldcover map of Legnaro in Fig. 1 (Zanaga et al., 2021). The Worldcover layer provides eleven surface classes in total, out of which Legnaro comprises six: i) tree cover, ii) shrubland, iii) grassland, iv) cropland, v) built-up, and vi) bare/sparse vegetation.

Regarding data, surface radiative properties, including solar absorptance (α) and emissivity (ε), are derived from high-resolution Landsat 8/9 Collection 2 Level 2 imagery to enable differentiation among key surface classes, such as vegetated/agricultural areas and built or industrial surfaces.

On the other hand, time-varying weather conditions, including global solar irradiance (I) and ambient air temperature (T_{air}), are retrieved from the local meteorological station of Legnaro on an hourly basis (ARPAV, 2026).

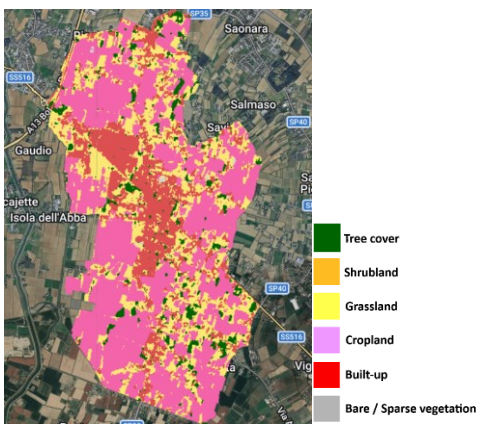

Fig. 1: ESA WorldCover 2021 map of the study area (Legnaro)

2. METHODOLOGY AND MATHEMATICAL MODELLING

The workflow of the proposed SEB-based approach for pixelwise modelling of urban surface temperature (T_s) is described step by step as follows:

1. Landsat 8/9 Collection 2 Level-2 imagery was retrieved and processed over the area of interest (AOI) for 1 January 2024-31 December 2024 using the Google Earth Engine (GEE) platform. Scenes were cloud- and shadow-masked using QA_PIXEL bit flags. Images were then quality-filtered by retaining only acquisitions with ≥ 0.90 clear-sky (unmasked) pixel coverage. This screening resulted in the shortlisting of 16 clear-sky images spanning throughout 2024, with 90% valid clear-sky pixels within the study area. The selected clear-sky dates have been shown in Table 1.

2. The thermal band ST_B10 and surface reflectance bands (SR_B*) of the image collection were scaled according to the official scale/offset (USGS, 2026). This scaling was done to compute LST for model validation (T_s) and to estimate parameters, such as solar absorptance (α) and emissivity (ε), for input into the SEB model.

3. The surface emissivity, over all surface classes, was estimated using an NDVI-based fractional vegetation method, with the resulting values clamped to a physically plausible range (0.96–0.99). While this approach is more appropriate for natural and mixed soil–vegetation surfaces, for built-up areas it should be interpreted as an effective bulk emissivity approximation rather than material-specific property. Consequently, it may smooth emissivity contrasts among roofs, pavements, and other impervious materials, which in turn may introduce local biases in longwave flux estimation and surface temperature.

Solar absorptance was computed from broadband shortwave albedo as α = 1 – albedo, using the following formulation, often attributed to normalized Landsat albedo calculation methods (Liang 2001).

$$\alpha = \frac{0.356B + 0.130R + 0.373NIR + 0.085SWIR1 + 0.072SWIR2 - 0.018}{1.016} \quad (1)$$

Afterwards, a multiband image was built by stacking these thermal (LST) and optical (α, ε) parameters with various land cover types (classes) driven from ESA WorldCover (v200). This class band was included as the key for assigning per-class thermal properties, i.e., conductivity, density, specific heat, and selecting the model configuration for each pixel. The image was sampled over the AOI at 30m to produce a per-pixel table to use for reference in SEB modelling.

4. Hourly meteorological measurements of air temperature and global shortwave solar radiation were obtained from the local weather station of Legnaro for all 16 clear-sky dates at satellite overpass hour (e.g., 2024-08-01 at 10:00). The sky temperature used to evaluate longwave radiative heat transfer is derived from the air temperature through the following relation:

$$T_{sky} = 0.0552T_{air}^{1.5} \quad (2)$$

A deep ground temperature boundary $T_{g,k}$ was computed using the Kusuda–Achenbach model driven by the annual air-temperature cycle and thermal diffusivity. Monthly mean air temperature was used to estimate annual mean temperature and seasonal amplitude, and the resulting damped sinusoidal $T_{g,k}$ was evaluated at a fixed lower boundary depth of 2 meter. The thermal diffusivity of soil (subsurface) was assumed constant ($\approx 3 \times 10^{-7} \mathrm{m^2 s^{-1}}$) across all landcover classes, while only the top surface properties vary between classes. The soil diffusivity was computed as $\frac{\lambda}{\rho c_p}$ by using conductivity (λ), density (ρ), and specific heat (c_p) of soil equal to 0.6 $\mathrm{W\,m^{-1}K^{-1}}$, 1200 $\mathrm{Kg\,m^{-3}}$, and 1670 $\mathrm{J\,kg^{-1}K^{-1}}$ respectively.

5. Next, using Landsat-driven parameters (α, ε) and meteorological forcing, the proposed 2-node dynamic SEB model is applied to perform per-pixel LST calculation for all different landcover classes within AOI (Fig. 1) in accordance with the corresponding surface properties of each class.

Class-wise allocation of the stated physical properties was performed only to the surface layer (top node) of the SEB model; on the other hand, fixed values were used for the deep ground layer (second node).

6. The estimated surface temperature (T_s) was converted to a projected GeoDataFrame and then rasterised onto a 30m grid to ensure spatial alignment with the Landsat grid. Subsequently, model accuracy was verified by comparing residuals between the calculated surface temperatures and satellite LST, as reported in the results section.

2.1 SEB Model

A simple dynamic 2-node surface energy balance (SEB) model was developed to track the spatial and temporal patterns of the surface temperature over the area of interest (AOI). The surface node represents the upper layer for which the surface temperature is estimated. A lower ground node is included to simulate heat conduction and heat storage within the soil layer beneath the surface. The structure of the 2-node model is shown in Fig. 2; the energy balances of the surface and ground node are presented in Eqs. 3 and 4, respectively.

$$\rho_s c_s z_s \frac{\mathrm{d}T_s}{\mathrm{d}\tau} = \alpha I - \varepsilon\sigma\left(T_s^4 - T_{sky}^4\right) - h_c(T_s - T_{air}) - \frac{T_s - T_g}{\frac{\lambda_s}{z_s} + \frac{\lambda_g}{z_{g,up}}} \quad (3)$$

$$\rho_g c_g \left(z_{g,up} + z_{g,low}\right) \frac{\mathrm{d}T_g}{\mathrm{d}\tau} = \frac{T_s - T_g}{\frac{\lambda_s}{z_s} + \frac{\lambda_g}{z_{g,up}}} - \frac{T_g - T_{g,k}}{\frac{\lambda_g}{z_{g,low}}} \quad (4)$$

The first energy balance (Eq. 3) states that the heat stored in the surface layer equates to the incoming energy (i.e., absorbed solar radiation) minus the outgoing heat fluxes (i.e., convection exchange with near-surface air, net longwave radiative exchange with the sky, heat conduction through the soil).

In the equation, T_s is the land surface temperature [K]; T_{sky}, T_{air} and T_g are sky, air and ground-node temperatures [K]; I is the total solar irradiance on the horizontal plane [W/m^2]; ρ_s, c_s, λ_s are density [kg/m^3], specific heat [J/(kg K)] and thermal conductivity [W/(m K)] of the surface layer material; λ_g is the thermal conductivity [W/(m K)] of the soil; σ is the Stefan-Boltzmann constant (5.67*10^{-8} W/(m^2 K^4)); α and ε are the surface absorptance and emissivity; z_s and $z_{g,up}$ are the surface layer thickness and the depth of the upper part of the soil layer, respectively, set to $z_s = 0.10$ m and $z_{g,\mathrm{up}} = 1.0$ m; h_c is the convective heat transfer coefficient, fixed at 15 W/(m^2 K), following the standard definition of a convective surface coefficient (ASHRAE, 2017). The coefficient was prescribed rather than dynamically estimated to avoid additional aerodynamic parameterization based on wind speed and atmospheric stability, and thereby to preserve the simplified formulation of the model.

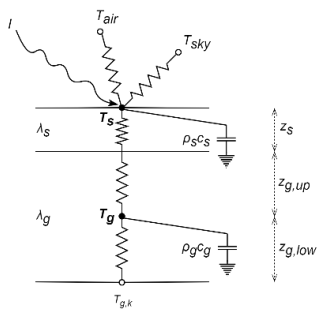

Fig. 2: (a) Structure of the 2-node dynamic SEB model

Similarly, in the soil energy balance (Eq. 4), the heat storage is the net difference between the conductive heat exchanges with the surface node and the deeper ground layers. In the equation, ρ_g and c_g are the soil density [kg/m^3] and specific heat [J/(kg K)], $z_{g,low}$ represents the depth of the lower part of the soil layer, set equal to 1.0 m, and $T_{g,k}$ is the deeper ground temperature set as a boundary condition through the Kusuda model (Kusuda & Achenbach 1965).

The presented 2-node SEB model only considers the sensible heat fluxes, neglecting the latent heat flux. It is presented in a general form, and it can be adapted to predict the temperature of different types of surfaces (vegetated areas, bare soil, fields with brown crops, paved roads, concrete-based built areas, etc.). The system of equations allows to calculate the dynamic evolution of LST over a period of time once weather conditions, the ground's Kusuda boundary temperature, surface and soil properties are set.

3. RESULTS AND DISCUSSION

Fig. 3(a) shows the modelled surface temperature map for 9 August 2024 at 10:00 EST (an hour closer to overpass time 9:57 a.m.). The temperature ranges from 33.6°C to 38.6°C, with a mean value of 36.2°C across the area of study. Build-up areas exhibited relatively higher surface temperature, consistent with effective thermal inertia, while the vegetated classes (tree, shrub, and croplands) exhibited cooler conditions, reflecting their lower net heating due to low absorptance and higher emissive properties of the built surfaces. Overall, the spatial temperature patterns predicted by the SEB model are consistent with the Landsat LST image captured on the same summer morning, as highlighted in Fig. 3(b).

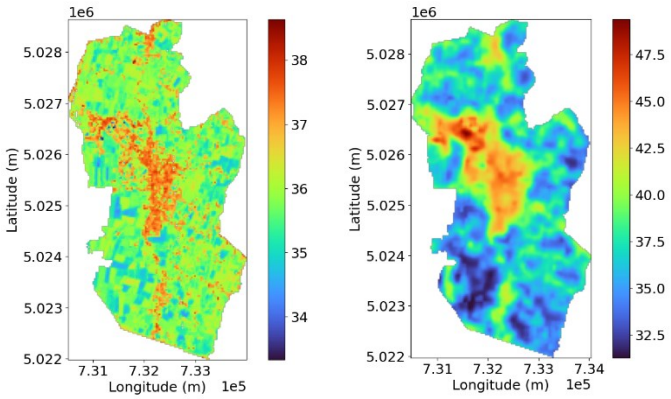

Fig. 3: (a) Surface temperature (T_s) map predicted by the SEB model (b) Landsat-8/9 driven LST

Satellite LST spans from 31.3°C to 49.1°C, with a mean value of 37.5°C. The residual map in Fig. 4 highlights in shades of red the areas where the model underestimates the surface temperature (T_s < LST); in contrast, the blue coloured patches represent the areas where model overestimates the surface temperature (T_s > LST). From the histogram plot of the residuals shown in Fig. 5, it is clear that most of the pixel-wise residuals in the area lie between –2.5°C and 2.5°C, with a mean value of 1.3°C on the selected day (9 August 2024). However, the minimum and maximum deviations across the entire AOI are –4.8°C and 12.9°C, respectively, suggesting that the model is not yet capable of completely describing the physical phenomena affecting the land surface temperature and further refinements are needed.

Dark red areas in Fig 4, where the model is producing the highest residuals, are industrial zones and residential building roofs, while the blue patches are the vegetated areas. Therefore, the model underestimates the surface temperature on the built-up areas, while a general overestimation is observed in the vegetated areas, likely due to some missing fluxes like latent cooling for vegetation-covered zones. This assumption of neglecting latent

heat flux in current formulation is more appropriate for dry impervious urban surfaces, where evapotranspiration is limited and sensible heat flux dominates. However, for vegetated areas, this simplification may have led to an overestimation of surface temperature due to the absence of evaporative cooling, hence representing an important direction for future model improvements. Moreover, a refined surface classification of urban built areas into, i.e. roads, roofs based on material types and surface colours, and similarly the vegetated areas to low, moderate, and dense vegetation classes can further refine the model results.

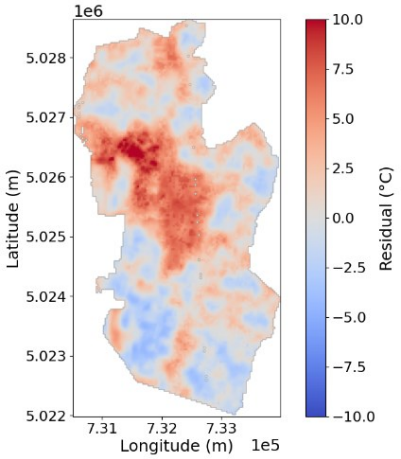

Fig. 4: Residual map on 9 August 2024

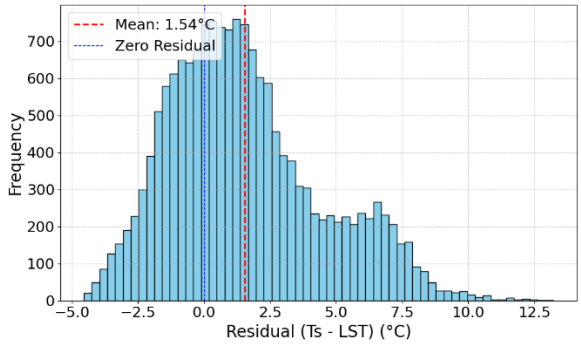

Fig. 5: Frequency histogram of residuals on 9 August 2024

However, despite the above-mentioned weaknesses, the model successfully reproduces the main spatial temperature contrasts, meaning that the cooler vegetated belts versus the warmer built areas are in line with the satellite LST mosaics. Mean spatial residuals are centred around 1°C, showing that the baseline Physics is directionally correct. This is further ensured by the plot in Fig. 6 and Table 1, which report the temporal comparison between surface temperature from the model and LST averaged across the study area for 16 selected clear-sky days. It is clear that T_s is capturing the seasonal progression and magnitude of Landsat LST reasonably well, especially during peak summer days (June–August). Most differences are within ~1–3 °C across the year.

Lastly, Fig.7 shows a pronounced diurnal cycle of mean T_s, peaking in the early afternoon and remaining consistently higher than mean air temperature throughout the day of 9 August 2024, highlighting the stronger surface heating during daytime hours. Also, mean LST (red marker) aligns closely with the modelled T_s (orange curve) at the satellite overpass time, indicating good agreement between the model and observations.

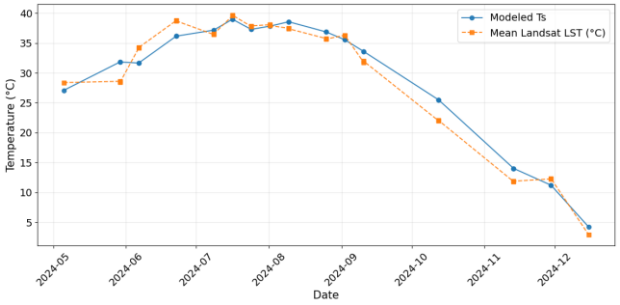

Fig. 6: Seasonal variability and comparison of spatially averaged modelled surface temperature (Ts) and LST across AOI on clear-sky days of 2024

Lastly, Fig.7 shows a pronounced diurnal cycle of mean T_s, peaking in the early afternoon and remaining consistently higher than mean air temperature throughout the day of 9 August 2024, highlighting the stronger surface heating during daytime hours. Also, mean LST (red marker) aligns closely with the modelled T_s (orange curve) at the satellite overpass time, indicating good agreement between the model and observations.

Table. 1: Modelled Ts and LST measurements

Selected (clear sky) dates (2024)	Mean Ts	Mean LST
5 May	27.1	28.4
29 May	31.8	28.6
6 June	31.6	34.2
22 June	36.2	38.8
8 July	37.2	36.4
16 July	38.9	39.6
24 July	37.3	37.8
1 August	37.8	37.9
9 August	38.5	37.3
25 August	36.8	35.7
2 September	35.5	36.2
10 September	33.6	31.9
12 October	23.7	22.1
13 November	12.7	11.8
29 November	10.2	12.3
15 December	3.9	2.9

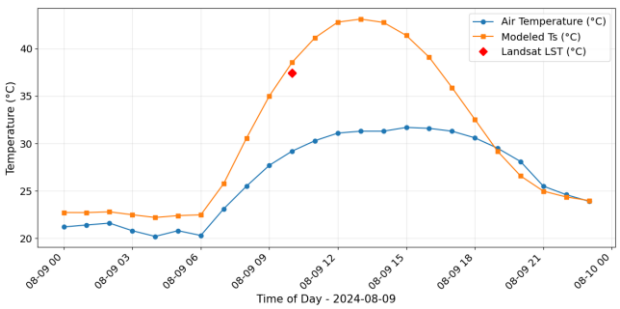

Fig. 7: Hourly mean surface temperature and air temperature across AOI on 9 August 2024

4. CONCLUSIONS

This study presents land surface temperature mapping using a physics-inspired approach known as surface energy balance, aided by surface absorptance and emissivity derived from Landsat-8/9 under clear-sky conditions. By integrating these remotely sensed parameters with the meteorological

measurements of air temperature and solar irradiance, the model is generating spatially continuous surface temperature estimates in the study area (Legnaro) at a 30-meter scale. Results show that, in comparison to LST, the model tends to underestimate surface temperature in built-up areas while overestimating it in green spaces. Despite these deviations, it successfully reproduces the main spatial patterns, which are consistent with the Landsat LST. With future refinements, such as detailed surface classification and integrating enhanced physical processes (i.e. latent heat, anthropogenic heat, etc.), the model accuracy could be significantly improved, thereby providing a scalable foundation for better urban climate monitoring and mitigation.
The work lays the ground to future studies where more sophisticated machine learning techniques can be integrated in the proposed physics-inspired model to fully capture the thermal behaviour of urban environments.

ACKNOWLEDGEMENTS

This study was carried out within Space It Up! project funded by the Italian Space Agency, ASI, and the Ministry of University and Research, MUR, under contract n. 2024-5-E.0 - CUP n. I53D24000060005 UNIPD C53C24000150006.

REFERENCES

ARPAV, 2026. *Legnaro meteorological station: hourly weather observations*. Agenzia Regionale per la Prevenzione e Protezione Ambientale del Veneto. https://meteo.arpa.veneto.it/meteo/dati_meteo/GrafStaz.html?sens=TEMP&staz=111

Evren, M.F., Ozsunar, A., Biyikoglu, A., and Kilkis, B., 2017. Determination of heat transfer coefficient between heated floor and space using the principles of ANSI/ASHRAE standard 138 test chamber. *ASHRAE Transactions*, 123(1), 71–82.

Hu, Y., Tang, R., Jiang, X., Li, Z.-L., Jiang, Y., Liu, M., Gao, C., Zhou, X., 2023. A physical method for downscaling land surface temperatures using surface energy balance theory. *Remote Sensing of Environment* 286, 113421. https://doi.org/10.1016/j.rse.2022.113421

Kusuda, T., Achenbach, P.R., 1965. Earth temperatures and thermal diffusivity at selected stations in the United States. *ASHRAE Transactions* 71(1), 61–74.

Liang, S., 2001. Narrowband to broadband conversions of land surface albedo I: Algorithms. *Remote Sensing of Environment* 76(2), 213–238. https://doi.org/10.1016/S0034-4257(00)00205-4

Mei, S.-J., Chen, G., Hang, J., Sun, T., 2025. GUST1.0: A GPU-accelerated 3D urban surface temperature model. *Geoscientific Model Development* 18(24), 10143–10167. https://doi.org/10.5194/gmd-18-10143-2025

Nogueira, M., Hurduc, A., Ermida, S., Lima, D.C.A., Soares, P.M.M., Johannsen, F., Dutra, E., 2022. Assessment of the Paris urban heat island in ERA5 and offline SURFEX-TEB (v8.1) simulations using the METEOSAT land surface temperature product. *Geoscientific Model Development* 15(14), 5949–5965. https://doi.org/10.5194/gmd-15-5949-2022

Salvati, A., Kolokotroni, M., 2023. Urban microclimate and climate change impact on the thermal performance and ventilation of multi-family residential buildings. *Energy and Buildings* 294, 113224. https://doi.org/10.1016/j.enbuild.2023.113224

USGS, 2026. *How to use scale factors with Landsat Level-2 science products*. U.S. Geological Survey. https://www.usgs.gov/faqs/how-do-i-use-a-scale-factor-landsat-level-2-science-products

Zanaga, D., Van De Kerchove, R., Daems, D., De Keersmaecker, W., Brockmann, C., Kirches, G., Wevers, J., Cartus, O., Santoro, M., Fritz, S., Lesiv, M., Herold, M., Tsendbazar, N.E., Xu, P., Ramoino, F., Arino, O., 2022. *ESA WorldCover 10 m 2021 v200* (dataset). European Space Agency WorldCover project. https://doi.org/10.5281/zenodo.7254221

Zhan, W., Chen, Y., Zhou, J., Wang, J., Liu, W., Voogt, J., Zhu, X., Quan, J., Li, J., 2013. Disaggregation of remotely sensed land surface temperature: Literature survey, taxonomy, issues, and caveats. *Remote Sensing of Environment* 131, 119–139. https://doi.org/10.1016/j.rse.2012.12.014

This work is licensed under a Creative Commons Attribution-No Derivatives 4.0 International License.

A GEOSPATIAL DECISION-SUPPORT FRAMEWORK FOR URBAN AND SUBURBAN PHOTOVOLTAIC DEPLOYMENT

M. Moretti *, E. Tricomi, M. Koren , M. Gianinetto

Department of Architecture, Built Environment and Construction Engineering, Politecnico di Milano
(margherita.moretti, mattia.koren, marco.gianinetto)@polimi.it

KEY WORDS: Renewable energy transition, Geospatial information, Earth Observation (EO), Photovoltaic site selection, Copernicus

ABSTRACT:
The transition towards renewable energy in Italy is progressing at a slower pace than required, partly due to a structural lack of coherent, up-to-date, and easily accessible geospatial information to support investment decision-making.
This research is conducted within the *Space It Up* project, funded by the Italian Space Agency (ASI) and the Ministry of University and Research (MUR), and aims to develop an operational tool to support industrial stakeholders in the identification of suitable sites for photovoltaic deployment by integrating Earth Observation (EO) data, geospatial information, regulatory constraints, incentives, and system productivity.
The methodology is applied to a case study in Regione Lombardia, in the context of the "Aree Idonee" decree issued in July 2024, which defines criteria for the identification of suitable and unsuitable areas for renewable energy installations and introduces simplified authorization procedures for photovoltaic plants in specific zones. Accordingly, the regulatory framework established by the decree is explicitly incorporated into the analysis. Official datasets from Regione Lombardia, the Ministry of the Environment and Energy Security (MASE), CORINE Land Cover, Copernicus products, and other EO-derived data are jointly exploited.
In addition, the study addresses rooftop characterization through the development of a multispectral approach for detecting existing photovoltaic installations, enabling the assessment of retrofit potential, the identification of suitable surfaces for solar energy production, and the evaluation of industrial areas for rooftop photovoltaic deployment.

1. INTRODUCTION

This project is framed within the European policy context defined by the commitment to reduce greenhouse gas emissions by 55% by 2030 and to achieve climate neutrality by 2050 under the *Fit for 55* package. In parallel, in response to recent energy challenges the European Union launched the *REPowerEU* programme to strengthen energy security and reduce external dependencies. This policy sets a target of 45% renewables by 2030 and promotes simplified authorization procedures for new solar installations.
The Integrated National Energy and Climate Plan (PNIEC, 2024) identifies photovoltaics as a key technology for achieving European targets and explicitly calls for the development of tools and methodologies for mapping photovoltaic potential, including solar cadastres, at both urban and national scales.
An assessment of existing tools reveals the widespread availability of solar cadastres, particularly in urban contexts, including initiatives implemented in Switzerland, Tirol, Wien, St. Pölten, Podgorzyn and Chrastava, London, Calgary, Bolzano, Baden, Hannover, Hessen, Amsterdam, and other European and non-European cities. These instruments typically provide building-scale assessments of rooftop solar potential.
Given the relevance and timeliness of the topic, this study aims to develop an operational mapping tool that integrates solar potential with the set of regulatory, spatial, and technical information. To this end, key stakeholders of the photovoltaic sector operating in Italy were consulted to identify the main criteria guiding site scouting activities. The interviews indicate that the primary assets of interest are ground-mounted photovoltaic systems exceeding 10 hectares and rooftop installations with a surface area larger than 1,000 m².
This work focuses on two main aspects:
– *Permitting*: the collection and spatial representation of regulatory incentives and constraints within a georeferenced framework (Section 2),
– *Detection of existing photovoltaic systems*: the development of a method to identify rooftop-mounted solar installations using Sentinel imagery (Section 3).

2. PERMITTING

Authorization procedures for photovoltaic systems are governed by the "Aree Idonee" Decree, which defines four distinct authorisation regimes (Table 1). Under this framework, areas classified as suitable are subject to simplified and accelerated authorisation procedures, whereas areas identified as unsuitable, are subject to more restrictive regulatory conditions.

Table 1. Authorisation regimes defined by the "Aree Idonee" Decree.

Class	Authorisation regime	Regulation reference
a)	Suitable Area	Legislative Decree No 190, 25 November 2024, N. 190, Art 11-bis
b)	Unsuitable Area	«Linee guida per l'autorizzazione degli impianti alimentati da fonti rinnovabili» (2010)
c)	Ordinary Area	Not specified
d)	Forbidden Area	Legislative Decree No 190, 25 November 2024, N. 190, Art 11-bis

2.1 Data and Methods

Data were retrieved from the Geoportale Lombardia, the "Carta Nazionale di Consumo del Suolo 2023" (CNCS2023) compiled by ISPRA, and the CORINE Land Cover 2018 (CLC2018) dataset, and subsequently processed using QGIS software. The

* Corresponding author

most recent source available for each dataset was selected. The temporal discrepancies are considered acceptable for the purposes of the preliminary site-screening process. The prototype was developed for the Regione Lombardia case study area.

2.1.1 Suitable areas

Areas classified as suitable pursuant to Article 20, paragraph 8 of Legislative Decree No. 199/2021 include:

a) *Existing photovoltaic installations undergoing modification or refurbishment:*
Corresponding to "ground mounted photovoltaic installations" class of CNCS2023 dataset. The detection of rooftop-mounted systems is addressed separately in Section 3.

b) *Sites subject to environmental remediation as defined under Title V, Part IV of Legislative Decree No. 152 of 3 April 2006:*
Obtained from AGISCO database (Registry and Integrated Management of Contaminated Sites).

c) *Quarries and mines that are no longer in operation, have not been reclaimed, have been abandoned, or are in a state of environmental degradation:*
Closed quarries with an area larger then 10.000 m2 were selected from the quarry registry provided by Geoportale Lombardia.
A distinction was made between dry and water-filled quarries, as the latter may be suitable for floating photovoltaic installations:
– Closed dry quarries: Quarries intersecting areas classified as "non-renaturalized extraction areas" in the CNCS2023 dataset and as "mineral extraction sites" in the CLC2018 dataset were selected. This category includes quarries with more than 50% of their surface not flooded or with a non-water surface exceeding 15,000 m².
– Closed submerged quarries: Areas classified as water bodies in the DUSAF 6.0 (2018) dataset were extracted from the regional quarry registry. Only quarries with a submerged area larger than 20,000 m² were considered.

[…]

c-ter)
2) Areas within industrial plants and agricultural areas enclosed within a perimeter whose boundary points are located no more than 500 m from the same plant:
Corresponding to industrial buildings and their surrounding areas within a 500 m buffer, intersecting land classified as agricultural in the CLC2018 dataset.
3) Areas adjacent to the motorway network within a maximum distance of 300 m.
A 300 m buffer around motorway was generated to delineate agricultural areas potentially suitable for photovoltaic deployment.

2.1.2 Unsuitable areas

Areas deemed unsuitable for the installation of photovoltaic systems are defined by Regional Council Resolution (Giunta Regionale) No. 9/3298 of 18 April 2012, Part V, in accordance with the Ministerial Decree of 10 September 2010. While photovoltaic installations are not explicitly prohibited in these areas, they are not eligible for accelerated or simplified authorisation procedures. The classification of unsuitable areas accounts for landscape, environmental, cultural, hydrogeological, and infrastructural constraints.

2.1.3 Integrated Suitability Analysis

Suitable and unsuitable areas are subsequently integrated into a single map, supporting the identification of locations most appropriate for photovoltaic deployment and allowing a suitability analysis. Figure 1 illustrates the results for a representative case study area, where several agricultural parcels fall within the buffer zones of highways or industrial facilities (shown in green) but are simultaneously included within a PLIS protected park (shown in orange). As a result, feasibility assessments should focus on agricultural areas that are not subject to park-related constraints.

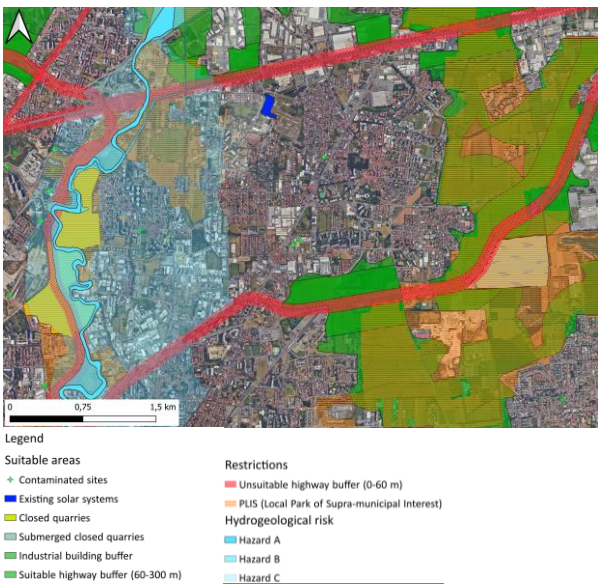

Figure 1. Spatial overlap between areas classified as suitable and unsuitable for photovoltaic installation.

3. DETECTION OF EXISTING SOLAR SYSTEMS ON ROOFTOP

Rooftop surfaces represent a significant opportunity for solar energy deployment while avoiding additional land take. Information on existing rooftop-mounted photovoltaic systems is analysed and integrated into the mapping framework. To this end, a method for detecting existing installations is developed to identify available roof surfaces. The presence of rooftop photovoltaic systems is also used as an indirect proxy for grid connectivity.

3.1 Data and methods

The datasets used for this analysis include a Sentinel-2B L2A image tile 32TNR acquired on 19 June 2025 and polygonal data for commercial and industrial buildings obtained from the Database Geo-Topografico (DBT) of Regione Lombardia, limited to features with a surface area greater than 10,000 m².
Spectral signatures were extracted for 411 buildings from the Sentinel-2B imagery using SNAP software. The sample includes both buildings equipped with rooftop photovoltaic systems and buildings without rooftop installations. Samples were selected to ensure a uniform spatial distribution across industrial areas and were manually labelled as "simple roof" or "solar panel" based on visual interpretation of Qgis basemaps Google satellite and Bing satellite, which have generally an update time of months, but in the worst cases it can go up to three years. Nevertheless, the comparison of the two basemaps was the best option available, as the most recent orthophoto dates to 2021.
An average spectral signature representative of photovoltaic panels was derived from the point samples extracted in SNAP (Figure 2). The resulting average signature is comparable to the

theoretical signature defined in the "Roof Material Spectral Library" (C. Wyard et al., 2023). Both are characterised by low reflectance in the visible and near-infrared regions, followed by a peak in the B11 band (SWIR1) and a decrease in the B12 band (SWIR2). Hyperspectral datasets additionally reveal an absorption feature at approximately 1730 nm, which cannot be resolved by the spectral bands of Sentinel-2.

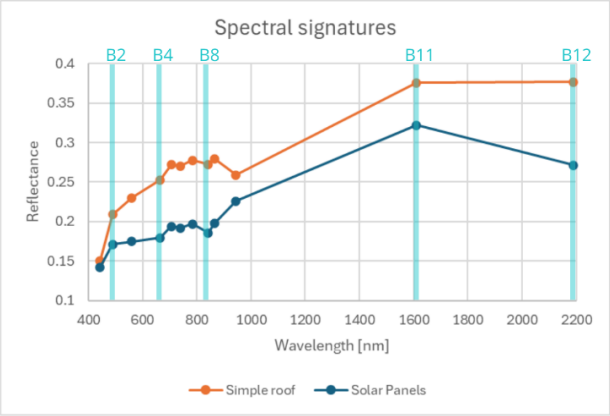

Figure 2. Average Sentinel-2 spectral signature of rooftop-mounted photovoltaic panels. Bands used in the indices are highlighted in light blue.

3.1.1 Classification model

The classification model was developed by combining three spectral indices selected for their compatibility with Sentinel-2 spectral bands and their operational capability to discriminate between rooftops with and without photovoltaic installations.

Enhanced Photovoltaic Index (EPVI)

The Enhanced Photovoltaic Index was introduced by Wang *et al.* (2024) to detect photovoltaic installations by emphasising the reflectance peak in the SWIR1 band (B11) relative to the near-infrared (B8) and SWIR2 (B12) bands:

$$EPVI = \frac{2 \cdot B11 - B12 - B8}{2 \cdot B11 + B12 + B8} \quad (1)$$

Solar Photovoltaic Index (SPI)

The Solar Photovoltaic Index was originally developed by Tian *et al.* (2022) for Landsat-8 OLI imagery and is here adapted to Sentinel-2 spectral bands. Like EPVI, this index exploits the reflectance peak observed in the B11 band to enhance the spectral response of photovoltaic panels:

$$SPI = \frac{(2 \cdot B11 - (B8 + B12)) - |\, B8 - B4 \,| - |\, B8 - B12 \,|}{2 \cdot B11 + (B8 + B12)} \quad (2)$$

B2/B4 ratio

The B2/B4 ratio exploits the relatively higher reflectance of photovoltaic panels in the blue band (B2) compared to the red band (B4):

$$B2/B4 = \frac{B2}{B4} \quad (3)$$

The three indices are based on bands with geometric resolution of 10 m or 20 m, resampled at 10 m. For each index, the discriminative capability was evaluated based on the separation between classes, quantified as the difference between the 75th percentile of the "simple roof" class and the 25th percentile of the "rooftop photovoltaic" class. Since all indices exhibit higher values for photovoltaic panels, this metric was used to assess their suitability for rooftop PV detection within the proposed framework. The three indices are used to classify the pixels in Solar Panel (PV) and Simple rooftop (T), on the base of the distance from centroids of solar panel sample and rooftop sample. Some pixels presenting comparable distance are considered Non-classified (NC).

3.1.2 Results

Validation was performed using an independent a posteriori sample, yielding an overall accuracy of 0.83 and a Cohen's Kappa coefficient of 0.66. User accuracy and Producer accuracy are reported in Table 2 and Table 3. The metrics are computed from around 160 samples per class, disregarding the non-classified pixels.

Table 2: User accuracy of validation sample

		Real classes	
		Solar panel	Simple roof
Classification	Solar Panel	74%	26%
	Simple roof	7%	93%

Table 3: Producer accuracy of validation sample

		Real classes	
		Solar Panel	Simple roof
Classification	Solar Panel	91%	22%
	Simple roof	9%	78%

Figure 3 shows an example of the resulting classification at the pixel level, representing PV pixels in blue, T pixels in orange and NC pixels with black.

An index representing the expected presence of rooftop photovoltaic installations (PAF) was computed for each building to aggregate pixel-level classification results at the building scale. To this end, the proportion of pixels assigned to each class was calculated. The index formulation accounts for the performance of the classification model by weighting each class according to its user accuracy. The PAF index was computed as:

$$PAF = PV_perc \cdot 0.74 + NC_perc \cdot 0.28 + T_perc \cdot 0.07 \quad (4)$$

Figure 4 illustrates the spatial distribution of the PAF values, with higher values represented by darker blue tones and lower values by lighter shades.

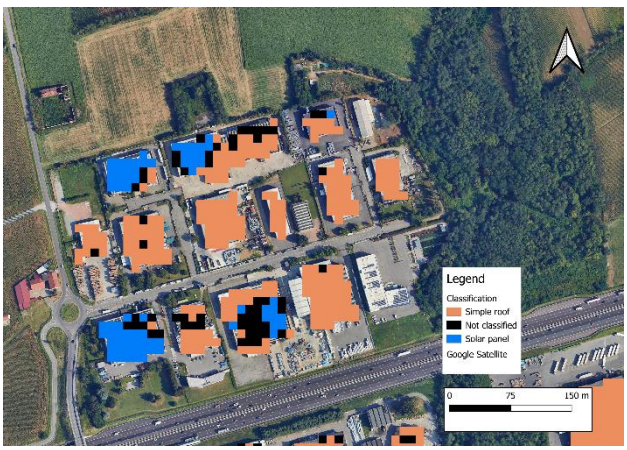

Figure 3. Building-level classification of the 10 m pixels

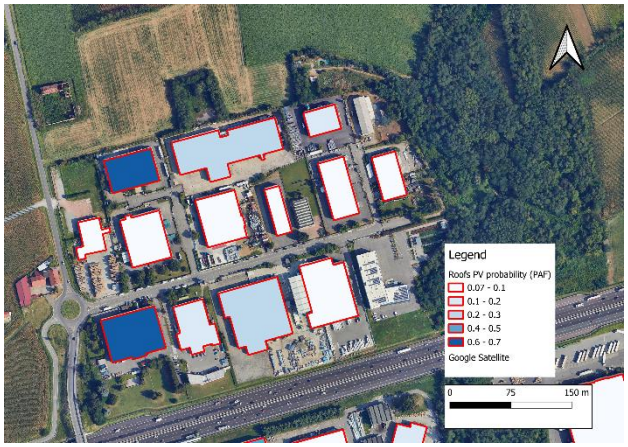

Figure 4. Building-level distribution of the PAF index derived from rooftop photovoltaic detection.

3.1.3 Robustness evaluation

The same classification approach was applied to the 8 buffer tiles of tile 32TNR, to cover the whole Lombardy region. The selected scenes date to summer 2025, as well. To assess the classification accuracy, a validation sampling was conducted. Around 50 pixels per tile were sampled among rooftops in Lombardy area, with user accuracy reported in Table 4. Only UA of Solar Panels class is assessed, as it is the class with lowest accuracy. The UA is quite variable among the tiles, but the weighted average of 77% is very close to the UA of tile 32TNR, confirming the robustness of the method for Sentinel-2.

Table 4: User accuracy of solar panel class performed with buffer tiles. Tiles are indicated with the last two letters, i.e. 32TPQ is PQ.

Tile	**PR**	**PQ**	**PS**	**NS**	**MS**
UA Solar panel %	71	72	88	84	60
Sampling points	55	47	50	49	50
Tile	**MR**	**MQ**	**NQ**	**All tiles**	
UA Solar panel %	67	86	90	77	
Sampling points	48	50	50	399	

4. CONCLUSIONS

This study demonstrates the integration of heterogeneous geospatial datasets into an operational framework supporting industrial-scale energy transition. The work successfully gathered all the indications required by current regulations in a single tool, and, therefore, it facilitates a potential user in efficiently identifying suitable sites, accelerating the scouting process. It is remarked that the selected datasets refer to different sources and inevitably present different spatial resolutions and temporal updates, although only official institutional datasets were used, and the most up-to-date version available for each source was selected. The framework should be updated whenever new data are released or when relevant regulatory provisions are modified.

Furthermore, a methodology for detecting rooftop-mounted photovoltaic systems was developed to identify available roof surfaces while providing an indirect proxy for grid connectivity, which is often difficult to assess using publicly available data. The proposed approach yields results that are adequate for the intended operational context; however, its ability to discriminate between photovoltaic installations and roof materials with similar spectral characteristics remains limited. This constraint could be addressed through the integration of hyperspectral data, such as PRISMA imagery. Another clear limit is the coarse spatial resolution of S2 bands, compared to the relatively small size of the rooftops, which influences the classification with border effects. Future developments will also consider additional information on electrical grid connectivity and roof geometry derived from LiDAR data, to assess sites suitability for photovoltaic panels installation.

ACKNOWLEDGEMENTS

This study was carried out within the SpaceItUp! project funded by the Italian Space Agency (ASI) and the Ministry of University and Research (MUR), under contract Nr. 2024-5-E.0, CUP (master) I53D24000060005 (CUP POLIMI: D43C24000350006).

REFERENCES

Piano Nazionale Integrato per l'Energia e il clima, Ministero dell'Ambiente e della Sicurezza Energetica, June 2024

ISPRA, «Carta Nazionale Consumo di Suolo 2023»

SINAnet, 29 November 2024. [Online]. Available at: https://groupware.sinanet.isprambiente.it/uso-copertura-e-consumo-di-suolo/library/consumo-di-suolo/carta-nazionale-consumo-suolo-2023

«CORINE Land Cover 2018». European Union's Copernicus Land Monitoring Service information. doi: https://doi.org/10.2909/71c95a07-e296-44fc-b22b-415f42acfdf0

Geoportale Lombardia. Available at: https://www.geoportale.regione.lombardia.it/

C. Wyard, R. Marion, e E. Hallot, «WaRM: A Roof Material Spectral Library for Wallonia, Belgium», MDPI, vol. 8, fasc. 3, 2023, doi: https://doi.org/10.3390/data8030059.

Wang et al., «Mapping national-scale photovoltaic power stations using a novel enhanced photovoltaic index and evaluating carbon reduction benefits», Energy Convers. Manag., vol. 318, ott. 2024, doi: https://doi.org/10.1016/j.enconman.2024.118894.

H. Tian, J. Qiao, Y. Qin, X. Jiao, e S. Wang, «A cloud platform-based automatic identification method for global solar photovoltaic panel remote sensing», CN114419463B, 30 September 2022

Autorità di bacino distrettuale del fiume Po, «PAI Po Limite Fascia A vigente». Geoportale del distretto Po, 8 August 2025. [Shapefile]. Available at: https://webgis.adbpo.it/catalogue/#/dataset/1745

This work is licensed under a Creative Commons Attribution-No Derivatives 4.0 International License

Environment, climate risk

MAP OF LAND COVER PARTIAL AGREEMENT: A PROBABILISTIC FUSION

Qiongjie Xu [1]*, Maria Antonia Brovelli [2]

[1] Department of Civil and Environmental Engineering (DICA), [2] Politecnico di Milano, Italy
(qiongjie.xu, maria.brovelli)@polimi.it

KEYWORDS: Land Cover Mapping, Data Fusion, Probabilistic Mapping, Ensemble Framework, Decision Strategies, Spatial Agreement, High-resolution Land Cover

ABSTRACT:

High-resolution land cover (LC) mapping has advanced rapidly with the increasing availability of satellite data and recent progress in artificial intelligence. However, the lack of large, reliable samples remains a major bottleneck. Consensus-based approaches such as the Map of Land Cover Agreement (MOLCA) help generate high-confidence samples from existing LC products, but their strict agreement rules limit spatial coverage and discard useful information in areas of partial consistency. To address these limits, we propose MOLCOPA, a novel multi-source fusion framework designed to integrate existing land cover maps into a unified probabilistic output. Unlike traditional methods that enforce a single label immediately, our approach computes the probability of each land cover type for each pixel from multi-class maps and leverages logical constraints from binary maps to filter conflicts. We further evaluate the conversion of MOLCOPA into discrete land cover maps using strategies ranging from "overall consistency" (which ensures high reliability) to "majority probability" (which ensures effective map coverage). The results highlight a key trade-off: overall consistency yields high-confidence labels suitable for training machine learning models, while probabilistic strategies preserve the spatial integrity required for regional analysis. This framework provides a transparent and flexible solution for generating consistent land cover data, enabling researchers to effectively address the uncertainties introduced by heterogeneous products.

1. INTRODUCTION

High-resolution Land Cover (LC) products are essential for environmental monitoring. In recent years, the combination of increasingly accessible satellite imagery, greater computational capacity and rapid progress in artificial intelligence has enabled the generation of large-scale, high-resolution LC maps (Xu et al., 2025). Despite these developments, getting reliable samples is still a major challenge. This problem is even more serious for modern deep learning models, which require far more diverse samples than traditional machine learning methods.

To address this challenge, Map of Land Cover Agreement (MOLCA) was created by combining several existing LC datasets based on consensus (Bratic et al., 2023). Although this dataset achieved a high estimated overall accuracy of about 96%, its spatial coverage was limit. For example, only 40% of Africa and 43% of Siberia have valid pixels. Besides, the areas without consensus, which currently are removed from MOLCA, still contain useful information that could support probabilistic modeling.

Therefore, building upon the core ideas of MOLCA, this paper introduces the **Map of Land Cover Partial Agreement (MOLCOPA)**. Unlike MOLCA, MOLCOPA is designed not only as a source of training data, but also to achieve flexible probabilistic mapping. Our framework extends existing methods by: (1) computing class-wise probabilities to preserve information in uncertain areas; (2) integrating binary maps as strict logical constraints to filter out invalid predictions; and (3) providing configurable decision strategies that allow users to balance label reliability and spatial completeness according to their needs.

2. METHODOLOGY

The MOLCOPA framework transforms heterogeneous input maps into a unified, probabilistic representation of land cover agreement. The workflow consists of three main steps: (1) Data Harmonization, (2) Probabilistic Fusion, and (3) Land Cover Mapping Strategy implementation.

2.1 Data harmonization

To ensure spatial and thematic consistency, all input LC products are first harmonized. Spatially, each dataset is converted to the WGS84 Coordinate Reference System (CRS) and resample to a common 10-m resolution. Thematically, to reduce differences in class definitions across products, all legends are mapped to a single classification scheme derived from MOLCA, which includes 10 land-cover classes (e.g., Shrubland, Grassland, Cropland, Built-up, Bareland, Permanent Ice and Snow, Water, Wetland, Lichens and Mosses, Forest).

2.2 Probabilistic fusion

After harmonization, the multi-class input maps are used to derive an initial class probability. For each pixel p and target class c, this probability is computed as the proportion of sources assigning class c to pixel p, as defined in Equation (1).

$$P_{ini}(c;p) = \frac{K}{N_{multi}(p)} \quad (1)$$

where K = number of multi-class maps that classify pixel p as class c
$N_{multi}(p)$ = total number of valid (non-NoData) multi-class maps for pixel p

* Corresponding author

Subsequently, binary maps are integrated to resolve logical inconsistencies. Unlike multi-class maps which often balance accuracy and completeness, binary maps typically provide high-confidence validation for specific classes. Accordingly, the initial probability $P_{ini}(c;p)$ is refined to $P_{fin}(c;p)$ following logical rules:

1. **Invalidation**. If a binary map excludes a given class while the initial probability is positive ($P_{ini}(c;p) > 0$), that class is explicitly invalidated at that pixel and its probability is set to NoData ($P_{fin}(c;p) = NoData$).
2. **Conflict**. If a binary map indicates that pixel p belongs to a specific class, but the corresponding probability is zero or missing, it is treated as a conflict. In such cases, all class probabilities for that pixel are discarded ($P_{fin}(\forall\, c;p) = NoData$).
3. Otherwise, $P_{fin}(c;p) = P_{ini}(c;p)$.

2.3 Land cover mapping strategies

The final probabilistic layers allow user to derive discrete LC maps based on flexible requirements. We evaluate three primary strategies:

1. **Overall Agreement (N)**: A label c is assigned if and only if all N sources agree ($P_{fin}(c;p) = 1$). This strategy maximizes precision but results in low coverage.
2. **N-1 Agreement**: A label is assigned if at least $N-1$ sources agree. This relaxes the strict consensus to accommodate minor noise or single-source outliers.
3. **Majority Agreement (T)**: The class with the highest probability is selected, provided it exceeds a defined confidence threshold T (e.g., $T > 0.5$). This strategy maximizes spatial coverage, filling gaps left by stricter rules.

3. EXPERIMENTS AND RESULTS

3.1 Study area and data

As shown in Figure 1, we applied this framework to a study area in the Sahel region of West Africa. A set of recent global LC products (Figure 2) is served as input, including six multi-class maps such as Google's Dynamic World (Brown et al., 2022) and ESA's WorldCover (Zanaga et al., 2021), as well as seven binary maps, like DLR's World Settlement Footprint (WSF) (Marconcini et al., 2021). Each of them has a spatial resolution of at least 30 m. We used 2019 as the reference year. If a product did not provide a map for 2019, the closest available year was selected to preserve temporal consistency as much as possible.

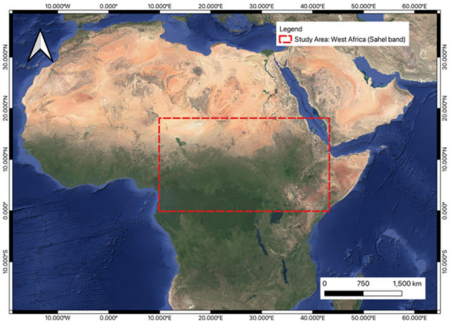

Figure 1. Study area

Name of LC Map	Provider	Temporal Resolution	Spatial Resolution	LC Focus	Accuracy (%)	
Global 30 m land-cover (dynamics monitoring) product with a fine classification system (GLC_FCS30/D)	Aerospace Information Research Institute, Chinese Academy of Sciences	1985,1990,1995,2000-2022 (map for every year)	30m	General (35 classes)	OA(2015)=82.5 OA(2000)=80.88 OA(2005,2010,2022,2015,2018)=82.14, 81.99, 81.97, 81.92, 81.64	Number of Multi-class Maps = 6
Dynamic World	World Resources Institute, Google	From 27/06/2015	10 m	General (9 classes)	OA(Overall)=73.8	
LULC Annual v2	Impact Observatory, Microsoft, and Esri	2017-2023 (map for every year)	10 m	General (10 classes)	OA(Overall)=85	
WorldCover	ESA	2020,2021	10 m	General (11 classes)	OA(2020)=74.4, OA(2021)=76.7	
GlobeLand30 (GLC)	NGCC	2000,2010,2019	30 m	General (10 classes)	OA(2010)=80, OA(2000)=78.6	
FROM-GLC	Tsinghua University	2010, 2015, 2017	30 m	General (10 classes)	OA(2017)=72.76, OA(2015)=70.17 OA(2010)=67.08	
Global annual wetland dataset at 30m with a fine classification system (GWL_FCS30/D)	Aerospace Information Research Institute, Chinese Academy of Sciences	2000-2022 (map for every year)	30 m	Wetland (8 classes)	OA(2020)=87.7, OA(2020)=86.95	Number of Binary Maps = 7
Global Surface Water (GSW) seasonality	JRC	1984-2021 (map for every year)	30 m	Water (3 classes)	UA(1990,1995,2000,2005,2010,2015,2018)=96 PA(1990,1995,2000,2005,2010,2015,2018)=96	
Global Forest Cover (GFC)	JRC	2020	10m	Forest (1 class)	OA(2020)=78.6	
Forest/Non-Forest (FNF)	JAXA, EORC	2007 - 2010 (map for every year) 2015 - 2020 (map for every year)	25 m	Forest (3 classes)	OA(2010)=87.14, 91.13 OA(2007)=89.19, 96.49	
Global 30m impervious-surface dynamic dataset (GHSD30)	Aerospace Information Research Institute, Chinese Academy of Sciences	1985–2020	30 m	Built-Up (1 class)	OA(1985, 1985–1990, 1990–1995, 1995–2000, 2000–2005, 2005–2010, 2010–2015 and 2015–2020)=90.1	
GHS-BUILT-S R2023A	JRC	2018	10 m	Built-Up surface proportion (continuous 0-100)	OA(2018)=90.6	
World Settlement Footprint (WSF)	DLR	2015, 2019	10 m	Built-Up (2 classes)	Balanced accuracy (2015) = 83.27	

Figure 2. Information of LC products used in this study

Validation was performed using the SRS_Val dataset (Liangyun Liu, 2023), a 2020 global validation dataset developed by stratified random sampling. We filtered out sample points falling within the study area and aligned their legends with ours (Table 1).

SRS_Val Land cover type	MOLCOPA Label
Rain-fed cropland	Croplands
Irrigated cropland	
Evergreen broadleaved forest	Forest
Deciduous broadleaved forest	
Evergreen needleaved forest	
Deciduous needleaved forest	
Mixed forest	-
Shrubland	Shrubland
Grassland	Grassland
Lichens and mosses	Lichen and Mosses
Sparse vegetation (fc<0.15)	Bareland
Wetlands	Wetland
Impervious surfaces	Built-up
Bare areas	Bareland
Water body	Water
Permanent snow/ice	Permanent ice and snow

Table 1. Legend matches between SRS_Val and MOLCOPA

3.2 Spatial coverage and visual assessment

We first compared the different decision strategies in terms of spatial coverage, measured using the ratio of pixels with clearly assigned labels to the total study area. The results show a clear trade-off between coverage and consensus strictness (Table 2). As the consensus degree becomes stricter, spatial coverage decreases dramatically. The majority agreement strategy retains a large proportion of valid pixels, achieving approximately 72.8% coverage. On the other hands, raising the rule to "overall agreement" reduced coverage to below 32.5%, resulting in approximately two-thirds of the study area being labeled as "NoData".

	Overall Agreement	N-1 Agreement	Majority Agreement
Valid Pixel Ratio (%)	32.34	59.34	72.77

Table 2. Valid pixel ratio using different strategies

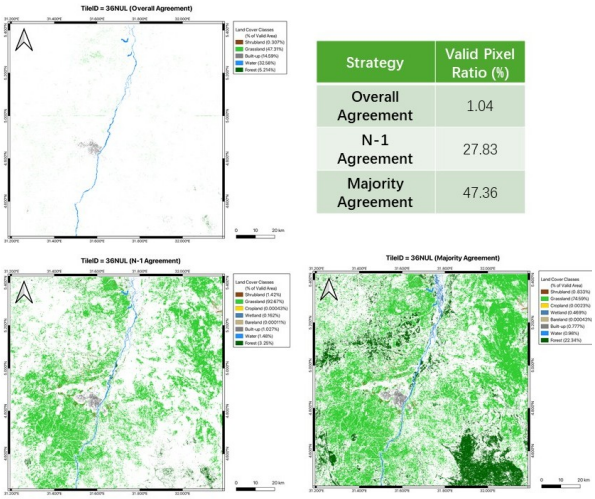

Strategy	Valid Pixel Ratio (%)
Overall Agreement	1.04
N-1 Agreement	27.83
Majority Agreement	47.36

Figure 3. Visual comparison of fusion strategies for Tile **36NUL**. White areas indicate NoData.

To understand the geographic distribution of these data gaps, we conducted a visual inspection of a representative tile (TileID = 36NUL) as an example (Figure 3). The map generated based on the overall agreement contains a large number of data gaps (only 1.04% of the pixels are valid). These gaps, shown as white areas, indicate that at least one input LC product disagrees with others. They are especially concentrated in the transition zone between shrubland and grassland, indicating the high uncertainty in these transitional zones. In contrast, the majority agreement strategy migrates conflicts by assigning each pixel the class with the highest probability, significantly increasing the valid pixel ratio to 47.36%. This approach largely preserves spatial continuity and provides substantially broader spatial coverage than strict consistency rules, making it more suitable for regional-scale mapping applications.

3.3 Quantitative analysis based on reference samples

We assessed these strategies using independent validation samples. Table 3 summarizes the trade-off between the classification accuracy and sample availability under different strategies.

	Overall Agreement	N-1 Agreement	Majority Agreement
Support (count)	779	1629	2004
Support (%)	25.17	52.63	64.75%
OA (%)	93.32	80.17	74.45
Kappa	0.8888	0.7364	0.6673

Table 3. Statics of different strategies

As the consensus become stricter, overall accuracy (OA) significantly improves, from 74.5% under the majority agreement strategy to 93.3% under the overall agreement. The Kappa coefficient shows a similar trend, increasing from 0.67 to 0.89. However, this improvement in accuracy comes at the cost of a significant reduction in the number of available samples, with validation points dropping from 2004 to 779 out of the original 3095 total samples. These results highlight the clear trade-off between label reliability and spatial support. The N-1 agreement strategy offers a practical compromise. It achieves an OA of 80.2% and a Kappa coefficient of 0.74 while retaining 1629 samples, more than twice the number of samples under the overall agreement strategy. This shows that allowing disagreement from a single source helps remove major errors but keeps valuable samples in areas with minor differences.

To better understand this trade-off, we further how sample distribution across land classes varies under each strategy (Figure 4). Highly consistent land cover classes, such as “Forest” and “Water”, maintain relatively stable sample proportions across all decision strategies. By contrast, classes prone to spectral confusion, particularly Grassland and Shrubland, suffer substantial sample loss as the consensus criterion becomes stricter. This suggests that MOLCOPA’s consensus mechanism effectively removes uncertain labels in transitional areas. It therefore retains high-confidence samples suitable for model training, while exposing classes and regions that may require probabilistic handling or expert interpretation.

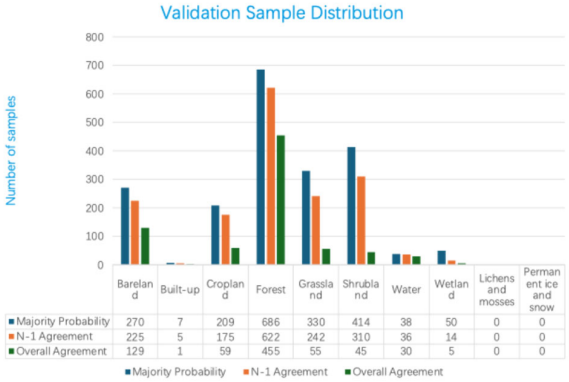

Figure 4. Sample distribution of different strategies

4. CONCLUSIONS

This study presented MOLCOPA, a novel framework for fusing heterogenous land cover products into a unified, probabilistic representation. Unlike its predecessor, MOLCA, which discards conflicting data, MOLCOPA explicitly computes the degree of agreement for each land cover class at the pixel level, and utilizes binary expert constraints to filter out logical inconsistencies. The framework offers a scalable and flexible alternative to rigid classification approaches. It allows user to adjust decision strategies to balance reliability and spatial completeness. For instances, users can adopt the most stringent strategy (overall agreement) to generate high-precision “golden samples” for model training, or choose the most lenient strategy (majority agreement) to preserve as much spatial continuity as possible for regional monitoring. User can also choose a compromise strategy, N-1 agreement, balancing accuracy and spatial coverage.

Some land cover classes, such as “Built-up,” “Lichen and Mosses,” and “Permanent Ice and Snow,” were rare or absent in our study area and reference sample set, limiting evaluation for these classes. Future work will focus on two main directions: (1) expanding the reference sample set within West Africa to better access the under-represented classes like “Built-up”; and (2) applying MOLCOPA to geographically diverse regions, such as Siberia and Amazonia, to validate its performance on the land cover classes not present in the Sahel (e.g., Lichen and Mosses).

ACKNOWLEDGEMENTS

This research was funded by the European Space Agency (ESA) Climate Change Initiative Extension (CCI+) Phase 2---New Essential Climate Variables (NEW ECVS) ---High Resolution Land Cover project (Grant No. 4000125259/18/I-NB).

REFERENCES

Bratic, G., Oxoli, D., Brovelli, M.A., 2023. Map of Land Cover Agreement: Ensambling Existing Datasets for Large-Scale Training Data Provision. *Remote Sensing*, 15(15). https://doi.org/10.3390/rs15153774

Brown, C.F., Brumby, S.P., Guzder-Williams, B., Birch, T., Hyde, S.B., Mazzariello, J., Czerwinski, W., Pasquarella, V.J., Haertel, R., Ilyushchenko, S., Schwehr, K., Weisse, M., Stolle, F., Hanson, C., Guinan, O., Moore, R., Tait, A.M., 2022. Dynamic World, Near real-time global 10 m land use land cover mapping. Sci Data 9, 251. https://doi.org/10.1038/s41597-022-01307-4

Liangyun Liu, T.Z., Xiao Zhang, 2023. A novel stratified random sampling global validation dataset in 2020—SRS_Val dataset. https://doi.org/10.5281/zenodo.7846090

Marconcini, M., Metz-Marconcini, A., Esch, T., Gorelick, N., 2021. Understanding current trends in global urbanisation-the world settlement footprint suite. GI_Forum 9, 33–38.

Xu, Q., Yordanov, V., Bruzzone, L., Brovelli, M.A., 2025. High-Resolution Global Land Cover Maps and Their Assessment Strategies. *ISPRS International Journal of Geo-Information*, 14(6). https://doi.org/10.3390/ijgi14060235

Zanaga, D., Van De Kerchove, R., De Keersmaecker, W., Souverijns, N., Brockmann, C., Quast, R., Wevers, J., Grosu, A., Paccini, A., Vergnaud, S., Cartus, O., Santoro, M., Fritz, S., Georgieva, I., Lesiv, M., Carter, S., Herold, M., Li, L., Tsendbazar, N.-E., Ramoino, F., Arino, O., 2021. ESA WorldCover 10 m 2020 v100. https://doi.org/10.5281/zenodo.5571936

This work is licensed under a Creative Commons Attribution-No Derivatives 4.0 International License.

A STANDALONE SOFTWARE FOR POST-FIRE EROSION SUSCEPTIBILITY ASSESSMENT DURING THE EMERGENCY PHASE

C. Pala[1]*, M.T. Melis[1] , M.T. Brunetti[2] C. Collu[1,6], R. Sarro[3] , P.V. Miranda Garcia[3] , J.P. Galve Arnedo[4] , A. Millares[5]

[1] Department of Chemical and Geological Sciences, University of Cagliari, Monserrato, Italy
[2] Research Institute for the Hydrogeologic Protection – National Research Council, Via Madonna Alta 126, 06128 Perugia, Italy
[3] Department of Geohazards and Climate Change, Geological and Mining Institute of Spain, Ríos Rosas 23, 28003, Madrid, Spain;
[4] Departamento de Geodinámica, Universidad de Granada, Campus de Fuentenueva s/n, 18071 Granada, Spain;
[5] Environmental Fluid Dynamics Group, Andalusian Institute for Earth System Research, Avda. del Mediterráneo s/n 18006, Granada, Spain;
[6] Department of Civil, Constructional and Environmental Engineering, Sapienza University of Rome, Rome, Italy

KEYWORDS: post-fire, susceptibility mapping, sediment connectivity, software, remote sensing, burned area, post-fire debris flow

ABSTRACT: Wildfire occurrence and frequency are increasing globally due to human and natural factors. The increased wildland-urban interface increases the probability of wildfire, with ignition commonly linked to electrical failures and arson. Wildfires decrease water infiltration, while increasing soil erodibility, enhance rock erosion and, sharply, increase sediment connectivity. As a result, post-fire debris flows can be observed during low-intensity post-fire rainfall, exposing neighbouring communities to a new hazard. By combining the existing knowledge about sediment connectivity, fire and vegetation indexes and erosion mitigation by land management, we propose a novel empirical equation for post-fire erosion susceptibility assessment. The equation is designed to be used in the emergency phase to produce a post-fire erosion susceptibility map and it is implemented through a python-based standalone, multithreaded software, called INteractive and User-friendly Emergency tool (INUE). We applied the equation to the burned areas after the 2021 Montiferru and 2022 Los Guájares wildfires, under different hazard scenarios. Evidence for post-fire debris flows occurrence is found in both study cases. Both areas are rocky and have thin soil cover, different geology, vegetation density and land cover. Despite these differences, debris is produced through the same processes: rockfall, thermal spalling, overland flow, and channel erosion. Terraces were excavated before the fire in both areas and effectively mitigated post-fire erosional processes. The performance of the resulting post-fire erosion susceptibility maps is evaluated at the watershed scale, based on the presence or absence of debris flow deposits. The equation gives better results in the Montiferru study case. Different performances can be related to differences in sediment connectivity distribution and prefire vegetation density.

1. INTRODUCTION

1.1 State of the art

Wildfires cause significant damage to ecosystems, human lives, and finances (Lloyd's, 2020), and their frequency is expected to rise by 90% due to socioeconomic and climatic factors, with burned areas shifting towards higher latitudes, affecting shrublands, tundra, and boreal forests (Moritz et al., 2012).

Besides their direct impacts on human life and economic assets, wildfires cause significant geomorphological changes by increasing sediment production, availability, storage, and transfer, leading to Post-Wildfire Debris Flows (PWDF). As an example, in the Western United States of America, sediment transfer is expected to rise by 10% in most watersheds and by 100% in over a third (Sankey et al., 2017). These changes result from vegetation loss, soil and hydrological modifications (DeBano, 1991), and rock erosion during the fire (Buckman et al., 2021; Kendrick et al., 2016; Pala et al., 2025), which increase Sediment Connectivity — the likelihood of particles reaching a sink or river network (Borselli et al., 2008).

An effective way to model sediment connectivity is through indices, such as the Index of Connectivity (IC) (Borselli et al., 2008). IC accounts for upslope and downslope factors, including flow path lengths, contributing area, slope, and custom impedance factors (W). The effects of wildfire on IC distribution are characterized of IC increases that are well correlated with burn severity (Martini, Faes, Scalari, et al., 2020). Furthermore, Difference of IC (DoIC) maps have been proposed to consider the effects of fire on sediment transfers in burned watersheds (Martini, Faes, Picco et al. 2020). In addition to these natural settings, anthropogenic landforms can play a key role in mitigating post-fire sediment delivery. Terraces and roads help reduce or modify post-fire sediment delivery by disrupting connectivity pathways (Dunning et al., 1998; Hammad et al., 2006; Garcia-Ruiz et al., 2013; Chen et al., 2017; Rutebuka et al., 2021). As an example, terracing, a long-standing cultivating practice, improves water infiltration, lowers slope gradient and length, and is able to reduce erosion and sediment connectivity when properly maintained (Calsamiglia et al., 2018). In the late post-fire phase, the regrowth of vegetation reduces sediment movement and often prevents debris flows even when if the recovery is incomplete (Graber et al., 2023; Cerdá & Doerr, 2005; Kim et al., 2021). In this study, we propose an equation that uses existing knowledge of sediment connectivity, burn severity, and sediment dysconnectivity to create a practical tool for swiftly identifying areas at high risk of post-fire sediment hazards. Its aims to help land managers prioritize interventions and allocate resources efficiently to reduce the risk associated with erosion and sediment movement.

1.2 Study Areas

The study compares two Mediterranean burned areas. Montiferru (Italy, burned in 2021) is characterized by volcanic rocks and dense vegetation, with 63% of the area suffering High to Moderate-High burn severity. Conversely, Los Guájares (Spain, burned in 2022) features carbonate and metamorphic rock with sparse vegetation, where 87% of the area showed Moderate-Low to Low burn severity. After the wildfires, significant vegetation

* Corresponding author

recovery is observed only in Montiferru. After the wildfire, 33 PWDF deposits are observed in Montiferru and 36 in Los Guájares linked to three and one rainstorm events, respectively.

2 METHODOLOGY

FIREX (FIRe Erosion indeX) is a geomorphological, empirically derived composite index designed to quantify post-fire erosion susceptibility. It integrates sediment connectivity, fire-induced disturbance, and dysconnectivity induced by structural and post-fire vegetation recovery processes.
The factors are systematized in the following equation (1):

$$FIREX = \frac{ICnorm * dNBRnorm}{gDI} * VRf * cf \qquad (1)$$

where ICnorm is the normalized Connectivity Index, dNBRnorm the normalized dNBR (i.e. the difference between the prefire and the postfire normalized burned ratio), gDI the geomorphological dysconnectivity index, VRf the vegetation recovery factor and cf a customization factor.
The equation is derived from the existing knowledge and methodologies on sediment connectivity and dysconnectivity, related to (but not only) burned areas (Borselli et al., 2008; Calsamiglia et al., 2018; Cerdá & Doerr, 2005; Kim et al., 2021; Martini, Faes, Picco, et al., 2020; Martini, Faes, Scalari, et al., 2020; Pala et al., 2025; Tarolli et al., 2014).
ICnorm is calculated by normalizing the Index of Connectivity IC, proposed in Borselli et al. 2008 but calculated with the D-infinity method as proposed in (Cavalli et al., 2013). IC has been calculated using the RI – Roughness index proposed in (Cavalli et al., 2008) as the W impedance factor since vegetation is lacking.
dNBRnorm is calculated by normalizing the immediate post-fire dNBR index.
To prevent the loss of polarity signs during multiplication, both terms are normalized to a non-negative range [0, 1], ensuring that the product consistently reflects the underlying magnitude.
It simplifies the procedure to calculate the Difference of the IC - DoIC map proposed by Martini, Faes, Picco, et al., (2020), making it possible to perform this calculation across the entire Burned Area in a short time. Furthermore, it allows DoIC map integration with sediment dysconnectivity factors.
The geomorphological dysconnectivity factor (gDI) is an empirical spatial correction term and represents the impeded sediment connection due to the presence of landforms able to retain sediment. gDI is equal to 1 in undisturbed areas and 2 in terraced areas.
The vegetation recovery factor (VRf) is a temporally varying, threshold-based index that represents post-fire vegetation regrowth dynamics and their effect on sediment mobilization potential.
VRf quantification follows a five-step workflow:

1) Delineation of the Burned Watershed Area (BWA). The spatial extent of the watershed affected by the wildfire is identified and mapped.
2) Monthly NDVI majority calculation within the BWA. NDVI values are computed in a GIS environment at monthly intervals, from fire occurrence to the last recorded debris flow event. In this study, the Zonal Statistics Majority tool in QGIS 3.28 was applied using the BWA as the aggregation unit. This produces a representative NDVI majority value for each month.
3) Temporal analysis of NDVI trends. Monthly NDVI values are plotted over time and compared with the timing of observed post-wildfire debris flows (PWDF), to identify possible correlations between vegetation recovery and debris flow occurrence.
4) Threshold identification (ζ, zeta). A threshold value (ζ) is defined, corresponding to the NDVI level above which no PWDF events are observed.
5) NDVI-based reclassification prior to rainfall events. NDVI values calculated before rainfall events expected to trigger PWDF are reclassified using ζ:
NDVI > ζ → 0 (no risk)
NDVI ≤ ζ → 1 (potential risk)

NDVI is derived from satellite imagery and provides a proxy for vegetation biomass. Its use is intentional: although it is less sensitive to sparse vegetation, this limitation acts here as a conservative filter, ensuring that areas with limited vegetation recovery are still classified as potentially susceptible to debris flows (Rouse et al., 1974).
The customization factor is optional and introduced to let the user integrate the FIREX with triggering or mitigating factors or local variables (e.g., surficial cover thickness or debris availability).
Equation (1) allows to define four hazard scenarios (HS):

- HS1: the area is burned and fully connected
- HS2: the area is burned and some areas may suffer from sediment fluxes impediment due to the presence of anthropic modifications
- HS3: is the evolution of HS1 scenario after partial vegetation recovery
- HS4: is the evolution of HS2 scenario after partial vegetation recovery

2.1 The Algorithm: INUE

SUBSTR8 (Pala, 2026), a modular platform based on Python 3.13 and designed for creating efficient tools for spatial analysis, was used to develop the **INteractive and User-friendly Emergency** tool for burned areas (INUE). INUE is made by 7 modules based on SUBSTR8 functions (Pala, 2025). A INUE's key feature is **TauExecuter**, which integrates external TauDEM (Tarboton, 2016) commands for the required hydrological calculations. INUE's modularity allows its use also for the assessment of sediment connectivity (IC) and remotely sensed fire indexes such as NBR, dNBR, and Burn Severity. The INUE software, implementing the extraction of FIREX (1), was developed and tested on a legacy consumer-grade notebook equipped with Windows 11 (64-bit), an AMD A9-9425 processor, 8 GB RAM (6.9 available). The software is available at (https://zenodo.org/records/17464802) while the code is available at https://github.com/constantineshovel/inue.

2.2 Materials

We used 10 m resolution DEMs retrieved from https://www.sardegnageoportale.it and https://www.centrodescargas.cnig.es. Red, NIR and SWIR imagery are from the ESA Sentinel 2 mission at the L2A level. Shapefiles for the road network are retrieved from https://www.geofabrik.de, while shapefiles for terraces and study areas are manually inferred from satellite imagery interpretation. PWDF deposit locations are from (Pala et al., 2025).

2.3 FIREX application and validation

The significant vegetation recovery observed in Montiferru allows us to test the HS4 scenario for the Montiferru 2022 events only. HS2 is tested in both areas for the 2021 Montiferru and 2022 Los Guájares events.

To validate the FIREX index, we combined field surveys with statistical performance metrics, including ROC-AUC, PR-AUC, F1-score, and Accuracy. We applied these metrics at the watershed scale, utilizing the occurrence of debris flow deposits in the burned basins as a binary classifier (0 = no deposits, 1 = deposits present). Finally, we verified the reliability of the index by calculating the mean FIREX value within the BWA and comparing it with the occurrence or non-occurrence of PWDF evidence.

3 RESULTS

3.1 Wildfire impacts and Sediment Connectivity patterns

Montiferru fire impacts are classified as High/Moderate-High severity. The Los Guájares impacts are classified as Low severity. IC calculations via INUE reveal distinct patterns in the study areas, with sediment connectivity being parallel in Montiferru (Fig 1a) and longitudinal in Los Guájares (Fig 1b). Field validation is consistent with these results, with significant sediment transfers from slope to channel observed in Montiferru only. In Los Guájares, sediment is mainly reworked within the channel. Rare slope erosion occurring in Los Guájares indicates the fire did not drastically alter sediment transfer dynamics compared to pre-fire conditions. The opposite occurs in Montiferru.

3.2 Geomorphologic Disconnection Factor Calculation

Terraced slopes are detected in both areas and a gDI value of 2 is assigned to evaluate the sediment retention in these areas.
Terraced areas have the same characteristics as the undisturbed ones where debris flow was detected: high amounts of debris formed prefire due to rockfall activity and during the wildfire (synfire) owing to rock erosion driven by thermal spalling of tephrite-phonolite lavas (Montiferru, Pala et al. 2025) and marbles (Los Guájares, Miranda et al., 2025, Pala, 2026).

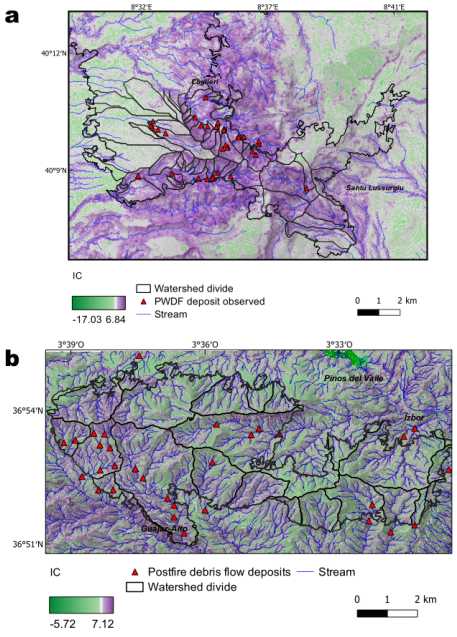

Figure 1 Sediment Connectivity Index (IC) distribution in the study areas. a) 2021 Montiferru Fire Burned Area b) 2022 Los Guájares Fire Burned Area. Green: disconnected areas Purple: connected areas.

3.3 Vegetation Recovery Factor Calculation

VRf is calculated only in the 2021 Montiferru Fire burned area because it is the only one with effective post-fire vegetation growth. When debris flow activity is observed in the second rainfall season after fire, PWDF are observed when NDVI is lower than 0.25 in the corresponding upstream BWA. By comparing the NDVI timeseries with debris flow occurrence after wildfire, we established a ζ equal to 0.25. These observations are extended to all areas through the VRf.

3.4 Application of the FIREX equation with the INUE software. Index and computing performances

In this paragraph, we will first disclose the application of the equation and assess its predictive performance. Then, we will provide details about the computing performance of INUE.

3.5 Hazard Scenario 2: Integrating the structural dysconnectivity factors

FIREX maps are compared with PWDF deposit occurrence, showing the strong correlation of high susceptibility areas with PWDF occurrence in Montiferru (Fig 2 a, c). The correlation is weaker in Los Guájares, showing poorer predictive power under longitudinal connectivity (Tab 1). The integration of gDI improves the map by lowering the FIREX index in these sectors and excluding them from risky areas.

3.6 Hazard Scenario 4

Montiferru area experienced significant vegetation recovery in a few months, with diffuse dense herbaceous cover with plants up to 2 meters in height at the periphery of the area after the first postfire rainy season. On the other hand, some areas in the center of the burned area had only sparse vegetation recovery, limited to shoots from oaks and shrubberies. This context was ideal to test the VRf. Two PWDF events occurred in the second post-fire winter in Montiferru, on 30 September 2022, immediately after the summer, and on 21 November 2022, after some months of heavy rain. The health of the biomass was different between the two events. We tested the VRf using satellite imagery produced immediately before the events to calculate the VRf. We obtained poor results for the 30 September 2022 event but very good results for the November 2022 event (Tab 1, Fig 2 c).

Area	HS	Event	Best Th.	AUC (ROC)	AUC (PR)	F1 score	Ac.
MF	2	3 Nov 2021	0.66	0.83	0.6	0.73	0.76
MF	4	30 Sep 2022	0.50	0.63	0.25	0.17	0.59
MF	4	21 Nov 2022	0.41	0.97	0.87	0.75	0.95
LG	2	14 Dec 2022	0.56	0.65	0.53	0.52	0.65

Table 1 Performance of the FIREX Model. MF: Montiferru Area LG: Los Guájares Area. HS: Hazard Scenario Best Th: Best Threshold Ac: Accuracy

3.7 INUE Computing Performance

The longest workflow required 0:13:8.325874 (h:m:s.ms) for the calculations under the HS4 scenario in Montiferru. For testing purposes, the computing area is significantly higher than the burned scar and 700 km^2 wide. Imagery has 10 m resolution.

4 DISCUSSION AND CONCLUSIONS

A novel equation for producing post-fire erosion susceptibility maps is proposed and implemented with a standalone software (INUE). The methodology builds upon existing knowledge and established approaches, systematized through targeted simplifications and resulting in the new empirical FIREX index. FIREX has demonstrated to be a good empirical proxy in areas characterized by parallel connectivity. The IC model effectively captured sediment connectivity patterns in both study areas: in Montiferru, sediment transfer is mainly driven by slope processes, resulting in efficient delivery to the channel network. On the other hand, in Los Guájares, debris flows occurrence are mainly related to sediment reworking within channels, reducing the predictive performance of FIREX. The integration of the empirical dysconnectivity factors successfully excluded areas where PWDF were not observed, improving the reliability of susceptibility maps. VRf is highly sensitive to biomass health as demonstrated by the totally different predictive performance achieved for the two HS4 scenarios in Montiferru. VRf should be calculated using the imagery representative of the best vegetation health to be effective. INUE demonstrated high computational efficiency, driven by the efficiency of the functions provided by SUBSTR8. These results indicate that FIREX and INUE, because of the global availability of the inputs and computing efficiency, can effectively support BAER teams, Civil Protection agencies, and land managers during the emergency phase following wildfire events, providing rapid operational assessments despite their conceptual simplicity and limited number of input data required. The application of FIREX is not restricted to the immediate post-fire phase but can support hazard assessment until full erosion mitigation is observed. FIREX and INUE are conceived as a screening post-fire emergency assessment tool to be integrated with more advanced modelling approaches. Further research could focus on the calibration and validation of gDI and ζ values in other burned areas but also integrating other variables through the cf such as triggering and mitigating conditions or data about sediment sources.

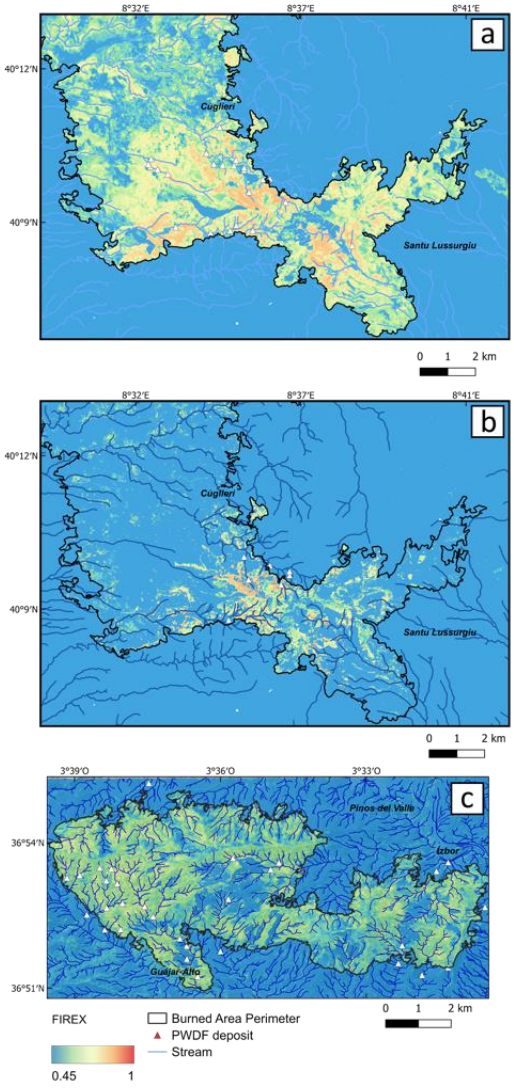

Figure 2. Maps for FIREX value distributions across the burned areas for the selected events. a) Montiferru area, 3 November 2021, HS2 b) Montiferru area, 21 November 2022, HS4 c) Los Guájares area, 16 December 2022

3 REFERENCES

Borselli, L., Cassi, P., & Torri, D. (2008). Prolegomena to sediment and flow connectivity in the landscape: A GIS and field numerical assessment. *CATENA*, *75*(3), 268–277. https://doi.org/10.1016/j.catena.2008.07.006

Buckman, S., Morris, R. H., & Bourman, R. P. (2021). Fire-induced rock spalling as a mechanism of weathering responsible fo r flared slope and inselberg development. *Nature Communications*, *12*(1), 2150. DOI.org (Crossref). https://doi.org/10.1038/s41467-021-22451-2

Calsamiglia, A., Fortesa, J., García-Comendador, J., Lucas-Borja, M. E., Calvo-Cases, A., & Estrany, J. (2018). Spatial patterns of sediment connectivity in terraced lands: Anthropogenic controls of catchment sensitivity. *Land Degradation & Development*, *29*(4), 1198–1210. https://doi.org/10.1002/ldr.2840

Cavalli, M., Tarolli, P., Marchi, L., & Dalla Fontana, G. (2008). The effectiveness of airborne LiDAR data in the recognition of channel-bed morphology. *CATENA*, *73*(3), 249–260. https://doi.org/10.1016/j.catena.2007.11.001

Cavalli, M., Trevisani, S., Comiti, F., & Marchi, L. (2013). Geomorphometric assessment of spatial sediment connectivity in small Alpine catchments. *Geomorphology*, *188*, 31–41. https://doi.org/10.1016/j.geomorph.2012.05.007

Cerdá, A., & Doerr, S. H. (2005). Influence of vegetation recovery on soil hydrology and erodibility following fire: An 11-year investigation. *International Journal of Wildland Fire*, *14*(4), 423. https://doi.org/10.1071/WF05044

Chen, D., Wei, W., & Chen, L. (2017). Effects of terracing practices on water erosion control in China: A meta-analysis. *Earth-Science Reviews*, *173*, 109–121. https://doi.org/10.1016/j.earscirev.2017.08.007

DeBano, L. F. (1991). *The effect of fire on soil properties*. U.S. Department of Agriculture, Forest Service, Intermountain Research Station.

Dunning, N., Beach, T., Farrell, P., & Luzzadder-Beach, S. (1998). Prehispanic Agrosystems and Adaptive Regions in the Maya Lowlands. *Culture & Agriculture*, *20*(2–3), 87–101. https://doi.org/10.1525/cag.1998.20.2-3.87

Garcia-Ruiz, J. M., Arnaez, J., Gomez-Villar, A., Ortigosa, L., & Lana-Renault, N. (2013). Fire-related debris-flows in the Iberian Range, Spain. *Geomorphology*, *196*. https://doi.org/10.1016/j.geomorph.2012.03.032

Graber, A. P., Thomas, M. A., & Kean, J. W. (2023). How Long Do Runoff-Generated Debris-Flow Hazards Persist After Wildfire? *Geophysical Research Letters*, *50*(19), e2023GL105101. https://doi.org/10.1029/2023GL105101

Hammad, A. H. A., Børresen, T., & Haugen, L. E. (2006). Effects of rain characteristics and terracing on runoff and erosion under the Mediterranean. *Soil and Tillage Research*, *87*(1), 39–47. https://doi.org/10.1016/j.still.2005.02.037

Kendrick, K. J., Partin, C. A., & Graham, R. C. (2016). Granitic Boulder Erosion Caused by Chaparral Wildfire: Implications for Cosmogenic Radionuclide Dating of Bedrock Surfaces. *The Journal of Geology*, *124*(4), 529–539. https://doi.org/10.1086/686273

Kim, Y., Kim, C.-G., Lee, K. S., & Choung, Y. (2021). Effects of Post-Fire Vegetation Recovery on Soil Erosion in Vulnerable Montane Regions in a Monsoon Climate: A Decade of Monitoring. *Journal of Plant Biology*, *64*(2), 123–133. https://doi.org/10.1007/s12374-020-09283-1

Lloyd's. (2020). *Wildfire: A burning issue for insurers?* (p. 36).

Martini, L., Faes, L., Picco, L., Iroumé, A., Lingua, E., Garbarino, M., & Cavalli, M. (2020). Assessing the effect of fire severity on sediment connectivity in central Chile. *Science of The Total Environment*, *728*, 139006. https://doi.org/10.1016/j.scitotenv.2020.139006

Martini, L., Faes, L., Scalari, C., Pellegrini, G., Iroumé, A., Lenzi, M. A., & Picco, L. (2020). Evaluating the Effects of Forest Cover Changes on Sediment Connectivity in a Catchment Affected by Multiple Wildfires. In A. Coppola, G. C. Di Renzo, G. Altieri, & P. D'Antonio (Eds.), *Innovative Biosystems Engineering for Sustainable Agriculture, Forestry and Food Production* (Vol. 67, pp. 13–20). Springer International Publishing. https://doi.org/10.1007/978-3-030-39299-4_2

Miranda, P., Pala, C., Mateos Ruiz, R. M., Galve, J. P., Millares, A., Martínez Corbella, M., López-Vinielles, J., Azañón, J. M., & Sarro Trigueros, R. (2025). *Evaluación de inestabilidades del terreno para la recuperación de áreas quemadas: El incendio de los Guájares (Granada).* Centro Internacional de Métodos Numéricos en Ingeniería. https://digital.csic.es/handle/10261/425062

Moritz, M. A., Parisien, M.-A., Batllori, E., Krawchuk, M. A., Van Dorn, J., Ganz, D. J., & Hayhoe, K. (2012). Climate change and disruptions to global fire activity. *Ecosphere*, *3*(6), 1–22. https://doi.org/10.1890/ES11-00345.1

Pala, C. (2025). *INteractive and Userfriendly Emergency tool for burnt areas* (Version 1.0.0 "άλφα") [Computer software]. Zenodo. https://doi.org/10.5281/ZENODO.17464801

Pala, C. (2026). *SUBSTR8—An open platform for building GIS applications* (Version 1.0 Assíle) [Computer software]. Zenodo. https://doi.org/10.5281/ZENODO.19462380

Pala, C., Melis, M. T., Pioli, L., Sarro, R., Loddo, S., Cinus, S., & Brunetti, M. T. (2025). Sediment generation through thermal spalling during the 2021 montiferru planargia wildfire and its contribution to postfire debris flows. *Scientific Reports*, *15*(1), 30918. https://doi.org/10.1038/s41598-025-15527-2

Rouse, J. W., Haas, R. H., Schell, J. A., & Deering, D. W. (1974). *Monitoring Vegetation Systems in the Great Plains with ERTS. NASA SP-351*, *1*, 309–317. https://ntrs.nasa.gov/citations/19740022614

Rutebuka, J., Munyeshuli Uwimanzi, A., Nkundwakazi, O., Mbarushimana Kagabo, D., Mbonigaba, J. J. M., Vermeir, P., & Verdoodt, A. (2021). Effectiveness of terracing techniques for controlling soil erosion by water in Rwanda. *Journal of Environmental Management*, *277*, 111369. https://doi.org/10.1016/j.jenvman.2020.111369

Sankey, J. B., Kreitler, J., Hawbaker, T. J., McVay, J. L., Miller, M. E., Mueller, E. R., Vaillant, N. M., Lowe, S. E., & Sankey, T. T. (2017). Climate, wildfire, and erosion ensemble foretells more sediment in western USA watersheds. *Geophysical Research Letters*, *44*(17), 8884–8892. https://doi.org/10.1002/2017GL073979

Tarboton, D. G. (2016). *TauDEM* (Version 5.3.7) [Computer software]. Utah State University, Hydrology Research Group, David Tarboton.

Tarolli, P., Preti, F., & Romano, N. (2014). Terraced landscapes: From an old best practice to a potential hazard for soil degradation due to land abandonment. *Anthropocene*, *6*, 10–25. https://doi.org/10.1016/j.ancene.2014.03.002

This work is licensed under a Creative Commons Attribution-No Derivatives 4.0 International License.

INTEGRATION OF BIOINDICATION AND REMOTE SENSING: UAV AND STRATOSPHERIC PLATFORMS FOR ENVIRONMENTAL MONITORING

M. Gargiulo*, C. Savarese, S. Parrilli, F. Tufano, M. De Mizio
CIRA - Italian Aerospace Research Centre, Via Maiorise snc, 81043 Capua, Italy
*Corresponding author: m.gargiulo@cira.it

KEY WORDS: remote sensing, data integration, UAV, stratospheric platforms, environmental monitoring, bioindication

ABSTRACT:

Vegetation functions as a reliable bioindicator of environmental stress, including soil contamination. This study presents a UAV-based remote sensing workflow to discriminate maize (Zea mays L.) cultivated in healthy versus contaminated soils using a semi-controlled "scaled field" setup. Multispectral (MicaSense Altum) and hyperspectral (Cubert Ultris 5) imagery were processed through a modular pipeline: pre-processing, vegetation masking, feature extraction, and pixel-wise supervised classification. Results demonstrated that hyperspectral data consistently outperformed multispectral data, with a Support Vector Machine (SVM) classifier achieving an F1-score of 0.838. When hyperspectral data were degraded to a spatial resolution comparable to stratospheric platforms (High-Altitude Pseudo-Satellites, HAPS), classification remained robust (F1=0.778). Compared to multispectral imagery, hyperspectral data improved classification performance by approximately 0.05–0.16 in terms of F1-score, highlighting the critical role of spectral resolution over classifier complexity. These results confirm the potential of UAV-based bioindication for soil contamination detection and demonstrate the scalability of the proposed workflow toward High-Altitude Pseudo-Satellite (HAPS) observation scenarios.

1 INTRODUCTION

Vegetation represents a reliable bioindicator of environmental quality, as plant physiological, morphological, and spectral responses are strongly influenced by abiotic stresses, including soil contamination [1]. Contaminants such as heavy metals and polycyclic aromatic hydrocarbons can alter plant development and canopy structure, inducing detectable spectral variations at both leaf and canopy scales, particularly in the visible and near-infrared regions [2], [3]. Remote sensing (RS) enables non-destructive, spatially extensive and repeatable monitoring of vegetation responses[4]. In this context, UAV platforms have emerged as effective tools for environmental and agricultural monitoring, providing high spatial resolution and flexible acquisition strategies that are well suited for canopy-scale analysis [5]. Previous studies have demonstrated the potential of UAV-based multispectral and hyperspectral data for detecting stress-related spectral signatures associated with soil contamination and vegetation health [6].

Despite these advances, operational remote sensing platforms often face trade-offs between spatial resolution, temporal revisit, and coverage, which may limit early stress detection. High-Altitude Pseudo-Satellites (HAPS) represent a promising solution by enabling persistent observation and proximity-to-target advantages compared to conventional satellite systems. However, the limited availability of HAPS platforms during validation phases makes UAV-based experiments a necessary intermediate step to define sensor requirements and assess algorithmic robustness prior to stratospheric deployment. Building on this framework, the present study introduces a UAV-based remote sensing workflow to discriminate maize (*Zea mays L.*) grown in control and contaminated soils using a semi-controlled "scaled field" experimental setup. Soil contamination was induced using selected heavy metals and hydrocarbons, and canopy responses were analyzed through multispectral and hyperspectral imagery. Feature-based and shallow machine learning approaches were deliberately adopted to ensure model interpretability, robustness under limited training data, and transferability toward future HAPS scenarios. In addition to evaluating classification performance, this work explicitly investigates the scalability of the proposed workflow toward coarser spatial resolutions representative of stratospheric platforms. This work does not aim at proposing a novel classifier, but rather at quantitatively validating a transferable UAV-based bioindication workflow, explicitly designed to assess performance degradation when moving from UAV to stratospheric-like spatial resolutions. The paper is structured as follows. Section 2 describes the experimental setup, data acquisition, and processing workflow. Section 3 presents the spectral analysis and classification results. Section 4 discusses the main findings and outlines future research directions.

Figure 1: Experimental design of seven bins.

2 MATERIALS AND METHOD

2.1 Experimental set-up: "scaled field" bins and contamination treatments

Zea mays L. was growth in large bins (order of 1.05 × 1.05 m footprint) under field condition (ambient temperature and natural light) to isolate pollutants, while enabling sufficient canopy development. As shown in Figure 1, the experimental design included three bin-containers filled with an healthy agricultural soil (control, C1-C3), two bins with the same soil experimentally spiked at fourfold the legal threshold concentrations (T1-T3), and one bin with the same contaminants at threefold the legal threshold concentrations (T4). Doses of pollutants (Cr, Pb, Zn and benzo[a]pyrene) were selected according to the Italian soil threshold values (D.Lgs. 152/2006).

* Corresponding author

Table 1: Spectral and spatial resolution comparison (Altum vs Ultris 5).

Key specs	MicaSense Altum	Cubert Ultris 5
Spectral resolution	6 discrete VNIR bands + LWIR	51 contiguous bands (450–850 nm)
Sampling / BW	Fixed BW per band (10–40 nm)	8 nm sampling; FWHM 26 nm @ 532 nm
Spatial resolution	2048×1536 px (MS)	290×275 px
GSD @ 120 m	∼4.0 cm/px (MS)	∼7.2 cm/px

A nearby weather station monitored the environmental conditions, and the soil's water-holding capacity was kept between 40% and 70%. Experiments were conducted in summer 2024. For this experimental setup, we tested the use of the UAV (shown in Fig. 2) data for soil contamination monitoring, in particular the usage of (i) multispectral (MS) imagery from Micasense Altum (5 bands in VIS-NIR spectrum) and (ii) hyperspectral (HS) imagery from Cubert Ultris 5 (51 bands, 450–850 nm), both acquired at low altitude to achieve centimeter-scale Ground Sample Distance (GSD). Specifically, we flew at 25–30 m altitude, thus we achieved a GSD of approximately 2 cm/pixel for HS and of approx 1 cm/px for MS. Given the HS native GSD, to emulate a HAPS-like GSD, we applied Gaussian blurring followed by a 4× image downsampling. More details in Tab. 1.

(a) (b) (c)

Figure 2: (a) The quadcopter used for the flights, and two sensors mounted on it: (b) MicaSense Altum and (c) Cubert Ultris.

2.2 Proposed workflow: from feature extraction to classification

The proposed workflow, schematized in Figure 3, was designed as a modular and sensor-independent pipeline applicable to both multispectral (MS) and hyperspectral (HS) UAV datasets. The overall procedure includes data pre-processing, vegetation masking, feature extraction, feature standardization and selection, model training/validation, pixel-wise inference, and output generation. In addition, a dedicated scalability assessment was performed to evaluate the transferability of the workflow to HAPS scenario.

In the PRE (pre-processing) phase, raw UAV data were converted into radiometrically calibrated and georeferenced orthomosaics. This step was applied to both MS and HS acquisitions, despite their different native spatial and spectral characteristics. In the MSK (vegetation masking) phase, the analysis was restricted to canopy pixels only. Background, bare soil, and non-vegetated pixels were excluded by applying an NDVI-based threshold (NDVI > τ), thus reducing the impact of background effects and shadows on the subsequent classification stages. On the masked orthomosaics, the FEAT (feature engineering) phase was performed. For MS imagery, the candidate features mainly consisted of vegetation indices computed from the available discrete spectral bands. For HS imagery, the feature space included both analogous vegetation indices and additional hyperspectral descriptors derived from the denser VIS–NIR spectral sampling. The indices considered are the same as those analyzed in [6], [7], [8]. Candidate features were initially screened based on their discriminative ability between control and contaminated conditions, using ANOVA-based analysis. Before classification, all retained features were standardized by z-score normalization (STD) in order to ensure comparability across variables and sensors. A subsequent FS (feature selection) step, based on Random Forest feature importance, was then used to reduce dimensionality and mitigate redundancy, especially for the HS-derived feature set. For model development, the dataset used for calibration was split into 80% training and 20% validation subsets (SPL). The validation subset was used only within the calibration stage, together with cross-validation and hyperparameter tuning, to optimize model configuration and reduce overfitting. Importantly, the calibration dataset (training + validation) was spatially independent from the dataset used in the final testing/inference phase. In this way, no overlap occurred between samples used for model calibration and those used for performance assessment on independent orthomosaics. The CLS (classification) phase involved the training of multiple supervised models, namely Support Vector Machine (SVM), Random Forest (RF), Multi-Layer Perceptron (MLP), and XGBoost, all applied to the same standardized and selected feature set. After calibration, the trained models were applied in the inference and output generation stage (INF/OUT) to produce pixel-wise classification maps over the full orthomosaics. Classification performance was then quantified through confusion-matrix-derived metrics, including accuracy, precision, recall, and F1-score. Finally, the workflow included a HAPS scalability assessment, explicitly represented in Figure 3 but here described in detail. To simulate a stratospheric observation scenario, the native UAV hyperspectral orthomosaic was spatially resampled to a coarser ground sampling distance comparable to that expected for a HAPS platform (GSD of approximately 8 cm). The purpose of this step was not to simply resize the final classification map, but to evaluate whether the full workflow remained effective under reduced spatial detail. Therefore, after spatial degradation, the feature extraction, standardization, feature selection, classification, and output generation steps were repeated on the resampled dataset. The resulting classification performance was then compared with that obtained from the native UAV-resolution HS dataset. In Tab. 2, the acronym HS_4 refers to the hyperspectral dataset after spatial degradation to the HAPS-like resolution level adopted in this experiment.

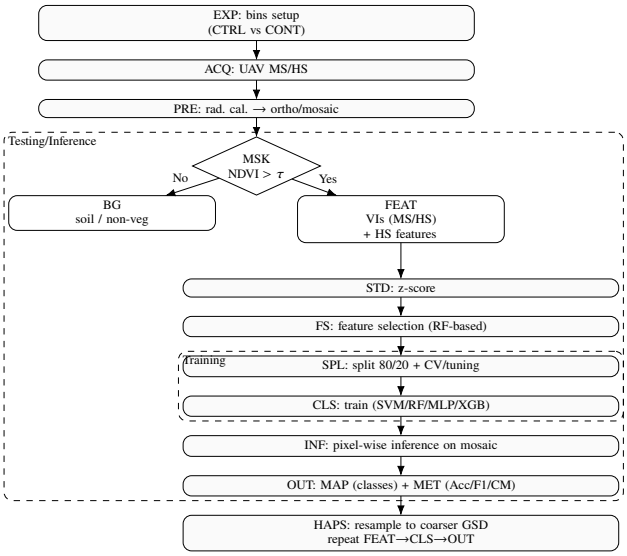

Figure 3: Proposed workflow on HS and MS data.

3 RESULTS

3.1 Canopy spectral signatures: MS vs HS evidence

Spectral "signatures" extracted from the orthomosaics show a consistent separation between control and contaminated canopies. For the multispectral sensor (Fig. 4), mean canopy reflectance trends highlight differences that become more evident in the red-edge/NIR region, which is typically sensitive to canopy structure and chlorophyll-related absorption features.

The hyperspectral signatures (Fig. 5) strengthen this evidence by resolving the spectral response across all 51 bands, and by explicitly comparing the full HS curve against the subset of HS bands corresponding to the MS spectral channels. This visualization supports the interpretation that spectral resolution (i.e., denser sampling across VNIR) provides additional discriminative cues for contamination-driven stress.

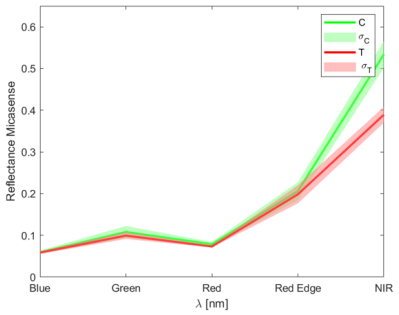

Figure 4: Spectral "signatures" of control bins and contaminated ones for Micasense Altum sensor.

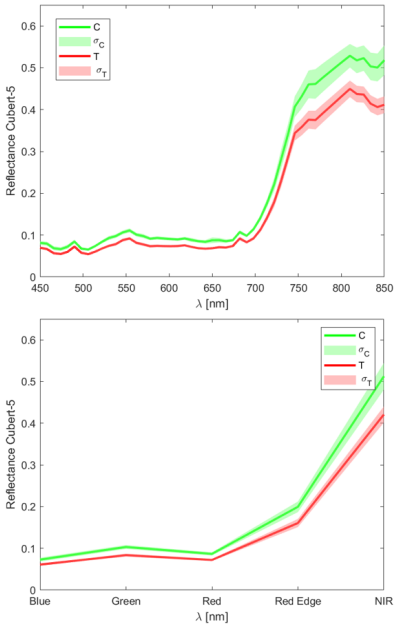

Figure 5: Spectral signatures of control bins and contaminated ones for Cubert Ultris-5 for all 51 bands and for the 5 bands corresponding to the Micasense Altum bands.

Similar spectral separability patterns under stress conditions have been reported in both proximal and UAV-based hyperspectral studies [9], [10].

Table 2: Performance metrics, i.e. accuracy/precision/recall/F1 that are exacted from confusion matrix. HS4 denotes the hyperspectral dataset after spatial degradation to the HAPS-like GSD adopted in the scalability analysis.

Method	Sensors	Accuracy	Precision	Recall	F1
SVM	MS	0.676	0.731	0.720	0.726
	HS	0.805	0.828	0.849	0.838
RF	MS	0.723	0.767	0.767	0.767
	HS	0.781	0.810	0.825	0.818
MLP	MS	0.657	0.716	0.701	0.709
	HS	0.802	0.825	0.846	0.836
XGBoost	MS	0.682	0.736	0.726	0.731
	HS	0.784	0.812	0.828	0.820
SVM	HS_4	0.745	0.743	0.814	0.778

3.2 Visual analysis and numerical performance

Visual inspection reveals systematic differences at the canopy level between the control and contaminated bins, consistent with the nature of the experiment (Fig. 6). This work also notes that NIR-related information appears particularly distinctive for both multispectral and hyperspectral cameras, consistent with stress/structure separability. Pixel-wise classification correctly separates control vs treated bins in most cases; ambiguity is mainly observed for the bin with the alternative contamination level/treatment (x3), in line with the observation (Fig. 7). Numerical accuracies show a consistent advantage for hyperspectral data in multiple models, as shown in Tab. 2. In particular, hyperspectral inputs consistently outperform multispectral data for all tested classifiers and all metrics considered, which allows us to conclude that the higher spectral resolution has a greater impact than the choice of learning algorithm.

For the SVM-HS configuration, the result indicates a strong separability with large true-positive and true-negative counts.

A key step toward HAPS applicability is assessing the robustness of supervised classification when moving to coarser spatial resolutions comparable to stratospheric payloads. To assess HAPS scalability, the hyperspectral orthomosaic was first spatially resampled by a factor of 4 (i.e., its spatial resolution was reduced fourfold) to a coarser GSD representative of a stratospheric acquisition scenario. The classification workflow was then re-applied to the resampled data, including feature extraction and model inference, rather than simply rescaling the output maps. The corresponding results are reported as HS_4 in Tab. 2. This approach allows for evaluating the robustness of the classification workflow under reduced spatial detail, simulating a HAPS-like observation scenario.

4 CONCLUSIONS

This study shows how well a UAV-based bioindication workflow can distinguish between contaminated and control maize grown in semi-controlled environments. The proposed method is based on supervised pixel-wise classification and vegetation masking. Hyperspectral data consistently outperform multispectral imagery across classifiers, confirming the key role of spectral resolution. Additionally, the workflow is specifically made to facilitate scalability toward coarser spatial resolutions, offering a methodological link between future HAPS-based environmental monitoring and UAV observations. Although spatial downsampling cannot fully reproduce stratospheric sensing conditions (e.g., SNR and atmospheric effects), the reported results provide a first-order indication of algorithmic robustness under reduced spatial detail, which is a necessary prerequisite for future HAPS validation campaigns. The

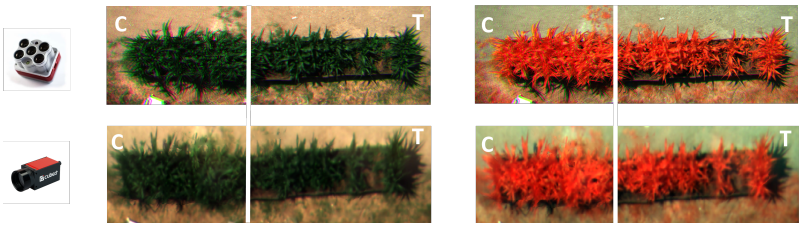

Figure 6: Visual inspection: first column, a RGB composite; second column, a NGB composite.

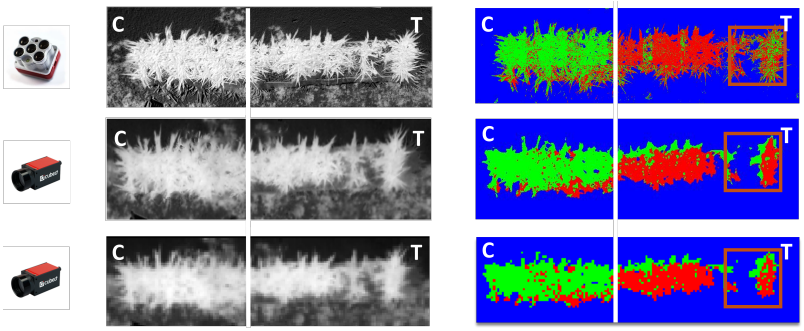

Figure 7: Supervised classification results: first row, example of index (NDVI) and classification for MS; second row, NDVI and classification for HS; third row, NDVI and classification for HS_4

main limitation of this study lies in the reduced spatial extent and controlled nature of the experimental setup; however, the objective was methodological validation rather than large-scale generalization. As larger and more structured training datasets become available, future work will focus on expanding the bioindicator–contaminant combinations and integrating advanced learning techniques, including deep learning approaches for hyperspectral data analysis [11], [12].

ACKNOWLEDGEMENTS

The authors gratefully acknowledge the Italian Space Agency for funding the STOPP project. Additionally, appreciation to CERMANU for managing the experimental setup.

REFERENCES

[1] J. Burger, "Bioindicators: A review of their use in the environmental literature 1970–2005," *Environmental Bioindicators*, vol. 1, no. 2, pp. 136–144, 2006.

[2] C. Boente, L. Salgado, E. Romero-Macías, A. Colina, C. A. López-Sánchez, and J. L. R. Gallego, "Correlation between geochemical and multispectral patterns in an area severely contaminated by former hg-as mining," *ISPRS International Journal of Geo-Information*, vol. 9, no. 12, p. 739, 2020.

[3] S. Gürtler, C. Souza Filho, I. Sanches, M. Alves, and W. Oliveira, "Determination of changes in leaf and canopy spectra of plants grown in soils contaminated with petroleum hydrocarbons," *ISPRS Journal of Photogrammetry and Remote Sensing*, vol. 146, pp. 272–288, 2018.

[4] A. Gholizadeh and V. Kopačková, "Detecting vegetation stress as a soil contamination proxy: A review of optical proximal and remote sensing techniques," *International Journal of Environmental Science and Technology*, vol. 16, pp. 2511–2524, 2019.

[5] M. T. Abdullayeva and G. T. Parpiyev, "The importance of using drones in monitoring agricultural crops," *American Journal Of Agriculture And Horticulture Innovations*, vol. 2, no. 10, pp. 24–31, 2022.

[6] M. Gargiulo et al., "Assessing the impact of soil contamination on maize plant development using uav-based multispectral indices," in *2023 International Conference on Unmanned Aircraft Systems (ICUAS)*, IEEE, 2023, pp. 343–348.

[7] H. Genc, L. Genc, H. Turhan, S. Smith, and J. Nation, "Vegetation indices as indicators of damage by the sunn pest (hemiptera: Scutelleridae) to field grown wheat," *African Journal of Biotechnology*, vol. 7, no. 2, 2008.

[8] D. Moshou et al., "Simultaneous identification of plant stresses and diseases in arable crops using proximal optical sensing and self-organising maps," *Precision Agriculture*, vol. 7, no. 3, pp. 149–164, 2006.

[9] D. Amitrano, L. Cicala, M. De Mizio, and F. Tufano, "Uav hyperspectral characterization of vegetation using entropy-based active sampling for partial least square regression models," *Applied Sciences*, vol. 13, no. 8, p. 4812, 2023.

[10] T. Ishida et al., "A novel approach for vegetation classification using uav-based hyperspectral imaging," *Computers and electronics in agriculture*, vol. 144, pp. 80–85, 2018.

[11] N. Audebert, B. Le Saux, and S. Lefèvre, "Deep learning for classification of hyperspectral data: A comparative review," *IEEE geoscience and remote sensing magazine*, vol. 7, no. 2, pp. 159–173, 2019.

[12] C. Nguyen, V. Sagan, M. Maimaitiyiming, M. Maimaitijiang, S. Bhadra, and M. T. Kwasniewski, "Early detection of plant viral disease using hyperspectral imaging and deep learning," *Sensors*, vol. 21, no. 3, p. 742, 2021.

This work is licensed under a Creative Commons Attribution-No Derivatives 4.0 International License.

MONITORING GLACIER SNOW COVER OF ALPINE GLACIERS WITH THE TENDIS INDEX

N. Genzano *, R. Zinelli, M. Scaioni

Department of Architecture, Built Environment and Construction Engineering, Politecnico di Milano – nicola.genzanoo@polimi.it

KEY WORDS: Snow cover persistence, NDSI, Spectral–temporal index, Landsat, Sentinel-2, Multi-temporal analysis

ABSTRACT:

Mountain glaciers are highly sensitive indicators of climate change, with Alpine glaciers experiencing accelerated mass loss over recent decades. Monitoring these changes is essential to understand their environmental and socio-economic impacts. This study applies the Temporal Normalized Difference Index for Snow cover (TeNDIS), a novel spectral–temporal index designed to quantify glacier snow persistence by exploiting the seasonal evolution of NDSI derived from multi-decadal satellite archives. TeNDIS compares winter and summer NDSI maximum value composites to distinguish persistently snow-covered areas from seasonally exposed surfaces. The method was applied to Landsat 5/8/9 and Sentinel-2 imagery (1985–2024) over four Alpine glaciers: Lauteraar, Mer de Glace, Miage, and Brenva. Results reveal a consistent long-term decline in persistent snow cover across all sites, indicating a progressive reduction of accumulation areas. TeNDIS provides a dynamic, process-oriented framework for long-term glacier monitoring under ongoing climatic warming.

1. INTRODUCTION

Mountain glaciers constitute one of the most dynamic components of the Earth's cryosphere and serve as critical indicators of ongoing climate change. The European Alps, with nearly 4,000 glaciers distributed across Switzerland, Italy, France, and Austria, represent a key mid-latitude glacier system that profoundly influences regional hydrology, ecosystems, and socio-economic sectors. Glacier retreat and mass loss in the Alps have accelerated markedly over recent decades, driven by increased air temperatures and altered precipitation regimes, with far-reaching impacts on freshwater availability and natural hazards.

The seasonal persistence of snow cover plays a pivotal role in modulating surface albedo, energy balance, and melt rates. The timing of snow disappearance determines the exposure of bare ice, thereby influencing the duration and intensity of the ablation season. Under warming conditions, shifts in snow persistence alter the equilibrium between accumulation and ablation zones, directly impacting glacier survival. Consequently, robust and long-term monitoring of glacier snow cover persistence is essential for understanding both short-term variability and long-term climate-driven trends.

Field-based measurements provide high-accuracy observations but remain spatially sparse and logistically constrained in high-altitude environments. In contrast, satellite remote sensing enables systematic, spatially extensive, and multi-decadal observation of glacier surfaces. Optical multispectral imagery has proven particularly effective for snow detection, owing to the distinct spectral signature of snow characterized by high reflectance in the visible range and strong absorption in the shortwave infrared (SWIR). The Normalized Difference Snow Index (NDSI; Dozier, 1989), originally introduced for global snow mapping applications (e.g., Hall et al., 1995), exploits this spectral contrast and has one of the most widely used indices for snow cover detection. Its operational implementation in MODIS products significantly improved the consistency of large-scale snow monitoring (Hall et al., 2002). Further developments demonstrated the capability of NDSI-based approaches to estimate fractional snow cover (e.g., Salomonson and Appel, 2004) and to support persistent snow and ice mapping over extended periods (e.g., Selkowitz and Forster, 2016).

Despite its widespread adoption, traditional NDSI-based methods typically rely on single-date thresholding approaches, implicitly assuming that snow detection is a static classification problem. However, glacier surfaces are intrinsically dynamic and heterogeneous, consisting of fresh snow, firn, bare ice, and debris-covered ice. These surface types may exhibit overlapping spectral responses, particularly under varying illumination conditions. Moreover, single-scene classifications fail to capture the temporal persistence of snow cover.

Recent research has highlighted the value of multi-temporal approaches and adaptive thresholds to improve snow detection in complex alpine environments (e.g., Awasthi & Varade, 2021; Ma and Zhang, 2022). Integrating temporal information with spectral indices can enhances the mapping of snow and ice persistence, offering new perspectives for distinguishing between perennial snow zones and seasonally exposed surfaces under evolving climate conditions. In this context, recent studies have introduced the concept of glacier "phenology", exploiting long-term satellite time series to derive metrics related to the timing and duration of the ablation season. For example, Di Mauro and Fugazza (2022) used MODIS-derived albedo time series to quantify shifts in glacier phenology across the European Alps, revealing widespread albedo decline and a significant increase in ablation season length over the last two decades. Despite recent efforts to incorporate temporal aggregation and adaptive thresholding in snow cover monitoring, few approaches fully exploit the temporal evolution of NDSI to derive a continuous metric of snow persistence.

In this study, we address this methodological gap by applying the Temporal Normalized Difference Index for Snow cover (TeNDIS), a spectral–temporal index specifically designed to quantify and discriminate glacier snow persistence regimes. TeNDIS extends the conceptual foundation of the NDSI by incorporating its temporal evolution derived from multi-decadal satellite archives. The central hypothesis underlying TeNDIS is

* Corresponding author

that distinct glacier surface types exhibit particular temporal NDSI signatures: persistently snow-covered areas maintain consistently high values with limited seasonal variability, whereas seasonally exposed zones show marked intra-annual fluctuations and progressive long-term trends under climatic forcing. By explicitly encoding these temporal behaviors, TeNDIS transforms snow detection from a static classification task into a dynamic process-based characterization of glacier surfaces.

Here, we apply the TeNDIS framework to a continuous archive of optical satellite imagery spanning 1985–2024, integrating data from Landsat 5 TM, Landsat 8/9 OLI/OLI-2, and Sentinel-2 MSI. The methodology is tested on representative Alpine glaciers with contrasting morphologies and climatic settings, such as Mar de Glace, Brenva, Miage and Lauteraar glaciers.

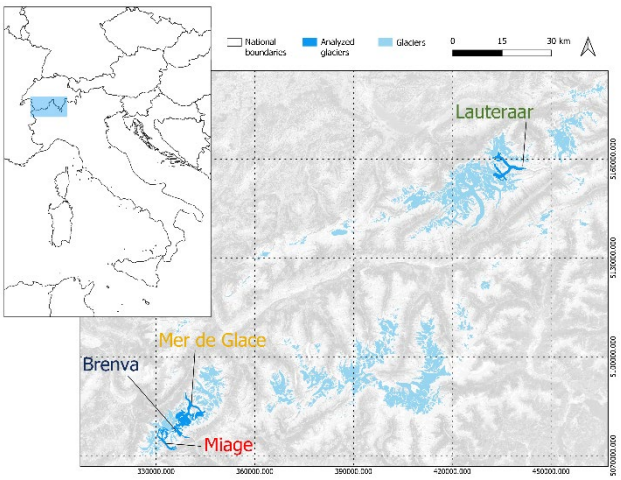

Figure 1. Localization of four glaciers to be investigated

2. DATA AND METHOD

2.1 Used satellite data

Optical satellite data at medium–high spatial resolution, including LANDSAT 5-TM (Thematic Mapper), LANDSAT 8/9-OLI/OLI2 (Operational Land Imager), and Sentinel-2 MSI (Multispectral Instrument), acquired over the period 1985–2024, were employed to investigate the long-term evolution of snow cover over the studied glaciers. These sensors provide multispectral imagery with spatial resolutions ranging from 10 to 30 meters, enabling consistent monitoring of snow cover dynamics over nearly four decades.

The extensive temporal coverage of the Landsat archive, combined with the higher spatial and temporal resolution offered by Sentinel-2 in recent years, allows for a comprehensive reconstruction of seasonal and interannual snow-cover variability, as well as the identification of long-term trends potentially related to climate change.

The satellite image time series were processed and analysed within the Google Earth Engine (GEE) cloud-based platform (Gorelick et al., 2017), which provides access to a vast archive of remote sensing data and high-performance computational resources.

2.2. TeNDIS index

The Temporal Normalized Difference Index for Snow cover (TeNDIS) was preliminarily introduced in Eskandari et al. (2024) with the aim of discriminating among various glacier surface types. Conceptually, TeNDIS builds upon the rationale of the pioneering TeNDI (Temporal NDVI Difference Index; Filizzola et al., 2018), which demonstrated the advantage of adopting a multi-temporal approach for the analysis of spectral indices. Unlike single-date image classification, which may not be sufficient to discriminate land cover types based solely on instantaneous spectral signatures (Jewell, 1989; Van Niel and McVicar, 2004), temporal approaches exploit seasonal variability to enhance separability among surface classes.

TeNDIS utilizesthe Normalized Difference Snow Index (NDSI; Dozier, 1989) as its core spectral variable within a spectral–temporal framework. The underlying assumption is that different glacier surface types, including fresh snow, firn, clean ice, and impure or debris-covered ice (see for example Rossini et al., 2023), exhibit unique seasonal NDSI dynamics. Areas characterized by persistent snow cover maintain consistently high NDSI values throughout the year due to the stable spectral response of snow in the visible and shortwave infrared bands. In contrast, glacier zones subject to seasonal ablation, where winter snow depletes to reveal firn or bare glacier ice show a marked decrease in NDSI values during the summer.

Accordingly, by comparing NDSI values across different periods of the year (e.g., winter versus summer), it becomes possible to distinguish persistently snow-covered areas from seasonally exposed glacier surfaces. To enhance the separability of these glacier cover types based on their spectral–temporal behavior, the TeNDIS (Temporal Normalized Difference Index for Snow cover) is computed as follows:

$$TeNDIS(x, y, t_w, t_s) = NDSI_{MVC}(x, y, t_w) - NDSI_{MVC}(x, y, t_s) \quad (1)$$

where $NDSI_{MVC}$ is the Maximum Value Composite (MVC - Holben, 1986) of the NDSI for each pixel (x,y) during the winter t_w (i.e., January, February, and March) and summer t_s (i.e., July, August and September) periods. It should be noted that the choice to use the maximum value composite of NDSI rather than a single date image has been considered to minimize residual cloud contamination and other possible effects due to different observational conditions (e.g., atmospheric transmittance, satellite view angle).

2.3 TeNDIS implementation

The TeNDIS index was implemented using LANDSAT (321 scenes for Miage, Brenva and Mer de Glase, 407 scenes for Lauterar) and Sentinel-2 (294 scenes for Miage, Brenva and Mer de Glase, 225 scenes for Lauterar) observations according to the following procedure:

- Top of Atmosphere (TOA) imagery acquired between January–March and July–September for the period 1985–2024 was selected from the GEE catalogue. Only scenes with cloud cover lower than 30% were retained.
- It should be noted that Top of Atmosphere (TOA) imagery has been favoured over Bottom of Atmosphere (BOA) imagery in order to maximise consistency within the long-term, multi-sensor archive (1985–2024) and to avoid artefacts or discrepancies resulting from the application of different atmospheric correction algorithms. Furthermore, the MVC technique is used specifically for the normalised difference snow index (NDSI) to mitigate the effects of

residual atmosphere, such as varying transmittance and cloud contamination. These effects can be particularly challenging to correct uniformly in high-altitude alpine environments over four decades.Standard cloud masks provided with TM, OLI/OLI-2, and MSI products were applied to distinguish clear-sky pixels from cloudy ones.

- For each clear pixel, the NDSI was calculated using TOA reflectance values in the green (~0.52–0.60 μm) and shortwave infrared (SWIR; ~1.55–1.75 μm) bands.
- For each glacier pixel and for each year, the TeNDI index was computed according to Equation (1).
- Annual composite images representing glacier coverage were generated, and yearly snow cover was mapped for both glaciers. The Otsu algorithm (Otsu, 1979) was applied to automatically determine the optimal threshold for discriminating snow from non-snow areas.

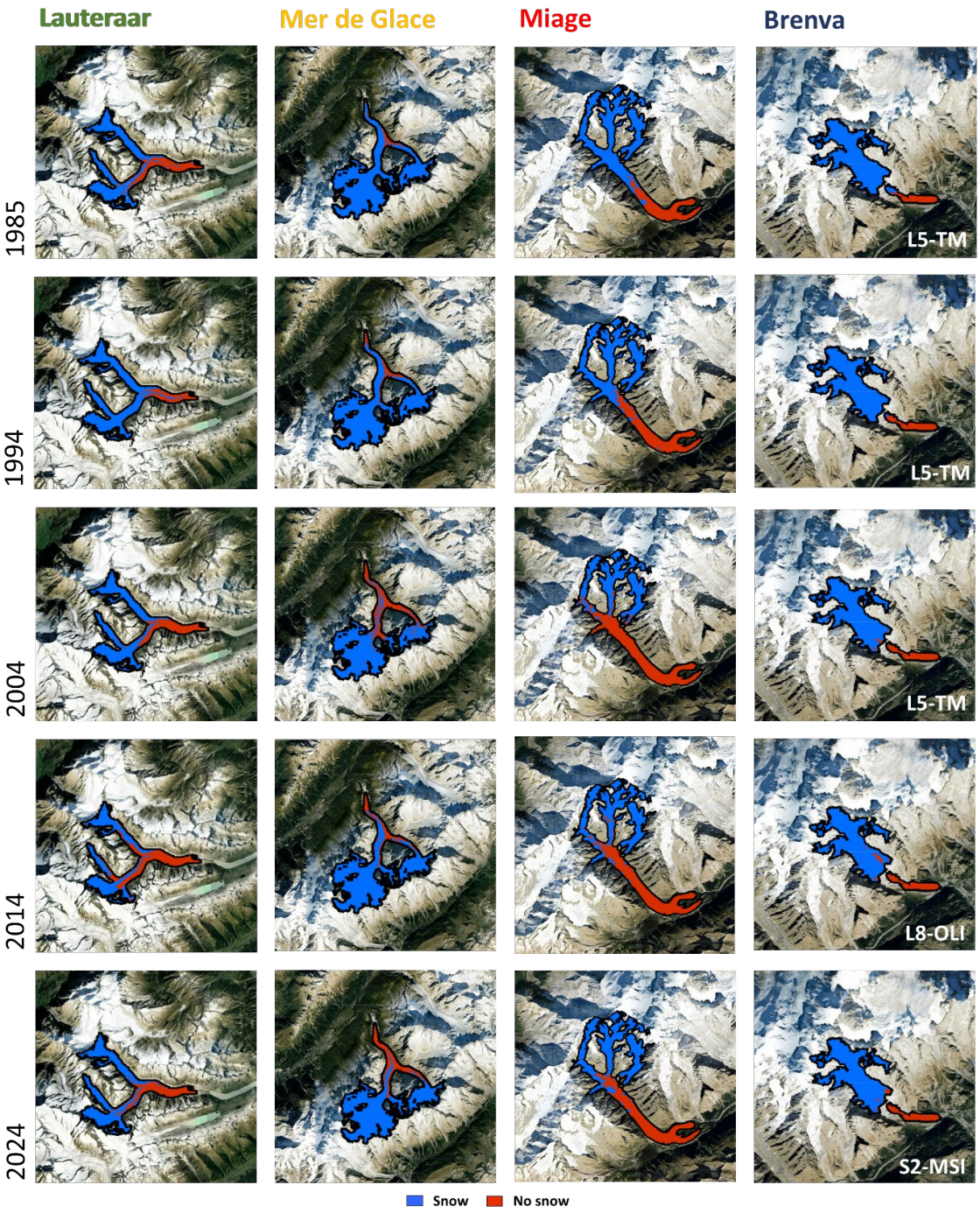

Figure 2. TeNDIS maps based on Landsat and Sentinel 2 observations for Lauteraar, Mer de Glace, Miage, and Brenva Glaciers. In blue are depicted the locations covered by a persistent snow cover, whilst in red those locations not affected by snow coverage during the whole year (background map from Google®).

.

3. RESULTS

Figure 2 presents a time series of TeNDIS-derived maps obtained from L5-TM, L8-OLI, and S2-MSI observations for the four investigated glaciers over the period 1985–2024. In the maps, blue areas indicate glacier portions persistently covered by snow throughout the year, whereas red areas identify zones where snow cover disappears during the summer season. A visual comparison of the maps clearly reveals a progressive reduction in the extent of persistent snow cover for all analyzed glaciers over time.

To further investigate snow cover variability over the 40-year study period (1985–2024), Figure 3 shows the temporal trends of persistent snow cover. For each glacier, the fraction of pixels classified as snow in TeNDIS images derived from L5-TM and L8/9-OLI/OLI-2 observations was calculated. Glacier outlines were obtained from the Alpine glacier inventory by Paul et al. (2020). Only years in which at least 95% of glacier pixels were available for TeNDIS computation were included in the analysis to ensure data reliability.

The trends shown in Figure 3 indicate a clear and consistent decline in persistent snow cover for all investigated glaciers. This decrease suggests a progressive reduction in snow accumulation areas over time. Moreover, the long-term reduction in persistent snow cover detected by TeNDIS is consistent with the well-documented upward shift of the equilibrium line altitude (ELA) and seasonal snow line under ongoing warming. In this sense, TeNDIS acts as a diagnostic remote-sensing indicator of changes in accumulation persistence rather than as a direct estimator of ELA.

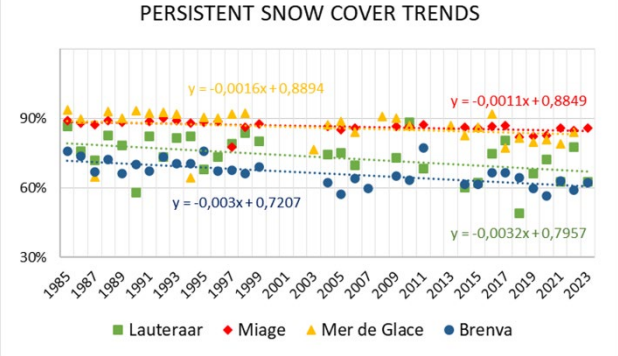

Figure 3. Trends of the persistent snow covers for Lauteraar, Mer de Glace, Miage, and Brenva Glaciers during 1985-2024 according to TeNDIS synthetic images based on LANDSAT 5-TM and LANDSAT 8/8- OLI/OLI2 observations.

4. CONCLUSIONS

In this study, we evaluated the multi-temporal and multi-spectral TeNDIS approach for mapping glacier snow cover using medium-to-high spatial resolution optical imagery. By analyzing approximately four decades of Landsat 5/8/9 and Sentinel-2 data, we assessed the spatial variability and long-term evolution of snow cover over the Lauteraar, Mer de Glace, Miage, and Brenva glaciers. The results consistently indicate a year-by-year decline in persistent snow-covered areas Nevertheless, a dedicated statistical analysis is required to quantitatively assess the significance of the observed trends.Although the proposed methodology requires further validation using independent datasets and/or comparison with alternative snow-mapping approaches, the encouraging results support continued refinement of the method. Future improvements may include the adoption of more advanced cloud-masking techniques beyond standard products and the extension of the analysis to additional glacier systems.

REFERENCES

Awasthi, S., & Varade, D., 2021. Recent advances in the remote sensing of alpine snow: a review. *GIScience & Remote Sensing*, *58*(6), 852–888. https://doi.org/10.1080/15481603.2021.1946938

Di Mauro, B., & Fugazza, D. (2022). Pan-Alpine glacier phenology reveals lowering albedo and increase in ablation season length. *Remote Sensing of Environment*, 279, 113119. https://doi.org/10.1016/J.RSE.2022.113119

Dozier, J., 1989. Spectral signature of alpine snow cover from the Landsat Thematic Mapper. *Remote Sens. Environ*. 28, 9-22. https://doi.org/10.1016/0034-4257(89)90101-6

Eskandari, R., Genzano, N., Fugazza, D., Scaioni, M., 2024. Investigation on Miage/Brenva Glaciers in The Alps From 50s to-date Based on Remote-Sensing Data, *Int. Arch. Photogramm. Remote Sens. Spatial Inf. Sci*., XLVIII-3-2024, 147–154, https://doi.org/10.5194/isprs-archives-XLVIII-3-2024-147-2024

Filizzola, C., Corrado, R., Falconieri, A., Faruolo, M., Genzano, N., Lisi, M., Mazzeo, G., Paciello, R. Pergola, N., Tramutoli, V., 2018: On the use of temporal vegetation indices in support of eligibility controls for EU aids in agriculture. *Int. J. Remote Sens.* 39(14), 4572-4598. https://doi.org/10.1080/01431161.2017.1395973

Gorelick, N., Hancher, M., Dixon, M., Ilyushchenko, S., Thau, D., Moore, R., 2017. Google Earth Engine: Planetary-scale geospatial analysis for everyone. *Remote Sens. Environ.* 202, 18-27. https://doi.org/10.1016/j.rse.2017.06.031

Hall, D.K., Riggs, G.A., Salomonson, V.V., 1995. Development of methods for mapping global snow cover using moderate resolution imaging spectroradiometer data. *Remote Sens. Environ*. 54(2), 127-140, https://doi.org/10.1016/0034-4257(95)00137-P.

Hall, D.K., Riggs, G.A., Salomonson, V.V., Di Girolamo N.E., Bayr, K.J. 2002. MODIS snow-cover products. *Remote Sens. Environ*. 83 (1-2), 181–194, Pages 181-194, https://doi.org/10.1016/S0034-4257(02)00095-0.

Holben, B.N., 1986. Characteristics of Maximum-Value Composite Images from Temporal AVHRR Data. *Int. J. Remote Sens.* 7, 1417-1434. https://doi.org/10.1080/01431168608948945

Jewell, N. 1989. An Evaluation of Multi-Date SPOT Data for Agriculture and Land Use Mapping in the United Kingdom. *Int. J. Remote Sens.* 10, 939-951. https://doi.org/10.1080/01431168908903936

Salomonson, V.V., Appel, I., 2004. Estimating fractional snow cover from MODIS using the normalized difference snow index. *Remote Sens. Environ*. 89 (3), 351–360. https://doi.org/10.1016/j.rse.2003.10.016.

Selkowitz, D.J., Forster, R.R., 2016. An Automated Approach for Mapping Persistent Ice and Snow Cover over High Latitude Regions. *Remote Sensing*, *8*(1), 16. https://doi.org/10.3390/rs8010016.

Ma, Y., Zhang, Y., 2022. Improved on snow cover extraction in mountainous areas based on multi-factor ndsi dynamic threshold. Int. Arch. Photogramm. Remote Sens. Spatial Inf. Sci., XLIII-B3-2022, 771–778, https://doi.org/10.5194/isprs-archives-XLIII-B3-2022-771-2022.

Otsu, N., 1979. A threshold selection method from gray-level histograms. *IEEE Trans. Syst. Man. Cybern*. 9, 62-66. https://doi.org/10.1109/TSMC.1979.4310076

Paul, F., Rastner, P., Azzoni, R.S., Diolaiuti, G., Fugazza, D., Le Bris, R., Nemec, J., Rabatel, A., Ramusovic, M., Schwaizer, G., Smiraglia, C., 2020. Glacier shrinkage in the Alps continues unabated as revealed by a new glacier inventory from Sentinel-2. *Earth Syst. Sci. Data* 12, 1805-1821. https://doi.org/10.5194/essd-12-1805-2020

Rossini, M.; Garzonio, R.; Panigada, C.; Tagliabue, G.; Bramati, G.; Vezzoli, G.; Cogliati, S.; Colombo, R.; Di Mauro, B. Mapping Surface Features of an Alpine Glacier through Multispectral and Thermal Drone Surveys. *Remote Sens.* 2023, 15, 3429. https://doi.org/10.3390/rs15133429"

Van Niel, T.G., Mac Vicar, T.R., 2004. Determining Temporal Windows for Crop Dissemination with Remote Sensing: A Case Study in the South-Eastern Australia. *Comput. Electr. Agric.* 45, 91–108. https://doi.org/10.1016/j.compag.2004.06.003

This work is licensed under a Creative Commons Attribution-No Derivatives 4.0 International License.

MONITORING THE DRYING DYNAMICS OF THE SAL'E PORCUS SALT POND USING SENTINEL-1 TIME SERIES: A PRELIMINARY STUDY FOR CLIMATE-DRIVEN SURFACE EVOLUTION

C. Collu[1,2]*, M. Casu[1,2], I. Nobile[1], C. Nieddu[1], M. Musacchio[3], K. Onačillov[4], J. Šašak[4], Michal Galley[4], M.T. Melis[1]

[1] Dept. of Chemical and Geological Sciences, University of Cagliari, Monserrato, Italy
[2] Dept. of Civil, Constructional and Environmental Engineering, Sapienza University of Rome, Rome, Italy
[3] National Institute of Geophysics and Volcanology (INGV), Rome, Italy
[4] Pavol Jozef Šafárik University in Košice (UPJŠ), Košice, Slovakia.

KEY WORDS: Time Series Analysis, Sentinel-1, Sentinel-2, Climate change, Desiccation dynamics, Salt pond, Surface Hydrology;

ABSTRACT:

Sal'e Porcus, Europe's largest natural salt pond undergoes pronounced seasonal drying and wetting cycles, making it an ideal natural laboratory to investigate climate-driven surface dynamics. This study examines the temporal evolution of the pond's surface over 2015–2024 by integrating Sentinel-1 C-band radar (VV) and Sentinel-2 multispectral (NDWI) time series with local meteorological data, including rainfall and air temperature. Time series were analyzed at weekly, biweekly, and monthly scales to identify the temporal aggregation that best captures the interaction between climatic forcing and surface response. The Standardized Precipitation Evapotranspiration Index (SPEI) was computed using daily precipitation and potential evapotranspiration estimated via the FAO-56 Penman-Monteith equation, with a historical baseline (1984–2014) to standardize deviations from long-term climatology. Pearson correlation analysis indicates moderate relationships between satellite indices and SPEI, strongest at the biweekly scale (NDWI: r = 0.50; VV: r = –0.55), with weaker correlations at the monthly scale due to aggregation effects and surface heterogeneity. Cross-correlation reveals a lag of approximately one month for VV backscatter to respond to SPEI variations, reflecting delayed surface adjustments, including salt crust formation and hydrological inertia. These findings demonstrate the importance of temporal resolution in capturing climate–surface interactions and highlight the combined use of SAR and optical data as a robust approach for monitoring fragile salt-flat ecosystems under changing climatic conditions.

1. INTRODUCTION

Sal'e Porcus is the largest natural salt pond in Europe, located along the central-western coast of Sardinia (Italy), covering more than 3.3 km². Its considerable size, surface homogeneity and marked seasonal variability make it an ideal candidate for satellite calibration and validation (CAL/VAL) activities (Musacchio et al., 2024). In fact, a recent campaign — carried out in the framework of the International Remote Sensing Summer School supported by the Italian Space Agency — has produced the first spectral and LiDAR dataset for the site, leading to the release of a preliminary spectral library of surface minerals and a detailed morphological characterisation of the salt flat (Melis et al., 2024).

Simultaneously, the cyclical desiccation that affects the pond during dry summer periods presents a unique opportunity to study temporal surface processes triggered by climatic and hydrological forcing. In particular, such salt-flat systems are highly sensitive to fluctuations in water presence, evaporation rates, and brine dynamics, which in turn influence surface roughness, dielectric properties and salt crystallization (Delsouc et al., 2020; Verlanti et al.,).

In recent years, the intensification of temperature extremes and the alteration of rainfall regimes have heightened concerns regarding the future stability of these fragile environments. Such climatic pressures are expected to influence not only the timing and duration of wet and dry phases, but also the underlying hydrological and geochemical processes that govern the evolution of salt-flat ecosystems. As evaporation rates increase and precipitation becomes more irregular, the balance between water input, moisture retention, and salt crystallization may shift in unpredictable ways, potentially altering surface properties, mineral formation dynamics, and overall ecosystem resilience.

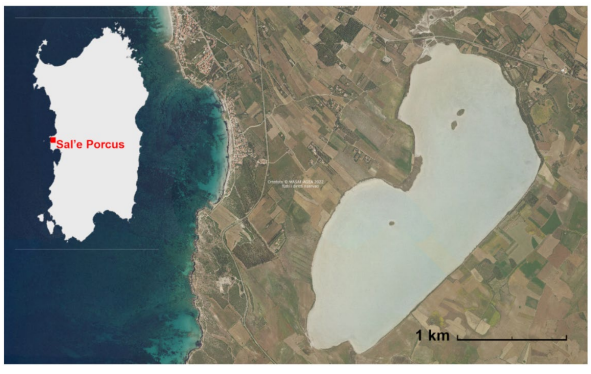

Figure 1. Location of Sal'e Porcus pond.

This preliminary study aims to analyze in detail the temporal evolution of the pond's drying process by integrating Sentinel-1 C-band radar data and Sentinel-2 multispectral time series with available local meteorological observations, including rainfall and air temperature. Time series of Sentinel-1 VV backscatter coefficients and Sentinel-2 NDWI (Normalized Difference Water Index) are used to characterize the surface response across different drying stages. In addition, the incorporation of local climatic data enables the investigation of how variations in surface conditions relate to seasonal meteorological patterns,

* Corresponding author

providing insight into the interplay between environmental dynamics, hydrological evolution, and climatic fluctuations throughout the last ten years.

2. DATA AND METHODS

A multi-source dataset was assembled to investigate the temporal evolution of surface conditions and drying dynamics within the study area. The analysis integrates synthetic aperture radar (SAR) observations, multispectral optical data, and ground-based meteorological measurements, allowing a comprehensive assessment of both surface processes and their relationship with climatic forcing. The combination of radar sensitivity to structural and moisture-related changes with optical indices linked to water content provides a robust framework for characterizing seasonal and interannual variability.

2.1 Data

The analysis relies on satellite data from the Sentinel missions, part of the Copernicus Programme operated by the European Space Agency (ESA). Sentinel-1 provides C-band synthetic aperture radar (SAR) observations, while Sentinel-2 offers multispectral optical imagery across 13 bands. For this study, a total of 465 Sentinel-1 GRD images (VV polarization, ascending orbit, 10 m resolution, 2015–2024) and 545 Sentinel-2 Level-2A images (10–20 m resolution, 2017–2024) were collected and pre-processed using the Google Earth Engine platform. Pre-processing steps speckle filtering border noise correction radiometric terrain normalization for Sentinel-1 (Mullissa et al., 2021), and cloud masking, using Sentinel Hub's Cloud Probability map, the Scene Classification Layer (SCL) in the Level-2A product, applying a probability threshold of 30%, and index computation (e.g., NDWI) for Sentinel-2.
To complement satellite observations, meteorological data were obtained from the San Vero Milis station (ilmeteo.it, 2025), which provides both a long-term historical record (1984–2014) and measurements covering the study period (2015–2024). Daily rainfall, air temperature (maximum, minimum and mean temperature), relative humidity, atmospheric pressure and wind speed were used to assess local climatic variability and to examine the relationship between meteorological forcing and the surface conditions observed in the satellite time series.

2.2 Methods

The analysis employed a multi-step methodological framework to investigate the temporal evolution of the Sal'e Porcus salt pond's drying process and its relationship with climatic forcing. This framework is comprised of three primary components: time series extraction and smoothing, Standardized Precipitation Evapotranspiration Index (SPEI) computation, and correlation analysis. The satellite and meteorological time series were analyzed at multiple temporal resolutions — weekly, biweekly, and monthly — in order to assess the aggregation scale that maximizes the correlation between surface dynamics captured by Sentinel data and local climatic variability. For Sentinel-1 and Sentinel-2, values were averaged over each time window, while for SPEI, cumulative values were computed over the corresponding periods. This approach allowed the investigation of temporal patterns across different scales and the identification of the temporal resolution at which climate–surface interactions are most pronounced, as demonstrated in recent studies on multi-temporal remote sensing and drought indices (Ferrentino et al., 2024; Mueller et al., 2022).

2.2.1 Time Series Extraction and Smoothing

To characterize the surface conditions over time, Sentinel-1 VV backscatter and the Sentinel-2 Normalized Difference Water Index (NDWI) time series were extracted for the study area, covering the 2015–2024 period, calculating the mean value over the basin area. The raw time series data inherently contain noise, particularly due to atmospheric effects, residual cloud contamination, and speckle in the SAR data.
To facilitate the analysis of underlying seasonal and inter-annual trends, the time series were smoothed using the Savitzky–Golay filter (Gorry, 1990; Savitzky & Golay, 1964).

2.2.2 SPEI computation

To quantify the combined influence of precipitation and atmospheric evaporative demand on the study area, the Standardized Precipitation Evapotranspiration Index (SPEI) was computed. SPEI is a widely used drought index based on the difference between precipitation (P) and potential evapotranspiration (PET), providing a standardized measure of water deficit or surplus. Potential evapotranspiration was estimated using the FAO-56 Penman-Monteith equation (Allen et al., 1998), employing daily meteorological observations from the San Vero Milis station for the study period 2015–2024. A historical reference period (1984–2014) was used to fit the probability distribution of the water-balance anomaly (P – PET) for each aggregation scale. The resulting parameters were then applied to standardize the drought index over the full study period (2015–2024). Such an approach ensures that SPEI values reflect departures from the long-term local climatology (Falzoi et al., 2019). The daily water balance (P−PET) was calculated and subsequently aggregated into cumulative sums over weekly, biweekly, and monthly intervals. This procedure resulted in three distinct SPEI time series, each representing climatic forcing over a different temporal integration period.

2.2.3 Correlation Analysis

A comprehensive correlation analysis was performed to investigate the relationship between surface conditions (Sentinel-1 VV and Sentinel-2 NDWI) and the local climate dynamics (SPEI). Pearson correlation coefficients (Benesty et al., 2009) were computed for all combinations of the Sentinel time series and the SPEI, specifically across the weekly, biweekly, and monthly scales. The primary goal was to identify which temporal aggregation scale resulted in the strongest correlation, indicating the most relevant climatic timescale driving the observed surface changes.
Following the identification of the optimal timescale, a cross-correlation analysis was conducted to determine the specific temporal lag between SPEI variations and the satellite responses. This lag represents the system's inherent response time. The final step involved lagged regression modelling to quantify the strength of the relationship at this optimal timescale and lag.

3. RESULTS

The correlation analysis performed to quantify the linear relationship between satellite indices (Sentinel-1 VV and Sentinel-2 NDWI), and the SPEI at three different temporal aggregation scales (weekly, biweekly and monthly), highlights the importance of the aggregation time scale.
The Pearson correlation analysis (Figure 2) shows a moderate relationship between satellite indices and SPEI, with stronger correlations at 14-day temporal scale. The lower correlations at monthly scale likely reflect the smoothing effect of aggregation and the integration of multiple surface processes that weaken linear relationships with SPEI. Overall, the correlations are consistent with previous studies, where moderate values are

common due to satellite data noise and surface heterogeneity (Mliyeh et al., 2025; Mueller et al., 2022). These results highlight the importance of temporal resolution: beweekly windows better capture the dynamic response of surface conditions to climatic forcing.

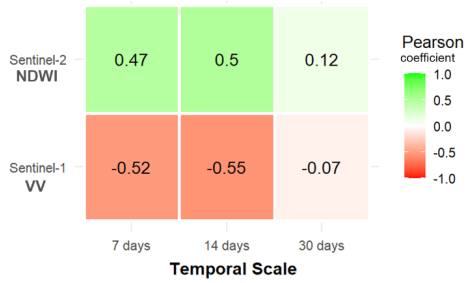

Figure 2. Pearson correlation heatmap.

Based on this finding, the subsequent cross-correlation analysis should focus on the Sentinel-1/SPEI aggregated at the 14-day scale to investigate the specific temporal lag that maximizes this correlation (Figure 3). The result of this analysis shows an optimal lag as -2 time units (-2 bi-weeks = -1 month), thus a change in the climatic water balance (SPEI) requires an average of one month to fully manifest as a change in the surface roughness and dielectric properties of the salt flat, as captured by the Sentinel-1 VV backscatter. The maximum cross-correlation coefficient at the optimal lag is r = - 0.3. This is weaker than the Pearson correlation (r = -0.55). This suggests that the relationship, while significant, is influenced by factors not fully captured by the linear biweekly lag analysis, or that the process of surface evolution (e.g., salt crust formation) is inherently non-linear and complex.

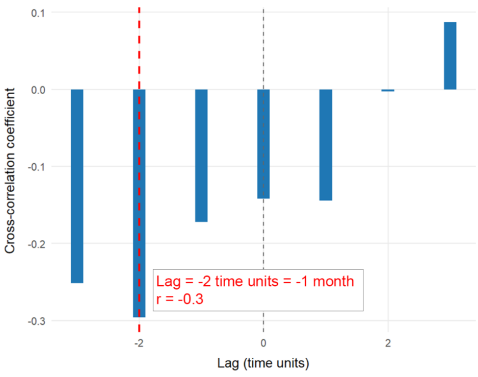

Figure 3. Cross-correlation results with lag analysis.

While the overall relationship shows a clear negative correlation between the Biweekly SPEI and Sentinel-1 VV backscatter, with a notable one-month lag (as established by the cross-correlation), the time series plot reveals periods of discrepancy (Figure 4). Specifically, in years like 2017, the high VV backscatter persisted despite the absence of extreme drought conditions (SPEI near zero). This suggests a physical inertia or legacy effect, where the surface roughness (e.g., highly developed salt crusts) established during a previous dry period requires a substantial or prolonged climatic reversal to be fully erased. Conversely, in 2019, the VV backscatter began to rise sharply earlier than expected based on the SPEI's minimum, indicating that the surface drying process may sometimes be accelerated by non-climatic factors like rapid sub-surface drainage, high evaporation rates, or specific operational regimes of the pond that are not fully captured by the aggregated SPEI index.

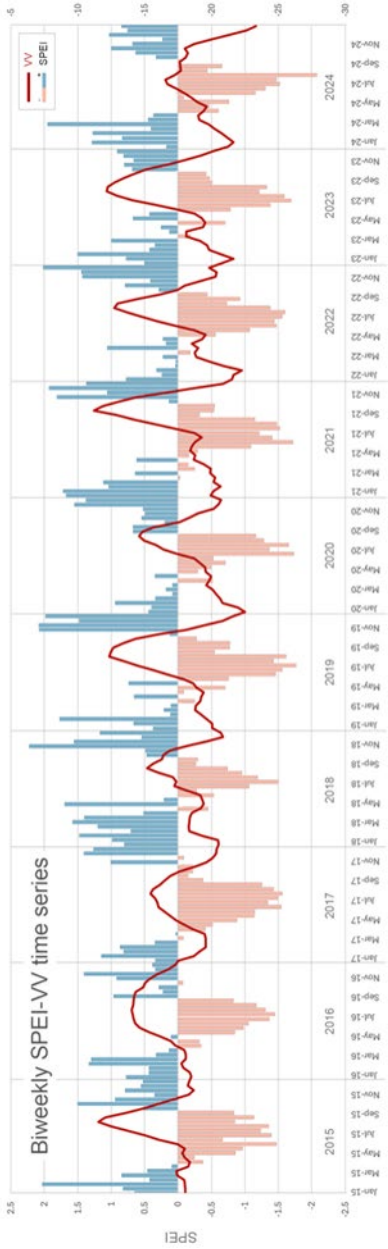

Figure 4. Biweekly time series (2015–2024) comparing the SPEI (bar chart, left y-axis) and the Sentinel-1 VV backscatter coefficient (red line, right y-axis).

4. CONCLUSIONS

The preliminary analysis successfully quantified the temporal relationship between local climatic forcing and the observed surface dynamics of the Sal'e Porcus salt flat over a ten-year period (2015–2024), utilizing the Standardized Precipitation Evapotranspiration Index (SPEI) and Sentinel time series (VV and NDWI). The cross-correlation analysis confirms that the surface evolution of the salt pond, as observed by Sentinel-1 VV backscatter, is a delayed process relative to the climatic forcing. The optimal temporal lag is identified as 1 month, confirming the existence of a lag between climatic input and the full physical manifestation of the surface response. Despite the strong overall correlation, our time series analysis identified instances where climatic variability (SPEI) does not fully explain the observed surface wetting–drying dynamicsof drying/wetting dynamics on the salt flat surface. Despite the strong biweekly SPEI-VV

correlation, analysis of the time series reveals that the wetting–drying dynamics are not fully climatically explained, displaying atypical behaviour such as the persistence of high VV backscatter (e.g., in 2017) due to physical inertia from rough salt crust structures established during prior extreme dry phases (e.g., 2016), or are influenced by local hydrology and management (like drainage). Conversely, the increase of VV backscatter to extreme values during extended desiccation phases (e.g., late 2019) strongly indicates a transition from simple exposure to a more complex, highly scattering crystalline and porous crust texture, underscoring the potential of SAR data for crust morphological characterization.

Future work will focus on periodic field campaigns to collect in-situ measurements of surface and near-surface soil moisture, which will allow for a direct correlation between Sentinel-1 VV backscatter and actual hydrological conditions. These ground-truth observations are expected to improve the interpretation of radar signals in terms of water content and surface roughness, providing a more robust framework to understand the physical processes underlying observed temporal patterns. Additionally, further investigations will aim to refine the analysis of the relationship between surface dynamics and meteorological forcing, exploring potential additional factors such as salt crust development and pond drainage management.

Concurrently, ongoing studies on the site's mineralogy, including the collection of spectral and compositional data from recent campaigns (Melis et al., 2024), offer complementary information that can help link changes in surface reflectance and radar backscatter to specific mineralogical and textural transformations. Integrating these datasets will provide a comprehensive perspective on the coupled hydrological, geochemical, and morphological processes driving the evolution of the Sal'e Porcus salt flat under current and future climatic conditions.

5. REFERENCES

Allen, R. G., Pereira, L. S., Raes, D., & Smith, M. (1998). *Crop evapotranspiration — Guidelines for computing crop water requirements*.

Benesty, J., Chen, J., Huang, Y., & Cohen, I. (2009). *Pearson Correlation Coefficient* (pp. 1–4). https://doi.org/10.1007/978-3-642-00296-0_5

Delsouc, A., Barber, M., Gallaud, A., Grings, F., Vidal-Páez, P., Pérez-Martínez, W., & Briceño-De-Urbaneja, I. (2020). Seasonality Analysis of Sentinel-1 and ALOS-2/PALSAR-2 Backscattered Power over Salar de Aguas Calientes Sur, Chile. *Remote Sensing*, *12*(6), 941. https://doi.org/10.3390/rs12060941

Falzoi, S., Acquaotta, F., Pulina, M. A., & Fratianni, S. (2019). Hydrological drought analysis in Continental Temperate and Mediterranean environment during the period 1981-2017. *Italian Journal of Agrometeorology*, 13–23.

Ferrentino, E., Polcari, M., Silverii, F., Bignami, C., Nunziata, F., Stramondo, S., & Migliaccio, M. (2024). On the joint use of SAR and meteo-climatological information to monitor the Po River under nominal and drought conditions. *International Journal of Applied Earth Observation and Geoinformation*, *133*, 104095. https://doi.org/10.1016/j.jag.2024.104095

Gorry, P. A. (1990). General least-squares smoothing and differentiation by the convolution (Savitzky-Golay) method. *Analytical Chemistry*, *62*(6), 570–573. https://doi.org/10.1021/ac00205a007

ilmeteo.it. (2025). *Archivio storico*. https://www.ilmeteo.it/portale/archivio-meteo/

Melis, M. T., Musacchio, M., Casu, M., Collu, C., Correa, M., Sedda, L., Silvestri, M., Buongiorno, F., Rabuffi, F., Andreucci, S., Kanuk, J., Gallay, M., Onacillova, K., Sasak, J., Naitza, S., Fantini, G., Dessì, F., & Noli, S. (2024). First results of the spectral characterisation of a salt flat in Europe: the Sal 'e Porcus salty pond. *The International Archives of the Photogrammetry, Remote Sensing and Spatial Information Sciences*, *XLVIII-3–2024*, 337–343. https://doi.org/10.5194/isprs-archives-XLVIII-3-2024-337-2024

Mliyeh, M. M., Aqnouy, M., Laaraj, M., Bouizrou, I., Tariq, A., Benaabidate, L., Kraiem, H., & Shitu, K. (2025). Assessing drought dynamics in a semi-arid basin: a multi-index approach using hydrological and remote-sensing indicators. *Environmental Sciences Europe*, *37*(1), 180. https://doi.org/10.1186/s12302-025-01240-4

Mueller, M. M., Dubois, C., Jagdhuber, T., Hellwig, F. M., Pathe, C., Schmullius, C., & Steele-Dunne, S. (2022a). Sentinel-1 Backscatter Time Series for Characterization of Evapotranspiration Dynamics over Temperate Coniferous Forests. *Remote Sensing*, *14*(24), 6384. https://doi.org/10.3390/rs14246384

Mullissa, A., Vollrath, A., Odongo-Braun, C., Slagter, B., Balling, J., Gou, Y., Gorelick, N., & Reiche, J. (2021). Sentinel-1 SAR Backscatter Analysis Ready Data Preparation in Google Earth Engine. *Remote Sensing*, *13*(10), 1954. https://doi.org/10.3390/rs13101954

Musacchio, M., Silvestri, M., Romaniello, V., Casu, M., Buongiorno, M. F., & Melis, M. T. (2024). Comparison of ASI-PRISMA Data, DLR-EnMAP Data, and Field Spectrometer Measurements on "Sale 'e Porcus", a Salty Pond (Sardinia, Italy). Remote Sensing, 16(6), 1092. https://doi.org/10.3390/rs16061092Savitzky, Abraham., & Golay, M. J. E. (1964). Smoothing and Differentiation of Data by Simplified Least Squares Procedures. *Analytical Chemistry*, *36*(8), 1627–1639. https://doi.org/10.1021/ac60214a047

Verlanti, A., Nunziata, F., Migliaccio, M., Melis, M.T., Bignami, C., & Musacchio, M. (2024). Speckle-Related Parameters to Monitor Water Area Coverage of Salty Ponds. IGARSS 2024 - 2024 IEEE International Geoscience and Remote Sensing Symposium, 4815-4818.

This work is licensed under a Creative Commons Attribution-No Derivatives 4.0 International License.

HEAT WAVE AND HEAT STRESS SPACE-TIME PATTERNS ASSESSMENT IN LOMBARDY USING CLIMATE REANALYSIS DATA AND IN SITU MEASUREMENTS

A. Vavassori *, M. Žgela , F. Bissi , M.A. Brovelli

Department of Civil and Environmental Engineering, Politecnico di Milano, Piazza Leonardo da Vinci 32, 20133, Milan, Italy - (alberto.vavassori, matej.zgela, maria.brovelli)@polimi.it, filippo.bissi@mail.polimi.it

KEY WORDS: Heat wave, heat stress, space-time patterns, climate reanalysis, VHR-REA_IT dataset, in situ measurements

ABSTRACT:

Extreme heat represents an increasing climate-related risk in Europe, with particularly severe impacts in densely populated and urbanised regions. This study investigates long-term trends in heat waves (HWs) and spatial-temporal patterns of heat stress (HS) across the Lombardy Region (northern Italy) over the period 1981-2024. HWs are identified using a climatological threshold-based approach applied to daily maximum air temperature, while HS conditions are assessed using the Humidex index derived from high-resolution climate reanalysis data. The analysis integrates ground-based observations from the Italian Air Force Meteorological Service with the VHR-REA_IT reanalysis dataset, enabling a detailed assessment of HW frequency, duration, and intensity, as well as HS exceedance patterns during daytime and nighttime conditions. Results show a clear regional warming trend of up to 1°C per decade, along with a marked increase in the frequency of HW events. The persistence of hazardous HS conditions increases substantially as well. In particular, the frequency of Humidex threshold exceedances rises by up to 5-7 days per decade in lowland and urban areas. To complement the regional-scale analysis, a mobile field survey conducted in the city of Milan provides qualitative insight into fine-scale thermal variability. Overall, the study highlights the intensification of heat-related hazards and demonstrates the value of combining multi-scale datasets to support heat-risk assessments and adaptation planning.

1. INTRODUCTION

Extreme heat is recognised as one of the most critical climate-related risks that Europe will face in the coming decades (European Environment Agency 2024). The growing frequency, duration, and intensity of heat wave (HW) events pose severe threats to human health and ecosystems, contributing to increased mortality, particularly among vulnerable populations such as the elderly (Campbell et al., 2018). Climate projections indicate that these impacts will be especially pronounced in the Mediterranean region, which is identified as a climate change hotspot, where temperatures are expected to rise approximately 20% faster than the global average (Hilmi et al., 2022). The effects of extreme heat are further amplified in dense urban environments due to the urban heat island (UHI) effect, which results in higher temperatures compared to surrounding rural areas, particularly under clear-sky and low-wind conditions that often prevail during HW events (Li et al., 2024).

Although several definitions have been proposed, HWs are traditionally identified using a climatological approach in which the daily maximum temperature is compared with long-term climatological thresholds. Numerous studies have highlighted a relationship between high air temperature and excess mortality during HW events (Campbell et al., 2018). However, the impacts of extreme heat on human health depend on a combination of meteorological variables, including air temperature, humidity, wind speed, and solar radiation. For instance, high humidity reduces the ability of the human body to regulate its internal temperature through evaporation; as a result, dangerous heat stress (HS) conditions may occur at relatively moderate air temperatures when humidity is high (Mora et al., 2017). For this reason, multiple HS indices have been developed that account for near-surface air temperature together with other meteorological parameters (primarily humidity) to assess the impact of extreme heat on human well-being (Yasmeen and Liu, 2019).

The meteorological variables required to identify HW events and compute HS indices are typically measured by in situ weather stations belonging to both authoritative and crowdsourced networks, which provide observations at high temporal resolution. However, professional monitoring networks are often characterised by limited spatial coverage, especially in densely urbanised areas, due to installation, maintenance, and siting constraints (Muller et al., 2013). To enhance the spatial coverage of these observations, citizen weather stations and portable sensors can be exploited, enabling the collection of weather variable transects, typically at the street level (Tsin et al., 2016). Conversely, climate reanalysis products, such as ERA5, combine observations with numerical weather prediction models to deliver spatially continuous datasets; however, their typically coarse spatial resolution limits their ability to capture local-scale thermal variability.

In this work, we integrate climate reanalysis data with in situ measurements to investigate the spatial and temporal patterns of extreme heat over the Lombardy Region in northern Italy. In particular, we leverage the VHR-REA_IT (Very High-Resolution dynamical downscaling of ERA5 Reanalysis over Italy) reanalysis dataset and ground-based measurements of air temperature from the Italian Air Force Meteorological Service network. The objectives are to assess the trends in HW frequency, duration, and intensity, as well as the spatial and temporal patterns of severe HS conditions. To complement the regional-scale analysis of HS, we also present the results of a field survey carried out in the city of Milan using portable sensors, highlighting local-scale variability.

* Corresponding author

2. MATERIALS AND METHODS

2.1 Case study and data

The study focuses on the Lombardy Region in northern Italy, which covers an area of approximately 23,844 km^2 and has a population of about 10 million inhabitants. The metropolitan city of Milan, located in the western part of the region, is the third largest in Italy after Naples and Rome and represents a major economic and urban hub. Lombardy is characterised by pronounced climatic heterogeneity, due to substantial elevation gradients, the presence of large inland water bodies, and extensive urbanised areas. According to the Köppen-Geiger classification (Kottek et al., 2006), Lombardy spans multiple climate types, ranging from humid subtropical conditions in the lowlands (Cfa) to temperate oceanic climates near the Alpine foothills (Cfb) and colder continental (Dfb) and Alpine tundra (EF) climates at higher elevations.

The analysis spans the period 1981-2024 (44 years), which is sufficiently long to investigate recent climatic trends. In order to identify HW events, daily maximum temperature records were extracted from SCIA, the "Italian national system for climate data collection, processing, and dissemination" (Desiato et al., 2011), accessible through a dedicated web portal (https://scia.isprambiente.it/, last access 3 January 2026). This platform integrates data from multiple meteorological networks, including the synoptic network of the Italian Air Force Meteorological Service, which is used in the present study.

For the HS analysis, 2 m air temperature and 2 m dew point temperature for the same period were retrieved from the VHR-REA_IT reanalysis dataset. This product was developed by the Euro-Mediterranean Centre on Climate Change (Centro Euro-Mediterraneo sui Cambiamenti Climatici, CMCC) through the dynamical downscaling of the ERA5 reanalysis using the COSMO-CLM regional climate model (Raffa et al., 2021). The dataset is particularly well-suited for the present analysis, as it provides hourly data at a spatial resolution of 2.2 km over the period 1981-2024, thereby enabling the computation of HS indices at relatively high spatial and temporal resolutions. The dataset was retrieved programmatically through the dedicated Python library *ddsapi* (https://pypi.org/project/ddsapi/, last access 5 January 2026), which provides access to the CMCC Data Delivery System via an Application Programming Interface.

To complement the reanalysis-based HS assessment, crowdsourced data were collected through a field survey conducted with portable MeteoTracker (MT) instruments. The survey was carried out in the city of Milan on 29 July 2025, between approximately 18:20 and 19:30 local time. MT instruments are low-cost, portable weather stations capable of measuring several meteorological variables, including air temperature and relative humidity, while on the go; they also provide an estimate of thermal comfort conditions in terms of Humidex index (Barbano et al., 2024). In particular, three MT sensors were deployed to collect simultaneous transects of meteorological variables across different urban neighbourhoods and adjacent rural areas.

2.2 HW identification and trend

Ground-based station data were used in conjunction with the reanalysis dataset to assess trends in daily maximum air temperature for each calendar day over the Lombardy Region, thereby quantifying the magnitude and seasonal variability of the warming trend.

HWs were identified as periods of at least three consecutive days during which the daily maximum temperature exceeds a climatological threshold. This threshold is defined, for each calendar day, as the 90th percentile of daily maximum temperature computed over the long-term reference period 1981-2024 and smoothed using a centred 15-day moving window (Perkins and Alexander, 2013). The threshold was calculated independently for each calendar day and for each VHR-REA_IT grid pixel. However, given the limited spatial extent of the Lombardy Region and the fact that HWs typically develop at synoptic to regional scales, a day was classified as an HW day only if more than 90% of the pixels exceeded their respective thresholds.

Once all HW events were identified over the study period, their annual frequency, mean duration, and mean intensity were computed. In particular, the intensity of each HW event is defined as the exceedance of daily maximum temperature above the corresponding climatological threshold, averaged over all days of the event and across all pixels. Linear regression was then applied to quantify annual and decadal trends in the frequency, duration, and intensity of HWs.

2.3 HS patterns and trend analysis

HS conditions were assessed using the Humidex index, which is defined as a function of near-surface air temperature and dew point temperature. Accordingly, it was computed using the VHR-REA_IT dataset for each grid pixel. In fact, given the complex topography of the Lombardy Region, HS conditions are expected to vary substantially across the area. The analysis was restricted to the warm half of the year, from April to September, and focused on two representative hours of the day, i.e. 3 PM and 6 AM (local time). The former was selected as it corresponds to mid-afternoon, when daily maximum air temperatures are most likely to occur; the latter was chosen to represent early-morning conditions, when minimum temperatures usually occur during summertime, in order to assess whether thermal discomfort persists even during periods that are normally associated with nighttime relief.

For each of the two reference hours, the annual number of Humidex threshold exceedances was computed for every pixel. A Humidex threshold of 30, corresponding to "some" discomfort, was adopted for nighttime conditions (6 AM), while a higher threshold of 40, corresponding to "great" discomfort, was used for daytime conditions (3 PM) (Schwingshackl et al., 2021; Government of Canada 2024). The average number of yearly exceedance occurrences was then calculated for each decade (1981-1990, 1991-2000, 2001-2010, and 2011-2024). In addition, a trend analysis was performed on the annual exceedance counts to investigate long-term changes in thermal discomfort conditions across the Lombardy Region.

Lastly, the results of the field survey conducted with MT instruments are presented to investigate fine-scale spatial variations in air temperature, relative humidity, and the corresponding Humidex across different parts of the city of Milan. These observations provide high-resolution, street-level information that complements the regional-scale analysis. The results are presented qualitatively and represent a snapshot of thermal conditions during a single time window in the late afternoon.

3. RESULTS AND DISCUSSION

The decadal trend in daily maximum temperatures over the period 1981-2024 reveals a clear and spatially consistent warming across the Lombardy Region, with rates reaching up to 1°C per decade and some intra-annual variability (Figure 1). The most pronounced warming occurs during the summer months, particularly in June, whereas only the second half of September does not show a significant trend. Overall, the ground-station dataset indicates slightly stronger warming trends than the reanalysis product; nevertheless, the two datasets show good agreement in both magnitude and temporal evolution.

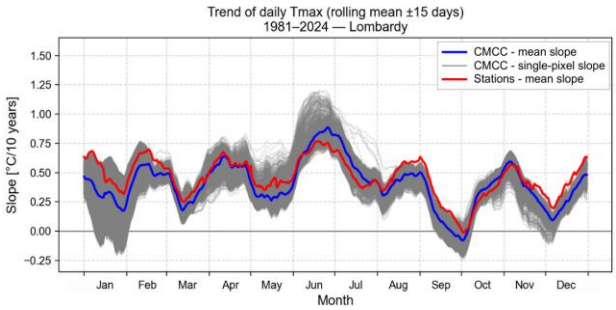

Figure 1. Temporal trend of daily maximum temperature in Lombardy (temperature series were smoothed using a ±15-day rolling mean).

In parallel with the increase in daily maximum temperatures, the HW analysis highlights a substantial rise in both the annual number of HW events and the corresponding total number of HW days. The trend analysis indicates that the number of HW events increases by 1.1 per decade. In contrast, the average duration and mean intensity of individual HW events exhibit weak upward trends, as illustrated in Figure 2.

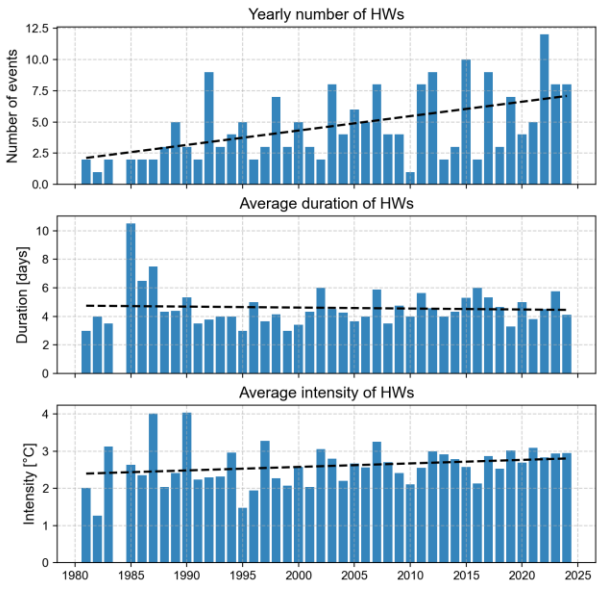

Figure 2. Annual number, average duration, and average intensity of HW events in Lombardy Region.

The increasing frequency of HWs is accompanied by a growing persistence of hazardous thermal comfort conditions during the warm season, as reflected by the Humidex index. Notably, distinct spatial patterns emerge between daytime and nighttime conditions. During the daytime, thermal discomfort is strongly modulated by elevation, with lower-elevation areas experiencing more severe HS conditions. During the nighttime, however, large urban centres clearly stand out as hotspots of thermal discomfort, reflecting the influence of the UHI effect.

The annual average number of Humidex threshold exceedances increases significantly over the decades. The trend analysis highlights pronounced spatial heterogeneity in heat-related discomfort trends, consistent with the complex topography of the region (Figure 3). In particular, a significant decadal increase in the number of days with great discomfort (Humidex > 40 at 3 PM) is observed, reaching up to 7 additional days per decade in lowland areas. A comparable increase is also detected during the early morning hours, reflecting the rising frequency of tropical nights in summer; in this case, the trend in nighttime thermal discomfort (Humidex > 30 at 6 AM) reaches up to 5 additional days per decade in the lowland areas.

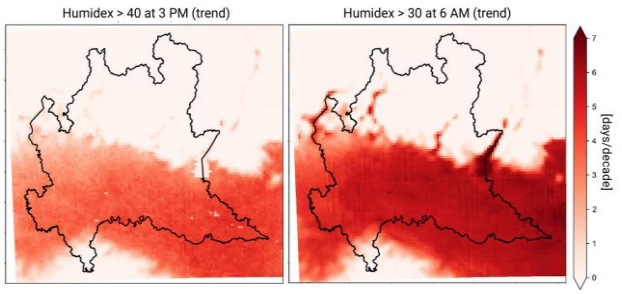

Figure 3. Average decadal increase in the number of days with severe thermal discomfort conditions at (Humidex > 40 at 3 PM and Humidex > 30 at 6 AM).

Lastly, the map derived from the in situ survey conducted with MT instruments depicts the spatial variability of the Humidex index along three transects across the city of Milan (Figure 4).

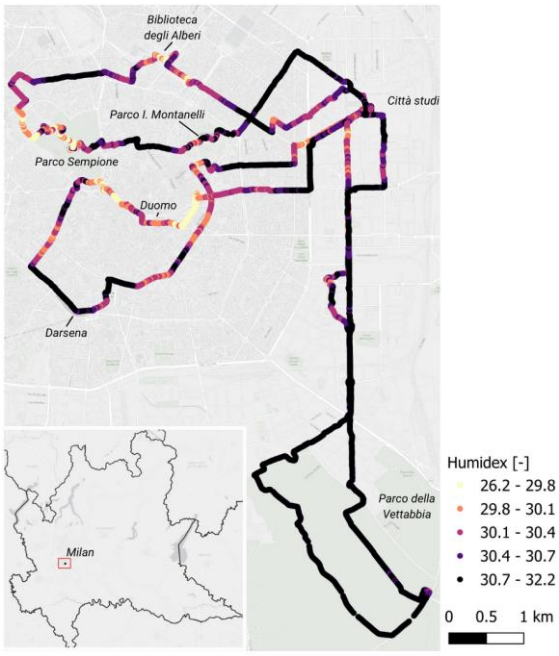

Figure 4. Humidex index recorded by MT instruments between 18:20 and 19:30 on 29th July 2025 in the city of Milan.

Higher Humidex values are observed in areas characterised by either elevated air temperature or higher relative humidity (or both). Air temperature is generally higher within the dense

urban fabric, while a clear cooling effect (approximately 1-2°C) is evident in urban parks and becomes more pronounced toward peri-urban and rural areas. In contrast, relative humidity tends to be lower in the urban core and higher in greener and rural zones, resulting in a partially compensating effect and, overall, a limited spatial variability of the Humidex across the study area.

It is important to note that the survey was conducted on a day without pronounced HS conditions (maximum air temperature < 30 °C and relative humidity < 45%) and therefore does not represent extreme summer conditions. Rather, it provides a baseline snapshot of local-scale thermal discomfort patterns, offering useful insight into the spatial structure of heat conditions within the urban environment.

4. CONCLUSIONS

This study presents an integrated assessment of HW and HS spatial and temporal patterns across the Lombardy Region by combining long-term in situ observations, high-resolution climate reanalysis data, and mobile field measurements.

The results reveal a clear and spatially consistent warming trend over the period 1981-2024, along with a substantial increase in the frequency of HW events. The analysis of HS highlights spatial heterogeneity in the pattern of thermal discomfort conditions, driven by the complex topography and strong urbanisation of the study area. The frequency of HS threshold exceedances increases markedly over time, with trends reaching up to approximately 5-7 additional days per decade in lowland and urban areas. These results underscore the importance of complementing the HW analysis with HS metrics to better understand the trends in heat-related risks.

Overall, this work highlights the intensification of heat-related hazards in the Lombardy Region and emphasises the need for targeted regional adaptation strategies. While Lombardy represents a suitable test bed, due to the topographic diversity and high urbanisation, the broader objective is to develop a scalable, open-source methodology that enables the assessment of heat extremes and their impacts at the Italian and continental scales.

ACKNOWLEDGEMENTS

This study was carried out within the Space It Up! project funded by the Italian Space Agency, ASI, and the Ministry of University and Research, MUR, under contract n. 2024-5-E.0 - CUP n. I53D24000060005.

REFERENCES

Barbano, F., Brattich, E., Cintolesi, C. et al., 2024. Performance Evaluation of MeteoTracker Mobile Sensor for Outdoor Applications. *Atmospheric Measurement Techniques*, 17(10) pp. 3255-3278. doi.org/10.5194/amt-17-3255-2024.

Campbell, S., Remenyi, T.A., White, C.J., Johnston, F.H., 2018. Heatwave and Health Impact Research: A Global Review. *Health & Place*, 53, pp. 210-18. doi.org/10.1016/j.healthplace.2018.08.017.

Desiato, F., Fioravanti, G., Fraschetti, P., Perconti, W., Toreti, A., 2011. Climate Indicators for Italy: Calculation and Dissemination. *Advances in Science and Research*, 6(1), pp. 147-50. doi.org/10.5194/asr-6-147-2011.

European Environment Agency, 2024. *European climate risk assessment*, Copenhagen. https://www.eea.europa.eu/en/analysis/publications/europeanclimate-risk-assessment (29 October 2025).

Government of Canada, Canadian Centre for Occupational Health and Safety, 2024. CCOHS: Humidex Rating and Work. https://www.ccohs.ca/oshanswers/phys_agents/humidex.html (28 August 2025).

Hilmi, N., Ali, E., Cols, J.C. et al., 2022. IPCC AR6 WGII Cross-Chapter Paper 4: Mediterranean Region. *EGU General Assembly 2022*, Vienna, Austria. doi.org/10.5194/egusphere-egu22-10590.

Kottek, M., Grieser, J., Beck, C., Rudolf, B., Rubel, F., 2006. World Map of the Köppen-Geiger Climate Classification Updated. *Meteorologische Zeitschrift*, 15(3), pp. 259-263. doi.org/10.1127/0941-2948/2006/0130.

Li, X., Wang, G., Zaitchik, B., Hsu, A., Chakraborty, Tc., 2024. Sensitivity and Vulnerability to Summer Heat Extremes in Major Cities of the United States. *Environmental Research Letters*, 19(9), 094039. doi.org/10.1088/1748-9326/ad6c64.

Mora, C., Dousset, B., Caldwell, I.R. et al., 2017. Global Risk of Deadly Heat. *Nature Climate Change*, 7(7), pp. 501-506. doi.org/10.1038/nclimate3322.

Muller, C.L., Chapman, L., Grimmond, C.S.B., Duick T.Y., and Cai, X., 2013. Sensors and the City: A Review of Urban Meteorological Networks. *International Journal of Climatology*, 33(7), pp. 1585-1600. doi.org/10.1002/joc.3678.

Perkins, S.E., Alexander, L.V., 2013. On the Measurement of Heat Waves. *Journal of Climate*, 26(13), pp. 4500-4517. doi.org/10.1175/JCLI-D-12-00383.1.

Raffa, M., Reder, A., Marras, G.F. et al., 2021. VHR-REA_IT Dataset: Very High Resolution Dynamical Downscaling of ERA5 Reanalysis over Italy by COSMO-CLM. *Data*, 6(8), 88. doi.org/10.3390/data6080088.

Schwingshackl, C., Sillmann, J., Vicedo-Cabrera, A.M., Sandstad, M., Aunan, K., 2021. Heat Stress Indicators in CMIP6: Estimating Future Trends and Exceedances of Impact-Relevant Thresholds. *Earth's Future*, 9(3), e2020EF001885. doi.org/10.1029/2020EF001885.

Tsin, P.K., Knudby, A., Scott Krayenhoff, E., Ho, H.C., Brauer, M., Henderson, S.B., 2016. Microscale Mobile Monitoring of Urban Air Temperature. *Urban Climate*, 18, pp. 58-72. doi.org/10.1016/j.uclim.2016.10.001.

Yasmeen, S., Liu, H., 2019. Evaluation of Thermal Comfort and Heat Stress Indices in Different Countries and Regions – A Review. *IOP Conference Series: Materials Science and Engineering*, 609(59), 052037. doi.org/10.1088/1757-899X/609/5/052037.

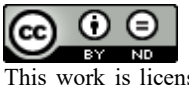

This work is licensed under a Creative Commons Attribution-No Derivatives 4.0 International License.

LONG TERM "X" PRESERVATION AND LONG TIME SERIES GENERATION FOR CLIMATE CHANGE

M.Albani[1] , R.Biasutti[1], I. Maggio[2*], S.Folco[2]

[2]STARION Italia S.p.A., Frascati, Italy – (i.maggio, s.folco)@stariongroup.eu
[1]European Space Agency, ESRIN, Frascati, Italy – (mirko.albani, roberto.biasutti)@esa.int

KEY WORDS: Data Preservation, Lifecycle, Data Valorisation, Earth Observation, Heritage Data Programme, Long Time Data Series, Fundamental Climate Data Record, European Space Agency.

ABSTRACT:

The need for accessing historical Earth Observation (EO) data series strongly increased in the last ten years, particularly for long-term science and environmental monitoring applications. This trend is likely to increase even more in the future, in particular regarding the growing interest in global change monitoring which is driving users to request time-series of data spanning 20 years and more. The contents of EO data archives are continuously growing from a few years to decades and therefore, their value as a scientific time-series is ever-increasing. There is a strong need to preserve the EO space data without time constraints and to ensure that they are accessible and exploitable by the community. The preservation of EO space data can also be considered as a responsibility of the Space Agencies or data owners as they constitute a humankind asset. ESA EO Heritage Data Holdings consists of 150+ ESA and Third Party missions (TPM) & ESA EO Campaigns data (mid 70's) providing a unique capability to look back in time. These assets are preserved, maintained accessible and curated in order to recover unique data from old media and private/public entities not providing access and generate new products from heritage data and build long time series with newer missions. The Heritage Space Programme responds to the mandate of preserving, making accessible, and valorising ESA heritage space data and associated information holdings generated by payloads and instruments on-board space platforms from ESA and ESA-managed TPM with a strong focus on their accessibility and exploitability.

1. INTRODUCTION

The ESA Heritage Space Programme (HSP) responds to the mandate of preserving, making accessible, and valorising ESA heritage space data and associated information holdings generated by payloads and instruments on-board space platforms from ESA and ESA-managed TPM with a strong focus on their accessibility and exploitability. Over 40 Earth Observation missions and 80 EO campaigns are included in the Heritage Space programme.

Figure 1. Missions under Heritage Space Programme

As part of the programme activities, a particular focus is put on the recovery, reprocessing and the generation of long time series of coherent data in support of climate change monitoring activities, needs and related applications.

1.1 ESA heritage Space Programme

The Earth Observation part of the ESA Heritage Space Programme covers data from ESA missions and TPM available at ESA through specific agreements nominally starting five years after the effective end of life of the mission or five years after end of the agreement (in case of the TPMs). The ESA Heritage Space Programme consists of five main streams of activities in Earth Observation:

1. Heritage Space ESA Inter-directorate Joint Activities
2. EO Heritage Space International Cooperation and Outreach
3. EO Space Data Preservation Systems and Services
4. EO Heritage Space Missions Discovery and Access
5. EO Heritage Space Missions Specific Activities

The last two areas focus particularly on the ESA Historical Dataset rescuing, preservation and valorisation according to user communities' needs. The results of user consultations aimed at capturing and understanding Earth Science users' needs in terms of long-term preservation (including accessibility and exploitability aspects) has highlighted that the preservation of Earth Science data and associated knowledge is vital to support their research and application activities. The same need was also identified in the frame of discussions and cooperation ongoing between the Data Access and Preservation (DAP) Working Group European space members and ESA Climate Change Initiative (CCI) representatives and projects [3].

The definitions of datasets composing the Fundamental Climate Data Records (FCDR) (i.e. processing levels and algorithms, formats, quality, orthorectification, etc.) have big impacts on the CCI projects' products and results and need to be clearly identified and documented.

ESA Earth observation data is freely available to the public, scientists, and commercial users and available on the ESA Earth Online Portal [4]. Access is granted after user registration. In cases where products are to be generated upon specific user requests, or due to access policy, technical and/or financial constraints, access to some datasets is subject to prior approval. This group of datasets is called the 'restrained datasets', requiring from the user a data access request. Upon approval, data is always provided free of charge.

The ESA Earth Online Portal [4] functions as access point for a wide variety of Earth observation resources. It features a directory to locate available missions and datasets and provides direct access to satellite data, operational news, events and tools in support of the data use.

* Corresponding author

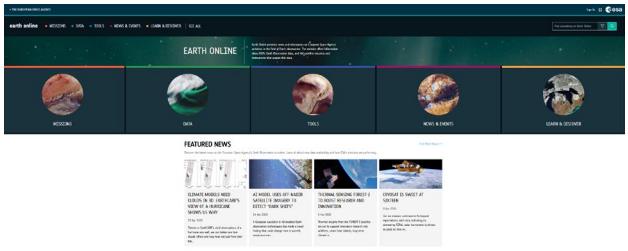

Figure 2. ESA Earth Online Portal

2. LONG TIME DATA SERIES GENERATION

The management of ESA EO data holdings (including data from TPM's archived at ESA) is formally covered within the ESA Heritage Space Programme starting 5 years after their end of life (or end of ESA agreement).

The ESA involvement in the last 45 years on TPM missions could notably differ mission to mission, ranging from the full ground segment chain (task, acquire, process and data delivery) to only data delivery. For this reason, the holding could be quite different: for some missions we have from the raw data (i.e. satellite data stream) for other only the L1 processed data.

The following set of activities is being implemented in accordance with the LTDP Core standard documents (i.e. EO Data Preservation Guidelines Best Practices [1], EO Preserved Dataset Content (PDSC) [1], the Long Term Preservation of Earth Observation Space Data: Preservation Workflow [1]) defined in cooperation with international partners and organisations:

1. Assessment of archived data and information holdings versus "Preserved Dataset Content Best Practice" [1] for all ESA and ESA managed TPMs.
2. Consolidation of Level-0 (or Level-1 if Level-0 is not available) datasets (and associated information), and generation of two copies to be stored in two different locations.
3. Ingestion in robotic tape libraries in the format of Open Archival Information System (OAIS) standard Submission Information Packages (SIPs).
4. Full datasets reprocessing, when feasible, for alignment with the most recent or future missions.
5. Ensuring basic discoverability and dissemination through ESA standard systems.
6. Progressive historical archives rationalisation.

The Section 2 is organised considering the Long Time Data Series projects managed and currently under finalization in the frame of the Heritage Space Programme.

2.1 SEASAT Recovery and Reprocessing

The satellite was launched in 1978 by NASA's Jet Propulsion Laboratory, and was the first satellite designed for remote sensing of the Earth's oceans with the first Synthetic Aperture Radar (SAR) onboard. Its data over Europe were acquired by the European Space Agency in the Oakhanger-UK station. The activity started with the recovery of the complete Seasat-SAR (L-band SAR) data holdings available at ESA and acquired during the short operational time span of the mission (August to October 1978). During its brief lifetime of just over 100 days, the satellite acquired information on ocean phenomena, such as surface and internal waves, currents and sea-surface winds for the study of ocean circulation. It also captured imagery of glaciers, sea ice, coastal regions, volcanoes, forests and land cover. These data (all Level-0 acquired over Europe and a few higher-level products) were migrated in the past years from old technology media to new ones and were stored, together with some supporting documentation, at ESA-ESRIN (Italy) and at Deutsches Zentrum für Luft-und Raumfahrt (DLR). In the framework of this activity, the information necessary to understand and use the Seasat-SAR data was recovered.

Figure 3 – ESA's Seasat data holdings coverage

The information on SAR data format has allowed the Level-0 data to be read again and the visualisation of the available higher-level products through proper configuration of commercial tools. The following steps consisted of the definition of a consolidation procedure for the SAR dataset, in the inventorying and consolidation of the full dataset and of the associated documentation paving the way for any possible future exploitation. Due to the unavailability of the original data processor and therefore, the impossibility of re-processing Level-0 data, the Level-1 recovered products were finally used in a pilot application exercise for glaciers monitoring over Greenland in combination with data from ERS-2 mission to demonstrate the achievements and usefulness of this recovery exercise. The project was the first practical exercise of historical Earth Observation space-borne dataset recovery based on the application of the LTDP Guidelines [1] and provided as such also a valuable contribution for their consolidation and improvement. Comparing data from three generations of radar missions – Seasat, ERS and Sentinel-1 – the retreat of two large glaciers in southeast Greenland over a 36-year period is evident in figure 4 below. This preliminary analysis shows that the effects of climate change on the world's second largest ice sheet have had a major impact over the past three decades. The glaciers show significant retreat, with the upper glacier receding by about 5.5 km over the past 36 years. This melt is contributing to sea-level rise and the release of more freshwater into the North Atlantic.

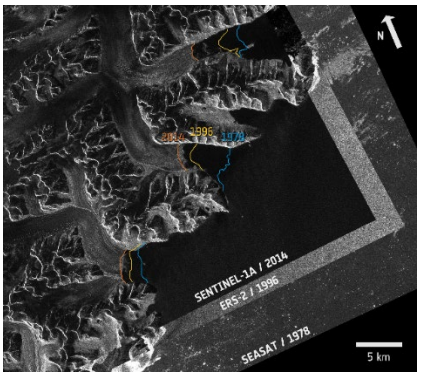

Figure 4 – Greenland glaciers seen by three generations of radar missions

2.2 JERS-1/SEASAT/ALOS – L-BAND RADAR

The importance of L-band radar has been analysed in M. Ottinger and C. Kuenzer, 2020 (https://doi.org/10.3390/rs12142228), L-

band SAR is particularly useful for geoscientific research on wetland and forest change mapping. The capability to penetrate canopy with long radar wavelength (L-band SAR) has been widely applied and investigated for mapping and monitoring of flooded vegetation, the retrieval of aboveground biomass, and the estimation of soil moisture and coastal area monitoring. Human activities and climate change-induced impacts are currently causing land degradation, deforestation and land use change. Long term data series are very important to address research into ecosystems sustainability and land modification climate-change-related, both in the past decades, in current days with SAR L-Band satellites such as the SAOCOM-1 constellation (Argentina’s space agency CONAE) and in the future with the proposed ESA’s ROSE-L. The recovery and consolidation of the SEASAT SAR heritage mission dataset available at ESA has been aligned with JERS-1 L-Band SAR and ALOS PALSAR missions data in terms of processing chain and output format. As a result of these activities, the complete SEASAT and JERS-1 SAR datasets have been reprocessed and aligned to the more recent ALOS PALSAR dataset producing a long time series of coherent data spanning from 1978 to 2011 (with gaps between the three missions operational lifetime). These SAR data are now accessible on an open and free basis for all users through ESA.
JERS-1, launched in 1992 by JAXA, carried on-board an L-band HH polarization SAR instrument and an optical VNIR/SWIR one (unfortunately the SWIR broke at the beginning of the operations) up to 1998. ESA acquired, process and disseminate (during the satellite lifetime through a commercial partner, now directly) JERS-1 data in Tromsø (N) and Fucino (I) ground stations. JERS-1 optical instrument (OPS) had 4 Bands, 3 looking at nadir and the 4th one (same wavelength of the 3rd) with off-nadir viewing (15.33 forward in-flight direction) allowing to make stereo pairs (an effective two-line stereoscopic along-track imaging capability). The stereo images are useful for geomorphology and digital elevation model (DEM) construction. These data are accessible as well on an open and free basis for all users through ESA. ALOS-1 (aka Daichi), launched in 2006 by JAXA, carried on board a polarimetric L-band SAR (PALSAR) instrument and 2 optical instruments: PRISM (Panchromatic Remote-sensing Instrument for Stereo Mapping) with 2.5m resolution and AVNIR-2 (Advanced Visible and Near-Infrared Radiometer 2, and evolution of the sensor that was present on ADEOS) with 4 bands at 10m. The mission ended in 2011. At the time, PRISM data were of extremely high resolution and are now often used to verify the geometry of other satellites from that period. PALSAR and AVNIR-2 data are accessible on free basis (a simple registration is needed) for all non-commercial users through ESA.

2.3 LANDSAT Long Time Data Series

USGS (United States Geological Survey) Landsat satellites’ series are the world's longest running system of satellites for optical remote sensing of land, coastal areas, and shallow waters. ESA’s data acquisitions, started in 1975, were part of an international agreement to get, to store and to distribute data over Europe and Africa sectors. The ESA Landsat dataset is a unique heritage to maintain and valorise for its peculiarity and historical value. Landsat satellites hosted onboard different types of optical medium-resolution sensors, evolved with the evolution of the satellite and technical evolutions, starting with MSS (MultiSpectral Scanner) instrument with only 4 bands in the VIS-NIR, going through TM (Thematic Mapper) and ETM+ (Enhanced Thematic Mapper Plus), arriving now to the updated OLI-TIRS (Operational Land Imager - Thermal Infrared Sensor) with 9 band in VIS-NIR-SWIR and also two band in the Thermal Infrared.

The objectives of the Landsat Series are to:

1. Image repetitively Earth's land and coastal areas with the aim of monitoring changes to those areas over time.
2. Provide moderate-resolution optical remote sensing for land, coastal areas and shallow waters.
3. Provide Earth observation data to support work in agriculture, geology, forestry, education, mapping, emergency response and disaster relief, as well as providing a long-term record of natural and human-induced changes to the Earth.

The programme opened entirely new fields of research, providing insights into geologic, agricultural, and land-use surveys, eventually leading to new paths of resource exploration - in all, for a better understanding of our planet's system. The success of the Landsat programme stimulated new approaches to data analysis and gave impetus to new sensor designs: for instance, the Copernicus Sentinel-2 sensor was designed in order to keep full compatibility with this fundamental dataset and expand it in terms of spatial resolution, spectral band set and revisit frequency. From 1975, ESA began with its own ground systems, to acquire, process and archive data from Landsat, under the Earthnet program. Starting with a single satellite ground station, located in Fucino (Italy), the acquisition capability was increased in the following years with Kiruna (Sweden– operating April to October), Maspalomas (Canary Islands – Spain – operating on campaigns), Matera (Italy) and Neustrelitz (Germany –Landsat 7 only) plus Landsat 5 data acquired with DLR portable station (Bishkek, Chetumal and Libreville). At the time being the satellites did not have a recorder on board, therefore the data could be taken only during the visibility of a ground station. The resulting dataset of the seven Landsat satellites, with over 1.8 million scenes, is now fully available under the Heritage Space Programme as open and free. As part of the International Ground Station (IGS) community, ESA is continuously maintaining efforts to distribute new Landsat 8 data under Earthnet’s TPM.
ESA's 45 years’ worth of Landsat historical data observed over Continental Europe, African regions and the Arctic has become massive. Major efforts have been undertaken to improve processing and then produce the most up to date Level-1 products for the community. The Multi Spectral Scanner (MSS) instrument on board the Landsat 1 to 5 satellites was built by SBRC (Santa Barbara Research Center) of Hughes Aircraft Company in Goleta, CA. In the context of the Landsat archive reprocessing, major improvements have been conducted regarding the MSS geometric processing. The product generation system of MSS has been aligned to the TM and ETM+ ones. The MSS telemetry is generally affected by missing and corrupted data, mainly because of mission ageing and archive degradation, resulting in a poor quality geometric model. The orbit, attitude and data from the Payload Control Data (PCD) stream are generally used to compute the geometric model. To overcome corrupted data issues, satellite position bias and attitude angle corrections are estimated as part of the geometric model refinement process, using the Ground Control Points (GCP) originating from the NASA GLS2000 dataset (http://glcf.umd.edu/data/gls/) for which the geolocation accuracy is estimated to be 25 m (RMSE). The geometric model is, then, calibrated by using information obtained over the complete orbit and not a single WRS (Word Reference System) scene. Hence, block adjustment techniques have been implemented to estimate an accurate georeferencing model and in order to perform subsequent ortho-rectification [2].

2.3.1 Landsat 1-5 MSS Current Status

The project for the definition of the algorithms to be used to generate a Landsat 1 – 5 MSS ARD product has been completed

(without the cloud cover AI algorithm). The components of the current ESA Level-1 processor that have been identified as requiring significant effort to reach all threshold requirements are Geometric Corrections, Atmospheric Corrections and Cloud and Cloud Shadow Masking. Study results show that cloud cover masking needs further developments and seems to be the most critical item. Implementation of an updated/new IPF would be the ideal case, however it is also possible to propose a Level-1 to Level-2 post-processing. This second approach could be an interim (prototype) solution, supporting further testing and gauging user interest. An alignment with the USGS science team is very important to proceed with a common approach. ESA and USGS is working together in the definition of the targets to be achieved in order to have a successful ARD product definition. On ESA side as initial step a post-processor prototype will be developed based on the study results to assess the algorithms to be used and to improve the clouds detection. One additional collection including data ranging from 1976 to recent days over Marmolada Glacier, Rome, Vienna and Valencia creating a time-lapse of those coverages was generated and used during the Living Planet Symposium 2025 to demonstrate the importance and added value of heritage data in change detection (glaciers, vegetation and urbanization).

2.3.2 Landsat 5-7 TM/ETM+ Current Status

The full Landsat Thematic Mapper (TM) and Enhanced Thematic Mapper (ETM+) data are available for direct download to the users on the dissemination service. Three cloud-free coverages of Landsat 5 TM products have been produced and made available to users:

1. Landsat 5 TM Europe and North Africa Coverage 1984-85
2. Landsat 5 TM Europe and North Africa Coverage 1986-89
3. Landsat 5 TM Europe and North Africa Coverage 1995-98

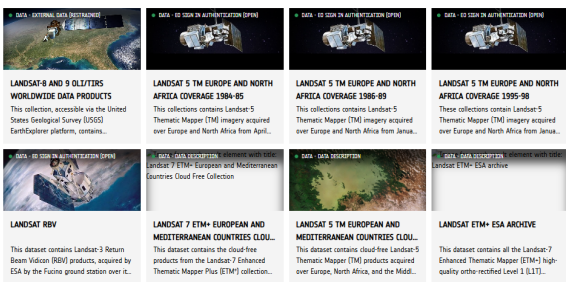

Figure 5. LANDSAT dataset in catalogue

2.4 AVHRR timeline

This long period fulfils the requirements of the World Meteorological Organization for a statistical sound analysis to study climate change induced shifts of Essential Climate Variables (ECV). Beside the central NOAA, CLASS archive exists many local archives, which are partly not accessible or the data holdings are not well maintained to be used by research teams. A few archives in Europe have data holdings covering Europe on a daily basis but are not homogenised and consolidated. In the frame of ESA HSP the data holdings of University of Bern (Switzerland), European Space Agency, and Dundee Satellite Receiving Station (UK) are combined, redundancy removed and validated to proof readability of the AVHRR LAC (1 km resolution) level 1b data. In a final step, metafiles and quick looks are generated to be included in a data container (SIP). The metafiles include some quality indicators to guarantee the usability of the dataset. This may help the user to select the needed files for their own investigations. Finally, the homogenised dataset was transferred to ESA to keep the unique AVHRR images alive for the next +50 years and make it accessible for all interested parties via ESA web interfaces.

The four to six band multi-spectral AVHRR data constitute a valuable data source for deriving time series of surface parameters, such as snow cover, land surface temperature or vegetation indices for monitoring global change. AVHRR data are residing in various archives worldwide, including several ESA facilities. The AVHRR Curation project aims at consolidating the AVHRR ESA Level 0 data holdings and at defining the technical approaches and solutions for the possible generation of a coherent European AVHRR dataset consisting of the combination of datasets from different organisations.

In this context, an AVHRR Level 0 dataset consolidation procedure was defined in coordination with AVHRR data users and experts, to ensure consistency and homogeneity of the datasets.

The project has outlined the importance of assuring that the long-term series datasets are:

- homogeneous (data gap consolidation procedure shall be in place during operations or at mission end);
- Consistent (inter-sensor consistency is one of the main requirements from the user community using long-term data series, i.e. to preserve the data and the knowledge of the family of sensor consistency and evolution and cross-validation assessment within the same family of sensors as AVHRR);
- Include the measure of the uncertainty (it is of utmost importance to foster practices for sensor degradation measurement and preserve the measure of uncertainty in the product w.r.t the original mission requirements, quality performances expectation, and to keep track of sensor performance degradation).

The whole process for consolidation of the AVHRR data was in-line with the recommendations of the CEOS Working Group on Information Systems and Services (WGISS) to fulfil the needs for data management and stewardship maturity [1].

CONCLUSIONS

The emergence of large volumes of data raises new issues in terms of discovery, access, exploitation, and visualisation of data, with profound implications on how users do “data-intensive” Earth Science. In line with LTDP framework guidelines and strategy for the preservation of long time series and to foster the exploitation of the dataset with the new emerging technology for big data analysis and reprocessing, various projects were started by the Agency. These projects have outlined the importance of assuring that long-term series datasets are: homogeneous (data gap consolidation procedure shall be in place during operations or at mission end); consistent and include not only measure of the uncertainty (inter-sensor performance degradation) but also all ancillary data, like telemetry are not lost, and have demonstrated that data and/or metadata must be broken out of silos in order to be mined, proximity of data to the streaming processing chain and data locality is vital for cross-fertilisation and discovery of new products and services to the EO community.

REFERENCES

[1] CEOS WGISS Preservation Guidelines and Best Practices - https://ceos.org/ourwork/workinggroups/wgiss/preservation/
[2] LANDSAT Products Description Document - IDEAS-VEG-SRV-REP-1320 v.6.0
[3] http://cci.esa.int/
[4] https://earth.esa.int/eogateway

This work is licensed under a Creative Commons Attribution-No Derivatives 4.0 International License.

INTEGRATED GNSS AND INSAR DATASETS FOR THE MONITORING OF LAND SUBSIDENCE IN THE PO RIVER DELTA

A. Danti [1] *, M. Fabris [2], C. Masetto [3], U. Trivelloni [3]

[1] Department of Industrial Engineering, University of Padova, Italy - alice.danti@unipd.it
[2] Department of Civil, Environmental and Architectural Engineering, University of Padova, Italy - massimo.fabris@unipd.it
[3] Regione del Veneto, Venezia, Italy - (carlo.masetto, umberto.trivelloni)@regione.veneto.it

KEY WORDS: Po River Delta, Land Subsidence, GNSS, InSAR, Calibration, Validation, Integration

ABSTRACT:

This study proposes an integrated approach to monitoring land subsidence in the Po River Delta by combining GNSS data with InSAR products from the Copernicus European Ground Motion Service (EGMS) and the Veneto Regional Monitoring Program. The aim is to assess the accuracy of EGMS Calibrated (L2b) and regional datasets by comparing them with the PO DELta NETwork (PODELNET) GNSS network. Analyses performed on data acquired in the 2018–2022 period, projecting GNSS velocities along the LOS and comparing them with Permanent Scatterers (PSs) within 200 m, reveal that about 70% of EGMS comparisons fall within a ±2 mm/year interval, with more than 50% within ±1.5 mm/year. On the contrary, the regional dataset shows systematic differences that exceed 2 mm/year, highlighting the need for recalibration. These findings confirm the reliability of EGMS products for regional-scale land subsidence monitoring and emphasize the importance of local validation for operational use in geologically sensitive areas.

1. INTRODUCTION

Land subsidence involves many and large areas worldwide, representing a serious problem for infrastructures and human activities because it exacerbates the risk of flooding (Syvitski et al., 2009). This phenomenon can be particularly harmful in transitional environments such as river deltas, most of the time densely populated and characterised by significant economic activities (Ericson et al., 2006).

The deformation monitoring of areas affected by land subsidence is crucial for implementing risk mitigation strategies; while in the past only geometric levelling was used, currently the Global Navigation Satellite System (GNSS) and Interferometry Synthetic Aperture Radar (InSAR) have proven highly effective (Martins et al., 2024). In this context, since 2021, the European Ground Motion Service (EGMS) of the Copernicus program has provided continental-scale ground motion data processed using radar interferometric techniques based on Permanent Scatterers (PSs). These points (targets that exhibit high coherence across time series of radar images) are generally located on artificial structures, such as buildings, or on rock outcrops. Part of the Copernicus Land Monitoring Service portfolio, the EGMS stands out for the high technical quality of its products and its complete open access, which makes it a potentially revolutionary tool for managing ground deformation data in Europe (Crosetto et al., 2025). Together with EGMS information, InSAR velocities from the Veneto Region database were used in this study. Since GNSS and InSAR information must agree on the same area, in this work the velocities obtained from the two techniques and related to the same period were compared in the Po River Delta (PRD), an area subject to land subsidence in northern Italy (Figure 1). In the case of differences in velocities greater than a threshold value, the interferometric data were calibrated using ground-based GNSS data. After calibration and validation, using independent velocities, the data were integrated to provide a deformation monitoring system for the area under investigation.

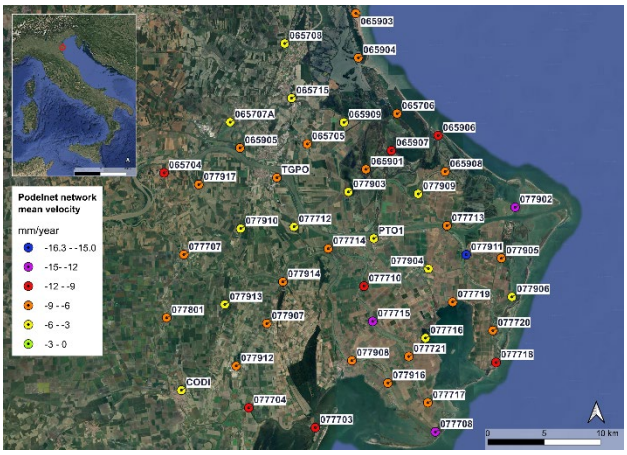

Figure 1. Location of the study area in northern Italy and vertical velocities of the PODELNET GNSS network.

2. MATERIALS AND METHODS

2.1 The study area

The Po River Delta (PRD) is a complex ecosystem located in northern Italy. It is the result of natural sedimentary processes linked to human activities, such as reclamation of wetlands and engineering activities (Cencini, 1998). Land subsidence in this area is due to natural and anthropogenic components: the natural contribution is correlated with the age of highly compressible Holocene deposits in the first 30–40 m of the sedimentary sequence (Teatini et al., 2011) and with tectonic movements (Carminati et al., 2003), with deformation velocities on the order of 2–4 mm/year (Teatini et al., 2011). The anthropogenic contribution is related to the intensive exploitation of aquifers (Martinelli et al., 2014) and can reach velocities of tens to hundreds of mm/year (Cenni et al., 2021). Currently, a large portion of the PRD lies below the mean sea level, without

* Corresponding author

receiving sediments due to artificial levees built to prevent flooding (Correggiari et al., 2005).

2.2 GNSS measurements

The GNSS data used in this work are derived from the PO DELta NETwork (PODELNET). It is composed of 46 non-permanent sites (NPS) integrated with the Continuous GNSS (CGNSS) stations of Taglio di Po (TGPO), Porto Tolle (PTO1), and Codigoro (CODI) (the last was replaced by the Vaccolino – VCCL station from 2020). The network, developed in 2016 in agreement with the University of Padova, the Italian Military Geographic Institute (IGMI), and the Veneto Region, was measured every two years and the sites were uniformly distributed throughout the PRD, both in urbanized and rural areas.
In this work, data acquired from 2018 to 2022 were analysed, maintaining the time overlap with the InSAR information. Surveys were carried out fixing the same parameters each time; measuring the same 130 baselines, with the same sampling rates, a minimum stationing of 3 hours, and, when possible, with the same instruments. In the first surveys, GPS receivers were used most of the time, while in the latest measurements, GNSS receivers, capable of receiving the GPS, GLONASS, GALILEO, and BEIDOU constellations were used. The TGPO and CODI stations used receivers capable of acquiring only the GPS constellation; for this reason, all available constellations were selected when calculating the baselines. The GNSS observations of the PODELNET network were processed using data from the three CGNSS reference stations. In a first step, the coordinates of the three permanent stations were calculated in the ITRF2014 reference system, specifically in the ETRF2014 implementation, using Bernese software during the processing of the Italian GNSS network, an infrastructure composed by about 600 stations in the Italian and surrounding areas. In a second phase, the coordinates of the 46 NPS points were calculated for each survey by fixing the coordinates of the CGNSS stations using Leica Infinity software; from the coordinates obtained for each point (both permanent and NPS), the velocities were obtained by comparing the multitemporal data (Fabris et al., 2022) (Figure 1).

2.3 InSAR data

The interferometric data used in this study were derived from the EGMS service of the Copernicus program (EGMS, 2025) and the Veneto Region database (Veneto Region, 2024). Both services provide open access data related to Line-Of-Sight (LOS) velocities, obtained through Advanced-DInSAR processing of SAR images acquired by the Sentinel-1 satellite.
The EGMS service provides three different products: Basic, Calibrated, and Ortho (Capes, Passera, 2025; Crosetto et al., 2021). In this study, the Calibrated data were used; they consist of points derived from interferometric analysis of Sentinel-1 images, similar to the Basic, but referring to a model based on data from the European GNSS station network.
In detail, to cover the PRD area, the ascending track 44 (scenes 264, 265, 266, 267) and the descending track 95 (scenes 806, 807, 808, 809) of the EGMS and the descending track 95 of the Veneto Region database were used. All data were referred to the period 2018-2022, and overlapped with the GNSS velocities.

2.4 Comparison for validation

The geospatial analysis of InSAR and GNSS data was carried out in QGIS software. GNSS and PSs velocities were compared within a 200 m buffer, selected to account for differing environmental conditions: the CGNSS stations were typically located in urban areas with a high density of PS, while many PODELNET NPS points were placed in vegetated areas where PS were sparse or absent nearby. Previous tests using CGNSS stations evaluated buffer distances of 50, 100, 150, and 200 m, showing that 200 m provides a suitable compromise between PS availability and spatial representativeness, given the heterogeneous distribution of InSAR points.
For each GNSS station, the LOS-projected 3D GNSS velocities were compared with the InSAR velocities, calculated as the mean of PS within the 200 m buffer; this approach was applied to both the CGNSS and the 46 NPS stations.
The definition of the threshold value related to the differences between velocities is crucial to evaluate the agreement between the results obtained with the two techniques and to assess the reliability of the estimated deformations. Moreover, this threshold value must be defined on the basis of the spatial scale of the analysis and the application context. In the literature different studies showed that, under ideal conditions, displacement velocities obtained from Sentinel-1 data can reach sub-millimeter accuracies (Cigna et al., 2021). Ng et al. (2023) compared the InSAR data with the CGNSS measurements in Sydney, obtaining mean differences less than 1 mm/year and RMS (root mean square) of the order of 1 mm/year, although in some cases differences exceeding ±2 mm/year were observed. Huang et al. (2024) studied the structural safety of high buildings located in Guangzhou–Foshan area (China). The authors compared the velocities obtained from 45 InSAR points with the deformation velocity of the GUAN CGNSS station. The results provided an overall RMSE of 1.50 mm/year. In this study, in agreement with the proposal of Martins et al. (2024) in a similar context of land subsidence caused by groundwater extraction in the Lorca area (Spain), a threshold of ±2 mm/year was adopted to assess the alignment between the GNSS velocities projected along the LOS and the InSAR rates. This value seems to represent a good compromise for analyses on a regional or territorial scale. However, in highly critical infrastructure contexts, more restrictive threshold values are preferable; Fabris et al. (2025) proposed a threshold of ±1.5 mm/year for monitoring the MOSE structures in Venice. Taking into account the nature of the phenomenon under investigation and the known land subsidence rates in the PRD, in this work both the thresholds, ±1.5 mm/year and ±2 mm/year, were used to classify the obtained results.

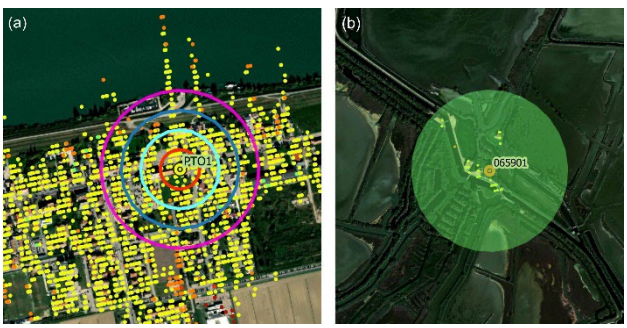

Figure 2. Definition of the analysed buffers centered on the CGNSS stations (radius of 50 m, 100 m, 150 m, and 200 m, in urbanized areas) (a) and those centered on the NPS points (radius of 200 m, in rural areas) (b).

3. RESULTS

3.1 Comparison CGNSS – InSAR velocities

The comparison between the CGNSS velocities of the continuous stations and the mean values of the PSs up to 200 m is reported in Table 1.

Continuous Station	Differences CGNSS – InSAR (mm/year)		
	EGMS Track 44	EGMS Track 95	Veneto Region Track 95
TGPO	-1.1	-0.8	-4.3
PTO1	0.3	-0.3	-4.0
CODI	-	-1.7	-

Table 1. Differences between velocities (CGNSS – InSAR)

Table 1 shows a good agreement between velocities, as the differences for the EGMS data were lower than the threshold value. In contrast, for the Veneto Region dataset, the differences were greater than the threshold value, both for the TGPO and PTO1 CGNSS stations, demonstrating that a local calibration is required.

3.2 Classification of the differences between velocities

The comparison between velocities was then performed using the data related to the 46 NPS stations. Using the original InSAR velocities, the differences (Δv) were classified into four classes with an upper limit of 13.2 mm/year:

$$|\Delta v| \leq 1.5 \text{ mm/year (class A)}$$
$$1.5 \text{ mm/year} < |\Delta v| \leq 2.0 \text{ mm/year (class B)}$$
$$2.0 \text{ mm/year} < |\Delta v| \leq 4.0 \text{ mm/year (class C)}$$
$$4.0 \text{ mm/year} < |\Delta v| \leq 13.2 \text{ mm/year (class D)}$$

Figure 3 shows the distribution of the differences between the velocities of the 46 GNSS NPS points and the mean values of the InSAR measurements within a buffer zone centered on each NPS, with a radius of 200 m.

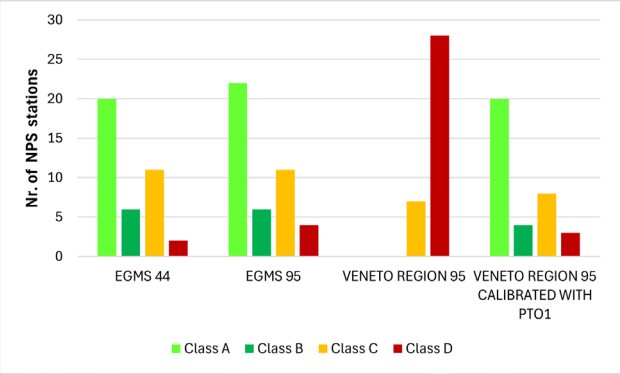

Figure 3. Distribution of the differences between velocities in four classes: $|\Delta v| \leq 1.5$ mm/year (class A); 1.5 mm/year $< |\Delta v| \leq$ 2.0 mm/year (class B); 2.0 mm/year $<|\Delta v| \leq 4.0$ mm/year (class C); 4.0 mm/year $<|\Delta v| \leq 13.2$ mm/year (class D)

Figure 3 shows that about 70% of the differences between velocities were lower than ±2.0 mm/year for the EGMS data (with 50-60% lower than ±1.5 mm/year), while class D contains differences where GNSS and InSAR velocities strongly disagree. In contrast, all differences between the velocities involved in the Veneto Region dataset were greater than ±2.0 mm/year. However, by recalibrating the data using the reference CGNSS station of PTO1, the new distribution of the three classes was very similar to the EGMS data (Figure 3).

3.3 Integrated monitoring system

InSAR data, calibrated and validated, were then integrated with GNSS velocities to provide a monitoring system of land subsidence in the PRD.

Figure 4 reports the GNSS velocities projected along the LOS together with the InSAR data, ascending track 44, of the EGMS service.

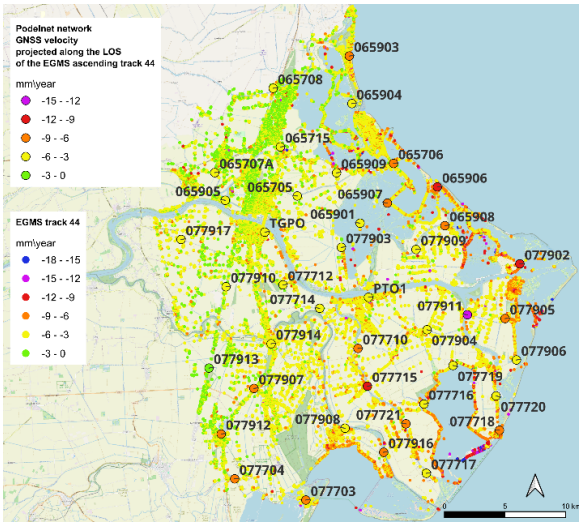

Figure 4. Line-Of-Sight (LOS) velocities of the GNSS points integrated with the EGMS InSAR data, ascending track 44.

Similarly, Figure 5 shows the GNSS data projected along the LOS integrated with the InSAR velocities, descending track 95, of the EGMS dataset.

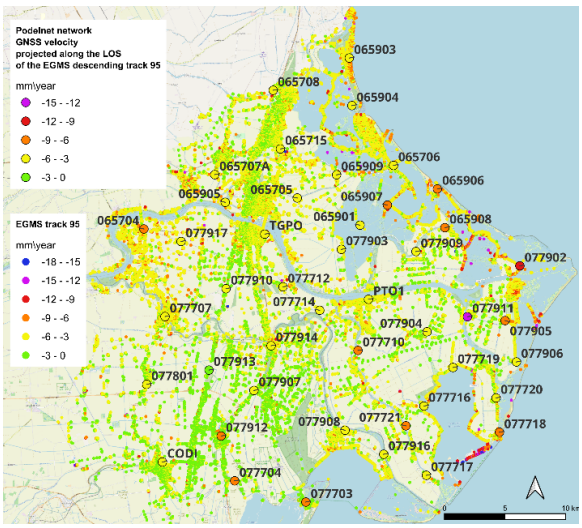

Figure 5. LOS velocities of the GNSS PODELNET network integrated with the EGMS InSAR data, descending track 95.

Finally, Figure 6 represents the GNSS velocities projected along the LOS together with the interferometric information, descending track 95, of the Veneto Region dataset, before (a) and after (b) calibration using the PTO1 CGNSS station as reference.

4. CONCLUSIONS

The results obtained in this work confirm that the EGMS data, Calibrated product, represent reliable information for land subsidence monitoring at the regional scale. Compared to ground-based GNSS data, approximately 70% of the differences between velocities showed values lower than ±2 mm/year, and more than 50% fell within the more restrictive threshold interval of ±1.5 mm/year. These data support the usability of information for environmental surveillance and land planning applications in the PRD.

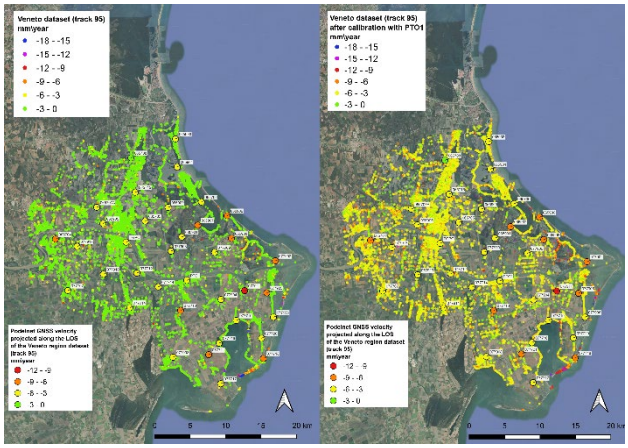

Figure 6. LOS velocities of the GNSS PODELNET network integrated with the Veneto Region dataset (track 95) before (left) and after (right) calibration using the PTO1 CGNSS station.

In contrast, the regional dataset showed systematic deviations from GNSS velocities, with differences always exceeding 2 mm/year. This result highlights the need for recalibration or careful interpretation before using these data in quantitative analyses.

REFERENCES

Cenni, N., Fiaschi, S., Fabris, M., 2021. Monitoring of Land Subsidence in the Po River Delta (Northern Italy) Using Geodetic Networks. *Remote Sens.*, 13, 1488.

Cigna, F., Ramírez, R.E., Tapete, D., 2021. Accuracy of Sentinel-1 PSI and SBAS InSAR Displacement Velocities against GNSS and Geodetic Leveling Monitoring Data. *Remote Sens.*, 13, 4800.

Crosetto, M., Crippa, B., Mróz, M., Cuevas-González, M., Shahbazi, S., 2025. Applications based on EGMS products: A review. *Remote Sensing Applications: Society and Environment*, 37, 101452.

Crosetto, M., Solari, L., Balasis-Levinsen, J., Bateson, L., Casagli, N., Frei, M., Oyen, A., Moldestad, D. A., Mróz, M., 2021. Deformation monitoring at European scale: the Copernicus Ground Motion Service. In: The International Archives of the Photogrammetry, *Remote Sensing and Spatial Information Sciences*, Vol. XLIII-B3, pp. 141-146.

EGMS 2025 https://egms.land.copernicus.eu/ (16 September 2025)

Ericson, J.P., Vörösmarty, C.J., Dingman, S.L., Ward, L.G., Meybeck, M., 2006. Effective sea-level rise and deltas: Causes of change and human dimension implications. *Global and Planetary Change*, 50(1-2), pp. 63-82.

Fabris, M., Battaglia, M., Chen, X., Menin, A., Monego, M., Floris, M., 2022. An Integrated InSAR and GNSS Approach to Monitor Land Subsidence in the Po River Delta (Italy). *Remote Sensing*, 14(21), 5578.

Fabris, M., Floris, M., 2025. Integrated GNSS and InSAR Analysis for Monitoring the Shoulder Structures of the MOSE System in Venice, Italy. *Remote Sensing*, 17, 1059.

Capes, R., Passera, E., 2025. End-to-end implementation and operation of the European Ground Motion Service (EGMS). Product Description and Format Specification. Foundation https://land.copernicus.eu/en/technical-library/egms-product-description-document/@@download/file (15 September 2025).

Carminati, E., Martinelli, G., Severi, P., 2003. Influence of glacial cycles and tectonics on natural subsidence in the Po Plain (Northern Italy): Insights from 14 C ages. *Geochemistry, Geophysics, Geosystems*, 4(10).

Cencini, C., 1998. Physical Processes and Human Activities in the Evolution of the Po Delta. Italy. *Journal of Coastal Research*, 14(3), pp. 774-793.

Correggiari, A., Cattaneo, A., Trincardi, F. (2005). The modern Po Delta system: Lobe switching and asymmetric prodelta growth. *Marine Geology*, 222-223(1-4), pp. 49-74.

Huang, D., Qi, Z., Lin, S., Gu, Y., Song, W., and Lv, Q., 2024. Investigating the structural health of high-rise buildings and its influencing factors using Sentinel-1 synthetic aperture radar imagery: a case Study of the Guangzhou–Foshan metropolitan area. *Buildings*, 14, 4074.

Martinelli, G., Chahoud, A., Dadomo, A., Fava, A., 2014. Isotopic features of Emilia-Romagna region (North Italy) groundwaters: Environmental and climatological implications. *Journal of Hydrology*, 519(PB), pp. 1928-1938.

Martins, J.E., Cuenca, M.C., Davids, B., Zhai, G., González-Alonso, E., Boncori, J.P.M., Kristersen, L., Sala, J., Solari, L., 2024. Validation of the European Ground Motion Service with Global Navigation Satellite Systems and Corner Reflectors over Deforming Areas. *International Geoscience and Remote Sensing Symposium (IGARSS)*, pp. 7537-7541.

Ng, A.H-M., Liu, Z., Du, Z., Huang, H., Wang, H., Ge, L., 2023. A novel framework for combining polarimetric Sentinel-1 InSAR time series in subsidence monitoring—A case study of Sydney. *Remote Sens. Environ.*, 295, 113694.

Syvitski, J.P.M., Kettner, A.J., Overeem, I., Hutton, E.W.H., Hannon, M.T., Brakenridge, G.R., Day, J., Vörösmarty, C., Saito, Y., Giosan, L., & Nicholls, R.J., 2009. Sinking deltas due to human activities. *Nature Geoscience*, 2(10), pp. 681-686.

Teatini, P., Tosi, L., Strozzi, T., 2011. Quantitative evidence that compaction of Holocene sediments drives the present land subsidence of the Po Delta, Italy. *Journal of Geophysical Research: Solid Earth*, 116(8).

Tosi, L., Da Lio, C., Strozzi, T., Teatini, P., 2016. Combining L- and X-Band SAR Interferometry to Assess Ground Displacements in Heterogeneous Coastal Environments: The Po River Delta and Venice Lagoon, Italy. *Remote Sensing*, 8(4), 308.

Veneto Region https://idt2.regione.veneto.it/portfolio/webgis-dei-dati-sentinel-1-ps/ (25 July 2024).

This work is licensed under a Creative Commons Attribution-No Derivatives 4.0 International License.

SYNTHETIC APERTURE RADAR BASED FLOOD EXTENT MAPPING IN COMPLEX LAND COVER AREAS: A CASE STUDY OF TANA RIVER DELTA, KENYA

D.M. Muriithi [1,2] *, F. Mutwiri [1,2], A. Vitti [2]

[1] Department of Civil, Building and Environmental Engineering, Sapienza Università di Roma, Italy
(davidmwenda.muriithi, faithkagwiria.mutwiri)@uniroma1.it
[2] Department of Civil, Environmental and Mechanical Engineering Università di Trento, Italy
(davidmwenda.muriithi, faith.mutwiri, alfonso.vitti,)@unitn.it

KEY WORDS: Flood extent mapping, Synthetic aperture radar (SAR), Sentinel-1

ABSTRACT:

Flooding is one of the most dangerous natural hazards in terms of frequency and impact with flood risk highest in Global South countries where disaster risk reduction (DRR) systems are limited. However, operational flood risk reduction demands near real-time (NRT) inundation mapping. Consequently, synthetic aperture radar (SAR) based solutions are preferred due to their 'all weather', day or night and canopy penetration capabilities. Nevertheless, due to SAR image formation dynamics, the post flood scene presents a complex scene made up of different inundated land cover types that further complicate SAR image analysis for automated NRT flood detection. This necessitates continuous improvement of SAR flood mapping techniques to meet the operational requirements of the DRR stakeholders. This study carried out comparative analysis of three flood detection techniques namely global thresholding (Otsu), multi-temporal change detection (CD) and a hybrid (Otsu + CD) technique using Sentinel-1 C-SAR imagery. The area of interest was set in Tana Delta in Kenya, a complex landscape made up of fragmented land cover types and supporting diverse ecosystem services. Analysis done for the 14th April 2024 flood event showed the flood area detected differed significantly for the VH and VV channels across all techniques. The VV channel return was higher than the VH by 70%, 50% and 87% for the Otsu, CD and hybrid techniques respectively. However, there was close agreement between the VH results for the dual image approaches. A major limitation of the study was the lack of validation data.

1. INTRODUCTION

1.1 Background

Flooding is one of the most dangerous natural hazards in terms of frequency and impact. In the last two decades, over 40% of natural disaster events recorded globally were associated with floods(CRED,2025). Given the increasing effects of climate change and variability, flood events are likely to increase with devastating impacts to lives and livelihoods. This applies especially to developing and other Global South countries where disaster risk reduction (DRR) systems are limited (Amitrano et al 2024).

Geospatial technologies have been used for many years in the DRR domain as decision making support tools for disaster preparedness, early warning and monitoring. However, the use of satellite remote sensing increased sharply over the last decade with the increase in earth observation (EO) satellite missions more so in constellation configuration (Schumann, 2024). This coupled with modern day developments in computing have driven the pursuit of automated global disaster monitoring solutions.

In the context of flood monitoring, operational flood risk reduction demands near real-time (NRT) inundation mapping (Shen et al, 2019). Consequently, SAR based solutions are preferred due to their 'all weather', day or night and frequency dependent canopy penetration capabilities (Landuyt et al, 2019). Nevertheless, SAR backscatter depends on surface roughness with respect to incident wavelength and the resultant scattering mode as well as dielectric properties. In addition to these, sensor acquisition properties such as the polarisation and incidence angle affect backscatter across the image swath while SAR side-looking imaging introduces geometric distortions.

In view of the foregoing, the post flood scene presents a complex environment made up of different inundated urban or rural land cover types that further complicate SAR image analysis for flood extent mapping (Amitrano et al 2024).

1.2 State of the Art

Researchers have over the years proposed ensemble methodologies aimed at overcoming inherent SAR limitations (C. Krullikowski, 2023). (Hlavá˘cová et al, 2021) automated open flood detection by combining Sentinel-1 change detection and thresholding with a fuzzy and region growing component. The AUTOWADE (AUTOmaticWater Areas DEtector) combines clustering, edge filtering, automatic thresholding and region growing for open flood and permanent water mapping with a fuzzy logic gap filling algorithm for vegetated areas (Pulvirenti et al, 2021). ESA's Global Flood Monitoring (GFM) service on the other hand uses an ensemble algorithm approach that combines single plus dual image and time-series classifiers albeit with an exclusion mask for dense vegetation, urban, non-water low backscatter, topographic distorting, radar shadow and insufficient coverage areas (Wagner et al, 2026). Additionally, many solutions are going beyond flood mapping to impact assessment including affected population and building (Nhangumbe et al, 2023) or crop (D. P Samuele et al, 2021) damage assessment.

However, many flood mapping methods focus on northern temperate latitudes thus the need to develop or test flood delineation methods in complex landscapes characterized by mixed land covers, land use and extreme seasonal fluctuations oscillating from drought to wet (Zhang et al, 2020). This study carried out comparative analysis and ensemble of three (3) SAR based flood detection techniques namely global thresholding (Otsu), multi-temporal change detection (CD) and a hybrid (Otsu + CD) technique in a complex land cover area, the Tana Delta in Kenya.

* Corresponding author

2. STUDY AREA AND METHODS

2.1 Study Area

The Tana River is Kenya's longest river covering approximately 1000 km with a catchment area of approximately 126,026 Km^2 that stretches from the Mt. Kenya and Aberdare highlands to the Indian Ocean (WRA, 2020). It is arguably the country's most important river basin given its contribution to national food, water, energy and environmental security.

At the lowest end of the basin, the Tana Delta presents a complex landscape consisting of forests, woodlands, floodplain grasslands and mixed wetlands supporting diverse bird and wildlife populations as well as anthropogenic activities (Duvail et al, 2012). The area's ecosystem depends heavily on the river's annual flooding cycles, with peaks in May and November. However, the flood onset, extent and duration vary from year to year due to climate variability, a changing river channel and upstream land use practices (UNESCO, 2010).

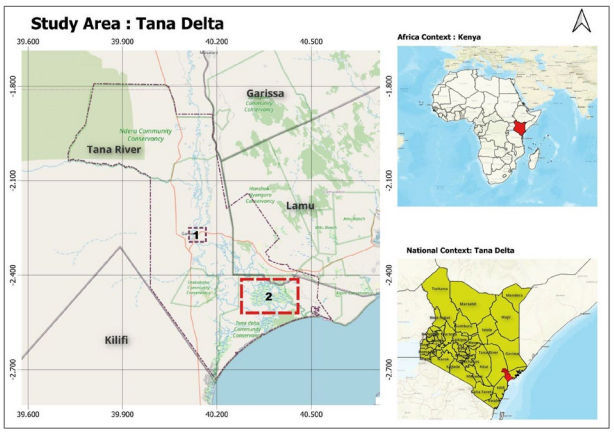

Figure 1. Tana Delta national and continental context map

2.2 April 2024 Tana Delta Flooding Event

In 2024, Kenya experienced above-average rainfall during the March-April-May (MAM) long rain season, resulting in heavy flooding across the country. In April 2024, the Tana River burst its banks at various points south of Garissa with devastating impact on lives and livelihoods.

2.3 Earth Observation Datasets

This study used three (3) products of Copernicus, the Earth Observation (EO) component of the European Union (EU) Space Program, namely: Sentinel-1 (S1) ground range detected (GRD) SAR, Sentinel-2 (S2) optical, and the Copernicus digital elevation model (GLO-30 DEM). The S1 acquisitions for the 2nd and 14th April were used as reference and crisis image respectively. S1 was used as the primary flood detection dataset while S2 and DEM were used to define the permanent water mask and slope condition respectively during post processing.

2.4 Methods

The data acquisition and processing were implemented on the Google Earth Engine (GEE) platform using the GEE Python API on Google Colab. The pre-event and post-event S1 images were filtered using a 50m focal mean kernel to reduce speckle noise and clipped to the area of interest (AOI).

Three (3) SAR flood detection approaches were then applied on the VH (vertical transmission-horizontal reception) and VV (vertical transmission and reception) polarization channels of S1 GRD imagery namely: Global Thresholding (Otsu), multi-temporal SAR change detection (CD) and a Hybrid (Otsu + CD).

Subsequently, the pixel with highest likelihood of flood was identified by raster multiplication of VV and VH binary flood maps of the three techniques. A similar raster multiplication was repeated for the Otsu, CD and Hybrid flood maps and validated against the GFM flood map after masking out the exclusion mask.

2.4.1 Global Thresholding (Otsu Threshold)

Thresholding water detection techniques aim to identify the optimal image binarization value that distinguishes water from non-water clusters. Examples of such thresholding approaches include the Otsu method, Kittler-Illingworth algorithm, Normal and Least Median of Squares(LMedS) method, Poisson method and the outlier detection method (Nhangumbe et al, 2023). However, the target flood cluster only covers a small fraction of the overall scene and may fail to stand out in the histogram, hence the continuous improvement of thresholding techniques by the research community (Rossi et al, 2023)

Otsu's method determines the optimal threshold that minimizes intra-class variance while maximizing inter-class variance between the foreground (water) and background (non-water) pixels (Landuyt et al 2019). This between-class variance can be calculated as :

$$\sigma_B^2 = \omega^f \omega_b (\mu_f - \mu_b)^2 \quad (1)$$

where μ_f = *mean intensity of the foreground pixels*
μ_b = *mean intensity of the background pixels*
ω_f = *foreground class buckets*
ω_b = *background class buckets.*

Thresholding performs best when the image histogram assumes a bimodal balanced gaussian distribution although this requirement can be loosened for large areas by using a 'core flooding area' to initialize the water distribution (Shen et al 2019). This 'core flooding area' approach was applied on the post flood (crisis) S1 image and repeated independently for the VV and VH polarisation bands.

2.4.2 Multi-temporal SAR change detection (CD)

As the name suggests, this approach involves the analysis of at least two images acquired over the same area before the flood (reference image) and during the flood event (crisis image). A difference image is generally obtained from the log ratio of the two images which corresponds to the difference of the log scaled (dB) backscatter images. Also, the ratio is used because when comparing two uncorrelated multi-look images the variances sum up resulting in difference pixels where brighter areas have a higher variance than those in darker areas (Amitrano et al 2024).

This case study implemented a simple image difference CD approach between the pre-event (median composite image of S1 acquisitions of February 2024) and the post-event image acquired on 26th April 2024. A change threshold of 1.25 was applied as per the UN-SPIDER recommended practice on flood mapping.

2.4.3 Hybrid (Otsu + CD)

Thresholding techniques have the inherent limitation of flooded pixel over estimation due to false positives from 'radiometric water like' surfaces while CD approaches tend to overestimate floods due to identification of isolated flood pixel as false positives. The hybrid of the automatic image thresholding and CD is proposed in literature to overcome these shortcomings (Landuyt et al 2019).

For this case study, the Otsu threshold was applied on both the reference and crisis S1 images before the CD was performed on the resultant binary image. This was repeated for both the VH and the VV channels.

2.4.4 **Post Processing**

A post processing step was performed for the three (3) aforementioned approaches to generate the flood extent map. This involved removal of permanent water defined as using the median Modified Normalized Difference Water Index (MNDWI) of the entire S2 collection. Next a slope condition parameter was derived from the GLO-30 DEM with flooded pixels identified in areas with a slope greater than 5% removed. However, due to the gentle terrain of the AOI a higher accuracy DEM would yield better results.

2.4.5 **Validation**

Due to the lack of insitu data, the results were compared against the GFM flood map product for the 14th of April 2024.

3. RESULTS

The Otsu threshold method identified floods in 223.41 Km^2 and 1261.75 Km^2 for the VH and VV channels respectively. As for the CD technique the output was 36.75 Km^2 and 111.14 Km^2 for the VH and VV channels respectively. Lastly, the hybrid approach identified 33.82 Km^2 for the VH and 468.51 Km^2 for VV channels. The dual-channel results were 216.66 Km^2, 29.77 Km^2 and 25.82 Km^2 for the Otsu, CD and Hybrid respectively. The highest flood likelihood map from the ensemble of the three approaches returned a flood area of 19.51Km^2.

The flooded area detected differed significantly for the VH and VV channels across the three SAR techniques. The VV channel return was higher than the VH by 70%, 50% and 87% for the Otsu, CD and hybrid techniques respectively. However, there was close agreement between the result for the dual image CD and Hybrid approaches which were close to the UN-SPIDER Recommended Practice on Flood Mapping using Sentinel-1(SAR) which returned a flood area of 34.37 Km^2 and 97.63 Km^2 for the VH and VV channels respectively. The combination of the three techniques returned 19.51 Km^2 against GFM's 3.03 Km^2.

Figures 2 to 4 and 5 show a zoom view of areas marked [1] and [2] on Figure 1.

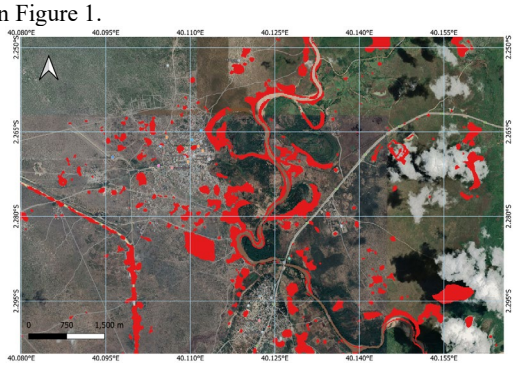

Figure 2. S1 Otsu thresholding flood extent map

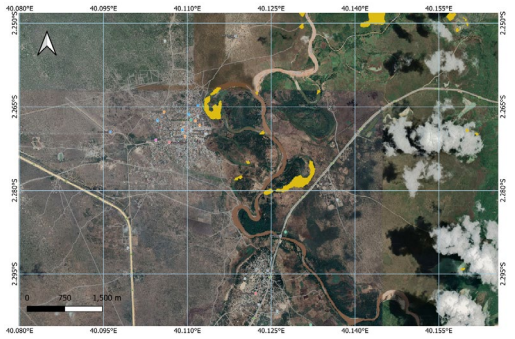

Figure 3. S1 CD flood extent map

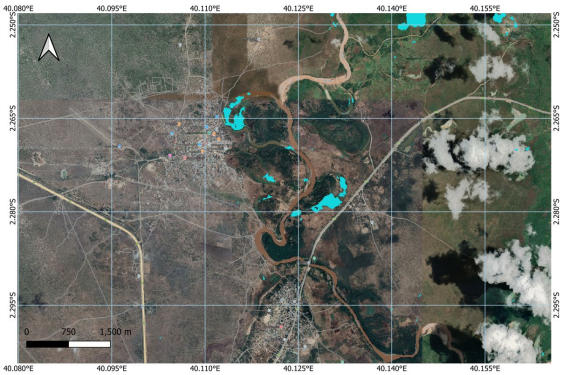

Figure 4. S1 Hybrid (Otsu + CD) flood extent map

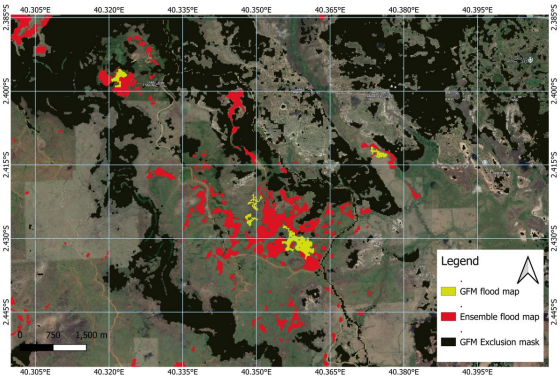

Figure 5. Otsu/CD/Hybrid ensemble flood extent map vs GFM

Satellite	Band	Flood Detected (Km^2)	Method
S1	VH	223.41	Otsu
	VV	1261.75	
	VV & VH	216.66	
	VH	36.75	CD
	VV	111.14	
	VV & VH	29.77	
	VH	33.82	Hybrid
	VV	468.51	
	VV & VH	25.82	
		19.51	Ensemble
	VH	34.37	UN-SPIDER (CD)
	VV	97.63	
	VV	3.03	GFM (Ensemble Algorithms)

Table 1. S1 flood mapping approaches results

3.1 Discussion

The VV returned larger areas than VH due to the mixed land cover which had volumetric scatterers that depolarized the VV channel. The single image Otsu threshold method had the highest flood areas due to confusion with smooth water-like surfaces. This is seen by the false positive along the highway in figure 2. Also, although a single water-non-water window was used to initialize the water distribution, the land cover complexity of the AOI demands more such windows to determine the optimal threshold. Additionally, while the thresholding method focuses on water detection in low backscatter areas, vegetation or urban flooding scenarios exhibit double bounce returns that result in higher backscatter (Shen et al, 2019).

The CD approach had a smaller flood area than the Otsu method, probably overcoming the latter's confusion in 'water-like' land cover. However, changes between the reference and crisis SAR images could have non-flood contributions from other factors such as wind, vegetation water content, incidence angles and inherent speckle noise. These effects were reduced by using pre and post flood images from the same orbit to reduce geometric errors and temporally close image pairs to reduce effects of vegetation phenological variations.

The hybrid (Otsu + CD) technique returned slightly higher flood areas than the CD approach in the VV but relatively low areas in the VH. However, this requires further investigation. Alternatively, the CD could be performed before the Otsu thresholding for comparative analysis (D. P Samuele et al, 2021).

These results could be further analysed by incorporating the accurate land cover maps, customizing exclusion mask generation and performing pixelwise accuracy assessments.

3.2 Conclusions

Effective SAR based flood detection needs to take into account the underlying complexity of the landscape under observation. The heterogeneity of complex land cover types complicates the automated identification of inundated vegetation (backscatter enhancement) and open flood (low backscatter). However, analysis of the SAR coherence as well as machine learning (ML) and deep learning (DL) approaches may hold the key to unpacking this complexity.

References

Amitrano, D.; Di Martino, G.; Di Simone, A.; Imperatore, P. Flood Detection with SAR: A Review of Techniques and Datasets. Remote Sens. 2024, 16, 656. https://doi.org/10.3390/rs16040656

Centre for Research on the Epidemiology of Disasters (CRED), International Disaster Database (EM-DAT): https://www.emdat.be/ (Accessed on 4th March 2025)

C. Krullikowski Candace Chow, Marc Wieland, Sandro Martinis, Bernhard Bauer-Marschallinger, Florian Roth, Patrick Matgen, Marco Chini Senior Member, IEEE, Renaud Hostache, Yu Li, Peter Salamonl., Estimating Ensemble Likelihoods for the Sentinel-1-Based Global Flood Monitoring Product of the Copernicus Emergency Management Service, in IEEE Journal of Selected Topics in Applied Earth Observations and Remote Sensing, vol. 16, pp. 6917-6930, 2023, doi:10.1109/JSTARS.2023.3292350.

De Petris Samuele, Sarvia Filippo & Borgogno-Mondino Enrico (2021) Multi-temporal mapping of flood damage to crops using sentinel-1 imagery: a case study of the Sesia River (October 2020), Remote Sensing Letters, 12:5, 459-469, DOI: 10.1080/2150704X.2021.1890262

Duvail, S.; Médard, C.; Hamerlynck, O. and Nyingi, D.W. 2012. Land and water grabbing in an East African coastal wetland: The case of the Tana delta. Water Alternatives 5(2): 322-343

Hlavá˘cová, I.; Ka˘cma˘rík, M.; Lazecký, M.; Struhár, J.; Rapant, P. Automatic OpenWater Flood Detection from Sentinel-1 Multi-Temporal Imagery. Water 2021, 13, 3392. https://doi.org/10.3390/w13233392

J-P. Schumann G (2024), Breakthroughs in satellite remote sensing of floods. Front. Remote Sens. 4:1280654. doi: 10.3389/frsen.2023.1280654

L. Landuyt , A. Van Wesemael, G.J.-P. Schumann , R. Hostache, N. E. C. Verhoest , and F.M. B. Van Coillie , Flood Mapping Based on Synthetic Aperture Radar: An Assessment of Established Approaches IEEE Transactions on Geoscience and Remote Sensing, Vol. 57, No. 2, February 2019, DOI 10.1109/TGRS.2018.2860054

M. Zhang, F. Chen, D. Liang , B. Tian and A. Yang, Use of Sentinel-1 GRD SAR Images to Delineate Flood Extent in Pakistan, Sustainability 2020, 12, 5784; doi:10.3390/su12145784

Nhangumbe, M.; Nascetti, A.; Ban, Y. Multi-Temporal Sentinel-1 SAR and Sentinel-2 MSI Data for Flood Mapping and Damage Assessment in Mozambique. ISPRS Int. J. Geo-Inf. 2023, 12, 53. https://doi.org/10.3390/ijgi12020053

Pulvirenti, L.; Squicciarino, G.; Fiori, E.; Ferraris, L.; Puca, S. A Tool for Pre-Operational Daily Mapping of Floods and Permanent Water Using Sentinel-1 Data. Remote Sens. 2021, 13, 1342. https://doi.org/10.3390/rs13071342

Rossi, D.; Zolezzi, G.; Bertoldi, W.; Vitti, A. Monitoring Braided River-Bed Dynamics at the Sub-Event Time Scale Using Time Series of Sentinel-1 SAR Imagery. Remote Sens. 2023, 15, 3622. https://doi.org/10.3390/rs15143622

UNESCO World Heritage Convention tentative lists, 2010 https://whc.unesco.org/en/tentativelists/5514/ (Accessed on 4th December 2025)

W. Wagner et al, The fully-automatic Sentinel-1 Global Flood Monitoring service: Scientific challenges and future directions, Remote Sensing of Environment 333 (2026) https://doi.org/10.1016/j.rse.2025.115108

Water Resources Authority (WRA), Water Resources Situation Report for the period July 2019 to June 2020, 2020.

UN-SPIDER Recommended Practice on Flood Mapping using Sentinel-1(SAR) Imagery and Google Earth Engine https://www.un-spider.org/advisory-support/recommended-practices/recommended-practice-radar-based-flood-mapping (Accessed on 30th January 2026)

X. Shen, D. Wang , K. Mao, E. Anagnostou, and Y. Hong , Inundation Extent Mapping by Synthetic Aperture Radar: A Review, Remote Sens. 2019, 11, 879; doi:10.3390/rs11070879

This work is licensed under a Creative Commons Attribution-No Derivatives 4.0 International License.

FAST BAYESIAN INFERENCE FOR FLOOD DETECTION USING GPU-ACCELERATED STATISTICAL ANALYSIS OF MULTI-TEMPORAL SAR STACKS

R. Paudice [1,2] *, F. P. Lovergine [2], A. Refice [2]

[1] Department of Earth and Geoenvironmental Sciences, University of Bari, Italy - rita.paudice@uniba.it
[2] Institute for Electromagnetic Sensing of the Environment, National Research Council (CNR-IREA), Italy
(francesco.lovergine, alberto.refice)@cnr.it

KEY WORDS: Flood monitoring, Bayesian Inference, SAR Time Series analysis, CUDA Acceleration, High Performance Computing, Parallel Processing

ABSTRACT:

High-resolution flood monitoring can be effectively conducted through a multi-temporal analysis of SAR datasets implemented within a semi-automated processing framework. By applying a Bayesian inference approach, posterior probabilities of floodwater presence can be rigorously quantified for each spatial pixel and time. Within the Bayesian approach, conditioned no-flood data probabilities, or likelihoods, can be estimated in time by approximating each pixel's value distribution as a Gaussian P.D.F., so that values corresponding to flood occurrences stand out as outliers. To this end, SAR observable time series can be modelled as smooth functions plus a noise component. This modelling can be achieved effectively through Gaussian Process Regression (GPR) algorithms.
While statistically robust, GPR traditionally suffers from computational bottlenecks, which hinder its application in a serial framework to the processing of large data cubes. To overcome this, a Python-based implementation has been developed to leverage the power of CUDA-enabled NVIDIA graphics units. This approach transforms the workflow —where time series are analyzed sequentially— into an efficient parallel architecture. By dynamically organizing time series into batches, the algorithm maximizes parallel computation on GPUs while maintaining statistical consistency.
Benchmarks comparing CPU-based and GPU-based versions demonstrate a dramatic reduction in computational time of over 96%. Validation and optimization are currently ongoing on the LEONARDO supercomputer (CINECA). This framework is well-suited for modeling long time series, and is thus applicable also to other kinds of remotely sensed data processing, addressing the growing need to extract actionable information from massive Earth Observation archives in progressively shorter timeframes.

1. INTRODUCTION

The growing frequency of extreme weather events, exacerbated by climate change, has established flood monitoring as a priority for disaster risk reduction strategies. In this context, different Synthetic Aperture Radar (SAR) satellite constellations, including Sentinel-1 by ESA, have revolutionized Earth Observation (EO) by providing high-resolution data with systematic global coverage and relatively short revisit times (Wagner et al., 2025). However, the sheer volume of this "Big Data" stream poses a significant challenge: extracting actionable information in short- or Near Real-Time (NRT) requires processing capabilities that often exceed standard computational resources. While methods such as change detection or thresholding are computationally inexpensive, they often suffer from false alarms in complex environments. Conversely, advanced statistical methods that model the temporal evolution of the signal offer superior accuracy but incur a prohibitive computational cost when applied to large-scale scenarios.
This work focuses on optimizing a robust flood detection framework based on Bayesian inference, in which a substantial novelty is constituted by the modelling of time series of SAR observables, both intensities and "cascaded" InSAR coherences, through GPR (Colacicco et al., 2024; Refice et al., 2024). The original implementation of this algorithm, developed in a MATLAB environment, proved effective for local-scale analysis and methodological validation. However, its reliance on a serial execution model—where the statistical analysis is performed sequentially for each pixel—creates a substantial bottleneck. Profiling of the legacy code revealed that the pixel-wise matrix operations required by the GP model resulted in linear time complexity relative to the image size ($O(n)$), making the processing of large-scale mosaics unfeasible within convenient timeframes. Furthermore, the dependency on proprietary software licensing may limit the deployability of the solution on cloud and High-Performance Computing (HPC) infrastructures.
To address these limitations, the whole processing chain was re-engineered from the CPU-based prototype to a high-performance Python architecture, accelerated by NVIDIA CUDA (Compute Unified Device Architecture) processing (NVIDIA Corporation, 2023). The primary objective of this migration is to exploit the massive parallelism of modern Graphics Processing Units (GPUs) to parallelize the Bayesian inference task. By shifting from a "loop-based" serial approach to a "batch-based" parallel approach, the proposed framework aims to drastically reduce computational time while maintaining the mathematical rigor of the original method. The following sections detail the architectural changes, the memory management strategies adopted for GPU processing, and the performance benchmarks obtained on both local workstations and the LEONARDO supercomputer.

2. METHODOLOGY

2.1 Theoretical framework

While traditional methods such as change detection or intensity thresholding are computationally inexpensive and have been widely explored for SAR-based water extraction (e.g., Pulvirenti et al., 2013), they often suffer from false alarms in complex environments.

* Corresponding author

For instance, thresholding techniques are inherently sensitive to transient surface roughness (e.g., wind-induced backscatter increase) and radar shadow misclassifications, whereas simple change detection algorithms frequently struggle to decouple true flood anomalies from natural phenological cycles or seasonal soil moisture variations.

To overcome these structural limitations, the presented flood detection strategy relies on a probabilistic machine learning framework grounded in Bayesian inference: the core objective is to rigorously quantify the posterior probability of floodwater presence by modelling the temporal evolution of SAR backscatter and InSAR coherence.

Unlike black-box deep learning approaches, this framework explicitly models physical uncertainty. Specifically, Gaussian Process Regression (GPR) is leveraged to estimate the likelihood of no-flood condition: by capturing the intrinsic seasonal and temporal signature of each individual pixel, the GPR creates a reliable baseline that natively accounts for natural backscatter fluctuations; furthermore, the Bayesian approach provides a robust probabilistic fusion of remotely sensed data with static ancillary variables (e.g., HAND and slope). This integration is crucial to systematically mask topographically induced false positives that would otherwise deceive standard radiometric thresholds. Finally, by subtracting the GP-fitted baseline from the observed SAR data, flood occurrences are identified as short-lived statistical anomalies within the residual space. This approach to anomaly detection effectively suppresses the false alarms typical of standard empirical methods, ensuring thematic accuracy while maintaining mathematical rigor and physical interpretability.

To benchmark this proposed architecture, a comprehensive multi-temporal dataset comprising 407 Sentinel-1 SAR acquisitions was used.

The operational validation was performed on a specific, purposely small spatial subset (100 x 100 pixels) to evaluate both the computational scalability and the memory footprint under realistic EO data volumes.

2.2 CUDA-Accelerated Implementation

While the calculation of priors is computationally inexpensive (as it relies on static maps), the GP modelling involves intensive algebra operations—specifically matrix inversions—for every single pixel in the temporal stack. In a traditional CPU-based serial implementation, this results in a prohibitive processing time for large-scale monitoring. To address this issue, the workflow was refactored into a Python-based parallel architecture utilizing NVIDIA CUDA via the PyTorch framework (Paszke et al., 2019).

2.2.1 Memory Management and Data Structure: to minimize the overhead of data transfer between Host (CPU) and Device (GPU), the PyTorch library was chosen, as capable of providing a high-performance interface for tensor manipulation directly on NVIDIA GPUs; the input SAR temporal stacks, in fact, are stored as multi-dimensional tensors. Before processing, these are reshaped into a flattened 2D structure where rows represent the spatial index (number of time series) and columns represent the time-series depth (number of time points).

This alignment ensures *memory coalescing*, allowing the GPU to access contiguous memory blocks efficiently and maximizing the throughput of the global memory bus.

2.2.2 Parallel GP Kernel and Libraries: the core of the methodology—Gaussian Process (GP) regression and Bayesian inference—was parallelized to run concurrently across thousands of CUDA cores. To achieve this, GPyTorch was leveraged, a highly optimized library that implements Blackbox Matrix-Matrix Multiplication (BBMM) to accelerate GP inference (Gardner et al., 2018).

By treating each pixel as an independent task, the $O(n^3)$ complexity of standard matrix inversion was bypassed. A custom kernel was implemented within the framework to accurately model the temporal behaviour of SAR backscatter by subclassing the base *gpytorch.kernels.Kernel* class. Unlike standard kernels, this custom implementation explicitly models two distinct physical components: a short-term exponential component and a long-term seasonal trend. The framework automatically optimizes the relevant hyperparameters—specifically the signal amplitude, decorrelation time, and seasonality weight—for each pixel via the L-BFGS algorithm (Liu & Nocedal, 1989). This approach enables a fully parallelized pixel-wise Bayesian processing, where likelihoods are computed concurrently across the GPU, ensuring a dramatic drop in computational time limited only by the number of available Streaming Multiprocessors.

2.2.3 Dynamic Batching and LEONARDO Integration: to handle large-scale satellite imagery that exceeds the physical VRAM (Video RAM) of a single GPU, a Stream-based Adaptive Batching Controller was developed. This module automatically calculates the optimal "chunk size" by monitoring the available hardware memory in real-time via the NVML module. The system dynamically adjusts the batch size—reducing it in case of memory pressure or increasing it to saturate GPU cores—preventing Out-Of-Memory (OOM) errors. This architecture was specifically tuned for the LEONARDO supercomputer, utilizing its high-speed interconnects and A100 nodes to enable the processing of very large-scale datasets in minutes rather than days.

3. RESULTS

The experimental evaluation was conducted in two logical phases: a preliminary scalability benchmark on synthetic data (executed on a local workstation) to validate the parallel architecture, followed by the operational deployment on real Sentinel-1 data using the LEONARDO supercomputer.

3.1 Phase I - Scalability Benchmarking (Synthetic Data)

Initially, the theoretical speedup was assessed by comparing a serial CPU implementation based on Scikit-Learn library for GPs computation (Pedregosa et al., 2011) against the parallel GPU architecture (GPyTorch), using different numbers (N) of synthetic time series. Tests were performed on a local workstation powered with a GPU NVIDIA Quadro RTX 4000 (8 GB).

As illustrated in Figure 1, the analysis confirms the decisive superiority of the parallel approach, although the gain exhibits a regime-dependent behavior. Despite the initial overhead observed on small workloads ($N < 500$)—where the "warm-up" cost of CUDA context initialization limits the speedup to ~ 8 times—the architecture proves its dominance in the long run.

As the workload increases ($N \geq 500$), GPU massive parallelism effectively amortizes this fixed startup cost.

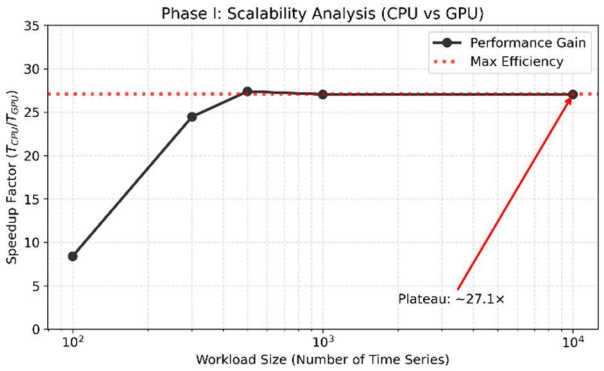

Figure 1: Computational speedup factor (T_{CPU}/ T_{GPU}) as a function of workload size (number of time series).

Consequently, the performance gain stabilizes at a sustained speedup plateau of ~ 27.1 times, drastically reducing the processing time for 10000 series from over 54 minutes (CPU) to under 2 minutes (GPU) (Table 1).

N Series	CPU Time (s)	GPU Time (s)	Avg GPU usage (%)	Speedup Factor (×)
100	34.04	4.05	22.75	8.4
300	99.10	4.05	48.00	24.5
500	167.15	6.10	57.67	27.4
1000	329.32	12.17	61.42	27.1
10000	3223.19	119.10	71.31	27.1

Table 1: Comparison of processing times and speedup factors for different workloads.

3.2. Phase II: Operational Efficiency on Sentinel-1 data

Following the successful validation on synthetic data, the workflow was migrated to the Booster module of the supercomputer LEONARDO for full-scale processing of a Sentinel-1 tile (100 x 100 pixels, 407 temporal acquisitions). Each node in the partition is powered by four NVIDIA A100 SXM4 64GB GPUs, and their computational capacity was accessible thanks to resources provided within the framework of the research activities of the ICSC "National Research Centre in High Performance Computing, Big Data and Quantum Computing" (Spoke 5 – Environment & Natural Disasters).
In this operational phase, the memory management efficiency was evaluated by contrasting the limitations of a standard Fixed Batching strategy with the performance of a custom Adaptive Batching Controller (Figure 2).

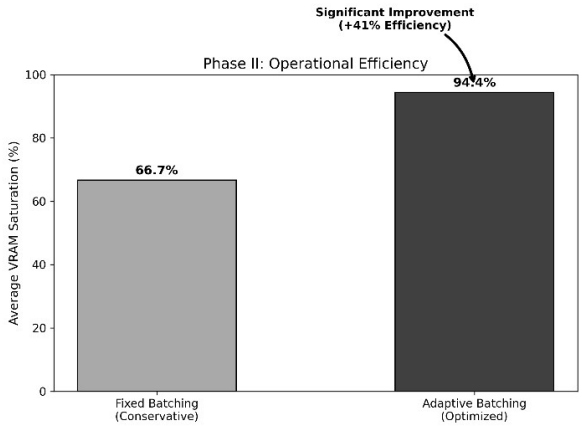

Figure 2: Comparison of GPU memory efficiency between Fixed and Adaptive batching strategies.

- Fixed Batching Constraints: due to memory constraints on the local workstation, an arbitrary batch size of 200 series was selected, as the precise ratio between the processing computational cost and the hardware capability was unknown. In the HPC setting, where GPUs drastically outperformed the local workstation, the risk of hardware under-saturation increased exponentially. Consequently, a change in approach was required, as simply adopting a conservative fixed batch size (e.g., 1000 series) became insufficient to fully leverage the hardware capabilities, since previous metrics showed GPU computational usage peaking at a maximum of only 70%.
- Adaptive Batching Performance: the adaptive controller eliminated the need for manual calibration across different hardware. By estimating the memory footprint of covariance matrices in real-time, the system automatically scales the workload to 7520 series per batch on the HPC nodes. This resulted in a peak memory utilization of almost 95%, maximizing throughput and ensuring that the operational pipeline is both hardware-agnostic and robust against Out-Of-Memory events.

Note that this substantial computational acceleration is achieved without altering the conceptual framework of the original flood detection algorithm: the GPU-accelerated probabilistic machine learning outputs match the baseline serial implementation from a mathematical standpoint. This confirms that the parallelization strategy acts exclusively as a computational optimization; it successfully preserves the statistical properties and reliability of the original method, drastically reducing the time-to-insight for large-scale processing without introducing any hardware-induced artifacts or methodological deviations.

4. DISCUSSIONS AND CONCLUSIONS

This study demonstrated that re-engineering the Bayesian flood detection framework from a traditional serial CPU-based approach to a parallel GPU-accelerated architecture effectively reduces the computational bottlenecks that hinder large-scale SAR processing. The transition to a High-Performance Computing environment allowed the system to go beyond simple acceleration: by enabling distributed parallelization across multiple GPUs, the proposed architecture introduces a second level of efficiency. This multi-layered parallelism ensures that the immense computational throughput of modern accelerators is fully exploited, scaling seamlessly with the available hardware resources.
From a quantitative perspective, the experiments confirm a major efficiency gain, recording a processing time reduction of over 96%. This acceleration not only compresses the analysis time for single tiles (stacks of 10000+ series) but also makes the processing of massive Sentinel-1 archives feasible (e.g. by assigning distinct tiles to parallel processing units, the system may be scaled to handle very large-scale datasets).
A critical component of this success is the introduction of the Stream-based Adaptive Batching Controller. This mechanism proved essential for ensuring operational robustness and flexibility. Thanks to the combination of dynamic intra-GPU memory probing and a Round Robin scheduling strategy across multiple GPUs, the system is capable of handling virtually any data load without manual intervention or tuning. This approach maximizes hardware saturation (reaching 94.4% VRAM utilization) while preventing resource exhaustion, ensuring cross-hardware portability.

Beyond the specific application to Synthetic Aperture Radar data, this work establishes a versatile methodological workflow suitable for the analysis of generic massive time-series. The architectural principles defined here are data-agnostic and can be adapted to other domains requiring intensive parallel processing of temporal data.
Future developments will focus on extending this architecture to support multi-sensor data fusion and integrating the pipeline into Near Real-Time (NRT) disaster response services. Furthermore, future research will be dedicated to fine-tuning the algorithmic core: specific evaluations will be conducted on different combinations of optimizers and parameter initialization strategies, with the aim of identifying the configuration that offers the optimal trade-off between the mathematical reliability of the fit and the execution speed.

ACKNOWLEDGMENTS

The authors gratefully acknowledge the ICSC – National Research Centre in High Performance Computing, Big Data and Quantum Computing for providing access to the LEONARDO supercomputer resources through Spoke 5 – Environment & Natural Disasters.

REFERENCES

Colacicco, R., Refice, A., Nutricato, R., Bovenga, F., Caporusso, G., D'Addabbo, A., La Salandra, M., Lovergine, F. P., Nitti, D. O., Capolongo D. (2024). High-Resolution Flood Monitoring Based on Advanced Statistical Modeling of Sentinel-1 Multi-Temporal Stacks. Remote Sensing, 16(2), 294. https://doi.org/10.3390/rs16020294

Gardner, J., Pleiss, G., Weinberger, K. Q., Bindel, D., & Wilson, A. G. (2018). GPyTorch: Blackbox Matrix-Matrix Gaussian Process Inference with GPU Acceleration. Advances in Neural Information Processing Systems, 31. https://papers.nips.cc/paper_files/paper/2018/hash/27e8e17134dd7083b050476733207ea1-Abstract.html

Liu, D. C., & Nocedal, J. (1989). On The Limited Memory BFGS Method for Large Scale Optimization. Mathematical Programming, 45(1), 503–528. https://link.springer.com/article/10.1007/BF01589116

NVIDIA Corporation. (2023). NVIDIA CUDA Toolkit (Version 12.1) [Computer software]. Santa Clara, CA, USA. https://developer.nvidia.com/cuda-toolkit

Paszke, A., Gross, S., Massa, F., Lerer, A., Bradbury, J., Chanan, G., Killeen, T., Lin, Z., Gimelshein, N., Antiga, L., Desmaison, A., Kopf, A., Yang, E., DeVito, Z., Raison, M., Tejani, A., Chilamkurthy, S., Steiner, B., Fang, L., Bai, J., & Chintala, S. (2019). PyTorch: An Imperative Style, High-Performance Deep Learning Library. Advances in Neural Information Processing Systems, 32, 8024–8035. http://papers.neurips.cc/paper/9015-pytorch-an-imperative-style-high-performance-deep-learning-library.pdf

Pedregosa, F., Varoquaux, G., Gramfort, A., Michel, V., Thirion, B., Grisel, O., Blondel, M., Prettenhofer, P., Weiss, R., Dubourg, V., Vanderplas, J., Passos, A., Cournapeau, D., Brucher, M., Perrot, M., & Duchesnay, E. (2011). Scikit-learn: Machine Learning in Python. Journal of Machine Learning Research, 12, 2825–2830. http://www.jmlr.org/papers/v12/pedregosa11a.html

Pulvirenti, L., Pierdicca, N., Chini, M., Guerriero, L. (2013). Monitoring Flood Evolution in Vegetated Areas Using COSMO-SkyMed Data: The Tuscany 2009 Case Study. IEEE Journal of Selected Topics in Applied Earth Observations and Remote Sensing, 6(4), 1807-1816. https://doi.org/10.1109/JSTARS.2012.2219509

Refice, A., Caporusso, G., Lovergine, F. P., Nutricato, R., Nitti, D. O., Parisi, A., Colacicco, R., Capolongo, D., Virelli, M., Tapete, D., & Ursi, A. (2024). On The Integration of Intensity, Interferometric Coherence and Polarization Diversity in Flood Detection from Long Stacks of Multi-Frequency SAR Data Through a Bayesian Framework. IGARSS 2024 - 2024 IEEE International Geoscience and Remote Sensing Symposium, 1506–1509. https://doi.org/10.1109/IGARSS53475.2024.10641731

Rennó, C. D., Nobre, A. D., Cuartas, L. A., Soares, J. V., Hodnett, M. G., Tomasella, J., & Waterloo, M. J. (2008). HAND, a New Terrain Descriptor Using SRTM-DEM: Mapping Terra-firme Rainforest Environments in Amazonia. Remote Sensing of Environment, 112(9), 3469–3481. https://doi.org/10.1016/j.rse.2008.03.018

Wagner, W., Bauer-Marschallinger, B., Roth, F., Raiger-Stachl, T., Reimer, C., McCormick, N., Matgen, P., Chini, M., Li, Y., Martinis, S., Wieland, M., Kraft, F., Festa, D., Hassaan, M., Tupas, M. E., Zhao, J., Seewald, M., Riffler, M., Molini, L., … Salamon, P. (2025). The Fully-automatic Sentinel-1 Global Flood Monitoring Service: Scientific Challenges and Future Directions. Remote Sensing of Environment, 333, 115108. https://doi.org/10.1016/j.rse.2025.115108

This work is licensed under a Creative Commons Attribution-No Derivatives 4.0 International License.

Agriculture & forestry

Estimating Agronomic Variables in Paddy Rice with Field and Spaceborne Hyperspectral Spectroscopy

R. Ceriani[1,2], F. Fava[2], F. Nutini [3], G. Candiani [3], M. Pepe [3], A. Crema[3], L. Parigi[3], S. Ambrosini[2], M. Boschetti[3]

[1] Department of Agricultural and Environmental Sciences - Production, Landscape, Agroenergy (DiSAA), University of Milan, Italy – rodolfo.ceriani@unimi.it

[2] Department of Environmental Science and Policy (ESP), University of Milan, Italy – francesco.fava@unimi.it

[3] Institute of Electromagnetic Sensing of Environment (IREA), Italian National Research Council, Italy – mirco.boschetti@unimi.it

KEY WORDS: Precision agriculture, Hyperspectral Imaging, Rice crop monitoring, PRISMA

ABSTRACT:

Agronomic management in paddy rice is critical, as nutritional deficit limits both growth and yield, while excessive or poorly timed fertilization causes low nutrient use efficiency and environmental problems. While multispectral sensors like Sentinel-2 are widely used for crop monitoring, their broad spectral bands limit the detection of biochemical traits needed for crop nutrients management. Second-generation hyperspectral satellite missions (e.g., PRISMA) offer high spectral resolution (10 nm) across the 400-2500 nm range, providing enhanced potential for precision agriculture. This study evaluates the capability of hyperspectral spaceborne sensors to monitor rice traits at field scale. During 2023 and 2024, five field campaigns were conducted in Jolanda di Savoia (FE, Italy) to collect hyperspectral field measurements and agronomic data, including aboveground biomass (AGB), leaf area index (LAI) and nitrogen content (N). Gaussian Process Regression (GPR) models were trained on 2023 ground spectral measurements (n=120) resampled to PRISMA and applied on real satellite images acquired in 2024. The models effectively monitored crop development on the 2024 independent test set (n=80), showing good predictive performance for LAI [-] (R^2: 0.83, RMSE: 0.30, nRMSE: 9.30%), AGB [$g \cdot m^{-2}$] (R^2: 0.72, RMSE: 627.27, nRMSE: 14.86%), chlorophyll content at leaf level [$\mu g \cdot cm^{-2}$] (R^2: 0.58, RMSE: 3.40, nRMSE: 16.84%), and modest fit for N content at leaf [$mg \cdot m^{-2}$] (R^2: 0.34, RMSE: 225.51, nRMSE: 19.35%) and canopy level [$g \cdot m^{-2}$] (R^2: 0.56, RMSE: 0.77, nRMSE: 13.51%). Our findings demonstrate that satellite hyperspectral spectroscopy can complement operational multi-spectral missions, adding key information about agroecosystems nutritional status. Furthermore, the use of pre-trained machine learning models enables accurate trait retrieval without synchronous ground truth acquisition, offering a scalable solution for landscape-scale agroecosystem monitoring.

1. INTRODUCTION

Characterizing leaf biochemical and canopy structural dynamics can effectively support precision agriculture practices (Lu et al., 2020). In paddy rice cultivation, digital agronomic management can improve the use efficiency of external inputs, such as fertilizers and water (Alfred et al., 2021). While nutritional deficits limit yield, excessive fertilization encourages luxury consumption, which provides no additional growth and, at extreme levels, can lead to toxicity-induced growth reduction. This inefficiency is further compounded by environmental degradation, such as groundwater leaching and run-off (Van Wijk et al., 2003).

Effective monitoring requires the quantification of key traits, including Leaf Area Index (LAI), Aboveground Biomass (AGB), and chlorophyll and nitrogen (N) content at leaf and canopy level. While operational multispectral satellite sensors like Sentinel-2 provide valuable data on canopy structure, but their broad spectral bands often fail to detect specific biochemical absorption features (De Clerck et al., 2024). This is particularly true for nitrogen; while it is often indirectly estimated with chlorophyll correlation, protein-related absorption features within the shortwave infrared (SWIR) region – features that require high spectral resolution to resolve – provide an option for direct retrieval (Cerasola et al., 2025).

Second-generation satellite hyperspectral missions, such as PRISMA (PRecursore IperSpettrale della Missione Applicativa) and EnMAP (Environmental Mapping and Analysis Program), represent a paradigm shift, opening new opportunities for the direct agronomic traits retrieval (Guanter et al., 2015). These sensors provide hundreds of narrow, continuous bands across the 400–2500 nm range, offering the potential to decouple biochemical traits from canopy structure (Tagliabue et al., 2022).

However, the transition to hyperspectral data introduces significant computational and statistical challenges. The continuous spectrum leads to multicollinearity among adjacent narrow bands, which poses challenges to traditional regression models (Dalponte et al., 2009). Furthermore, the high data dimensionality may induce model overfitting (Hughes phenomenon; Hughes 1968), unless a sufficient number of training samples or robust dimensionality reduction techniques are employed. To address these complexities, advanced retrieval schemes such as non-parametric machine learning and hybrid models are required (Féret et al., 2021).

* Corresponding author

Despite the potential of hyperspectral technology, its application through satellite sensors remains poorly evaluated for rice agronomic trait retrieval. Recent research has predominantly focused on UAV-based hyperspectral sensing for estimating nitrogen nutrition indices, biomass, and yield-related traits (Yu et al., 2023; Xu et al., 2024; Zhang et al., 2025). Other studies have utilized field sensors to characterize nutrient stress, physiological traits variation, and leaf-level chlorophyll (Ting et al., 2023; Wang et al., 2024). While these proximal sensing approaches provide high spatial resolution, they are limited at district scales. The transition to spaceborne hyperspectral missions offers a path toward regional and large farms monitoring and management applications, yet research specifically validating these satellite-scale retrievals against field-scale agronomic data remains scarce.

This study evaluates the capacity of hyperspectral spaceborne sensors to monitor rice agronomic traits at the field scale in Jolanda di Savoia, Italy. First, we conducted 5 field campaigns during 2023-2024 growing seasons in rice paddies located in Jolanda di Savoia (NE Italy) to collect field hyperspectral and agronomic data across different phenological stages, including AGB, LAI, chlorophyll and N content. Then, GPR models were calibrated on 2023 reference samples obtained by spectral convolution to simulate PRISMA bands. Finally, the models were demonstrated on real PRISMA hyperspectral scene, and the estimations were validated against a temporal independent (2024) test set.

2. MAIN BODY

2.1 Study area and field data collection

The study was conducted at the Bonifiche Ferraresi S.p.A. agricultural estate, a large-scale farm of approximately 3,850 ha located in Jolanda di Savoia (Ferrara, NE Italy; 44.855° N, 11.952° E), within the Po delta (Fig. 1).

During the 2023–2024 growing seasons, five field campaigns were organized to coincide with different phenological stages of rice. Specifically, three campaigns were conducted in 2023 to provide a robust dataset for model calibration (comprising 120 points), while two additional campaigns were performed in 2024 to create a temporally independent dataset (comprising 80 points) for testing model exportability and transferability. All field measurements were carried out within Elementary Sampling Units (ESUs) of approximately 60x60 m^2, a scale chosen to ensure spatial representativeness when compared against the 30 m ground sampling distance (GSD) of PRISMA imagery. In-situ canopy reflectance was measured across the 350–2500 nm range using a Spectral Evolution NaturaSpec™ spectroradiometer.

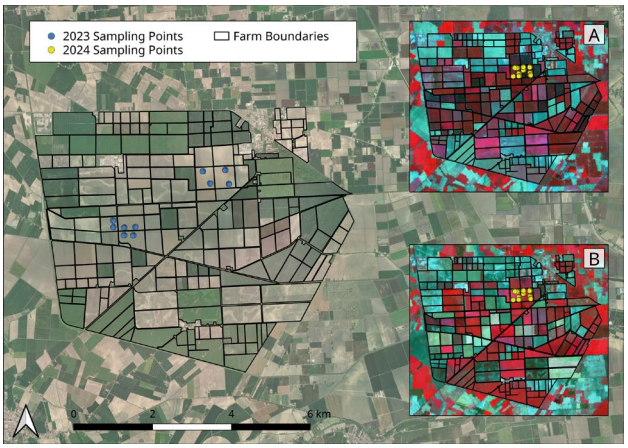

Figure 1: Overview of the study site in Jolanda di Savoia (NE Italy). The dotted line represents the boundaries of the Bonifiche Ferraresi S.p.A. agricultural estate. Blue and yellow circles indicate the location of the Elementary Sampling Units (ESUs) monitored during the 2023 and 2024 growing seasons, respectively. Insets show PRISMA false-color composites (R=854.9 nm, G=650.5 nm, B=546.3 nm) captured on (A) 26 July and (B) 30 August 2024. [PRISMA product L1 2024-07-26/2024-08-30©Italian Space Agency (ASI) (2024). All rights reserved].

Agronomic traits were characterized through a combination of structural and biochemical measurements following standardized protocols. The Leaf Area Index (LAI) was non-destructively measured using a LAI-2200 plant analyzer, while biochemical traits were derived from destructive sampling. Leaf Nitrogen Content (LNC) was determined via dry combustion using a nitrogen elemental analyzer, and Leaf Chlorophyll Content (LCC) was estimated in the field, using the Apogee MC-100 chlorophyll concentration meter, and in the laboratory through methanol extraction and spectrophotometry. Furthermore, Leaf Water Content (LWC) and Leaf Mass per Area (LMA) were calculated through gravimetric analysis by weighing leaf disk samples before and after oven-drying at 65°C for 48 hours.

These field-measured traits provided the fundamental ground-reference data required for the training and validation of the GPR models used in this study.

2.2 Machine Learning Models

The retrieval of rice agronomic traits was performed using a hybrid machine learning workflow based on GPR (Williams and Rasmussen, 1995). To address the challenges of high dimensionality and multicollinearity, inherent in hyperspectral data, a multi-step pipeline was implemented. First, spectral data were standardized using a Z-score normalization to ensure that all wavelengths contributed equally to the model calibration. Subsequently, dimensionality reduction was performed via Principal Component Analysis (PCA), extracting the first 15 principal components. This step was critical to mitigate the "Hughes phenomenon" and to compress the continuous spectral information into a manageable set of uncorrelated features that capture most of the spectral variance.

The non-parametric Bayesian GPR model was configured with a composite kernel consisting of a Radial Basis Function (RBF) to capture non-linear relationships and a White Kernel to account for the inherent noise in the spectral signal (Halme et al., 2019). The kernel hyperparameters were optimized during the training phase by maximizing the log-marginal likelihood, utilizing ten restarts of the optimizer to ensure global convergence (Pedregosa et al., 2011). This configuration allowed the model to maintain flexibility in trait estimation while providing a robust assessment of prediction uncertainty (Verrelst et al., 2013).

The performance of the GPR model was evaluated through a dual validation strategy. Internal consistency and model generalization were first assessed using a 10-fold cross-validation on the 2023 calibration dataset (Fushiki, 2011). To determine the practical utility and robustness of the models for operational monitoring, an independent validation was conducted by applying the calibrated models to real PRISMA scenes acquired in 2024. The predictive accuracy for all investigated traits—including LAI, AGB, and N content—was quantified using the coefficient of determination (R^2), Root Mean Square Error (RMSE), and Normalized Root Mean Square Error (nRMSE).

This rigorous validation scheme ensured that the models were not only accurate within their training domain but also transferable across different growing seasons.

2.3 PRISMA hyperspectral imagery

The PRISMA satellite of the Italian Space Agency (ASI) is a push-broom imaging spectrometer featuring 240 spectral bands across the visible (VIS), near-infrared (NIR) and shortwave infrared (SWIR) regions (400–2500 nm) (Loizzo et al., 2018). It provides a nominal spectral sampling interval of < 11 nm, a bandwidth of < 15 nm, and a ground spatial resolution of 30 m (Cogliati et al., 2021).

For this study, two PRISMA scenes were acquired contextually to the 2024 field campaigns on 26 July 2024 (Fig. 1A) and 30 August 2024 (Fig. 1B). The following pre-processing steps were conducted before further analyses:

1. **Data gathering:** Level 1 (Top of Atmosphere radiance) products were processed into a single hyperspectral data cube, including basic geometric corrections, using the *prismaread* R package (Busetto and Ranghetti, 2020).

2. **Co-registration:** To ensure sub-pixel spatial accuracy, geocoding and co-registration were performed using a Sentinel-2 Level-2A image acquired on the same day as a master reference, using the *AROSICS* and *GDAL* Python packages (Scheffler et al., 2017; Rouault et al., 2025).

3. **Atmospheric correction:** Units of radiance were converted to surface reflectance using ATCOR-3 software (ReSe Applications GmbH, Zurich, Switzerland). Columnar water vapour was retrieved using the absorption band at 1130nm, and Aerosol Optical Depth (AOD) was sourced from the daily MODIS product (MCD19A2).

4. **Spectral cleaning:** Bad bands were removed, specifically excluding regions with low signal-to-noise ratios or Gaussian-like noise (407–425 nm and 2343–2477 nm). Additionally, the atmospheric water absorption regions (1350–1510 nm and 1795–2000 nm) were filtered out. A cubic smoothing spline was applied to the remaining bands to reduce residual noise (Spirito et al., 2025).

2.4 Validation results

The performance of the GPR models was evaluated by comparing the satellite-derived estimates against the independent ground-truth dataset collected during the 2024 growing season (Fig. 2). This validation step is particularly significant as it assesses the transferability of the models across different years and the transition from proximal (ground-based) to spaceborne (satellite-based) spectral signatures.

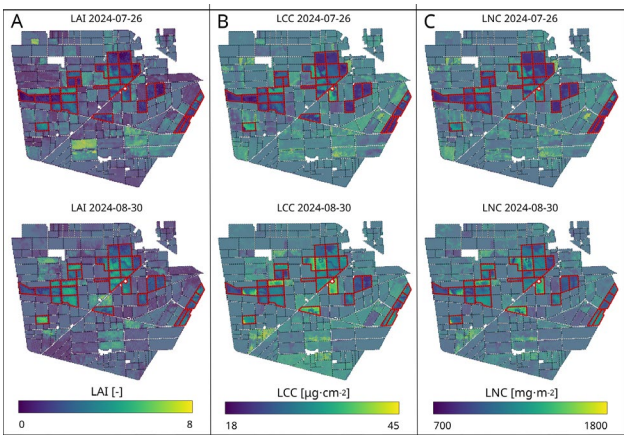

Figure 2: Spatio-temporal mapping of rice agronomic traits derived from PRISMA hyperspectral imagery for (A) Leaf Area Index (LAI), (B) Leaf Chlorophyll Content (LCC), and (C) Leaf Nitrogen Content (LNC). The top row (2024-07-26) corresponds to the stem elongation stage (BBCH = 31), while the bottom row (2024-08-30) captures the crops during fruit development phase (BBCH = 75). Red polygons highlight the rice paddies monitored in this study.

Structural traits demonstrated the highest retrieval accuracy, confirming the strong influence of canopy architecture on the hyperspectral signal. The models effectively estimated LAI, achieving an R^2 of 0.83 and an RMSE of 0.30 [-] (nRMSE: 9.30%). Similarly, aboveground biomass (AGB) was retrieved with high precision (R^2: 0.72; RMSE: 627.27 g·m^{-2}, nRMSE: 14.86%), indicating that the combination of VIS-NIR and SWIR bands effectively captures the variations in rice volume and density throughout the reproductive stages.

Regarding biochemical traits, LCC was retrieved with good accuracy (R^2: 0.58, RMSE: 3.40 µg·cm^{-2}, nRMSE: 16.84%), benefiting from the narrow bands in the visible and red-edge

regions, which are highly sensitive to pigment concentrations. N quantification showed varying levels of accuracy depending on the scale of observation. Canopy Nitrogen Content (CNC), which integrates both leaf biochemistry and total biomass, was retrieved with moderate-to-high accuracy (R^2: 0.56; RMSE: 0.77 $g \cdot m^{-2}$, nRMSE: 13.51%). At the leaf level, the retrieval of N content proved more challenging (R^2: 0.34; RMSE: 225.51 $mg \cdot m^{-2}$, nRMSE: 19.35%). This lower performance at the leaf scale is consistent with the "dilution effect" and the structural interference of the canopy, which can mask individual biochemical absorption features (Asner, 1998). However, the statistically significant correlation at both scales highlights the advantage of the high spectral resolution of PRISMA, particularly within the SWIR region, in detecting protein-related N absorption features that are typically not detectable with broad-band multispectral sensors.

The validation results point toward the potential of using pre-trained GPR models to bridge the gap between field-scale measurements and satellite observations. While performance varies by trait, the consistent retrieval of structural and biochemical variables highlights a pathway for monitoring rice development without requiring contemporaneous ground data.

3. CONCLUSIONS

This study demonstrates that second-generation hyperspectral satellite missions, such as PRISMA, provide an effective and reliable platform for the quantitative monitoring of rice agronomic traits at the field scale. By coupling spaceborne imaging spectroscopy with GPR models optimized through dimensionality reduction, we successfully retrieved both structural (LAI, AGB) and biochemical (chlorophyll, N) traits across independent growing seasons.

A key finding of this research is the operational feasibility of transferring models trained on ground-based proximal measurements to spaceborne scenes. The successful validation against a temporally independent dataset (2024) indicates that pre-trained machine learning models look promising to monitor rice paddies without the necessity for synchronous and labor-intensive ground truth acquisition. This offers a scalable solution for landscape-scale agronomic management.

In conclusion, the integration of satellite hyperspectral data into digital agriculture workflows provides a potential tool for optimizing nitrogen use efficiency and enhancing the sustainability of rice production. Future research should focus on the multi-temporal integration of these products with crop growth models to support real-time fertilization decision systems at regional and national scales.

ACKNOWLEDGEMENTS

This work was supported by the European Space Agency (ESA) within the framework of the EO4NUTRI project (“Earth Observation for estimating and predicting crop nutrients”), in response to the EXPRO+ AO/1-11144/22/I-EF for Agriculture Science Precursors. The authors acknowledge P. Sacco from the Italian Space Agency (ASI) for supporting the PRISMA image acquisitions. We further thank C. Zanella (DIAGRAM) for the logistic support and the provision of geo-spatial information on the crops' distribution and agricultural practices, as well as M. Gallina and R. Fuccella (UNIMI) for their assistance with laboratory measurements.

REFERENCES

Alfred, Rayner, et al. "Towards paddy rice smart farming: a review on big data, machine learning, and rice production tasks." IEE Access 9 (2021): 50358-50380.

Asner, Gregory P. "Biophysical and biochemical sources of variability in canopy reflectance." Remote Sensing of Environment 64.3 (1998): 234-253.

Busetto, L., Ranghetti, L. (2020) prismaread: A tool for facilitating access and analysis of PRISMA L1/L2 hyperspectral imagery v1.0.0, doi: https://doi.org/10.5281/zenodo.4019081

Cerasola, Vito Aurelio, et al. "Hyperspectral imaging for precision nitrogen management: A comparative exploration of two methodological approaches to estimate optimal nitrogen rate in processing tomato." Smart Agricultural Technology 10 (2025): 100802.

Cogliati, Sergio, et al. "The PRISMA imaging spectroscopy mission: overview and first performance analysis." Remote Sensing of environment 262 (2021): 112499.

Dalponte, Michele, et al. "The role of spectral resolution and classifier complexity in the analysis of hyperspectral images of forest areas." Remote Sensing of environment 113.11 (2009): 2345-2355.

De Clerck, Emma, et al. "Optimizing hybrid models for canopy nitrogen mapping from Sentinel-2 in Google Earth Engine." ISPRS Journal of Photogrammetry and Remote Sensing 218 (2024): 530-545.

Féret, Jean-Baptiste, et al. "PROSPECT-PRO for estimating content of nitrogen-containing leaf proteins and other carbon-based constituents." Remote Sensing of Environment 252 (2021): 112173.

Fushiki, Tadayoshi. "Estimation of prediction error by using K-fold cross-validation." Statistics and Computing 21.2 (2011): 137-146.

Guanter, Luis, et al. "The EnMAP spaceborne imaging spectroscopy mission for earth observation." Remote Sensing 7.7 (2015): 8830-8857.

Halme, Eelis, Petri Pellikka, and Matti Mõttus. "Utility of hyperspectral compared to multispectral remote sensing data in estimating forest biomass and structure variables in Finnish boreal forest." International Journal of Applied Earth Observation and Geoinformation 83 (2019): 101942.

Hughes, Gordon. "On the mean accuracy of statistical pattern recognizers." IEEE transactions on information theory 14.1 (1968): 55-63.

Loizzo, Rosa, et al. "PRISMA: The Italian hyperspectral mission." IGARSS 2018-2018 IEEE international geoscience and remote sensing symposium. IEEE, 2018.

Lu, Bing, et al. "Recent advances of hyperspectral imaging technology and applications in agriculture." Remote Sensing 12.16 (2020): 2659.

Pedregosa, Fabian, et al. "Scikit-learn: Machine learning in Python." the Journal of Machine Learning research 12 (2011): 2825-2830.

Rouault, Even, et al. "Gdal." Zenodo (2025).

Scheffler, Daniel, et al. "AROSICS: An automated and robust open-source image co-registration software for multi-sensor satellite data." Remote sensing 9.7 (2017): 676.

Spirito, E., et al. “PRISTAR-GEOSPEC: PRISma Tools for Analysis in R for GEOcoding and SPECtral Refinement” (2025).

Tagliabue, Giulia, et al. "Hybrid retrieval of crop traits from multi-temporal PRISMA hyperspectral imagery." ISPRS Journal of Photogrammetry and Remote Sensing 187 (2022): 362-377.

Ting, To-Chia, et al. "Quantifying physiological trait variation with automated hyperspectral imaging in rice." Frontiers in Plant Science 14 (2023): 1229161.

Van Wijk, Mark T., et al. "Luxury consumption of soil nutrients: a possible competitive strategy in above-ground and below-ground biomass allocation and root morphology for slow-growing arctic vegetation?." Journal of Ecology 91.4 (2003): 664-676.

Verrelst, Jochem, et al. "Gaussian processes uncertainty estimates in experimental Sentinel-2 LAI and leaf chlorophyll content retrieval." ISPRS Journal of photogrammetry and remote sensing 86 (2013): 157-167.

Wang, Jinfeng, et al. "Characterization and identification of NPK stress in rice using terrestrial hyperspectral images." Plant Phenomics 6 (2024): 0197.

Williams, Christopher, and Carl Rasmussen. "Gaussian processes for regression." Advances in neural information processing systems 8 (1995).

Xu, Tianyue, et al. "Multi-scale monitoring of rice aboveground biomass by combining spectral and textural information from UAV hyperspectral images." International Journal of Applied Earth Observation and Geoinformation 127 (2024): 103655.

Yu, Fenghua, et al. "Estimating the rice nitrogen nutrition index based on hyperspectral transform technology." Frontiers in Plant Science 14 (2023): 1118098.

Zhang, Yufen, et al. "Estimating rice yield-related traits using machine learning models integrating hyperspectral and texture features." Frontiers in Plant Science 16 (2025): 1713014.

This work is licensed under a Creative Commons Attribution-No Derivatives 4.0 International License.

ASSESSING MACHINE LEARNING REGRESSION ALGORITHMS FOR WHEAT GRAIN PROTEIN CONTENT (GPC) ESTIMATION EXPLOITING GROUND SPECTRAL DATA AND CROP TRAITS

L. Miazzo [1] *, M. Boschetti [1], M. Marshall[2], M. Belgiu[2], L. Parigi [1], G. Candiani [1]

1 National Research Council of Italy (CNR), Institute for Electromagnetic Sensing of Environment (IREA) Via A. Corti 12, 20133 Milan, Italy (miazzo.l, boschetti.m, parigi.l, candiani.g)@irea.cnr.it

2 Faculty of Geo-Information Science and Earth Observation, University of Twente, PO Box 217, Drienerlolaan 5, 7500 AE Enschede, The Netherlands (m.t.marshall, m.belgiu)@utwente.nl

KEY WORDS: Grain protein content, machine learning, wheat, ground spectral data, crop traits

ABSTRACT:

Wheat is a fundamental staple food and grain protein content (GPC) is a key quality trait that affects both nutritional and economic factors. Timely GPC predictions could support proper nitrogen fertiliser management at field level, potentially reducing N waste, making agricultural production more sustainable. The objective of this study was (i) to explore the relation between GPC and either ground spectral data (resampled to PRISMA-like spectra) or crop traits and (ii) test the capability of five popular machine learning regression algorithms (MLRA) combined with different preprocessing steps to estimate GPC. Input ground data include measurements collected in the vegetative (VEG) phase, the reproductive (REP) phase or a combination of both (VEG+REP). The results show how GPC is closely related to crop nitrogen uptake according to both ground spectral data and crop traits analysis. The machine learning analysis highlighted the capability of single layer neural network (NN) and partial least square regression (PLSR) to estimate GPC achieving good accuracy (NRMSE ~ 14%) when exploiting spectral data collected during REP or VEG+REP. Similar results are obtained when crop traits are used, with the best performances achieved by VEG+REP models. These results confirm the relation between nitrogen and GPC and the capability of MLRA to estimate GPC exploiting ground spectral data or crop traits.

1. INTRODUCTION

Wheat is the most widely cultivated crop in terms of global surface area and provides 20% of calories and protein in the global diet, making it a fundamental staple food (Erenstein *et al.*, 2022). Grain quality is primarily determined by its protein content (GPC) and gluten properties, which define the range of end products that can be produced (Poutanen *et al.*, 2022). Traditional laboratory tests and analytical methods for determining grain protein content (GPC), such as the Kjeldahl test, are widely reported in the literature for their high accuracy. However, these approaches typically rely on point sampling after harvest and require labour-intensive chemical analyses (Z. Li *et al.*, 2024). In practice, they are not well suited for optimizing crop management before harvest or for monitoring large-scale areas. Recently, remote sensing has shown its potential in estimating crop traits at leaf level (*e.g.* LNC, LCC, LWC) and canopy level (*e.g.* LAI, CNC, CCC, CWC) achieving good results (Candiani *et al.*, 2022; Tagliabue *et al.*, 2022; D. Li *et al.*, 2024). Due to the demonstrated accuracy of remote sensing approaches, numerous studies have sought to estimate GPC (Longmire *et al.*, 2023; Z. Li *et al.*, 2024). Compared with destructive laboratory assays or spectroscopy-based methods, remote sensing offers the advantage of capturing within-field variability and has the potential to predict GPC (Barmeier *et al.*, 2017; Zhao *et al.*, 2019; Longmire *et al.*, 2023). A range of methodologies for estimating GPC from multispectral or hyperspectral optical data have been exploited, including regression-based approaches utilising vegetation indices, machine learning approaches, radiative transfer model inversion approaches, and physically-based approaches that exploit crop models and assimilation techniques (Ma *et al.*, 2022; Z. Li *et al.*, 2024). However, modelling the relationship between spectral data and GPC remains inherently complex (Longmire *et al.*, 2023; Z. Li *et al.*, 2024), reflecting both the intricate physiological dynamics of source–sink interactions during flowering and grain filling and the influence of genome–environment interactions (Kong *et al.*, 2016). In this framework, an explorative analysis to assess the relation of either crop traits or spectra with GPC has been conducted exploiting ground spectral data (resampled to PRISMA-like reflectance) and crop traits, collected during the wheat crop cycle. Moreover, five commonly used machine learning regression algorithms (MLRAs) and several input pre-processing and combinations were tested to estimate GPC.

2. MATERIAL

2.1 Ground measurements dataset

Ground reference data were collected within the ESA EO4NUTRI project at Jolanda di Savoia (JDS; 44°53′N; 11°59′E, Emilia Romania, Italy) during the 2023 and 2024 seasons and consisted of wheat canopy spectra (resampled to PRISMA-like reflectance), crop traits measured throughout the growing season at different phenological stages, and harvest data including grain protein content (GPC) and yield. In addition, two experimental campaigns conducted at different locations and years in Arborea (ARB; 39°46′N; 8°34′E, Sardigna Italy; E-CROP project) and in Torrazza Coste, Riccagioia (RIC; 44°57′N 9°05′E, Lombardy-Italy AGRITECH project) were included to increase data diversity and robustness (see table 1). The EO4NUTRI datasets were acquired in real farm condition while the other datasets derive from controlled field experiments, with replicated plots

* Corresponding author

and/or different nitrogen fertilization treatments and/or multiple wheat varieties. Physiological traits and spectral data were measured during the vegetative (VEG) and reproductive (REP) phase of wheat (table 1), including leaf area index (LAI [m^2/m^2]), leaf chlorophyll content (LCC [µg/cm^2]), leaf nitrogen content (LNC [g/cm^2]), leaf water content (LWC [g/cm^2]) and leaf mass per area (LMA [g/cm^2]). Canopy traits were calculated multiplying LAI and the relative leaf traits to obtain canopy chlorophyll content (CCC [g/m^2]), canopy nitrogen content (CNC [g/m^2]) and canopy water content (CWC [g/m^2]). Information on sampling strategies can be found in Tagliabue *et al.*, (2022) and Heidarian Dehkordi *et al.*, (2024). At the end of the season, yield and grain protein content were also collected. GPC was determined as:

$$GPC[\%] = N_{grain}[\%]*6.25 \quad (1)$$

Where N_{grain}[%] is the percentage of nitrogen in the grain at harvest determined by near-infrared (NIR) spectroscopy.

Location	Year	Type of data	Crop	Sampling date	BBCH	Phenology	Cardinality
Arborea	2022	spectra	durum wheat	14/05/2022	37	VEG	89
				28/05/2022	69	REP	90
		crop traits	durum wheat	14/05/2022	37	VEG	23
				28/05/2022	69	REP	21
Riccagioia	2024	spectra	soft wheat	12/04/2024	32	VEG	12
				13/05/2024	67	REP	12
		crop traits	soft wheat	12/04/2024	32	VEG	11
				13/05/2024	67	REP	11
Jolanda di Savoia	2023	spectra	durum wheat	04/04/2023	37	VEG	20
				23/05/2023	75	REP	20
			soft wheat	04/04/2023	37	VEG	20
				23/05/2023	69	REP	20
		crop traits	durum wheat	05/04/2023	37	VEG	20
				23/05/2023	75	REP	20
			soft wheat	05/04/2023	37	VEG	20
				23/05/2023	69	REP	20
	2024	spectra	soft wheat	04/04/2024	31	VEG	39
				09/05/2024	65	REP	39
		crop traits	soft wheat	04/04/2024	31	VEG	17
				09/05/2024	65	REP	19

Table 1. Characteristics of measurements dataset (ARB22, RIC24, JDS23 and JDS24)

3. METHODS

3.1 Correlation analysis

A correlation analysis has been conducted to ascertain the relation between crop traits at leaf and canopy level, and GPC considering phenology of data acquisition (VEGetative and REProductive phase) and species (soft and durum wheat).

3.2 Analysis of important spectral regions for GPC estimation

A preliminary analysis was conducted using Minimum Redundancy Maximum Relevance (mRMR) algorithm to identify which spectral regions (visible, red-edge, NIR, SWIR1, and SWIR2) contributed most to GPC estimation. mRMR is an agnostic feature selection method based on information theory (Peng et al. 2005). The algorithm aims to identify the subset of features that are both highly relevant to the target variable and minimally redundant with each other. This approach produces an ordered ranking of features, enabling the identification of the most informative bands and spectral regions for GPC prediction.

3.3 Machine learning modelling of either spectra or crop traits and GPC

An exploratory analysis was conducted to evaluate the ability of five commonly used machine learning regression algorithms (MLRAs) to estimate the grain protein content (GPC) of wheat using either ground-based spectral data or crop traits. The selected MLRAs were: Partial Least Square Regression (**PLSR**, Wold *et al.*, 2001), Gaussian Process Regression (**GPR**, Rasmussen and Williams, 2006), Random Forest (**RF**, Breiman, 2001), Light Gradient Boosting (**LGB**, Ke *et al.*, 2017), Single layer Neural Network (**NN**, Goodfellow *et al.*, 2016).

All algorithms were trained on the **ARB22**, **RIC24**, **JDS23**, and **JDS24** datasets to estimate GPC using leaf traits, canopy traits, and PRISMA-like spectra. Inputs were used either in raw form or transformed via PCA, while PRISMA-like data were also tested using the 20 most relevant bands selected by mRMR. Models were trained using five-fold cross-validation repeated ten times, considering vegetative (VEG), reproductive (REP), or combined (VEG+REP) phases. Because **JDS24** included observations beyond the reproductive stage (BBCH 75, table 1), analyses were performed with and without these data, but only results excluding them are reported unless otherwise noted. Model performance was evaluated using NRMSE (normalised on data range) computed on out-of-fold predictions from the best hyperparameter configuration. Friedman tests were applied to NRMSE values to assess differences among algorithms, input configurations, and phenological phases (Demšar, 2006). When significant, post-hoc pairwise comparisons were conducted using the Wilcoxon signed-rank test, with p-values adjusted using the Shaffer procedure (Demšar, 2006). Analyses were performed separately for crop trait–based and PRISMA-based models when evaluating preprocessing methods and phenology.

4. RESULTS

4.1 Correlation analysis

Crop	Phenology	LCC	LNC	LWC	LMA	Cardinality
Soft and	VEG	0.710***	0.600***	0.632***	0.306**	91
Durum wheat	REP	0.565***	0.174	0.521***	0.450***	91
Crop	**Phenology**	**LAI**	**CCC**	**CNC**	**CWC**	**Cardinality**
Soft and	VEG	0.278**	0.437***	0.428***	0.412***	91
Durum wheat	REP	0.516***	0.607***	0.425***	0.670***	91

Table 2. Correlation analysis results (Pearson correlation coefficient, r) between crop traits and GPC. Significance levels: *** p-value ≤ 0.001, ** 0.001 < p-value ≤ 0.01, * 0.01 < p ≤ 0.05, 0.05 < p ≤ 0.1

Table 2 summarizes the correlations between leaf- and canopy-level crop traits and GPC. Canopy traits (LAI, CCC, CNC, CWC) showed overall positive relationships, particularly for nitrogen- and water-related traits, with the highest correlations observed during the reproductive stage, in agreement with physiological knowledge (Wang *et al.*, 2014; Kong *et al.*, 2016; Zhao *et al.*, 2019). Leaf parameters (LCC, LWC, LMA, LNC) show an higher correlation value compared to the corresponding canopy traits during vegetative phase, but lower during the reproductive phase, probably due to the beginning of nitrogen remobilization and the onset of senescence (Kong *et al.*, 2016). LAI exhibited a weak correlation during vegetative phase, while a strong one during the reproductive phase, indicating how canopy traits are driven by LAI and how this trait is important especially during the reproductive phase. Given the moderate strength of the

correlations, non-linear modelling approaches were adopted to relate crop traits to GPC.

4.2 Band importance analysis

Figure 3 show the top 20 PRISMA bands related to GPC, for vegetative (VEG) and reproductive (REP) phases, selected by mRMR and their resulting relative importance. Most of the selected bands for VEG and REP phases are located in VIS , RED-EDGE and SWIR2 (second part of the short wave infra-red) regions and are mostly related to green vegetation features and specific chlorophyll, nitrogen and protein absorption, as reported by Curran (1989). This is also in accordance with physiological knowledge, as reported by Kong *et al.* (2016), considering that approximately 40-95% of grain N originates from the remobilization of stored nitrogen in plant tissues prior to anthesis in wheat. Additional bands are related to structural components (e.g. cellulose and lignin) and photosynthetic products (e.g. sugars and starch) characterizing plant biomass.

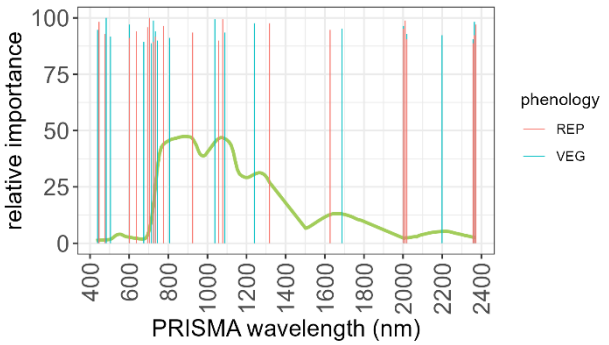

Figure 3. Band importance for VEG (blue) and REP (red) spectra from mRMR analysis. The green line shows an average wheat spectra during reproductive phase.

4.3 MLRA analysis

Figure 4-a shows the MLRA performance metrics computed from out-of-fold predictions obtained during cross-validation, using the best hyperparameter configuration for each model. In general, the results are good, highlighting how either ground spectral data or crop traits acquired during the season can be effectively exploited to estimate GPC. Friedman tests revealed significant differences among the five algorithms (χ^2 (4) = 37.105, p = 1.71 × 10^{-7}). Post-hoc Wilcoxon tests indicated that NN and PLSR, which consistently ranked highest (mean ranks of 1.71 and 2.38, respectively), significantly outperformed RF (mean rank = 3.95; $p < 0.01$) and LGB (mean rank = 4.19; $p < 0.01$). The performance difference between NN and PLSR was marginal ($p = 0.07$). NN showed a slightly better performance than GPR (mean rank = 2.76; $p = 0.046$), whereas no significant differences were observed between PLSR and GPR ($p = 0.37$). No significant effects of preprocessing strategy (raw, PCA, or mRMR) were detected, either for PRISMA-based models or for models trained using crop traits as input.

Regarding phenological phases, significant differences were found for both PRISMA ($\chi^2(2) = 6.33$, p = .042) and crop traits models ($\chi^2(2) = 9.75$, p = .008). For PRISMA, post-hoc tests indicated that REP and VEG+REP, which achieved the highest rank (REP = 1.50, VEG+REP = 1.67), outperformed the vegetative phase; for crop traits models, VEG+REP (mean rank = 1.12) outperformed both the vegetative and reproductive phases. The statistical analysis of the phenological phases confirms what is widely reported in the scientific literature: the reproductive phase is the most suitable period for estimating GPC, particularly when spectral data are used. The analysis also highlights the value of temporal information when predictors closely linked to crop physiology are considered (Wang *et al.*, 2014; Zhao *et al.*, 2019; Longmire *et al.*, 2023). Moreover, if data collected beyond the reproductive phase had been included in the phenological analysis (i.e. data in BBCH 75), no significant differences between VEG, REP, VEG+REP would have been observed for PRISMA-based models, due to the lower performances, emphasizing how spectral data can be sensitive to abrupt changes in crop behaviour in maturity phase. Figure 4-b shows some of the best-performing models, including NN trained on PCA-reduced PRISMA data from the REP phase (left panel) and a NN trained on PCA-reduced leaf trait data combining vegetative and reproductive phases (VEG+REP).

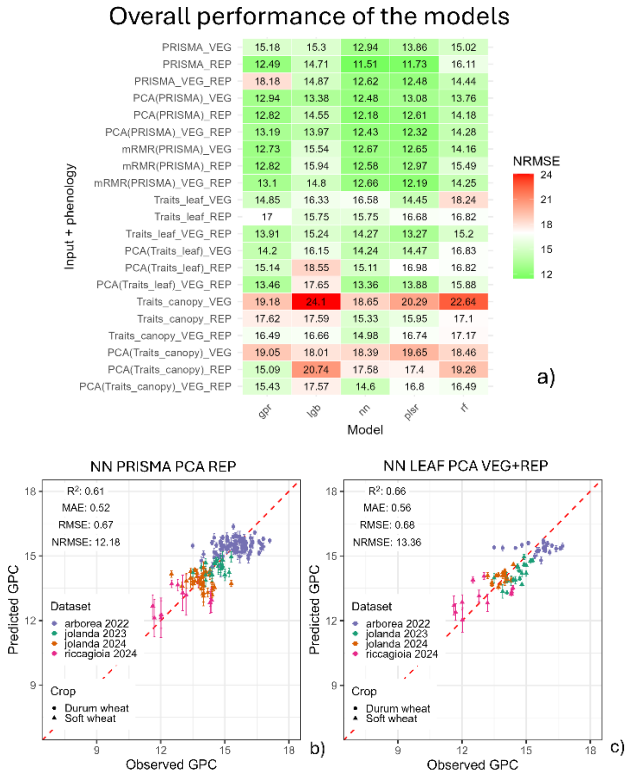

Figure 4. Cross-validation performance for GCP in terms of NRMSE across all tested combinations (a). Results for the best-performing NN models using PCA-reduced PRISMA REP data (b, 160 samples) and leaf traits VEG+REP data (c, 71 samples) as inputs. Error bars show the standard deviation of the out-of-fold predictions.

5. CONCLUSIONS

In this study an exploratory analysis has been conducted to investigate the potential of ground spectral data and crop traits to estimate GPC, exploiting data collected in different years and locations across Italy. Several algorithms were tested with different combination of data source (PRISMA-like or crop traits), preprocessing (raw, PCA, mRMR) and temporal feature (VEG, REP, VEG+REP). Statistical analysis has been conducted to assess significative differences in the performances of the models (Algorithm x data source x preprocessing x phenological stage). NN and PLSR were found as the best performing

algorithms for this specific task given the low amount of available data. REP and VEG+REP were found as the most relevant phenological stages to estimate GPC when using spectral data, while VEG+REP when exploiting crop traits. No differences were found between the tested preprocessing approaches. The achieved performances for the best models are promising (NRMSE ~ 14%) highlighting how both ground hyperspectral data and crop traits potentially can be valid predictors for estimating GPC.

ACKNOWLEDGEMENTS

This study was conducted within the EO4NUTRI project, funded by the European Space Agency (ESA) under the Agriculture Science Precursor grant (No. 4000140875/23/I-EF).

REFERENCES

Barmeier, G., Hofer, K. and Schmidhalter, U. (2017) 'Mid-season prediction of grain yield and protein content of spring barley cultivars using high-throughput spectral sensing', *European Journal of Agronomy*, 90, pp. 108–116. Available at: https://doi.org/10.1016/j.eja.2017.07.005.

Breiman, L. (2001) 'Random Forests', *Machine Learning*, 45(1), pp. 5–32. Available at: https://doi.org/10.1023/A:1010933404324.

Candiani, G. *et al.* (2022) 'Evaluation of Hybrid Models to Estimate Chlorophyll and Nitrogen Content of Maize Crops in the Framework of the Future CHIME Mission', *Remote Sensing*, 14(8), p. 1792. Available at: https://doi.org/10.3390/rs14081792.

Curran, P.J. (1989) 'Remote sensing of foliar chemistry', *Remote Sensing of Environment*, 30(3), pp. 271–278. Available at: https://doi.org/10.1016/0034-4257(89)90069-2.

Demšar, J. (2006) 'Statistical Comparisons of Classifiers over Multiple Data Sets', *The Journal of Machine Learning Research*, 7, pp. 1–30. Available at: https://doi.org/10.5555/1248547.1248548.

Erenstein, O. *et al.* (2022) 'Global Trends in Wheat Production, Consumption and Trade', in M.P. Reynolds and H.-J. Braun (eds) *Wheat Improvement: Food Security in a Changing Climate*. Cham: Springer International Publishing, pp. 47–66. Available at: https://doi.org/10.1007/978-3-030-90673-3_4.

Goodfellow, I., Bengio, Y. and Courville, A. (2016) *Deep Learning*. Cambridge, MA: MIT Press. Available at: https://www.deeplearningbook.org/.

Heidarian Dehkordi, R. *et al.* (2024) 'Towards an Improved High-Throughput Phenotyping Approach: Utilizing MLRA and Dimensionality Reduction Techniques for Transferring Hyperspectral Proximal-Based Model to Airborne Images', *Remote Sensing*, 16(3), p. 492. Available at: https://doi.org/10.3390/rs16030492.

Ke, G. *et al.* (2017) 'LightGBM: A Highly Efficient Gradient Boosting Decision Tree', *31st Conference on Neural Information Processing Systems*, Long Beach, CA, USA.

Kong, L. *et al.* (2016) 'Remobilization of vegetative nitrogen to developing grain in wheat (Triticum aestivum L.)', *Field Crops Research*, 196, pp. 134–144. Available at: https://doi.org/10.1016/j.fcr.2016.06.015.

Li, D. *et al.* (2024) 'Estimating canopy nitrogen content by coupling PROSAIL-PRO with a nitrogen allocation model', *International Journal of Applied Earth Observation and Geoinformation*, 135, p. 104280. Available at: https://doi.org/10.1016/j.jag.2024.104280.

Li, Z. *et al.* (2024) 'Remote sensing of quality traits in cereal and arable production systems: A review', *The Crop Journal*, 12(1), pp. 45–57. Available at: https://doi.org/10.1016/j.cj.2023.10.005.

Longmire, A. *et al.* (2023) 'Estimation of grain protein content in commercial bread and durum wheat fields via traits inverted by radiative transfer modelling from Sentinel-2 timeseries', *ISPRS Journal of Photogrammetry and Remote Sensing*, 206, pp. 49–62. Available at: https://doi.org/10.1016/j.isprsjprs.2023.10.018.

Ma, J., Zheng, B. and He, Y. (2022) 'Applications of a Hyperspectral Imaging System Used to Estimate Wheat Grain Protein: A Review', *Frontiers in Plant Science*, 13. Available at: https://doi.org/10.3389/fpls.2022.837200.

Peng, H., Long, F. and Ding, C. (2005) 'Feature selection based on mutual information criteria of max-dependency, max-relevance, and min-redundancy', *IEEE Transactions on Pattern Analysis and Machine Intelligence*, 27(8), pp. 1226–1238. Available at: https://doi.org/10.1109/TPAMI.2005.159.

Poutanen, K.S. *et al.* (2022) 'Grains – a major source of sustainable protein for health', *Nutrition Reviews*, 80(6), pp. 1648–1663. Available at: https://doi.org/10.1093/nutrit/nuab084.

Rasmussen, C.E. and Williams, C.K.I. (2006) *Gaussian processes for machine learning*. Cambridge, Mass: MIT Press (Adaptive computation and machine learning).

Tagliabue, G. *et al.* (2022) 'Hybrid retrieval of crop traits from multi-temporal PRISMA hyperspectral imagery', *ISPRS Journal of Photogrammetry and Remote Sensing*, 187, pp. 362–377. Available at: https://doi.org/10.1016/j.isprsjprs.2022.03.014.

Wang, L. *et al.* (2014) 'Predicting grain yield and protein content in wheat by fusing multi-sensor and multi-temporal remote-sensing images', *Field Crops Research*, 164, pp. 178–188. Available at: https://doi.org/10.1016/j.fcr.2014.05.001.

Wold, S., Sjöström, M. and Eriksson, L. (2001) 'PLS-regression: a basic tool of chemometrics', *Chemometrics and Intelligent Laboratory Systems*, 58(2), pp. 109–130. Available at: https://doi.org/10.1016/S0169-7439(01)00155-1.

Zhao, H. *et al.* (2019) 'Monitoring of Nitrogen and Grain Protein Content in Winter Wheat Based on Sentinel-2A Data', *Remote Sensing*, 11(14), p. 1724. Available at: https://doi.org/10.3390/rs11141724.

This work is licensed under a Creative Commons Attribution-No Derivatives 4.0 International License.

Mapping Tillage and Crop Residue presence Using Planet and Sentinel-2 Imagery

G. Tellina[1], M. Boschetti[1], M. Pepe[1], A. Ferrarini[2], F. Filipponi[3], F. Zucca[4], F. Nutini[1*]

[1] CNR-IREA, Via Alfonso Corti 12, Milan, Italy (tellina.g, boschetti.a, pepe.m, nutini.f)@irea.cnr.it
[2] UCSC - DI.PRO.VE.S., Via E. Parmense 84, Piacenza, Italy - andrea.ferrarini@unicatt.it
[3] CNR-IGAG, Montelibretti (RM), Italy - federico.filipponi@cnr.it
[4] UniPV DSTA, Via Ferrata 1, Pavia, Italy - francesco.zucca@unipv.it

KEY WORDS: Carbon Farming, Change Detection, PlanetScope, Machine Learning

ABSTRACT:

Carbon farming aims to mitigate climate change by increasing soil organic carbon (SOC) through practices such as reduced tillage and crop residue retention. To ensure transparency and effectiveness, these practices require robust Monitoring, Reporting, and Verification (MRV) protocols. Satellite remote sensing plays a central role in MRV frameworks by providing spatially explicit and temporally consistent observations of agricultural practices. This study assesses the potential of high-resolution (PlanetScope) and medium-resolution (Sentinel-2) multispectral imageries to detect soil management practices relevant to carbon farming. Objectives of the study are to: (i) evaluate the capability of PlanetScope data to detect spectral changes associated with harvesting and tillage events; (ii) test the performance of a Random Forests classifier for field-level management practice classification; and (iii) transfer the approach to Sentinel-2 data to assess their suitability for large-scale monitoring using open-access satellite products. The study was conducted in the Emilia-Romagna region (Piacenza and Parma provinces, Italy) within the REMOTE-C project and focused on the 2022 agronomic season during the winter crop harvesting period (June–August). Approximately 200 agricultural fields were visually interpreted using daily PlanetScope imagery and classified into eight classes representing different land-cover and soil / crop residue management. A mapping demonstration using two PlanetScope acquisitions (10 and 15 July 2022) and the classification model using Random Forests algorithm achieved an overall accuracy of 86%. The resulting map was used to train a Sentinel-2-based model, which reached an overall accuracy of 89%. These results demonstrate the potential of multitemporal and spectral satellite data and machine learning for operational MRV of carbon farming practices.

1. INTRODUCTION

1.1 Carbon farming and MRV

In the context of climate change mitigation, agriculture is increasingly recognized not only as a source of greenhouse gas (GHG) emissions but also as a potential sink, particularly through soil organic carbon (SOC) sequestration (Smith et al., 2020). Among the strategies aimed at enhancing this potential, carbon farming encompasses a set of conservation and regenerative practices—such as conservation tillage, cover cropping, and crop residue retention—that promote the accumulation of soil organic carbon (SOC) in agricultural soils. To support the implementation of carbon farming at scale, robust Monitoring, Reporting, and Verification (MRV) systems are required to quantify, validate, and certify actual carbon (C) sequestration benefits. Remote sensing, particularly through satellite imagery, is a recognised cornerstone of MRV systems due to its ability to monitor large areas with high spatial and temporal resolution, providing objective, repeatable, and spatially explicit data on crop development and management practices (https://climate.ec.europa.eu/eu-action/carbon-removals-and-carbon-farming_en) .

1.2 Remote Sensing monitoring of crop residue

Among agricultural practices, crop residue management plays a critical role in maintaining SOC levels. However, monitoring residue presence and post-harvest soil preparation (e.g., tillage) remains challenging using traditional field-based methods due to their labour intensity and limited spatial coverage. Diagnostic detection and quantification of crop residues (CR) from remote sensing can be achieved using narrowband shortwave infrared (SWIR) data, which enable the identification of spectral features associated with non-photosynthetic vegetation (NPV), primarily related to carbon-based constituents (CBCs) such as lignin and cellulose. Previous studies have demonstrated that hyperspectral imagery enables accurate mapping of crop residues (Pepe et al., 2023). Although hyperspectral data provide clear advantages, multispectral imagery has also been successfully applied for CR detection (Hively et al., 2021).

In this context, the multi-temporal dimension of operational Earth Observation (EO) systems, such as the Copernicus Sentinel-2 mission, offers additional value by enabling change-detection analyses capable of identifying abrupt spectral changes in agricultural fields associated with soil management operations (Yang et al., 2025). Moreover, the availability of commercial missions such as PlanetScope, which provide near-daily imagery at 3 m spatial resolution, offers further potential to monitor the temporal evolution of field conditions and to capture rapid changes driven by management practices.

1.3 Objective

Within this framework, the study investigates the potential of multispectral satellite imagery to detect harvesting and tillage operations and to assess the feasibility of identifying crop residue management practices through spectral change analysis. Developed within the REMOTE-C project, the research explores the complementary use of high-resolution (HR) PlanetScope and medium-resolution (MR) Sentinel-2 data to support MRV workflows for carbon farming practices.

The overall objective is to evaluate the capability of daily HR PlanetScope imagery to capture field-level changes related to crop management and to use this information to build a reliable training dataset for supervised classification based on operational Sentinel-2 data. Notably, the study aims at:

1. detecting spectral changes associated with harvesting and tillage operations at the field scale;
2. assessing the feasibility of using multispectral optical data to identify crop residue management practices relevant to carbon farming;

* Corresponding author

3. evaluating the scalability of the proposed approach for district level monitoring using Sentinel-2 imagery.

2. MATERIAL AND METHOD

2.1 Study area

The study area is located in northern Italy in Emilia-Romagna region within the Province of Piacenza and Parma, (Figure 1). In this area we focused on the 2022 agronomic season during the winter crop harvesting period (June–August).

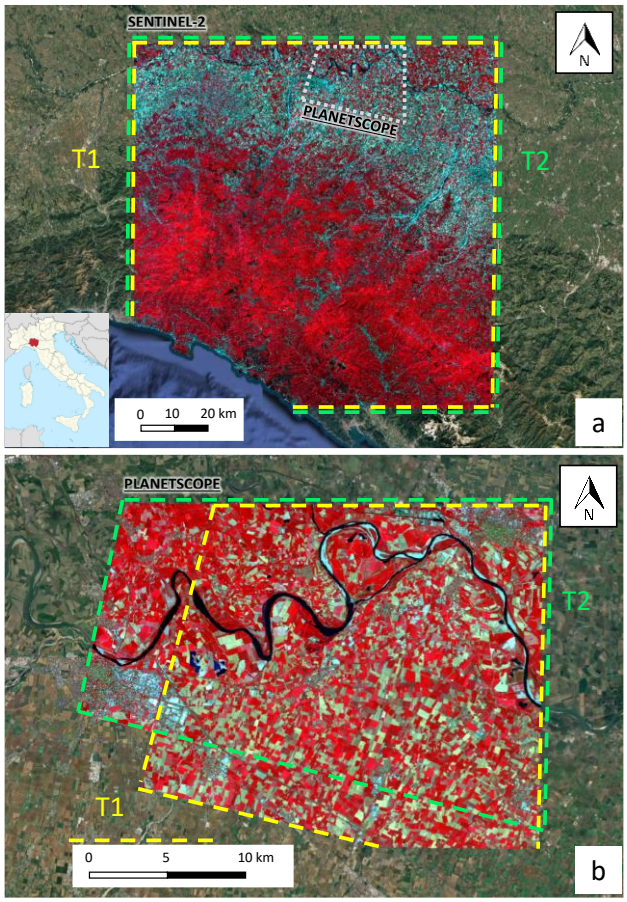

Figure 1. Overview of the study area and satellite data coverage. a) Sentinel-2 imagery and b) PlanetScope imageries. T1 (10 July 2022) and T2 (15 July 2022) extent are in yellow and green respectively.

2.2 Reference data and target land cover classes

Two types of reference data were available for this study: (i) ten experimental fields managed by UCSC, with different crop residue management practices, to analyse the spectral response of such agricultural surfaces in multispectral EO data; and (ii) photo-interpretation of approximately 200 crop fields used to calibrate the PlanetScope-based mapping algorithm. For both datasets, the sequence of land management operations (e.g. harvesting, residue retention, and tillage) was reconstructed over the study period. Table 1 summarizes the target land cover and management classes, defined according to the field conditions observed in the first (T1) and second (T2) consecutive satellite acquisitions as a consequence of agricultural operations.

Class type	Land cover condition in T1 and T2	Operation /status
Class 1 – C	Green crop to crop residue	Mowing
Class 2 – C	Crop residue to bare soil (wet)	Tillering
Class 3 – NC	Green crop unchanged	Crop
Class 4 – NC	Bare soil unchanged	Bare soil
Class 5 – NC	Crop residue unchanged	Residue
Class 6 – C	Bare dry soil to wet soil	Tillering
Class 7 – C	Mature crop to crop residue	Harvesting
Class 8 – C	Bare soil to green crop.	Growing
C =Change; NC = No Change		

Table 1. Target land cover status and changes

2.3 Remote sensing datasets and features for machine-learning classification

Two EO datasets were used to cover the 2022 cropping season: PlanetScope (PS) and Sentinel-2 (S2). PS provides near-daily multispectral imagery at 3 m spatial resolution, with eight VIS–NIR bands including red-edge and coastal blue, enabling enhanced sensitivity to vegetation and soil surface conditions. Sentinel-2 offers multispectral imagery in the VNIR–SWIR domain at 10–20 m spatial resolution, with a 2/3-day revisit time from the combined S2A/S2B/S2C constellation. Two consecutive cloud-free acquisitions (10 and 15 July 2022) were selected from both sensors to exploit spectral, textural, and temporal changes associated with known management operations (e.g., harvesting and tillage) as observed in the experimental fields.

Among other machine learning algorithms, Random Forests (RF) - implemented in R (Liaw and Wiener, 2002) and configured with 500 decision trees and predictors variable importance calculated through permutation - was selected because it offers the best compromise between model accuracy and processing speed, and is therefore widespread used in remote-sensing applications to generate robust mapping products (Agrillo et al., 2021). Predictor variables included spectral bands (8 for PS, 10 for S2), NDVI, and texture entropy computed on the NIR band using a 5 × 5 pixel window (Iqbal et al., 2021). All these features were extracted from the second acquisition (T2) and from temporal differences between the two dates ($\Delta = T2 - T1$). In total 20 and 24 predictors were available for PS and S2 classification respectively. Reference pixels extracted from training polygons were used to train the PS-RF model. The resulting PS classification, resampled to 20 m with a majority, was then used as training data for the S2-RF model to assess scalability using operational and open-access imagery.

2.4 Map validation

Map validation was performed using two sets, one per EO dataset, of 320 stratified random points (40 per class) distributed across the study area, masking non-agricultural areas and non-flat areas for S2. The points were independently photo-interpreted using PS and S2 imagery to build a reference dataset. Observed and predicted class labels were compared through a confusion matrix, from which standard accuracy metrics were derived.

3. RESULTS AND DISCUSSION

3.1 PlanetScope spectral change detection

Figure 2 reports the average spectra extracted from PS and S2 imagery at T1 and T2. Classes associated with stable surface conditions, such as standing crops (Class 3), bare soil (Class 4),

and persistent residues (Class 5), show nearly overlapping spectral behavior between T1 and T2. This temporal consistency supports the classification of these surfaces as "no change." Conversely, classes related to active field transitions (Classes 1, 2, 6, 7, and 8) exhibit distinct spectral shifts, particularly in the red edge, NIR and SWIR (where available) bands, which are sensitive to vegetation status and biomass. These changes reflect surface transformations consistent with mowing, tillage, harvesting, and early regrowth.

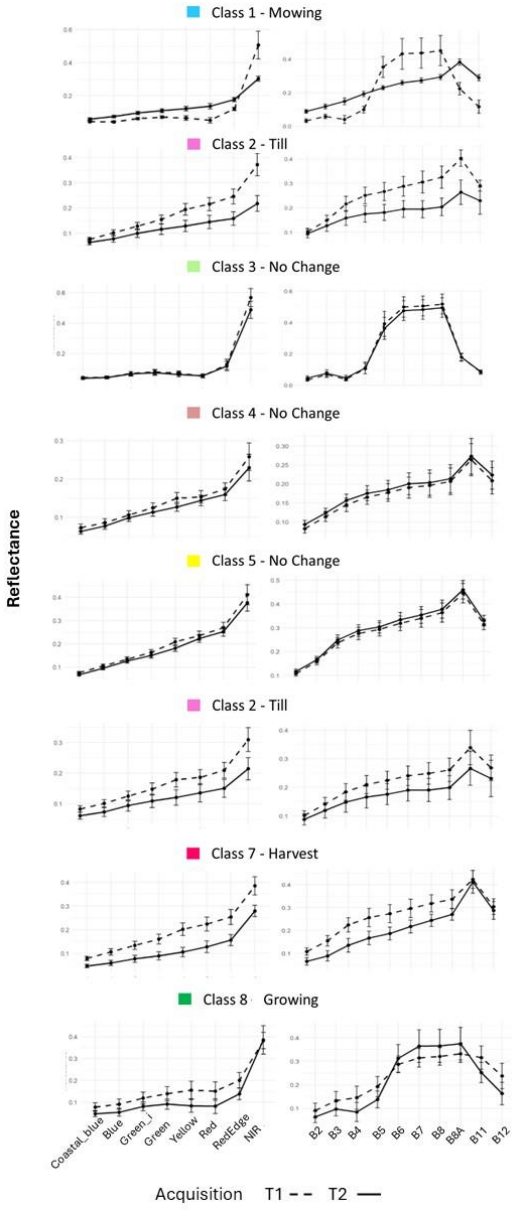

Figure 2. Mean spectral signatures for PS (left panels) and S2 (right panels) of the target land cover classes at times T1 (dashed lines) and T2 (solid lines), highlighting spectral changes associated with management operations.

The RF classification using PS data successfully enabled the identification of all eight classes. The classification output showed high spatial detail, clearly recognizing different post-harvest conditions (e.g., fields with crop residues vs. tilled soil). The confusion matrix indicated an OA of 86%. At class level there is a reliable identification of interest classes like tillage (Class 2 – 91% PA) and residual cover (Class 5 – 92% UA); some spectral confusion occurred for harvesting (Class 7 – 0.59 PA%), often confused with Class 8. Harvesting was not very common between T1 and T2, hence the statistical sample has little significant.

3.2 Sentinel-2 Scalability Test

When applied to S2 data the RF trained using PS map provide very good results (OA 89%). Despite the coarser spatial resolution (10–20 m), the combination of spectral bands and indices allowed for effective detection of key changes: such as transition from residual cover to bare soil, persistence of crop residues after harvest, and detection of wet or recently tilled soil. Although some detail was lost compared to PS, the spectral richness of S2 (Figure 2, right panel) compensated for the spatial resolution gap allowing to identify tillage (Class 2 – 98% PA) and residue presence (Class 5 – 95% UA). On the other hand, some harvesting was classified as tillage resulting in poor UA for Class 2 (75%) and some residue were misclassified as bare soil, resulting in low PA for Class 5 (79%). This last confusion was expected due to similar spectral responses at specific wavelengths (Figure 2 right panels).

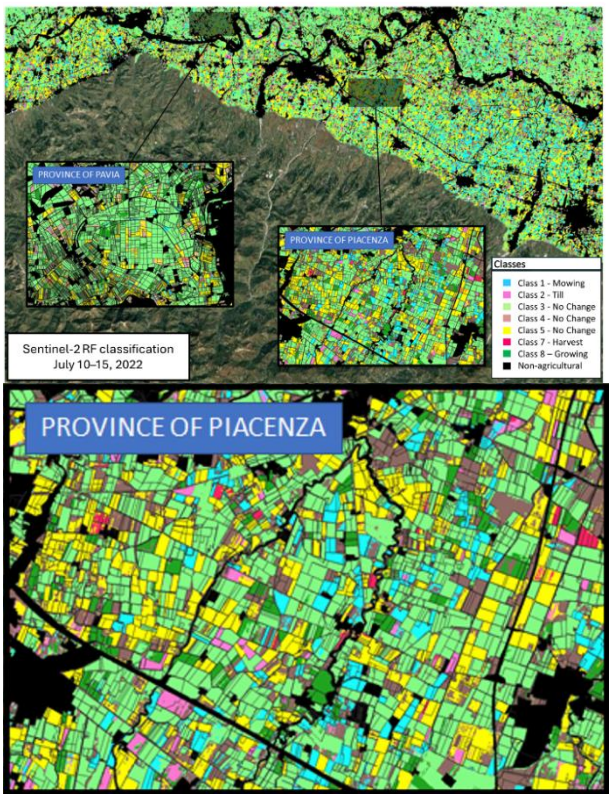

Figure 3. Land surface classification map derived from S2 imagery for the study area (Top) and detail for Piacenza Province (Bottom). Non-arable land is masked in black.

3.3 Analysis of PS variable importance

The final analysis focuses on class-specific RF importance rather than global RF importance metrics, in order to highlight predictors that may have limited overall relevance but are highly informative for specific classes.

Figure 4 shows the class-specific importance scores of the 20 predictors derived from PS data for four classes that were robustly identified and/or are of particular relevance in carbon

farming studies: two change classes (mowing and tillering) and two no-change classes (crop and residue).
The heatmap highlights a clear differentiation between change and no-change classes. Predictors based on reflectance differences (Δ) and ΔNDVI exhibit higher importance for change classes, indicating their sensitivity to management-induced surface changes. In particular, ΔNIR is most informative for mapping tillering (Class 2), while Δred and ΔNDVI are key predictors for distinguishing mowing (Class 1).
No-change classes are primarily characterized by spectral conditions at T2: NDVI at T2 is most important for identifying crop presence (Class 3), whereas red and red-edge reflectance at T2 contribute to the detection of permanent residues (Class 5). Texture metrics generally show low importance across classes, but provide a modest contribution for Class 2, likely because the 3 m spatial resolution allows the detection of fine-scale changes in field patterns and surface roughness induced by management operations.

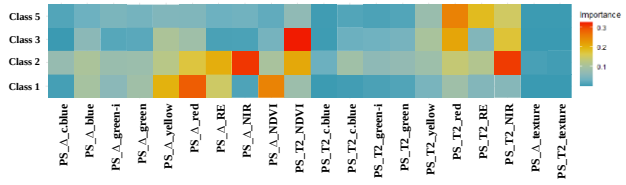

Figure 4. heatmap of class-specific RF importance scores for Classes 1, 2, 3 and 5, using PS data.

4. CONCLUSION

This study demonstrates the feasibility of using optical satellite imagery—from both PS and S2 missions—to monitor agricultural practices relevant to carbon farming, with a specific focus on detecting crop residue cover and tillage events. The proposed workflow, based on RF classification of pre- and post-event imagery, effectively identifies key surface transitions associated with soil management, achieving consistent and promising performance across both high- and medium-resolution datasets.
A key outcome is the ability to discriminate between fields with and without crop residues and to detect the occurrence and spatial extent of tillage operations. These capabilities are highly relevant for MRV systems. Indeed, the resulting spatial products can support soil carbon turnover modelling and help identify areas with higher carbon sequestration potential, thereby enabling targeted management strategies and incentive mechanisms.

PS, with its finer spatial resolution and quasi-daily acquisitions, enables detailed field-scale analyses and the detection of rapid management changes, while S2 supports scalable district- to regional-level mapping using open-access operational data. In this context, the former can be exploited to generate spatially distributed reference data for training S2 classification models, enabling an effective scaling-up strategy.

Future work will focus on two main aspects: (i) improving mapping performance and transferability; and (ii) assessing the contribution of Earth Observation information to soil carbon modelling. For the first aspect, the calibrated models will be tested using multiple pairs of consecutive PS and S2 images acquired throughout the winter crop harvesting period (from late June to September), with additional reference data collected to evaluate temporal and spatial transferability. For the second aspect, reconstructed time series of land management practices, including crop residue presence and persistence, will be integrated into the RothC carbon model (https://www.rothamsted.ac.uk/rothamsted-carbon-model-rothc) to assess the long-term impacts of residue and tillage management.

5. ACKNOWLEDGEMENTS

This study was financed by a grant from the Italian Ministry of Education, University and Research (PRIN 2022, Project Remote-C "Remote-C - Scaling soil C sequestration in croplands with operational remote sensing-based MRV tools", Prot. 2022J97KYT). Access to PlanetScope acquisitions was granted by project PNRR NODES, which has received funding from the MUR – M4C2 1.5 of PNRR funded by the European Union - NextGeneration EU (Grant agreement no. ECS00000036). The authors used ChatGPT-5 to improve the grammar of this article.

6. REFERENCES

Agrillo, E., Filipponi, F., Pezzarossa, A., Casella, L., Smiraglia, D., Orasi, A., Attorre, F., Taramelli, A., 2021. Earth Observation and Biodiversity Big Data for Forest Habitat Types Classification and Mapping. Remote Sens. 13. https://doi.org/10.3390/rs13071231

Hively, W.D., Lamb, B.T., Daughtry, C.S.T., Serbin, G., Dennison, P., Kokaly, R.F., Wu, Z., Masek, J.G., 2021. Evaluation of SWIR Crop Residue Bands for the Landsat Next Mission. Remote Sens. 2021, Vol. 13, 13. https://doi.org/10.3390/RS13183718

Iqbal, N., Sha, U., Mohammad, S., 2021. Gray level co-occurrence matrix (GLCM) texture based crop classi fi cation using low altitude remote sensing platforms. https://doi.org/10.7717/peerj-cs.536

Liaw, A., Wiener, M., 2002. Classification and Regression by randomForest. R News 2, 18–22.

Pepe, M., Pompilio, L., Ranghetti, L., Nutini, F., Boschetti, M., 2023. Mapping spatial distribution of crop residues using PRISMA satellite imaging spectroscopy. Eur. J. Remote Sens. 56. https://doi.org/10.1080/22797254.2022.2122872

Smith, P., Soussana, J.-F., Angers, D., Schipper, L., Chenu, C., Rasse, D.P., Batjes, N.H., van Egmond, F., McNeill, S., Kuhnert, M., Arias-Navarro, C., Olesen, J.E., Chirinda, N., Fornara, D., Wollenberg, E., Álvaro-Fuentes, J., Sanz-Cobena, A., Klumpp, K., 2020. How to measure, report and verify soil carbon change to realize the potential of soil carbon sequestration for atmospheric greenhouse gas removal. Glob. Chang. Biol. 26, 219–241. https://doi.org/10.1111/gcb.14815

Yang, L., Lu, B., Schmidt, M., Natesan, S., Mccaffrey, D., 2025. Smart Agricultural Technology Applications of remote sensing for crop residue cover mapping. Smart Agric. Technol. 11, 100880. https://doi.org/10.1016/j.atech.2025.100880

This work is licensed under a Creative Commons Attribution-No Derivatives 4.0 International License.

INVESTIGATING CROP RESIDUES PRESENCE AND PERSISTENCE FROM SENTINEL-2 TIME SERIES

C. Bossio [1], E. Spirito [1]*, F. Filipponi[2], F. Nutini [1], G. Tellina [1], A. Ferrarini [3], F. Zucca[4], M. Boschetti [1], M. Pepe [1]

[1] CNR-IREA, Via A. Corti 12, Milano, Italy - (spirito.e, nutini.f, tellina.g, boschetti.m, pepe.m)@irea.cnr.it, chiara.bossio@studenti.unipr.it

[2] CNR-IGAG, Strada Provinciale 35, Montelibretti, Italy – federico.filipponi@cnr it

[3] UCSC - DI.PRO.VE.S., Via E. Parmense 84, Piacenza, Italy – andrea.ferrarini@unicatt.it

[4] UniPV DSTA, Via Ferrata 1, Pavia, Italy - francesco.zucca@unipv.it

KEY WORDS: Sentinel-2, carbon farming, time series, crop residues

ABSTRACT:

Crop residue cover (CRC) is a key indicator for monitoring conservative agriculture, as its presence, quantity, and persistence reflect sustainable soil management practices, which are useful for Monitoring, Reporting and Verification in the framework of carbon farming. While the literature shows that accurate CRC quantification requires hyperspectral satellite data—particularly exploiting lignin–cellulose absorption features in the short-wave infrared (SWIR)—such data are not yet operational. Current multispectral missions lack the necessary spectral resolution, despite future platforms (e.g. Sentinel-2 NG, Landsat-Next) will bring improvements. Given these constraints, this study focuses on detecting CRC presence and persistence rather than precise quantification, exploiting multitemporal Sentinel-2 imagery. To achieve this objective, we analysed time series of different non-photosynthetic vegetation indices together with bare soil index and LAI (Leaf Area Index) to recognise trends and discontinuities of such indicators in time, as representative of crop development and of key management events (harvesting and incorporation). This analysis was preliminary to set up a machine-learning classification approach to identify five classes of soil cover conditions, representing the sequence: (0) crop development; (1) crop senescence; (2) standing dead vegetation; (3) crop residues and (4) bare soil. The analysis was performed using ground truth for winter wheat fields in the Piacenza district (2022 season), where key event dates were obtained through field observations or PlanetScope imagery photointerpretation. Results show the potentiality of optical spectral temporal features to detect changes in soil conditions due to management. Promising results were achieved by a preliminary test of a random forest classifier for the 5 target classes, overall Cohen's Kappa of ~0.87 and a balanced accuracy of 0.95 were obtained for the crucial CR class. The results confirm the feasibility of using Sentinel-2–based ML classification for end-of-season MRV of crop residue management in carbon farming.

1. MOTIVATION

Crop residues, together with cover crops, are key practices for conservative agriculture, for their role in hydrological, bio-physical and chemical balance and maintenance of soils. So that crop residues are considered as key agricultural variables in EO derived products for a sustainable development. In addition, the perspective of The European Climate Law and the goal of EU of becoming carbon-neutral by 2050 raised attention to carbon removals in agriculture, asking for new Monitoring, Verification and Reporting (MVR) tools, as demonstrated by the inclusion of remote sensing techniques in the upcoming Carbon Removals and Carbon Farming Certification (CRCF) Regulation. Multispectral data have proved to be suitable only for CR detection (Hively et al. 2021) rather than quantification, which is mapped accurately enough only by the use of hyperspectral data (Kokaly et al 2009, Hank et al. 2019, Pepe et al. 2022, Verrelst et al., 2023), while resolving subtle absorption features, and the ones diagnostic for carbon base constituent (CBC) in the SWIR, a spectral region where both past and current satellite multispectral missions offer limited data. For that reason, both ESA and NASA designed next generation multispectral missions, namely Sentinel 2 NG and Landsat neXt, for which the SWIR bands configuration is suitable also for the purpose of CR fraction evaluation.

Notwithstanding the limitation of current multispectral operational data for CR accurate quantification, there is a need of information about the soil coverage and the CR management that could be still gathered from such missions to be effectively assimilated into carbon turn-over models. In fact, knowledge about presence of crop residues and their persistence, occurring between the two key management events: crop harvest (HAR) and residues incorporation into the soil (INC), are undoubtfully important to properly calibrate soil models. The use of remotely sensed time series could thus provide actual soil cover information to be assimilated to model soil carbon budgets, instead of using practises data envisaged from crop calendars and general indicators.

Given that importance of CR presence and persistence in MRV for carbon farming, this study is aimed at exploiting Sentinel-2 data series to: i) investigate non-photosynthetic vegetation indices to represent CR and bare soil dynamics besides provide information on soil cover changes throughout the season; ii) evaluate the contribution of time features, and sequence of events related to crop growth and agro-practices in predicting soil cover conditions; iii) test of ML approach as a potential approach for CR persistence mapping.

To this aim several NPV (Non-Photosynthetic Vegetation) spectral indices from the literature were considered, together with a bare soil index, in their temporal dynamics in a season, to evaluate their potentials as predictors of CR presence and persistence, one by one and as an ensemble.

At the same time Leaf Area Index (LAI) and some main crop development pheno-metrics (start, peak and end of season), calculated from LAI time series, were used to account for crop development and to provide some keystones for the

* Corresponding author

identification of practises of interest (i.e. HAR and INC). Then, spectral indices (SI), LAI, together with temporal indicators - including SI changes in time – calculated based on pheno-metrics, were analysed as predictors of soil cover classes in a machine learning classification framework. Such approach was chosen since the relationships between the predictors and the soil cover classes is multivariate, complex and not linear.

2. MATERIALS AND METHODS

2.1 Study area an RS data

The study area is in the province of Piacenza (western Po River Valley), is a highly productive agricultural district, characterized by fertile soils, abundant water resources, and a temperate continental climate with cold, wet winters and hot, dry summers, all of which strongly influence cropping systems. The focus of the study is winter wheat, which is the dominant crop in the area see Figure 1 crop distribution panel, due to its importance. Ground truth information was available from specific farms were crop residues management experiment were conducted. The remotely sensed data-set is constituted by a dense time series of Sentinel-2 A and B, acquired during the cropping season of 2022, since the area is at the intersection of two adjacent orbits (22 and 65). The overall revisit time is increased from the nominal 5 days to 2 / 3 days alternately.
PlanetScope constellation data, over the same period and covering the North-Eastern area of the province (see image footprint in Figure 1), were acquired. They were used for the creation of reference data regarding main management events - harvesting and incorporation – because of their very high spatial (GSD 3 m) and temporal resolution (daily). Overall, a complete daily sequence over 91 winter wheat fields was analysed.

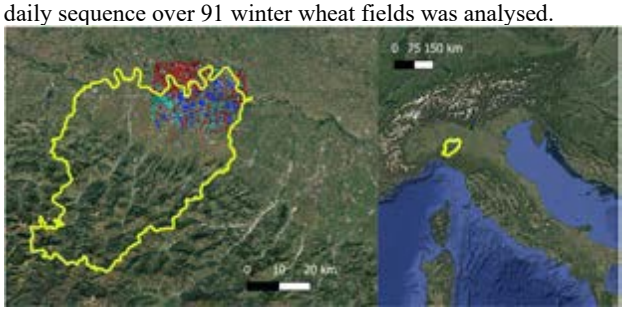

Figure 1. Piacenza province (yellow outline), a PlanetScope VHR imagery (false colour composite) is overlayed to show the footprint, and in blue the 91 Piacenza reference fields

In most of the reference fields HAR and INC dates were recognised by photointerpretation of false colour composites' series of VHR images in the August 2021 - October 2022 period, for a total of 290 PlanetScope images (see figure 2); only for 10 fields the information regarding such dates were available from ground observation acquired during experimental activities conducted locally by UCSC.

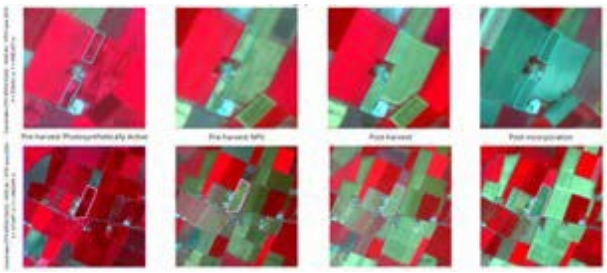

Figure 2. Examples of changes in PlanetScope false colour RGB in relation to crop development and HAR and INC events

2.2 Methodological approach for CR detection: soil cover classes

Since the CR management dynamics are closely linked to seasonal soil cover conditions, specific soil cover classes were defined for this study and are reported, together with their descriptions, in Table 1. The classes are primarily related to changes in field status due to crop phenological changes encompassing: emergence; developing crop; senescence till completely mature condition (standing dead vegetation – STD); and then harvesting, and residue incorporation operations. The underlying rationale is that, on the one side, class 3 (Post harvest condition) identify the CR presence; on the other side, by identifying the dates of the two changeovers between class 2 and 3 (approximately the harvest date), and class 3 and 4 (roughly the residues incorporation date) also CR persistence in the field could be estimated.

2.3 Predictors for machine learning classification

2.3.1 Exploratory analyses of NPV SI time series

To assess the feasibility of the proposed classification workflow, an exploratory analysis was performed: i) analysing the NPV indices' sensitivity to crop residues cover, as derived from the spectral library data; ii) by analysing, for the available experimental fields, the temporal behaviour of the candidate NPV SIs with respect to crop phenological development and known harvesting (HARV) and residue incorporation (INC) events.

2.3.2 Calculation of spectral and temporal predictors

As regards spectral predictors, 3 different categories of spectral predictors and corresponding indicators have been considered to characterise field conditions: i) green vegetation (LAI); ii) crop residues presence (DFI, NDFI, NDI5, NDI7, NDSVI, NDTI and SRNDI, Li and Guo, 2016); and iii) bare soil (BI, Diek et al., 2017)[1]. Moreover, the five S2 spectral bands (Blue, Red, NIR broad, SWIR1 and SWIR2) used in NPV SI calculations, were included as predictors.
For what concerns temporal features, Position Of Peak (POP) and End of Season (EOS) were detected exploiting the EO4PM algorithm (Filipponi et al. 2022). Starting from S2 data EO4PM is based on three main steps: i) LAI retrieval with SANP-Biophysical processor (Weiss et al., 2021); ii) creation of daily LAI time series, by gap filling and smoothing; and iii) estimation of pheno-metrics.
Additionally, spectral/temporal features related to NPV SI temporal changes have been computed as follow:

$$\Delta SI_{NPV(i)}(t) = MAX_{t' \in (EOS-15d;EOS+15d)}\left[SI_{NPV(i)}(t')\right] - SI_{NPV(i)}(t) \qquad \text{(eq. 1)}$$

Where $SI_{NPV(i)}$ is the i-th NPV spectral index and t is the moment of S2 acquisition. For each SI Max is computed in a 30 days window centered on the detected occurrence of EOS.
Finally, together with $\Delta SI_{NPV(i)}$, as a temporal feature, the time difference between each acquisition and the date of EOS is included.

2.3.3 ML selection, training and test

The envisaged classification workflow is supervised and object-based, using agricultural fields—defined by Land Parcel System (LPAS) records—as classification units. For each parcel, the median value of each predictor was computed from all pixels

[1] Formulas for indexes used in this study refer to: https://github.com/emanuelespiritowork/spectral_index_db

within the field, excluding a 10 m internal buffer along parcel boundaries, and used as input to the classifier.
Random Forest (RF) was selected as the classification algorithm due to its well-documented performance and robustness in remote sensing applications. The RF model was trained using the predictors described above. The final version of the model is the one using the top 95% predictors importance according to RF-ranking (*varImp*) using the R package caret (Breiman, 2001). Each field was classified at every available Sentinel-2 overpass during the study period, excluding cloud-contaminated observations identified using the standard L2A cloud mask. Overall, approximately 60 Sentinel-2 images were available between 1 August 2021 and 31 October 2022, resulting in a temporal sequence of soil-cover class assignments for each field, with each date classified into one of the five defined soil-cover classes

	Class	Phase Name	Period	Description
	0	Vegetative phase	Start of season → Peak (POP)	Active growth; soil cover from none to full.
	1	Phase towards senescence	Peak (POP) → End of season (EOS)	Maximum cover followed by progressive vegetative decline.
	2	Senescent vegetation	End of season (EOS) → Harvest	Dry, inactive crop still present in the field.
	3	Post-harvest	After harvest → Before incorporation	Presence of residues (stubble, straw); heterogeneous cover.
	4	Post-incorporation	After residue incorporation	Bare soil; no active or residual vegetation.

Table 1. Soil cover condition classes definition

3. RESULTS AND DISCUSSION

3.1 Exploratory analyses

3.1.1 Spectral/ temporal predictors trends

Figure 4 reports the temporal trend of different indicator of soil condition status for a wheat field traditionally managed from emergence to CR incorporation. Vertical lines indicate the occurrence of POP and EOS and harvesting and incorporation events. LAI clearly show crop development with a decreasing trend after POP and a near zero values after harvesting. Similarly, but reversely, BI increase from POP to harvest reaching its maximum in non-vegetation conditions. Anyway, the soil indicator does not show differences between bare and residue-covered soils. On the other and NPV indices (DFI, NDTI and NDFI) shows changes in relation to the quantity of NPV with a clear drop after harvesting and a decreasing trend afterwards.

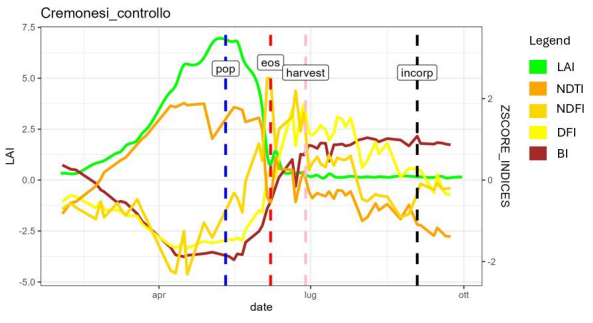

Figure 4. Trends and discontinuities of the different predictors for a wheat field in the training data in Piacenza province.

Figure 5 presents the trend of DFI for part of the same wheat field with different only in CR management: standard straw management (control- gold line) vs conservative practices (test. Orange line). After harvesting the two lines deviate with test condition showing higher DFI values due to straw presence. After CR incorporation in test parcel the DFI show a significant drop. After this moment the two parcels behave similarly.

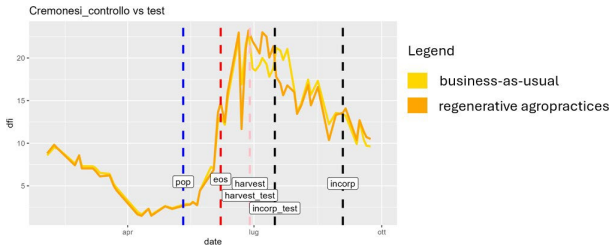

Figure 5. Trends and discontinuities of DFI predictor on two bordering wheat fields in Piacenza province.

These results demonstrate the usefulness of NPV-based indices for crop residue (CR) detection, as well as, the inclusion of green vegetation and soil indicators contributes to a more complete characterization of the investigated system. Anyway, it is also clear that spectral and biophysical indicator - SIs and LAI – are not diagnostic *per se*, and that only by means of their trends and changes, information regarding practises could be detected. This is the reason why also pheno-metrics are considered to extract some indicators which are useful for representing the sequence of field conditions: time difference between acquisition and EOS (Λt); trends in NPV SIs according to eq. 1 ($\Lambda SI_{NPV(i)}$). Such predictors could be exploited within a machine learning framework, as it enables the identification of non-linear relationships that better explain soil cover conditions and their temporal dynamics.

3.2 ML results analysis

A Random Forest model was trained on reference dataset and tested on another reference dataset as described above (§2.33): the 91 reference fields, considering the cloud-masked time series, resulted in 8255 samples in total. RF model achieved very good performances. Overall accuracy was estimated with 80-vs-20 random split of reference samples for training and test, reaching 0.938 and 0.942 in cross-validation (5-fold) and validation, respectively, with Cohen's K coefficients of 0.916 and 0.923. After evaluation of this first RF model trained with all 22 predictors (S2 bands, SIs, and spatial/temporal features), the predictors importance (see Fig. 6) was analysed to be interpreted for model optimization.

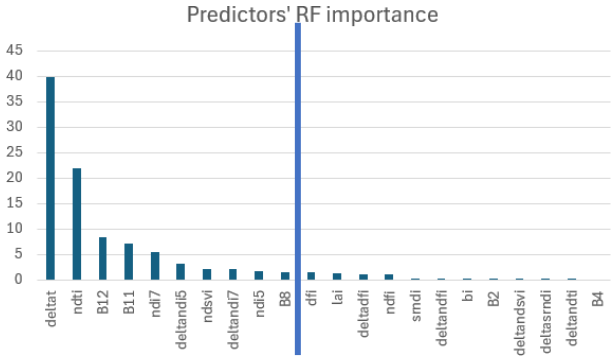

Figure 6. Percentages of predictors importance as Random Forest variable importance feature of caret

The ranking in Figure 4 confirms the importance of those spectral predictors, expected from their underpinning physics (i.e., NPV SIs and SWIR bands), while the diagnostic power of

temporal (Λt) and spectral/temporal features (ΛSI_{NPV} for NDI5, NDI7) is clearly apparent.
After completing the analysis, a second model was trained on the top-ranking predictors—specifically, those 10 features that together accounted for more than 95% of the total importance (those at the left side of the dashed line in fig.4).

		Reference						
		class 0	class 1	class 2	class 3	class 4	TOT	UA
Prediction	class 0	99	7	0	0	0	106	0.93
	class 1	4	115	0	0	0	119	0.97
	class 2	0	0	80	7	0	87	0.92
	class 3	0	0	5	206	13	224	0.92
	class 4	0	0	0	25	312	337	0.93
	TOT	103	122	85	238	325	873	
	PA	0.96	0.94	0.94	0.87	0.96	**O.A.**	**0.93**

Table 2. Confusion Matrix for optimized RF model (test)

The performance of this optimized model is: in cross-validation the OA reaches 0.94 and over the test set, it hits 0.93 (see table 2); with a Cohen's K coefficient of 0.92 and 0.91 respectively, the model proved to be robust, with omission and commission errors that are overall low and quite balanced, as regards classes of main interest (2, 3 and 4), with the commission error for class which is due to the fact that in same operations (i.e. secondary tillage) some CR is still present.

4. CONCLUSIONS

Monitoring crop residues management is a key information in the framework of conservative agriculture. Remote sensing is acknowledged to be useful as a technique for MRV of conservation practices in carbon farming. Currently, operational missions are restricted to multispectral sensors, which are not optimal for Crop Residue Cover quantification; nevertheless, good results could be achieved as regards residues presence and persistence. In this preliminary study Sentinel 2 time series were exploited to understand their potentials in the detection of harvest and incorporation key events and this is accomplished by exploratory analyses of spectral and temporal indices as predictors of soil-cover classes related to such events. The classification is carried out by a Random Forest paradigm, trained and tested on reference field data. Results are encouraging, with overall accuracy around 90% both in cross validation (0.94) and test (0.93). The time dimension proved to be required to achieve accurate results. Further work will encompass: i) the identification of harvest and incorporation dates, starting from soil-cover maps; ii) mapping of key events at a district level; iii) their assimilation in a soil carbon turn-over model; iv) robustness assessment by application in other regions and to other crops.

ACKNOWLEDGEMENTS

This study was financed by a grant from the Italian Ministry of Education, University and Research (PRIN 2022, Project Remote-C "Remote-C - Scaling soil C sequestration in croplands with operational remote sensing-based MRV tools", Prot. 2022J97KYT).
Access to PlanetScope acquisitions was granted by project PNRR NODES, which has received funding from the MUR – M4C2 1.5 of PNRR funded by the European Union - NextGeneration EU (Grant agreement no. ECS00000036).

REFERENCES

Breiman, L., 2001. Random Forests. *Machine Learning,* 45, pp. 5–32. doi.org/10.1023/A:1010933404324

Diek, S., Fornallaz, F., Schaepman, M.E., de Jong, R., 2017. Barest Pixel Composite for agricultural areas using Landsat time series. *Remote Sensing*, 9(12), 1245. doi.org/10.3390/rs9121245

Filipponi, F., Smiraglia, D., Agrillo, E., 2022. Earth Observation for Phenological Metrics (EO4PM): Temporal Discriminant to Characterize Forest Ecosystems. *Remote Sensing*, 14(3), 721. doi.org/10.3390/rs14030721

Hank, T.B., Berger, K., Bach, H., Clevers, J.G.P.W., Gitelson, A., Zarco-Tejada, P., Mauser, W., 2019. Spaceborne Imaging Spectroscopy for Sustainable Agriculture: Contributions and Challenges. *Survey in Geophysics*, 40, pp. 515–551. dx.doi.org/10.1007/s10712-018-9492-0

Hively, W. D., Lamb, B. T., Daughtry, C. S., Serbin, G., Dennison, P., Kokaly, R. F., Wu, Z., Masek, J. G., 2021. Evaluation of SWIR crop residue bands for the Landsat neXt mission. *Remote Sensing*, 13(18), 3718. doi.org/10.3390/rs13183718

Kokaly, R.F., Asner, G.P., Ollinger, S.V., Martin, M. E., Wessman, C.A., 2009. Characterizing canopy biochemistry from imaging spectroscopy and its application to ecosystem studies, *Remote Sensing of Environment*, 113(sup. 1), pp. S78-S91. doi.org/10.1016/j.rse.2008.10.018

Lamb, B.T., Daughtry, C.S.T., Serbin, G., Dennison, P., Kokaly, R.F., Wu, Z., Masek, J.G., 2021. Evaluation of SWIR Crop Residue Bands for the Landsat Next Mission. *Remote Sensing,* 13, 3718. doi.org/10.3390/rs13183718

Li, Z., Guo, X., 2016. Remote sensing of terrestrial non-photosynthetic vegetation using hyperspectral, multispectral, SAR, and LiDAR data. *Progress in Physical Geography,* 40(2), pp. 276-304. doi.org/10.1177/0309133315582005

Pepe, M., Pompilio, L., Ranghetti, L., Nutini, F., Boschetti, M., 2023. Mapping spatial distribution of crop residues using PRISMA satellite imaging spectroscopy. *European Journal of Remote Sensing*, 56(1). doi.org/10.1080/22797254.2022.2122872

Verrelst, J., Halabuk, A., Atzberger, C., Hank, T., Steinhauser, S., Berger, K., 2023. A comprehensive survey on quantifying non-photosynthetic vegetation cover and biomass from imaging spectroscopy. *Ecological Indicators*, 155, 110911. doi.org/10.1016/j.ecolind.2023.110911

Weiss, M., Baret, F., Jay, S., 2021. S2toolbox level 2 products. Version 2.1. step.esa.int/docs/extra/ATBD_S2ToolBox_V2.1.pdf (last visited January 2026)

This work is licensed under a Creative Commons Attribution-No Derivatives 4.0 International License.

Wheat yield estimation from sequences of hyperspectral images: preliminary investigation of spectral temporal information with Neural Network

L. Parigi[1,2] *, L. Miazzo[1], F. Nutini[1], G. Candiani[1], M. Marshall[3], M. Belgiu[3], M. Borschetti[1]

[1] National Research Council of Italy (CNR), Institute for Electromagnetic Sensing of Environment (IREA) Via A. Corti 12, 20133 Milan, Italy (parigi.l, miazzo.l, nutini.f, candiani.g, boschetti.m)@irea.cnr.it
[2] Department of Civil, Constructional and Environmental Engineering, Sapienza University of Rome, Rome, Italy
[3] Faculty of Geo-Information Science and Earth Observation, University of Twente, PO Box 217, Drienerlolaan 5, 7500 AE Enschede, The Netherlands

KEY WORDS: Yield, Wheat, Hyperspectral, Multispectral, Time series, Neural Networks

ABSTRACT:

Agriculture faces major challenges due to climate change. Yield is a key information for improving crop-management planning and resource allocation to support food security. Multispectral satellite data are widely used to estimate yield, typically by exploiting time series of indices or crop traits derived from the images. Hyperspectral data are less frequently used, and in most cases yield is estimated from a single acquisition taken at a key phenological stage and rarely from spaceborne sensors. Current scientific hyperspectral (PRISMA and EnMAP) and planned missions (CHIME and SBG) enable collection of multiple images during the cropping season over large areas, allowing exploitation of both dense spectral information and the temporal dimension. This work assesses the contribution of hyperspectral sequences, combined with multispectral data, to end-of-season yield estimation using neural network models. Three baseline models were trained on a single modality (Sentinel-2 LAI time series, S2 derived phenological metrics, or hyperspectral sequences from PRISMA and EnMAP). To evaluate the added value of hyperspectral data, two combination models were then trained that pair hyperspectral sequences with phenological metrics or with LAI time series. The best results were obtained with LAI time series model (R^2: 0,67; RMSE: 1.26), while the hyperspectral-only model scored the worst results (R^2: 0.41; RMSE 1.60). Combining hyperspectral data with LAI (R^2: 0.6; RMSE 1.33) did not increase the performance relative to the LAI-only model.

1. INTRODUCTION

Agriculture faces multiple challenges from climate change to an ever-growing population that require enough food production. Yield information is valuable to a range of stakeholders: farmers can use yield estimates to plan field operations efficiently, while administrative bodies can use them to design local and regional interventions that support food security (De Clercq & Mahdi, 2025; Weiss et al., 2020).

Remote sensing is a valuable tool because it provides frequent observations over large areas. Multispectral satellites such as MODIS, Landsat and Sentinel-2 are widely used for yield estimation because of their accessibility and revisit time, which enable monitoring of seasonal dynamics. These data are used to compute time series of vegetation indices (e.g. Normalised Difference Vegetation Index, NDVI; Enhanced Vegetation Index, EVI) or to estimate crop traits such as Leaf Area Index (LAI). These information are often correlated with crop biomass and its seasonal dynamics; consequently, their values at key phenological stages (e.g. LAI at peak season) or temporal aggregates of the time series (for example monthly averages or seasonal cumulate) can be used to estimate yield (Darra et al., 2023; De Clercq & Mahdi, 2025).

Hyperspectral data contain a large number of narrow bands that characterise the spectral signature of a target in great detail. In recent years two scientific hyperspectral missions, ASI-PRISMA and DLR-EnMAP, have been launched; these sensors are precursors to future operational missions such as ESA-CHIME and NASA-SBG. Hyperspectral data have been used to estimate many in-season crop traits (LAI, Chlorophyll and Nitrogen content in leaf and canopy, …) (Candiani et al., 2022; Parigi et al., 2024; Verrelst et al., 2019). However, hyperspectral data have rarely been used for direct yield estimation (De Clercq & Mahdi, 2025), and most works employ single-date images acquired at key phenological stages and apply some form of dimensionality reduction (indices, Principal Components Analysis - PCA, …) (Marshall et al., 2022; Ranghetti et al., 2023). The scarcity of studies using sequences of full-range hyperspectral images may be due to the only recent availability of these satellites, their long revisit time and the cost and logistical challenges of assembling long time series using field spectrometers or unmanned aerial vehicles. Nevertheless, hyperspectral data have produced promising results in single-date predictions, suggesting potential gains if multiple hyperspectral acquisitions can be combined for yield prediction (Tan et al., 2025).

Machine learning methods, and in particular Neural Networks (NN), are widely used for yield estimation because they can learn complex relationships and exploit structured inputs such as time series or spectra. Convolutional neural networks (CNN) can extract important features from sequential data and have been applied successfully to yield prediction tasks (Darra et al., 2023; De Clercq & Mahdi, 2025; Sun et al., 2022).

The objective of this preliminary study is to estimate end-of-season wheat yield using sequences of hyperspectral images and to assess the contribution of hyperspectral information to multispectral data models. To address these objectives, we test two scenarios: baseline and combination. In the baseline scenario, models are trained on a single spectral modality: (i) phenological metrics PHENO or (ii) LAI time series derived

* Corresponding author

from Sentinel-2 multispectral data LAI_TS, or (iii) hyperspectral data from PRISMA and EnMAP satellites HYPER. The combination scenario comprises two models that combine multispectral and hyperspectral inputs to quantify the change in performance when hyperspectral information is added to multispectral predictors; the two combination designs are (i) phenological metrics and hyperspectral data (PHENO-HYPER), and (ii) LAI time series and hyperspectral data (LAI_TS-HYPER.

2. MATERIALS AND METHODS

2.1 Yield data

Yield data were collected between 2020 and 2024 at the Bonifiche Ferraresi farm (Jolanda di Savoia, FE, Italy) from fields of durum wheat, soft wheat, barley, and spelt (Table 1). During this period, we carried out multiple georeferenced sampling campaigns; each campaign comprised destructive harvesting of plots of known area immediately prior to harvest. Grains were separated from the plant biomass and weighed. The farm also provided field-scale harvested yield for 2020-2023. All yield data were standardised to 13% moisture content. The two yield sources were merged into a single dataset. Samples from lodged fields and observations with yield values inconsistent with the LAI curve were excluded.

Year	Durum wheat	Soft wheat	Barley	Spelt
2020	44	33		
2021	17	22	4	1
2022	21	10	23	3
2023	21	52		
2024		40		
Total	**103**	**157**	**27**	**4**
		291		

Table 1 Number of yield samples divided by year and species.

2.2 Multispectral data

The time series of Sentinel-2 images (2019-2024) over Bonifiche Ferraresi farm was processed in SNAP to derive Leaf Area Index (LAI) time series. The LAI series were then smoothed and interpolated to daily time steps (Filipponi et al., 2022). We used the R package Sen2Rts (Ranghetti, 2021) to calculate the day of year (DOY) for the following phenological metrics derived from the LAI curve: Start of Season (SOS), End of Season (EOS) and Peak of Season (POS). The threshold method at 5% and 10% levels was applied to compute SOS (SOS05, SOS10) and EOS (EOS05, EOS10).

From the DOY values for SOS05, SOS10, EOS05, EOS10 and POS we derived additional metrics: interval length (days) between two phenological dates, cumulative LAI between two dates (sum of LAI), difference in LAI between two dates, growth rate between dates, and the LAI value at each phenological DOY. Many of these metrics were collinear or highly correlated, so redundant predictors were removed using the "findLinearCombos" function from the caret package (Kuhn & Max, 2008) generating the final feature set for PHENO baseline.

We also used the interpolated daily LAI time series directly as model input. For this purpose, the series were truncated to the period between 1 March and 1 June, which covers an important part of the cropping season for the target cereals (LAI_TS baseline).

2.3 Hyperspectral data

For the period 2020-2024, a total of 24 PRISMA and 4 EnMAP images were collected over Bonifiche Ferraresi farm. The PRISMA images were geometrically corrected, regridded, and spectrally smoothed using Savitzky-Golay smoothing. Bands with low signal-to-noise ratio or strong atmospheric interference were removed following the procedure described by Candiani et al. (2024); of the original 230 PRISMA bands, 170 bands were selected. EnMAP images were regridded and spectrally resampled to match the PRISMA spectral configuration, and the same 170 bands were selected. For both sensors, clouds over the farm were identified and masked manually.

2020	2021	2022	2023	2024
14/2	14/2			
			4/3	
			28/3	
		1/4	**4/4**	
7/4	7/4		7/4	7/4
	24/4	30/4		
5/5			**5/5**	
11/5		12/5		12/5
17/5			**21/5**	
23/5	23/5		24/5	
	4/6			10/6
26/6	21/6	27/6		27/6

Table 2 Acquisition dates of the hyperspectral satellites. Bold dates indicate EnMAP acquisitions, while the remaining dates correspond to PRISMA acquisitions. Grey cells denote the four selected time steps and the images available for those periods.

The hyperspectral acquisitions span from early February to late June (Table 2), but in most years they were concentrated between April and June. To minimise the number of missing time steps across years, we used only images acquired in April and May and defined four time steps corresponding to the first and second halves of each month. In most cases only one image was available for each time step. If two acquisitions fell within the same time step, the image with an acquisition date closest to that used in other years for the same time step was designated the primary image and the other the fallback. If the conflict was between a PRISMA and an EnMAP image, the PRISMA image was selected as primary. Fallback images were used when areas of interest in the primary image were obscured by clouds.

We extracted the spectrum of the pixel containing each sampling point, provided that an image for the given time step was available and the pixel was cloud-free. For field-level averages, we computed the mean of the cloud-free pixels within each field.

2.4 Neural networks models

Neural networks (NNs) were implemented in PyTorch (Paszke et al., 2019). The architecture comprised two modules: a feature-extraction module and a regression module. We implemented different feature-extraction architectures depending on the input modality:

- PHENO baseline was a tabular (24 variables) and were processed with a fully connected network.
- LAI_TS baseline was one-dimensional (93 time steps) and were processed with a one-dimensional convolutional network.

- HYPER data were arranged as a two-dimensional matrix (4 time steps and 170 bands) and were processed with a two-dimensional convolutional network.
- Ancillary data were tabular, consisting of two entries representing crop species, and were processed with a fully connected network.

Outputs from the feature-extraction modules were concatenated and passed to a fully connected regression network. The Rectified Linear Unit (ReLU) was used as the activation function in the network hidden layers. The Adaptive Moment Estimation (Adam) optimiser was used with tuneable learning rate.

For both fully connected networks and CNN, the numbers of layers and neurons were treated as hyperparameters and optimised during training. The CNN modules were composed of 1D or 2D convolution layer followed by the activation function and a 1D or 2D max pooling layer. Then, a sequence of convolution, activation and dropout layers was repeated, the number of repetitions was a tuneable hyperparameter, a max pool layer was placed every two repetitions. The fully-connected NN was composed by repeated of linear, activation and dropout layers.

Five models were developed. Three baseline models used a single modality (PHENO, LAI_TS and HYPER) together with ancillary data to assess the predictive power of each individual modality. Two combination models incorporated multispectral and hyperspectral inputs together with ancillary data (PHENO-HYPER and LAI_TS-HYPER) were tested to evaluate the change in performance when hyperspectral information is added to multispectral input.

2.5 Training and test of the models

The dataset was randomly split into training (80%) and test (20%) sets. Model development and hyperparameter optimisation were performed using five-fold cross-validation on the training set. The goal of this work is to predict wheat yield, so spelt and barley were always part of the training and never appear in the validation fold or the test set. Hyperparameters were optimised with the Ray Tune framework (Liaw et al., 2018), using Optuna (Akiba et al., 2019) as the search algorithm and the ASHA scheduler (Asynchronous Successive Halving Algorithm) (Li et al., 2020). Models were trained for up to 300 epochs, unless terminated earlier by the scheduler. Mean squared error (MSE) was used as the loss function during training. After identifying the best hyperparameter configuration and the optimal number of epochs for each model, we retrained the model on the complete training set and assessed performance on the held-out test set. Model performance was reported using the coefficient of determination (R^2) and the root mean squared error (RMSE).

3. RESULTS

The scatterplots of the models are showed in Figure 3. The baseline model using only LAI time series (LAI_TS) showed the best performance in yield estimation (R^2 = 0.67 and RMSE = 1.259). The HYPER model performed worst (R^2 = 0.41 and RMSE = 1.601), and the model based on phenological metrics (PHENO) also performed poorly (R^2 = 0.45 and RMSE = 1.613). In the multi-modality experiments, adding hyperspectral data to multispectral data did not improve performance. When hyperspectral data were added to phenological metrics (PHENO-HYPER) performance remained similar (R^2 0.45 and RMSE 1.639), while combining hyperspectral data with LAI

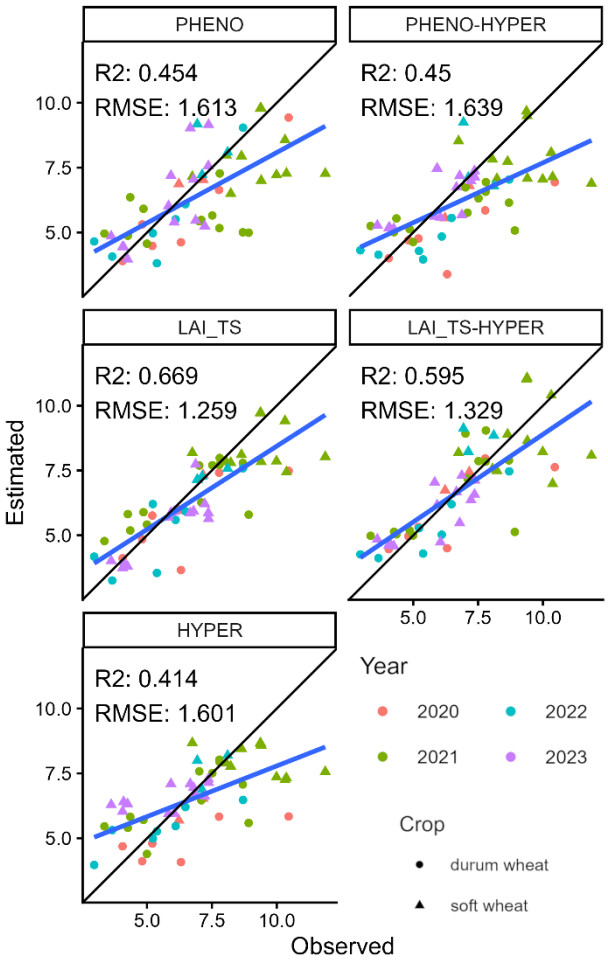

Figure 3 Scatterplots of the NN models. The colour represents the year of the sampling, and the shape of the points represents the species and the origin of the sample (point sample or field average)

(LAI_TS-HYPER) reduced performance relative to the LAI-only model (R^2 = 0.60 and RMSE = 1.329).

4. DISCUSSION

The model that used hyperspectral data performed poorly in end-of-season yield prediction. The main cause of this poor performance is the data sparsity. To feed the 2D CNN, we adopted a rigid structure of four time steps intended to represent the main growth period occurring in April and May. Unfortunately, due to cloud cover and sensor unavailability, all samples contained at least one missing time step, which hindered the models' ability to learn and generalise (R^2 0.60 and RMSE 1.329). Another factor that may have reduced performance was the limited seasonal coverage, which precluded observation of the early growth period (February and March). The inability to learn important features from the hyperspectral sequences was also visible when hyperspectral data were combined with multispectral inputs. In those experiments the models did not improve relative to multispectral-only counterparts, indicating that the hyperspectral modality did not provide additional predictive value.

By contrast, multispectral data in the form of LAI time series produced good estimation performance. This highlights the importance of the temporal dimension, from which the models

autonomously extracted informative features that supported accurate yield estimation. Instead, predefined features, such as phenological metrics derived from the LAI curve, performed poorly. These results suggest that NN can efficiently extract predictive features from raw temporal inputs, reducing the need for manual feature engineering or other kinds of dimensionality reduction.

5. CONCLUSION AND FUTURE PERSEPCTIVE

NN models that used LAI performed best in the estimation of end-of-season yield, whereas the hyperspectral models did not show good results and their addition to multispectral data reduced the estimation performance. The main cause of the poor hyperspectral performance appears to be the combination of CNN requiring a rigid input structure and the temporal sparsity of hyperspectral acquisitions across years.

In future work, more flexible architectures should be considered, such as recurrent neural networks (RNN) or transformer-based models, which may allow exploitation of all available images each year, regardless of sequence length, and extract time-dependent features that the CNN could not capture.

In this study Sentinel-2 data underwent multiple transformations that reduced dimensionality and complexity to produce LAI time series and phenological metrics. The use of RNNs or transformer would also enable use of LAI time series without temporal interpolation, or the direct use of Sentinel-2 spectral data, thereby allowing the model to learn relevant features from less-processed inputs.

6. REFERENCES

Akiba, T., Sano, S., Yanase, T., Ohta, T., & Koyama, M. 2019. Optuna: A Next-generation Hyperparameter Optimization Framework. *Proceedings of the 25th ACM SIGKDD International Conference on Knowledge Discovery & Data Mining*, 2623–2631. https://doi.org/10.1145/3292500.3330701

Candiani, G., Nutini, F., Parigi, L., Pepe, M., & Boschetti, M. 2024. Crop Traits Retrival from Prisma Imagery with Machine Learning: A Comparison of Data Driven and Hybrid Approach with a Multi-Year Multi-Crop Dataset. *2024 14th Workshop on Hyperspectral Imaging and Signal Processing: Evolution in Remote Sensing (WHISPERS)*, 1–5. https://doi.org/10.1109/WHISPERS65427.2024.10876467

Candiani, G., Tagliabue, G., Panigada, C., Verrelst, J., Picchi, V., Rivera Caicedo, J. P., & Boschetti, M. 2022. Evaluation of Hybrid Models to Estimate Chlorophyll and Nitrogen Content of Maize Crops in the Framework of the Future CHIME Mission. *Remote Sensing*, *14*(8), 1792. https://doi.org/10.3390/rs14081792

Darra, N., Anastasiou, E., Kriezi, O., Lazarou, E., Kalivas, D., & Fountas, S. 2023. Can Yield Prediction Be Fully Digitilized? A Systematic Review. *Agronomy*, *13*(9), 2441. https://doi.org/10.3390/agronomy13092441

De Clercq, D., & Mahdi, A. 2025. Modern computational approaches for rice yield prediction: A systematic review of statistical and machine learning-based methods. *Computers and Electronics in Agriculture*, *231*, 109852. https://doi.org/10.1016/j.compag.2024.109852

Filipponi, F., Smiraglia, D., & Agrillo, E. 2022. Earth Observation for Phenological Metrics (EO4PM): Temporal Discriminant to Characterize Forest Ecosystems. *Remote Sensing*, *14*(3), 721. https://doi.org/10.3390/rs14030721

Kuhn & Max. 2008. Building predictive models in R using the caret package. *Journal of Statistical Software*, *28*(5), 1–26. https://doi.org/10.18637/jss.v028.i05

Li, L., Jamieson, K., Rostamizadeh, A., Gonina, E., Hardt, M., Recht, B., & Talwalkar, A. 2020. *A System for Massively Parallel Hyperparameter Tuning* (arXiv:1810.05934). arXiv. https://doi.org/10.48550/arXiv.1810.05934

Liaw, R., Liang, E., Nishihara, R., Moritz, P., Gonzalez, J. E., & Stoica, I. 2018. *Tune: A Research Platform for Distributed Model Selection and Training* (arXiv:1807.05118). arXiv. https://doi.org/10.48550/arXiv.1807.05118

Marshall, M., Belgiu, M., Boschetti, M., Pepe, M., Stein, A., & Nelson, A. 2022. Field-level crop yield estimation with PRISMA and Sentinel-2. *ISPRS Journal of Photogrammetry and Remote Sensing*, *187*, 191–210. https://doi.org/10.1016/j.isprsjprs.2022.03.008

Parigi, L., Candiani, G., Gallo, I., Toscano, P., & Boschetti, M. 2024. *Towards crop traits estimation from hyperspectral data: evaluation of neural network models trained with real multi-site data or synthetic RTM simulations*. 475–484. https://doi.org/10.15439/2024F4108

Paszke, A., Gross, S., Massa, F., Lerer, A., Bradbury, J., Chanan, G., Killeen, T., Lin, Z., Gimelshein, N., Antiga, L., Desmaison, A., Köpf, A., Yang, E., DeVito, Z., Raison, M., Tejani, A., Chilamkurthy, S., Steiner, B., Fang, L., … Chintala, S. 2019. *PyTorch: An Imperative Style, High-Performance Deep Learning Library* (arXiv:1912.01703). arXiv. http://arxiv.org/abs/1912.01703

Ranghetti, L. 2021. *sen2rts: Build and Analyse Sentinel-2 Time Series*. https://doi.org/10.5281/zenodo.4682829

Ranghetti, M., Boschetti, M., Nutini, F., Rossini, M., & Candiani, G. 2023. Assessing Wheat Yield and Grain Protein Content with Machine Learning and Satellite Hyperspectral Data: Multi-Year Explorative Analysis. *2023 13th Workshop on Hyperspectral Imaging and Signal Processing: Evolution in Remote Sensing (WHISPERS)*, 1–5. https://doi.org/10.1109/WHISPERS61460.2023.10430546

Sun, Z., Li, Q., Jin, S., Song, Y., Xu, S., Wang, X., Cai, J., Zhou, Q., Ge, Y., Zhang, R., Zang, J., & Jiang, D. 2022. Simultaneous Prediction of Wheat Yield and Grain Protein Content Using Multitask Deep Learning from Time-Series Proximal Sensing. *Plant Phenomics*, *2022*, 9757948. https://doi.org/10.34133/2022/9757948

Tan, S., Pei, J., Zou, Y., Fang, H., Wang, T., & Huang, J. 2025. Improving rice yield prediction with multi-modal UAV data: hyperspectral, thermal, and LiDAR integration. *Geo-Spatial Information Science*, 1–20. https://doi.org/10.1080/10095020.2025.2535524

Verrelst, J., Malenovský, Z., Van der Tol, C., Camps-Valls, G., Gastellu-Etchegorry, J.-P., Lewis, P., North, P., & Moreno, J. 2019. Quantifying Vegetation Biophysical Variables from Imaging Spectroscopy Data: A Review on Retrieval Methods. *Surveys in Geophysics*, *40*(3), 589–629. https://doi.org/10.1007/s10712-018-9478-y

Weiss, M., Jacob, F., & Duveiller, G. 2020. Remote sensing for agricultural applications: A meta-review. *Remote Sensing of Environment*, *236*, 111402. https://doi.org/10.1016/j.rse.2019.111402

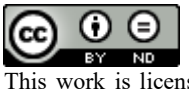

This work is licensed under a Creative Commons Attribution-No Derivatives 4.0 International License.

MULTI-SOURCE EARTH OBSERVATION DATA INTEGRATION FOR PRECISION AGRICULTURE: A CORN CROP MONITORING CASE STUDY

L. Cicala[1], M. Gargiulo[1]*, C. Savarese[1], S. Parrilli[1], C.V. Angelino[1], F. Tufano[1], M. De Mizio[1]

[1]CIRA - Italian Aerospace Research Centre, Via Maiorise snc, 81043 Capua, Italy

*Corresponding author: m.gargiulo@cira.it

KEY WORDS: precision agriculture, UAV multispectral/hyperspectral imaging, proximal sensing, vegetation indices, maize yield prediction, data fusion

ABSTRACT:

Multi-platform Earth Observation (EO) strategies enhance crop monitoring by synergizing satellite time series for broad-scale continuity with UAV imagery for ultra-high-resolution diagnostics. This study presents a multi-temporal, multi-sensor workflow applied to an open-field maize fertilization experiment (Castel Volturno, Italy) to evaluate four treatments and demonstrate a practical data-fusion pathway from satellite screening to detailed UAV-based diagnostics. The experimental design comprised four fertilization strategies (A: traditional mineral; B: coffee compost+biochar; C: coffee compost; D: mineral+humic substances from compost), replicated four times (16 plots, 40m^2 each). Ground measurements (SPAD, LAI) and UAV multispectral/hyperspectral data were collected in two campaigns (July and September 2023). Results showed consistent treatment-driven trends: A and D had higher SPAD/LAI and vigor, while B underperformed. In multispectral and hyperspectral data, NDRE emerged as the most representative index (ρ = 0.6–0.75), enabling robust linear estimation of SPAD and LAI . The potential of UAV-derived products for plot-scale management decisions in precision agriculture is demonstrated by proposed pixel-based SPAD and LAI maps.

1 INTRODUCTION

The growing demand for sustainable agriculture and food security necessitates robust, scalable technologies for timely crop monitoring [1]. A key challenge is reconciling (i) frequent, large-area observations, (ii) fine spatial detail at field scale, and (iii) quantitative, physiologically meaningful indicators for agronomic decisions [2]. Satellites offer extensive coverage and temporal consistency, valuable for contextual screening and trend analysis [3]. In the proposed framework, satellite data are not intended for direct biophysical estimation at plot scale, but rather as a statistically driven trigger to activate UAV surveys only when inter-treatment differences become detectable. In this study, PlanetScope time series served as a screening layer, using multispectral indices (e.g., NDVI) to identify inter-treatment anomalies and guide targeted UAV deployments [4]. UAVs provide complementary rapid deployment, ultra-high spatial resolution, and acquisition flexibility, making them ideal for precision agriculture and plot-level experimentation [5]. However, remote sensing products gain operational value only when linked to ground-truth physiological and morphological parameters [6]. SPAD, a proxy for leaf chlorophyll related to photosynthetic capacity and stress [7], and LAI, a structural descriptor of canopy development linked to biomass [8], were measured with handheld devices (MultispeQ V2.0, LAIpen LP 110) for validation and calibration.

Data fusion frameworks integrating satellite, UAV, and proximal sensing are emerging as powerful tools for enhanced crop characterization [9], [10]. For instance, satellite-guided UAV campaigns optimize resource use, while UAV-derived products, calibrated with ground data, enable detailed biophysical mapping [11], [12]. This work focuses on a satellite-UAV activation strategy that strives for operationalization, unlike other data fusion approaches that tend to increase algorithmic complexity. Scalability and agronomic interpretability are the top priorities in the proposed framework, which leverages high-spatial-resolution satellite time series to target UAV deployments only when statistically significant differences are detected. This paper presents a practical integration workflow applied to a maize fertilization experiment. It aims to: (i) demonstrate satellite time series for guiding anomaly detection using Planetscope imagery; (ii) quantify treatment effects via in-situ SPAD/LAI and UAV VIs; (iii) identify the most informative spectral indices; and (iv) showcase spatialized products (pixel-based SPAD maps) for plot-scale decision support. Although PlanetScope provides a commercial solution with high temporal resolution and relatively fine spatial detail, its operational use implies non-negligible acquisition costs. In this context, the proposed workflow is designed to minimize such costs by using satellite data only as a triggering mechanism for UAV acquisitions, rather than for continuous monitoring or direct biophysical estimation. From a scalability perspective, similar logic could be implemented using freely available satellite data such as Sentinel-2, at the expense of reduced temporal resolution and coarser spatial detail. However, this limitation may be partially mitigated through the integration of multi-date observations or the application of super-resolution techniques, as widely explored in the literature. Therefore, the proposed framework is not strictly dependent on commercial data, but can be adapted to different cost–performance trade-offs depending on operational constraints. A key outcome is the validation of NDRE as a robust, cross-sensor index for estimating SPAD and LAI, forming a "rapid tool" concept for precision fertilization management. The paper is structured as follows: Section 2 details the experimental site and design; Section 3 describes the proposed multi-source methodology; results and discussion are presented in Section 4; and conclusions are drawn in Section 5.

2 EXPERIMENTAL SITE AND DESIGN

The case study was an open-field maize (Zea mays L.) cultivation in the Campania region (Castel Volturno, Italy). In this case, we have observed with satellite date all growing period from

* Corresponding author

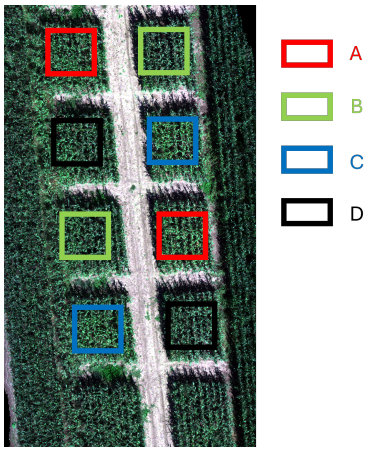

Figure 1: The experimental setup designed as a randomized complete block with four treatments per block and four replications (here two replications).

sowing occurred in June 2023 to harvest in October 2023. The experimental design included four different fertilization treatments: (A) Traditional mineral fertilizer, (B) Coffee compost + biochar, (C) Coffee compost, (D) Mineral fertilizer + humic substances (HS) extracted from coffee compost.

The design used four replications per each treatment, for a total of 16 plots. The plot size was 40 m^2 (8×5 m) and sowing density was 7 plants m^{-2}. The area of each plot is sufficient to use Planet data at 3m. Obviously, the data may be subject to "noise" due to mixing between different land covers.

Field data were acquired by drone for two dates: July 27, 2023 (early season characterization) and September 28, 2023 (pre-harvest characterization). These dates were intended to verify any changes induced by the different treatments considered and to potentially allow for a potential interpretation related to yield.

3 PROPOSED MULTI-SOURCE APPROACH

In Fig. 2, the proposed workflow is shown. This workflow is composed by three different data sources, from satellite (for screening phase), UAV (detailed analysis phase) and on-ground (validation and operational phase).

3.1 Satellite, UAV, and on-ground data

PlanetScope imagery was used at the screening level, leveraging its high temporal resolution to support drone acquisitions, providing eight spectral bands from VIS to NIR with a spatial resolution of approximately 3 m. Satellite data is conceptually used to observe temporal trends (e.g., NDVI trajectories) on a large scale, providing an initial indication of differences between treatments before proceeding with drone flights, which require more time, resources, and costs. Conversely, UAV acquisitions are designed to provide detailed multispectral and hyperspectral information (see Tab. 1 for some details about spectral–spatial characteristics of the considered cameras).

Eventually, to validate the drone data and combine it with physiological and morphological information, data were also collected using ground-based instruments:

- SPAD using MultispeQ V2.0 (chlorophyll proxy; sensitive to changes in growth conditions, including water/nutrient stress);
- LAI using LAIPen LP 110 (canopy development proxy; higher values generally indicate more developed plants with better nutritional status).

Table 1: Spectral–spatial trade-off summary (Micasense Altum vs Cubert Ultris 5).

Focus	MicaSense Altum	Cubert Ultris 5
Spectral content	6 discrete VNIR + thermal	HS cube: 51 bands (450–850 nm)
Spectral detail	Band BW 10–40 nm	Contiguous; 8 nm sampling
Spatial detail	2048×1536 px; ~4.0 cm/px @120 m	290×275 px; ~7.2 cm/px @120 m
Acquisition mode	Multi-lens discrete bands (co-registered)	Snapshot hyperspectral (2D spatial–spectral)

3.2 Satellite, UAV and on-ground data: Interoperability

Planetscope satellite data were used in the first screening phase for potential differences between the different treatments. Using these data, it was possible to calculate some of the indices selected in [13], in particular NDVI, NDRE, and EVI2, which proved to be the most discriminating in this first phase. Thanks to the temporal resolution of the Planetscope, it was possible to obtain, net of the cloud cover over the observed scene, a time series with an almost daily frequency. On each individual date, statistical tests were performed to determine whether or not it was appropriate to conduct a drone flight on a specific date (ANOVA and Wilcoxon Test [14]). Therefore, where the differences between the different treatments exceeded the statistical tests, with a p-value < 0.05, a flight was scheduled. Once the flight with the hyperspectral and multispectral cameras has been completed, UAV images are processed into orthomosaics, then used to compute vegetation indices (VIs), as in [13]. The orthomosaic workflow, implemented in Agisoft Metashape software includes photo alignment, dense point cloud generation, definition of reconstruction region, orthomosaic building, and export for the following spectral analysis. Vegetation indices were extracted from multispectral and hyperspectral data. Finally, on-ground data were acquired manually in the field.

To evaluate the relationship between remote indices and ground parameters, correlation analysis and statistical significance assessment were performed, i.e. Pearson correlation coefficient (ρ) between each VI and SPAD/LAI and ANOVA to evaluate statistical significance of correlations (p-value driven selection)

Once better index is selected as in [13], SPAD and LAI were estimated through linear regression:

$$OGP = \beta_0 + \beta_1 \cdot VI_{Oct} + \epsilon, \tag{1}$$

OGP corresponds to on-ground parameter, i.e. SPAD and LAI, β_0 and β_1 are the coefficient of linear regressor and ϵ is the error related to the estimate. In accordance with operational precision-agriculture constraints, we have chosen linear models to maintain robustness and interpretability. The predictive performance was assessed through RMSE, MAPE, and ρ. For model validation, the workflow included an 80% calibration / 20% validation split and K-fold cross validation (K=5).

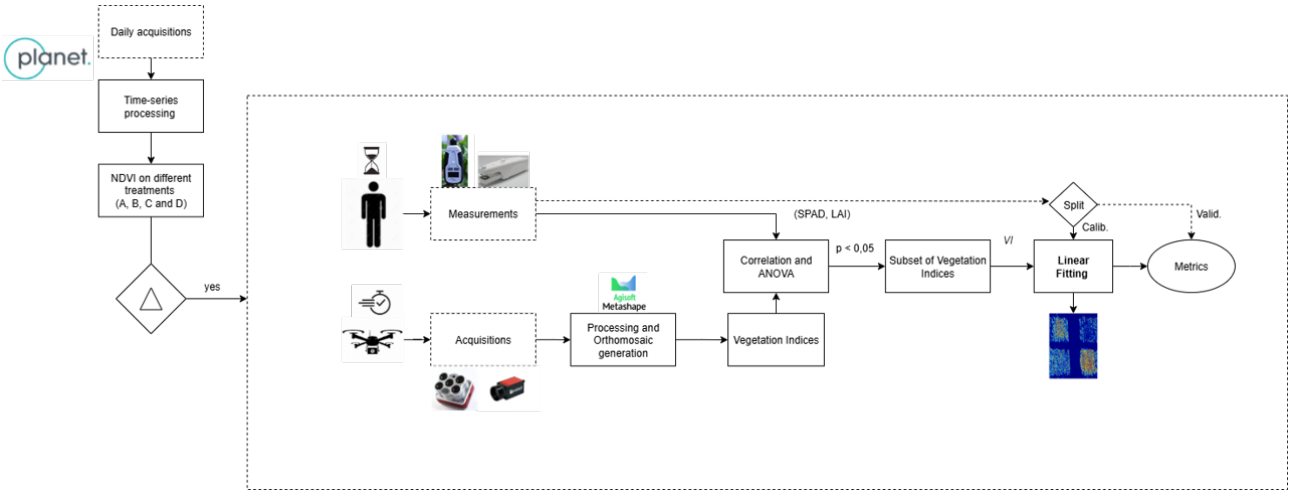

Figure 2: Proposed multi-source strategy.

4 RESULTS AND DISCUSSION

4.1 Treatment effects on ground parameters (SPAD, LAI)

Ground measurements indicated a consistent separation among fertilization strategies. SPAD and LAI showed a clear trend: the compost+biochar treatment (B) produced the lowest values, compost alone (C) slightly improved relative to B, while mineral fertilization (A) and mineral + humic substances (D) showed similar and generally higher SPAD and LAI. This implies that treatments A and D encouraged increased canopy formation and chlorophyll content.

4.2 UAV vegetation indices and the role of NDRE as a representative index

The same treatment-driven trend observed in SPAD and LAI was reflected in most UAV-derived vegetation indices computed from multispectral and hyperspectral imagery, with higher vigor signatures for A and D and weaker performance for B. Among the tested indices, NDRE emerged as the most statistically significant and practically robust descriptor for both sensor types, having consistent correlations with SPAD and LAI (ρ =0.6–0.75) and resulting errors within acceptable agronomic ranges.NDRE leverages the red-edge region, which improves sensitivity to chlorophyll-related changes and avoids some saturation effects typical of NDVI in dense canopies; in this experiment it consistently captured treatment differences similarly to SPAD/LAI patterns.

4.3 Multi-source interoperability: from time-series satellite to detailed on-ground information

First of all, we proceed with the calculation of the average value of the NDRE, NDVI, EVI2 indices with the planet data for the plots analyzed, from the sowing phase to the harvest phase. NDVI time series, shown in Fig. 3-(a), followed the expected maize phenological trajectory, with statistically significant inter-treatment differences emerging only in September. However, by performing an ANOVA and Wilcoxon analysis, as shown in Tab.2, only in September these data appear slightly statistically significant, which prompted us to proceed with a flight aimed at a more detailed observation of this trend. A further flight, as described previously, was carried out in July, but obviously it proved to be not very discriminating in terms of the indices considered. The reported values refer to the acquisition date in which statistically significant differences between treatments were observed. Furthermore, this table also reports the standard deviation and p-values obtained from the two tests considered. This allowed us to confirm that the satellite data is in line with the on-ground data and, as seen in [13], also with the drone data, which obviously allow us to obtain greater detail than the satellite data. Therefore, all the data confirm a condition of canopy development and greater vigor for the maize plants in plots A and D compared to B and C. Furthermore, thanks to the regression model, tested on multispectral and hyperspectral data, we can show an example, reported in Fig.3-(c), of detailed result starting from the NDRE index to predict the SPAD and LAI values. NDRE was considered the most significant for SPAD and LAI prediction in [13]. Eventually, with this UAV-based visual analysis we are able to provide greater spatial detail of a particular case study than the satellite data and greater coverage than the data acquired on-ground. This workflow ensures operational scalability from satellite-driven screening to targeted UAV acquisitions and ground-based physiological validation.

Table 2: Mean ± SD of vegetation indices computed on Planetscope data (September 27th, 2023) by treatment (A–D) and related statistical tests.

Index	Trt	$\mu \pm \sigma$	p-value		
			ANOVA (4-class)	ANOVA (2-class)	Wilcoxon (ranksum)
NDRE	A	0.5314 ± 0.0368	0.0572	0.0211	0.0313
	B	0.5037 ± 0.0424			
	C	0.5092 ± 0.0256			
	D	0.5295 ± 0.0434			
EVI2	A	0.4153 ± 0.0230	0.0846	0.026571	0.0190
	B	0.3964 ± 0.0300			
	C	0.3905 ± 0.0238			
	D	0.4164 ± 0.0278			
NDVI	A	0.6630 ± 0.0330	0.044	0.000859	0.0011
	B	0.6358 ± 0.0472			
	C	0.6432 ± 0.0337			
	D	0.6710 ± 0.0449			

5 CONCLUSIONS

This work presented a practical multi-source EO workflow for maize monitoring in an open-field fertilization experiment. Limita-

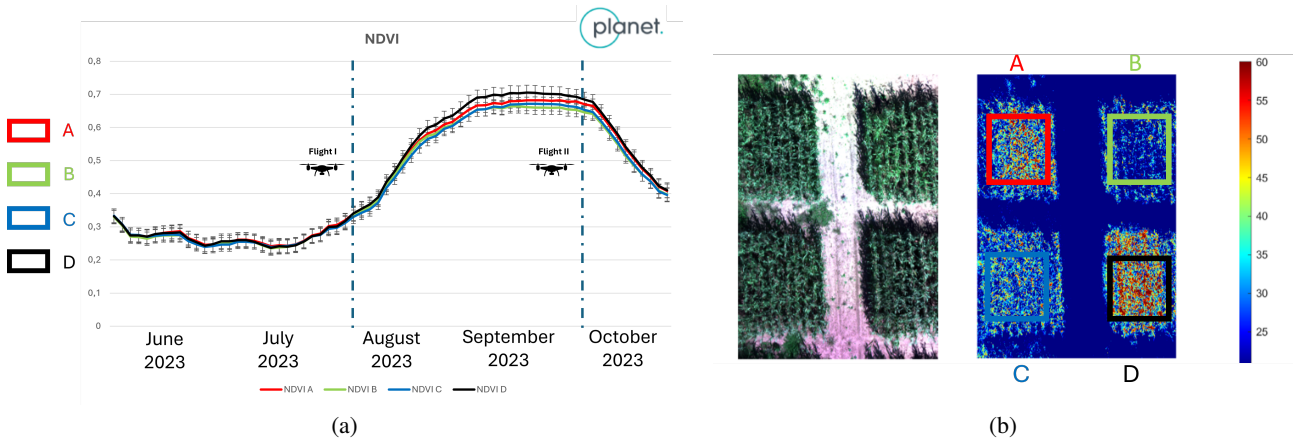

Figure 3: (a) The NDVI timeseries from June 2023 to October 2023 with vertical lines to represent the dates of the two UAV flights (I: 27 July; II: 28 September 2023). The spatial (b) zoom on statistical significance date.

tions include the limited number of UAV acquisition dates and the plot-scale experimental design, which may constrain generalization to larger or more heterogeneous fields. A two-date, multi-temporal design (27 July and 28 September 2023) enabled early-season and pre-harvest assessment, combining satellite time-series screening with UAV multispectral/hyperspectral diagnostics and ground validation via SPAD and LAI instruments. Across treatments, both ground parameters (SPAD, LAI) and UAV vegetation indices showed coherent trends, with mineral fertilization (A) and mineral + humic substances (D) generally associated with stronger crop status than compost-based treatments, particularly compost+biochar (B). Overall, the study supports a scalable "from satellite to detailed monitoring" paradigm in which satellite time series guide the deployment of UAV surveys, while ground measurements provide physiological meaning and validation—forming a rapid, quantitative tool concept for precision fertilization management.

ACKNOWLEDGEMENTS

This study was carried out within the Space It Up project funded by the Italian Space Agency, ASI, and the Ministry of University and Research, MUR, under contract n. 2024-5-E.0 - CUP n. I53D24000060005.

REFERENCES

[1] D. K. Ray, N. D. Mueller, P. C. West, and J. A. Foley, "Yield trends are insufficient to double global crop production by 2050," *PloS one*, vol. 8, no. 6, e66428, 2013.

[2] D. Panday, N. Bhusal, S. Das, and A. Ghalehgolabbehbahani, "Rooted in nature: The rise, challenges, and potential of organic farming and fertilizers in agroecosystems," *Sustainability*, vol. 16, no. 4, p. 1530, 2024.

[3] D. Radočaj, A. Šiljeg, R. Marinović, and M. Jurišić, "State of major vegetation indices in precision agriculture studies indexed in web of science: A review," *Agriculture*, vol. 13, no. 3, p. 707, 2023.

[4] J. Yuan, Y. Zhang, Z. Zheng, W. Yao, W. Wang, and L. Guo, "Grain crop yield prediction using machine learning based on uav remote sensing: A systematic literature review," *Drones*, vol. 8, no. 10, p. 559, 2024.

[5] S. Chatterjee, A. Adak, S. Wilde, S. Nakasagga, and S. C. Murray, "Cumulative temporal vegetation indices from unoccupied aerial systems allow maize (zea mays l.) hybrid yield to be estimated across environments with fewer flights," *PLoS One*, vol. 18, no. 1, e0277804, 2023.

[6] S. Liu, Z. Hu, J. Han, Y. Li, and T. Zhou, "Predicting grain yield and protein content of winter wheat at different growth stages by hyperspectral data integrated with growth monitor index," *Computers and Electronics in Agriculture*, vol. 200, p. 107 235, 2022.

[7] J. Fan et al., "Estimation of maize yield and flowering time using multi-temporal uav-based hyperspectral data," *Remote Sensing*, vol. 14, no. 13, p. 3052, 2022.

[8] P. Killeen, I. Kiringa, T. Yeap, and P. Branco, "Corn grain yield prediction using uav-based high spatiotemporal resolution imagery, machine learning, and spatial cross-validation," *Remote Sensing*, vol. 16, no. 4, p. 683, 2024.

[9] M. Weiss, F. Jacob, and G. Duveiller, "Remote sensing for agricultural applications: A meta-review," *Remote sensing of environment*, vol. 236, p. 111 402, 2020.

[10] A. R. Allu and S. Mesapam, "Fusion of satellite and uav imagery for crop monitoring," *ISPRS Annals of the Photogrammetry, Remote Sensing and Spatial Information Sciences*, pp. 71–79, 2025.

[11] P. Singh et al., "Hyperspectral remote sensing in precision agriculture: Present status, challenges, and future trends," in *Hyperspectral remote sensing*, Elsevier, 2020, pp. 121–146.

[12] A. Matese and S. F. Di Gennaro, "Practical applications of a multisensor uav platform based on multispectral, thermal and rgb high resolution images in precision viticulture," *Agriculture*, vol. 8, no. 7, p. 116, 2018.

[13] M. Gargiulo, C. Savarese, M. De Mizio, F. Tufano, and S. Parrilli, "Rapid monitoring of maize plant status using uav-based multispectral and hyperspectral data," in *2024 IEEE International Workshop on Metrology for Agriculture and Forestry (MetroAgriFor)*, IEEE, 2024, pp. 7–12.

[14] D. W. Zimmerman and B. D. Zumbo, "Relative power of the wilcoxon test, the friedman test, and repeated-measures anova on ranks," *The Journal of Experimental Education*, vol. 62, no. 1, pp. 75–86, 1993.

This work is licensed under a Creative Commons Attribution-No Derivatives 4.0 International License.

EXPLORING VINEYARD PHENOLOGICAL VARIABILITY THROUGH UNSUPERVISED BI-TEMPORAL ANALYSIS OF UAV MULTISPECTRAL AND THERMAL DATA

A. Capolupo * and E. Tarantino

Department of Civil, Environmental, Land, Construction and Chemistry (DICATECh), Politecnico di Bari, Italy
(alessandra.capolupo, eufemia.tarantino)@poliba.it

KEYWORDS: Vineyard monitoring, Unsupervised learning, Multi-temporal analysis, Continuous spatial variability, UAV remote sensing, Phenological gradients

ABSTRACT:

High-resolution Unmanned Aerial Vehicle (UAV) imagery is frequently used in precision viticulture to delineate spatial management zones, implicitly assuming that phenological variability is organized into discrete units. This study proposes an unsupervised bi-temporal analytical framework explicitly designed to evaluate whether UAV-derived phenological variability exhibits intrinsic clustering or is more consistently described as a continuous spatial gradient. Multispectral vegetation indices and thermal imagery acquired at two contrasting phenological stages were processed through pixel-wise temporal differences and explored using a Self-Organizing Map. Model diagnostics based on Quantization Error and Topographic Error, together with sensitivity analysis across input configurations and random initializations, were used to assess representation stability and topological coherence. Results indicate that multispectral temporal differences generate a stable feature-space organization; however, no robust or well-separated clusters emerge across configurations. Instead, spatial projections reveal gradual transitions consistent with gradient-like organization. The inclusion of thermal temporal differences increases representation error and reduces coherence, suggesting limited structural contribution in the bi-temporal clustering context, although thermal data provide complementary descriptive information. While limited to two acquisition dates, the framework demonstrates how unsupervised topology-preserving methods can be used diagnostically to assess the structural validity of zonation assumptions in Earth observation studies.

1. INTRODUCTION

Unmanned Aerial Vehicles (UAVs) have significantly expanded the capacity of Earth observation for agricultural monitoring, providing high spatial resolution and flexible temporal acquisition (Nex and Remondino, 2014). In viticulture, UAV-based multispectral and thermal imagery are commonly used to assess canopy vigour, water status, and spatial variability, often with the objective of delineating management zones (Velusamy et al., 2021). These capabilities have motivated a growing number of studies aimed at mapping vineyard variability to support phenological assessment and site-specific management (Pádua et al., 2019; Santesteban et al., 2017).

Most vineyard variability studies adopt clustering or zonation strategies that partition fields into discrete spatial units (Capolupo and Tarantino, 2025). While effective under heterogeneous environmental or management conditions, such approaches implicitly assume that phenological responses are organized into separable classes. However, plant phenology is inherently continuous, and the extent to which discrete zonation accurately reflects spatial organization remains insufficiently examined, particularly in vineyards characterized by homogeneous management and limited environmental gradients.

Unsupervised learning techniques provide an opportunity to explore spatial structure without imposing predefined labels. Among them, the Self-Organizing Map (SOM) performs topology-preserving projection of high-dimensional data onto a low-dimensional lattice, enabling investigation of intrinsic feature-space organization (Vesanto, 1999). Rather than using unsupervised learning to produce management zones, it can also be employed diagnostically to evaluate whether intrinsic clustering exists at all (Ferro and Catania, 2023; Matese et al., 2019).

The objective of this study is therefore not to delineate management zones but to evaluate the structural validity of zonation assumptions in bi-temporal UAV-derived phenological variability. By analysing pixel-wise temporal differences through a SOM and systematically assessing representation stability, the study investigates whether intrinsic partitioning emerges or whether variability is more consistently described as spatially continuous.

2. MATERIAL AND METHODS

The analysis was implemented through a custom Python-based pipeline to ensure reproducibility and explicit control over data processing and model evaluation. The workflow comprises four main steps: (i) pre-processing and geometric harmonization of bi-temporal UAV data; (ii) computation of multispectral Vegetation Indices (VIs) and pixel-wise temporal differences; (iii) exploratory analysis of the resulting feature space using a SOM; and (iv) quality assessment and sensitivity analysis. Each step is described in detail in the following sections.

2.1 Data acquisition and pre-processing

The study was conducted in a commercial vineyard located near Avellino (Campania, southern Italy), covering approximately 21,000 m² and planted with *Vitis vinifera* L. cv. Aglianico. (Picariello et al., 2020). The vineyard reached its final layout in 2015 and has since been managed under homogeneous agronomic conditions.

UAV data were collected at two campaigns corresponding to distinct phenological stages (the 5th of June 2025 and 20th of

* Corresponding author

August 2025). For each campaign, two separate UAV flights were conducted using the DJI Matrice 4T platform. The first one was dedicated to multispectral acquisition while the other one to thermal acquisition. Multispectral imagery was acquired using a sensor with a detector pixel size of 2.4 μm and a focal length of 6.72 mm, while thermal imagery was collected using a sensor characterized by a detector pixel size of 12 μm and a focal length of 12 mm. The multispectral flight was carried out at approximately 650 m above ground level, while the thermal flight was conducted at approximately 500 m above ground level in order to obtain a comparable ground sampling distance.
All raster products were reprojected to a common metric coordinate reference system (WGS 84 / UTM zone 33N) and resampled using bilinear interpolation onto a shared grid defined by a target pixel size of 0.10 m to ensure pixel-wise comparability between sensors and acquisition dates. Pixels lacking valid observations in either acquisition were excluded from subsequent processing to prevent artificial variability in the computation of temporal differences.

2.2 Vegetation indices computation

Vegetation condition and phenological variability were characterized using a set of multispectral VIs designed to capture complementary structural and physiological properties of the canopy. These VIs exploit differential reflectance responses in the visible, near-infrared (NIR), and red-edge (RE) spectral regions, which are sensitive to variations in pigment concentration, canopy structure, and photosynthetic activity (Weiser et al., 1986; Munden et al., 1994).
The following VIs were computed for each acquisition date:

$$NDVI = \frac{NIR-RED}{NIR+RED} \text{ (Rouse et al., 1974)} \quad (1)$$

$$OSAVI = \frac{NIR-RED}{NIR+RED+0.16} \text{ (Rondeaux et al., 1996)} \quad (2)$$

$$GNDVI = \frac{NIR-GREEN}{NIR+GREEN} \text{ (Wu, 2014)} \quad (3)$$

$$LCI = \frac{NIR-RED}{NIR+RED} * \frac{NIR}{RED} \text{ (Sakuno and Kunii, 2015)} \quad (4)$$

$$NDRE = \frac{NIR-RE}{NIR+RE} \text{ (Boiarskii and Hasegawa, 2019)} \quad (5)$$

The selected indices jointly describe different aspects of canopy status, including vegetation vigour (NDVI, OSAVI), chlorophyll-related variability (GNDVI, NDRE), and combined structural-physiological responses (LCI) (Capolupo et al., 2020). To focus on phenological variation, pixel-wise temporal differences were calculated between the two acquisition dates. This approach emphasizes relative change and reduces sensitivity to inter-date radiometric offsets.

2.3 Thermal data processing

Thermal imagery was geometrically harmonized with multispectral data, as described in Section 2.1. Given the sensitivity of UAV-based thermal observations to environmental conditions, thermal values were normalized independently for each date relative to their spatial distribution within the vineyard (Maes and Steppe, 2019; Prashar and Jones, 2014). Normalized thermal differences were derived between acquisition dates and retained for descriptive analysis of spatial variability. To evaluate their structural contribution, thermal temporal differences were tested both as clustering inputs and as complementary variables. While limited to two acquisition dates, this design captures marked differences in canopy development and allows assessment of bi-temporal phenological variation. The analytical framework is designed to be scalable to denser temporal sampling.

2.4 SOM analysis

The multi-dimensional feature space derived from temporal differences was explored using a SOM (Kohonen, 2001; Kiviluoto, 1996). Let $x_j \in R^d$ denote the j-th input vector and w_i the weight vector of the i-th SOM node. For each input vector, the Best Matching Unit (BMU) was identified as:

$$BMU\left(\boldsymbol{x}_j\right) = \arg min_i \|x_i - w_i\| \quad (6)$$

Input variables were standardized prior to training to ensure comparable influence (Li and Eastman, 2010). A two-dimensional rectangular lattice (12 × 12) was adopted following preliminary tuning experiments. For visualization purposes only, SOM codebook vectors were subsequently grouped using k-means clustering (MacQueen, 1967), without implying the existence of discrete phenological classes.

2.5 Quality assessment and sensitivity analysis

Model behaviour was evaluated using Quantization Error (QE) and Topographic Error (TE), which respectively measure representation accuracy and preservation of topological relationships within the SOM (Park et al., 2003; Kohonen, 2012):

$$QE = \frac{1}{N}\sum_{j=1}^{N}\left\|x_i - w_{BMU(j)}\right\| \quad (7)$$

$$TE = \frac{1}{N}\sum_{j=1}^{N} u_j \quad (8)$$

where u_j=1 if the two closest nodes to x_j are not adjacent on the lattice, and u_j=0 otherwise.
A targeted sensitivity analysis was conducted to assess the influence of input feature selection and SOM configuration, including comparisons between multispectral-only and multispectral-plus-thermal inputs, different map sizes, training durations, and random initializations (Asan and Ercan, 2012). These experiments were used to evaluate stability and coherence.

3. RESULTS AND DISCUSSION

In this study, SOM was selected as an exploratory technique capable of organizing multi-dimensional phenological information while preserving neighborhood relationships without relying on labeled data. Model configuration was not fixed a priori but defined through a series of tuning experiments. As reported in Table 1, input feature selection had the strongest influence on model behaviour. Configurations combining multispectral and thermal temporal differences resulted in increased QE, indicating reduced representational efficiency, while configurations based exclusively on thermal differences exhibited very low QE but extremely high TE, reflecting poor preservation of neighbourhood relationships due to reduced dimensionality. The configuration based exclusively on multispectral temporal differences achieved the most balanced outcome, with lower QE and consistently low TE, and was therefore selected as the reference model for subsequent analysis.

ID	Input features	SOM size	Epochs	Seed	QE	TE
A	Δ Multispectral + Δ Thermal	12×12	2000	0	2.08	0.0998

B	Δ Multispectral	12×12	2000	0	1.29	0.125
C	Δ Thermal	12×12	2000	0	0.034	0.95

Table 1. Input feature sensitivity. Δ indicates pixel-wise temporal differences between acquisitions.

The SOM architecture was set to a 12 × 12 lattice and trained for 2000 epochs, which provided stable convergence without introducing overfitting effects. Preliminary tests using alternative map sizes or substantially longer training durations did not alter the qualitative behaviour of the model and either reduced topological stability or increased representation error. The robustness of the selected configuration with respect to random initialization was evaluated through repeated runs using different seeds. As shown in Table 2, variations in QE and TE across seeds were limited, indicating moderate sensitivity to initialization but no qualitative changes in the organization of phenological responses. In all cases, the SOM produced a coherent representation of the feature space without revealing stable or well-separated clusters.

ID	Input features	SOM size	Epochs	Seed	QE	TE
B-S0	Δ Multispectral	12×12	2000	0	1.29	0.125
B-S7	Δ Multispectral	12×12	2000	7	1.20	0.169
B-S42	Δ Multispectral	12×12	2000	42	1.19	0.215

Table 2. Sensitivity of SOM results to random initialization (seed)

When the SOM output corresponding to the selected configuration was projected back into the spatial domain, phenological responses were distributed smoothly across the vineyard. No abrupt transitions or persistent boundaries were observed, and the spatial organization of BMU reflected gradual variations rather than segmented structures. This behaviour was consistent across all tested configurations and parameter settings, supporting the conclusion that the absence of clustering is not an artifact of model choice but reflects the intrinsic structure of the data.

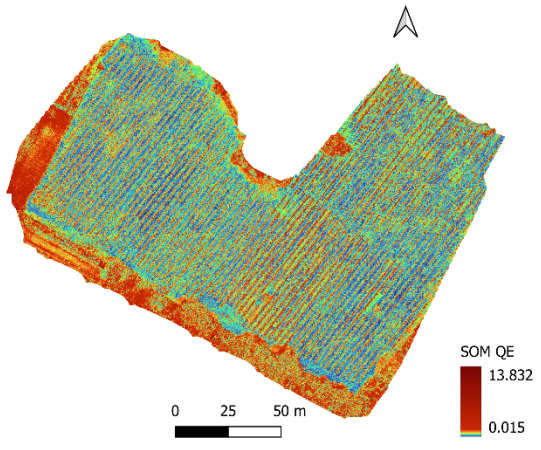

Figure 1. Continuous phenological gradient derived from the SOM output.

Thermal temporal differences exhibited greater spatial variability than multispectral indices but did not align with the organization of the multispectral phenological feature space. Including thermal differences as clustering inputs consistently increased representation error without improving topological preservation, as documented in Table 1. Consequently, thermal data were retained exclusively for descriptive interpretation, where they provided complementary information on surface temperature variability without structuring phenological responses.

The findings highlight a broader consideration for high-resolution Earth observation analyses. Clustering-based zonation is often applied as a default analytical strategy. However, when variability is intrinsically continuous, enforcing categorical partitioning may introduce artificial boundaries and overinterpretation. Topology-preserving unsupervised learning can serve as a diagnostic instrument to evaluate whether discretization is structurally supported. The absence of stable clustering should therefore be interpreted cautiously: not as definitive proof of continuity, but as evidence that gradient-based representations may provide a more parsimonious and robust description under the tested conditions.

Adopting exploratory frameworks capable of distinguishing between discrete and continuous organization prior to implementing management zoning can improve methodological transparency and reduce algorithm-driven ecological misinterpretation.

4. CONCLUSION

This study introduced an unsupervised bi-temporal framework to evaluate whether UAV-derived vineyard phenological variability supports discrete zonation or continuous representation. Multispectral temporal differences produced a stable and coherent feature-space organization; however, no robust clusters emerged across configurations. Spatial projections indicated gradual transitions consistent with gradient-like organization. The inclusion of thermal differences increased representation error without improving topological coherence, suggesting limited structural contribution in the investigated bi-temporal context.

While restricted to two acquisition dates and a single vineyard, the results demonstrate how unsupervised topology-preserving methods can be used diagnostically to assess the structural validity of zonation assumptions. The proposed framework provides a transparent approach for exploratory multi-temporal UAV analysis and can be extended to denser temporal sampling and additional agro-ecosystem contexts.

ACKNOWLEDGEMENTS

This research was funded by the European Union-NextGenerationUE, Progetto PRIN-PNRR WIN-RIESCO (CUP: D53D23017750001 - PNRR - Missione “Istruzione e Ricerca”-componente “Dalla Ricerca all’Impresa” Investimento “Fondo per il Programma Nazionale di Ricerca e Progetti di Rilevante Interesse Nazionale (PRIN)”

REFERENCES

Asan, U. and Ercan, S. An introduction to self-organizing maps. In Computational Intelligence Systems in Industrial Engineering: With Recent Theory and Applications (Proc. Atlantis Press), Atlantis Press (2012).

Capolupo, A., and Tarantino, E. (2025, October). Addressing climate-induced aridity in vineyards through a data-driven approach based on open-access EO: the case study of Negramaro in the Puglia region. In *Remote Sensing for Agriculture, Ecosystems, and Hydrology XXVII* (Vol. 13666, pp. 346-356). SPIE.

Capolupo, A., Monterisi, C., Caporusso, G. and Tarantino, E. Extracting land cover data using GEE: A review of classification indices. Computational Science and Its Applications – ICCSA 2020 (Proc.), Springer International Publishing (2020).

Ferro, M. V., and Catania, P. (2023). Technologies and innovative methods for precision viticulture: a comprehensive review. *Horticulturae*, *9*(3), 399.

Jackson, R. D. Canopy temperature and crop water stress. In Advances in Irrigation, vol. 1, Elsevier (1982). (context for thermal interpretation)

Kiviluoto, K. Topology preservation in self-organizing maps. In Proc. IEEE Int. Conf. on Neural Networks (ICNN '96), IEEE, 294–299 (1996).

Kohonen, T. Self-Organizing Maps. Springer Series in Information Sciences (3rd ed.), Springer (2012).

Li, Z. and Eastman, J. R. Commitment and typicality measures for the Self-Organizing Map. International Journal of Remote Sensing, 31(16):4265–4280. https://doi.org/10.1080/01431161003734518 (2010).

Maes, W. H. and Steppe, K. Perspectives for remote sensing with unmanned aerial vehicles in precision agriculture. Trends in Plant Science, 24(2):152–164. https://doi.org/10.1016/j.tplants.2018.11.007 (2019).

Matese, A., Di Gennaro, S. F., and Santesteban, L. G. (2019). Methods to compare the spatial variability of UAV-based spectral and geometric information with ground autocorrelated data. A case of study for precision viticulture. *Computers and Electronics in Agriculture*, *162*, 931-940.

Munden, R., Curran, P. J. and Catt, J. A. The relationship between red edge and chlorophyll concentration. International Journal of Remote Sensing, 15(4):705–709. https://doi.org/10.1080/01431169408954149 (1994).

Nex, F., and Remondino, F. (2014). UAV for 3D mapping applications: a review. *Applied geomatics*, 6(1), 1-15.

Pádua, L., Marques, P., Adão, T., Guimarães, N., Sousa, A., Peres, E., and Sousa, J. J. (2019). Vineyard variability analysis through UAV-based vigour maps to assess climate change impacts. *Agronomy*, *9*(10), 581.

Park, Y. S., Céréghino, R., Compin, A. and Lek, S. Applications of artificial neural networks for patterning and predicting aquatic insect species richness. Ecological Modelling, 160(3):265–280. https://doi.org/10.1016/S0304-3800(02)00278-5 (2003).

Picariello, L., Rinaldi, A., Forino, M., Errichiello, F., Moio, L. and Gambuti, A. Effect of different enological tannins on Aglianico wine evolution. Molecules, 25(20):4607. https://doi.org/10.3390/molecules25204607 (2020).

Prashar, A. and Jones, H. G. Infra-Red Thermography as a High-Throughput Tool for Field Phenotyping. Agronomy, 4(3):397–417. https://doi.org/10.3390/agronomy4030397 (2014).

Rondeaux, G., Steven, M. and Baret, F. Optimization of soil-adjusted vegetation indices. Remote Sensing of Environment, 55:95–107. https://doi.org/10.1016/0034-4257(95)00188-4 (1996).

Rouse, J. W., Haas, R. H., Schell, J. A. and Deering, D. W. Monitoring vegetation systems in the Great Plains with ERTS. NASA SP-351 I, 309–317 (1974).

Sakuno, Y. and Kunii, H. Chlorophyll-a estimation from Landsat-8 using the Linear Combination Index (LCI). In Proc. 2015 IEEE Int. Geoscience and Remote Sensing Symposium (IGARSS), IEEE (2015).

Santesteban, L. G., Di Gennaro, S. F., Herrero-Langreo, A., Miranda, C., Royo, J. B. and Matese, A. High-resolution UAV-based thermal imaging for plant water status within vineyards. Agricultural Water Management, 183:49–59. https://doi.org/10.1016/j.agwat.2016.09.010 (2017).

Tucker, C. J. Red and photographic infrared linear combinations for monitoring vegetation. Remote Sensing of Environment, 8(2):127–150. https://doi.org/10.1016/0034-4257(79)90013-0 (1979). (classic context for vegetation indices)

Velusamy, P., Rajendran, S., Mahendran, R. K., Naseer, S., Shafiq, M., and Choi, J. G. (2021). Unmanned Aerial Vehicles (UAV) in precision agriculture: Applications and challenges. *Energies*, *15*(1), 217.

Vesanto, J. SOM-based data visualization methods. Intelligent Data Analysis, 3(2):111–126. https://doi.org/10.1078/1089-828X-00034 (1999).

Weiser, R. L., Asrar, G., Miller, G. P. and Kanemasu, T. Assessing grassland biophysical characteristics from spectral measurements. Remote Sensing of Environment, 20:141–151. https://doi.org/10.1016/0034-4257(86)90031-1 (1986).

Wu, W. The generalized difference vegetation index (GDVI) for dryland characterization. Remote Sensing, 6:1211–1233. https://doi.org/10.3390/rs6031211 (2014).

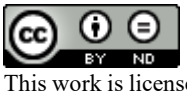

This work is licensed under a Creative Commons Attribution-No Derivatives 4.0 International License.

INTEGRATION OF MODIS NDVI DATA INTO TUSCANY METEOROLOGICAL FIRE RISK BULLETIN

R. Mari[1,2*], G. Bartolini[2], G. Betti[1,2], L. Bottai[2], M. Chiesi[1], L. Fibbi[1,2], F. Maselli[1], F. Pasi[1,2], B. Gozzini[1,2]

1 Institute of Bioeconomy, National Research Council (IBE-CNR), Via Madonna del Piano 10, 50019 Sesto Fiorentino (FI), Italy
2 LaMMA Consortium, Via Madonna del Piano 10, 50019 Sesto Fiorentino (FI), Italy
* Corresponding author: riccardo.mari@cnr.it

KEY WORDS: wildfire danger rating; Fire Weather Index; MODIS; NDVI; remote sensing; spatial decision support system; Tuscany; operational bulletin; SDSS.

ABSTRACT:

The Regional Government of Tuscany (Central Italy), together with the LaMMA Consortium and the National Research Council – Institute for BioEconomy (CNR IBE), have implemented an operational workflow and a Spatial Decision Support System (SDSS) which provide a daily wildfire danger rating for each municipality in the region. The system is driven by the Canadian Forest Fire Weather Index (FWI), the components of which are calculated from in-situ observations and numerical weather predictions to quantify the predisposition of forest fuels to ignition and spread. During the peak risk season (approximately from June to September), a dedicated Bulletin is produced daily, containing FWI metrics, fire-weather indices and additional atmospheric parameters over the administrative areas (municipalities) of Tuscany Region. The AIB on-duty operator uses this information to provide operational guidance on anticipated fires, their behaviors, and regional hotspots requiring heightened readiness. Because NDVI reflects vegetation stress and fuel condition, this work explores the integration of vegetation status information from MODIS NDVI images into the bulletin. Fire statistics for Tuscany (number of fires) over 25 years (2000–2024) are therefore analyzed together with MOD13Q1 NDVI imagery (16-day, 250 m) and negative relationships with fire activity are defined, mostly complementary to meteorological danger indices. A preliminary composite FWI+NDVI indicator was tested and compared to the conventional FWI. The results obtained show an improvement in the model capability to predict the number of fires. On average, the determination coefficient between the conventional and modified indices increases from 0.38 to 0.51, suggesting that NDVI can provide additional predictive information. These findings open the way to operationally include an NDVI-based layer/index in the Tuscany fire risk bulletin.

1. INTRODUCTION

Wildfire danger assessment is a core tool for prevention, early warning and suppression; it is formally embedded in the Tuscany Wildfire Management Plan (Piano AIB 2023-2025), the three-year policy framework that allocates strategies, resources and procedures in a risk landscape exacerbated by climate change, wildland–urban interface expansion and farmland abandonment. Its overarching goals are to keep fire events within the regional suppression capacity, minimize burned areas and safeguard Tuscany's forest and infrastructure assets. The Tuscany forest fire fighting (anti incendi boschivi, AIB) organization relies on a meteorological fire risk bulletin supported by a Spatial Decision Support System (SDSS) that provides daily maps and summary indicators at municipality scale (Tuscany, that occupies an area of about 23000 km2, is divided into 273 municipalities).

The bulletin is currently based on the Canadian Forest Fire Weather Index System (FWI) (Van Wagner and Pickett, 1987), which is computed from meteorological variables and summarizes the expected potential fire behavior. However, meteorological danger indices do not explicitly account for seasonal and inter-annual changes in vegetation condition and fuel availability, which can modulate ignition probability and spread. These indices, in fact, do not consider the contribution of vegetation status, which depends not only on meteorology, but also on other environmental factors (e.g. soil and plant types) and on local disturbance history.

This information can be derived from optical satellite data, which can detect land surface features synoptically and frequently over large areas (Zeng et al., 2022). The integration of weather indices and remotely sensed data is therefore potentially useful to improve the operational assessment of forest fire risk (Maselli et al., 2003).

Based on these premises, the current work investigates the operational value of adding MODIS NDVI information to the Tuscany fire risk bulletin, with the aim of capturing vegetation stress signals that are complementary to meteorological predictors and may therefore improve the relationship with the observed forest fire activity. The study is carried out utilizing the eight zones of the region that the AIB organization has identified based on homogeneous eco-climatic conditions (Figure 1).

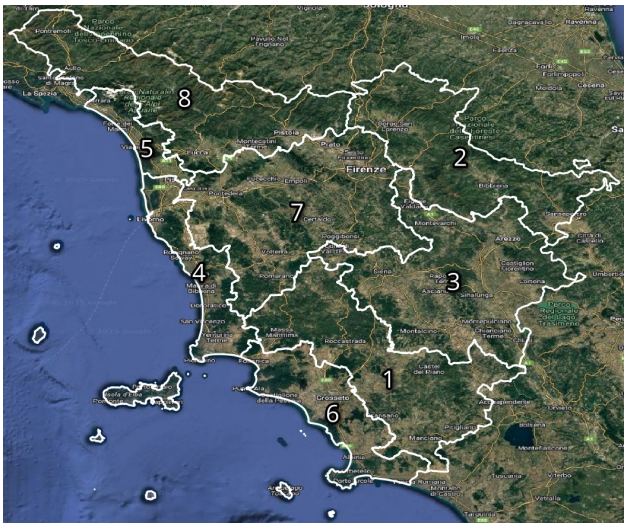

Figure 1. Google Earth image of the Tuscany region with superimposed the eight zones defined according to their mean eco-climatic conditions.

* Corresponding author

2. MATERIALS AND METHODS

2.1. AIB chain

The operational AIB chain integrates ground meteorological observations and numerical weather predictions to compute the daily FWI components and derived indices. In this work, the FWI is computed using the open-source Python library xclim through its fire-weather module (xclim.indices.fire) (Bourgault et al., 2023). More specifically, daily ground meteorological observations of air temperature, relative humidity, wind speed and precipitation are collected from the LaMMA Consortium database (https://www.lamma.toscana.it) and spatially extended over the whole Tuscany region by applying the DAYMET algorithm (Thornton et al., 1997). In such a way, daily maps of the main meteorological drivers are obtained at a 250-m spatial resolution; the same maps are then used to compute the classical FWI. In addition to the observed and interpolated data, daily weather predictions are also computed and utilized within the fire risk bulletin.

The FWI outputs are disseminated through a Spatial Decision Support System (SDSS) and summarized in a daily bulletin produced during the peak season (i.e., approximately from June to September) (Figure 2; OSGeo, 2026; GeoSolutions, n.d.; OSI, 2024). When very high-risk conditions (i.e., red FWI index) occur, the Forestry Department, by 12:00 p.m., sends via email the Wildfire Meteorological Analysis Bulletin (Figure 3) to i) the AIB Analysts, ii) the Fire Operational Directors, iii) the Permanent Unified Operational Room (Sala Operativa Unificata Permanente, SOUP), iv) the AIB Provincial Operational Centers (COP AIB), and v) the AIB Volunteer Organizations. The AIB Meteorological Analysis Bulletin consists of two sections: “what we had / what we expect”. The “what we had” section reports information on the number, geographic distribution and characteristics of wildfires that occurred in Tuscany during the previous day. In addition, the “what we expect” section provides a detailed analysis of the forecasted meteorological conditions for the day, broken down by time intervals.

2.2. Remote sensing data integration

The evaluation of the FWI capability to predict fire risk was based on the collection and analysis of the main statistics about forest fires (i.e., number of fires, extension, location). These data were derived from the Regional dataset and refer to a 25-year period (2000-2024).
Remotely sensed MODIS NDVI imagery (MOD13Q1 product) at 250-m spatial resolution and 16-day temporal frequency were downloaded from the NASA website (https://www.earthdata.nasa.gov/data/catalog/lpcloud-mod13q1-006) for the same period and further treated to remove abrupt decreases due to atmospheric disturbances, following Maselli et al. (2014).

The NDVI time series obtained, which describe the vegetation status, were then extracted for the eight major eco-climatic zones of the region (Figure 1) and aggregated to support the comparison with the number of fires for the 2000-2024 period.

The relationship between fire frequency and the conventional FWI was first investigated by performing a simple linear regression between the index and the number of fires detected during the 25 study years, for each zone and period considered (i.e. from the end of May to the end of September). Similar regression analyses were performed to assess the prediction power of forest NDVI.

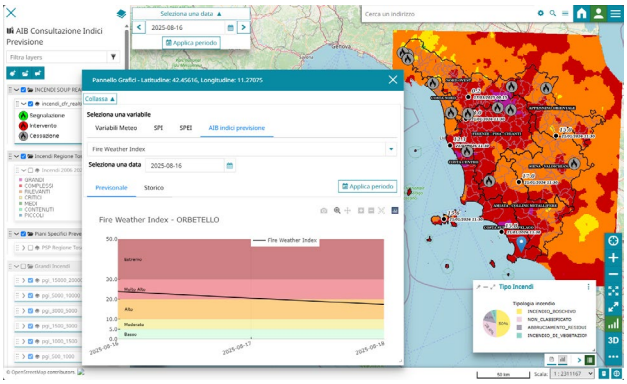

Figure 2. Example of SDSS interface used to visualize the wildfire danger indices for Tuscany.

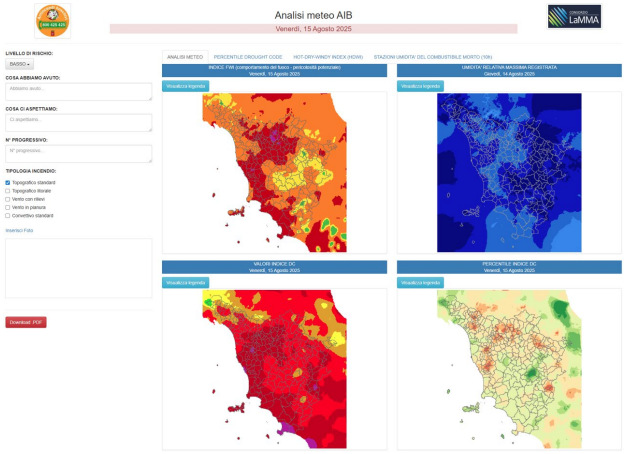

Figure 3. Example of daily risk-level products and ancillary layers available to support the Tuscany AIB bulletin.

Finally, multiple regressions were carried out by using contemporaneously FWI and NDVI as predictors. The prediction capabilities in the two cases were then assessed by pooling the eight periods for each zone, i.e. over 200 sample points.

3. RESULTS

Across the 25-year study period, an overall negative relationship is found between NDVI and fire activity (data not shown), which is consistent with the interpretation of NDVI as a proxy of vegetation vigor and fuel moisture conditions.
Figures 4 and 5 show the scatter plots which describe the fire prediction capabilities found for the largest eco-climatic zone of the region (zone 7). The number of fires occurred, evaluated in terms of pixels affected by forest fires per each scene, varies from 0 to about 16 and mostly depends on the meteorological conditions occurred during the investigated years. The sole use of the FWI induces a moderate prediction capability, i.e. a r^2 = 0.42 between the index and the number of fires occurred (Figure 4). When the MODIS NDVI information is included through the described FWI–NDVI indicator, the regression skill increases to $r^2 = 0.53$ (Figure 5). This indicates that NDVI provides additional predictive information beyond meteorological danger alone.

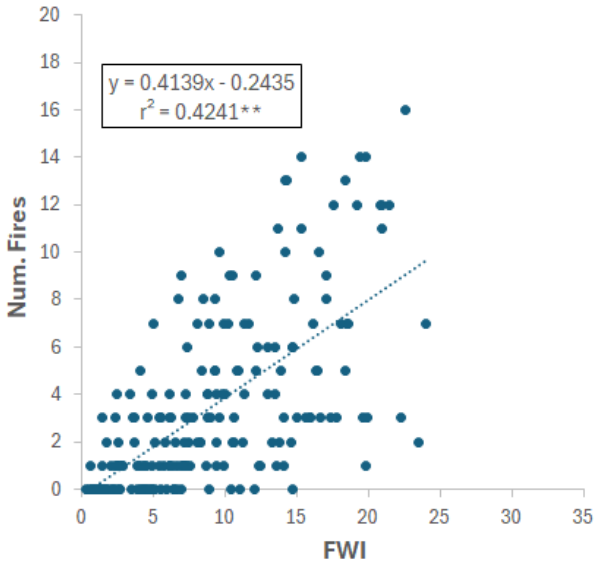

Figure 4. Linear regression of the number of fires occurred from the end of May till the end of September over Tuscany area number 7 versus the classical FWI (i.e., eight 16-day periods per 25 years). Data refer to the years 2000-2024 (** = highly significant correlation coefficient, $P < 0.01$).

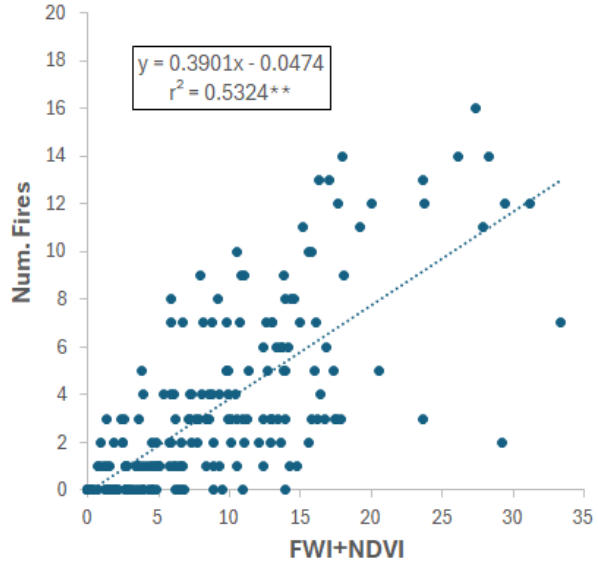

Figure 5. Linear regression of the number of fires occurred from the end of May till the end of September over Tuscany area number 7 versus the FWI integrated with NDVI (i.e., eight 16-day periods per 25 years) (FWI+NDVI). Data refer to the years 2000-2024 (** = highly significant correlation coefficient, $P < 0.01$).

Similar results are found for the other seven eco-climatic zones, which are summarized in Figure 6. On average, R^2 increases from 0.38 to 0.51. The lowest and highest accuracies are obtained for the zones number 4 and 8, respectively; this might be attributed to the prevalent arson origin of fires in the former zone and to the lowest human influence in the latter. While, in fact, the former is a coastal zone that is densely frequented especially during the most critical summer season, the latter is prevalently a mountain area where more humid conditions usually occur and human activities are more limited.

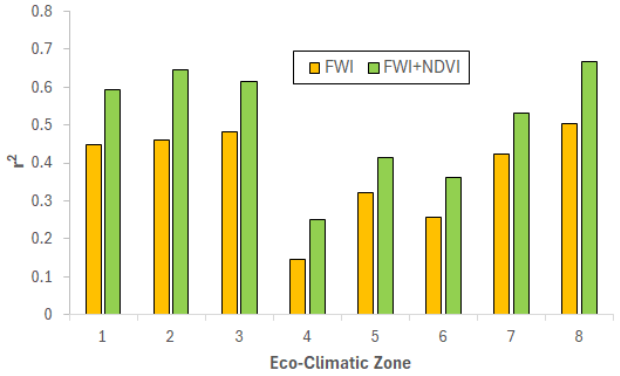

Figure 6. Coefficients of determination obtained between the two indices considered and the number of fires occurred during the 25 study years in the eight eco-climatic zones of Tuscany.

4. OPERATIONAL INTEGRATION

NDVI is available at 16-day frequency, which is compatible with monitoring seasonal fuel condition. For operational use, the latest NDVI composite image can be included among updates and displayed as an additional layer in the SDSS, together with a derived percentile/anomaly map relative to a multi-year baseline.

Within the bulletin, NDVI-based products are intended to complement the current "what we had / what we expect" structure, supporting the identification of regional hotspots, municipal readiness levels, and situational awareness for decision makers during the most critical periods.

Two exemplary maps of the original FWI and the integrated index obtained using the NDVI image of the second half of August 2025 are shown in Figure 7 and Figure 8, respectively. The higher information content of the integrated FWI+NDVI index with respect to the original is clearly evident in the second figure.

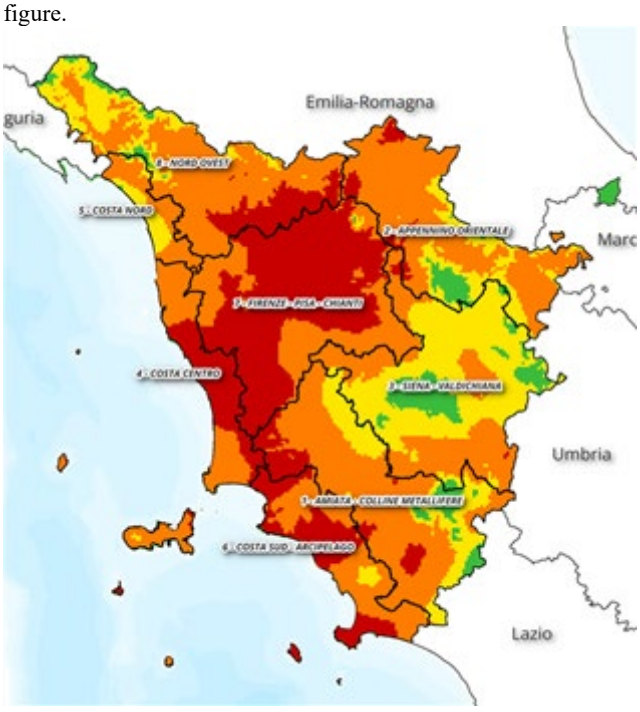

Figure 7. Map of the FWI obtained for the second half of August 2025 over the whole Tuscany region (green, yellow, orange and red colors correspond to low, moderate, high and very high FWI, respectively).

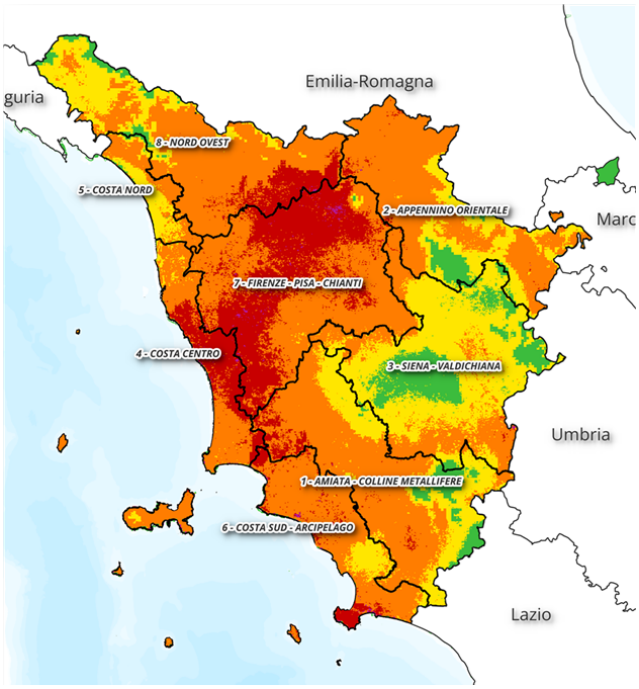

Figure 8. Map of the new index obtained in Tuscany integrating the original FWI and the NDVI imagery for the second half of August 2025 (green, yellow, orange and red colors correspond to low, moderate, high and very high FWI, respectively).

5. CONCLUSIONS

The preliminary integration of MODIS NDVI images into the Tuscany meteorological fire risk bulletin supports the possibility of obtaining a significant improvement in the prediction of forest fire occurrences. NDVI, in fact, can provide information on fuel/vegetation conditions that is complementary to the meteorological indices. In addition to NDVI, however, other remotely sensed indices sensitive to fuel moisture, hence related to fire risk, might be tested (Sivrikaya et al., 2024).

Future work will therefore be directed to a) refine the composite indicator, b) assess its robustness across seasons and zones, and c) explore alternative higher-resolution satellite data sources (e.g., Sentinel-2) in sight of improved near-real-time monitoring and enhanced spatial detail.

ACKNOWLEDGEMENTS

The authors acknowledge the Tuscany Regional Government, the LaMMA Consortium and CNR IBE for supporting the operational fire danger rating service and for providing access to the fire statistics and processing infrastructure.

REFERENCES

Byram, G.M., 1959. Combustion of forest fuels. In: Forest Fire: Control and Use. McGraw-Hill, New York.

Bourgault, P., Huard, D., Smith, T.J., et al., 2023. xclim: xarray-based climate data analytics. Journal of Open Source Software, 8(85), 5415. https://doi.org/10.21105/joss.05415

GeoSolutions, n.d. MapStore Documentation: MapStore2 WebGIS framework. https://docs.mapstore.geosolutionsgroup.com/en/latest/ (last access on 21st January 2026).

Maselli, F., Romanelli S., Bottai, L., Zipoli, G., 2003. Use of NOAA-AVHRR NDVI images for the estimation of dynamic fire risk in Mediterranean areas. *Remote Sensing of Environment*, 86(2), 187-197.

Maselli, F., Cherubini, P., Chiesi, M., Gilabert, M.A., Lombardi, F., Moreno, A., Teobaldelli, M., Tognetti, R., 2014. Start of the dry season as a main determinant of inter-annual Mediterranean forest production variations. *Agricultural and Forest Meteorology*, 194, 197-206.

Open Source Initiative (OSI), 2024. The Open Source Definition. https://opensource.org/osd (last access on 21st January 2026).

OSGeo, 2026. GeoServer User Manual: Overview (v2.28.x). https://docs.geoserver.org/stable/en/user/introduction/overview.html (last access on 21st January 2026).

Sivrikaya, F., Günlü, A., Küçük, O., Ürker, O., 2024. Forest fire risk mapping with Landsat 8 OLI images: Evaluation of the potential use of vegetation indices. *Ecological Informatics*, 79, 102461.

Thornton, P.E., Running, S.W., White, M.A., 1997. Generating surfaces of daily meteorological variables over large regions of complex terrain. *Journal of Hydrology*, 190, 214–251.

Van Wagner, C.E., Pickett, T.L., 1987. Equations and FORTRAN program for the Canadian Forest Fire Weather Index System. Canadian Forestry Service, Forestry Technical Report 33.

Zeng, Y., Hao, D., Huete, A., Dechant, B., Berry, J., Chen, J.M., Joiner, J., Frankenberg, C., Bond-Lamberty, B., Ryu, Y., Xiao, J., Asrar, G.R., Chen, M., 2022. Optical vegetation indices for monitoring terrestrial ecosystems globally. *Nature Reviews Earth & Environment*, 3, 477–493.

This work is licensed under a Creative Commons Attribution-No Derivatives 4.0 International License.

Leveraging Geospatial Techniques to Monitor Restoration Efforts and Assess Associated Forest Ecosystem Services in Kenya: Case Study of Maasai Mau Forest in Kenya

F.K. Mutwiri [1,2,*], D.M. Muriithi [1,2.], A. Vitti [2]

[1] Department of Civil, Environmental and Mechanical Engineering, Sapienza Università di Roma, Italy
(faithkagwiria.mutwiri, davidmwenda.muriithi)@uniroma1.it
[2] Department of Civil, Environmental and Mechanical Engineering, Università di Trento, Italy
(faith.mutwiri, davidmwenda.muriithi, alfonso.vitti)@unitn.it

KEY WORDS: Tropical forest restoration, Data fusion, Ecosystem service

ABSTRACT

Forests are essential resources for climate change mitigation, biodiversity conservation, and livelihood support. Maasai Mau Forest is part of East Africa's most vital tropical water towers. However, this ecosystem is threatened by forest degradation, deforestation, and encroachment, leading to carbon emissions into the atmosphere. Countries aim to enhance removals through afforestation and reforestation, aligning with initiatives such as REDD+, FLR, AFR100, and SDG 15 to promote sustainable forest management and ecosystem restoration.

This research aims to fuse Sentinel-1 and Sentinel-2 satellite images to map restored areas and determine spatial, temporal, and volumetric changes between 2019 and 2025. Radar vegetation index, VV/VH ratios, and optical selected bands and vegetation indices were derived from the images and fused. Principal component analysis (PCA) was performed, the first four components were selected and clustered using K-means, then merged into forest and non-forest classes. The NDVI was also categorised into three classes using thresholds to sparse, moderate, and dense vegetation. Change detection was performed to identify areas of forest loss and gain.

Results show coherence between the NDVI categorization and PCA classification, indicating an increase in forest cover and a decline in non-forest, except for a minor downward fluctuation in 2023. The forest area rose from 32,424 Ha in 2019 to 36,791 Ha in 2025. The data derived will be the baseline for assessing ecosystem services in the next phase of this research, with a focus on incorporating other missions to facilitate the estimation of biomass and sequestered carbon as a key ecosystem service.

1. INTRODUCTION

Trees and forests are invaluable to our environment and human well-being. They provide habitats for numerous species of flora and fauna, firewood for cooking and heating, and building materials (Kenya Forest Service, 2021). Forests are also places of spiritual, cultural, and recreational importance. They are also essential resources for climate change mitigation, biodiversity conservation, and supporting livelihoods. (Food and Agriculture Organization of the United Nations, 2020).

However, forest and landscape degradation is a significant global issue, threatening biodiversity, ecosystem services, and climate stability (Quiñones-Sánchez et al., 2025). In forest ecosystems, deforestation, forest degradation, habitat fragmentation, loss of biodiversity, and unsustainable land-use practices continue to endanger these critical ecosystems, particularly in developing nations (MENR, 2016), leading to the release of carbon dioxide (CO_2) into the atmosphere.

Maasai Mau Forest (MMF) is an important water catchment area and one of the forest blocks in the Mau Forest Complex (MFC). The MFC covers approximately 400,000Ha (Government of Kenya, Office of the Prime Minister, 2009). The complex, which is one of the five main "water towers" of Kenya and one of the few remaining extensive tracts of natural forest in East Africa, the others being Mt. Elgon, Mt. Kenya, the Aberdare Ranges, and the Cherangany Hills (Mutwiri et al., 2017). In addition to other ecological benefits, the complex is a water source for 12 rivers that feed into lakes Natron, Victoria, and Turkana. The Mau Forest Complex supports the livelihoods of more than 3 million rural people who live in the Lake Victoria Basin and up to 2 million more in urban areas (Jebiwott et al., 2021).

The Maasai Mau Forest, like many other forest ecosystems, was heavily impacted by encroachment, especially on the western side, unauthorized livestock grazing, and illegal extraction of forest resources (MENR, 2018), (Were et al., 2013).

Although some restoration processes have been initiated in the Maasai Mau Forest (MMF) to reverse patterns of forest loss and degradation, the major challenge lies in the lack of ways to assess and monitor the success. There is also a need to generate data frequently and accurately for national planning and international processes, such as establishing Forest Reference Levels (FRL) and compiling Greenhouse Gas Inventories (GHGI). In addition, the country lacks an efficient way to map and monitor efforts to restore degraded forests and landscapes, along with the associated biomass, to support sustainable resource management.

Currently, forest and biomass monitoring in Kenya is limited due to the complex ecology of the forest ecosystems. These ecosystems encompass high species diversity, which makes generic models inaccurate, insufficient data for model calibration, since Kenya lacks a national forest inventory, and high costs associated with advanced technologies like LiDAR and specialized expertise (Mkuzi et al., 2025).

To address these challenges, studies are moving toward integrative frameworks that incorporate field information and machine learning. The growing access to open source satellite data, such as Sentinel, Landsat, and spaceborne LiDAR like GEDI, offers a relatively inexpensive and scalable way to enhance the precision of national biomass surveillance. (De Almeida et al., 2025)

Therefore, this research aims to leverage geospatial data fusion to identify and map restoration areas over time. The broader project aims to assess the spatial (3D) dimensional changes in the

* Corresponding author

restored areas and estimate the associated carbon sequestered, as the main ecosystem service. This paper focuses on developing the fusion-based classification and mapping framework as the foundational step.

2. METHODS

2.1 Study area

The study area is part of the Mau Forest Complex, located in the south-west part of Kenya, spanning from latitudes 0.66° S to 0.92° S and Longitudes 35.5° E to 35.9° E. It is in Narok County, approx. 17 kilometers north of Narok Town, as shown in Figure 1. The Maasai Mau Forest (MMF) is a Trust Land with approximately 46,000 ha, managed by the Narok County Government (NCG).

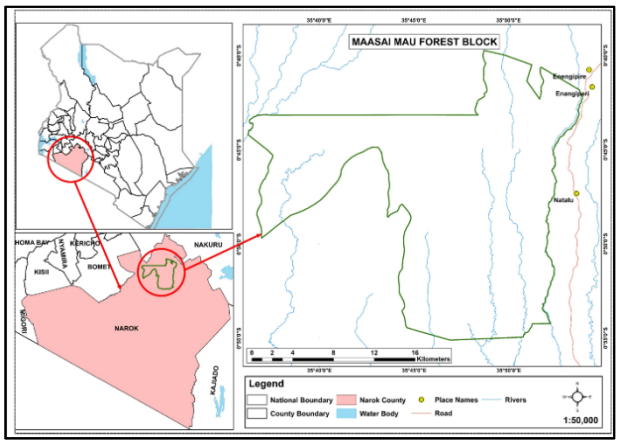

Figure 1: Location of Maasai Mau Forest in Kenya

It is dominated by mixed indigenous forest, with patches of bamboo, grassland, and shrubland. It's characterised by a high-altitude climate, with elevations ranging from 1,800 to 3,000 meters above sea level.

Over time, large scale restoration initiatives have been implemented across multiple blocks of the Mau Forest complex. These efforts include tree planting, fencing for natural regeneration, and community-based forest rehabilitation. The restored sites now form a mosaic of young plantations, regenerating forest, and remnant natural stands. Figure 2 shows a section of the Maasai Mau forest before and after restoration.

Figure 2: Google Earth Image of 2017 and 2025 showing restored areas

2.2 Methodology

The study focused on the use of fused satellite images, as shown in Figure 3. Sentinel-1 (Synthetic Aperture Radar) for its strength of penetrating cloud, which makes it possible to have a consistent time series for restoration monitoring; Sentinel-2 optical image for its high resolution and ability to calculate vegetation indices, and support of the multi-year comparison.

The images were acquired from January to March, the dry season in the study area, in 2019, 2021, 2023, and 2025 to minimize seasonal effects.

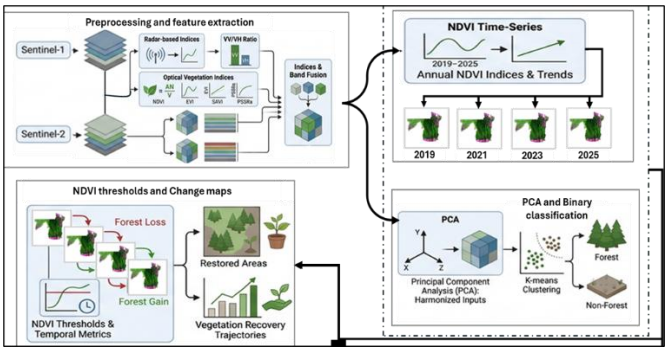

Figure 3: Methodology

2.2.1 Preprocessing and feature extraction

The satellite images from radar and optical sensors for the period indicated within the region of interest were processed using Google Earth Engine (https://earthengine.google.com/). The Sentinel-1 Radar bands VV and VH were corrected and speckle-filtered using the refined Lee method, while the Sentinel-2 optical bands were cloud-masked in preparation for deriving indices. Radar vegetation Index and VV/VH ratios were derived from Sentinel-1, while optical vegetation indices (NDVI, EVI, SAVI, PSSRa) were derived from Sentinel-2. The derived indices and selected optical bands (B2, B3, B4, and B8) were fused to create annual composites as shown in Figure 4.

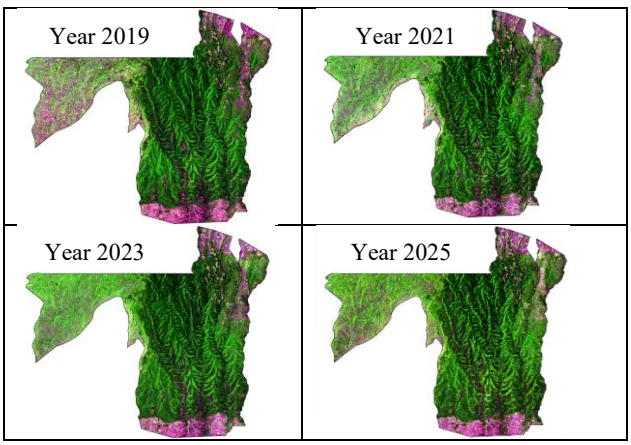

Figure 4: Fused Sentinel-1 and Sentinel-2 (SWIR, NIR, and red bands) composite

2.2.2 Principal Component Analysis

From the created composites, principal component analysis (PCA) was performed to generate harmonized inputs for classification. The first four PCA Bands were retained for classification. The selection was based on their eigenvalues and the proportion of variance in percentage. Components with minimal variance were discarded, while those capturing the highest information content were retained. The final set of PCA

bands was determined using a cumulative variance threshold of 90%, as indicated in Figure 5.

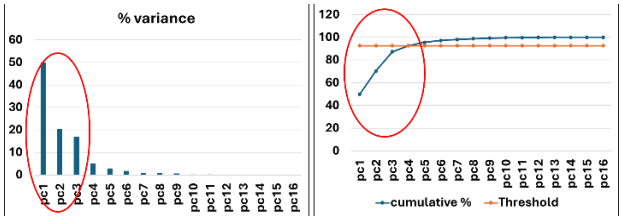

Figure 5: Selection of the PCA bands for K-means classification

K-means clustering was applied to the PCA bands, generating 8 clusters, which were subsequently reclassified into forest and non-forest classes as shown in Figure 6. Changes between the two classes were made to get areas of forest loss and gain.

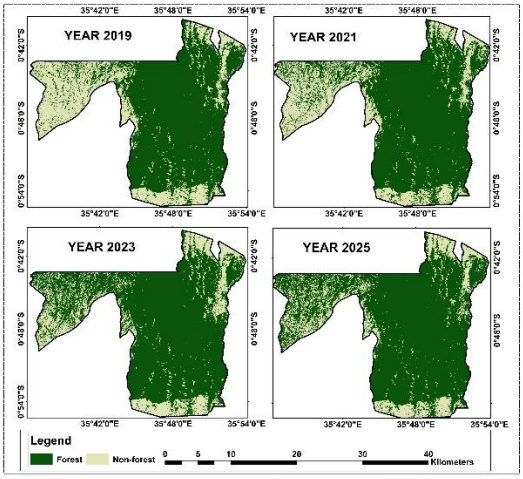

Figure 6: Forest and non-forest classification

2.2.3 NDVI time series and change maps

The NDVI was categorised into three classes based on thresholds, where values below 0.4 indicate sparse or no vegetation, 0.4 to 0.7 indicate Moderate Vegetation, and values above 0.7 indicate Dense Vegetation. (Nazhifah et al., 2025); (Nițu et al., 2025) as shown in Figure 7. Change detection was performed to identify areas of forest loss and gain.

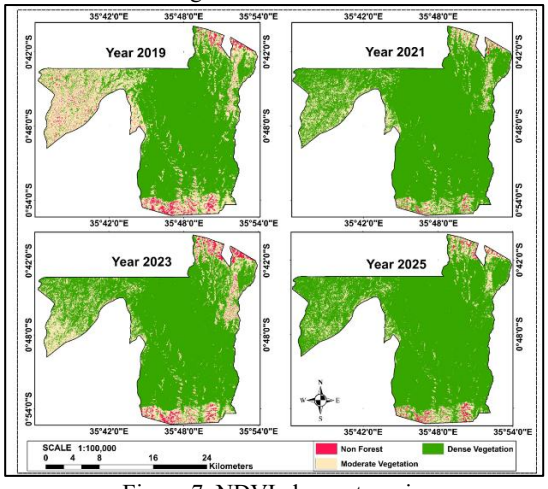

Figure 7: NDVI class categories

Separately, NDVI was also used to derive annual indices and assess time-series trends. This trend was to validate the classification trend from the fused images. NDVI-based thresholds and temporal metrics were combined with classified outputs to identify restored areas and map vegetation recovery trajectories.

3. RESULTS

3.1 Classification of fused images

Classification from the fused images indicated a positive forest trend from 2019 to 2025. The area of forest increased from 32,424Ha in 2019 to 36,791Ha in 2025, while the non-forest area decreased from 13,751Ha to 9,385 Ha in the same years, as shown in Table 1.

Area in ha	2019	2021	2023	2025
Forest	32,424	34,073	33,002	36,791
Non forest	13,751	12,102	13,173	9,385

Table 1: Forest areas in Hectares

3.2 NDVI categorization

The NDVI values across the years also indicate a positive forest trend with fluctuations in 2023, as shown in Figure 8.

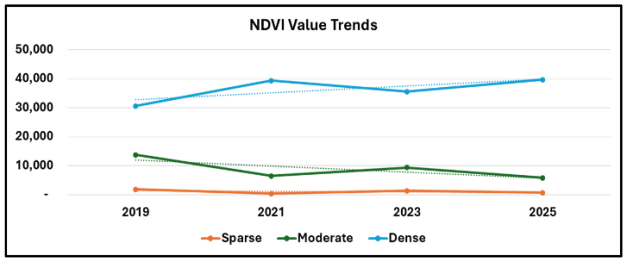

Figure 8: NDVI trends

Using randomly generated points, a confusion matrix was produced to assess the coherence between the two maps from both methods, yielding an accuracy of 90.86%. The remaining inaccuracies were visually inspected and occurred mostly at the transition zones between classes.

3.3 Areas of change

Areas of change were obtained by comparing outputs of two consecutive years. The remaining forest areas are termed stable forest; the remaining non-forest areas are termed stable non-forest; areas converted from forest to non-forest are termed forest loss; and areas converted from non-forest to forest are termed forest gain. Though the assessment's primary focus was the forest gain interpreted as restoration, there were some areas of forest loss. This is shown in Figure 9.

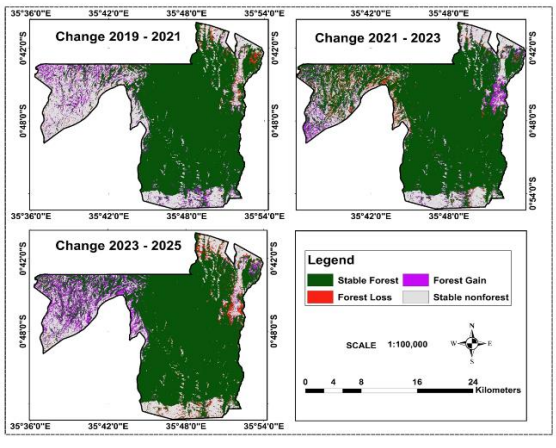

Figure 9: Areas of change

4. DISCUSSIONS AND CONCLUSIONS

The integration of Sentinel-1 radar and Sentinel-2 optical data through Google Earth Engine offers a comprehensive, multimodal approach to land cover monitoring that overcomes the traditional limitations of optical sensors, such as cloud cover.

By using the structural sensitivity of radar (VV/VH ratios) and optical indices with the spectral richness, the methodology captured a more comprehensive "fingerprint" of the landscape than a single-sensor approach could offer. The use of Principal Component Analysis (PCA) to retain 90% of the cumulative variance ensured reduction of data redundancy and retained the most critical information for K-means clustering.

Results show coherence between the NDVI categorization and PCA classification, indicating an increase in forest cover and a decline in non-forest, except for a minor downward fluctuation in 2023. Using randomly generated points, the coherence between the two methods was assessed yielding an accuracy of 90.86%. The remaining inaccuracies were visually inspected and occurred mostly at the transition zones between classes. However, there is still a need for improvement to address misclassification.

These classification trends offer a critical baseline for assessing ecosystem services; consequently, the next phase of this research will focus on the estimation of biomass. In addition to the generated data, the study will incorporate data from other remote sensing missions to facilitate the estimation of sequestered carbon as a key ecosystem service and to support forest monitoring systems.

In conclusion, the integration of satellite images from different sensors with machine learning techniques for processing indicates that it's a reliable way to track and monitor forest dynamics over time. The increase in forest area from 32,424 Ha in 2019 to 36,791 Ha observed in 2025 indicates a positive restoration trajectory and enhanced carbon sequestration potential.

REFERENCES

De Almeida, D. R. A., Vedovato, L. B., Fuza, M., Molin, P., Cassol, H., Resende, A. F., Krainovic, P. M., De Almeida, C. T., Amaral, C., Haneda, L., Albuquerque, R. W., Gorgens, E., Romanelli, J., Ferreira, M., Salk, C., Espinoza, N., Silva, C., Broadbent, E., & Brancalion, P. H. S. (2025). Remote sensing approaches to monitor tropical forest restoration: Current methods and future possibilities. Journal of Applied Ecology, 62(2), 188–206. https://doi.org/10.1111/1365-2664.14830

Food and Agriculture Organization of the United Nations. (2020). Global Forest Resources Assessment 2020: Main Report, Rome. https://doi.org/10.4060/ca9825en

Government of Kenya, Office of the Prime Minister. (2009). Rehabilitation of the Mau Forest Ecosystem. https://www.kws.go.ke/sites/default/files/2019-11/Mau%20Forest%20Complex%20-%20Concept%20paper.pdf

Jebiwott, A., Ogendi, G. M., Agbeja, B. O., Alo, A. A., & Kibet, R. (2021). Mapping the trends of forest cover change and associated drivers in Mau Forest, Kenya. Remote Sensing Applications: Society and Environment, 23, 100586. https://doi.org/10.1016/j.rsase.2021.100586

Kenya Forest Service. (2021). National Forest Resources Assessment Report 2021 Kenya. https://www.kenyaforestservice.org/national-forest-resources-assesment-report-2021-kenya/

MENR. (2016). Technical Report on the National Assessment of the Forest and Landscape Restoration Opportunities in Kenya 2016. Ministry of Environment and Natural Resources. https://afr100.org/sites/default/files/2022-11/Kenya_Technical%20Report_Assessment%20of%20National%20Forest%20and%20Landscape%20Resto..._0.pdf

MENR. (2018). Taskforce Report on Forest Resources Management and Logging Activities in Kenya. Ministry of Environment and Natural Resources.

Mkuzi, H. T., Ocansey, C. M., Maghanga, J., Gulyás, M., Penksza, K., Szentes, S., Michéli, E., Fuchs, M., & Boros, N. (2025). A Review of Biomass Estimation Methods for Forest Ecosystems in Kenya: Techniques, Challenges, and Future Perspectives. Land, 14(9). https://doi.org/10.3390/land14091873

Mutwiri, F. K., Odera, P. A., & Kinyanjui, M. J. (2017). Estimation of Tree Height and Forest Biomass Using Airborne LiDAR Data: A Case Study of Londiani Forest Block in the Mau Complex, Kenya. Open Journal of Forestry, 7(2), 255–269. https://doi.org/10.4236/ojf.2017.72016

Nazhifah, S., Maulyanda, Putri, A., & Kiftiyani, U. (2025). Comparative Evaluation of NDVI-Based Vegetation Classification Using Rule-Based Thresholding and Random Forest Models. Cyberspace: Jurnal Pendidikan Teknologi Informasi, 9, 22–32. https://doi.org/10.22373/agmq9j89

Nițu, A., Florea, C., Ivanovici, M., & Racoviteanu, A. (2025). NDVI and Beyond: Vegetation Indices as Features for Crop Recognition and Segmentation in Hyperspectral Data. Sensors, 25(12). https://doi.org/10.3390/s25123817

Quiñones-Sánchez, E., Bolaños-González, M. A., López-Pérez, A., Báez-Pérez, A., Adán, V.-H., & Eduardo, R.-S. A. (2025). Impacts of forest loss on soil carbon sequestration in an area under anthropogenic threats. Research Square. https://doi.org/10.21203/rs.3.rs-6414503/v1

Were, K. O., Dick, Ø. B., & Singh, B. R. (2013). Remotely sensing the spatial and temporal land cover changes in Eastern Mau forest reserve and Lake Nakuru drainage basin, Kenya. Applied Geography, 41, 75–86. https://doi.org/10.1016/j.apgeog.2013.03.017

This work is licensed under a Creative Commons Attribution-No Derivatives 4.0 International License.

MONITOR POST-FIRE VEGETATION DYNAMICS IN FOREST ECOSYSTEMS USING SENTINEL-2 AND PLANETSCOPE TIME SERIES

F. Filipponi [1] *, E. D'Andrea [2], F. Zucca [3]

[1] Institute of Environmental Geology and Geoengineering (IGAG), National Research Council (CNR), Italy - federico.filipponi@cnr.it
[2] Research Institute on Terrestrial Ecosystems (IRET), National Research Council (CNR), Italy – ettore.dandrea@cnr.it
[3] Department of Earth and Environmental Sciences, University of Pavia, Italy – francesco.zucca@unipv.it

KEY WORDS: wildfires, post-fire recovery, time series analysis, forest ecosystem, Sentinel-2, PlanetScope

ABSTRACT:

Satellite earth observation has been demonstrated to be an effective tool to characterize pre-fire conditions, quantify fire severity, and monitor post-fire dynamics. Medium and long-term time series of satellite-derived thematic information for the monitoring of post-fire conditions and trends can support the identification of forest dieback and the monitoring of the recovery of natural ecosystems. In this framework, post-fire time series analysis was performed using Copernicus Sentinel-2 and PlanetScope satellite acquisitions over the period 2016-2024 at Monte Morrone (Abruzzo, Itay), disturbed by two wildfire events: about 2000 hectares burned during August 2017, and about 400 hectares burned during July 2023. Results show changes in dominant plant functional types in areas subject to high fire severity, where natural grassland ecosystems have temporarily replaced previously existing forest ecosystems. In situ measurements confirms the change in dominant plant functional types in black pine stands and beech forests characterized by high fire severity. Results demonstrate that the exploitation of medium-term time series of the vegetation indices estimated from satellite data can be a suitable tool to identify, describe, and monitor vegetation post-fire dynamics in ecosystems disturbed by wildfires.

1. INTRODUCTION

Wildfires represent major disturbance in forest ecosystems and are recently increasing under climate change. Primary damage due to wildfires on forest ecosystem can be estimated using fire severity as a proxy. Secondary damage due to wildfires, sometimes in combination with other stressors, may lead to forest dieback, that is the decline in vitality of a forest ecosystem. Although many communities will remain resilient to changing fire regimes in the short-term, longer-term changes to vegetation structure, demography and species composition are susceptible if exposed to repeated short-interval fire in combination with other stressors (e.g drought, heatwaves, insect outbreaks) (Nolan et al., 2021).

Medium and long-term time series of satellite-derived thematic information for the monitoring of post-fire conditions and trends can support the identification of forest dieback, besides the well-known monitoring of the recovery of natural ecosystems. A significant contribution for the monitoring of post-fire conditions is offered by existing and forthcoming constellations of standard and cubesat Earth observation satellites having high revisit frequency, observation scenario and guaranteed continuity. Plant phenology, studying the succession of plant cycle phases and their development in relation to abiotic and biotic factors, can be investigated by exploiting dense time series of vegetation index, calculated from satellite observations, by analysing seasonal trajectories and by estimating phenological metrics (Filipponi et al., 2022).

Previous studies used phenological metrics estimated from Leaf Area Index (LAI), in combination with environmental variables, to evaluate the vegetation restoration and landslide susceptibility for different land use classes (Filipponi et al., 2019). Another study using phenological analysis of satellite observation, aimed at providing quantitative insights into complex post-fire vegetation dynamics, found that fire induces a shift of the start and end of growing season in forest ecosystems but has no effect on prairies (Di Mauro et al., 2014). Analysis of post-fire recovery trajectories in Pinus ponderosa forests of the southwestern United States highlighted an increasingly shifting away from pre-burn vegetation communities, exhibiting changes in NDVI values with significantly lower mean amplitude, higher mean base value, higher mean peak value, and later peak date (Walker et al., 2019). Synergizing satellite imagery from multiple sources is critical to reconstruct the dense temporal trajectories required to accurately characterize the rapid and complex post-fire vegetation recovery dynamics.

In this framework, post-fire time series analysis was performed using Copernicus Sentinel-2 and PlanetScope satellite acquisitions over the period 2016-2024 at Monte Morrone (Abruzzo, Itay), disturbed by two wildfire events in August 2017 and July 2023. Objectives of this research study are: i) identify burned areas from satellite imagery; ii) monitor post-fire recovery dynamics; iii) demonstrate the capability of multiple constellations of satellites to produce denser time series for forest ecosystems monitoring.

2. MATERIALS AND METHODS

2.1 Study area

Monte Morrone (Abruzzo, Italy) was selected as study site, covering an area of 90 km^2. It has been disturbed by two wildfire events in recent years, resulting in a surface of about 2000 hectares burned during August 2017 and about 400 hectares burned during July 2023.

Vegetation in Morrone grades with altitude. There are four distinct phytoclimatic belts located at various altitudinal range; Mediterranean (below 400/500 m), sub-Mediterranean (500–

* Corresponding author

900/1000 m), temperate Montane (900–1600/1700 m) and subalpine (above 1700 m). The forest types are evergreen oak woods (comprising 1 % of the area), deciduous oak woods (31 %), black pine stands (26 %), hop-hornbeam forest (11 %) and beech forest (31 %).

2.2 Satellite data

Satellite imagery from MultiSpectral Instrument (MSI) onboard Copernicus Sentinel-2 satellites constellation, acquired over the period 2016-2024, were used for the analysis. Collected data (a total of 961 single day acquisitions) consists of bottom-of-atmosphere reflectances at a spatial resolution of 10 and 20 m, with spectral bands in visible, red-edge, near-infrared and short-wave infrared radiometric intervals. Single images were spatially clipped to the study area extent and masked from bad pixels (cloud, cloud shadow, snow, anomalous reflectance, topographic shadow).
Satellite imagery from Dove and SuperDove multispectral sensors onboard PlanetScope satellites constellation, acquired over the period 2016-2024, were also used for the analysis. Collected data (a total of 4621 scenes) consists of bottom-of-atmosphere reflectances at a spatial resolution of 3 m, with spectral bands in visible and near-infrared radiometric intervals (red-edge band available only from SuperDove sensor). Single PlanetScope scenes were mosaicked and spatially clipped to the study area extent, masked from bad pixels (cloud, cloud shadow, snow, anomalous reflectance, topographic shadow) and a radiometric terrain correction was applied. Topographic shadow area mask is not available in PlanetScope *Usable Data Mask*, therefore it was calculated using module *r.sun* available in *GRASS GIS* software.

2.3 Field data

Field measurements for the collection of forest structure parameters and for deadwood assessment were performed inside circular buffers, centred on the sampling point coordinates identified by stratified random sampling analysis, based on fire severity level and elevation. Inside each sampling plots, crown and stem damages were assessed for each damaged tree, considering the percentage of destroyed crown, the height of fire signs along the stem and the percentage of damages around the stems. Field data were used for a comparison exercise with the different seasonal trajectories identified from post-fire vegetation indices time series.

2.4 Methods

Burned area mapping for fire event of August 2017 and July 2023 was realized using a bi-temporal approach integrating multiple spectral indices, in order to optimize product accuracy (Smiraglia et al., 2020). Burned area polygons distributed by EFFIS through the Burnt Area database (https://forest-fire.emergency.copernicus.eu/applications/data-and-services) were used for comparison purpose.
Calculation of fire severity according to USGS classes based on difference Normalized Burnt Ratio (NBR), was used to support the selection sampling points within the study area.
The kernel Normalized Difference Vegetation Index (kNDVI) vegetation index (Camps-Valls et al., 2021) was calculated for each single Sentinel-2 and PlanetScope observation, at 10 m and 3 m spatial resolutions respectively. In addition, LAI biophysical index was estimated for each Sentinel-2 satellite observation at 20 m spatial resolution from the full bottom-of-atmosphere bands set at 20 m using the *Biophysical Processor* available in *ESA SNAP* software.

Single kNDVI and LAI raster data were temporally stacked for the full period of analysis 2016 – 2024. Later, time series were processed through a pixel-based approach (Filipponi et al., 2022) following two main steps: i) small drops and spikes identification and removal; ii) daily interpolation and smoothing through iterative weighted Whittaker smoother. The resulting vegetation indices time series at daily timesteps provide seasonal trajectories for the interpretation of phenology and multi-annual trends, aimed at monitoring post-fire vegetation dynamics.
Difference analysis between post-fire and pre-fire conditions was realized by comparing spectral indices and LAI for a pair of acquisitions over time, to produce differenced kNDVI and LAI mapping products. The specific purpose is complementing fire severity derived from NBR with a more physically based quantitative estimate, as well as assessing the feasibility of using kNDVI as a proxy for LAI.

3. RESULTS AND DISCUSSION

Burned area polygons generated using Sentinel-2 MSI data differs from polygons available from EFFIS. On one side, the EFFIS polygons delineate the edge of the burned area with greater approximation (Figure 1a and Figure 2a), on the other side, identification of burnt scars from Sentinel-2 data did not account for fire propagation in the understory with limited impact on tree canopy.

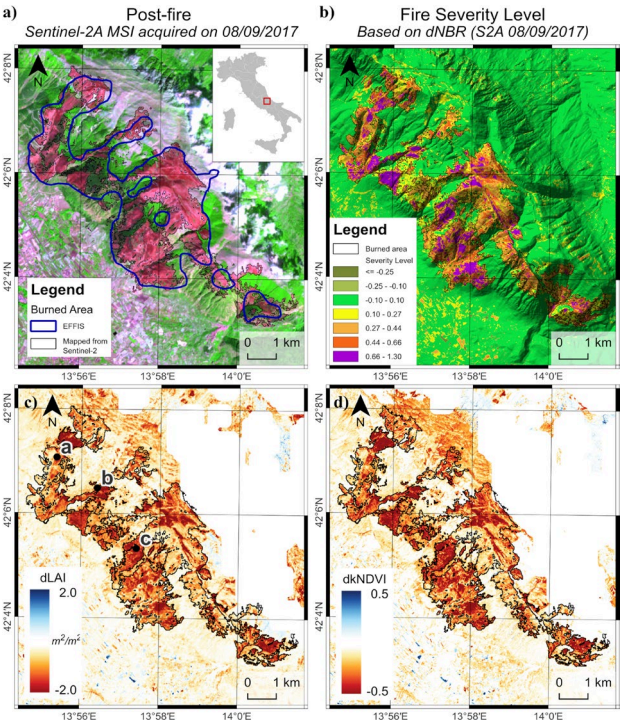

Figure 1. Mapping product of wildfire event in August 2017. a) comparison of burned area mapped from Sentinel-2 and EFFIS burned area polygons (bg: post-fire false color composite); b) fire severity level based on dNBR; c) differenced LAI calculated from pre- and post-fire acquisitions; d) differenced kNDVI calculated from pre- and post-fire acquisitions.

Wildfire event of July 2023 partially spread through the burned area of the August 2017 fire event, resulting in lower values of differenced vegetation indices.
Seasonal trajectories allowed to examine the phenological cycles, by interpreting the temporal behaviour of single pixels.

First, it allowed to establish the dominant plant functional type in the pixel before the fire events (i.e. deciduous broadleaved, evergreen needleleaved, evergreen broadleaved, herbaceous).

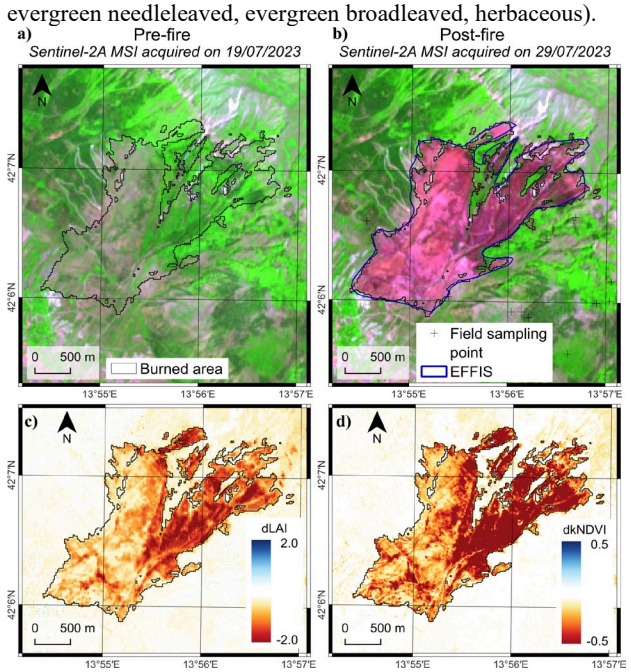

Figure 2. Mapping product of wildfire event in July 2023. a) burned area mapped from Sentinel-2 data (background: pre-fire post-fire false color composite); b) burned area mapped from Sentinel-2 data and by EFFIS (background: post-fire post-fire false color composite); c) differenced LAI calculated from pre- and post-fire acquisitions; d) differenced kNDVI calculated from pre- and post-fire acquisitions.

Considering the launch dates of PlanetScope satellites, as well as the limited number of available PlanetScope scenes prior the fire event in summer 2017, there were not enough acquisitions to characterize the pre-fire vegetation properties (year 2016) through the analysis of vegetation time series. For this reason, dominant plant functional type was determined solely by Sentinel-2 time series.

Interpretation of seasonal trajectories identified from post-fire vegetation indices time series in the area allowed to distinguish the following main vegetation cover categories: dense deciduous broadleaved forest (main phenological cycle with a single peak); sparse deciduous broadleaved forest (main phenological cycle with a main single peak, followed by a secondary peak from understory); dense evergreen needleleaved forest (high base value); area dominated by herbaceous cover (characterized by short length of maturity plateau, sometimes in combination with a weaker temporal signal from single trees in areas subject to high fire severity). In terms of multi-annual trends, positive slope of the time series suggests post-fire vegetation recovery, while negative slope indicates potential forest dieback. Figure 3 shows time series for three selected locations burned, specifically: a) evergreen needleleaved forest burned in both 2017 and 2023; b) deciduous broadleved forest (moderate fire severity in 2017); c) deciduous broadleved forest (high fire severity in 2017). Corresponding geographic locations for the three selected time series are represented in Figure 1c.

Faster recovery of natural grasslands ecosystems was found when compared against forests ecosystems, in agreement with previous studies (Di Mauro et al., 2014). Results show changes in dominant plant functional types in areas subject to high fire severity, where natural grassland ecosystems have temporarily replaced previously existing forest ecosystems. In situ measurements confirms the change in dominant plant functional types in black pine stands and beech forests characterized by high fire severity. Some of the identified sampling points show vegetation index reduction in the post-fire, suggesting secondary damage due to wildfires. In the context of climate change, the increased frequency of extreme weather events (e.g., drought and late frost), which may greatly modify the contribution of processes related to wood formation, stem CO2 efflux, and in general the C cycle, can have an impact on vegetation recovery and their effect on tree performance (D'Andrea et al., 2020). The Mont Morrone site experienced few years following the fire event of summer 2017 characterized by prolonged drought periods. These conditions likely initiated processes of secondary damage due to wildfires, resulting in a decline in vitality of forest ecosystems (dieback). According to the field measurements, fire impact of radial growth is hidden by the drought long stress effects. In fact, post-fire years were characterized by prolonged drought periods. Moreover, the competition reduction stimulated the growth of survived trees.

4. LESSONS LEARNED AND FUTURE DEVELOPMENTS

Compared to a previous investigation on post-fire vegetation monitoring after Monte Morrone fire in summer 2017, using LAI estimates to monitor post-fire vegetation dynamics and identify trends through linear regression (Filipponi et al., 2024), this study aimed to observe the time series in deeper detail, also facilitated by the use of satellite acquisition with higher revisit time. The specific objective is not merely to analyse the overall trend but rather to interpret the variations in terms of plant functional types.

The results of this in-depth study allowed to define requirements to better interpret time-series signal of post-fire vegetation condition. Future developments should quantitatively estimate phenological metrics for quantitative characterization of changes in plant functional types. To this aim, the identification of multiple vegetation cycles in a year it is of paramount importance, because it would allow the seasonal trajectories of deciduous forests, grasslands and understory to be effectively distinguished.

kNDVI represents a valid alternative to use Sentinel-2 MSI imagery in synergy with PlanetScope imagery acquired by both Dove and SuperDove sensors, as shown in Figure 1c,d and Figure 2c,d. In fact, kNDVI is a solution that allows the use of a vegetation index linearly correlated with biophysical parameters (such as LAI), without the need for a set of spectral bands over a wide radiometric range. It can be calculated from a wide variety of remote sensing optical sensors, although it is still affected by signal saturation at high canopy cover.

While small drops and spikes identification and removal allowed to clean the PlanetScope time series signal, characterized by noise interference due to inconsistent surface reflectance among images, time series comparison highlighted a need for bias correction through adjustment coefficients to integrate Sentinel-2 and PlanetScope data. It is essential to establish a stronger and more comprehensive relationship between LAI and kNDVI, with particular emphasis on addressing the issue of kNDVI saturation.

Further research is required to assess the extent to which PlanetScope acquisitions can enhance the analysis of spatial variability within a single Sentinel-2 pixel, particularly in identifying and monitoring individual trees. However, this operation requires accurate geolocation of the data, which translates into the need to use image co-registration algorithms.

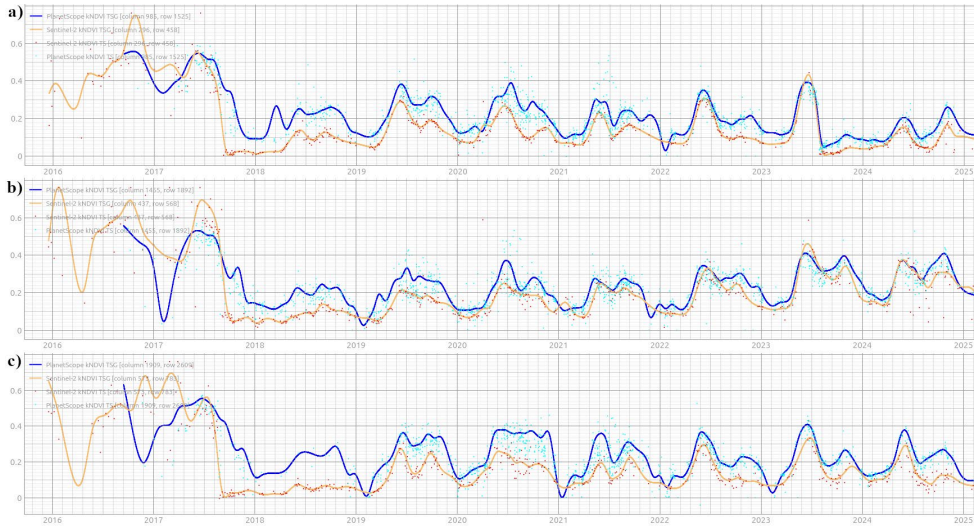

Figure 3. Time series of Sentinel-2 MSI raw (red points), Sentinel-2 MSI daily interpolated and smoothed (orange line), PlanetScope raw (cyan points), PlanetScope daily interpolated and smoothed (blue line) for burned pixel (location are represented in Figure 1c).

5. CONCLUSIONS

Exploitation of medium-term time series of the vegetation indices estimated from satellite data is a suitable tool to identify, describe, and monitor vegetation post-fire dynamics in ecosystems disturbed by wildfires. Virtual constellations of satellite, integrating multiple sensors, allow the generation of denser vegetation indices time series, contributing to improve vegetation time trajectories, examine phenology cycles, and consequently enhancing forest ecosystems monitoring capacity. Exploitation of medium-term time series of the vegetation indices estimated from satellite data is a suitable tool to identify, describe, and monitor vegetation post-fire dynamics in ecosystems disturbed by wildfires, strengthening the need of forest monitoring tools for supporting sustainable ecosystem management, especially under climate change scenario.

ACKNOWLEDGEMENTS

Contains modified Copernicus data (2025). Access to PlanetScope acquisitions was granted by project PNRR NODES, which has received funding from the MUR – M4C2 1.5 of PNRR funded by the European Union - NextGeneration EU (Grant agreement no. ECS00000036). The authors acknowledge NextGenerationEU in the framework of the NBFC (National Biodiversity Future Center) of Italy (funded by the European Union), and colleagues who contributed to the collection of field data in this context.

REFERENCES

Camps-Valls, G., Campos-Taberner, M., Moreno-Martínez, Á., Walther, S., Duveiller, G., Cescatti, A., ... & Running, S. W., 2021. A unified vegetation index for quantifying the terrestrial biosphere. *Science Advances*, 7(9), eabc7447. https://doi.org/10.1126/sciadv.abc7447.

D'Andrea, E., Rezaie, N., Prislan, P., Gričar, J., Collalti, A., Muhr, J., Matteucci, G., 2020. Frost and drought: Effects of extreme weather events on stem carbon dynamics in a Mediterranean beech forest. *Plant, Cell & Environment*, 43(10), 2365-2379. https://doi.org/10.1111/pce.13858.

Di Mauro, B., Fava, F., Busetto, L., Crosta, G. F., Colombo, R., 2014. Post-fire resilience in the Alpine region estimated from MODIS satellite multispectral data. *International Journal of Applied Earth Observation and Geoinformation*, 32, 163-172. https://doi.org/10.1016/j.jag.2014.04.010.

Filipponi, F., Manfron, G., 2019. Observing Post-Fire Vegetation Regeneration Dynamics Exploiting High-Resolution Sentinel-2 Data. *Proceedings*, 18, 10. https://doi.org/10.3390/ECRS-3-06200.

Filipponi, F., Smiraglia, D., Agrillo, E., 2022. Earth Observation for Phenological Metrics (EO4PM): Temporal discriminant to characterize forest ecosystems. *Remote Sensing*, 14(3), 721. https://doi.org/10.3390/rs14030721.

Filipponi, F., Sarti, M., Rezaei Sangsaraki, N., Adducci, F., D'Andrea, E., 2024. Monitor Post-Fire Vegetation Dynamics in Forest Ecosystems at Monte Morrone (Abruzzo, Italy). In: *13th EARSeL Workshop on Forest Fires 2024, Remote Sensing of Forest Fires: Lessons learned and future challenges under a changing climate*, pp. 138-140.

Nolan, R. H., Collins, L., Leigh, A., Ooi, M. K., Curran, T. J., Fairman, T. A., ... & Bradstock, R., 2021. Limits to post-fire vegetation recovery under climate change. *Plant, cell & environment*, 44(11), 3471-3489. https://doi.org/10.1111/pce.14176.

Smiraglia, D., Filipponi, F., Mandrone, S., Tornato, A., Taramelli, A., 2020. Agreement index for burned area mapping: Integration of multiple spectral indices using Sentinel-2 satellite images. *Remote Sensing*, 12(11), 1862. https://doi.org/10.3390/rs12111862.

Walker, J. J., Soulard, C. E., 2019. Phenology patterns indicate recovery trajectories of ponderosa pine forests after high-severity fires. *Remote Sensing*, 11(23), 2782. https://doi.org/10.3390/rs11232782.

This work is licensed under a Creative Commons Attribution-No Derivatives 4.0 International License.

Evapotranspiration, soil moisture and irrigation

Bayesian-Optimized LSTM Fusion of SAOCOM L-Band, Sentinel-1 C-Band, Sentinel-2 NDVI, and Meteorological Forcings for High-Resolution Soil Moisture Retrieval in No-Till Croplands

J. O. Ondieki[1]*, M. Marsella[1], G. Laneve[2], M. Collins[3]
[1] Department of Mechanical and Aerospace Engineering (DIMA), Sapienza University of Rome, Italy
[2] School of Aerospace Engineering, Sapienza University of Rome, Italy
[3] Department of Physics, University of Nairobi, Kenya

ABSTRACT

Accurate retrieval of surface soil moisture remains a major challenge in agricultural regions, especially in conservation tillage systems. These systems have vegetation residues and surface roughness that alter microwave scattering. This study introduces a novel, multi-sensor deep learning framework, which integrates SAOCOM L-band quad-polarimetric SAR, Sentinel-1 C-band dual-pol SAR, Sentinel-2 NDVI, and ERA5-Land meteorological data. The framework uses a Bayesian-optimized Long Short-Term Memory (LSTM) architecture to estimate soil moisture in a no-till cropland, located in Monte Buey, Córdoba Province, Argentina. For this research, a harmonized 2022 dataset was compiled, which includes 11 SAOCOM acquisitions, time-paired Sentinel-1 passes, Sentinel-2 NDVI, and 4,831 quality-controlled in situ moisture measurements. This data was used to train and validate the model at a resolution of 10 meters. Results show that the fused LSTM model achieves remarkable accuracy, with an $R = 0.93$, $R^2 = 0.84$, and RMSE = 0.024 m^3/m^3, surpassing standalone single-sensor methods. Ablation study highlight a strong synergy between L-band, C-band, NDVI, and meteorological features, while seasonal analysis shows the framework's robust performance under residue-dominated and fully vegetated conditions. The proposed framework offers a scalable and practical solution for high-resolution soil moisture retrieval in complex agricultural ecosystems.

KEYWORDS

Surface soil moisture; SAOCOM; Sentinel-1; Sentinel-2 NDVI; LSTM; Bayesian optimization; multi-sensor fusion; L-band SAR; C-band SAR

1. INTRODUCTION

Surface soil moisture (SSM) is not just critical for agriculture, but also for hydrology, drought early warnings, and land–atmosphere interactions (Mittelbach & Seneviratne, 2012; Seneviratne et al., 2010). Retrieving SSM from satellite data is particularly challenging in croplands, where dense vegetation, dynamic roughness, and persistent residue layers, resulting from no-till farming practices, pose significant obstacles(Singh & Gaurav, 2023) . Traditional C-band SAR retrievals often struggle with challenges like vegetation attenuation and roughness-induced uncertainties (Shilpa et al., 2023) , while coarse-resolution passive microwave products fail to capture the variability at the field scale. By fusing multiple SAR frequencies, particularly the L-band and C-band, we can access complementary information. For example, the L-band can penetrate deeper through vegetation and residue layers, while the C-band remains sensitive to surface scattering. When combined with optical vegetation indices and meteorological data, deep learning methods can effectively harness these synergistic contributions (Abdikan et al,.2023,Anconitano, G. 2025,Chen et al,.2021) . Our study introduces a feature-level fusion framework that integrates data from SAOCOM L-band quad-pol SAR, Sentinel-1 C-band SAR, Sentinel-2 NDVI, and meteorological variables into a temporally aware LSTM model. Using Bayesian optimization, we identify optimal hyperparameters. The goal is to achieve high-accuracy SSM retrievals across different phenological stages in regions practicing no-till farming.

2. STUDY AREA AND DATASETS

Monte Buey, located in the Córdoba Province of Argentina (32.91°S, 62.45°W), serves as our study site. This region is primarily characterized by the rotation of maize, soybean, and wheat under a continuous no-till farming approach. The landscape here is gently rolling, rising approximately 101 meters above sea level, and features rich Mollisols that are high in organic matter. The area receives an average of 920 mm of rainfall annually, and experiences a temperate climate with a mean temperature of 17.4°C.The Monte Buey site has been recognized as a reference site for the calibration and validation of soil moisture products, especially due to its dense sensor network and agricultural conditions. The site has a dense sensor network of Hydra Probe sensors installed at a depth of 5 cm, providing quality soil moisture data, and has been used for the calibration and validation of various satellite missions, such as SMAP, SMOS, and SAOCOM, among others (Maertens et al., 2021). The site has also been specifically designed for SAR calibration and validation, with dense sensor networks supporting the evaluation of different scales of soil moisture algorithm development (Grings et al., 2016; Kim et al., 2017). Previous works have shown the suitability of the Monte Buey

* Corresponding author

site to benchmark the quality of soil moisture retrieval methods using L-band and C-band SAR images and satellite-based and land surface model products, validating the representativeness of the site with regard to agricultural conditions and no-till practices (Spennemann et al., 2020; Anconitano, 2024).

In situ and Satellite and datasets

Throughout 2022, a comprehensive network of Hydra Probe II sensors captured soil moisture data at a depth of 5 cm. To provide spatial context for the in situ measurements, a map of the study area and sensor distribution is presented in Figure 1. The locations of Hydra Probe II sensors are overlaid on the study area boundary derived from the shapefile. This visualization highlights the spatial representativeness of the ground measurements across the no-till cropland and supports the robustness of the training dataset used in this study. Once the data was filtered and synchronized with satellite overpass, we managed to retain 4,831 high-quality measurements. All datasets were carefully aligned in time, with sensor readings.

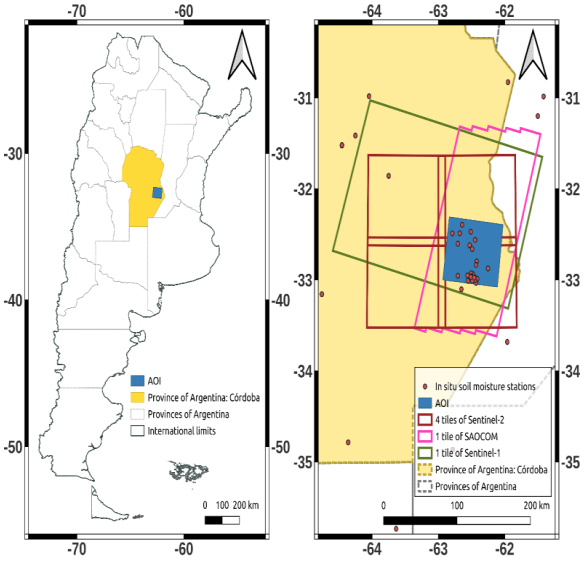

Figure 1. The study area, with red markers representing the locations of the in situ soil moisture monitoring stations.

3. METHODS

3.1 Preprocessing and Feature-Level Fusion

SAR images were radiometrically calibrated, terrain-corrected using SRTM DEM, and co-registered using SNAP. SAOCOM was resampled to 10 m to match Sentinel-1. Sentinel-2 NDVI and ERA5 variables were linearly interpolated to SAR acquisition dates. The fused feature vector per sample are a shown in table 1:

Table 1 Specific features used in the ML modeling and their source

Feature Category	Specific Features	Source
SAR Backscatter	σ VV, σ VH, σVV/σVH	Sentinel-1
Quad-pol SAR	σ VV,σ HH,σ VH,σ HV, σVV/σVH	SAOCOM
Vegetation Index	NDVI	Sentinel-2
Temporal Feature	Day of year (Fetcha)	Derived
Meteorological	temperature, precipitation	ERA5

3.2 LSTM Architecture and Bayesian Optimization

LSTM network was used in this work because it excels at capturing temporal patterns in the changes of soil moisture over time. The network's architecture features layers of LSTM units stacked on top of one another, which are then connected to fully connected layers. The main goal during optimization was to reduce the validation loss, measured as Mean Squared Error (MSE). To enable the model to generalize effectively, a time-causal expanding-window validation strategy was used. This approach provided a realistic evaluation of model performance.

3.3 Feature Importance and Ablation Analysis

LSTM importance scores were computed for vegetated (December) and residue-dominated (October) periods. Further, systematic ablation experiments removed NDVI, precipitation, temperature, or SAOCOM features to quantify their contribution.

4. RESULTS

4.1 Overall Model Performance

The full-fusion Bayesian-optimized LSTM model demonstrated a strong performance with a correlation coefficient of R = 0.93. It achieved an RMSE of 0.024 m^3/m^3. Furthermore, the residual distributions were narrow and centered around zero, indicating similar training and testing errors. This suggests minimal overfitting occurred. (Figure 2.)

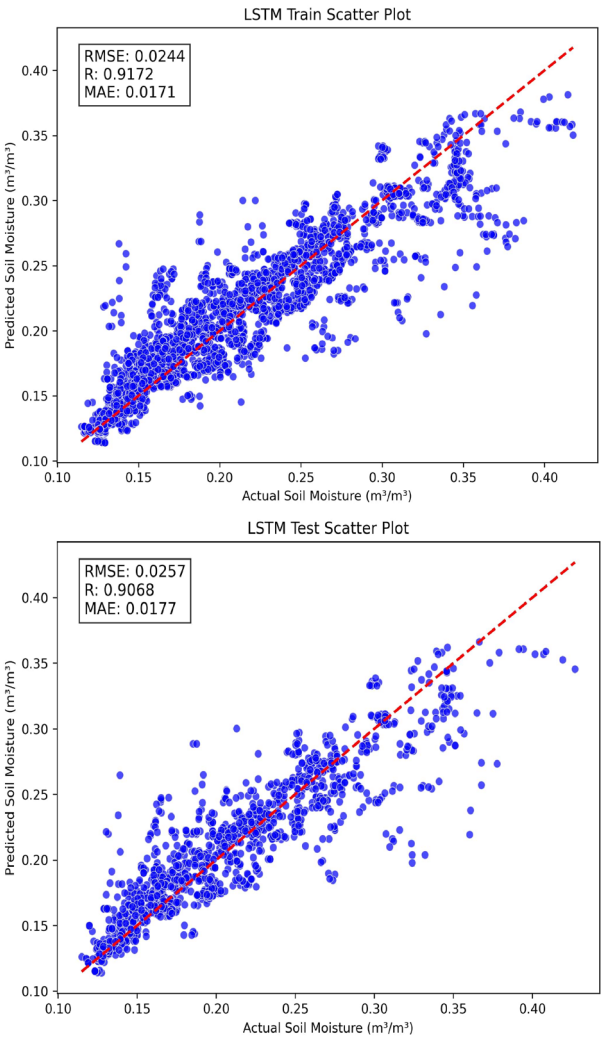

Figure 2. Scatter plots of predicted performance for training and testing datasets.

4.2 Seasonal Dynamics and Vegetation Effects

In residue-dominated months, Sentinel-1 C-band VV/VH and temperature were dominant features.During peak vegetation, SAOCOM L-band VV and HV, and NDVI gained importance due to enhanced canopy penetration (Figure 3).

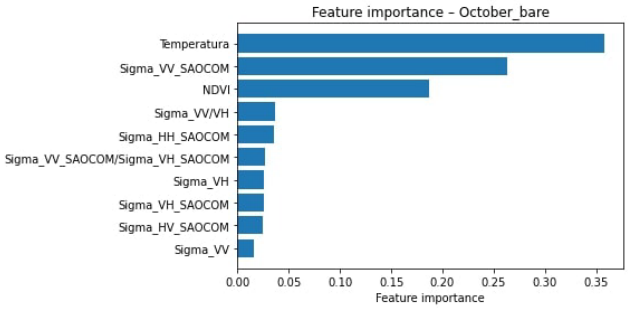

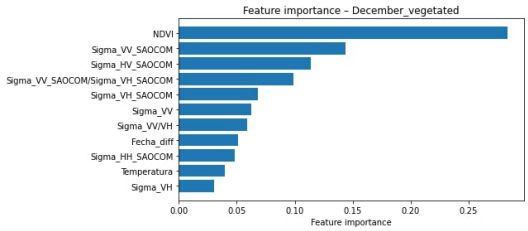

Figure3. (a)Feature importance during bare soil/less vegetated (b) vegetated state

4.3 Multi-Sensor Synergy

The ablation analysis results revealed that if we remove the SAOCOM L-band from our model, the correlation coefficient R drops significantly, from 0.93 to 0.72 Eliminating the NDVI data caused a 3.6% decrease in the coefficient of determination, R^2. On the other hand, removing temperature data resulted in a more noticeable 9.5% drop in R^2. Similarly, when precipitation was excluded, the R^2 value decreased by 11.9%.

Interestingly, when NDVI, temperature, and precipitation were all removed together, the reduction in R^2 was only 10.7%, which is less than the cumulative total of the individual losses (Table 2). This suggests that nonlinear compensatory interactions are occurring among the sensors.

Table 2 Performance of the ML soil moisture prediction models trained using a feature set

Excluded Features	R^2	R^2 Decrease (%)	RMSE m^3/m^3	RMSE Increase (%)	MAE m^3/m^3	MAE Increase (%)
None (All features)	0.84	0.00%	0.022	0.00%	0.016	0.00%
NDVI	0.81	3.57%	0.026	8.33%	0.017	6.25%
Surface Temperature	0.76	9.52%	0.029	20.83 %	0.020	25.00 %
Precipitation	0.74	11.90 %	0.031	29.17 %	0.021	31.25 %
NDVI + Temp + Precipitation	0.75	10.71 %	0.030	25.00 %	0.020	25.00 %

4.4 Spatial Mapping of Soil Moisture

To further evaluate the spatial performance of the proposed framework, a high-resolution soil moisture map derived from the

Bayesian-optimized LSTM model is presented in Figure 4 . The map illustrates the spatial variability of soil moisture across the study area at 10 m resolution, capturing field-scale heterogeneity influenced by vegetation cover, soil properties, and meteorological conditions. The results demonstrate the capability of the multi-sensor fusion approach to generate physically consistent and spatially detailed soil moisture estimates.

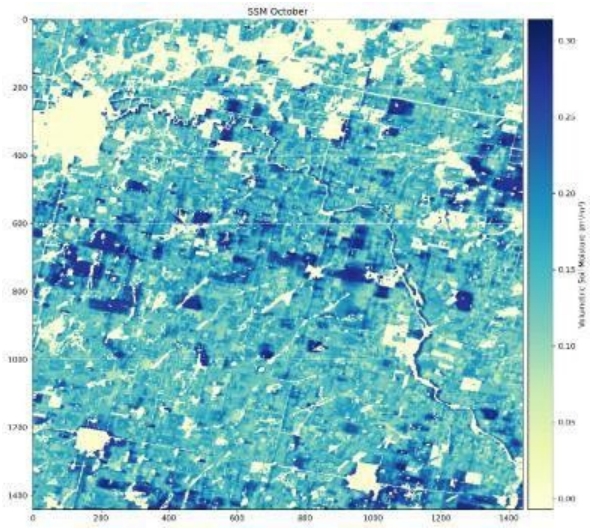

Figure 4. Spatial distribution of estimated surface soil moisture (m^3/m^3) derived from the Bayesian-optimized LSTM model over the Monte Buey study area.

5. DISCUSSION

This study revealed insightful information about SSM retrieval by solving four key gaps in SSM literature through integrated multi-sensor fusion and advanced machine learning: SAOCOM's full-polarization L-band capabilities proved indispensable for penetrating dense agricultural residues where C-band signals saturate.The L-band's ability to penetrate vegetation (Duc, 2024) and the C-band's sensitivity to surface changes (Hashemi et al., 2024) were combined to mitigate the limitations of each frequency when used in isolation, effectively counteracting signal saturation caused by dense vegetation and surface roughness This synergy between L-band's penetration depth and C-band's surface sensitivity yielded a $0.02 m^3/m^3$ RMSE compared to heuristic fusion approaches (Liu et al., 2024).

The ablation study (Table 2) revealed how optical/meteorological data compensate for SAR limitations and, therefore quantifying the multi-sensor synergy in our study. The NDVI captured reduced vegetation backscatter errors by 3.5 % in terms of coefficient of determination, and temperature captured 9.52% of evaporation-driven moisture loss, while precipitation omission caused the steepest performance drop (11.9% R^2). Critically, joint exclusion of non-SAR features caused non-additive degradation (10.7% R^2), demonstrating synergistic compensation mechanisms consistent with studies by (Xu et al., 2024).

The multi-source fusion framework, which consisted of integration of SAOCOM L band, Sentinel-1 C band, Sentinel-2 NDVI and meteorological data, outperformed existing approaches across key metrics. For instance, the multi-source multi-frequency fusion (L+C-band, NDVI and meteorological data) achieved R^2=0.84 (RMSE=0.02 m^3/m^3), surpassing single-frequency C-band approaches (Ondieki et al., 2023) R^2=0.71 for C-band in vegetated areas) by 13% in R^2. In residue-heavy no-till systems, it outperformed (Shilpa et al., 2023) by 14% (R^2=0.84 vs 0.70). The approach also exceeded triple-band (C/X/optical) fusion (Xu et al., 2024) by 3.4% in R^2.

6. CONCLUSIONS

This work introduces an innovative framework that is not only scalable and operational, but also offers clear physical interpretations for high-resolution soil surface moisture (SSM) retrieval in the complex landscapes of agriculture. The main takeaway points include how multi-sensor fusion, combining data from SAOCOM, Sentinel-1, Sentinel-2 NDVI, and meteorological sources, greatly boosts the accuracy of retrievals. Through Bayesian optimization, the Long Short-Term Memory (LSTM) model achieves an R^2 value of 0.84 and a Root Mean Square Error (RMSE) of 0.024, even under varied land surface conditions. The use of L-band Synthetic Aperture Radar (SAR) proves to be invaluable where there's dense vegetation and residue cover, providing crucial insights. The collaboration of SAR, NDVI, and meteorological data is vital for overcoming the limitations of using a single sensor. This framework can be adapted for transfer learning, and it supports near-real-time applications in agriculture. This method lays a solid foundation for operational soil surface moisture mapping, aiding hydrological forecasting and precision agriculture in regions where data is sparse.

ACKNOWLEDGEMENTS

The authors thank CONAE (Argentina) for providing SAOCOM data and field support, Sapienza University of Rome for funding and scientific guidance, and for research collaboration support.

REFERENCES

Anconitano, G. (2025). Soil moisture estimation and crop area classification from multi-frequency and multi-polarization SAR data.

Duc, B. P. (2024). Comparison of Synthetic Aperture Radar Sentinel-1 and ALOS-2 observations for lake monitoring. *Vietnam Journal of Earth Sciences*, *46*(3), Article 3. https://doi.org/10.15625/2615-9783/20639.

Hashemi, M. G. Z., Jalilvand, E., Alemohammad, H., Tan, P.-N., & Das, N. N. (2024). Review of synthetic aperture radar with deep learning in agricultural applications. *ISPRS Journal*

of Photogrammetry and Remote Sensing, *218*, 20–49. https://doi.org/10.1016/j.isprsjprs.2024.08.018.

Liu, J., Hao, Z., Ding, J., Zhang, Y., Miao, Z., Zheng, Y., Alimu, A., Cheng, H., & Li, X. (2024). Ensemble Machine-Learning-Based Framework for Estimating Surface Soil Moisture Using Sentinel-1/2 Data: A Case Study of an Arid Oasis in China. *Land*, *13*(10), Article 10. https://doi.org/10.3390/land13101635.

Mittelbach, H., & Seneviratne, S. I. (2012). A new perspective on the spatio-temporal variability of soil moisture: Temporal dynamics versus time-invariant contributions. *Hydrology and Earth System Sciences*, *16*(7), 2169–2179. https://doi.org/10.5194/hess-16-2169-2012.

Ondieki, J., Laneve, G., Marsella, M., & Mito, C. (2023). Enhancing Surface Soil Moisture Estimation through Integration of Artificial Neural Networks Machine Learning and Fusion of Meteorological, Sentinel-1A and Sentinel-2A Satellite Data. *Advances in Remote Sensing*, *12*, 99–122.

Cappelletti, L., Ruscica, R., Salvia, M. M., Sörensson, A., Jobbágy, E., Gattinoni, N., Spennemann, P., & Fernandez-Long, M. (2020). First surface soil drying validation in a productive area in central Argentina. *ISPRS Annals of the Photogrammetry, Remote Sensing and Spatial Information Sciences, IV-3/W2*, 33–40. https://doi.org/10.5194/isprs-annals-IV-3-W2-2020-33-2020

Thibeault, M., et al. (2015). Soil moisture monitoring network for the validation of satellite missions in the Pampas region (Monte Buey core site). *Proceedings of IGARSS 2015*. https://doi.org/10.1109/IGARSS.2015.7326117

Grings, F., Ferrazzoli, P., Jacobo-Berlles, J., Karszenbaum, H., Tedesco, M., & Prats-Iraola, P. (2016). The SAOCOM mission: SAR-based soil moisture retrieval and validation activities in Argentina. *IEEE Geoscience and Remote Sensing Letters, 13*(2), 266–270. https://doi.org/10.1109/LGRS.2016.2521643

Entekhabi, D., Njoku, E. G., O'Neill, P. E., Kellogg, K. H., Crow, W. T., Edelstein, W. N., Entin, J. K., Goodman, S. D., Jackson, T. J., Johnson, J., Kimball, J., Piepmeier, J. R., Koster, R. D., Martin, N., McDonald, K. C., Moghaddam, M., Moran, S., Reichle, R., Shi, J. C., Spencer, M. W., Thurman, S. W., Tsang, L., & Van Zyl, J. (2010). The Soil Moisture Active Passive (SMAP) mission. *Proceedings of the IEEE, 98*(5), 704–716. https://doi.org/10.1109/JPROC.2010.2043918

Kerr, Y. H., Waldteufel, P., Wigneron, J. P., Delwart, S., Cabot, F., Boutin, J., Escorihuela, M. J., Font, J., Reul, N., Gruhier, C., Juglea, S. E., Drinkwater, M. R., Hahne, A., Martin-Neira, M., & Mecklenburg, S. (2012). The SMOS mission: New tool for monitoring key elements of the global water cycle. *Proceedings of the IEEE, 98*(5), 666–687. https://doi.org/10.1109/JPROC.2010.2043032

Panciera, R., Walker, J. P., Kalma, J. D., Kim, E. J., Hacker, J. M., Merlin, O., Berger, M., Skou, N., Chanzy, A., & Wigneron, J. P. (2014). The Soil Moisture Active Passive Experiments (SMAPEx): Toward soil moisture retrieval from multi-frequency observations. *IEEE Transactions on Geoscience and Remote Sensing, 52*(8), 4909–4925. https://doi.org/10.1109/TGRS.2013.2283197

Singh, A., & Gaurav, K. (2023). Deep learning and data fusion to estimate surface soil moisture from multi-sensor satellite images. *Scientific Reports, 13*, 2251. https://doi.org/10.1038/s41598-023-28939-9

Shilpa, K., Suresh Raju, C., Mandal, D., Rao, Y. S., & Shetty, A. (2023). Soil Moisture Retrieval Over Crop Fields from Multi-polarization SAR Data. *Journal of the Indian Society of Remote Sensing*, *51*(5), 949–962. https://doi.org/10.1007/s12524-023-01682-4.

Singh, A., & Gaurav, K. (2023). Deep learning and data fusion to estimate surface soil moisture from multi-sensor satellite images. *Scientific Reports*, *13*(1), 2251. https://doi.org/10.1038/s41598-023-28939-9.

Seneviratne, S. I., Corti, T., Davin, E. L., Hirschi, M., Jaeger, E. B., Lehner, I., Orlowsky, B., & Teuling, A. J. (2010). Investigating soil moisture–climate interactions in a changing climate: A review. *Earth-Science Reviews*, *99*(3), 125–161. https://doi.org/10.1016/j.earscirev.2010.02.004.

Xu, C., Liu, Q., Wang, Y., Chen, Q., Sun, X., Zhao, H., Zhao, J., & Li, N. (2024). Inversion of Farmland Soil Moisture Based on Multi-Band Synthetic Aperture Radar Data and Optical Data. *Remote Sensing*, *16*(13), Article 13. https://doi.org/10.3390/rs16132296
paper does not exceed the limits given above.

This work is licensed under a Creative Commons Attribution-No Derivatives 4.0 International License.

INTEGRATED ANALYSIS OF EVAPOTRANSPIRATION IN THE PLANT-NURSERY DISTRICT OF PISTOIA

B. Rapi[1*], P. Battista[1], M. Chiesi[1], L. Fibbi[1-2], F. Sabatini[1], L. Incrocci[3], M. Pieri[1], F. Maselli[1]

[1] CNR – Institute of BioEconomy, Via Madonna del Piano 10, 50019 Sesto Fiorentino (FI), Italy - nome.cognome@cnr.it
[2] LaMMA Consortium, Via Madonna del Piano 10 – 50019 Sesto Fiorentino (FI), Italy - fibbi@lamma.toscana.it
[3] Department of Agriculture, Food and Environment, University of Pisa, via Borghetto, 80, 56124 Pisa, Italy - luca.incrocci@unipi.it

KEY WORDS: Remote Sensing; Sentinel-2 MSI; fractional Vegetation Cover, NDVI; Water balance, Kc.

ABSTRACT:

The production subsystems of the plant-nursery district of Pistoia (Italy) are characterized by high spatial and temporal variability driven by specific economic and techno-productive dynamics. This variability complicates management practices and reduces efficiency in terms of resource use (e.g. water, labor, and energy) and sustainability. The current study proposes an integrated methodology for analyzing actual evapotranspiration (ETa) in plant-nurseries by combining remote sensing (RS), field observations, and water-balance modelling to improve ETa estimates and irrigation requirement assessment at the plot scale. Five years (2020–2024) of field measurements and Sentinel-2 (S-2) data were analyzed in two representative nurseries. Results show: (a) a high sensitivity of S-2-derived Fractional Vegetation Cover (FVC) to spatial and temporal field dynamics related to vegetation growth, plant displacement, and thinning; and (b) improved water-balance performance when using a modified crop coefficient (Kcc) derived from NDVI compared to the standard FAO-56 Kc (the R^2 of the linear regression versus irrigation measurements increases from 0.74 to 0.86). Despite limitations associated with the spatial resolution of S-2, preliminary results indicate that integrating RS and field data for precision irrigation in ornamental nurseries could reduce water volumes by up to 40% without negatively affecting plant health, supporting more sustainable water management.

1. INTRODUCTION

Growing awareness of environmental challenges and technological opportunities has stimulated collaboration between horticultural producers and researchers, aimed at developing operational solutions to improve the efficiency of natural resource use. The adoption of automated irrigation systems (irrigation control units) or dedicated decision support systems (DSS), based on meteorological and soil-moisture sensors, can in principle enhance irrigation efficiency, but still faces limitations related to the management of the high variability among production plots (Pardossi et al., 2009).

The quantification of plant water requirements is a recognized priority in the plant-nursery district of Pistoia (Tuscany, Italy), where numerous projects have been carried out in recent years to develop efficient irrigation control strategies (Lazzerini et al., 2018). Among the factors limiting the adoption of proposed solutions, the most critical are the difficulties in determining actual water availability in pots and the marked heterogeneity within each production unit (Incrocci et al., 2014). While the first issue may be addressed through the installation of a representative number of soil moisture sensors, the acquisition of very high spatial- and temporal-resolution imagery from different platforms (fixed or mobile cameras; drones and satellites) can provide valuable information to support advanced modelling and precision-farming approaches.

Water requirements are commonly estimated using water-balance models that integrate ground data (agrometeorological stations and sensor nodes), field observations, and remote-sensing (RS) data. The latter are typically used to quantify the fraction of vegetation cover (FVC) throughout the year following an approach which was originally developed for MODIS NDVI imagery and subsequently extended to Sentinel-2 (S-2) Multi Spectral Imager (MSI) data (Maselli et al., 2020). In this context, RS imagery may support several tasks which include: (a) describing production dynamics; (b) defining plot-scale water requirements; (c) assessing the representativeness of local measurements; and (d) detecting spatial or temporal anomalies.

This study aims at evaluating these potentials by developing a methodology for the spatial and temporal analysis of FVC and the estimation of actual evapotranspiration (ETa) in plant nurseries, based on RS products. Very-high-spatial-resolution imagery acquired during the growing season, together with corresponding field agrotechnical measurements (e.g. plant species and size, pot density, canopy cover percentage), are analyzed to characterize the spatio-temporal variability and vegetation dynamics within production plots, and to support the validation of the S-2-based procedure.

To this aim, the classical dual crop coefficient (Kc) used in the water-balance approach (Allen et al., 2005) is replaced by a modified crop-coverage coefficient (Kcc), derived from NDVI (Maselli et al. 2020). This RS-based procedure addresses several limitations of classical water balance models and automatic irrigation management systems enabling spatial-temporal analysis of plant status and improving ETa estimation under diverse operational settings. The proposed method appears less complex and expensive than alternative techniques, while still providing adequate spatial and temporal detail.

2. MATERIAL AND METHODS

Two private production areas were selected within the plant-nursery district of Pistoia for their agrotechnical and managerial characteristics, plant species, and production assets (Fig. 1). During the study period (2020–2024), the production surfaces covered approximately 80,000 m² and 300,000 m², respectively, with plots ranging from 900 to 1,800 m². In both sites, evergreen and deciduous species were cultivated either in soil or in pots of different sizes. Irrigation management followed

* Corresponding author

the highest production standards commonly adopted for small- and medium-sized ornamental plants. This approach accounted for the pronounced spatial and temporal variability of plant cover within production plots (multiple parcels), which is driven by several technical and commercial factors.

Local monitoring networks, consisting of fully equipped agrometeorological stations (Davis Instruments) and sensor nodes measuring air temperature and relative humidity, were installed at central locations within each nursery to ensure the representativeness of hourly measurements with respect to local micrometeorological conditions.

Rain gauges were used to intercept irrigation water applied through sprinkler systems. Seasonal agrotechnical information and ground-truth data were provided by local experts across the entire production area and complemented by one-two very-high-resolution visible (HRv - Google Earth) satellite images per year. Information on vegetation cover, plant number and density within 30 plots selected as representative for different nursery conditions was further integrated with an automated estimation of FVC, obtained through MATLAB-based image analysis procedures. HRv imagery was used to define plot characteristics (e.g. shape, boundaries, crop type, plant density) and to assess the consistency of S-2-derived FVC by direct comparison (see Fig. 2).

The available S-2 MSI imagery covering the study area was downloaded in ortho-rectified, pre-processed Level-2A format from the European Space Agency repository and processed to generate 15-day Maximum Value Composite NDVI data series at 10 m spatial resolution for the Pistoia district. All images were further processed to remove abrupt variations attributable to atmospheric effects and to derive FVC for the selected sites following the methodology proposed by Maselli et al. (2014). These data were then used to evaluate the contribution of remote sensing information to the estimation of crop coefficients (Kc) and actual evapotranspiration (ETa) within a classical water-balance modelling framework and irrigation measurements collected during the study period.

a)

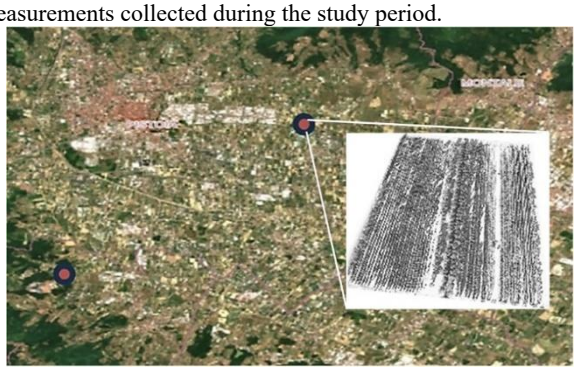

b)

Figure 1. (a) HRv image of the plant-nursery district of Pistoia showing the location of the two private nurseries (red dots), with a detailed view of a representative plot; (b) Local monitoring station and sensors installed in one of the test areas.

3. RESULTS AND DISCUSSION

Sentinel-2 imagery provides the opportunity to monitor land-use changes and plant development at spatial and temporal scales that are barely sufficient for plant-nursery applications. A direct comparison between Google Earth HRv and S-2 data for 31 plots, differing in plant species and vegetation cover percentage, indicates for the mid-July 2023 period an average error of approximately 25% in fractional vegetation cover (FVC) estimation (Fig. 2). This discrepancy is mainly attributable to imperfect image co-registration and to the inclusion of heterogeneous ground elements within 10-m pixels (e.g. paths, canals, boundary hedges). A visual comparison of the HRv and S-2 images (Fig. 2a and 2b) further highlights the difficulty of unambiguously assigning individual pixels to plot boundaries. In this analysis, a 50% threshold was adopted for pixel attribution to plots. This choice resulted in noticeable deviations from the reference condition defined by manual plot delineation, as well as evident distortions in parcel geometry. From a statistical perspective, average errors remain largely unchanged when FVC values are computed using relative pixel contributions based on areal overlap.

a)

b)

c)

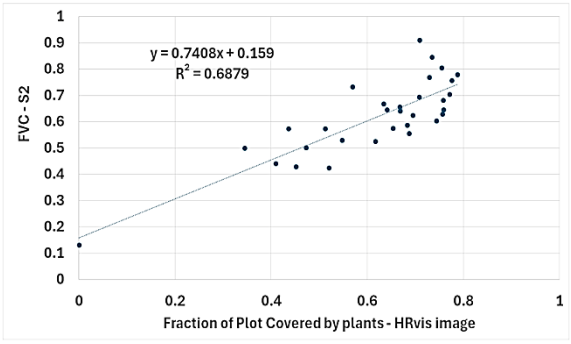

Figure 2. a) Example of a HRv image taken on 27th July 2023 with 31 individual plots identified; (b) extraction of the same plots from the corresponding S-2 image; (c) linear regression between reference and S-2-derived FVC.

Conversely, restricting the analysis to pixels fully contained within the plots reduces estimation errors but significantly decreases the number of usable pixels and requires near-perfect geometric alignment between plot masks and imagery, a condition that cannot be currently guaranteed (Vajasová et al., 2020). In Figure 2c, the lowest value refers to an additional plot without vegetation (zero reference), while the remaining plots exhibit varying degrees of vegetation cover. The internal spatial variability of production plots remains very high throughout the year, with patterns influenced by local technical and economic drivers as well as natural plant growth. Figure 3 illustrates this variability through the spatial distribution of NDVI values (Fig. 3a), the temporal evolution of FVC (Fig. 3b), and an assessment of the progressive loss of representativeness of a single image over time (Fig. 3c). The latter evaluation is based on common statistical indicators (Coefficient of determination - R^2, slope, and intercept). Results indicate that, for a period of approximately 30 days, information derived from a single image remains statistically representative of the average FVC of the production area (residual variance < 20%).

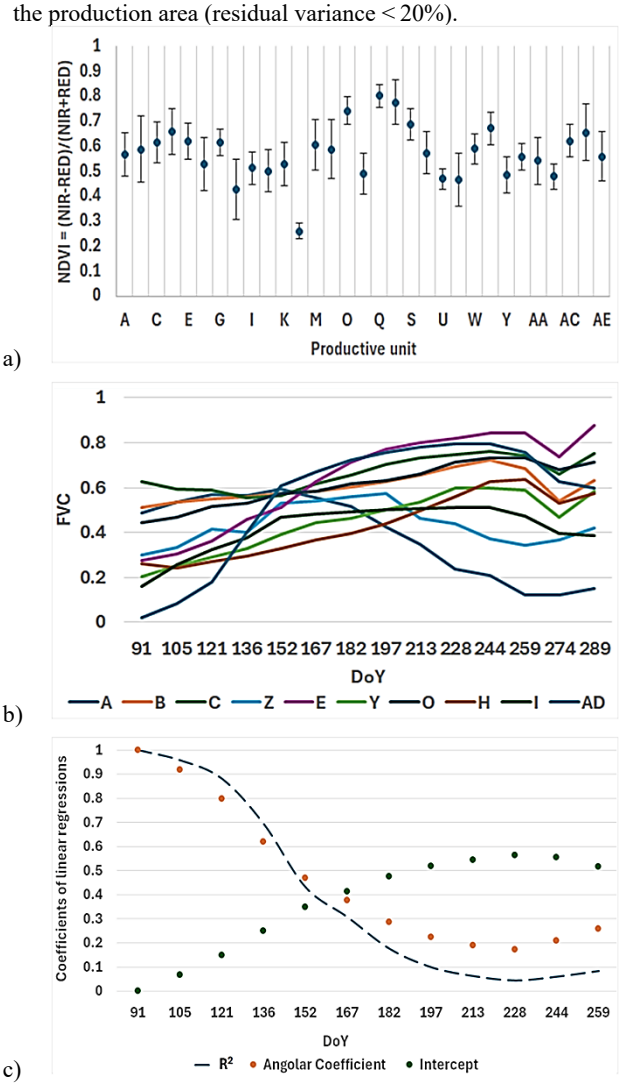

Figure 3. a) Mean NDVI values and corresponding standard deviations within 30 selected plots on a given date (mid-July 2023); (b) FVC dynamics within 10 reference plots from April to October 2023; (c) decrease in the coefficient of determination (R^2) and trends in intercepts and slopes of linear regressions obtained by comparing the initial (April 2023) FVC with subsequent 15-day observations.

Assuming that data provided by local monitoring networks, remotely sensed imagery, or technical surveys are routinely used as reference inputs for DSS models, key aspects of canopy dynamics—such as plant growth—may be tracked more accurately, limiting model drift in accordance with Bayesian data assimilation principles (Wang et al., 2024). Although spatial variability within plant nurseries depends on multiple factors, from an operational standpoint NDVI values can be directly related to green biomass and, consequently, to ETa at the plot scale. In this case study, replacing traditional crop coefficients (Kc) with S-2-derived coefficients (Kcc), while keeping all other model parameters unchanged, led to improved agreement between estimated and observed values of irrigation. Over the full study period (2020–2024), the R^2 of the related linear regression increased from 0.74 to 0.86, with a consistent improvement of the major performance metrics: mean squared error (MSE, −33%), root mean squared error (RMSE, −18%), mean squared relative error (MSRE, −65%), and mean absolute error (MAE, −21%).

Figure 4 illustrates (a) the modification of crop coefficients derived from S-2 FVC, (b) the resulting changes in irrigation requirement estimates, and (c) the non-linear regression between measured and estimated irrigation volumes for a representative plot over the five-year period.

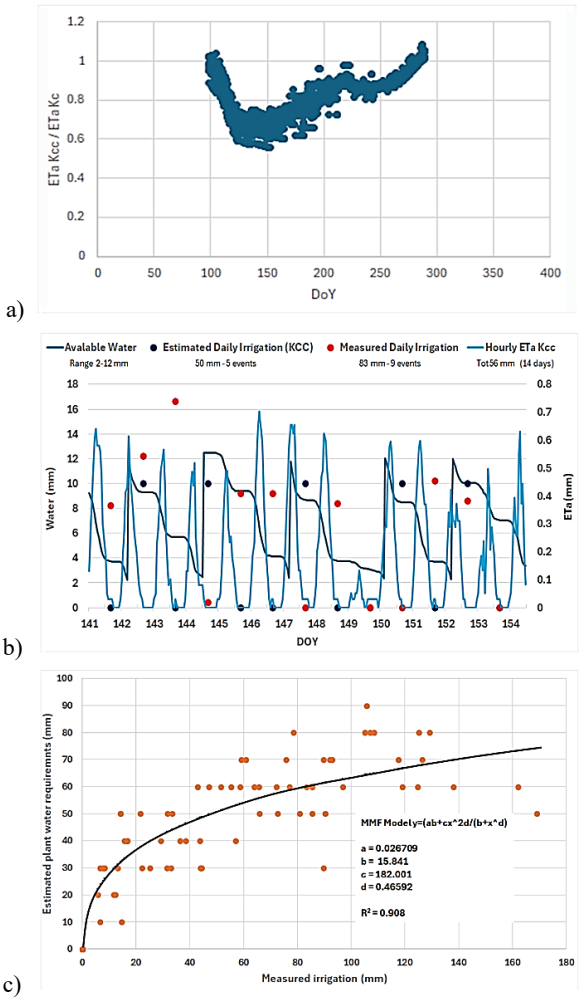

Figure 4. a) Average Five-year (2020–2024) ETa·Kcc/ETa·Kc average ratio; (b) example of available water, actual and simulated irrigation, and ETa values during May–June 2020; (c) observed VS estimated irrigation at 15-day time step 2020-2024 (Morgan–Mercer–Flodin, MMF, regression model).

Overall, Kcc values are generally lower than classical Kc values (Fig. 4a), reflecting the partial vegetation cover typical of nursery production systems. The resulting water-balance simulations (Fig. 4b) are more consistent with expert assessments and operational irrigation practices, although differences remain in recommended irrigation frequency and daily volumes, leading to an overall divergence of approximately 40% in estimated plant water requirements. These findings are supported by a direct comparison between measured and estimated 15-day cumulative irrigation doses, revealing a non-linear pattern (Fig. 4c), characterized by higher-than-expected water demand during cooler periods and lower demand during warmer ones. Accordingly, RS information could be used to optimize over-irrigation driven by environmental stress or to ensure substrate imbibition.

Recent studies support the effectiveness of remotely sensed indicators for irrigation management and monitoring. In Sapkota et al. (2025), for example, evapotranspiration (ET), crop water stress index (CWSI), and NDVI successfully delineate irrigation management zones in almond orchards, with ET and CWSI, being particularly sensitive to transient changes in water use and stress. More generally, the use of NDVI-derived crop coefficients for evapotranspiration estimation is a well-established approach in agricultural modelling and precision farming (Kamble, 2013). Consistent with these evidences, a preliminary analysis conducted over the Pistoia plant-nursery district using the operational ETa estimation method of Maselli et al., (2026), reveals an increase in water consume of more than 5% in the period 2020–2024, likely driven mostly by rising temperature and potential evapotranspiration.

4. CONCLUSIONS

This study demonstrates that the use of S-2 imagery with a 15-day temporal resolution significantly improves the assessment of actual vegetation cover within nursery production plots. The integration of remote-sensing products with ground-based monitoring data can provide a continuous and reliable description of canopy and environmental dynamics, representing a key prerequisite for the adoption of precision-agriculture practices in the plant-nursery sector.

The preliminary results obtained highlight the potential contribution of FVC derived from S-2 MSI data for the estimation of actual irrigation requirements at plot scale, yielding estimates that are more consistent with field conditions. In particular, the use of NDVI-derived crop coefficients improved the agreement between estimated and observed plant water requirements, increasing the R^2 from 0.74 to 0.86. Moreover, irrigation volumes could be optimized by exploiting imagery with adequate spatial and temporal resolutions, allowing program scheduling to better reflect the effective water demand of plants across different production sectors during the year.

In several cases, also considering operational constraints and the need to occasionally exceed theoretical plant water requirements (e.g. to ensure adequate substrate wetting), a significant wastage was detected. The adoption of automated control strategies supported by HRv and NDVI imagery could therefore enable alternative irrigation approaches, achieving potential water savings currently estimated at 20–40% or higher, depending on local agrotechnical practices.
These results suggest that efforts aimed at making such monitoring and modelling systems operational at the regional scale could support a progressive optimization of water use within the Pistoia plant-nursery district. Future work should therefore focus on improving image pre-processing techniques and strengthening the integration of this methodology within decision support systems, in order to maximize resource-use efficiency under highly variable production conditions.

AKNOWLEDGEMENTS

The authors thank the partner of the 3S Eco-Nursery Project (Smart Specialization Strategy) – Progetti Integrati di Filiera, Tuscany Region PSR 2014-2020, Measure 16.2 (PIF47/2015).

REFERENCES

Allen R.G., Pereira L.S., Smith M., Raes D., Wright J.L., (2005). FAO-56 dual crop coefficient method for estimating evaporation from soil and application extensions. *J. Irrig. Drain. Eng.*, 131(1), 2–13. Doi: 10.1061/(ASCE)0733-9437(2005)131:1(2).

Kamble, B., Kilic, A., & Hubbard, K. (2013). Estimating Crop Coefficients Using Remote Sensing-Based Vegetation Index. *Remote Sensing*, 5(4), 1588-1602. Doi:10.3390/rs5041588.

Lazzerini G., Merante P., Lucchetti S., and Nicese F.P. (2018) Assessing environmental sustainability of ornamental plant production: a nursery level approach in Pistoia District, Italy, *Agroecology and Sustainable Food Systems*, 42:8, 911-932. Doi: 10.1080/21683565.2018.1466755.

Maselli, F., Papale, D., Chiesi, M., Matteucci, G., Angeli, L., Raschi, A., Seufert, G. (2014). Operational monitoring of daily evapotranspiration by the combination of MODIS NDVI and ground meteorological data: Application and validation in Central Italy. *Remote Sensing of Environment*, 152, 279–290.

Maselli, F., Angeli, L., Battista, P., Fibbi, L., Gardin, L., Magno, R., Rapi, B., Chiesi, M. (2020). Evaluation of Terra/Aqua MODIS and Sentinel-2 MSI NDVI data for predicting actual evapotranspiration in Mediterranean regions. *International Journal of Remote Sensing*, 41(14), 5186-5205.

Maselli F. et al. (2026). High spatio-temporal resolution estimation of actual evapotranspiration by the use of Sentine-2 MSI data. Int. Journal of Applied Earth Observation and Geoinformation, in revision.

Pardossi A., Incrocci L., Incrocci G., Malorgio F., Battista P., Bacci L., Rapi B., Marzialetti P., Hemming J., Balendonck J. (2009). Root zone sensors for irrigation management in intensive agriculture. *Sensors*, 9(4), 2809-2835.

Sapkota A., Roby M., Peddinti S.R., Fulton A., Kisekka I. (2025). Comparative analysis of evapotranspiration (ET), crop water stress index (CWSI), and normalized difference vegetation index (NDVI) to delineate site-specific irrigation management zones in almond orchards. *Scientia Horticulturae*, V.339, 1.1.25, 113860.

Vajsová, B., Fasbender, D., Wirnhardt, C., Lemajic, S., & Devos, W. (2020). Assessing Spatial Limits of Sentinel-2 Data on Arable Crops in the Context of Checks by Monitoring. Remote Sensing, 12(14), 2195. Doi:10.3390/rs12142195.

Wang, J., Wang, Y., & Qi, Z. (2024). Remote Sensing Data Assimilation in Crop Growth Modeling from an Agricultural Perspective: New Insights on Challenges and Prospects. Agronomy, 14(9), 1920. Doi:10.3390/agronomy14091920.

This work is licensed under a Creative Commons Attribution-No Derivatives 4.0 International License.

EARLY ESTIMATION OF IRRIGATION NEEDS OF PROCESSING TOMATOES AT DISTRICT SCALE: FIELD IDENTIFICATION AND PHENOLOGY

M. Rinaldi [1], P. Garofalo [2], F. Ciavarella [1], G. Satalino [3], F. Mattia [3], A. Balenzano [3], L. Nardella [4], N. Noviello [4], R. Guarini [5], D. Tapete [5], S. Ruggieri [2]*

[1] Council for Agricultural Research and Economics, Research Centre for Cereal and Industrial Crops (CREA-CI), Foggia, Italy
michele.rinaldi@crea.gov.it; francesco.ciavarella@crea.gov.it
[2] Council for Agricultural Research and Economics, Research Centre for Agriculture and Environment (CREA-AA), Bari, Italy
pasquale.garofalo@crea.gov.it; sergio.ruggieri@crea.gov.it
[3] National Research Council of Italy, Institute for Electromagnetic Sensing of the Environment (CNR-IREA), Bari, Italy
giuseppe.satalino@cnr.it, francesco.mattia@cnr.it, anna.balenzano@cnr.it
[4] Consorzio per la Bonifica della Capitanata, Foggia, Italy
luigi.nardella@bonificacapitanata.it; nicoletta.noviello@bonificacapitanata.it
[5] Italian Space Agency (ASI), Rome, Italy
rocchina.guarini@asi.it; deodato.tapete@asi.it

KEY WORDS: processing tomatoes, irrigation scheduling, irrigation water requirements, crop modelling, decision support system

ABSTRACT:

The THETIS project has developed a spatial decision support system (SDSS) capable of providing early, watershed-scale estimates of crop water needs, in order to improve water supply management and enhance services provided to irrigation agencies. The SDSS integrates a hydrological and a crop growth model, driven by products derived from Earth Observation (EO) data as well as weather and climate variables. This paper focuses on the SDDS module dedicated to the early identification of irrigated areas for the upcoming season and to the estimation of transplanting dates of irrigated crops. This system has been applied to the Capitanata plain in southern Italy, with a specific focus on processing tomato crop, the dominant irrigated crop in the study area.
The early identification of tomato fields before the start of the crop season is based on statistical data of the occurrence of tomato in the same field (crop rotation), which are updated at the beginning of the crop season based on tilled fields detected through an EO data-driven algorithm. Crop rotations of tomato fields are obtained using historical georeferenced field data consisting of five-year surveyed land use, overlayed to a 100 m² grid and recording the presence or absence of tomato cultivation. This map is updated by using tilled field map information, thus achieving the best balance between timeliness and accuracy. The transplanting dates are identified using, in this case, data analysis of historical Leaf Area Index (LAI) signatures of tomato fields obtained utilizing the biophysical processor in European Space Agency's SNAP application. Results reveal that they are mainly concentrated in May and June (namely 15th May and 15th June), with a higher frequency in June.

1. INTRODUCTION

In the context of climate change and the resulting shifts in agricultural dynamics, the traditional model of continuous water distribution adopted by irrigation consortia is increasingly under strain. Rising temperature and precipitation variability are causing pronounced alternations between wet and dry periods. During rainy phases, irrigation demand decreases, whereas in dry seasons—intensified by extreme heat waves and reduced water availability—demand sharply increases. Farmers are also adapting by replacing highly water-intensive crops, such as tomatoes, with crops requiring only supplemental irrigation, such as wheat. This transition is producing a more heterogeneous irrigation demand across both time and space (Kourgialas, 2023). Under these conditions, the need for early informed decision-making with high spatial resolution becomes critical for irrigation consortia and water-resource management agencies, especially in regions where climate change impacts are accelerating, such as the Mediterranean basin. Responding to this challenge, the THETIS project (Satalino et al., 2024**a**), funded by the Italian Space Agency (ASI), has developed a Spatial Decision Support System (SDSS) for providing early estimates of crop water needs at the watershed scale.
Unlike conventional SDSS tools for irrigation water management that rely primarily on optical Earth Observation (EO) data after the crop season starts, THETIS integrates both Synthetic Aperture Radar (SAR) and optical data. It inputs EO-derived products into an integrated hydrological and crop growth model, incorporating forecasts of weather-and climate variables. This combination enables comprehensive monitoring of land use, crop conditions, soil moisture, and irrigated areas, providing a more holistic picture of agricultural systems.
The following sections present the results of an early estimate of the areas potentially under tomato cultivation and an analysis of the planting dates used by farmers in the area. This identification is based on crop rotation information and updates obtained from the EO products that identify tillage practices and the most frequent tomato transplanting dates. These parameters are essential for an early identification of irrigation needs at the district level from the crop growth model.

2. MATERIAL AND METHODS

THETIS SDSS integrates four main components: (i) a hydrological modelling framework (Iacobellis et al, 2024), (ii) a crop growth model (Rinaldi et al., 2024), (iii) multi-source EO data, and (iv) Artificial Intelligence (AI) techniques (Impedovo et al., 2024) for data processing and spatialization. The interaction among these components enables the early estimation of crop water requirements at both field and irrigation-district scales.

* Corresponding author

EO data, in particular the ESA's Sentinel-2 images and the LAI biophysical variable calculated using the "Biophysical Processor" in the SNAP application, were used to derive key crop management information for processing tomatoes in the Capitanata plain (Southern Italy), with a specific focus on crop spatial distribution and crop transplanting dates. This system has been applied in Irrigation District 6/B of the "Consorzio per la Bonifica della Capitanata" (CBC) to assess the likelihood and recurrence of tomato cultivation across agricultural fields.

2.1 Tomatoes field identification

THETIS SDSS was designed to generate irrigation requirement forecasts for tomatoes (i.e. a high irrigation water- demand crop) according to three distinct use cases, corresponding to different stages of the crop season and increasing levels of information availability (Fig. 1). They were defined in close interaction with the CBC to meet operational planning needs at the irrigation-district scale:

- **Use Case 1 (UC1)**: early pre-season forecast, issued around 1st April, before tomato transplanting and field operations begin;
- **Use Case 2 (UC2)**: early-season forecast, issued around 1st May, at the onset of the cropping season;
- **Use Case 3 (UC3)**: in-season forecast, issued around 1st June, when transplanting activities are ongoing or completed.

Moving from UC1 to UC3, forecasts progressively, incorporate crop rotation maps, that are updated based on EO-derived information on tillage identification, transplanting dates, and crop presence, thereby reducing uncertainty and improving the spatial accuracy of irrigation demand estimates.

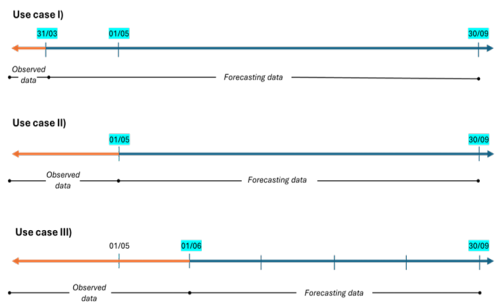

Figure 1. Temporal evolution of the three use cases.

The identification of tomato-cultivated areas (TCA) across the three use cases is a key prerequisite for the reliable estimation of irrigation water requirements. For Use Case 1, the early area identification is obtained by the crop rotation patterns through a statistical analysis of CBC land-use maps for District 6/B over the 2020–2024 period. For Use Cases 2 and 3, which correspond to May 1st and June 1st, respectively, TCA is updated using maps of tilled fields. These maps serve as a proxy for identifying fields that are likely to be cultivated, as well as determining the transplanting date. To accurately determine the area cultivated on each field for each year, both the tomato layer provided by CBC land use (CBC_LU) and the vegetation class from the Scene Classification Layer (vegSCL) of Sentinel-2 imagery were used. The land use data produced by the CBC involves recording the crops grown by farmers for each growing season on cadastral maps. The process began by estimating Summer Crops (SC map) through the subtraction of early autumn vegSCL images from summer vegSCL images. This approach excludes areas with herbaceous crops transplanted in late summer (e.g., cabbage and onion) and perennial crops such as orchards, olive groves, and vineyards, which are visible in the autumn imagery.
Subsequently, the annual SC maps were intersected with the corresponding CBC_LU tomato maps to isolate areas cultivated, excluding roads and non-agricultural features. The resulting summer crop maps (referred to as CBC_SC map) represent the effective TCA for each year from 2020 to 2024.
The union of the five annual CBC_SC maps was used to define the total area cultivated with tomatoes during the years. This area was then divided into a grid of cells measuring 100 m² each, resulting in a total of 681,300 cells, of which 479,397 were cultivated with tomato across the years (Fig. 2).
To gather crop rotation information, the district was divided into parcels, each assigned to a specific crop type annually. However, these parcels often include non-agricultural features such as sheds, dwellings, and water pools, in addition to cultivated land.

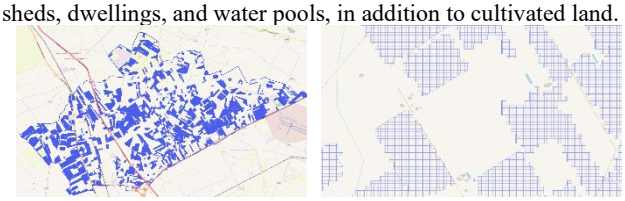

Figure 2. Cumulative area cultivated with tomatoes in the five-year period (2020 – 2024); a close-up of the 100 m² grid used to subdivide the area.

For Use Case 1, the provisional identification of tomatoes field locations was based on crop rotation information derived from the CBC_SC maps spanning from 2020 to 2024.
Based on the analysis, the field locations for Use Case 1 in 2023 and 2024 were obtained by selecting fields that had not been used for tomato cultivation in the previous two years. This estimate suggests that the area under tomato cultivation will be comparable to that of the previous two years.

A statistical analysis of the CBC_SC maps revealed that tomato is typically cultivated in the same fields after several years of rotation. In particular, the frequency of tomato cultivation was calculated for each plot planted with tomatoes across a total area of 4,828 hectares during the period 2020–2024:

- 77.90% of the field hosted tomato only once;
- 11.23% of the field hosted tomato twice;
- 10.87% of the field hosted tomato more than twice, either with only one-year interval or in consecutive years.

For Use Cases 2 and 3 (for 2023 and 2024), field identification was instead based on cumulative maps of tilled fields derived from EO provided by CNR-IREA (Satalino et al., 2024**b**). This analysis utilized both Sentinel-1 (ascending orbit on track 146) and Sentinel-2 data. The maps were clipped to District 6/B, and each field was classified as either rolled or ploughed. The map for Use Case 2 included tillage activities recorded from early March to late April, whereas the map for Use Case 3 included events through the end of May.

2.2 Transplanting Date

The transplanting date for tomatoes in each field was determined on the basis of statistical data relating to typical transplanting periods.
A multi-year phenological analysis of tomato crops was conducted, using the leaf area index (LAI) derived from Sentinel-2 images processed using ESA's SNAP application (Fig. 3). This made it possible to verify that, in the five-year period from 2020 to 2024, transplanting took place predominantly in May and June,

whereas in the fields flagged by CBC_LU, the LAI value was found to be below 0.5 (Fig. 3).

2.3 Additional field data

During the 2024 growing season, detailed land-use surveys were conducted in the Irrigation District 6/B of the CBC between June and August. The survey was carried out using a trekking app on a tablet capable of recording the location and land use of the fields on a Sentinel-2 image updated to the date of the survey.
A total of 273 processing tomato fields were identified, covering an area of approximately 1,264 ha. These additional surveyed fields were used as a reference dataset to evaluate the performance of early forecasts produced under the three use cases.

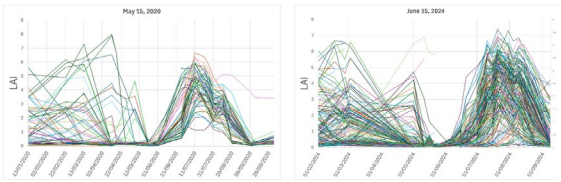

Figure 3. Changes in the LAI index (from SNAP S-2) in tomato fields in May 2020 (left) and June 2024 (right) in two of the five examined years, to identify the most common transplanting periods.

3. RESULTS AND DISCUSSION

The following section illustrates the validation of the area under tomato cultivation estimated in 2023 and 2024 from crop rotation information and tillage maps derived from EO data.

3.1 Tomatoes field identification-Season 2023

The area under tomato cultivation in 2023 was identified by intersecting the tomato layer provided by CBC land use and SC map of the vegetation class representing summer crops derived from Sentinel-2. The two areas were 1233 ha and 1548 ha, respectively. Their intersection, which represents the area actually cultivated with tomatoes (i.e. the CBC_SC map), was 76%, or 940 hectares (Fig. 4, left).
The area identified by CBC_SC map of 940 ha is used as a reference area for comparison with the areas identified early in the three Use Cases, which are:

- Use Case 1: from the crop rotations maps, i.e., selecting tomato cultivation areas that had not hosted tomatoes for at least the previous two years. The area covers approximately 759 ha.

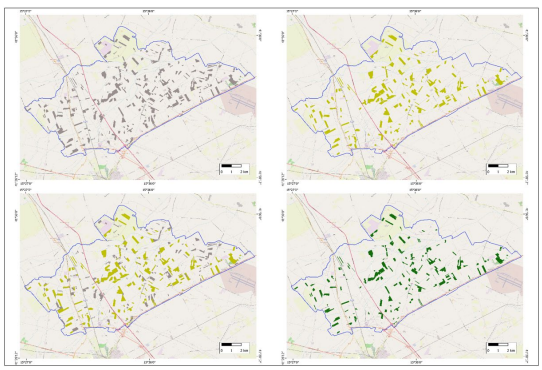

Figure 4. Top row: (left) tomatoes fields identified by the SC map in 2023; (right) tomatoes fields in the CBC Land Use. Bottom row: (left) overlap of the two previous maps; (right) intersection (CBC_SC map) between the two previous maps.

- Use Case 2: from the tilled maps, cumulated from February to April 2023; it covers approximately 957 ha.
- Use Case 3: from the tilled maps, cumulated from February to May 2023; it is about 1373 ha.

By comparing the overlap of the fields in the initial estimated maps and their intersection with the CBC_SC maps, the following results are obtained:

- Use Case 1: an underestimation of 19% and an intersection of 11%;
- Use Case 2: an overestimation of 2% and an intersection of 44%;
- Use Case 3: an overestimation of 46 % and intersection of 44%.

The estimated tomato-growing areas for Use Case 1 was based on crop rotation data that considers the return time of the tomatoes cultivation into the same fields. The Apulian Tavoliere is a region predominantly cultivated with wheat, and farmers typically wait for several years before replanting tomatoes in the same field. This practice helps prevent phytopathologies, pest infestations, and crop-specific diseases, which can complicate pest management.
The results obtained using crop rotation data are used to make an early estimate of the areas under tomato cultivation. By adding further years, we could determine whether there are any areas dedicated to tomato cultivation within CBC District 6/B.
For Use Cases 2 and 3, the identification of cultivation areas was based on tillage activity. The errors of these early estimates for the identification of tomato areas are because tillage is carried out not only to prepare the soil for planting or transplanting new crops, but also to incorporate the residues of previous crops, such as wheat, and to prevent the spread of wild plant species. Additionally, other summer crops such as bell peppers, eggplants, melons, and watermelons are also cultivated in the Tavoliere during the summer season.
According to CBC data, tomatoes account for approximately 10% of the total cultivated area in District 6/B, corresponding to about 1,300 hectares. Other summer crops represent around 1%, or approximately 120 hectares.

3.2 Tomatoes field identification-Season 2024

The CBC_SC map in 2024 was estimated as done in season 2023, i.e., by intersecting the tomato layer provided by CBC_LU and the vegetation class representing summer crops (SC map). The result is an area of 1284 ha, which is higher than the one obtained in 2023.
Moreover, this map was refined through field surveys. The data acquired, i.e., the GPS information, were over imposed to Sentinel-2 images for obtaining actual parcel borders. For less accessible areas, Sentinel-2 imagery (from April to October 2024) and CBC_SC were used. The resulting refined summer crop map (ref_SC) was considered to represent the actual tomato cultivation area in District 6/B for 2024, for an amount of 1264 ha. It was used as a reference for comparisons with CBC_SC map.
The identified area on CBC_LU and SC map was 1669 ha and 1678 ha, respectively. The intersection (CBC_SC map) is 1284 ha, i.e., approximately 77%. Whereas, the ref_SC map, which covers 1264 ha, when it is intersected with the CBC_SC area, returns an area of 1156 ha (i.e., 91%). This shows that the SC map refinement has interested approximately 9% of the CBC_SC map.

3.3 Transplanting dates

Results of the phenological analysis allowed the identification of two distinct transplanting windows: one in May and another in June. On average, these dates correspond to 15th May and 15th June, respectively. This was inferred from multi-annual LAI time series derived from Sentinel-2 imagery, which consistently exhibited values close to zero immediately prior to transplanting across the examined fields over the 2020–2024 period (Fig. 3).
The transplanting dates were then assigned to each field based on the tillage class identified in the tillage maps. For rolled fields, characterized by a smooth soil surface ready for sowing, a transplanting date of 15th May was assigned. In contrast, for ploughed fields, which have a rough soil surface not yet suitable for sowing, a later transplanting date of 15th June was used.
The temporal consistency of these patterns across multiple years supports the robustness of EO-derived phenological indicators for the identification of transplanting windows, even at early stages of the growing season.

3.4 Validation

The crop rotation analysis performed over an agricultural area of approximately 14,075 ha for the 2020–2024 period highlighted a limited temporal persistence of processing tomato cultivation. Approximately 65.7% of the area was not cultivated with tomatoes during the analyzed period, while 26.7% hosted tomato crops for only one year. Continuous or quasi-continuous tomato cultivation was relatively rare, with only 2.7% of the area cultivated for two or three consecutive years.
The remaining fraction of the area was planted with tomatoes twice over the five years (from 2.21% to 0.79% of the total cropped area), but with variable temporal gaps between plantings, ranging from one to three years. These findings confirm that crop rotation information alone can provide a reasonable, albeit uncertain, basis for very early forecasts of tomato cropped area (UC1), while also highlighting the intrinsic limitations of this approach.
The early forecast for tomato crop area showed an tendency toward overestimation for 2024, with an average deviation of approximately +25% compared to the areas derived from on-site land-use surveys. Among the three use cases, for 2023 and 2024, UC2 (early-season forecast issued on 1st May) provided the most accurate estimates, with an overestimation for the two years of approximately +2% and +15% compared to the reference surface observations (Fig. 5).

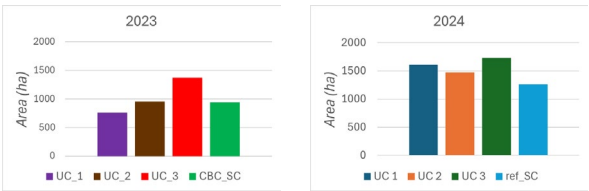

Figure 5. Total tomato field areas identified for the three Use Cases and the surfaces given by the CBC_SC map in 2023 (left) and from land-use surveys (ref_SC) map in 2024 (right).

UC1, based exclusively on crop rotation criteria, was affected by higher uncertainty, whereas UC3 benefited from the integration of additional EO information on tillage and transplanting activities, progressively reducing spatial misclassification errors. These results demonstrate the added value of incorporating EO-derived indicators as the season advances, enabling a gradual refinement of cropped-area estimates.
By integrating early identification of tomato fields with spatially distributed soil and climate information, the THETIS SDSS enabled the initialization of crop growth simulations for the 6/B irrigation district as early as the beginning of April (UC1).

4. CONCLUSIONS

This study demonstrates the potential of integrating EO-derived crop rotation, tillage identification, and phenological indicators for the early identification of tomato cultivation areas in the Apulian Tavoliere. For both 2023 and 2024, the intersection of CBC land-use data with Sentinel-2–based vegetation classes provided a robust reference for tomato area estimation, further improved with tillage information.
Among the early forecasting approaches, UC1, based solely on crop rotation, proved informative but was affected by higher uncertainty due to limited historical depth. UC2, relying on early-season tillage information, achieved the best balance between timeliness and accuracy, while UC3 showed increased overestimation linked to non-specific tillage practices and the presence of other summer crops.
The identification of consistent transplanting windows in May and June confirmed the reliability of EO-based phenological analysis.
Overall, the results highlight that the progressive integration of multi-source EO information significantly improves spatial accuracy and supports early-season decision-making. This demonstrates how EO-driven early field identification can shift irrigation planning from a reactive to a predictive approach at the irrigation-district scale. This approach enables the timely initialization of crop growth simulations within the THETIS SDSS, offering a valuable tool for early irrigation and agricultural management at the district scale.
In addition, the THETIS project delivered a dedicated WEBGIS platform (https://teti.irea.cnr.it/demo/) that allows authorized users to visualize and download spatial products, maps, and associated data, facilitating the operational uptake of SDSS outputs by irrigation managers and stakeholders.

ACKNOWLEDGEMENTS

The project “EarTH Observation for the Early forecast of Irrigation needS” (THETIS) has been funded by ASI under Agreement N. 2023-52-HH.0 and N. 2023-52-HH.1-2025 in the framework of ASI’s program “Innovation for Downstream Preparation for Science” (I4DP_SCIENCE).

REFERENCES

Iacobellis, V., et al., 2024. Advancing Sustainable Water Management in Southern Italy through Integrated Hydrological Modeling and Earth Observation. Lecture Notes in Computer Science, vol 14819. Springer, Cham., 217-229. https://doi.org/10.1007/978-3-031-65282-0_14.

Impedovo, D., et al., 2024. A Novel Multi-Speed Dilated Convolutional Deep Neural Network Architecture for Meteorological Forecasting. IEEE International Humanitarian Technologies Conference (IHTC), Bari, Italy, 1-7, doi: 10.1109/IHTC61819.2024.10855081.

Kourgialas, N.N. 2023. How Does Agricultural Water Resources Management Adapt to Climate Change? A Summary Approach. Water, 15, 3991. https://doi.org/10.3390/w15223991

Rinaldi, M., et al., 2024. A crop model for large scale and early irrigation requirements estimation, Proc. of the 2024 IEEE International Geoscience and Remote Sensing Symposium, pp. 2807- 2810, DOI: 10.1109/IGARSS53475.2024.10640683.

Satalino, G., et al., 2024**a**. Earth observation for the early forecast of irrigation needs, Proc. of the 2024 IEEE International Geoscience and Remote Sensing Symposium, pp. 4912- 4915, DOI: 10.1109/IGARSS53475.2024.10642240.

Satalino, G., et al., 2024**b**. Copernicus Sentinels for tillage change detection. Proc. of the 2024 IEEE International Geoscience and Remote Sensing Symposium, pp. 1249-1252, DOI: 10.1109/IGARSS53475.2024.10641126.

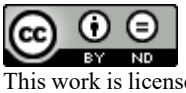

This work is licensed under a Creative Commons Attribution-No Derivatives 4.0 International License.

MODELING AND MAPPING KC DYNAMICS FROM NDVI TIME SERIES USING A DOUBLE LOGISTIC FUNCTION

Ronco E, De Petris S., Ghilardi F., Borgogno Mondino E.

Department of Agriculture, forestry and food, University of Turin, Italy
(edoardo.ronco, samuele.depetris, federica.ghilardi, enrico.borgogno)@unito.it

KEY WORDS: Kc timeseries; Kc-NDVI modeling; Double logistic; Sentinel-2

ABSTRACT:

Evapotranspiration (ET) is a major component of water loss in the soil–plant–atmosphere system and plays a critical role in irrigation management and crop yield estimation. Since direct ET measurements over large areas are rarely available, the FAO Penman–Monteith method is commonly used to estimate reference evapotranspiration (ET_0), which is combined with a crop coefficient (Kc) to calculate crop evapotranspiration. This study presents a method to derive dynamic crop coefficients for corn using Normalized Difference Vegetation Index (NDVI) time series from Copernicus Sentinel-2 imagery. NDVI is used as a spectral proxy of crop development to describe the seasonal evolution of Kc. The NDVI temporal profiles are modeled with a double logistic function, allowing the identification of key phenological stages, including the start of season, peak growth, and end of season. These phenological markers are then linked to the corresponding FAO crop coefficient values (initial, mid-season, and late-season Kc), enabling pixel-level estimation of Kc throughout the growing season. The approach was applied to corn fields in selected areas of the Piedmont region (northwestern Italy), demonstrating the potential of satellite-based phenological modeling to support spatially distributed estimation of crop evapotranspiration.

1. INTRODUCTION

Evapotranspiration (ET) is a key component of the agricultural water balance, critical for irrigation and water resource management under increasing water scarcity. Actual ET (ETa) is commonly estimated via the FAO56 approach (Allen et al., 1998) as the product of reference ET (ET_0) and a crop coefficient (Kc), with ET_0 derived from the FAO Penman-Monteith equation. FAO56 provides tabulated Kc values for discrete phenological stages; however, these coefficients assume ideal conditions and often fail to represent spatial variability, interannual climate effects, and differences in crop vigor or management (Allen et al., 2011).

Satellite remote sensing, particularly vegetation indices such as the Normalized Difference Vegetation Index (NDVI), has become a key tool for monitoring crop development and has been widely used to derive time-varying Kc (Glenn et al., 2011; Kamble et al., 2013a; Patel, 2016a), improving ET estimates when crops deviate from idealized growth curves (Reyes-González et al., 2018). However, linking NDVI to FAO56 Kc remains challenging due to the discrete nature of reference coefficients.

This study proposes a phenology-driven framework that positions FAO56 Kc values along NDVI-derived temporal profiles using a double logistic model to identify start, peak, and senescence stages. The goal is not to estimate ET directly, but to derive temporally explicit Kc profiles under standard conditions, with magnitude anchored to FAO56 reference values. Stress effects are not represented and would require an additional modelling step. This approach enables consistent, parcel-scale mapping of dynamic crop coefficients integrating FAO guidelines with satellite vegetation dynamics.

2. MATERIALS AND METHODS

2.1 Study area and corn parcels

The study was conducted in areas of interest (AOI - Fig.1) located in Piedmont region (northwestern Italy), a major agricultural area of the Po Valley where corn is one of the dominant summer crops. In this study, corn fields were selected within AOI using Geospatial Aid Application (GSAA) data. GSAA is a vector layer containing geometries that represent the declarations submitted by farmers for obtaining public contributions under the common agricultural policy. This dataset includes the parcels shape and the corresponding declared crop. GSAA data for the years 2021, 2022, and 2023 were collected, and 100 fields were selected, covering a total area of 425 ha, in which maize was continuously cultivated over the three-year period (Fig 1). Four parcels greater than 6 ha were selected as reference fields for validating proposed method having a spatial extent that ensure the consistency with raster data subsequently adopted.

2.2 Available data

2.2.1 Sentinel-2 imagery: All Sentinel-2 Level-2A (S2) imagery covering the area of interest (AOI) was acquired from the Sentinel-2 Harmonized (S2_HARMONIZED) collection available in Google Earth Engine (GEE). This collection provides atmospherically corrected surface reflectance data, ensuring radiometric consistency across sensors and acquisition dates. All available images within the study period were selected to maximize temporal coverage and support continuous monitoring of corn development over the AOI. About 230 images were analysed directly on GEE.

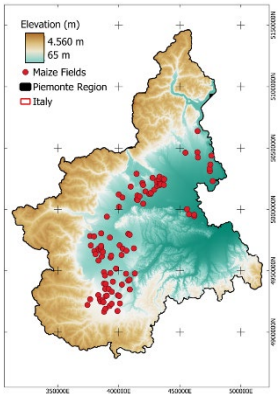

Figure 1. Selected corn areas locations within Piedmont region NW-Italy. The coordinates reference system is WGS84 / UTM32N.

* Corresponding author

2.2.2 FAO56 reference crop coefficients: Within the FAO56 framework, the Kc is a dimensionless parameter that accounts for crop-specific characteristics influencing evapotranspiration, including canopy development, aerodynamic resistance, and ground cover. For maize (*Zea mays* L.), FAO56 provides reference Kc values corresponding to three main growth stages under standard conditions: an initial stage coefficient (*Kc_ini* = 0.30) representative of bare soil or early crop emergence; a mid-season coefficient (*Kc_mid* = 1.20), associated with full canopy cover and maximum transpiration; and an end-season coefficient (*Kc_end* = 0.60), reflecting canopy senescence and reduced transpiration rates. These values describe the typical seasonal evolution of corn water dynamics under well-watered conditions and uniform crop development. Although widely adopted, FAO56 reference Kc values are defined for idealized conditions and fixed growth stages, and therefore do not explicitly account for spatial variability, interannual climate variability, or differences in actual crop phenology. This limitation motivates the integration of FAO reference coefficients with satellite-derived indicators of crop development to enable dynamic and spatially explicit estimation of Kc.

2.2.3 Reference data: To evaluate the performance of the proposed method for Kc estimation, reference data were derived from the FAO WaPOR (Water Productivity through Open access of Remotely sensed derived data). Specifically, WaPOR raster products at medium spatial resolution were used, providing spatially distributed estimates of both reference ET_0 and ETa. These data were obtained from the FAO WaPOR datasets available in the GEE data catalog. Specifically, the FAO/WAPOR/2 (and v3) Level-1 collections were used, which provide spatially distributed evapotranspiration products at medium spatial resolution (about 300 m). Both ETa (provided as actual evapotranspiration and interception, AETI) and ET_0 (reference evapotranspiration, RET) are available at a dekadal temporal resolution, with each image representing the average daily evapotranspiration over a ten-day period. These datasets ensure consistent spatial coverage and temporal continuity over the study period and allow the derivation of reference Kc maps by computing the ETa/ET_0 ratio for each pixel resulting in spatially explicit maps of reference Kc, which were used as an independent benchmark to assess the Kc estimates derived from the proposed NDVI-based methodology. To ensure temporal consistency with Sentinel-2 observations, only WaPOR decades closest to the corresponding Sentinel-2 acquisition dates were selected.

2.3 Data processing

2.3.1 NDVI time series generation: S2 imagery was processed directly within the GEE environment. Cloud and cloud-shadow contamination were removed using the Scene Classification Layer (SCL) provided with the Level-2A products, retaining only pixels classified as clear vegetation or bare soil. NDVI was computed for each cloud-free acquisition. For each corn parcel, a median NDVI value was extracted at each acquisition date in order to reduce the influence of outliers, mixed pixels, and boundary effects that may affect mean-based statistics. The resulting NDVI time series were then exported from GEE and further processed in the *R* environment for subsequent phenological analysis and modelling steps.

2.3.2 Start of season detection: The computation of the start of season (SOS) served two main purposes in this study. First, SOS was used to guide the temporal placement of *Kc_ini*, which represents the evapotranspiration conditions of the crop during the early growth stage, when vegetation cover is sparse and soil evaporation dominates following crop emergence. Because *Kc_ini* is defined at the onset of effective crop development, it can be consistently associated with the SOS identified from the NDVI time series. Second, SOS was used to detect and exclude potential double-cropping systems, ensuring that only summer maize phenological cycles were considered. To identify SOS from the NDVI time series, a threshold-based approach was adopted. Vegetation phenology studies commonly use either absolute or relative NDVI thresholds to detect transitions between phenophases, with thresholds empirically selected to match crop development patterns depending on crop type and local conditions (You et al., 2013). In this study, an absolute NDVI threshold of 0.3 was selected to indicate the onset of substantial vegetative activity, reflecting the emergence and rapid green-up typical of irrigated maize. The SOS was defined as the first date at which NDVI remained above this threshold continuously for at least two months, thereby minimizing the influence of short-lived fluctuations or noise in the time series. Similar threshold criteria have been shown to provide robust estimates of key phenological dates when adapted to specific crop characteristics, although optimal thresholds can vary by crop and environment (Li et al., 2023). This method ensured a consistent identification of the phenological onset of maize across the study area and formed the basis for subsequent linkage with crop coefficient dynamics. The computation of SOS was necessary not only to characterize crop phenology, but also to verify the temporal consistency of the declared crop type within the area of interest. Although the analyzed parcels were classified as corn according to GSAA records, the presence of double-cropping systems (e.g., winter crops followed by a summer crop) cannot be excluded. Therefore, parcels exhibiting an SOS before March (day of year < 90) were interpreted as winter crops, whereas parcels with SOS occurring after March were considered to represent summer crops, characterized by a phenological development starting in spring and ending in late summer. This criterion allowed the exclusion or appropriate interpretation of parcels not representative of the targeted irrigated maize growing season.

2.3.3 Placing Kc-NDVI values strategy: To establish a robust relationship between Kc and vegetation dynamics, NDVI temporal profiles were first modeled using a double logistic function fitted by nonlinear least squares. The fitting procedure was implemented in the *R* environment using the *nlsLM* algorithm, which ensures stable convergence for nonlinear models. The adopted double logistic model is defined as:

$$NDVI(t) = y_0 + (y_m - y_0)\left[\frac{1}{1+e^{-\alpha_1(t-t_1)}} - \frac{1}{1+e^{-\alpha_2(t-t_2)}}\right] \quad (1)$$

where y0 represents the baseline NDVI, ym the maximum NDVI, $\alpha 1$ and $\alpha 2$ control the rates of green-up and senescence, and t1 and t2 correspond to the inflection points of the growth and decline phases, respectively. From the fitted NDVI curve, three key phenological markers were extracted: (i) SOS point (t1) according to previous detection strategy, (ii) the time of maximum NDVI (t2), and (iii) the senescence inflection point (t3). These points were assumed to correspond to the initial, mid-season, and late-season growth stages defined in the FAO56 framework. Accordingly, standard FAO56 crop coefficient values (*Kc_ini, Kc_mid, Kc_end*) were temporally placed at t1, t2, and t3, respectively. The double logistic function assumes

smooth phenological transitions and may not fully capture abrupt disturbances or irregular dynamics. However, these effects are likely reduced by parcel-level NDVI aggregation and the relatively regular phenological development of irrigated maize in the study area.

2.3.4 Modelling and mapping Kc-NDVI coefficients: The proposed approach introduces a novel strategy to link Kc and remotely sensed vegetation dynamics by explicitly accounting for field-specific phenological timing. Although the FAO56 Kc values are fixed and identical for all fields, the use of the double logistic model allows these tabulated coefficients to be placed at different times for each field, thereby locally calibrating the Kc–NDVI relationship according to the observed phenological development. A second innovative aspect of the proposed methodology lies in the formulation of the Kc estimation model. For each field, a bivariate linear regression (eq. 2) without intercept was fitted using the FAO-anchored phenological points, where crop coefficients were expressed as a function of both NDVI and day of year (DoY).

$$K_c(i,t) = \beta_1 \cdot NDVI(i,t) + \beta_2 \cdot DOY(t) \quad (2)$$

where *Kc(i,t)* is the Kc value at *i-th* position and at time *t* denoting spatio-temporal dependence of Kc. The explicit inclusion of the temporal variable (DoY) addresses a key limitation of NDVI-based approaches: the same NDVI value may occur at different stages of the phenological cycle, for example during both the green-up and senescence phases, while corresponding to markedly different evapotranspiration conditions. The temporal term enables the model to disambiguate these situations by incorporating the seasonal context of each observation. The regression coefficients (β1, β2) were estimated and mapped using ordinary least squares and subsequently applied to the complete NDVI time series to derive continuous, field-specific Kc profiles. The spatial distribution of the estimated coefficients and their associated goodness-of-fit (R^2) was then mapped and statistically analyzed using boxplots. Boxplot and maps were computed separately per each year in order to explore spatial and temporal variability of proposed coefficients. Finally, a global model was proposed using the β1 and β2 mean values involving all years and spatial locations coefficients.

2.4 Model Validation

Model validation was performed using Kc values derived from the FAO WaPOR dataset. To ensure a reliable spatial comparison between S2-based estimates and WaPOR products, the validation was restricted to 4 irrigated corn fields with an area larger than 6 ha, selected to guarantee that at least one pure WaPOR pixel (300 m resolution) was fully contained within each field polygon, thus minimizing mixed-pixel effects from neighboring crops. For each selected field, reference Kc values were computed as the ratio between WaPOR ETa and ET_0. These values were then compared with Kc estimates obtained using the proposed NDVI-based method. Model performance was evaluated using the Mean Absolute Percentage Error (MAPE), calculated separately at monthly and annual time scales to assess both intra-annual and inter-annual variability. This validation strategy allowed a consistent evaluation of model accuracy across different temporal aggregations and growing seasons.

3. RESULST AND DISCUSSIONS

3.1 Modelling and mapping Kc-NDVI coefficients

The spatial and temporal patterns of the estimated coefficients (Fig. 2) reflect the combined effect of the data processing and modeling choices adopted in this study. The generation of parcel-based NDVI time series from S2 allowed the extraction of robust vegetation signals representative of field-scale dynamics, minimizing noise related to cloud contamination, mixed pixels, and parcel boundaries. The identification of the SOS further ensured a consistent phenological alignment across fields and years, supporting both the temporal placement of crop coefficients and the exclusion of double-cropping systems not representative of summer maize. Building on these steps, the double logistic modeling of NDVI profiles enabled the identification of key phenological markers and the field-specific placement of FAO56 crop coefficient values, while the bivariate Kc-NDVI-time model explicitly accounted for both spectral and temporal variability in crop development. The latter shows in general high R^2 values (Fig. 2). Looking at the spatial maps and statistical distributions of *Kc(i,t)* model coefficients, we can note not a clear spatial pattern in the estimated regression coefficients β1 and β2, nor in the associated R^2 values. This suggests that the proposed Kc-NDVI relationship is not controlled by localized spatial effects but captures a generalized phenological behavior of irrigated corn across the study area. Moreover, the coefficients remain largely stable over time, suggesting that the sensitivity of Kc to NDVI and seasonal timing is preserved under varying interannual conditions. Although a slight decrease in R^2 is observed in the most recent years, values consistently remain above 0.8, confirming a strong agreement between tabular FAO56-based reference Kc values and NDVI-derived Kc estimates. Overall, these results demonstrate the robustness of the proposed approach and its ability to reliably characterize crop coefficient dynamics across space and time.

3.2 Modelling validation

Finally, a global average model involving β1 = 1.300 and β2 = -0.001 values was proposed (eq. 2). The temporal pattern observed in the MAPE is consistent with findings in the remote sensing literature on NDVI-based crop coefficient estimation. The global Kc-NDVI model shows good agreement with reference values from June through August, when canopy cover is well developed and NDVI reliably reflects transpiration-dominated evapotranspiration. However, higher errors in April and May coincide with the early growth stage, where soil evaporation contributes significantly to total evapotranspiration but is not explicitly accounted for in a single-step crop coefficient formulation. Similar behavior has been documented in studies deriving Kc from NDVI: (Kamble et al., 2013b) found that NDVI-based Kc retrievals tend to diverge from reference evapotranspiration under conditions of sparse vegetation due to unmodeled soil evaporation components.

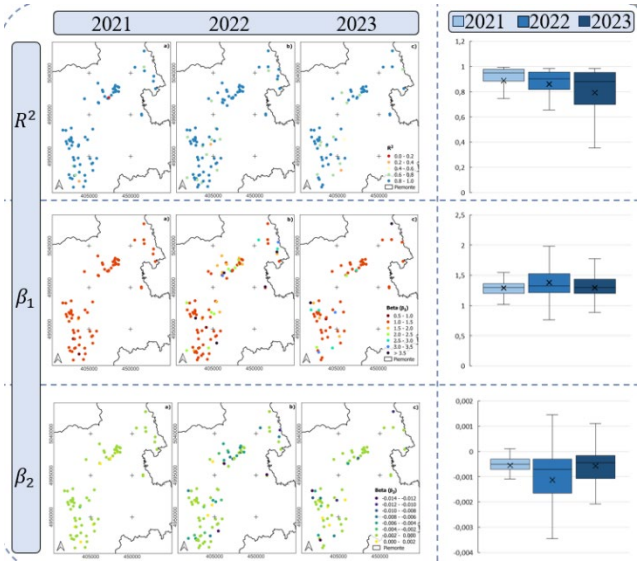

Figure 2. Maps of Kc-NDVI coefficients and related boxplots.

Furthermore, (Patel, 2016b) developed an NDVI-Kc regression model and noted that early season Kc estimates may be biased when canopy development is limited because NDVI predominantly captures vegetation signal but cannot separate transpiration from soil evaporation. These studies suggest the interpretation that a dual crop coefficient approach-distinguishing basal crop transpiration (Kcb) from soil evaporation (Ke)-could help reduce early-season bias and improve the estimation of Kc under incomplete canopy conditions. Therefore, future developments will try to decouple these contributions in Kc.

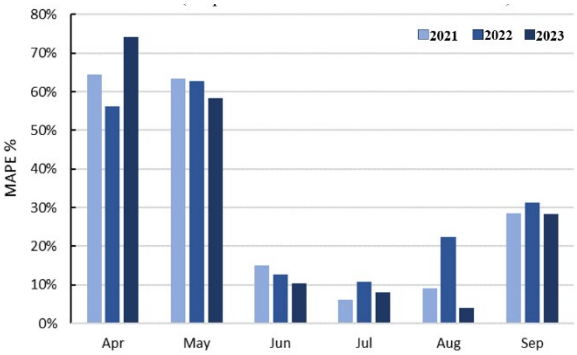

Figure 3. Error analysis of proposed general model.

4. CONCLUSIONS

This study presents a novel approach to estimate dynamic maize crop coefficients by integrating S2 NDVI time series with phenology-driven double logistic modeling. The method enables field-specific temporal placement of FAO56 Kc values and accounts for both spectral and temporal variability, improving the representation of crop evapotranspiration.

Validation against WaPOR reference data demonstrated high accuracy ($R^2 > 0.8$) and highlighted seasonal limitations in early growth stages due to soil evaporation. The workflow is robust across space and time, offering a practical framework for operational irrigation management. Future improvements could include a dual Kc formulation to further reduce early-season bias.

ACKNOWLEDGEMENTS

This research was supported with funding provided by the Italian Ministry of University and Research (MUR) through the Finanziamento dell'Unione Europea – Next Generation EU, Missione 4 "Istruzione e Ricerca" - componente C2 Investimento 1.1 "Fondo per il Programma Nazionale di Ricerca e Progetti di Rilevante Interesse Nazionale (PRIN)" – "Bando PRIN 2022 PNRR", Progetto "EO4DEMOC - Earth Observation For Drought Effects Monitoring On Crops", Prot. P2022MTRNX, CUP "D53D23022890001".

REFERENCES

Allen, R.G., Pereira, L.S., Howell, T.A., Jensen, M.E., 2011. Evapotranspiration information reporting: I. Factors governing measurement accuracy. Agricultural water management 98, 899–920.

Allen, R.G., Pereira, L.S., Raes, D., Smith, M., 1998. Crop evapotranspiration-Guidelines for computing crop water requirements-FAO Irrigation and drainage paper 56. Fao, Rome 300, D05109.

Glenn, E.P., Neale, C.M.U., Hunsaker, D.J., Nagler, P.L., 2011. Vegetation index-based crop coefficients to estimate evapotranspiration by remote sensing in agricultural and natural ecosystems. Hydrological Processes 25, 4050–4062. https://doi.org/10.1002/hyp.8392

Kamble, B., Kilic, A., Hubbard, K., 2013a. Estimating crop coefficients using remote sensing-based vegetation index. Remote sensing 5, 1588–1602.

Kamble, B., Kilic, A., Hubbard, K., 2013b. Estimating crop coefficients using remote sensing-based vegetation index. Remote sensing 5, 1588–1602.

Li, H., Li, F.Y., Guo, J., Gao, X., 2023. An improved dynamic threshold method for determining the start of the vegetation greening season in remote sensing monitoring: The case of Inner Mongolia. Ecological Informatics 78, 102378.

Patel, J.N., 2016a. Development of relationship between crop coefficient and NDVI using geospatial technology. Journal of Agrometeorology.

Patel, J.N., 2016b. Development of relationship between crop coefficient and NDVI using geospatial technology. Journal of Agrometeorology.

Reyes-González, A., Kjaersgaard, J., Trooien, T., Hay, C., Ahiablame, L., 2018. Assessing accuracy of vegetation index method to estimate actual evapotranspiration. Earth Sci 7, 227–235.

You, X., Meng, J., Zhang, M., Dong, T., 2013. Remote sensing based detection of crop phenology for agricultural zones in China using a new threshold method. Remote Sensing 5, 3190–3211.

This work is licensed under a Creative Commons Attribution-No Derivatives 4.0 International License.

TOWARDS A REGIONAL AGRICULTURAL DROUGHT MONITORING SYSTEM BASED ON EVAPOTRANSPIRATION MODIS PRODUCTS: FIRST ISSUES

E. Ronco [1]* , M. Balin [2], S. De Petris[1], S. Tuand[2], M. Gianinetto [2,] E. Borgogno Mondino[1]

[1] Department of Agriculture, Forestry and Food Sciences, University of Torino, Italy
(edoardo.ronco, samuele.depetris, enrico.borgogno)@unito.it
[2] Department of Architecture, Built Environment and Construction Engineering (DABC), Politecnico di Milano
(mirco.balin, marco.gianinetto)@polimi.it
Salvatore.tuand@mail.polimi.it

KEY WORDS: Reference evapotranspiration, MOD16, PET, regional calibration, ET_0 estimation

ABSTRACT:

Increasing frequency and severity of drought events are enhancing water stress in Italian agriculture, highlighting the need for reliable evapotranspiration information at regional scale. However, ground-based reference evapotranspiration (ET_0) data are often spatially sparse and insufficient to support irrigation management. This study proposes a regionally calibrated approach to derive ET_0 from the MOD16 potential evapotranspiration (PET) product over the Piemonte region (northern Italy), with a specific focus on the irrigation season (March–October). MOD16 PET estimates were locally calibrated against ET_0 computed from agrometeorological stations using the FAO Penman–Monteith method. The analysis shows that the PET–ET_0 relationship is temporally stable, allowing the use of multi-year averaged correction coefficients. Spatial variability in the correction is primarily controlled by elevation, which was therefore adopted as the sole explanatory variable in an altitude-dependent parameterization. The resulting model, based only on PET and elevation, substantially improves ET_0 estimates, reducing the median mean absolute percentage error from approximately 50–60% to about 20%, particularly during the irrigation season. These results demonstrate the potential of the proposed approach as a simple and effective tool for regional irrigation monitoring and water resource management.

1. INTRODUCTION

In recent years, Italy has experienced increasing climatic variability, with alternating periods of intense precipitation and prolonged drought, significantly affecting agricultural water management (ISPRA, 2023a; 2023b). These conditions have intensified the need for reliable, spatially distributed indicators to support irrigation planning and drought monitoring at regional scale.

Reference evapotranspiration (ET_0) is a key variable for agricultural water management and represents the basis for estimating crop water requirements according to the FAO-56 framework (Allen et al., 1998). ET_0 is defined over a standardized reference surface and depends exclusively on meteorological variables, making it independent of crop type and management practices. Crop evapotranspiration (ETc) is then derived by combining ET_0 with crop-specific coefficients (Kc), allowing the assessment of irrigation demand and water stress conditions.

Despite its central role, ET_0 is generally available only at point scale from meteorological stations or at coarse spatial resolution from reanalysis datasets. At present, no operational ET_0 product exists at spatial resolutions suitable for field- to district-scale agricultural applications. This limitation constrains the use of ET_0 for spatially explicit irrigation management and regional water planning.

Conversely, the MOD16 product provides estimates of potential evapotranspiration (PET) at relatively high spatial resolution. PET represents the atmospheric evaporative demand under non-limiting water conditions but is not formally equivalent to FAO-defined ET_0, as it is derived from a satellite-based implementation of the Penman–Monteith equation and incorporates assumptions related to land surface characteristics.

In this study, we propose a simple and operational method to derive ET_0 from MOD16 PET. The method is based on an empirical alignment between PET and ET_0 calculated from meteorological stations using the FAO-56 Penman–Monteith formulation. The resulting relationship is evaluated with respect to elevation variable to assess its spatial robustness and transferability. The approach is tested over the Piemonte region, with the aim of providing high-resolution ET_0 estimates suitable for operational agricultural and water management applications, prioritizing computational efficiency and data availability over full physical representation of all climatic drivers.

2. MATERIALS AND METHODS

2.1 Study Area

The study area selected for this work is the Piemonte region, located in northern Italy. The region covers approximately 2.7 million hectares, about 35% of which are devoted to agricultural use; of this agricultural area, approximately 59% is irrigated. Piemonte is therefore a region of major agricultural importance, with maize, rice, and forage crops among the dominant cultivated species.

Due to its geographical position at the foothills of the Alpine arc and upstream of the Po River, the region has historically benefited from abundant water availability. However, in recent years, increasing air temperatures, decreasing precipitation, and rising water demand have led to growing water stress, resulting in crop yield losses, particularly during severe drought events such as those observed in 2003, 2007, and 2022.

In this context, accurate hydrological monitoring and efficient water resource management have become essential. Furthermore, Piemonte exhibits pronounced spatial heterogeneity, ranging from plains to hilly and mountainous areas, which allows the proposed model to be tested and calibrated across a wide range of environmental conditions.

2.2 Available data

2.2.1 Satellite and elevation data

In this study the MOD16A2GF version 6.1 product derived from NASA's MODIS sensor was used to retrieve PET estimates. The MOD16 algorithm is based on a modified Penman-Monteith and

* Corresponding author

integrates meteorological reanalysis data with MODIS derived variables such as LAI/FPAR, albedo and land cover information. It was originally developed by Mu et al. 2007 and further refined by Mu et al. 2011 and it provides a global PET estimate at 500m spatial resolution and an 8-day temporal scale. The MOD16A2GF product was selected instead of MOD16A2, as recommended by the MODIS technical team, because the latter is not available for periods prior to 2023. Moreover, the gap-filled (GF) version represents an improved dataset, providing enhanced spatial continuity and data completeness.MOD16A2GF provides PET only over vegetated areas; stations falling within non-vegetated pixels (Section 2.2.3) were therefore excluded. The 8-day PET time series for 2010–2022 were retrieved from Google Earth Engine and extracted at station locations to ensure consistency with ground-based ET_0 observations.
The elevation data were derived from the TINITALY Digital Elevation Model developed by the Italian National Institute of Geophysics and Volcanology (INGV) (Tarquini et al. 2023).

2.2.2 Reference data

The data used to compute reference evapotranspiration, as described in Section 2.3.1, were obtained from the monitoring network of the Regional Agency for Environmental Protection (ARPA). Out of the 336 agrometeorological stations operating in the region, only 37 are equipped with all the sensors required for ET_0 computation and provide complete records for the study period (2010–2022). Of these, 9 stations are located within pixels for which no satellite data are available. The remaining 28 stations were divided into training and validation sets, comprising 23 and 5 stations, respectively. Their spatial distribution is shown in Figure 1.

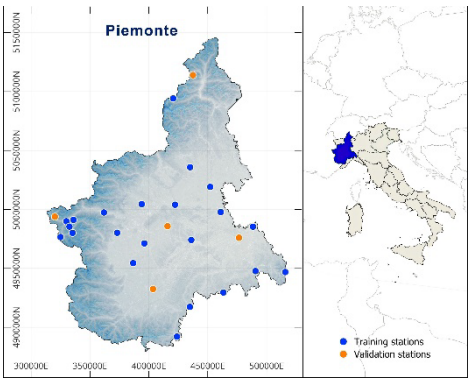

Figure 1. Agrometeorological stations spatial distribution

2.3 Data processing

2.3.1 ET_0 computation

ET_0 depends exclusively on climatic conditions and can therefore be computed using meteorological data. The FAO Penman–Monteith method is the recommended standard for this purpose and requires information on station elevation, latitude, and longitude, together with standard climatological variables: solar radiation (or sunshine duration), daily maximum and minimum air temperature, daily maximum and minimum relative humidity, and wind speed. To ensure computational consistency, all meteorological variables must be measured at a height of 2 m or converted accordingly. Since the ground stations are not equipped with barometers, atmospheric pressure was estimated following Allen et al. (1998).
Ground-station data were filtered to retain observations within the 2010–2022 reference period and further restricted to the months from March to October, corresponding to the irrigation season under the climatic conditions of the study area. Once all required variables were available, ET_0 was calculated using the FAO Penman–Monteith equation (Eq. 1). Daily ET_0 values were then aggregated to an 8-day temporal resolution to match the MOD16A2GF product, excluding aggregation periods with missing daily observations to ensure data consistency.

$$ET_0 = \frac{0.408\Delta(R_n - G) + \gamma \frac{900}{T+273} u_2 (e_s - e_a)}{\Delta + \gamma(1 + 0.34u_2)} \quad (1)$$

Where:

ETo reference evapotranspiration [mm day-1],
Rn net radiation at the crop surface [MJ m-2 day-1],
G soil heat flux density, set to 0 [MJ m-2 day-1],
T air temperature at 2 m height [°C],
u2 wind speed at 2 m height [m s-1],
es saturation vapour pressure [kPa],
ea actual vapour pressure [kPa],
es-ea saturation vapour pressure deficit [kPa],
Δ slope vapour pressure curve [kPa °C-1],
γ psychrometric constant [kPa °C-1]

2.3.2 PET vs ET_0 spatio-temporal comparison

An ordinary least squares (OLS) analysis was carried out in accordance with Eq. 2, modeling a linear relationship between the annual PET time series and the ET_0 one, in order to compare PET and ET_0 and investigate the differences.

$$\widehat{ET_0}(x,y,t) = a(x,y,t) \cdot PET(x,y,t) + b(x,y,t) \quad (2)$$

where x and y denote spatial coordinates (here set in WGS84/UTM32N reference system) and t is the *t-th* year along the full PET-ET_0 time series.
The OLS approach estimates the coefficients a and b, representing the linear gain and offset, respectively, for each meteorological station in the *t-th* year. The model described in Eq. 2 enables the estimation of ET_0 from PET maps derived from the MOD16A2 product. To investigate whether interannual climatic conditions within the AOI influence the variability of the coefficients, boxplots of $a(x, y, t)$ and $b(x, y, t)$ were computed and compared for each year of the analyzed period. Subsequently, the coefficients were averaged across all years to obtain $\bar{a}(x, y)$ and $\bar{b}(x, y)$. These maps represent the mean coefficient values for each meteorological station and summarize the relationship between PET and ET_0.

2.3.3 Modelling ET_0-PET transformation coefficients

Since $\bar{a}(x, y)$ and $\bar{b}(x, y)$ spatially vary, a multivariate regression model was proposed to explore how local environmental conditions, here summarized by altitude (it is related to mean temperature and biomes distribution), can affect coefficients distribution. From DTM the corresponding values at meteorological station location, $A(x, y)$, were sampled and involved in a regression by using OLS relating topographic conditions as independent variables and $\bar{a}(x, y)$ and $\bar{b}(x, y)$ as dependent ones. Therefore two different OLS linear models were fitted: one relating $\bar{a}(x, y)$ vs altitude and the second one relating $\bar{b}(x, y)$ vs altitude.
Estimates from these linear models were combined into a final model (FM) to estimate ET_0 from PET and altitude was proposed in Eq. 3.

$$\widehat{ET_0}(x,y) = [c \cdot A(x,y) + d] \cdot PET(x,y) + [e \cdot A(x,y) + f] \quad (3)$$

where c and e are gain values of linear regressions; $A\ (x, y)$ is the value of altitude at location (x, y); d and f are two offset values. The FM coefficients i.e., c, e, d and f, were calibrated using training sets for AOI. It is worth highlighting that FM in Eq. 3 is no longer dependent on meteorological station data but it depends only on topography making this model more generalizable.

2.4 Model validation

FM developed for AOI was evaluated using independent validation datasets, with performance assessed through the mean absolute percentage error (MAPE), calculated according to Eq. 4.

$$MAPE = \frac{1}{n} \cdot \sum_{i=1}^{n} \left| \frac{\hat{y} - y}{y} \right| \quad (4)$$

In this formulation, y represents the estimated ET_0, while $\hat{y}$ denotes the reference ET_0 values measured at the corresponding ground-based meteorological stations. The MAPE was computed separately to analyze both interannual and intra-annual errors, considering ET_0 values aggregated by year and by month, respectively.

3. RESULTS AND DISCUSSIONS

3.1 PET and ET_0 spatio-temporal comparison

The annual boxplots of the coefficients $a\ (x, y, t)$ and $b\ (x, y, t)$ computed for the Piemonte region (Fig. 2) indicate a weak inter-annual variability. Across the analysed period, both coefficients show stable distributions, with nearly constant median values and limited changes in their dispersion. This behaviour suggests that inter-annual climatic variability within the area of interest has a negligible effect on the estimated coefficients.

On the basis of this temporal stability, all yearly estimates were pooled to derive multi-year mean coefficient maps, $a\ (x, y)$ and $b\ (x, y)$.
These aggregated values provide a representative and robust description of the relationship between MOD16-derived PET and ground-based ET_0 at each station.

Fig. 3 illustrates the spatial patterns of the two coefficients over Piemonte. Higher gain values are mainly observed in the central lowland areas, indicating a strong correspondence between PET and ET_0 and confirming the ability of the model to capture the dominant spatial variability. Conversely, lower gain values are found in the northern, western, and southern sectors of the region, particularly in mountainous and topographically complex areas. Such patterns are consistent with previous findings showing larger discrepancies between PET and ET_0 at higher elevations, where topography and vegetation heterogeneity play a significant role (Dias et al. 2021).

The spatial distribution of errors (Fig. 3) further highlights that in the central plains and hilly zones, which are largely characterized by agricultural land use, PET values tend to exceed ET_0. This systematic behaviour implies the need for higher correction factors to obtain accurate ET_0 estimates from MOD16. Overall, the observed spatial patterns reflect the combined effects of land cover, topography on the PET–ET_0 relationship.

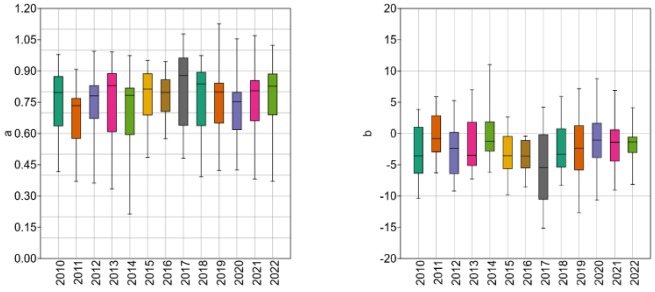

Figure 2. Annual boxplots of coefficient $a\ (x, y, t)$ (left panel) and $b\ (x, y, t)$ (right panel).

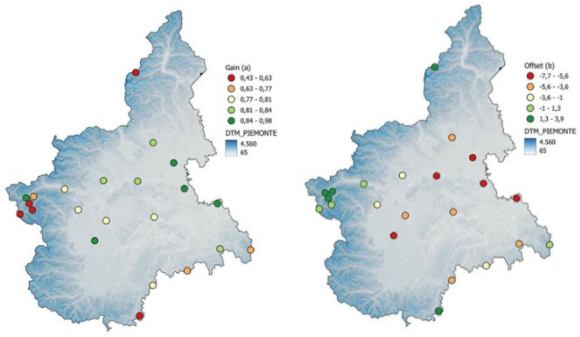

Figure 3. Spatial distribution of *a(x,y)* (left panel) and *b(x,y)* (right panel).

3.2 Modelling ET_0-PET transformation coefficients

The elevation-dependent formulation of ET_0 shows statistically robust and physically consistent behaviour in the Piemonte region. As reported in Table 1, the coefficient c is negative and highly significant, indicating a systematic reduction in the sensitivity of ET_0 to PET with increasing altitude, while the positive coefficient e represents a compensating additive effect associated with elevation. The PET-related term explains a large portion of the variability (R^2 = 0.76, Table 1), whereas the additive altitude-dependent term provides a secondary but non-negligible contribution. The overall model performance (R^2 = 0.65, Table 1) supports the relevance of an altitude-dependent parameterization, although part of the variability remains unexplained. Residual discrepancies suggest the influence of additional local or climatic drivers not explicitly accounted for in the model (e.g. local land cover or biomes).

	Coeff.	s.e.	t	p	r^2
c	-0.39	0.05	7.98	1.21E-07	0.76
d	0.88	0.02			
e	9.65	1.59	6.06	6.3E-06	0.65
f	-5.21	0.66			
r^2	0.65				

Table 1. ET_0-PET model parameters and performance metrics.

3.3 Model validation

Fig.4 and Fig.5 illustrates the mean absolute percentage error (MAPE) obtained from the original MOD16 product and from

the calibrated model for the Piemonte region, using annual and monthly boxplots.

At the annual scale, MAPE values remain highly consistent over the 2010–2022 period, indicating that year-to-year climatic variability has a limited impact on the performance of both MOD16 and the adjusted model. The similarity of the yearly distributions suggests a stable and robust error structure through time.

Seasonal differences become evident in the monthly analysis. Higher MAPE values are observed at the beginning and end of the irrigation season (March and October), while minimum errors occur during the summer months. This pattern reflects the lower evapotranspiration rates outside the core irrigation period, where small absolute errors translate into larger relative deviations, whereas higher summer ET_0 values reduce the relative error magnitude.

A clear improvement is observed when comparing the adjusted model with the original MOD16 estimates. MOD16 typically exhibits median MAPE values around 50–60%, while the calibrated model reduces the error to approximately 20%. This improvement is consistent across both annual and monthly scales. Moreover, the reduced interquartile ranges and shorter whiskers of the adjusted model indicate not only lower median errors but also decreased variability among meteorological stations.

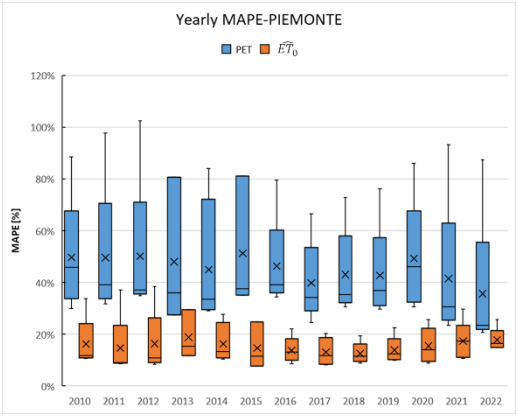

Figure 4. Annual MAPE for the Piemonte region.

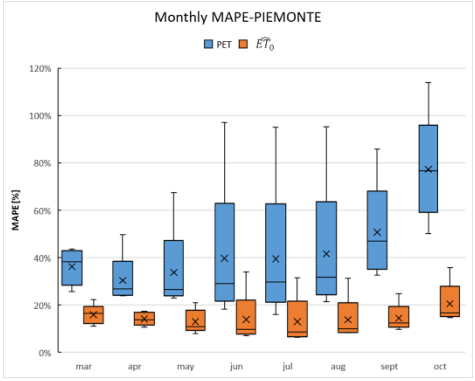

Figure 5. Monthly MAPE for Piemonte region.

4. CONCLUSION

This work introduces a region-specific calibration framework to estimate reference evapotranspiration (ET_0) from MOD16 potential evapotranspiration (PET), addressing the scarcity of high-resolution ET_0 information for agricultural purposes. The analysis shows that the relationship between PET and ET_0 is temporally consistent, allowing the use of correction parameters averaged over multiple years. Spatial variability in the calibration coefficients is primarily controlled by elevation, which emerges as the key explanatory factor in the Piemonte region. The resulting model, based solely on PET and elevation, significantly enhances ET_0 estimation accuracy, lowering the median MAPE from approximately 50–60% to about 20%, especially during the irrigation season. Although the model does not explicitly represent all drivers of the PET–ET_0 relationship (e.g., radiation), elevation provides a practical approximation of the main climatic gradients. This simplification may not capture all local variability, which can contribute to residual model errors, but enables rapid ET_0 estimation using readily available data for regional-scale applications.

ACKNOWLEDGEMENTS

This research was supported with funding provided by the Italian Ministry of University and Research (MUR) through the Finanziamento dell'Unione Europea – Next Generation EU, Missione 4 "Istruzione e Ricerca" - componente C2 Investimento 1.1 "Fondo per il Programma Nazionale di Ricerca e Progetti di Rilevante Interesse Nazionale (PRIN)" – "Bando PRIN 2022 PNRR", Progetto "EO4DEMOC - Earth Observation For Drought Effects Monitoring On Crops", Prot. P2022MTRNX, CUP "D53D23022890001".

REFERENCES

Allen, R. G., Pereira, L. S., Raes, D., Smith, M. (1998). *Crop evapotranspiration: Guidelines for computing crop water requirements*. FAO Irrigation and Drainage Paper No. 56. FAO, Rome, Italy.

Dias, Santos Henrique Brant, Roberto Filgueiras, Elpidio Inacio Fernandes Filho, et al. 2021. «Reference evapotranspiration of Brazil modeled with machine learning techniques and remote sensing». Plos one 16 (2): e0245834.

ISPRA – Istituto Superiore per la Protezione e la Ricerca Ambientale (2023a). *Clima: nuovo record nel 2023 (+1,20 °C delle temperature minime)*. Available online at: https://www.isprambiente.gov.it.

ISPRA – Istituto Superiore per la Protezione e la Ricerca Ambientale (2023b). *Eventi estremi*. Available online at: https://www.isprambiente.gov.it.

Mu, Qiaozhen, Faith Ann Heinsch, Maosheng Zhao, e Steven W. Running. 2007. «Development of a global evapotranspiration algorithm based on MODIS and global meteorology data». Remote sensing of Environment 111 (4): 519–36.

Mu, Qiaozhen, Maosheng Zhao, e Steven W. Running. 2011. «Improvements to a MODIS global terrestrial evapotranspiration algorithm». Remote sensing of environment 115 (8): 1781–800.

Tarquini S., I. Isola, M. Favalli, A. Battistini, G. Dotta (2023). TINITALY, a digital elevation model of Italy with a 10 meters cell size (Version 1.1). Istituto Nazionale di Geofisica e Vulcanologia (INGV). https://doi.org/10.13127/tinitaly/1.1.

This work is licensed under a Creative Commons Attribution-No Derivatives 4.0 International License.

Advancing High-Resolution Retrieval of Soil and Vegetation Water Content from C- and L-band SAR Observations: the SARWATER Project

F. Mattia*, A. Balenzano[1], D. Palmisano[1], S. Rossi[1,2], R. Roseto[1], F. Lovergine[1], A. Belmonte[1], A. Refice[1], F. Bovenga[1], G. Satalino[1], D. G. Miralles[3], N.Verhoest[3], H. Lievens[3], J. Massant[3], M. Rahmati[4], C. Montzka[4]

[1] Consiglio Nazionale delle Ricerche (CNR) - Istituto per il Rilevamento Elettromagnetico dell'Ambiente (IREA), Bari, Italy; Francesco.Mattia@cnr.it
[2] Department of Earth and Geoenvironmental Sciences, University of Bari, Italy
[3] Hydro-Climate Extremes Lab (H-CEL), Ghent University, Ghent, Belgium
[4] Institute of Bio- and Geosciences: Agrosphere (IBG-3), Forschungszentrum Jülich, 52428 Jülich, Germany

KEY WORDS: SAR, Soil Moisture, Vegetation Water Content, ROSE-L, Sentinel-1, NISAR, Change Detection, SMOSAR

ABSTRACT:

High-resolution retrieval of soil moisture (SM) and vegetation water content (VWC) from SAR remains challenging due to complex soil-vegetation interactions and strong sub-kilometre variability. Improving these retrievals is essential for hydrological modelling, agricultural management, weather prediction, and extreme-event monitoring. In the coming years, Sentinel-1 observations will be complemented by several L-band missions (e.g., NISAR, SAOCOM, ALOS-4), paving the way for ROSE-L and creating new opportunities for synergistic C-L band retrieval. This contribution presents the SARWATER project framework and ongoing methodological developments for SM and VWC estimation through multitemporal change-detection applied to polarimetric, incoherent, and coherent SAR observations. The methodology draws on extensive satellite, airborne, and ground-based datasets collected over diverse, well instrumented sites. Illustrative examples are provided, while comprehensive algorithm validation and the assessment of impacts on root-zone soil moisture, evaporation, and irrigation monitoring are currently being conducted within the SARWATER project.

1. INTRODUCTION

Synthetic Aperture Radar (SAR) systems are well-suited for the retrieval of soil moisture (SM) and vegetation water content (VWC), two key variables of the terrestrial water and energy cycles influencing agricultural productivity and hydro-meteorological forecasting. However, achieving robust SM and VWC retrieval, particularly at very high spatial resolution (e.g., $10^2 - 10^3$ m), remains challenging due to the complex scattering mechanisms and the strong spatial and temporal variability in land surface conditions.

Physically based scattering models provide valuable insight into soil-vegetation-radar interactions but often lead to ill-posed inversions due to the large number of unknowns. Machine learning approaches are promising but require large training datasets and may struggle under diverse environmental conditions. Multi-temporal change detection offers a robust alternative by exploiting the distinct temporal dynamics of SM, vegetation, and surface roughness. Operational exploitation of change detection has historically been limited by revisit frequency and coverage. Sentinel-1 changed this landscape, enabling improved monitoring and synergies with coarse-resolution SM products (Lievens et al., 2017). Still, the current Copernicus Soil Water Index (SWI) product at $\sim 10^3$ m resolution does not fully account for vegetation and roughness dynamics. Moreover, the methodology underlying the Copernicus product faces limitations when attempting to push the spatial resolution below 10^3 m. Several alternative approaches have been proposed (Rahmati et al., 2026), yet C-band backscatter remains strongly affected by crop canopies. The forthcoming L-band Radar Observing System for Europe (ROSE-L) mission will mitigate these limitations, and its orbital alignment with Sentinel-1 offers a unique opportunity to jointly exploit C- and L-band SAR observations. Within this context, SARWATER was selected under the European Space Agency (ESA) SAR *Fundamental Scientific Developments* call. The project develops and assesses advanced retrieval algorithms for high-resolution SM and VWC estimation using synergistic C- and L-band observations. This paper outlines the scientific motivations, describes the methodological strategies, and presents a case study illustrating the potential of the proposed framework.

2. WHY IS KILOMETRIC RESOLUTION FOR SM NOT SUFFICIENT?

Recent studies show that SM exhibits strong local heterogeneity driven by fine scale variations in soil properties, topography, land use, and climate (e.g., Vergopolan et al., 2022). Hyper-resolution SM datasets reveal multi-scale patterns that rapidly disappear when aggregated: nearly half of the spatial variability is lost at $\sim 10^3$ m resolution (Chaney et al., 2016). Consequently, operational products and land surface models at kilometre resolutions obscure most field scale SM variability. This scale dependence is illustrated in Figure 1, which shows a mosaic of SM maps at $\sim 10^3$ m resolution derived from Sentinel-1 IWS data acquired over seven adjacent descending orbits. The data were processed using the SMOSAR software developed at CNR IREA, implementing a Short Term Change Detection (STCD) approach consistent with multi temporal incoherent change detection (Balenzano et al., 2021). The mosaic extends from southern Spain to northern Italy. At this scale and resolution, the observed SM patterns primarily reflect the impact of large-scale

* Corresponding author

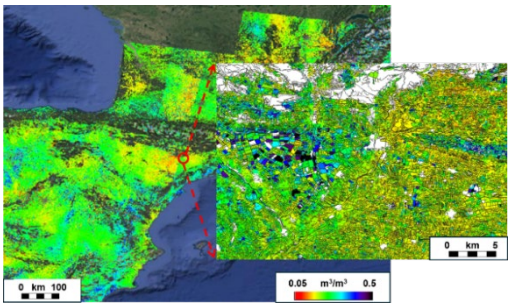

Figure 1. SMOSAR SM map from Sentinel-1 data (June 2018) at $\sim 10^3$ m resolution. The inset shows a $\sim 10^2$ m field-scale map of an irrigated area in Catalonia.

meteorological forces and significant topographic features. In this context, the effects of local land surface variability are mostly masked. However, when we examine smaller spatial scales with higher resolution, the influence of local drivers becomes evident. This is clearly illustrated in the inset in Figure 1, which provides a zoomed-in view of an area in the Ebro River basin in northern Spain. Here, an SM map with a resolution of ~ 100 m (40 m pixel size) is aggregated at the field scale using parcel boundaries, revealing detailed patterns at the landscape level.

These patterns reflect variations in land use, soil texture, and topography, which control key hydrological processes such as infiltration, runoff generation, and evaporation. Understanding the relationship between SM at sub-kilometre resolution and its physical drivers has important implications for agricultural management, weather forecasting, and the monitoring and mitigation of hydrological and meteorological extreme events. This creates a strong demand for accurate, high-resolution SM products below 10^3 m (Peng et al., 2021). At the same time, such products must be accompanied by reliable uncertainty estimates, which are essential for data assimilation and for the integration of independent observational datasets. Moreover, the joint retrieval of related variables, such as VWC and surface roughness, can further enhance the scientific and societal impact of high-resolution SAR based SM observations. The next section illustrates the main objectives, methodology, and assessment strategy adopted in SARWATER.

3. SARWATER: ADVANCING SM AND VWC RETRIEVAL

SARWATER responds to the demands from various user communities for SM products with spatial resolutions well below 10^3 m and temporal resolutions of a few days. To address these requirements, SARWATER explores multi-mission SAR data at both C- and L-band, leveraging a variety of acquisition modes, including polarimetric, interferometric, and bistatic observations, to support the development and assessment of high-resolution SM, VWC retrieval strategies.

3.1 Methodology

The core methodology is STCD and is based on two key assumptions: (i) vegetation effects on the sensitivity of SAR observations to soil moisture are negligible, such that the method can be applied over bare or moderately vegetated areas; and (ii) between two consecutive SAR acquisitions, soil moisture is the only variable that varies, while vegetation properties and surface roughness remain constant. To support assumption (i), dynamic masking of densely vegetated areas is applied in C-band (Satalino et al., 2013). The mathematical framework supporting STCD is derived from Radiative Transfer (RT) theory as it applies to soil and crop scattering. Eq. (1) focuses on the first-order solution of RT, specifically for soil attenuation scattering, while neglecting multiple reflections and volume scattering, which aligns with the requirements of STCD:

$$\begin{cases} \sigma_{0,t_n} \approx \sigma_0^s \cdot \tau^2 = \left|\alpha\left(\varepsilon_{t_n},\theta\right)\right|^2 \cdot \mathrm{F}\left(W_{t_n},\theta,k\right) \cdot \tau^2\left(VWC_{t_n}\right) \\ \frac{\sigma_{0,t_{n+1}}}{\sigma_{0,t_n}} \approx \frac{\left|\alpha\left(\varepsilon_{t_{n+1}},\theta\right)\right|^2}{\left|\alpha\left(\varepsilon_{t_n},\theta\right)\right|^2} \end{cases} \quad (1)$$

where

- σ_{0,t_n} is the radar backscatter observed at t_n, where n indexes the Sentinel-1 time series;
- $\left|\alpha\left(\varepsilon_{t_n},\theta\right)\right|$ is the soil reflection coefficient, which depends on the relative dielectric constant (ε_{t_n}) and the incidence angle (θ);
- $F\left(W_{t_n},\theta,k\right)$ is the Fourier transform of the surface roughness autocorrelation function (W) and k the wave number;
- $\tau^2\left(VWC_{t_n}\right)$ is the two-way vegetation attenuation, which depends on VWC (i.e., $\tau = exp[-b \cdot \sec\theta \cdot VWC]$, with b the vegetation parameter introduced by Jackson and Schmugge (1991).

The approximation in (1), known as "*alpha approximation*" (Balenzano et al., 2011), simplifies the retrieval process, accelerates data processing, and leads to the maximum likelihood analytical solution for the reflection coefficient ($\left|\alpha\left(\varepsilon_{t_n},\theta\right)\right|$), which is then inverted to SM. In SMOSAR, both mean and standard deviation (std) are provided at resolutions ranging between 10^2 and 10^3 m.

3.2 C- and L-band synergy

STCD is initially tailored in this work and will be further extended during the project, with performance assessed across extensive EO, ground, and modeled database. In particular, the synergy between C- and L-band SAR data will be explored under various scenarios. For acquisitions that are co-located in space and time, soil moisture derived from C-band (SM_C) and L-band (SM_L) will be fused through weighted averaging:

$$SM_{CL}(t_n) = w\, SM_C(t_n) + (1-w)\, SM_L(t_n). \quad (2)$$

The weight w depends on the pixel level uncertainty associated with the two estimates and can be computed using different approaches (Granger and Ramanathan, 1984; Cressie, 1993; Tarantola, 2005). For acquisitions that are co-located in space but offset in time, the most suitable fusion strategy will be identified during the project. Once SM_{CL} and the associated $\left|\alpha_{CL}(\varepsilon_{t_n},\theta)\right|$ are retrieved, it is possible to estimate $F(W_{t_n},\theta,k)$ under bare-soil conditions (i.e., when $VWC_{t_n} \approx 0$). Assuming that surface roughness remains approximately constant during the growing season, one can estimate the temporal evolution of vegetation attenuation as

$$\tau^2(VWC_{t_n}) \approx \frac{\sigma_{0,t_n}}{\left|\alpha_{CL}(\varepsilon_{t_n},\theta)\right|^2 \cdot F(W_{t_n},\theta,k)}. \quad (3)$$

The logarithm of τ yields the vegetation optical depth (VOD), from which the corresponding VWC can be retrieved. Eq. (3) can also be evaluated using $\left|\alpha_L(\varepsilon_{t_n},\theta)\right|^2$ instead of the combined C–L term. This alternative formulation is examined in Section 4, where the proposed approach is applied to a case study.

3.3 Database and validation

The SARWATER developments will be assessed at large scale using an extensive SAR database that includes satellite observations (e.g., Sentinel-1, ALOS-2, SAOCOM, NISAR) as well as airborne and ground-based radar datasets from ESA soil- and vegetation-monitoring campaigns (e.g., AGRISAR, SARSENSE, HydroSoil, SARSimHT-NG, AgriROSE-L). These datasets span diverse land-cover and climatic conditions and were acquired over well instrumented test sites, including the Apulian Tavoliere (Italy), Castilla y León (Spain), and the Rur catchment (Germany).

Validation of the improved algorithms will be carried out at the European scale following community standards (Montzka et al., 2021), assessing accuracy, robustness, and transferability across contrasting conditions. The validation strategy will include comparisons against *in situ* SM measurements from global networks (e.g., ISMN), consolidated coarse-resolution products (e.g., SMOS, SMAP), and reanalysis datasets (e.g., ERA5).

3.4 Impact Demonstration

Two demonstration cases illustrate potential impacts:

- Rur catchment (Germany): assimilation of C- and L-band SM/VWC retrievals into the Global Land Evaporation Amsterdam Model (GLEAM) (Miralles et al., 2025) to assess improvements in root-zone SM, vegetation stress detection, and evaporation.
- Apulian Tavoliere (Italy): field-scale irrigation detection and classification using high-resolution SM products, with validation from *in situ* observations.

4. CASE STUDY: AGRISAR CAMPAIGN

The AGRISAR campaign (Hajnsek et al., 2007) provides a well-characterized dataset for evaluating C–L synergy. From April to August 2006, sixteen European institutions conducted coordinated ground and airborne campaigns, including soil, vegetation, atmospheric, and radiometric measurements, as well as surface energy-budget estimates. The study area, located in northern Germany, is known as the Görmin test site (Figure 2). The analysis focused on the twelve C- and L-band acquisitions collected along the east-west track. Time series of SM and associated uncertainty maps (Figure 3) were independently derived from the C- and L-band airborne acquisitions using an appropriately adapted version of SMOSAR (Palmisano et al., 2020). Table 1 compares the metrics (ubRMSE, bias, and Pearson correlation) of the C- and L-band soil moisture retrievals in VV polarization. It is worth mentioning that the incidence angle ranges from ~30° to ~50°. Subsequently, the time series of VWC maps was derived using SM_L in Eq. (3).

SM	C-band Wheat (221, 230, 250)	L-band Wheat (221, 230, 250); Rape (110, 140)
ubRMSE (m^3/m^3)	0.05	0.08
Bias (m^3/m^3)	0.06	0.02
R	0.8	0.7
# points	33	55

Table 1. Metrics of SM retrieved vs observed

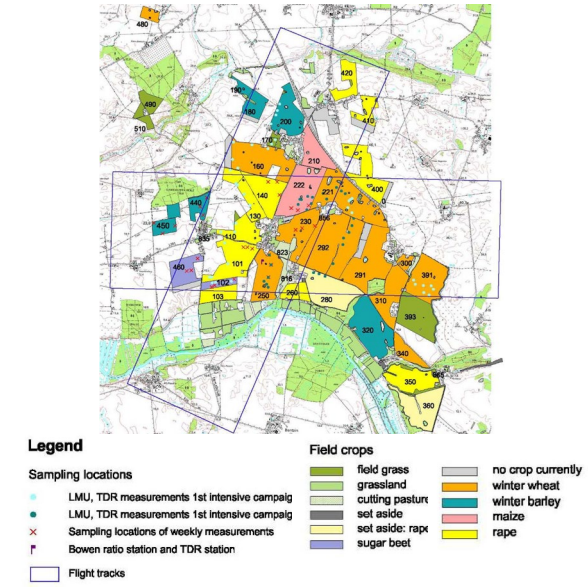

Figure 2. Görmin site showing field crops, *in situ* sampling locations, and east–west/north–south flight tracks used for the C- and L-band acquisitions (after Hajnsek et al., 2006).

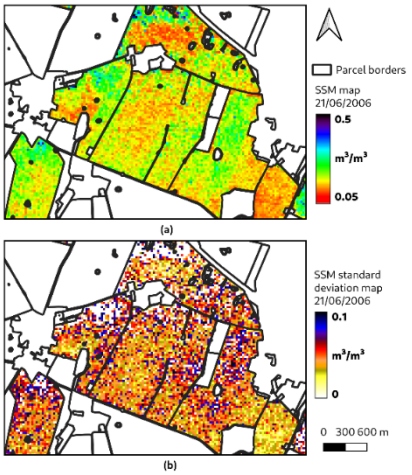

Figure 3. L-band maps of (a) SM and (b) the associated uncertainty over wheat fields on 21 June 2006.

The factor $F(W_{t_n}, \theta, k)$ was estimated at the end of the season (when wheat was either harvested or about to be) and kept constant throughout the analysis. Figure 4 presents an example of VWC map for June 21 and time series of retrieved and observed VWC over field 221. Table 2 reports the metrics for the comparison between the retrieved and observed VWC.

VWC	C-band Wheat (221, 230, 250)
ubRMSE (kg/m^2)	1.1
Bias (kg/m^2)	0.15
R	0.6
# points	20

Table 2. Metrics of VWC retrieved vs observed

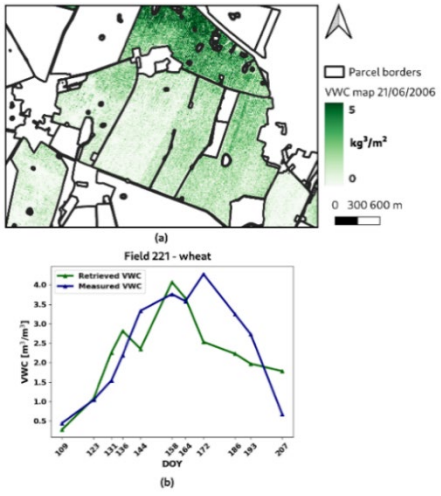

Figure 4. (a) VWC map on 21 June and (b) temporal evolution of retrieved and observed VWC for wheat field 221

5. SUMMARY & OUTLOOK

SARWATER aims to deliver a robust and scalable retrieval framework that integrates STCD with C–L multi-frequency sensing to enhance SM and VWC estimates and quantify their uncertainties. The project prioritizes physically based, robust methodology, harmonized processing across sensors, and standardized large-scale validation using ground networks and reference products. Demonstration activities will highlight end-user value by supporting irrigation detection and classification and by improving root-zone SM and evaporation estimation through data assimilation, thereby providing quantitative evidence of algorithm transferability (Balenzano et al., 2022; Rossi et al., 2026). Future developments will focus on optimizing C–L fusion schemes, refining canopy attenuation and $VOD - VWC$ relationships, and preparing for operational synergy between Sentinel-1 and ROSE-L, including open-access product dissemination. The case study presented here serves only as an illustrative application within this broader framework; comprehensive validation and performance assessment will be conducted at project scale.

ACKNOWLEDGEMENTS

The authors gratefully acknowledge funding from ESA through the SAR Retrieval of Soil and Vegetation WATER Content (SARWATER) project, under Contract No. 4000148119/25/I-EB-BGH.

REFERENCES

Balenzano, A., et al., 2011. Dense temporal series of C-and L-band SAR data for soil moisture retrieval over agricultural crops. IEEE Journal of Selected Topics in Applied Earth Observations and Remote Sensing, 4(2), pp.439-450.

Balenzano, A., et al., 2022. Sentinel-1 and Sentinel-2 data to detect irrigation events: Riaza Irrigation District (Spain) case study. Water, 14(19), p.3046.

Balenzano, A., et al., 2021. Sentinel-1 soil moisture at 1 km resolution: a validation study. Remote Sensing of Environment, 263, p.112554.

Chaney, N.W., et al., 2016. A field-scale resolving land surface model for application over continental extents. Hydrological processes. Sep 30;30(20):3543-59.

Cressie, N. 1993. Statistics for Spatial Data. Wiley.

Granger, C. W. J. and Ramanathan, R. 1984. Improved methods of combining forecasts. Journal of Forecasting, 3, 197–204.

Hajnsek, I., et al., 2007. AgriSAR 2006—Airborne SAR and optics campaigns for an improved monitoring of agricultural processes and practices. Geophys. Res. Abstr, Vol. 9, p. 04085.

Jackson, T.J. and Schmugge, T.J., 1991. Vegetation effects on the microwave emission of soils. Remote Sensing of Environment, 36(3), pp.203-212.

Lievens, H., et al., 2017. Joint Sentinel-1 and SMAP data assimilation to improve soil moisture estimates. Geophysical research letters 44.12: 6145-6153.

Miralles, D. G., et al., 2025. GLEAM4: global land evaporation and soil moisture dataset at 0.1 resolution from 1980 to near present. Scientific data, 12.1: 416.

Montzka, C., et al., 2021. Soil moisture product validation good practices protocol. *Version 1.0*. In: C. Montzka, M. Cosh, J. Nickeson, and F. Camacho (Eds.): Good Practices for Satellite Derived Land Product Validation (p. 123), Land Product Validation Subgroup (WGCV/CEOS).

Palmisano, D., et al., 2020. Sentinel-1 sensitivity to soil moisture at high incidence angle and the impact on retrieval over seasonal crops. IEEE Transactions on Geoscience and Remote Sensing, 59(9), pp.7308-7321.

Peng, J., et al., 2021. A roadmap for high-resolution satellite soil moisture applications–confronting product characteristics with user requirements. Remote Sensing of Environment, 252, p.112162.

Rahmati, M., et al., 2026. Soil moisture retrieval from Sentinel-1: Lessons learned after more than a decade in orbit. Remote Sensing of Environment, 333, p.115146.

Rossi, S., et al., 2026, Adaptive Unsupervised Detection of Field-Scale Irrigation from High-Resolution SAR Soil Moisture Maps. Remote Sensing. 2026; 18(12):1871..

Satalino, G., et al., 2013. C-band SAR data for mapping crops dominated by surface or volume scattering. IEEE Geoscience and Remote Sensing Letters, 11(2), pp.384-388.

Tarantola, A. 2005. Inverse Problem Theory and Methods for Model Parameter Estimation. SIAM.

Vergopolan, Noemi, et al., 2022. High-resolution soil moisture data reveal complex multi-scale spatial variability across the United States. Geophysical Research Letters, 49.15.

This work is licensed under a Creative Commons Attribution-No Derivatives 4.0 International License.

ADVANCED SATELLITE TECHNOLOGIES AND SYSTEMS FOR ENVIRONMENTAL MONITORING AND SUSTAINABILITY IN AGRICULTURE

L. Servadei *

CREA - Council for Agricultural Research and Agricultural Economics, Via della Navicella 2–4, 00184 Rome, Italy – (l.servadei@masaf.gov.it)

KEY WORDS: Space technologies, Remote sensing, Environmental sustainability, Monitoring, Precision agriculture, Sentinel, CAP, Eco-schemes

ABSTRACT:

The adoption of innovative solutions that leverage satellite observation and space technologies represents one of the most promising frontiers for addressing the challenges of environmental sustainability in agriculture. This paper provides a methodological and applicative review of Earth observation satellite technologies for agricultural monitoring and sustainability, illustrating the operational framework adopted in Italy as a concrete case study. The use of multispectral and radar data from the Sentinel-1 and Sentinel-2 missions of the Copernicus program, combined with IoT field sensors, machine learning algorithms, and forecasting models, enables the development of integrated solutions for the dynamic monitoring of agricultural practices and the mapping of environmental parameters. Specifically, the framework of the CAP Area Monitoring System (AMS), integrated with the SIAN - National Agricultural Information System, is described. This framework enables the automatic monitoring of 100% of declared parcels and the verification of commitments related to the CAP 2023–2027 eco-schemes. Finally, applications for precision agriculture and the prospects offered by integration with artificial intelligence and new satellite platforms are analyzed.

1. INTRODUCTION

The agricultural sector faces unprecedented challenges related to climate change, food security, and the need to preserve natural resources. In this context, space technologies are emerging as key tools for promoting more sustainable and resilient production models (Weiss et al., 2020).

Satellite Earth observation offers a tool for monitoring agricultural activities on a large scale, enabling the collection of timely and continuously updated data on crop health, soil properties, and environmental dynamics. The European Space Agency's Copernicus program, with its Sentinel missions, represents a strategic resource for monitoring and implementing decision support systems in agriculture (Segarra et al., 2020).

The integration of satellite technologies with national information systems and artificial intelligence tools opens up new opportunities for the implementation of the Common Agricultural Policy (CAP) 2023-2027, particularly with regard to controls relating to climate and environmental support schemes (eco-schemes) and enhanced cross-compliance. This paper provides a methodological and applicative review of satellite technologies for monitoring and environmental sustainability in agriculture. In addition to providing an overview of the main available technologies, the paper illustrates the operational framework adopted in Italy within the CAP Area Monitoring System (AMS), presenting it as a concrete case study of the integration between Copernicus data and the National Agricultural Information System (SIAN). The aim is to outline a reference framework that links satellite technological capabilities to the operational needs of sustainable agricultural management in the Italian context.

2. SATELLITE TECHNOLOGIES FOR THE OBSERVATION OF AGRICULTURAL AREAS

The Copernicus programme provides free and open Earth observation data through several satellite missions. The Sentinel-1 and Sentinel-2 missions are particularly relevant for agricultural applications due to their complementary technical characteristics (Filipponi, 2019).

Sentinel-1 is equipped with C-band synthetic aperture radar (SAR) sensors, capable of acquiring images regardless of weather and light conditions. This feature allows continuous monitoring even in the presence of cloud cover. SAR data are particularly useful for detecting soil moisture, monitoring irrigation practices, and identifying flood events (Mandal et al., 2020).

Sentinel-2, on the other hand, operates in the optical domain with a spatial resolution of up to 10 meters and a revisit frequency of 5 days. Its 13 spectral channels enable the calculation of numerous vegetation indices and detailed analysis of the phenological status of crops. The combination of optical and radar data allows for a comprehensive characterization of agricultural systems.

Multispectral data processing allows us to derive vegetation indices that provide quantitative information on crop health. The Normalized Difference Vegetation Index (NDVI) is the most widely used index for assessing vegetation development and estimating biomass.

The temporal analysis of these parameters allows us to monitor crop phenological development, identify water or nutritional stress, and detect diseases or pests early. Furthermore, comparison with historical series allows us to assess production anomalies and support risk management.

* Corresponding author

3. APPLICATIONS FOR ENVIRONMENTAL SUSTAINABILITY IN AGRICULTURE

Satellite technologies support the monitoring of agricultural practices critical to environmental sustainability. Crop rotation can be tracked through the temporal analysis of spectral signatures, allowing for verification of production diversification and compliance with agri-environmental commitments (Belgiu and Csillik, 2018). Methodologically, crop classification is based on the application of supervised algorithms, such as Random Forest and Support Vector Machine, to time series of vegetation indices (NDVI, EVI) derived from Sentinel-2, with overall accuracies exceeding 85% in heterogeneous agricultural contexts such as those in Italy.

The detection of winter cover crops that reduce erosion and increase carbon sequestration is facilitated by the integration of optical and radar data. In particular, Sentinel-1 SAR data allow the presence of vegetation cover to be detected even in persistent cloudiness, typical of winter, through the analysis of the backscatter coefficient in VH and VV polarization. Table 1 summarizes the main applications of satellite technologies for monitoring sustainable agricultural practices.

Agricultural Practice	Satellite	Monitored Parameters	Frequency
Crop Rotation	Sentinel-2	NDVI, Spectral Signatures Seasonal	Seasonal Critical
Cover Crops	Sentinel-1, Sentinel-2	Backscatter SAR, NDVI	Monthly
Residue Management	Sentinel-2	Crop Residue Indices	Post-harvest
Soil Erosion	Sentinel-2	Bare Soil Exposure	Criticism
Water Stress	Sentinel-1, Sentinel-2	Soil Moisture, NDWI	Weekly

Table 1. Main applications of Sentinel satellites for monitoring sustainable agricultural practices

Soil organic carbon (SOC) is a key indicator of soil fertility and carbon sequestration capacity. Remote sensing technologies integrated with in situ surveys and predictive models allow mapping the spatial distribution of SOC at large scales (Castaldi et al., 2019). Specifically, SOC estimation is based on spectral analysis of the visible and near-infrared bands (Sentinel-2 bands B4, B8, and B11) acquired on bare soil, using multivariate regression models such as Partial Least Squares Regression (PLSR).

Machine learning algorithms, such as Random Forest and neural networks, applied to multispectral data allow estimating organic carbon content with coefficients of determination (R^2) greater than 0.70 at the regional scale. These tools support the assessment of carbon stocks and the monitoring of temporal variations in relation to adopted agricultural management practices.

4. INTEGRATION WITH CAP INFORMATION SYSTEMS

The integration of satellite technologies with the SIAN – National Agricultural Information System – represents a significant innovation for the implementation of the CAP in Italy and is the main case study of this work. The Area Monitoring System (AMS), operational in Italy since 2023, uses Sentinel data to automatically verify compliance with farmers' declared commitments on over 4 million agricultural parcels georeferenced in the SIAN (Figure 1).

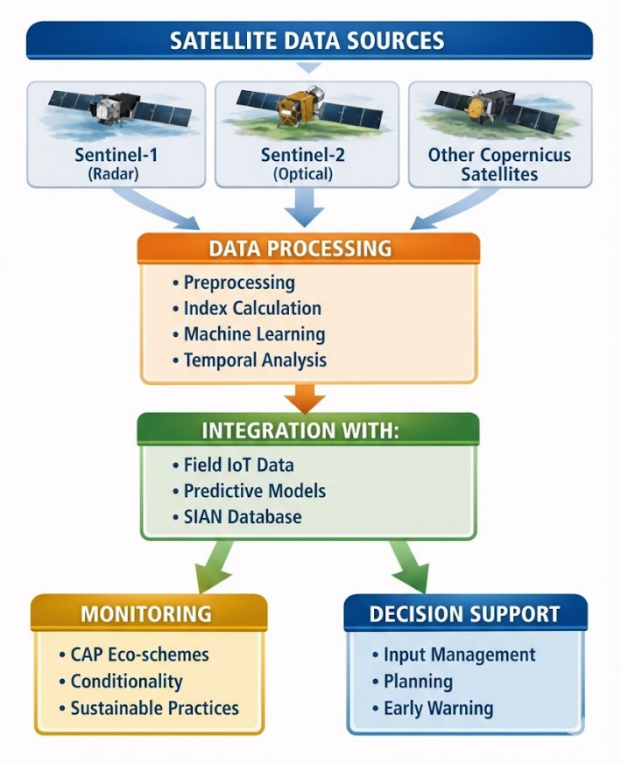

Figure 1. Integrated monitoring system based on satellite technologies for CAP implementation and agricultural sustainability

Pursuant to Regulation (EU) 2021/2116, the AMS is a mandatory component of the Integrated Administration and Control System (IACS), which relies on the use of satellite data from the Copernicus programme to assess the eligibility of agricultural areas and practices (Devos et al., 2019). The IACS represents the framework through which Member States collect, transmit, and validate geospatial information, ensuring data quality for monitoring, control, and reporting purposes under the CAP.

Operationally, the area monitoring system integrates multi-source data from the Sentinel-1 and Sentinel-2 satellites, high-resolution orthophotos, and vector information from Land Parcel Identification Systems (LPIS). In particular, Sentinel-2 imagery enables monitoring of the phenological cycle of crops through multi-temporal analysis of the NDVI vegetation index (Figure 2). The NDVI values are aggregated on a decadal basis ($NDVI_{10g}$) by extracting the maximum value pixel by pixel (Maximum Value Composite, MVC), after removing the areas affected by cloud cover using the Scene Classification Map (SCL) provided by the Sen2Cor processor. The analysis is conducted at the single plot level, applying a minimum threshold of two Sentinel-2 pixel

centroids (10 m) intersecting the plot, in order to guarantee the statistical reliability of the measurements and minimize edge effects.
The resulting NDVI temporal profile allows for the automatic identification of agronomic events such as sowing, flowering, ripening, and harvesting using change-point detection algorithms. The AMS infrastructure is managed nationally by AGEA – the Agency for Agricultural Payments – through full integration with the SIAN.
This approach significantly reduces the need for on-site inspections, with monitoring coverage increasing from 5-10% of traditional sampling to 100% of declared plots, resulting in a reduction in administrative costs and an increase in the overall effectiveness of inspections. Automatic algorithms analyze the time series of vegetation indices, applying decision rules based on NDVI and temporal variation thresholds to identify significant events, such as mowing, plowing, or practices that do not comply with the commitments undertaken. In cases where automatic monitoring does not produce a conclusive result, a second-level verification is carried out through photointerpretation of high-resolution images or field inspections.

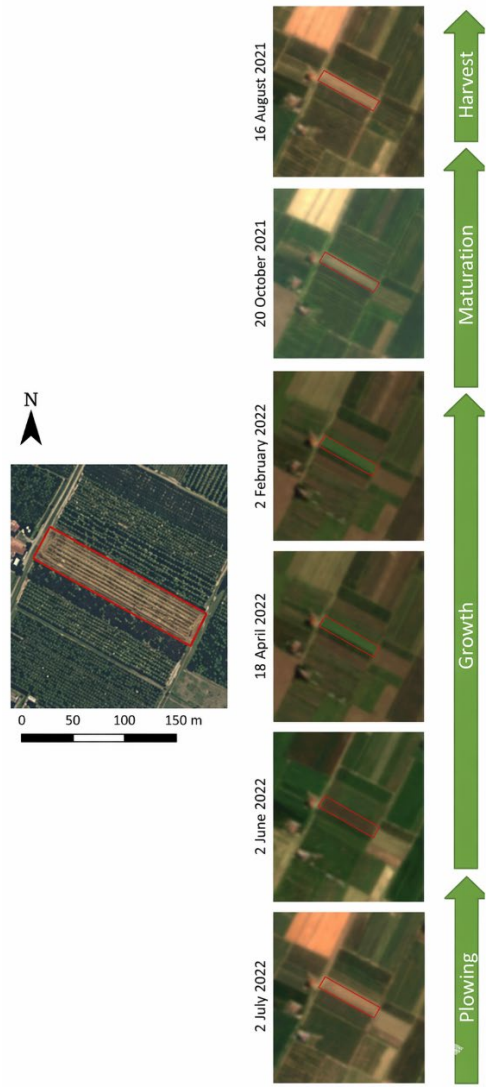

Figure 2. Visual monitoring of a wheat plot using Sentinel-2 multitemporal series. The images show the different phenological phases from sowing to harvest in the period 2021-2022 (Source: AGEA)

A particularly relevant application area for these monitoring systems is the eco-schemes introduced by the CAP 2023-2027, which provide voluntary payments linked to the adoption of agricultural practices beneficial for the environment and climate. In this context, satellite technologies are crucial for verifying the effective implementation of these commitments. For example, for Eco-scheme 4 (Extensive Forage Systems), satellite monitoring verifies compliance with the maximum livestock stocking rate by analyzing grazing intensity, as measured by seasonal variations in NDVI. For Eco-scheme 5 (Specific Measures for Pollinators), the presence of arable land dedicated to spontaneous flora is confirmed through the multitemporal classification of Sentinel-2 imagery.
The system allows tracking practices such as the grassing of tree crops, the presence of characteristic landscape elements, and the sustainable management of water resources. Automatic validation significantly reduces monitoring times and increases the system's transparency.

5. PRECISION FARMING

Satellite technologies also promote precision agriculture by enabling more efficient and targeted management of agronomic inputs based on actual crop needs. Specifically, mapping the spatial variability of soil parameters and vegetation status, achieved by zoning NDVI maps into homogeneous vigor classes, allows for the modulation of fertilizer, plant protection products, and water resources based on actual crop needs (Sishodia et al., 2020).
Satellite observation enables the acquisition of georeferenced and constantly updated data, facilitating differentiated and timely interventions with economic and environmental benefits.
Precision fertilization and irrigation, supported by vegetation cover maps derived from satellite data, enables more rational management of nutrient inputs, allowing for reductions in fertilizer use of up to 20–30% without negatively impacting yields, which in some cases even improve yields. These results are linked to the possibility of modulating doses based on the actual spatial variability of crops and soil and climate conditions (Zhang et al., 2019; Sishodia et al., 2020). Similarly, the targeted application of plant protection products, based on the early identification of areas with greater stress or susceptibility, allows for significantly reduced volumes distributed, limiting losses due to drift and runoff and limiting the overall environmental impact (Gebbers and Adamchuk, 2010).
Integration with IoT sensors in the field allows for further refinement of management choices, providing timely measurements of parameters such as soil moisture, temperature, and electrical conductivity. This synergy between satellite data and field sensors represents the evolution towards intelligent and interconnected agricultural systems.

6. MODEL ANALYSIS AND FORECASTING SCENARIOS

The use of forecasting models integrated with satellite data allows for the simulation of crop growth processes and the assessment of the impact of different management strategies. These tools also support the ex-ante evaluation of agricultural policies and the design of territorial interventions (Jones et al., 2017).
Water balance models, supported by satellite-derived evapotranspiration estimates, allow for irrigation optimization and the identification of areas vulnerable to drought. Similarly, greenhouse gas emission models can be calibrated with remote

sensing data to quantify the carbon footprint of different agricultural practices.
The ability to analyze alternative scenarios is particularly relevant in the context of climate change, allowing for the evaluation of specific adaptation strategies and the identification of the most resilient agricultural practices. These tools are essential for long-term environmentally sustainable agricultural planning.

7. CHALLENGES AND PROSPECTS

Despite the potential of satellite technologies, several barriers exist that limit their widespread adoption. The technical complexity of data processing requires specialized skills that are not always available locally. Therefore, it is necessary to invest in training operators and developing user-friendly interfaces that make these tools accessible to farmers as well (Klerkx et al., 2019).
Data interoperability represents another significant challenge. The integration of heterogeneous data sources requires common standards and adequate digital infrastructure. The lack of connectivity in rural areas also continues to be a barrier to accessing advanced digital services.
Furthermore, the regulatory framework should evolve to incentivize the adoption of innovative technologies, recognizing the value of agricultural data and ensuring operator privacy. The definition of certification protocols for satellite-based services can facilitate the use of these tools.
The future prospects for the use of satellite data are linked to the ongoing evolution of satellite platforms and processing algorithms. New missions, such as constellations of small satellites with high temporal resolution, will enable near-real-time monitoring of agricultural activities.
Furthermore, artificial intelligence and deep learning are revolutionizing satellite imagery analysis, enabling the extraction of increasingly detailed and complex information. Combining data from integrated sensors improves the accuracy of estimates and the robustness of monitoring systems.
Integration with emerging technologies such as agricultural drones and autonomous robots can create integrated digital ecosystems for the almost completely automated and optimized management of crop operations.

8. CONCLUSION

Satellite technologies represent an indispensable tool for addressing the challenges of environmental sustainability in agriculture. This paper provides a methodological review of the main Earth observation technologies applied to the agricultural sector, while also illustrating the operational framework of the Italian Area Monitoring System (AMS) as a concrete case study of the integration of Copernicus data, national information systems, and the CAP. The analysis highlighted how integrating satellite data with field sensors and forecasting models enables the development of operational solutions for monitoring agricultural practices, optimizing input management, and supporting the implementation of rural development policies.
The Italian CAP experience with the integration of the SIAN and satellite-based control systems demonstrates the technical feasibility and effectiveness of this approach. However, fully leveraging these technologies requires adequate investment in digital infrastructure, operator training, and a coherent regulatory framework capable of supporting their development and fostering their large-scale adoption.
Collaboration between public administrations, universities and research institutions, businesses, and farmers is also essential to transform technological innovation into locally-based solutions.
Satellite technologies can strengthen the agricultural system's ability to respond to environmental crises and can provide an opportunity to improve governance and promote the sustainable development of rural areas.
The evolution of satellite platforms and artificial intelligence tools will further expand application possibilities, opening new frontiers for smart, environmentally friendly agriculture.

REFERENCES

Belgiu, M., Csillik, O., 2018. Sentinel-2 cropland mapping using pixel-based and object-based time-weighted dynamic time warping analysis. *Remote Sensing of Environment*, 204, pp. 509–523.

Castaldi, F., Hueni, A., Chabrillat, S., Ward, K., Buttafuoco, G., Bomans, B., Vreys, K., Brell, M., van Wesemael, B., 2019. Evaluating the capability of Sentinel-2 data for soil organic carbon prediction in croplands. *ISPRS Journal of Photogrammetry and Remote Sensing*, 147, pp. 267–282.

Devos, W., Lemoine, G., Milenov, P., Fasbender, D., 2019. *Technical guidance on the decision to go for substitution of OTSC by monitoring*. JRC Technical Report, Publications Office of the European Union, Luxembourg.

Filipponi, F., 2019. Sentinel-1 GRD preprocessing workflow. *Proceedings*, 18(1), 11.

Gebbers, R., Adamchuk, V.I., 2010. Precision agriculture and food security. *Science*, 327(5967), pp. 828–831. https://doi.org/10.1126/science.1183899

Jones, J.W., Antle, J.M., Basso, B., Boote, K.J., Conant, R.T., Foster, I., Godfray, H.C.J., Herrero, M., Howitt, R.E., Janssen, S., Keating, B.A., 2017. Brief history of agricultural systems modeling. *Agricultural Systems*, 155, pp. 240–254.

Klerkx, L., Jakku, E., Labarthe, P., 2019. A review of social science on digital agriculture, smart farming and agriculture 4.0: New contributions and a future research agenda. *NJAS – Wageningen Journal of Life Sciences*, 90–91, 100315.

Mandal, D., Kumar, V., Bhattacharya, A., Rao, Y.S., Siqueira, P., Bera, S., 2020. Sen4Rice: A processing chain for differentiating early and late transplanted rice using time-series Sentinel-1 SAR data with Google Earth Engine. *IEEE Geoscience and Remote Sensing Letters*, 15(12), pp. 1947–1951.

Regulation (EU) 2021/2115 of the European Parliament and of the Council, 2021. Rules on support for CAP Strategic Plans for the period 2023–2027. *Official Journal of the European Union*, L435, pp. 1–186 (CELEX: 32021R2115).

Regulation (EU) 2021/2116 of the European Parliament and of the Council, 2021. Financing, management and monitoring of the CAP. Official Journal of the European Union, L435, pp. 187–262 (CELEX: 32021R2116).

Segarra, J., Buchaillot, M.L., Araus, J.L., Kefauver, S.C., 2020. Remote sensing for precision agriculture: Sentinel-2 improved features and applications. *Agronomy*, 10(5), 641.

Sishodia, R.P., Ray, R.L., Singh, S.K., 2020. Applications of remote sensing in precision agriculture: A review. *Remote Sensing*, 12(19), 3136.

Weiss, M., Jacob, F., Duveiller, G., 2020. Remote sensing for agricultural applications: A meta-review. *Remote Sensing of Environment*, 236, 111402.

Smith, J., 1987a. Close range photogrammetry for analyzing distressed trees. *Photogrammetria*, 42(1), pp. 47-56.

Smith, J., 1987b. Economic printing of color orthophotos. Report KRL-01234, Kennedy Research Laboratories, Arlington, VA, USA.

Smith, J., 1989. *Space Data from Earth Sciences*. Elsevier, Amsterdam, pp. 321-332.

Smith, J., 2000. Remote sensing to predict volcano outbursts. In: *The International Archives of the Photogrammetry, Remote Sensing and Spatial Information Sciences*, Vol. XXVII-B1, pp. 456-469.

This work is licensed under a Creative Commons Attribution-No Derivatives 4.0 International License.

Algorithm, tool and new mission

THE JOINT ASI-NASA/JPL SURFACE BIOLOGY AND GEOLOGY THERMAL INFRARED (SBG-TIR) MISSION

S. Venafra [1] *, S. Zoffoli [1], F. Longo [1], T. Scopa [1], R. Votta [1], G. Viavattene [1], F. Tataranni [1], A. Andrisani [1], D.K. Pallotti [1], V. Martucci [1], M. Orefice [1], R. Pellegrini [1], E. Ciocci [1], M.F. Buongiorno [2], M. Silvestri [2], G.L. Liberti [3], R. Colombo [4], S. Pignatti [5], C. Notarnicola [6], G. Laneve [7], V. Della Corte[8], A. Francioni [9], F. Antonacci [10], R. Basilio [11], S. Hook [11], K.C. Nicholson [11], S. Hunyadi-Lay [11], M. Larson[11], L. White [11], P. Xaypraseuth[11], S. Islas[11]

[1] Italian Space Agency (ASI), Roma, Italy
(* sara.venafra@asi.it)
[2] Istituto Nazionale di Geofisica e Vulcanologia (INGV), Roma, Italy
[3] CNR-ISMAR, Roma, Italy
[4] Università degli Studi di Milano Bicocca (UNIMIB), Milano, Italy
[5] CNR-IMAA, Roma, Italy
[6] EURAC, Bolzano, Italy
[7] Università La Sapienza, Roma, Italy
[8] Istituto Nazionale di Astro Fisica (INAF), Napoli, Italy
[9] Thales Alenia Space Italia (TAS.I), Roma, Italy
[10] Leonardo, Campi Bisenzio (FI), Italy
[11] NASA Jet Propulsion Laboratory, California Institute of Technology, Pasadena, USA

KEY WORDS: Thermal Remote Sensing, Land Surface Temperature and Emissivity, Volcanoes and Fires, Vegetation and Agriculture, Cryosphere, Coastal and inland waters, Urban microclimate monitoring

ABSTRACT:

The Joint ASI - NASA/JPL Surface Biology and Geology Thermal Infrared (SBG-TIR) Mission is designed to advance scientific understanding in areas such as of climate, ecosystem and natural resources, hydrology, weather and solid earth, in response to recommendations from Italian and American national users and communities. The SBG-TIR mission will embark two instruments: the NASA-provided Orbiting Terrestrial Thermal Emission Radiometer (OTTER) instrument and the ASI-provided Visible InfraRed Earth Observation (VIREO) Camera. High spatial resolution observations will be acquired on a global scale, with a 3-days revisit time, with standard and low latency products (available in less than 72 and 24 hours, respectively). The OTTER instrument will acquire data in MIR (3-5 µm) and TIR (8-12 µm) spectral bands during day and night time, while VIREO will provide observations in 3 VNIR spectral bands one PAN (centered at 750 nm) and two VNIR channels (VNIR-0 (centered at 655 nm) and VNIR-1 (centered at 835 nm)) during daytime with a spatial resolution at nadir of 60m over land and 1km over ocean water for OTTER and 30/60m over land for VIREO. All these requirements shall allow for the retrieval of a valuable source of information about geophysical parameters fundamental in the monitoring of natural and anthropogenic changes to the ecosystems, such as emissivity and land surface temperature, evapotranspiration (ET), surface reflectance, Normalized Difference Vegetation Index (NDVI), surface mineralogy, elevated temperature features, volcanic activity data products, etc. This work presents an overview of SBG-TIR mission, data products and their possible applications.

1. INTRODUCTION

1.1 SBG-TIR mission Overview

NASA/JPL and the Italian Space Agency (ASI) are jointly developing the Surface Biology and Geology - Thermal Infrared (SBG-TIR) mission. This partnership supports NASA's Earth System Observatory (ESO) (NASA, 2017a), established by the 2017 Earth Science Decadal Survey (NASA, 2017b), as well as ASI's 2020-2029 Strategic Vision Document for Space approved by the Interministerial Committee (COMINT) (ASI, 2020-2029).
The SBG-TIR mission (Basilio et al., 2022) will support the development of innovative approaches and methodologies that benefit both scientific research and practical applications across a broad field of applications in agriculture, food security, surface water management, conservation, wildfire management, volcanic risk assessment and detecting heat wave events.
The SBG-TIR mission will embark two sensors:

- TIR instrument, named Orbiting Terrestrial Thermal Emission Radiometer (OTTER), provided by NASA.
- VNIR instrument, named Visible InfraRed Earth Observation (VIREO) Camera, provided by ASI.

Multispectral radiometric estimations of surface emission and reflection from the Earth's land, including polar regions, inland water and coastal regions are expected from both instruments.
To maximize scientific impact and strengthen international cooperation, the SBG-TIR mission will collaborate with similar initiatives such as ESA-EC LSTM (ESA, 2020) and CNES-ISRO TRISHNA (CNES-ISRO, 2021). This coordination aims to leverage cross-validation and improve overall science returns, whenever possible.

1.2 SBG-TIR Instrumentation and Observation Mask

The SBG-TIR mission will deliver observations across 8 MIR and TIR spectral bands (3-5 µm and 8-12 µm) during both day and nighttime, provided by the OTTER instrument.

* Corresponding author

Additionally, it features three VNIR bands for daytime use: a PAN channel (centered at 750 nm) and two VNIR channels (centered at 655 nm and 835 nm, respectively), provided by VIREO camera. Comprehensive band specifications for both instruments are reported in the following tables.

Band #	Center Wavelength (μm)	Spectral Width (nm)
MIR-1	3.98	25
MIR-2	4.80	150
TIR-1	8.32	300
TIR-2	8.63	300
TIR-3	9.07	300
TIR-4	10.30	300
TIR-5	11.35	500
TIR-6	12.05	500

Table 1. OTTER Spectral bands

Band #	Center Wavelength (nm)	Spectral Width (nm)
VNIR-0	655	80
VNIR-1	835	80
PAN	750	300

Table 2. VIREO Spectral bands

Figures 1 and 2 illustrate OTTER and VIREO Spectral bands respectively, considering different contributions to the total transmission of the system, such as optical layout, filter transparency, scan mirror and detector quantum efficiency.

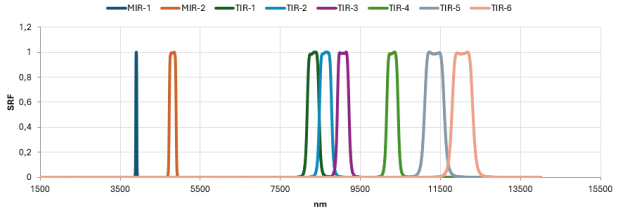

Figure 1. OTTER Spectral Response Functions

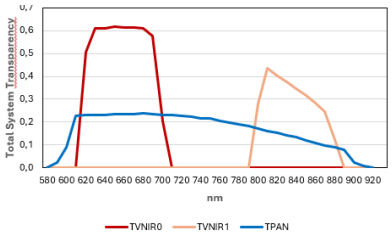

Figure 2. VIREO Spectral Response Functions

The SBG-TIR system will operate in a LEO repeating track sun-synchronous orbit, with a swath width of 935 km, a revisit time <= 3 days, and a spatial resolution of 60m at nadir.

The observations are intended to be acquired at global scale between ± 86° latitude, driven by the coverage mask illustrated in Fig. 3.

Two acquisition instrument modes are foreseen:

- High Resolution at 60m for land and coastal areas for both OTTER and VIREO instruments.
- Low Resolution at 960m for ocean pixels, for OTTER instrument only.

The red and pink areas in Fig. 3 represent where data will be acquired at 60m resolution and made available at 60m resolution at nadir. For the blue areas, the data will be resampled on board to almost a kilometer resolution and sent down at a reduced resolution to reduce data volumes. For these low-resolution areas VIREO will be off as well as during nighttime for all the acquisitions.

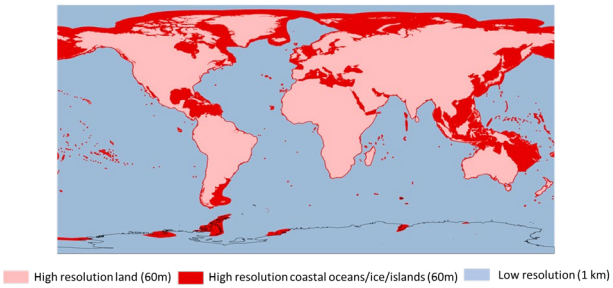

Figure 3. SBG-TIR observation mask

The observation mask can be sporadically updated (e.g. every three months or seasonally) with the aim of modifying the instrument mode to provide acquisitions in some new areas for both OTTER and VIREO instruments. Moreover, a temporary mask update is also available to switch the instrument mode in some areas defined by the user but limited to a potential weekly addition of a single scene of 1000 km along-track in high resolution area.

2. SBG-TIR PRODUCTS AND PROCESSING CHAINS

The SBG-TIR mission will provide a valuable source of information on geophysical parameters essential for monitoring both natural and anthropogenic ecosystem changes. Land Surface Temperature (LST), spectral emissivity and reflectance are critical variables for understanding and adapting to climate variability. Specifically, their knowledge enables sustainable water management for agriculture (e.g., irrigation), the mitigation of health stress during heatwaves (in conjunction with evapotranspiration and NDVI), drought prediction, the monitoring of coastal and inland waters, and understanding changes in the cryosphere and related water resources.

Furthermore, SBG-TIR data supports the identification of mineralogical species in raw materials and the topsoil key properties, while addressing natural hazards such as wildfires and volcanic activity. The mission also facilitates the integration of VNIR and MIR-TIR observations through simultaneous daytime acquisition across all spectral channels; this synergy enhances the spatial resolution of TIR imagery (TIR-sharpening) and improves Evapotranspiration (ET) estimation.

The SBG-TIR mission will deliver low-latency (LL) and standard products within 24 and 72 hours from the time of the instruments acquisition, respectively. Fig. 4 illustrates the organization of SBG-TIR science data products from Level 1 to Level 4: OTTER products are indicated in blue, while VIREO products are shown in orange. Many US products were originally developed for ECOSTRESS (ECOSTRESS, 2018), while new geology products, such as Elevated Temperature Features (ETF), Surface Mineralogy (SM), and Volcanic Activity (VA) are highlighted with green boxes in Figure 4.

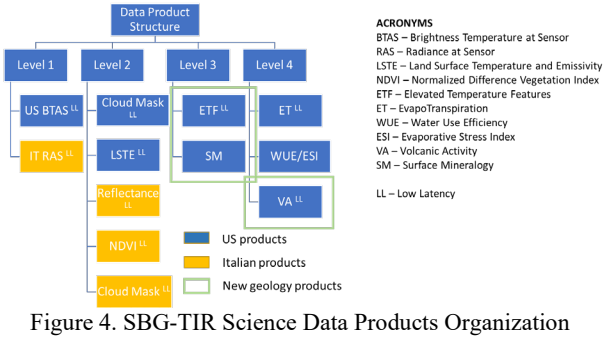

Figure 4. SBG-TIR Science Data Products Organization

All products from Level 1B to Level 4 will be distributed in NetCDF-4 format for swath data and Cloud Optimized GeoTIFF (COG) for tiled data. The tiling scheme will follow the Sentinel-2 tiling system, which consists of tiles approximately 109.8 km × 109.8 km in size.

Figure 5 illustrates the OTTER processing chain for both standard and low-latency products. Starting from geolocated radiance, the pipeline generates Land Surface Temperature and Emissivity, followed by several ecosystem products such as Evapotranspiration, Evaporative Stress Index and Water Use Efficiency. Additionally, it includes a suite of geological-related products focused on mapping lava flows, wildfires, volcanic activity and surface mineralogy.

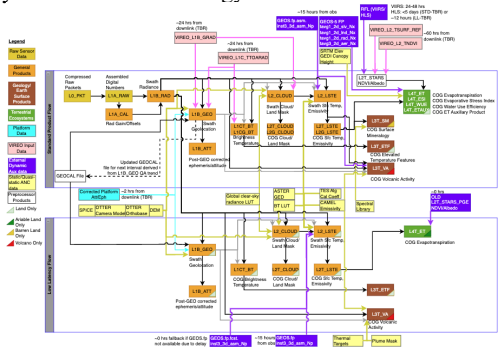

Figure 5. OTTER Product overflow

The VIREO processing chains are depicted in Figure 6. The primary distinctions between standard and low-latency products lie not only in their data latency but also in the specific methodologies employed, such as atmospheric correction and spatial enhancement techniques (e.g., super-resolution and pan-sharpening). Figure 6 highlights the direct links between the OTTER and VIREO chains, emphasizing the strategic integration of the two instruments. Specifically, VIREO data will refine OTTER's geolocation and co-registration, enable pan-sharpening to enhance LST spatial resolution, and improve Evapotranspiration (ET) estimation through VIREO surface reflectance and NDVI, and the possibility to exploit VIREO bands for Leaf Area Index (LAI) and Fractional Cover (FC) estimations. Furthermore, a joint cloud mask algorithm can be developed by exploiting both TIR and VNIR channels to improve accuracy.

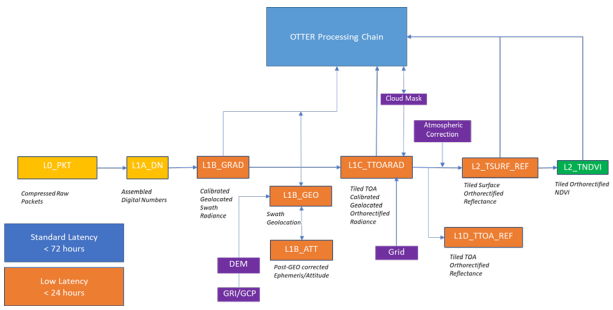

Figure 6. VIREO product overflow

Furthermore, a VIREO End-To-End (E2E) performance simulator is under development to serve as the foundation for future processors. By modeling the entire data chain, from the observed scene to the final geophysical parameters, this tool enables rigorous performance evaluations and supports the design of retrieval algorithms and data products specifically tailored for the VIREO camera. Moreover, two ASI scientific projects are currently underway: THERESA (THErmal infRarEd SBG Algorithms), which aims to refine data processing algorithms for the SBG-TIR mission by integrating visible and thermal imagery (Silvestri et al., 2024), and VEDRAI (VNIR Enhanced Dynamic RAnge Instrument) which focuses on developing a radiometric model and a super-resolution algorithm to optimize VIREO performances (Della Corte et al., 2025).

3. SBG-TIR SCIENCE & APPLICATIONS

The SBG-TIR mission will deliver high-resolution temperature and emissivity imagery, thus providing essential data for a wide range of scientific research and practical applications. The combination of optical and thermal data will provide different products such as:

- Food security and agriculture: by SGB-TIR Evapotranspiration (ET) data (Figure 7), more efficient irrigation practices (crop per drop, Figure 8) can be achieved, resulting in food production maximization.

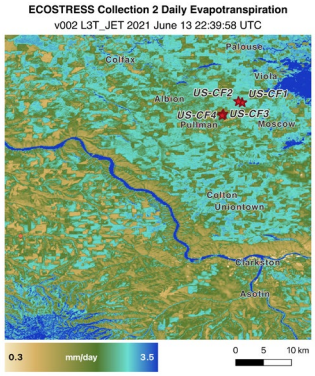

Figure 7. Example of ET daily estimation from ECOSTRESS

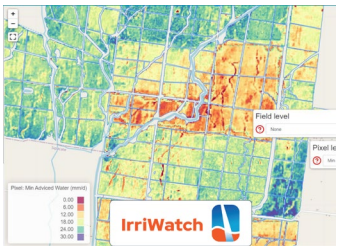

Figure 8. Example of irrigation application: IrriWatch integrates ECOSTRESS data into high quality estimates of water use and delivers irrigation advisories to over 18,000 fields in 25 countries around the world

- Mapping volcanic hazards (lava, anthropogenic targets, SO2 (Figure 9), ash concentrations, aerosol (SO4) plumes detection) and wildfires (Figure 10).

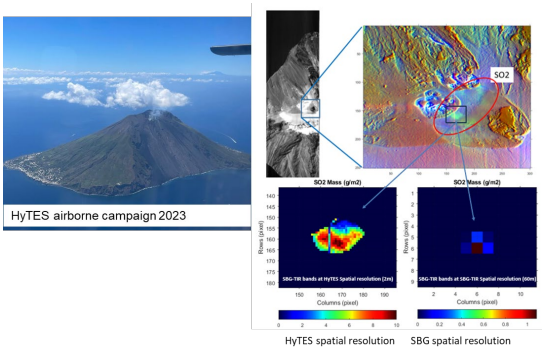

Figure 9. Example of SO2 retrieval applied to simulated SBG-TIR bands (8.7, 10.3, 11.3 µm) using HyTES data, over Stromboli Volcano (Italy) (ASI/THERESA project results)

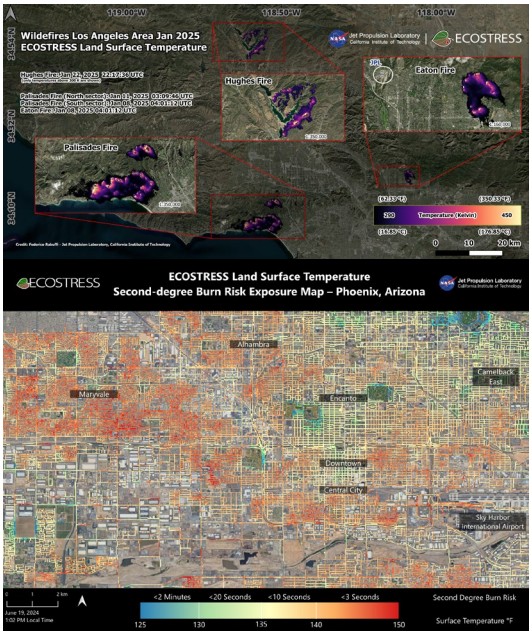

Figure 10. Example of ECOSTRESS active fire map in Los Angeles (top panel) and thermal burn risk mapping (bottom panel) in Phoenix (Arizona)

- Urban resilience: Keeping cities cool (Figure 11).

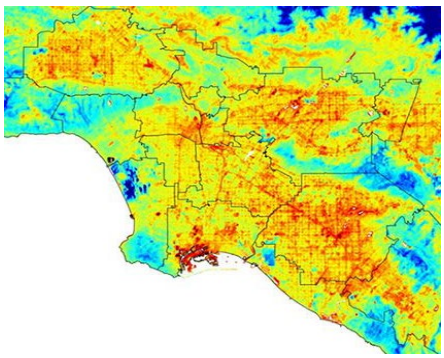

Figure 11. Example of LST retrieval from ECOSTRESS data

- Discovering critical minerals, energy resources and topsoil properties (Figure 12).

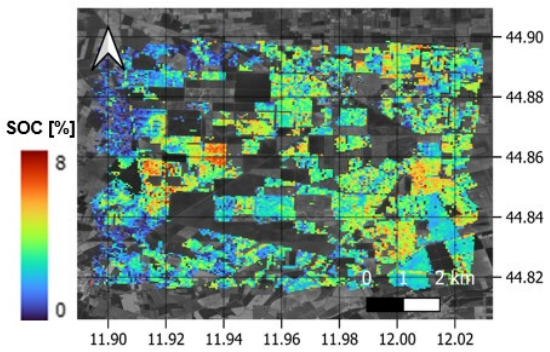

Figure 12. Example of Soil Organic Carbon (SOC) retrieval on Jolanda of Savoia site, using Hytes L1 (@9.8 µm) to simulate SBG-TIR radiances and NDVI from Sentinel-2 to simulate VIREO L2 product (ASI/THERESA project results)

4. CONCLUSIONS

The SBG-TIR mission, a joint NASA/JPL and ASI initiative, fulfills the objectives of the NASA Surface Biology & Geology (SBG) designated observable, the broader NASA Earth System Observatory (ESO), and the ASI Strategic Vision Document for Space 2020-2029.

The SBG-TIR data are intended to answer fundamental questions across ecosystems, natural resources, hydrology, solid Earth, and climate.

Furthermore, international partnerships with the TRISHNA and LSTM missions will ensure a long-term and consistent data record for climatic studies. During periods of overlapping operation, the synergy of these three satellites will enable high-frequency observations, potentially achieving daily and night-time global coverage.

REFERENCES

Basilio, R., Hook, S. J., Zoffoli, S., and Buongiorno, M. F., "Surface Biology and Geology (SBG) Thermal Infrared (TIR) Free -Flyer Concept," 2022 IEEE Aerospace Conference (AERO), Big Sky, MT, USA, 2022, pp. 01-09, doi: 10.1109/AERO53065.2022.9843292.

CNES-ISRO TRISHNA website, (2021): https://cnes.fr/projets/trishna

Della Corte, V., De Martino, C., Inno, L., Cozzolino, F., Da Deppo, V., Ruggiero, G., Venafra, S., Zuppella, P., Moualla, L. “Enhancing Small Satellite Imagery with Hybrid Super-Resolution”, AGU 2025, A43R-VR8026

ECOSTRESS NASA JPL website, (2018): https://ecostress.jpl.nasa.gov/.

ESA LSTM website, (2020): https://www.esa.int/ESA_Multimedia/Images/2020/11/LSTM.

Italian Space Agency (ASI) Strategic Vision Document for the Space 2020-2029 website: https://www.asi.it/lagenzia/documenti-istituzionali/

NASA Earth Science Observatory website (2017a): https://science.nasa.gov/earth-science/missions/earth-system-observatory.

NASA Surface Biology and Geology website, (2017b): https://science.nasa.gov/earth-science/decadal-sbg.

Silvestri M., Buongiorno, M. F., Laneve, G., Colombo, R., Notarnicola, C., Pignatti, S., Romaniello, V., Venafra, S., "Theresa Project: Study of Algorithms for SGB-TIR Mission," IGARSS 2024 - 2024 IEEE International Geoscience and Remote Sensing Symposium, Athens, Greece, 2024, pp. 3561-3563, doi: 10.1109/IGARSS53475.2024.10642352

This work is licensed under a Creative Commons Attribution-No Derivatives 4.0 International License.

TOWARDS FLEX FOR WATER: ANALYSIS OF GROUND AND AIRBORNE OBSERVATIONS IN LAKE GARDA

L. Panizza [1]*, M. Bresciani [1], C. Giardino [1], M. Pinardi [1], M. Austoni [2], R. Colombo [3], L. Caccetta [3], E. Canuti [4], B. Siegmann [5], P. Rademske [5], U. Rascher [5], K. Sakowska [6], L. Genesio [6], L. Vescovo [7] and S. Cogliati [3]

[1] Institute for Electromagnetic Sensing of the Environment, National Research Council, 20133 Milan, Italy - (panizza.l, bresciani.m, giardino.c, pinardi.m)@irea.cnr.it
[2] Water Research Institute, National Research Council, 28922 Verbania, Italy - marina.austoni@cnr.it
[3] University of Milano-Bicocca, 20126 Milano, Italy - l.caccetta@campus.unimib.it, (roberto.colombo, sergio.cogliati)@unimib.it
[4] Joint Research Centre - European Commission, 21027 Ispra (VA), Italy - Elisabetta.CANUTI@ec.europa.eu
[5] Institute for Bio- and Geosciences, IBG-2: Plant Science, Forschungszentrum Jülich GmbH, 52425 Jülich, Germany – (b.siegmann, p.rademske, u.rascher)@fz-juelich.de
[6] Institute of BioEconomy, National Research Council, 50145 Florence, Italy – (karolina.sakowska, lorenzo.genesio)@ibe.cnr.it
[7] Edmund Mach Foundation, 38098 Trento, Italy - loris.vescovo@fmach.it

KEY WORDS: Earth Observation, FLEX, Airborne Data, Inland Waters, Phytoplankton, In situ Measurements

ABSTRACT:

Phytoplankton play a fundamental role in global biogeochemical cycles, since, despite representing only ∽1–2% of the world's plant biomass, they account for about 40% of global carbon fixation. Monitoring their blooms intensity, spatial distribution and temporal variability is therefore crucial for understanding aquatic ecosystem dynamics at regional and global scales. In this context, the ESA's FLuorescence EXplorer (FLEX) mission, scheduled for launch in 2026, will provide global observations of Solar Induced Fluorescence, which in aquatic environments is commonly used as a proxy for Chlorophyll-a (Chl-a) concentration. This study, conducted within the FLEX-ITA project, investigates airborne hyperspectral acquisitions over Lake Garda, supported by extensive in situ spectroradiometric measurements. Particular emphasis is placed on data quality control as a prerequisite for reliable atmospheric correction and subsequent water quality product generation. Flight strips affected by sunglint are first identified, allowing the exclusion of unsuitable acquisitions, followed by a band-wise signal-to-noise ratio analysis to remove noisy bands. Atmospheric correction is applied using the 6SV radiative transfer model, and sunglint correction is performed, leading to improved accuracy of at surface reflectance products (R^2=0.96 in 2024 and R^2=0.66 in 2025). Chl-a concentration maps generated using the bio-optical model BOMBER show good agreement with in situ data (RMSE=0.2506 in 2024 and RMSE=0.6076 in 2025), although severe sunglint in 2025 prevents full spatial coverage. Overall, these findings highlight the importance of rigorous pre-processing and quality screening of airborne hyperspectral data to support robust validation activities and algorithm development in view of FLEX applications over aquatic environments.

1. INTRODUCTION

Phytoplankton are responsible for about half of the global photosynthetic oxygen production, making them key players in both the carbon cycle and Earth's climate regulation (Naselli-Flores & Padisák, 2023). They are responsible for regulating functions and services of not only aquatic ecosystems, but of the entire biosphere. For this reason, monitoring their spatial and temporal dynamics, as well as their physiological status, is crucial for understanding aquatic ecosystems. In this context, the ESA's FLuorescence EXplorer (FLEX), the 8th Earth Explorer mission scheduled for launch in 2026, aims to provide global estimates of Solar Induced Fluorescence (SIF) (Taccola et al., 2023). In aquatic environments, SIF is widely used as a proxy for Chlorophyll-a (Chl-a) concentration, which is commonly adopted as an indicator of phytoplankton biomass (Gupana et al., 2025). Although FLEX is primarily optimized for terrestrial vegetation, it will also represent a new source of hyperspectral data that can provide insights for assessing phytoplankton pigment concentrations and phytoplankton physiology in inland and coastal waters. Within this framework, the "FLEX Inland water and Terrestrial Airborne measurements and scientific exploitation" (FLEX-ITA), founded by the Italian Space Agency (ASI), aims to acquire high-quality data and to develop algorithms for mapping SIF, and exploiting FLEX-like measurements to improve phytoplankton characterization. For this reason, many field campaigns were organized within the project on both aquatic environments and terrestrial vegetation.

2. MATERIALS AND METHODS

2.1 Study Area and Fieldwork Activities

Fieldwork activities were carried out on Lake Garda, that is a deep, warm monomictic lake, situated in northern Italy (45.535 N, 10.596 E) that spans multiple provinces; it is the largest Italian lake (370 km^2), with an average depth of 136 m, a maximum depth of 346 m and a water volume of 50 km^3. The lake has many inflows, but the main one is the Sarca river, while the only outflow is the Mincio river. Lake Garda can be classified as meso-oligotrophic, with generally stable physical and chemical conditions and occasional high Chl-a concentrations (Bresciani et al., 2018). Chl-a exhibits a clear seasonal pattern, with higher values in winter and transitional periods and lower values in summer. The lake oligotrophication has been induced by climate warming, since the increase of water temperatures lead to an increase of total phosphorous that favoured cyanobacteria and large diatoms diffusion, decrease in the frequency of full mixing episodes, and decrease in nutrient supply to the upper layers (Salmaso et al., 2018). Considering the morphology, the lake can

* Corresponding author

be divided in two different areas; both field campaigns were conducted in the southern part, that is surrounded by morenic and alluvial plains and low hills with a mix of urbanised and rural land use (Giardino et al., 2014).
Two field campaigns were conducted to collect in situ data and support the assessment of water constituent retrieval from airborne imagery: the first on 2-9 July 2024, with synchronous airborne acquisition on the 4th, and the second on 10-11 June 2025, with synchronous airborne acquisition on the 11th. In total, 60 sampling stations were defined in deep waters (Figure 1), resulting in almost the same number of spectral signatures acquired using multiple spectroradiometers, including WISP-3, WISP Orca, Spectral Evolution and Hypstar. In addition to radiometric measurements, water samples were collected and filtered (GF/F glass fiber filters), to estimate the optically active constituents in the water column. Phytoplankton composition was characterised in terms of the main taxonomic groups (density and biomass) based on surface water samples (phytoplankton net). Chl-a was measured spectrophotometrically after extraction in 90% acetone (Lorenzen, 1967). High Performance Liquid Chromatography was also performed to identify photosynthetic pigments and related compounds. AquaFlash and CyanoFluor were used for chlorophyll fluorescence retrieval and cyanobacteria detection, while turbidity and water transparency were measured using the HACH instrument and a Secchi disk, respectively. Both campaigns involved high-resolution airborne hyperspectral data collected with the IBIS and HYPLANT system (comprising the DUAL and FLUO modules), although, in this study, we are focusing just on the products of the DUAL module.

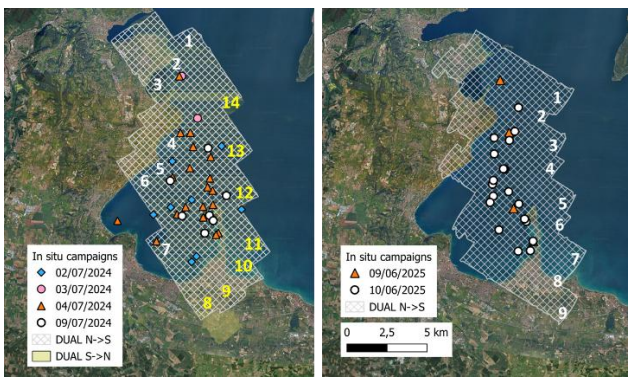

Figure 1. Sampling stations from fieldwork activities (2024 on the left and 2025 on the right).

2.2 Airborne Image Processing

The airborne acquisitions were in total 14 flight strips for 2024; the airplane acquired firstly from north to south, and then from south to north, for a total flight period of 1.15 hour. On 2025 the total number of acquisitions was 9 acquired from north to south in half an hour. Considering that in this time period the geometric, solar and atmospheric conditions changed, a sunglint index was computed on a ROI basis, and then standardized using a global SI Z-score (Equation 2) to identify the strips mostly disturbed. The same statistic was applied also to the mosaic generated from the strips, in order to identify the spatial regions highly affected by sunglint (Gao & Li, 2021).

$$SI = \frac{(R_{NIR} - R_{BLUE})}{(R_{NIR} + R_{BLUE})} \quad (1)$$

$$SI\ Z - score = \frac{SI - \mu(SI)}{\sigma(SI)} \quad (2)$$

where SI = Sunglint Index
R_{NIR}, R_{BLUE} = Reflectances in NIR (800 nm) and BLUE bands (490 nm)
$\mu(SI)$ = Sunglint Index mean
$\sigma(SI)$ = Sunglint Index standard deviation

After removing or correcting these portions from the mosaic, a noisy bands removal has been performed by identifying bands that were systematically showing minimal radiance across more than 80% of flight stripes, as they indicate persistent instrument or atmospheric noise. Therefore, the Signal to Noise Ratio (SNR) of the image has been computed automatically accordingly to the "homogeneous area" method (Gao, 1993). In particular, a block-based approach was applied to the radiance image, restricted to water pixels identified by a binary mask. For each spectral band, the image was cropped to the minimum bounding box containing valid water pixels and then divided into non-overlapping square blocks (5 × 5 pixels). Within each block, the local standard deviation of radiance was computed and used as an estimate of local noise. This procedure resulted in a distribution of noise estimates for each band. To obtain a robust band-wise noise estimate and to reduce the influence of disturbed areas, the 25th percentile of the block standard deviation distribution was selected as representative of the sensor noise floor (Fiete & Tantalo, 2001). The mean signal was computed as the average radiance over all water pixels in the band. Finally, the SNR for each spectral band was calculated as the ratio between the mean signal and the selected percentile-based noise estimate.

After band removal the 6SV radiative transfer model (Kotchenova et al., 2006) was applied on radiance data to perform atmospheric correction and derive surface remote sensing reflectance (Rrs). The algorithm accounts for target elevation, anisotropic and Lambertian surface reflectance, and gaseous absorption.

Since the image was still affected by sunglint, an additional correction was performed (Gao & Li, 2021). The method assumes that the sunglint component of Rrs is spectrally proportional to the Fresnel reflectance of the air–water interface and can be estimated using a near-infrared reference band, where the water-leaving signal is assumed negligible. A constant Fresnel reflectance spectrum was computed from the solar zenith angle and scaled by the ratio between measured reflectance and Fresnel reflectance at the reference wavelength. The scaled Fresnel spectrum was then subtracted from each spectral band.
Finally, the bio-optical model BOMBER (Giardino et al., 2012), a software package for simultaneous retrieval of the optical properties of water column and bottom from remotely sensed imagery was employed to derive Chl-a maps. The parametrization of BOMBER was done with specific Inherent Optical Properties acquired during the FLEX-ITA field campaigns. The Chl-a maps were generated for the entire mosaic using the "Deep Waters" model for 2024, and for only one strips for 2025.

3. RESULTS & DISCUSSION

3.1 Dependency on Illumination Conditions and Acquisition Geometry

The boxplots derived from the standardized SI represent SI Z-scores that quantify how anomalous each ROI is with respect to the entire dataset rather than within a single flight strip. This global normalization enables direct comparison of SI Z-scores among all strips. Since two acquisition directions were adopted during the 2024 field campaigns, this approach allowed

identification of the strips most affected by illumination conditions and acquisition geometry (Figure 2). In particular, strips acquired in the south–north direction and the first strip of the north–south sequence exhibit higher anomaly levels.

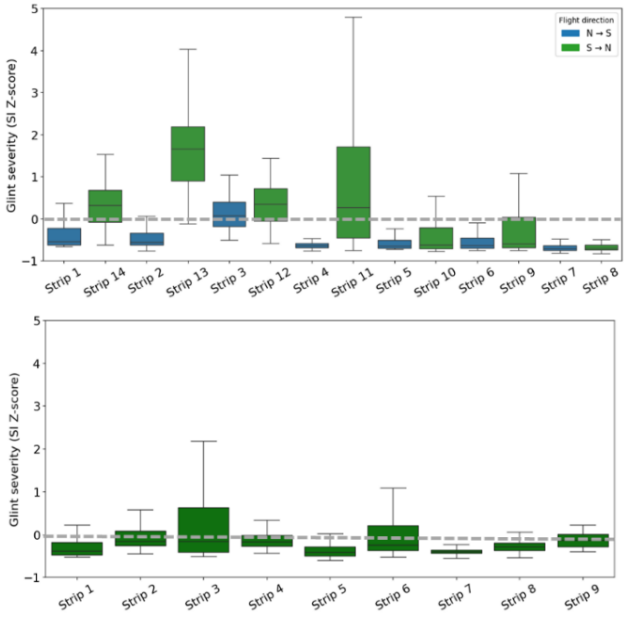

Figure 2. SI Z-score per each ROI, grouped by strip acquired in 2024 at the top and in 2025 at the bottom.

3.2 Noisy Bands Removal and Atmospheric Correction

The application of the SNR-based method led to the removal of approximately 5% of the total bands and improved the agreement with in situ data by about 3%. Figure 3 shows the validation of Rrs derived from airborne images after atmospheric correction using the 6SV algorithm and sunglint removal. The Rrs data were resampled to match the spectral configurations of the hyperspectral FLORIS sensor on the left (150 bands) and the multispectral OLCI sensor on the right, in view of the FLEX mission and its future tandem operation with Sentinel-3. A total of 12 OLCI bands were considered, in agreement with the ESA CCI product documentation (ESA, 2020), since some bands are not informative for the retrieval of water quality products, and are sometimes affected by low SNR over water.

Results show a systematic overestimation of in situ Rrs by the airborne data in both 2024 and 2025; this displacement from the 1:1 line is more pronounced in 2025 due to higher sunglint conditions. Particularly NIR bands (red dots) exhibit the largest deviations from the baseline. In 2024, the FLORIS configuration shows slightly lower agreement ($R^2 = 0.96$, RMSE = 0.0012 sr^{-1}) than OLCI configuration ($R^2 = 0.97$, RMSE = 0.0009 sr^{-1}), partly due to the different number of matchups. In contrast, in 2025 both configurations show worst performances, with lower R^2 values (0.66 for FLORIS and 0.70 for OLCI) and higher RMSE and bias values.

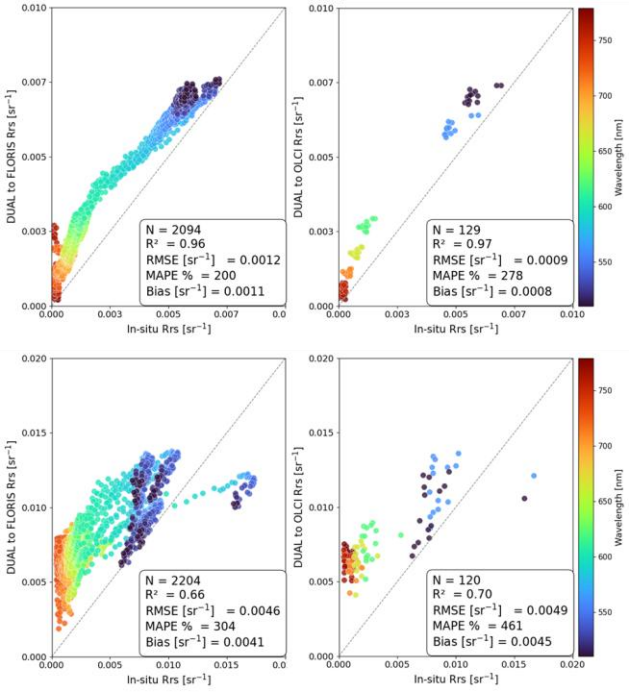

Figure 3. Scatterplot of Rrs from airborne data resampled to FLORIS (left) and OLCI (right) versus in situ Rrs: data from 2024 (top) and from 2025 (bottom). In dashed gray the 1:1 line.

3.3 Water Quality Products

Figure 4 shows the Chl-a maps generated for the deep portion of Lake Garda, defined by a shallow mask of 7 m depth. Due to the strong sunglint affecting the 2025 flight strips, the product could be generated for only one strip in that year (Figure 4b). Overall, higher Chl-a concentrations are observed in 2025, consistent with the different water quality conditions measured during the two campaigns. The mean deviation between estimated and in situ Chl-a values at the validation stations was below 15% in both years. Mean in situ Chl-a concentrations increased from 1.09 mg/m^3 in 2024 to 1.83 mg/m^3 in 2025. In addition, water transparency, measured using Secchi disk, decreased from approximately 8 m in 2024 to about 5 m in 2025. The contrasting water conditions are also evident in Figure 4d, which shows the mean spectral signatures derived from in situ measurements. While the 2024 spectrum exhibits the typical signature of clear oligotrophic waters, the 2025 spectrum shows higher reflectance peaks in the green region (up to ~0.01 sr^{-1}) and in the red region, which are characteristic of more phytoplanktonic water.

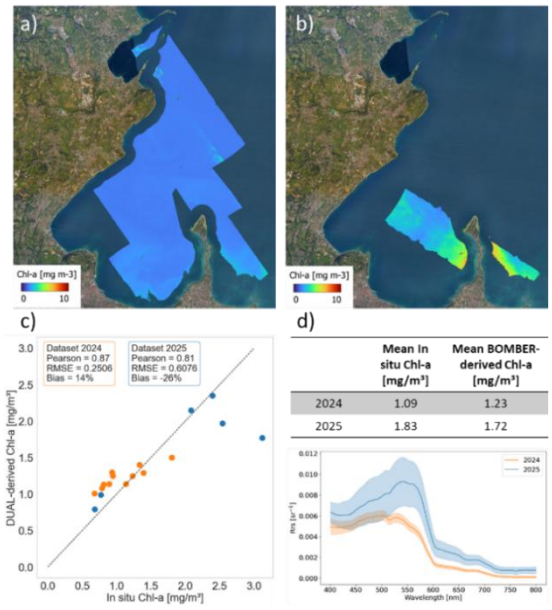

Figure 4. Chl-a maps for 2024-2025 (a, b), Chl-a validation (c), Mean Chl-a values per year at the top, and mean in situ spectral signatures at the bottom (d).

4. CONCLUSIONS

The main goal of this study was to illustrate the processing required for airborne hyperspectral data, specifically in relation with two field campaigns conducted in 2024 and 2025 within the FLEX-ITA project. The analysis highlighted the sensitivity of airborne data acquisition to several factors, such as acquisition geometry, atmospheric conditions, solar position, sensor orientation. Accurate processing is therefore essential to ensure reliable radiometric data to give in input to bio-optical algorithms for the generation of products, such as Chl-a concentration maps. These products could be integrated in a future prospective with SIF maps to enhance the characterization of phytoplankton dynamics and community structure, in order to have a more comprehensive knowledge of inland and coastal waters and support aquatic monitoring.

ACKNOWLEDGEMENTS

This work was supported by the Italian Space Agency (ASI) under contract no. 2023-6-HB.0, CUP F43C23000350001, within the FLEX-ITA project, and by the ESA (GA 4000139081/22/I-EF, HYPERNETS-POP), and the Horizon 2020 Framework Programme of European Union [GA 775983, HYPERNETS project]. Thanks to A. Pellegrino, S. Mangano and M. Musanti for fieldwork activities.

REFERENCES

Bresciani, M., Cazzaniga, I., Austoni, M., Sforzi, T., Buzzi, F., Morabito, G., & Giardino, C. (2018). Mapping phytoplankton blooms in deep subalpine lakes from Sentinel-2A and Landsat-8. Hydrobiologia, 824(1), 197–214. https://doi.org/10.1007/s10750-017-3462-2

ESA. (2020, October 23). Key Documents - ESA Climate Change Initiative.

Fiete, R., & Tantalo, T. (2001). Comparison of SNR image quality metrics for remote sensing systems. Optical Engineering, 40(4), 574. https://doi.org/10.1117/1.1355251

Gao, B.-C. (1993). An operational method for estimating signal to noise ratios from data acquired with imaging spectrometers. Remote Sensing of Environment, 43(1), 23–33. https://doi.org/10.1016/0034-4257(93)90061-2

Gao, B.-C., & Li, R.-R. (2021). Correction of Sunglint Effects in High Spatial Resolution Hyperspectral Imagery Using SWIR or NIR Bands and Taking Account of Spectral Variation of Refractive Index of Water. Advances in Environmental and Engineering Research, 02(03), 1–15. https://doi.org/10.21926/aeer.2103017

Giardino, C., Bresciani, M., Cazzaniga, I., Schenk, K., Rieger, P., Braga, F., Matta, E., & Brando, V. (2014). Evaluation of Multi-Resolution Satellite Sensors for Assessing Water Quality and Bottom Depth of Lake Garda. Sensors, 14(12), 24116–24131. https://doi.org/10.3390/s141224116

Giardino, C., Candiani, G., Bresciani, M., Lee, Z., Gagliano, S., & Pepe, M. (2012). BOMBER: A tool for estimating water quality and bottom properties from remote sensing images. Computers & Geosciences, 45, 313–318. https://doi.org/10.1016/j.cageo.2011.11.022

Gupana, R. S., Odermatt, D., Rahaghi, A. I., Minaudo, C., Werther, M., Giardino, C., & Damm, A. (2025). Remote Sensing of Sun-Induced Fluorescence in a Deep Lake: Disentangling Quenching Mechanisms Improves Relationship With Chlorophyll-a Concentration Estimates. IEEE Journal of Selected Topics in Applied Earth Observations and Remote Sensing, 18, 4410–4426. https://doi.org/10.1109/JSTARS.2025.3528911

Kotchenova, S. Y., Vermote, E. F., Matarrese, R., & Jr., F. J. K. (2006). Validation of a vector version of the 6S radiative transfer code for atmospheric correction of satellite data Part I: Path radiance. Applied Optics, 45(26), 6762. https://doi.org/10.1364/AO.45.006762

Lorenzen, C. J. (1967). Determination of chlorophyll and pheo-pigments: spectrophotometric equations 1. Limnology and Oceanography, 12(2), 343–346. https://doi.org/10.4319/lo.1967.12.2.0343

Naselli-Flores, L., & Padisák, J. (2023). Ecosystem services provided by marine and freshwater phytoplankton. Hydrobiologia, 850(12–13), 2691–2706. https://doi.org/10.1007/s10750-022-04795-y

Salmaso, N., Boscaini, A., Capelli, C., & Cerasino, L. (2018). Ongoing ecological shifts in a large lake are driven by climate change and eutrophication: evidences from a three-decade study in Lake Garda. Hydrobiologia, 824(1), 177–195. https://doi.org/10.1007/s10750-017-3402-1

Taccola, M., Da Mota Silva, S., Pereira do Carmo, J., Petitjean, G., Bock, R., Fratacci, O., Trastour, J., Baroni, M., Naldoni, S., Nuzzi, D., & Bittner, H. (2023). FLEX instrument: status, performances and lessons learnt. In K. Minoglou, N. Karafolas, & B. Cugny (Eds.), International Conference on Space Optics - ICSO 2022 (p. 18). SPIE. https://doi.org/10.1117/12.2688822

This work is licensed under a Creative Commons Attribution-No Derivatives 4.0 International License.

The EarthCARE mission: an overview of science objectives, data processing chain and products visualization

A. Piro,[1]* B. Abis [1], L. Di Ciolo,[2]* T. Hummel,[3] B. Frommknecht,[3] F. Capatano,[3]V. Tzallas,[3]

[1] Starion Group, Via di Grotte Portella 28, Frascati, Italy – a.piro@stariongroup.eu
[2]Serco Italia Spa, Via Bernardino Alimena, 111, 00173 Roma RM, Italy; - lorenzo.di-ciolo@serco.com
[3] European Space Agency (ESA), ESRIN, Frascati, Italy

KEY WORDS: Earth Observation, EarthCARE, atmosphere, aerosols, climate, data processing, data visualization

ABSTRACT:

The Earth Cloud Aerosol and Radiation Explorer (EarthCARE) is an operational satellite mission launched on 28th May 2024 and developed by the European Space Agency (ESA) in cooperation with the Japan Aerospace Exploration Agency (JAXA). The satellite embarks four instruments that provide collocated and synergistic observations: two active instruments, the Atmospheric LIDar (ATLID) and the Cloud Profiling Radar (CPR); and two passive instruments, the MultiSpectral Imager (MSI) and the Broadband Radiometer (BBR) with the aim to measure: vertical distributions and profiles of aerosols, clouds and precipitation properties together with radiative fluxes and derived heating rates.
EarthCARE's cloud profiling radar provides information on the vertical and internal structure of clouds and their dynamic; the atmospheric lidar reveals profiles of aerosols and thin clouds and provides cloud-top information; the multispectral imager provides a scene overview in multiple wavelengths and gives an overall visual context; and the broadband radiometer measures reflected solar radiation and outgoing infrared radiation coming from Earth.
The combination of these data and the complex processing chain through the synergistic products generation derived by the contribution of information coming from the four instruments, are being used in particular to evaluate the representation on global scale of clouds properties and classification, aerosols, precipitation, and associated radiative fluxes in weather forecasting and climate models.
This paper provides and overviews of the mission and the data processing chains, of level 1 and level 2 data products, their content and applications, and data exploitation and visualization.

1. INTRODUCTION

1.1 EarthCARE Mission

The Earth Cloud Aerosol and Radiation Explorer (EarthCARE) is an operational satellite mission launched on 28th May 2024 and developed by the European Space Agency (ESA) in collaboration with the Japan Aerospace Exploration Agency (JAXA) which provided the Cloud Profiling Radar (CPR) instrument. The satellite embarks four instruments that provide collocated and synergistic observations: two active instruments, the Atmospheric LIDar (ATLID) in addition to CPR; and two passive instruments, the MultiSpectral Imager (MSI) and the Broadband Radiometer (BBR) with the aim to measure: vertical distributions and profiles of aerosols, clouds and precipitation properties together with radiative fluxes and derived heating rates.

1.2 Cloud Profiling Radar (CPR)

Cloud Profiling Radar (CPR) provides information and measurements of the vertical and internal structure of clouds along the satellite track through the retrieval of their microscopic and macroscopic properties, and the measurement of the vertical velocity of cloud particles.

1.3 Atmospheric Lidar (ATLID)

The ATmospheric LIDar (ATLID) is a high spectral resolution atmospheric backscatter LIDAR allowing the detection of cloud boundaries and profiles of optically thin cloud and aerosols though three channels:

- Mie co-polar- backscatter from particles co-polarised compared to emitted pulse;
- Mie cross-polar- backscatter from particles cross-polarised compared to emitted pulse;
- Rayleigh-molecular backscatter.

1.4 Multispectral Imager (MSI)

The multispectral imager (MSI) provides a scene overview and additional data information on cloud type, texture, and cloud temperature in multiple channel wavelengths.

1.5 Broadband Radiometer (BBR)

The broadband radiometer (BBR) measures the co-located reflected solar and emitted thermal radiation.

2. MISSION OBJECTIVES

2.1 Cloud Aerosol Radiation Interaction

The main objective of the mission is the improvement of the understanding of cloud-aerosol-radiation interactions so as to include them correctly and reliably in climate and numerical weather prediction models. In detail, the scientific objectives are:

- The observation and measurements of the vertical distributions of atmospheric liquid water and ice on a global scale, their transport by clouds and their radiative impact.
- The observation and measurements of cloud distribution ('cloud overlap'), cloud-precipitation interactions and the characteristics of vertical motions within clouds.
- The observation and measurements of the vertical profiles of natural and anthropogenic aerosols on a global scale, their radiative properties and interaction with clouds.

* corresponding author

- The retrieval of profiles of atmospheric radiative heating and cooling through the combination of the retrieved aerosol and cloud properties.

The combination of the four instruments acquisitions data though the complex processing chain and the generation of the synergistic products, has allowed the analysis, the evaluation and representation on global scale of clouds properties and classification, aerosols, precipitation, and associated radiative fluxes providing the contribution of a better understating of weather forecasting and climate models.

2.2 Production Model

The EarthCARE ESA processing chain includes the following product levels:

- Level 0 (L0): annotated raw instrument science packets
- Level 1b (L1b): fully calibrated and geolocated instrument science measurements on the native instrument grid (for BBR also spatially integrated to several ground pixel sizes)
- Level 1c (L1c): MSI-only; L1b data re-sampled onto the grid of one selected MSI reference channel
- Level 1d (L1d): spatial grid shared by all instruments ("joint standard grid") and ECMWF meteorological fields limited to EarthCARE swath
- Level 2 (L2): derived geophysical variables, either at the same resolution and location as L1b data ("native grid") or re-sampled to the joint standard grid
- Level 2a (L2a): single-instrument geophysical products
- Level 2b (L2b): synergistic geophysical products (using data from two or more instruments)

The production model depicted in Figure 1 shows data produced by the ESA ground segment, except for externally generated products shown as dashed boxes which are used as inputs. These external inputs are:

- CPR L1b products, C-NOM, provided by JAXA
- Meteorological analysis and forecast fields L1d products, X-MET, provided by ECMWF.

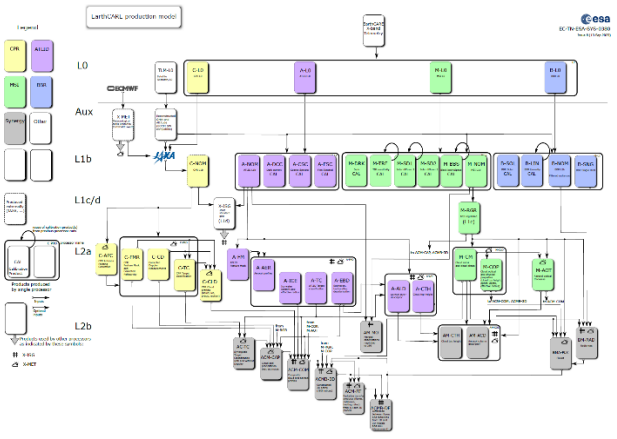

Figure 1. EarthCARE Production Model

Each of the small boxes represents a single EarthCARE data product, grouped by level (L0 at the top and L2 at the bottom) and processor that generates them. For each box, the product identifier (such as "AM-CTH") and a brief description of the main parameter (such as "cloud top height") are specified. Products are color-coded depending on the instrument retrieving the data. Synergistic products are represented by grey boxes. Additionally, the first part of the product identifier denotes the instrument or combination of instruments from which a product has been derived. A full description of all EarthCARE's products is beyond the scope of this paper. In the following, a brief description of the ESA's L1 and L2 products will be given.

2.2.1 L1 Products

The scientific L1 products contain calibrated instrument data processed to physical units, with error bars, quality flags and geolocated. The main science products are described in Table 1.

Product	Processor	Instrument	Content
A-NOM	A-L1	ATLID	Attenuated backscatter (Rayleigh and Mie)
B-NOM	B-L1	BBR	Integrated SW and TW radiances
B-SNG			Single pixel SW and TW radiances
C-NOM	C-L1	CPR	Radar reflectivity and Doppler velocities
M-NOM	M-L1	MSI	TOA radiances and brightness temperatures
M-RGR			Regridded TOA radiances and brightness temperatures

Table 1. L1 Products and Processors

2.2.2 L2 Products

L2 products contain derived geophysical variables, either at the same resolution and location as L1b data, i.e., on the native grid, or re-sampled to a common grid, called "joint standard grid". A brief description of ESA products is given in Table 2 and table 3, whereas the production model of Figure 1 reports which products follow the joint standard grid, i.e., those with JSG auxiliaries in input.

Product	Processor	Instrument	Content
C-FMR	C-PRO	CPR	Feature mask and corrected reflectivity
C-CD			Corrected Doppler
C-TC			Target classification
C-CLD	C-CLD	CPR	Cloud Profiles
A-FM	A-FM	ATLID	Feature mask
A-AER	A-PRO	ATLID	Aerosol profiles
A-ICE			Ice water content and effective radius
A-TC			Target classification
A-EBD			Extinction, backscatter, depolarisation
A-CTH	A-LAY	ATLID	Cloud top height
A-ALD			Aerosol layer descriptor
M-CM	M-CLD	MSI	Cloud mask and phase
M-COP			Cloud optical and physical properties
M-AOT	M-AOT	MSI	Aerosol optical thickness

Table 2. ESA L2A Products and Processors

Product	Processor	Instrument	Content
AM-CTH	AM-COL	ATLID, MSI	Cloud top height
AM-ACD			Aerosol column descriptor
AM-MO	AM-MO	ATLID, MSI	ATLID & MSI level 1b merged onto same grid
BM-RAD	BM-RAD	BBR, MSI	Broadband radiances
BMA-FLX	BMA-FLX	BBR, MSI, ATLID	Broadband fluxes
AC-TC	AC-TC	ATLID,	Synergistic target classification
ACM-CAP	ACM-CAP	ATLID, CPR, MSI	Cloud, aerosol, precipitation best estimates
ACM-COM	ACM-COM	ATLID, CPR, MSI	Composite cloud and aerosol profiles
ACMB-3D	ACMB-3D	ALL	Constructed three-dimensional scene
ACM-RT	ACM-RT	ATLID, CPR, MSI	Radiative transfer products – fluxes, radiances, heating rates
ACMB-DF	ACMB-DF	ALL	Differences between radiances and calculated from retrievals (ACM-RT) and BBR measurements

Table 3. ESA L2B Products and Processors

3. DATA VISUALIZATION AND EXPLOITATION

The full extent of EarthCARE applications is still being explored, and reporting all known cases would not fit in this manuscript. In the following, few novel examples will be provided on how EarthCARE observations can work in synergy to increase the understanding of various phenomena.

3.1 Typhoon Ragasa

Figure 2, using an MSI acquisition over Typhoon Ragasa near the Philippines on 20th September 2025 (EarthCARE lifts the clouds on climate models, 2025), shows how an RGB composition (Natural Colour RGB Quick Guide, 2023) can give a context overview of a cyclone, highlighting its main features.

During the same event, CPR can detect snow, rain and hail in large clouds, as depicted in Figure 3. Whereas ATLID can detect aerosol, ice particles and liquid droplets in thin clouds, as shown in Figure 4.

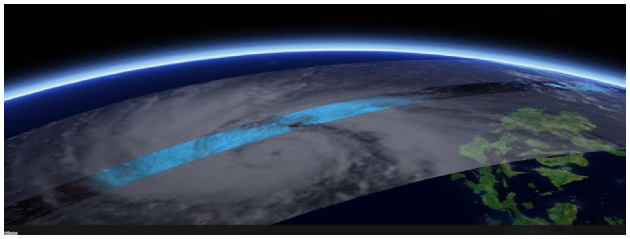

Figure 2. Typhoon Ragasa RGB

The CPR detects snow rain and hail in large clouds.

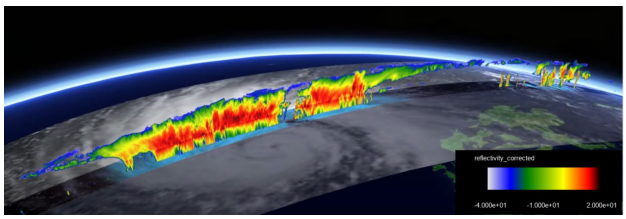

Figure 3. Typhoon Ragasa CPR Reflectivity

The ATLID detects aerosol, ice particles and liquid droplets in thin clouds.

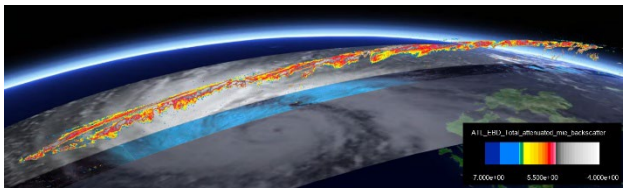

Figure 4. Typhoon Ragasa ATLID Mie Signal

EarthCARE ATLID, CPR, and MSI data are then combined to derive vertical curtains with cloud and precipitation properties, as shown in Figure 5. MSI imagery can be used to extrapolate and compute cloud profiles across the satellite's track. By identifying pixels with similar optical properties, the 3D cloud structure is reconstructed. Additionally, using a radiative transfer modelling technique, it is possible to estimate how incoming sunlight is scattered by cloud particles and Earth's surface, and consequently how much radiation is reflected to space. This computed reflected sunlight is then compared against the independent measurements made by BBR, as shown in Figure 5.

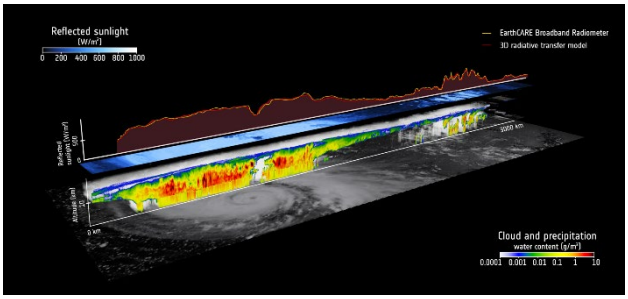

Figure 5. Typhoon Ragasa Total water content and 3D fluxes from radiative transfer model vs BBR fluxes

3.2 Klyuchevskaya Sopka Volcanic Eruption

Klyuchevskaya Sopka, an active volcano in Russia, emitted large ash plumes on 8th August 2025, visible in NASA satellite imagery and captured also by EarthCARE. Figure 6 shows the RGB composite image from NASA VIIRS instruments together with the EarthCARE MSI acquisition around 03:46.

A different combination of channels (Ash RGB Quick Guide, 2023) can be used to create an RGB image highlighting important aerosol components such as Sulphur dioxide and ash. Given that SO_2 has weak absorption around 8.8 micrometers, the TIR1 band can be used to highlight its presence. Figure 7 shows the EarthCARE volcanic ash and SO_2 plume detection during the Klyuchevskaya Sopka eruption event.

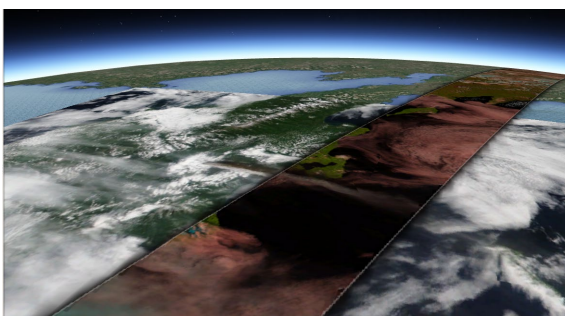

Figure 6. Klyuchevskaya Sopka MSI RGB natural colour

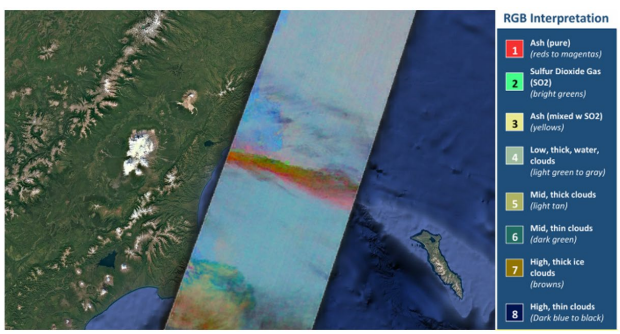

Figure 7. Klyuchevskaya Sopka MSI volcanic ash detection

Figure 8 shows the vertical aerosol classification provided by an ATLID product (ATL_AER) compared to the MSI RGB image composition, highlighting the synergy between instruments.

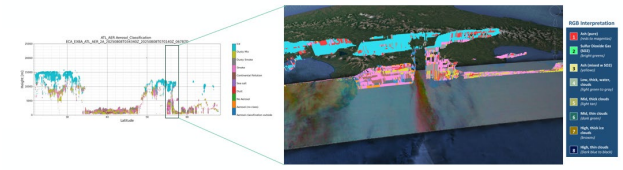

Figure 8. ATLID Aerosol classification (left) and MSI volcanic ash RGB (right)

3.3 Snow Detection and Monitoring

A combination of MSI spectral bands yields a Snow Detection Index, useful for distinguishing between snow on ground and ice from water clouds or ice clouds. On cloud-free areas, this corresponds to snow or ice detection (Snow RGB quick guide, 2023). Figure 9 (left) depicts snow-cover for the Alps using the EarthCARE daylight acquisition on 4th January 2026 over the Western Alps. Similarly, on the right of Figure 9, data from the 3rd February 2026 shows ice covering the surfaces of the Great Lakes. In particular, the Lake Nipigon is completely covered in ice, whereas Lake Superior shows frozen shorelines and islands.

Another interesting case can be seen with the acquisition on the Caspian Sea and Alborz and Zagros mountains (Iran) on the 5th February 2026, depicted in Figure 10. The MSI Snow Index (on the right) reveals ice cover over the northern Caspian Sea basin and snow cover over the Iranian mountains. The northern Caspian Sea often freezes over during the winter, with ice covering its shallow, less saline northern waters.

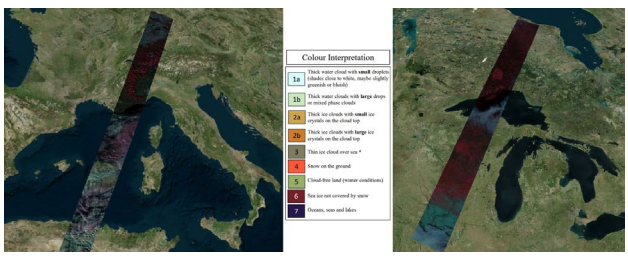

Figure 9. MSI Snow Index over the Alps (left) and the Great Lakes region (right)

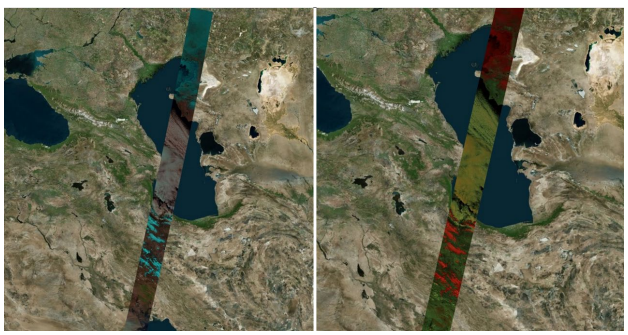

Figure 10. MSI natural RGB (left) and MSI Snow Index (right)

4. CONCLUSIONS

The EarthCARE mission is implemented by ESA in cooperation with JAXA to improve our understanding of the role of clouds, aerosol and radiation in climate.

EarthCARE allows scientists to evaluate the representation of cloud, aerosol, precipitation, and radiative flux in weather forecast and climate models, while improving parameterisations and reducing uncertainties in cloud processes.

In this paper, a description of the four main instruments, of the mission scientific objectives, and of ESA's production chain and products has been presented. Additionally, examples of novel applications of EarthCARE data for various types of events have been illustrated, with the explanation of the main variables and parameters of interest.

5. REFERENCES

5.1 References

Ash RGB Quick Guide, 2023
https://user.eumetsat.int/resources/user-guides/ash-rgb-quick-guide

EarthCARE lifts the clouds on climate models, 2025
https://www.esa.int/Applications/Observing_the_Earth/FutureEO/EarthCARE/EarthCARE_lifts_the_clouds_on_climate_models

Natural Colour RGB Quick Guide, 2023
https://user.eumetsat.int/resources/user-guides/natural-colour-rgb-quick-guide

Snow RGB Quick Guide, 2023
https://user.eumetsat.int/resources/user-guides/snow-rgb-quick-guide

Wehr, T., et al. "The EarthCARE mission–science and system overview." *Atmospheric Measurement Techniques* 16.15 (2023): 3581-3608. doi:https://doi.org/10.5194/amt-16-3581-2023

This work is licensed under a Creative Commons Attribution-No Derivatives 4.0 International License.

PRISTAR-GEOSPEC: PRISMA TOOLS FOR ANALYSIS IN R FOR GEOCODING AND SPECTRAL REFINEMENT

E. Spirito[1*], F. Filipponi[2], G. De Luca[3], L. Parigi[1], R. Ceriani [4], M. Boschetti[1], M. Pepe[1]

[1] CNR-IREA, Via A. Corti 12, Milano, Italy - (spirito.e, parigi.l, boschetti.m, pepe.m)@irea.cnr.it
[2] CNR-IGAG, Strada Provinciale 35, Montelibretti, Italy – federico.filipponi@cnr it
[3] CNR-IBE, Via Madonna del Piano 10, Sesto Fiorentino, Italy – giandomenico.deluca@cnr.it
[4] UNIMI-DISAA, Via Celoria 2, Milano, Italy – rodolfo.ceriani@unimi.it

KEY WORDS: PRISMA, preprocessing, OpenSource

ABSTRACT:

PRISMA (PRecursore IperSpettrale della Missione Applicativa) is an Italian hyperspectral satellite launched in 2019, focused on applications in agriculture, forestry, water monitoring, climate studies, and raw-material exploration. Working with its Level 1 (Top-of-Atmosphere radiance) and Level 2 (Bottom-of-Atmosphere reflectance) data presents three main challenges: the data are distributed in HDF format and split into two spectral stacks—VNIR and SWIR—which must be merged before use; the native geolocation accuracy of some products is poor and needs refinement; Level 1 data, required for custom atmospheric correction - for very low or very high reflective targets, such as water and snow - are not geocoded.
While some open-source tools to read and convert PRISMA products already exist, only commercial software offer geolocation refinement, and none provides geocoding for L1. To address this gap with open-source solutions, the authors developed a seamless preprocessing tool named PRISTAR-GEOSPEC (PRISma Tools for Analysis in R for GEOcoding and SPECtral refinement) that converts standard HDF files into geocoded L1 products and geolocation-refined L2 products, with additional options for spatial re-gridding and spectral-smoothing. The toolchain relies on the *prismaread* tool for data conversion/cube merging/metadata extraction, AROSICS and GDAL packages for geocoding. Spatial re-gridding supports multi-temporal analysis, while smoothing is applied to reflectance data for removing spectral artifacts. Realising the workflow in a RStudio Server Docker image connecting to GitHub public repository provides scripts easy for use with all dependencies resolved.

1. MOTIVATION

PRISMA (PRecursore IperSpettrale della Missione Applicativa) is a hyperspectral forerunner satellite mission offering a suite of standard products designed for general use. However, some preprocessing is still needed for some specific applications, which could need for high geocoding/ortho-projection accuracy (e.g. rugged terrains), *ad hoc* atmospheric correction (low/high reflectivity issues, adjacency and/or topographic effects), spatial alignment (time series analyses), spectral smoothing (diagnostic features).
In this framework PRISTAR-GEOSPEC was conceived as a seamless solution to offer some pre-processing functionalities for PRISMA users:

- Data import and metadata extraction
- L2 geocoding refinement
- L1 ortho-projection for rugged terrains
- Spatial Re-gridding
- Spectral smoothing with bad bands removal
- Cloud mask refinement for L1
- Sun-satellite geometry data extraction

The underpinning idea of PRISTAR-GEOSPEC is to provide scientific/expert users of some pre-processing functionalities – which could be found in different commercial, free and open-source software - in a unique environment, easy to install and use. The different functionalities are designed as modules to be combined in a user-defined workflow (some use-cases are reported in section 3).
Currently, there are different software suites dealing with PRISMA data, most of them for reading and exporting HDF5 image and metadata in more common formats. This is the case of ENVI® commercial software, Earthbit PRISMA Toolbox (Agrimano et al., 2024) – which is free but not open-source – and in the open-source domain: EnMAP-Box (Jakimow et al., 2023) and *prismaread* (Busetto et al., 2020).
While most of them offer also image analysis functionalities, they are not dedicated to preprocessing of standard products, and do not offer the possibility to process not-geocoded TOA radiance data to obtain a customized geocoded BOA reflectance product – possibly also re-gridded and cleaned from bad-bands, which is the most noticeable part of PRISTAR-GEOSPEC.
Any open-source package requires continuous dependency maintenance to keep each functionality stable over time, following all sub-version updates. Moreover, some packages used – such as AROSICS – are written and optimized in python. For these reasons, an Rstudio Docker image provided with both R and Python cores and all the PRISTAR-required packages has been created and shared in public domain via DockerHub, thus creating a standalone software.

2. FUNCTIONALITIES

2.1 *read*: data import with prismaread

PRISMA data are distributed from the ASI repository (prisma.asi.it) using HDF format with an he5 extension. In the framework of PRISTAR-GEOSPEC metadata and data in the HDF format are gathered and converted according to the PRISMA Product Specifications to address the extraction of relevant information (e.g. bandwidths, geometry angles, band order, raster content).
Open-source software commonly use portable formats as GeoTIFF, i.e. tiff extension, so to be ready to study PRISTAR provides the *read* function whose core is *prismaread* R package. The function extracts the image data and geolocation metadata,

* corresponding author

combine hyperspectral cubes (coregistered VNIR and SWIR) in a single data stack of all bands VNSWIR and export in GeoTIFF format. This is valid both for L1 and L2 PRISMA products; in the case of L1 *prismaread* applies also a bow-tie correction based on basic geolocation information, including gap-filling during projection to geographic coordinates (EPSG:4326) and extract the cloud mask; also sun zenith and azimuth angle are retained.

2.2 *coreg*: coregistration with AROSICS and GDAL

With the PRISTAR processor the user can project L1 product into ground coordinates or refine the geocoding of L2 product using the *coreg* function with built-in AROSICS python code which extracts spatial patterns similarities between a Sentinel-2 L2A single band image to the user-chosen corresponding band of PRISMA L1 product. AROSICS outcome is a validated tie points collection that becomes the input of GDAL warping functions to make a second-order polynomial transformation to the PRISMA image (which is not provided by AROSICS, which is originally designed only for co-registration).

2.3 *ortho*: DTM ortho-correction

In rugged terrains, the user may prefer a robust algorithm to exploit also the height information levels, when available, of a DTM (Digital Terrain Model), namely using PRISTAR *ortho* feature. Even if L2 are ortho-projected this do not apply to L1 images, and the user could anyway need consistency between the DTM used in geocoding with the one used in further processing. Given an L# product, tie points are extracted using AROSICS as in *coreg* feature, but they are now used to create a regression model between PRISMA L# and Sentinel-2 L2A images coordinates. A 3-pixels spaced grid (to account for the difference in GSD) on the Sentinel-2 L2A image along with z coordinates by DTM extraction is then passed to the trained regression model which results in a grid-like structure in PRISMA L# coordinates. Using the latter grid, the spectral information in the PRISMA image is extracted and then projected back to the grid in the S2 image coordinates, thus projecting the full PRISMA image in satellite coordinate onto the ground. A focal kernel is then spatially passed over the image to fill topographic shadows on the ground.

2.4 *smooth*: spectral refinement

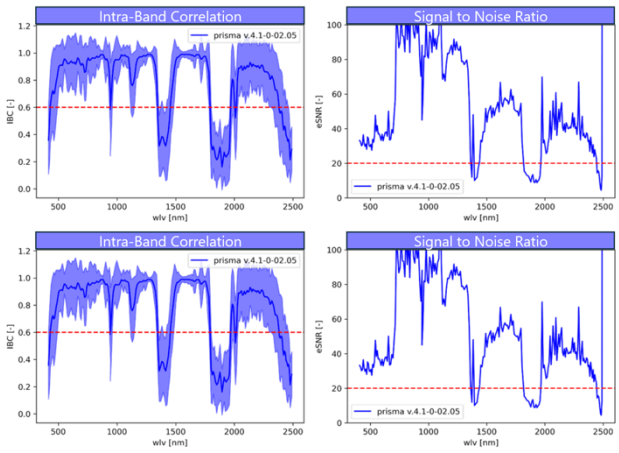

Figure 1. Examples of average IBC and eSNR over homogeneous agricultural targets collected in the field.

It is well known that for hyperspectral satellite data the radiometric calibration and atmospheric correction processes are very complex. There are two main issues related to the narrow band configuration of such systems: low signal to noise values (especially in the SWIR) and accurate calibration of band centres during satellite operation. Both issues could affect the BOA reflectance values and bring some artifacts after the atmospheric correction process. Artifacts occur because physical absorptions are not correctly centred in the band they should had been creating drop-peak features, while the SNR problems results in shifts in reflectance values.

Thus, for application relying on narrow bands, and absorption peak analysis, the PRISMA L2 products need bad-bands removal and spectral smoothing, i.e. *smooth* feature.

Bad-bands removal is done according to (Boschetti et al. 2025) which exploits SNR and intra-band correlation of homogenous targets, to reveal which bands are too noisy for poor signal and for being barely correlated to the neighbour ones – high inter-band correlation is a feature of hyperspectral data - ; such bands are labelled as bad-bands and hence discarded.

Spectral smoothing achieves the goal of drop-peak removal and improvements in SNR of specific bands using their neighbours. This is done with a 40-dof spline smoother using only valid bands. The user can choose to get reflectance (λ) only for valid bands – which are less than the ones of original products -or, using spline regression, reflectance on the full interpolated PRISMA spectrum. The specific dof number was optimized to balance the removal of high-frequency noise with the preservation of narrow diagnostic absorption features.

2.5 *regrid* and *crop*: time series analysis regridding

Time series analysis requires a stack of images whose pixel should geometrically match between layers. PRISTAR lets the user re-grid all the "slave" PRISMA images to a "master" PRISMA image. The *regrid* function continues the pixel grid of the "master" image beyond its borders up to covering all the "slave" image. Then a reprojection procedure makes a new image with "slave" spectral content into the "master" pixel grid using a user-defined reprojection strategy (nearest-neighbour, bilinear, cubic). The user can also choose the *crop* function to keep in the PRISMA "slave" image only pixels inside the master PRISMA image footprint.

2.6 *atcor:* data about acquisition geometry for atmospheric correction

When custom atmospheric correction is needed, the user downloads the PRISMA L1 product instead of the PRISMA L2 product. Every radiative transfer model for atmospheric correction needs sun-satellite-target geometry to be known, i.e. all geometry angles, namely sun azimuth, sun zenith, sensor azimuth and sensor zenith angles. From the PRISMA HDF file the first two are extracted using *prismaread* package while the other two are indirectly computed using the *read_PRISMA_vaa* (Giardino et al, 2025). Such data are computed and then stored in a csv file in the *atcor* feature. At the moment the PRISTAR tool does not provide for a RTM implementation to perform atmospheric correction.

2.7 *cloud*: cloud mask refinement

PRISMA has a defective pixel issue – also known as bad pixels – due to individual elements of the sensor constantly failing to operate correctly. This issue, resulting in dead vertical lines (columns) for some spectral bands, are corrected in L2 data, but still present in L1. Since the cloud mask belongs to L1 it presents many cases of non-physical strip-like structures targeted as clouds where instead they are due defective pixels, particularly in VIS range, used for cloud detection. Those problems can be

solved using erosion-dilation spatial neighbourhood mathematical-morphological filtering using the *cloud* function whose core is the R function erodil_raster of the package spatialist.

3. COMMON USE-CASES

As mentioned above, the PRISTAR-GEOSPEC suite is designed to address the preprocessing needs of a scientific/expert user as related to the functionalities described in the previously (section 2). Even if the code lets the user choose its own pre-processing chain, two explanatory and common workflows are detailed in the following (§3.1 and 3.2).

3.1 L1 preprocessing use-case

The PRISMA L1 product contains not geocoded Top-Of-Atmosphere radiances in satellite coordinates: hyperspectral data are stored in different data cubes, 2 of the aligned VNIR and SWIR data. Referring to the functions in Section 2 the standard preprocessing chain suggested by the authors is the following:

Input of the processing chain is the L1 PRISMA standard product distributed in HDF format whose name is <PRS_L1_STD_OFFL_datetimestart_datetimeend_tile.he5>.
The first step is to convert the HDF5 to a GeoTIFF containing a single raster stack of 230 spectral bands (aligned VNIR+SWIR), plus 1 layer for the cloud mask projected in EPSG:4326 (*read* function). The cloud mask is then cleaned for defective pixels (*cloud* function). The PAN band is not considered, could potentially been included, but its 5m GSD, and problems in spatial alignment between PAN and hypercubes, could hinder the co-registration with Sentinel 2.
Atmospheric correction by now is not part of the PRISTAR functionalities, but for geometry information extraction (*atcor* function). After the atmospheric correction is run in another environment, the geocoding (co-reg function) is accomplished using with a chosen band of a co-occurent (or nearly co-occurrent) Sentinel-2 acquisition at processing level L2A to be used as a reference image for coregistration in GeoTIFF format. A naming convention is set up for input and output data: both PRISMA and Sentinel-2 files must be stored into a given folder, namely *<put_PRISMA_he5_and_S2_tif_here>*. Optionally another input file is the DTM that should be a raster file in GeoTIFF format, stored in an appropriate folder – specifically *<DEM>* – already prepared in the distributed code.
Moreover if the image is to be part of a time series (*regrid* and *crop* functions) the master image should be a raster file in GeoTIFF format stored in the *<master_image_for_regridding>* folder.
The Sentinel-2 EPSG is chosen as default CRS for all the raster outputs if not else specified. DTM will be reprojected into the reference CRS if necessary. The main outputs are:

- the full raw VNIR+SWIR stack (suffix <FULL>) in GeoTIFF format bow-tie corrected and trasformed in WGS84 (EPSG:4326);
- the cloud mask (suffix <CLD> in GeoTIFF format in WGS84;
- the sun and sensor angles stored in csv format;
- the file containing bands' central wavelengths and FWHM stored in txt format.

Workflow outputs are the pre-processed images whose intermediate results are always stored at each step. The folder naming convention is coded according to the processing chain applied to the raw PRISMA image:

1. the coregistered and/or orthorectified raster file in GeoTIFF format;
2. the regridded raster file in GeoTIFF format. If input master image is not in the reference CRS there will be a runtime reprojection of it. The regrid strategy is user-defined selecting from nearest-neighbour, bilinear, cubic;
3. the cropped raster file in GeoTIFF format.

In this case the user will find the following directory tree:

1. <coreg> folder containing <prs_crs_translate_warp>;
2. <coreg_regrid> folder containing <PRISMA_resample>;
3. <coreg_regrid_crop> folder containing <PRISMA_crop>.

3.2 L2 preprocessing use-case

The PRISMA L2 product contains Bottom-Of-Atmosphere reflectances in ground geographical coordinates (WGS84): hyperspectral data are stored in different data cubes, 2 of the aligned VNIR and SWIR data. Referring to the functions in Section 2 the standard preprocessing chain suggested by the authors is the following:

Input of the processing chain is the L2C or L2D PRISMA distributed in HDF format whose name should be <PRS_L2#_STD_datetimestart_datetimeend_tile.he5>. The Sentinel-2 L2A reference band, the naming convention for files and folders, optional use of DTM and regrid, are the same of section 3.1.
Even in this case the Sentinel-2 EPSG is chosen as default CRS, if not else specified. DTM will be reprojected into the reference CRS where needed. The main outputs are:

- the full raw VNIR+SWIR reflectances stack (suffix <FULL>) in GeoTIFF format in the original geographic CRS WGS84;
- the file containing central wavelength and FWHM for each band in txt format.

Further outputs are the processed images resulting from intermediate steps that are all archived. The names of the folder are the left-to-right processing chain function names applied as suffixes to the raw PRISMA image:

1. the coregistered and/or orthorectified raster file in GeoTIFF format;
2. the regridded raster file in GeoTIFF format. If input master image is not in the reference CRS there will be a runtime reprojection of it. The regrid strategy is user-defined selecting from nearest-neighbor, bilinear, cubic;
3. the cropped raster file in GeoTIFF format;
4. the bad-bands cleaned and smoothed raster file in GeoTIFF format. The user can choose to have a 230 bands raster or only valid bands raster.

The folder structure is the same of the one exemplified in Section 3.1, except for adding a <smooth> folder to that chain.

4. DISCUSSION

PRISTAR workflow exemplified in Section 3.1 has shown its usefulness when dealing with calibration/validation activities, such as those performed in the framework of the ASI PRISCAV project (Cal/val scientific activities for the PRISMA mission) at the agricultural site of Bonifiche Ferraresi in Jolanda di Savoia, Ferrara, Italy. Here it was necessary to start from PRISMA L1 product to produce custom atmospheric corrected products,

matching up with field data, coming both from campaigns with portable spectroradiometer and from continuous monitoring with HYPSTAR (HYperspectral Pointable System for Terrestrial and Aquatic Radiometry) stations, also in the framework of HYPERNETS project. Another example is the use of this first use-case, is the ASI/SCIA (Sviluppo di algoritmi per lo studio della Criosfera mediante Immagini PrismA) project, for which rugged terrain and snow/ice coverage needed both the use of a certain DTM orthocorrection and custom atmospheric correction to include adjacency and slope effects. Other examples of applications, this time in agriculture and rangeland, are the ESA/HyRELIEF project – considering evapotraspiration in rangeland - and the ESA/EO4NUTRI (Earth Observation for estimating and predicting crop NUTRIents) project on nutrients retrieval, also of soil (by composite bare soil maps) where PRISTAR was used to create a consistent time series. In both projects a custom atmospheric correction was performed to provide more accurate spectra in input to modelling. Both goals have been achieved by PRISTAR.

In other context, using L2 standard products (case of section 3.2), PRISTAR was necessary, because before 2025 PRISMA L2 were not accurately geocoded: the geometric displacement in L2 data was found to be up to 80 till 250 m, with irregular distribution throughout the same scene and among scenes (De Luca et al., 2024). For cal/val purposes and many applications, when working at pixel scale, there was the need for a geocoding refinement of L2 products. Even after an accurate geocoding of L2 standard products was distributed by ASI, the creation of time series was still an issue addressed by PRISTAR, since regridding is mandatory to have a stack of images, with optionally further need of bad-bands removal and smoothing. This was the case of the ASI/PRIS4VEG project, PRISTAR-processed L2 PRISMA images made it possible to study crop traits and soil cover conditions (Boschetti et al., 2025) by RTM inversions.

5. CONCLUSIONS AND PERSPECTIVES

PRISTAR-GEOSPEC processing chain collects many pre-processing functions applicable to PRISMA L1 and L2 standard products, combining in a synergic software environment both R and Python cores, thus becoming versatile to further addition of features in the two most common programming languages in remote sensing coding. All the R and Python scripts are open-source and free and the full environment is inside a Linux-based Docker image freely available on a public repository with the advantage of freezing all the tools inside a standalone box, avoiding packages dependency issues and different OS and CLI running setups.

The quality of the workflow has been proven in many project applications of ASI and ESA, thus becoming reliable and trustable tool in our work. All the scripts are customizable so any user can adapt the processing in different domains and is warmly invited to share suggestions on the GitHub Issue page.

Future perspectives regard the creation of a metrics for data quality estimation, thus fine-tuning regulation of AROSICS parameters will be then possible, and inclusion of atmospheric correction open-source software (e.g. ISOFIT) for a full workflow implementation.

ACKNOWLEDGEMENTS

We acknowledge Agenzia Spaziale Italiana (ASI) for funding most of the projects in whose framework this tool has been tested. Special thanks to Patrizia Sacco and Ettore Lo Pinto, for their help in data procurement and their sharing of knowledge about the mission. ASI, in the framework of PRISCAV project is also funding the research scholarship of Emanuele Spirito, first Author of this contribution, who also wants to acknowledge the amazing team at CNR - IREA.

REFERENCES

Agrimano, L., Santoro, F., Amoruso, L., Abbattista, C., Drimaco, D., 2024. "PRISMA toolbox, a tool for ingestion, interaction and processing of hyperspectral EO data," Proceedings of the IAF Earth Observation Symposium, Milan, Italy, International Astronautical Federation (IAF), pp. 885-888. https://doi.org/10.52202/078362-0114. Last visit April 2026: URL: https://www.planetek.it/en/products/all_products/earthbit

Alvarez, M., 2025. Spatialist R package in cloud mask refinement.https://github.com/kamapu/spatialist/blob/main/R/erodil_raster.R (last visited January 2026)

Boschetti, M., Candiani, G., Pepe, M., 2025. Quantification of in-season crop traits and post-harvest residues with hyperspectral remote sensing. In: *Earth Observation, Carbon Fluxes and Biophysical Variables from Earth Observation*, pp. 91-151. Campos-Taberner, M., Martínez, B., Sánchez-Ruiz, S. (Eds.), Elsevier, ISBN 9780443299919, https://doi.org/10.1016/B978-0-443-29991-9.00007-0.

Busetto, L., Ranghetti, L., 2020. Prismaread: A tool for facilitating access and analysis of PRISMA L1/L2 hyperspectral imagery Version 1.0.0. https://doi.org/10.5281/zenodo.4019081

De Luca, G., Carotenuto, F., Genesio, L., Pepe, M., Toscano, P., Boschetti, M., Miglietta, F., Gioli, B., 2024. Improving PRISMA hyperspectral spatial resolution and geolocation by using Sentinel-2: development and test of an operational procedure in urban and rural areas. *ISPRS Journal of Photogrammetry and Remote Sensing*, 215, pp. 112-135. https://doi.org/10.1016/j.isprsjprs.2024.07.003.

Giardino, C., Pahlevan, N., Fabbretto, A., Panizza, L., Pellegrino, A., Vandermeulen, R., … Gascon, F., 2025. ACIX-III Aqua: evaluation of atmospheric correction for hyperspectral PRISMA imagery over inland and coastal waters. *International Journal of Remote Sensing*, 46(23), pp. 9066–9090. https://doi.org/10.1080/01431161.2025.2574517

Jakimow, B., Janz, A., Thiel, F., Okujeni, A., Hostert, P., and Van der Linden, S., 2023. "EnMAP-Box: Imaging spectroscopy in QGIS," SoftwareX, vol. 23, p. 101507. https://doi.org/10.1016/j.softx.2023.101507 URL: https://www.enmap.org/data_tools/enmapbox/ (last visit April 2026)

Scheffler, D., Hollstein, A., Diedrich, H., Segl, K., Hostert, P., 2017. AROSICS: An Automated and Robust Open-Source Image Co-Registration Software for Multi-Sensor Satellite Data. *Remote Sensing,* 9(7), p. 676. https://doi.org/10.3390/rs9070676

REPOSITORIES

DockerHub repository (last visit: April 2026): https://hub.docker.com/r/emanuelespiritowork/pristar-geospec/tags

GitHub repository (last visit: April 2026): https://github.com/emanuelespiritowork/PRISTAR-GEOSPEC

This work is licensed under a Creative Commons Attribution-No Derivatives 4.0 International License.

A GEOAI APPROACH TO LAND COVER CHANGE PREDICTION USING MULTILAYER PERCEPTRONS AND COPERNICUS EO DATA TO SUPPORT FUTURE TERRITORIAL PLANNING IN AOSTA VALLEY (NW ITALY)

T. Orusa[1]*, D. Cammareri[1], A. Viani[2]
[1]IN.VA spa, Brissogne Località L'Île-Blonde 5, Brissogne (AO), Italy
[2]Azienda Sanitaria Locale della Valle d'Aosta - AUSL Aosta - SC Sanità Animale, Quart (AO), Italy
*corresponding author e-mail: tommaso.orusa@gmail.com

KEY WORDS: GeoAI; Land Cover Change; Artificial Neural Network (ANN), Multilayer Perceptron (MLP); Copernicus Earth Observation Data; Territorial Planning; Legislative Rules; Aosta Valley

ABSTRACT: Mapping land cover, monitoring its evolution, and anticipating future changes are essential tasks for sustainable territorial planning, particularly in environmentally constrained mountain regions. This study presents a GeoAI-based framework for predicting land cover changes in the Aosta Valley (NW Italy), integrating Multilayer Perceptron (MLP) neural networks with Copernicus Earth Observation data. Sentinel-1 SAR and Sentinel-2 multispectral imagery are combined with validated land cover maps and demographic information to model land cover transitions under current territorial planning regulations. A key innovation of the proposed approach lies in the explicit integration of legislative and planning constraints as spatial layers within the GeoAI model, implemented as hard rules that restrict or guide land cover transitions. Population density and demographic trends are included as dominant drivers for transitions toward urban and anthropic land cover classes. Future land cover is simulated for the 2030 horizon and evaluated using standard accuracy metrics. Land cover transitions affecting populated classes between 2020 and 2030 are synthesized using Sankey and chord diagrams to highlight the magnitude and direction of change. Results indicate limited but spatially concentrated urban expansion, strongly constrained by demographic dynamics and regulatory frameworks. The proposed GeoAI framework provides a scalable and regulation-compliant decision-support tool for proactive land-use planning at the regional scale.

1. INTRODUCTION

Land cover and land use mapping constitute a core component of environmental monitoring, risk assessment, and spatial planning (Annalisa Viani et al., 2024). The rapid expansion of Earth Observation (EO) programs over the last two decades, coupled with open data policies, has significantly enhanced the capacity to monitor land surface processes at multiple spatial and temporal scales (Tommaso Orusa et al., 2024; Viani et al., 2025). In particular, Copernicus Sentinel-1 and Sentinel-2 missions provide dense temporal coverage and spatial resolutions suitable for capturing fine-scale landscape dynamics in heterogeneous environments (Orusa et al., 2020; Orusa, Viani, d'Alessio, et al., 2025). Despite this increased data availability, extracting actionable information from large EO archives remains challenging. GeoAI, defined as the integration of artificial intelligence techniques with geospatial data and GIS Science, has emerged as a powerful paradigm to address this challenge (Gao et al., 2023). GeoAI approaches enable the modelling of non-linear relationships between spatial drivers and observed land cover dynamics, supporting both descriptive and predictive analyses. Predictive land cover change modelling has a long tradition in GIS-based environmental studies, with Artificial Neural Networks (ANNs) and Multilayer Perceptrons (MLPs) widely adopted to simulate land cover transitions. Recent advances in open-source geospatial ecosystems and computational resources have renewed interest in these approaches, particularly when combined with regulatory and socio-demographic information (Carella et al., 2022; Orusa, Cammareri, et al., 2023). Mountain regions such as the Aosta Valley represent a critical test case for GeoAI-based modelling. Strong geomorphological constraints, limited buildable land, and strict territorial planning regulations interact with demographic decline and ageing, shaping land cover dynamics in complex ways (T Orusa et al., 2024; A Viani et al., 2024). In this context, predictive tools (De Petris et al., 2025; Orusa, Viani, Di Lorenzo, et al., 2025) must integrate EO data, population trends, and planning constraints to produce realistic and policy-relevant scenarios. This study proposes a GeoAI framework based on MLP neural networks to predict land cover changes in the Aosta Valley up to 2030.

2. MAIN BODY

The study area corresponds to the Aosta Valley Autonomous Region in north-western Italy (Figure 1).

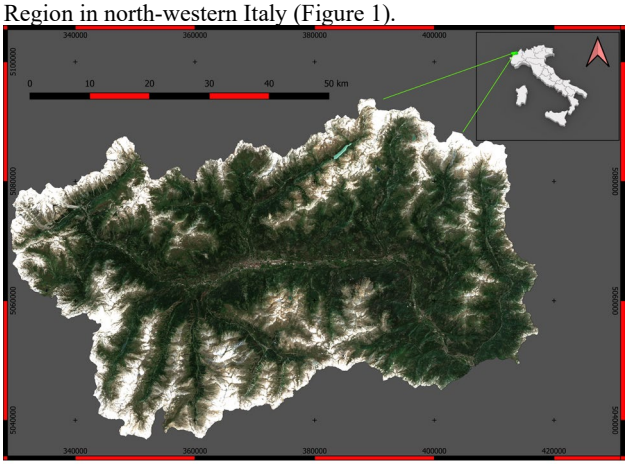

Figure 1 Aosta Valley Autonomous Region

Land cover information was derived from regional land cover maps SCT Geoportal produced using Sentinel-1 and Sentinel-2 imagery, following hierarchical classification approaches specifically designed for alpine environments according (Orusa et al., 2022a, 2022b). The 2020, 2022, and 2024 land cover maps available on the SCT Geoportal are all validated against independent ground truth data collected through field surveys (more details: https://geoportale.regione.vda.it/download/carta-copertura-suolo/). For this study, the validated 2020 and 2022 maps were used as input to train the GeoAI model. The model was then used to simulate the 2024 land cover map. The simulated 2024 output was compared against the observed 2024 land cover map to assess model performance. After this validation step, the model was applied to simulate future land cover scenario for the years following 2024.

* corresponding author

Land cover change modelling was implemented using the MOLUSCE plugin within QGIS (Amgoth et al., 2023), extended through open-source Python routines (https://github.com/nextgis/qgis_molusce). Transition potentials were estimated using a feed-forward Multilayer Perceptron (MLP) neural network (Boutayeb et al., 2025). Land cover maps of 2020 and 2022 have been used to model 2024 and the simulated map of 2024 has been used to assessing the model performance and forecasting land cover until 2030. These products have been retrieved from Aosta Valley SCT Geoportal (https://geoportale.regione.vda.it/download/carta-copertura-suolo/). Beyond these input maps also other products have been considered. Specifically, the input layers used to drive land cover transitions included: (i) topographic variables derived from a Digital Terrain Model (DTM with a vertical accuracy of 30-60 cm), specifically elevation and slope with 10 m GSD; (ii) proximity factors, such as Euclidean distance from water bodies and the main transport infrastructures with both reference nominal scale of 1:5.000; (iii) demographic variables, including population trends (Orusa, Viani, et al., 2023), were analysed through pixel-level modeling using a first-order polynomial regression applied to annual population estimates from the WorldPop project. The analysis was performed on a raster stack of yearly population data covering the period from 2000-2030 (https://hub.worldpop.org/geodata/listing?id=135 with a reference GSD of 100 m); (iv) legislative rules and planning constraints, derived from regional and municipal land-use plans (Ambiti; PTP, PRGC). It is worth noting that (i), (ii), (iv) data have been retrieved from Aosta Valley Geoportal SCT (https://geoportale.regione.vda.it/). The planning rules were translated into a map in which higher-level rules have priority and overlay lower-level ones, as reported in Table 1, following a hierarchical planning-rule approach.

Level	Tool	Effect	Legal Framework of regional laws*
1 (highest)	P4 Hazard Zones (high and very-high natural hazard areas)	Absolute or severe restrictions on building due to natural hazards (landslides, avalanches, debris flows, floods). These zones override all planning instruments.	Aosta Valley Regional Law 11/1998 – Soil protection and natural hazard regulation (Articles 35–38). Implementing acts: Regional Government Resolutions 1384/2006 (avalanches), 1949/2012 (hazard-zone procedures), 331/2020 (debris flows), 1194/2025 (landslides).
2	PTP Landscape Territorial Plan	Landscape protection, binding rules on land use, mandatory for all municipalities .	Legislative Decree 42/2004 – Cultural Heritage and Landscape Code (Articles 135–145). Regional Landscape Plan of Valle d'Aosta (joint approval with the Ministry of Culture).
3 (lowest)	PRGC Municipal Master Plan	Local urban planning instrument; must comply with both the Landscape Plan and hazard-zone regulations.	Must conform to: Regional Law 11/1998 (integration of P3–P4 hazard zones). Legislative Decree 42/2004 (compliance with the Landscape Plan). Municipal technical regulations.
*detailed information at https://www.consiglio.vda.it/app/leggieregolamenti			

Table 1. Hierarchy of Planning Regulations in Aosta Valley Region, Italy

Topographic layers were used to capture geomorphological limitations typical of alpine environments, while accessibility variables accounted for spatial proximity effects influencing urban development. Population-related layers were explicitly introduced as dominant drivers for transitions toward urban and anthropic land cover classes. Legislative rules were implemented as hard rules within the GeoAI model, preventing land cover transitions in legally restricted areas and prioritizing already buildable zones in compliance with the current planning framework (figure 2).

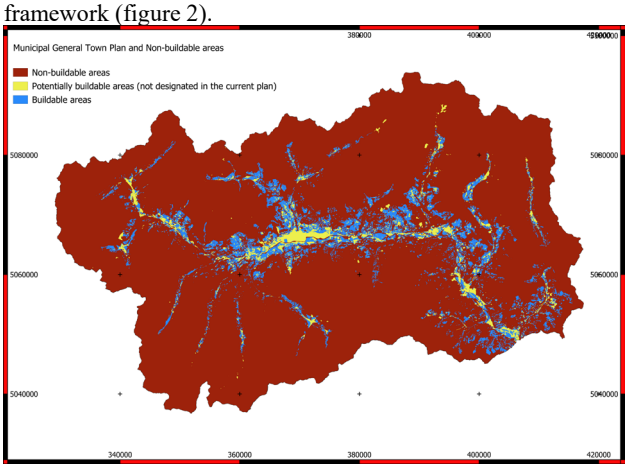

Figure 2. Regulation map ingested into the GeoAI model

The Pearson correlation matrix of the selected predictors, computed prior to modeling, showed mostly low to moderate correlations. Transportation proximity network (TNP) and water proximity network (HPG) were strongly correlated but retained due to the study area's geomorphology, with multicollinearity considered in variable selection. Specifically, TNP and DTM correlation also is not accidental but intrinsic to the geomorphology of the Aosta Valley, in fact the main TNP is concentrated almost exclusively along the valley bottoms, where elevation values are also lowest.

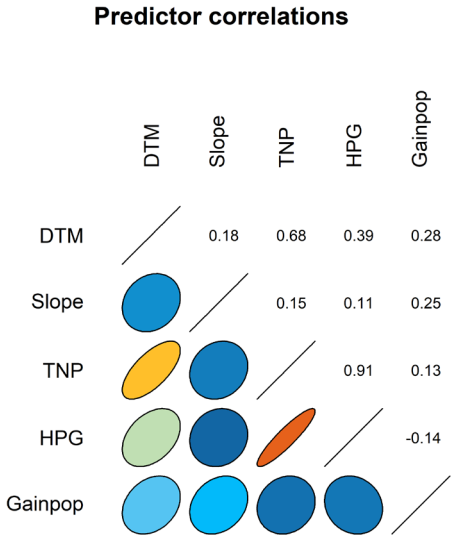

Figure 3. Pearson correlation matrix of input predictors.

Optimal ANN MLP hyperparameters were identified through an extensive hyperparameter tuning procedure. A randomized grid-search strategy was adopted to explore the hyperparameter space and select the configuration that minimized validation error while reducing the risk of overfitting (see table 2).

Hyperparameter	Explored range	Optimal value
Learning rate (η)	10^{-4} – 10^{-2}	0.001
Momentum (α)	0.0005 – 0.01	0.001
Hidden neurons (m)	5 – 30	10
Maximum iterations (t_{max})	1,000 – 5,000	3,000
Training sample size (N_{train})	10,000 – 50,000	20,000
Training / validation split	—	60% / 40%

Table 2. Hyperparameters detected after tuning

The Artificial Neural Network (ANN) MLP model exhibited stable learning behaviour and satisfactory classification performance across the classes. Figure 4 shows the evolution of training and validation accuracy across model iterations, confirming the stability of the learning process.

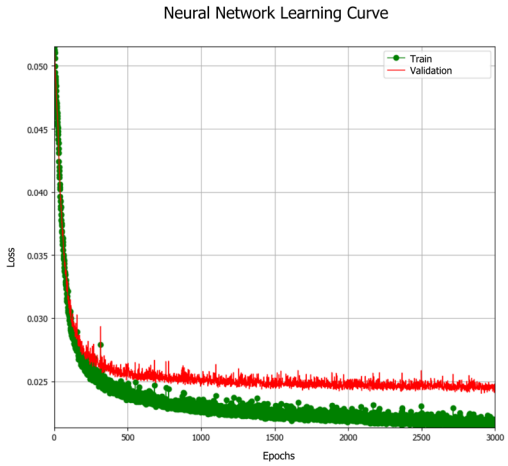

Figure 4. Learning curves of the neural network during training, showing progressive optimization and stabilization of the loss function across iterations for both training and validation datasets, with population gain as input.

Model performance was evaluated using standard classification accuracy metrics (overall accuracy, precision, recall, and F1-score) derived from the comparison between predicted and observed 2024 land cover maps. Validation results (Table 4) indicate good overall accuracy, with precision, recall, and F1-score values consistently above 0.80.

Metric	Value
Overall Accuracy	0.86
Overall Model Kappa	0.85
Model Kappa	0.84
Precision	0.90
Recall	0.81
F1-score	0.85

Table 4. Accuracy metrics

Spatially explicit prediction outputs were generated both in probabilistic and categorical form. SP (Soft Prediction) represents the probability of land-cover change for each spatial unit on a continuous scale (0-100%), preserving uncertainty and highlighting areas more susceptible to change. HP (Hard Prediction) is derived from SP by applying model-specific thresholds and decision rules, producing a discrete land-cover map where each unit is assigned a specific class according to the predefined transition rules. The transition from SP to HP is performed by applying a decision rule that assigns each pixel to a discrete land cover class based on the highest transition probability estimated by the ANN, while respecting hierarchical territorial constraints. Specifically, for each pixel: (a) the ANN outputs a set of transition probabilities y^k for each possible land cover transition class k; (b) the pixel is allocated to the class with the maximum transition probability only if the change is legally admissible according to the constraint mask derived from P4 hazard zones, the Landscape Territorial Plan (PTP), and the Municipal Master Plan (PRGC); (c) for transitions toward Urban and Anthropic Areas, the inclusion of the population-gain driver further conditions HP: urban expansion is simulated only in areas where positive demographic trends coexist with legal admissibility and high transition potential. Thus, the HP map represents a deterministic, regulation-compliant forecast where each pixel's new class is the most probable legally allowed transition, with urban change further moderated by population dynamics. SP and HP maps from 2024 to 2030 reported in figure 5 and 6 respectively.

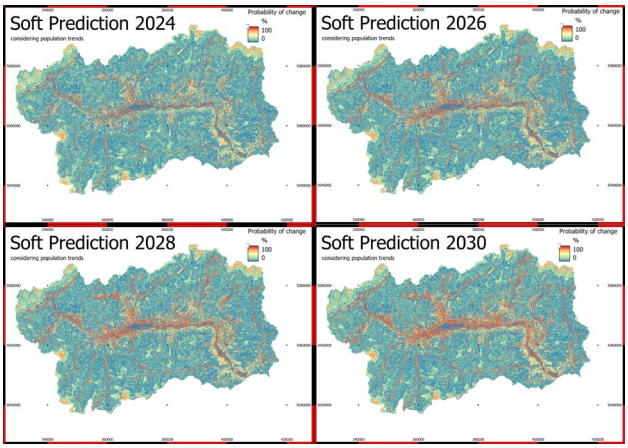

Figure 5. Soft prediction from 2024 to 2030

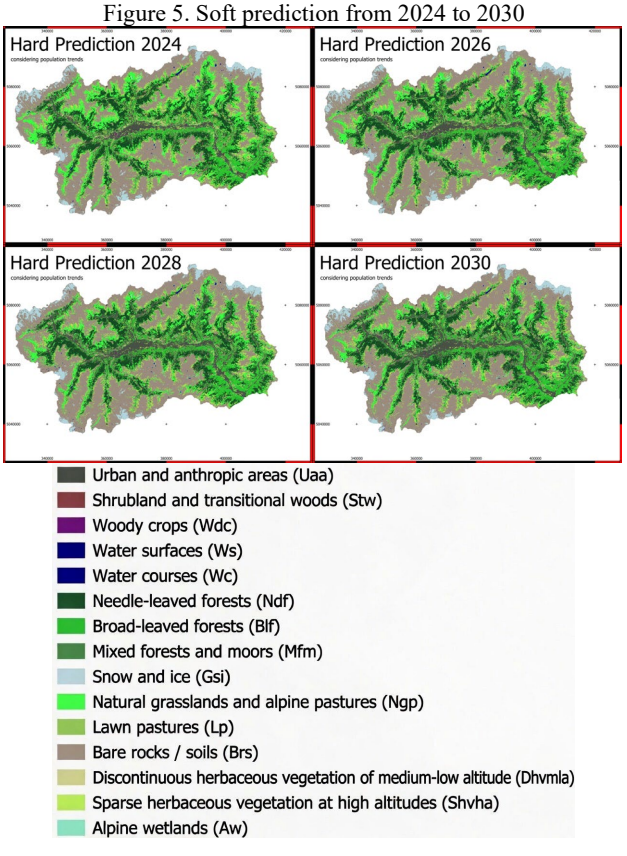

Figure 6. Hard prediction from 2024 to 2030.

Land cover transitions between 2020 and 2030 were synthesized using flow-based visualizations. In figure 7 the Sankey diagram highlights the dominant transitions. Focus on transitions affecting populated classes indicates limited but spatially concentrated urban expansion and ongoing land abandonment and climate change effects in marginal areas.

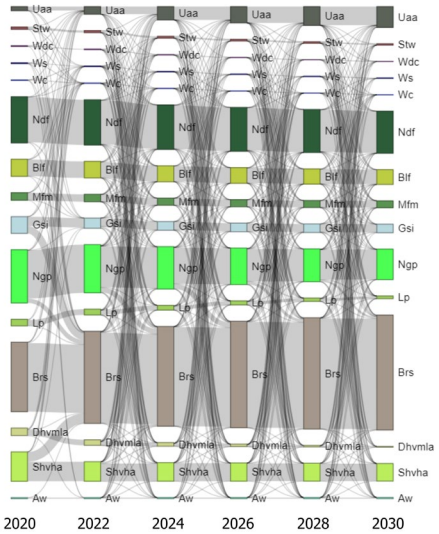

Figure 7 Sankey diagram. Thick flows = large-transformed areas; flows entering/leaving a node = net gain/loss.

3. CONCLUSIONS

This study proposes a GeoAI framework integrating Multilayer Perceptron neural networks, Copernicus EO data, demographic variables, and legislative constraints to predict land cover changes in the Aosta Valley. The inclusion of planning regulations as hard spatial layers enables more realistic and regulation-compliant scenarios achieving model's good performance. Results show limited but spatially concentrated urban expansion. Regarding transferability to other regions, three conditions are necessary: (i) validated multi-temporal land cover maps; (ii) medium-high resolution demographic data; (iii) a georeferenced, hierarchizable regulatory framework. The GeoAI architecture is location-independent, but regulatory implementation requires case-by-case adaptation. The proposed framework offers a scalable, regulation-compliant decision-support tool for proactive land-use planning in environmentally constrained regions.

REFERENCES

Amgoth, A., Rani, H. P., & Jayakumar, K. (2023). Exploring LULC changes in Pakhal Lake area, Telangana, India using QGIS MOLUSCE plugin. *Spatial Information Research*, *31*(4), 429–438.

Boutayeb, A., Lahsen-Cherif, I., & El Khadimi, A. (2025). When Machine Learning Meets Geospatial Data: A Comprehensive GeoAI Review. *IEEE Journal of Selected Topics in Applied Earth Observations and Remote Sensing*.

Carella, E., Orusa, T., Viani, A., Meloni, D., Borgogno-Mondino, E., & Orusa, R. (2022). An integrated, tentative remote-sensing approach based on NDVI entropy to model canine distemper virus in wildlife and to prompt science-based management policies. *Animals*, *12*(8), 1049.

De Petris, S., Orusa, T., Viani, A., Feliziani, F., Sordilli, M., Troisi, S., Zoppi, S., Ragionieri, M., Orusa, R., & Borgogno-Mondino, E. (2025). Spatio-Temporal Pattern Analysis of African Swine Fever Spreading in Northwestern Italy—The Role of Habitat Interfaces. *Animals*, *15*(19), 2886.

Gao, S., Hu, Y., & Li, W. (2023). Introduction to geospatial artificial intelligence (GeoAI). In *Handbook of geospatial artificial intelligence* (pp. 3–16). CRC Press.

Orusa, T., Cammareri, D., & Borgogno Mondino, E. (2022a). A Possible Land Cover EAGLE Approach to Overcome Remote Sensing Limitations in the Alps Based on Sentinel-1 and Sentinel-2: The Case of Aosta Valley (NW Italy). *Remote Sensing*, *15*(1), 178.

Orusa, T., Cammareri, D., & Borgogno Mondino, E. (2022b). A scalable earth observation service to map land cover in geomorphological complex areas beyond the dynamic world: An application in Aosta Valley (NW Italy). *Applied Sciences*, *13*(1), 390.

Orusa, T., Cammareri, D., Freppaz, D., Vuillermoz, P., & Borgogno Mondino, E. (2023). Sen4MUN: A Prototypal Service for the Distribution of Contributions to the European Municipalities from Copernicus Satellite Imagery. A Case in Aosta Valley (NW Italy). *Italian Conference on Geomatics and Geospatial Technologies*, 109–125.

Orusa, T, Farbo, A., De Petris, S., Sarvia, F., Cammareri, D., Borgogno-Mondino, E., & others. (2024). Characterization of alpine pastures using multitemporal earth observation data within the climate change framework. In *Earth Observation: Current challenges and opportunities for environmental monitoring* (Vol. 3, pp. 110–114). Associazione Italiana di Telerilevamento (AIT).

Orusa, T., Orusa, R., Viani, A., Carella, E., & Borgogno Mondino, E. (2020). Geomatics and EO data to support wildlife diseases assessment at landscape level: A pilot experience to map infectious keratoconjunctivitis in chamois and phenological trends in Aosta Valley (NW Italy). *Remote Sensing*, *12*(21), 3542.

Orusa, Tommaso, Viani, A., & Borgogno-Mondino, E. (2024). Earth Observation Data and Geospatial Deep Learning AI to Assign Contributions to European Municipalities Sen4MUN: An Empirical Application in Aosta Valley (NW Italy). *Land*, *13*(1), 80.

Orusa, T., Viani, A., d'Alessio, S. G., Orusa, R., & Caminade, C. (2025). One Health approaches and modeling in parasitology in the climate change framework and possible supporting tools adopting GIS and remote sensing. In *Frontiers in Parasitology* (Vol. 4, p. 1560799). Frontiers Media SA.

Orusa, T., Viani, A., Di Lorenzo, A., & Orusa, R. (2025). CerMapp: A Cloud-Based Geospatial Prototype for National Wildlife Disease Surveillance. *ISPRS International Journal of Geo-Information*, *14*(11), 453.

Orusa, T., Viani, A., Moyo, B., Cammareri, D., & Borgogno-Mondino, E. (2023). Risk assessment of rising temperatures using landsat 4–9 LST time series and meta® population dataset: An application in Aosta Valley, NW Italy. *Remote Sensing*, *15*(9), 2348.

Viani, A, Orusa, T., Divari, S., Lovisolo, S., Zanet, S., Borgogno-Mondino, E., Orusa, R., Bollo, E., & others. (2024). Bartonella spp. Distribution assessment in foxes coupling geospatially-based techniques. In *Earth Observation: Current challenges and opportunities for environmental monitoring*

(Vol. 3, pp. 50–55). Associazione Italiana di Telerilevamento (AIT).

Viani, A., Orusa, T., Divari, S., Lovisolo, S., Zanet, S., Orusa, R., Borgogno-Mondino, E., & Bollo, E. (2025). Detection of Bartonella spp. In foxes' populations in Piedmont and Aosta Valley (NW Italy) coupling geospatially-based techniques. *Frontiers in Veterinary Science*, *11*, 1388440.

Viani, Annalisa, Orusa, T., Mandola, M. L., Robetto, S., Nogarol, C., Mondino, E. B., & Orusa, R. (2024). Grading Habitats for Ticks by Mapping a Suitability Index based on Remotely Sensed Data and Meta® population dataset in Aosta Valley, NW Italy. *Veterinaria Italiana*, *60*(4).

This work is licensed under a Creative Commons Attribution-No Derivatives 4.0 International License.

Evaluation of Deep Learning models applied to remotely sensed imagery for object detection and segmentation tasks in territorial monitoring.

A. Demartis* and F. Giulio Tonolo

Politecnico di Torino, Department of Architecture and Design (DAD), Laboratory of Geomatics for Cultural Heritage (G4CH), Viale Pier Andrea Mattioli 39, 10125, Torino (TO)

KEY WORDS: Deep Learning, GeoAI, Satellite Imagery, RPAS Imagery, Wildfires, Floods

ABSTRACT:

Remote sensing applications such as agro-forestry monitoring, land classification, environmental surveillance, and border supervision increasingly rely on automated solutions to reduce manual interpretation. Artificial intelligence (AI), particularly deep learning (DL) applied to image analysis, represents the state of the art and has fostered the development of GeoAI, integrating geospatial analysis and AI to extract information from Earth Observation (EO) data. Satellite remote sensing is a primary EO data source due to its broad spatial coverage, high temporal resolution, and availability of open-access datasets such as the Copernicus Sentinel missions. Applications requiring very high spatial detail, including the detection of objects related to environmental crimes, benefit from data acquired by Remotely Piloted Aircraft Systems (RPASs), which provide flexible, centimeter-level resolution imagery. Despite the growing availability of EO data, DL workflows remain complex for non-experts. To address this limitation, pre-trained DL models and commercial software with graphical user interfaces have been developed. In object detection (OD), these include traditional class-specific approaches and prompt-based models (PBMs) that enable zero-shot detection through textual prompts, eliminating task-specific training. This study evaluates both categories, focusing on PBMs, using RPAS imagery for OD within the EU Horizon Europe EMERITUS project and Sentinel-2 data for land-cover classification.

1. INTRODUCTION

Remote Sensing based on satellite and aerial imagery plays a fundamental role in natural disaster monitoring, environmental surveillance, and land management. The increasing availability of multi-spectral and high-resolution data has significantly enhanced the capability to detect, classify, and monitor phenomena across spatial and temporal scales. In the context of GeoAI, DL has become the state of the art for image-based analysis. Despite the proven effectiveness of DL methods, their practical implementation usually remains challenging, especially in operationally oriented frameworks, such as the ones involving local law enforcements. Training, fine-tuning, and inferencing models typically require annotated datasets, computational resources, and coding expertise. To lower this barrier, commercial Geographic Information System platforms have integrated a DL interface through Graphical User Interfaces (GUIs), enabling inference directly within the software environment. These solutions allow end users to train, fine-tune, or inference DL pre-trained models without specific coding skills. In the context of the available pre-trained models, recent advancements in tasks such as OD have introduced PBMs that combine vision architectures with Large Language Models, enabling zero-shot detection through textual prompts. Despite the growing availability of pre-trained and prompt-based models in commercial GIS environments, systematic evaluations of their performance in operational EO scenarios remain limited. This study presents an exploratory analytical evaluation of traditional and prompt-based pre-trained DL models for object detection and semantic segmentation, using exclusively the inference capabilities available within the ESRI ArcGIS Pro DL environment. The research can be divided into two main parts: i) an analysis based on PBMs conducted on RPASs imagery acquired within the EU Horizon Europe "EMERITUS" project for environmental crime detection, and ii) an analysis based on available pre-trained DL models trained with Sentinel-2 imagery, including flooded areas and wildfires burn scars segmentation. The objective is to assess the effectiveness and practical applicability of these models in real-world remote sensing workflows.

* corresponding author

2. MAIN BODY

2.1 Materials

This OD and semantic segmentation tests were conducted in ArcGIS Pro (versions 3.4.2 to 3.5.3) using a workstation equipped with an Intel Core i9-14900KF CPU @ 3.20 GHz, 64 GB RAM, an NVIDIA GeForce RTX 4070 GPU with 12 GB VRAM, and Windows 11 Pro. The RPAS imagery used as input test data was collected within the EMERITUS Project, and consists of three orthoimages with centimetric resolution acquired in a semi-controlled environment in the period between October 2023 and June 2025. This environment, a former NATO base in Italy, was used to set up ad-hoc scenarios of illegal dumping by scattering waste objects, mainly tyres and barrels. The multispectral satellite imagery used as input test data was collected from the website of the Copernicus Mission Sentinel-2, selecting data acquired during flood and wildfire events for emergency related models, while an image of the Piemonte region was used for the other analyses. The data for the emergency related models were sensed in May and March 2025 for the floods of Emilia Romagna and Tuscany respectively, while data related to the wildfires of Sardinia and Pantelleria were sensed in the Augusts of 2020 and 2022 respectively. Regarding the Piemonte region, the sensing date is the 27th of October. The pre-trained model selection was performed through an exploration of the Living Atlas, Esri's platform for imagery, maps, and pre-trained DL models with different purposes.

For the RPAS-based analysis, Prompt-Based Models (PBMs) were selected, namely models that should be able to detect any object in the image by means of a user-defined text prompt. This is possible thanks to the usage of a Text Encoder (TE), an architecture that, through tokenization, can convert words into features. This type of encoder is usually trained using large text datasets, which allow them to retrace the features of the target object from text. The input image, instead, goes through a Feature Encoder (FE), that extracts feature representations from the image. Subsequently, the features extracted by the TE and the FE are projected into a shared embedding space where, if overlap is found, an output of the model is generated. The PBMs selected for this research are TextSAM (Spiegler *et al.*, 2025),

GroundingDINO (Liu *et al.*, 2024), and CLIPSeg (Lüddecke e Ecker, 2021), which perform Instance Segmentation, Object Detection, and Semantic Segmentation respectively. These models were chosen since their output can be interpreted within an object detection framework. Ground truth (GT) labels for the RPAS analyses were manually digitized from the orthoimagery for each object category under investigation.For the RPAS analyses, model performance was assessed using Precision, Recall, and F1-score metrics, given the object detection-oriented nature of the task. For the satellite-based analysis, four models compatible with Sentinel-2 imagery were selected. These include a Corine Land Cover (CLC) classification model and a Human Settlements segmentation model, representing traditional remote sensing applications. In addition, two fine-tuned versions of the Prithvi Foundation Model (Jain, 2023) were adopted for flood and burn scar segmentation tasks. For the satellite imagery applications, the CLC 2021 dataset (European Environment Agency, 2024) was used as GT for both the CLC classification model and the human settlements segmentation model, considering either the complete set of classes or a subset restricted to built-up areas, depending on the model configuration. For the evaluation of the fine-tuned Prithvi models, two flood events and two wildfire events were selected from the Copernicus Emergency Management Service archive. For the satellite imagery analyses, which correspond to pixel-level classification tasks, performance was evaluated using a confusion-matrix-based approach, computing Producer and User Accuracy.

2.2 Methods

All the tested models could be inferenced with different tools in ArcGIS Pro through GUIs. Specifically, TextSAM and GroundingDINO could be inferenced using the "Detect Object using Deep Learning" tool, while all the other models could be inferenced using the "Classify Pixel using Deep Learning" tool. As previously explained, the PBMs require as input, along with the orthoimage, a user defined text prompt. For the sake of this research, the prompt was kept as simple as possible, specifically "tyres" or "barrels". Along with the text prompt, it is possible to change some other hyperparameters. This part of the research focused on understanding if, changing the available hyperparameters, these models could be used for unsupervised monitoring applications. To do so, numerous inferences of the models with different hyperparametrization were launched across all orthoimages, obtaining around 220 outputs from the three PBMs. The target hyperparameters for the analysis were padding, tile size, and batch size. This last hyperparameter was chosen to investigate the interaction with padding, as ArcGIS Pro processes tiles in a square group, applying padding to the outer boundary of the groups. Consequently, identical padding values may lead to different effective contexts depending on the batch size. The models were also inferenced with default hyperparameters for comparison. After the inferences, all the outputs underwent a post-processing workflow, specifically TextSAM and GroundingDINO masks underwent a Non-Maximum-Suppression, a Dissolve and an Area Filter (0.2 m^2), while CLIPSeg rasters, after conversion into polygon underwent the same Area Filter. For satellite applications only the default settings of the related pre-trained models were considered. To evaluate the outputs the "Compute accuracy for object detection" tool was used for PBMs paired with previously described manually extracted labels. A deliberately low IoU=0.1 was adopted due to the different natures of the masks generated by the outputs. This choice was necessary to accommodate shape discrepancies between prediction types. For CLIPSeg, raster outputs were converted to polygons before object-level evaluation. For satellite applications the "Compute accuracy for pixel classification" tool was used paired with the vector layers provided by the CEMS activations in the case of emergency related tasks, and with CLC 2021 (or a subselection) for the CLC classification and Human Settlement Segmentation models. The bounding area of the accuracy assessment in this case is the area of interest provided by the CEMS.

2.3 Results and Discussion

The boxplots in Figure 1. A report the F-1 scores obtained by all the inferences of the PBMs with RPAS imagery, whose examples can be found in Figure 2. The graphs show how the F-1 scores are not significantly improved by a hyperparametrization different from the default one. This is highlighted by the heights of the boxes in the boxplots, which describes the variability of the results. The graphs highlight how the models, on average, perform worse with barrels than with tyres, especially in the third orthoimage. This happens probably because of the ambiguity in the text prompt which is harder for the TE to interpret; the prompt "tyres" can trace up to a consistent range of features (e.g. round, black, holey), while "barrels" could lead to less consistent features (e.g. wooden or metallic). Lastly, for each orthoimage, the model CLIPSeg performs better than the others scoring an F-1 Score of 0.89. In the boxplots in Figure 1.B and C are reported recall and precision respectively. The high recalls and low precision reported in the graphs, especially with barrels, are clear symptom of false positives. While this highly impact the possibility to use these models in unsupervised applications, the high recall could still be useful from an operational point of view in cases where the time constrain for the inspection of the monitored area can be relaxed. Regarding satellite applications, the output of the CLC model is reported in Figure 3. The producer and user accuracies per each class are reported in Table 1. The model returns high Producer Accuracies with the classes Urban fabric, Industrial/commercial/transport units, Arable land, Open Spaces with little to no vegetation, and Water, with values of 0.78, 0.58, 0.90, 0.94, and 0.58 respectively.

A)

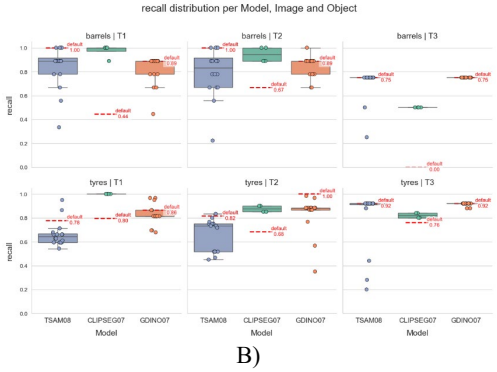

B)

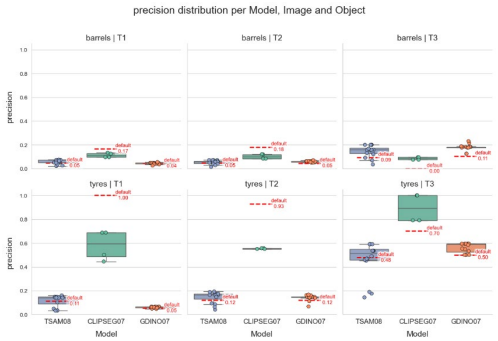

C)

Figure 1 Evaluation of the performances of the PBMs subdivided per model, object, and RPAS orthoimage

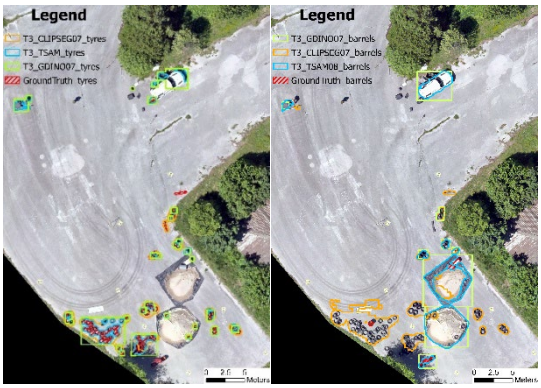

Figure 2 Examples of output of PBMs with GT in the an RPAS orthoimage

These values highlight high recall for these classes, while all the other classes are characterised by very low values, around 0.1. According to User Accuracy, 7 classes out of 11 have values higher than 0.5, with a maximum of 0.78 for Forests. These values, representative of the precision of the model, show that many false positives are generated. The Human Settlement Classification model output is reported in Figure 4, with its accuracies reported in

Table 2. In the test performed in this research, this model performed particularly well, with an overall accuracy of 0.96.

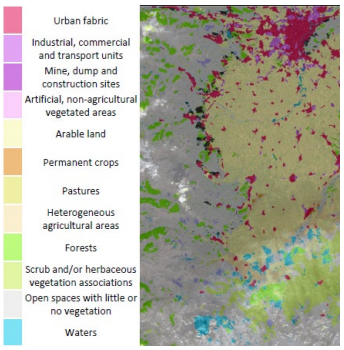

Figure 3 Output of the CLC classification model

Table 1 Producer and User accuracies per each class.

	Producer Accuracy	User Accuracy
Urban fabric	0.78	0.66
Industrial, commercial and transport units	0.58	0.70
Mine, dump and construction sites	0.06	0.75
Artificial, non-agricultural vegetated areas	0.14	0.34
Arable land	0.90	0.69
Permanent crops	0.03	0.59
Pastures	0.00	0.02
Heterogeneous agricultural areas	0.06	0.53
Forests	0.18	0.78
Scrub and/or herbaceous vegetation associations	0.06	0.10
Open spaces with little or no vegetation	0.94	0.35
Waters	0.58	0.04

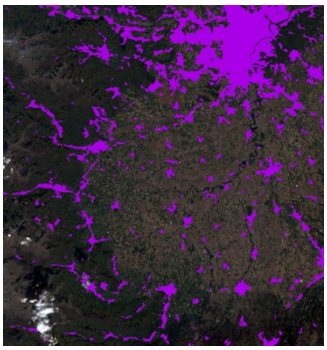

Figure 4 Output of the Human Settlement Classification model

Table 2 Summary accuracies table for the Human Settlement Classification model

	Producer Accuracy	User Accuracy
No Settlement	0.96	0.99
Human Settlements	0.93	0.72

The finetuned version of the Prithvi model for Flood Segmentation was tested on two case studies happened in Emilia Romagna (Left in Figure 5, Table 3) and in Tuscany (Right in Figure 5, Table 4). In both cases user and producer accuracies are close to 1 for the Non-Flooded class, while values around 0.5 reported for the flooded class. It is unclear if the large misclassification is due to the extraction of the GT, labelled using a different image and/or a different type of imagery, or to model's performances. The same procedure was performed for the finetuned version of the Prithvi model for Burn Area segmentation. The selected case studies are wildfires happened in Sardinia (Left in Figure 6, Table 5) and in Pantelleria (Right in Figure 6, Table 6). The accuracies in this case are slightly different across case study; the inference with the Sardinian wildfire has a close to perfect recall with false positives pixels in both classes, while in the Pantelleria's wildfire the false positive is mostly related to no Burnscar pixels misclassified as burned areas.

Figure 5 Red: Output of the Flood Segmentation Prithvi model. Blue: GT from CEMS. Left: Emilia Romagna flood. Right: Tuscany Flood.

Table 3 Summary Table of accuracies for the Privthi Flood Segmentation Model with the Emilia Romagna Flood.

	Producer Accuracy	User Accuracy
No Flood	0.99	0.98
Flood	0.48	0.59

Table 4 Summary Table of accuracies for the Privthi Flood Segmentation Model with the Tuscany Flood

	Producer Accuracy	User Accuracy
No Flood	0.97	0.98
Flood	0.71	0.55

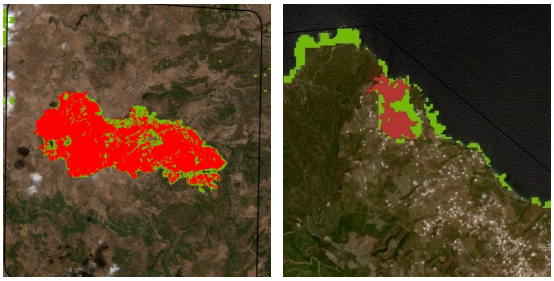

Figure 6 Red: Ground Truth from CEMS. Green: Output of the Burn Scar Segmentation Prithvi model. Left: Sardinia's Wildfire. Right: Pantelleria's Wildfire.

Table 5 Summary Table of accuracies for the Privthi Burn Scar Segmentation Model with the Sardinian Wildfire

	Producer Accuracy	User Accuracy
No BurnScar	0.78	0.99
BurnScar	0.99	0.78

Table 6 Summary Table of accuracies for the Privthi Burn Scar Segmentation Model with the Pantelleria Wildfire

	Producer Accuracy	User Accuracy
No BurnScar	0.98	0.99
BurnScar	0.94	0.3

3. CONCLUSIONS

This study wanted to evaluate the practical operability of the DL open-source models made available by the commercial GISsoftware ESRI ArcGIS Pro through a user friendly GUI, inferencing the pre-trained models available in their online framework. The results for the first part of the research, focused on PBMs and RPAS imagery, shows that the available pre-trained models can be used in operative conditions after preliminary testing with the target object. The models are not particularly sensitive to hyperparametrizations that deviates from the default one, which usually performs better and is therefore the advised one. The high recall returned by the models in almost all the inferences with barrels suggests their use can still be valuable for tasks not strongly related to time for the retrieval of the objects. Overall, satellite-based applications returned better results, which is probably linked to the abundance of training data compared to RPAS data. While the results for the automatic CLC model is not satisfactory for some classes, the tested Human Settlements segmentation model returned satisfactory results, showing how it could be already used in operational workflows. Fine-tuned segmentation models for floods and burned areas demonstrated good overall capacities for a preliminary delineation. The experiments indicate that the commercial GIS software ESRI ArcGIS Pro provides an accessible environment for deploying DL models, but that the accuracy of the outputs strongly depends on the task.

ACKNOWLEDGEMENTS

We would like to thank the DAD-Laboratory of Geomatics for CulturalHeritage and DIATI-Laboratory of GIS and Photogrammetry from Politecnico di Torino for the field data acquisition and the data processing resources. We would like to thank SAFE for their support in the planning of the acquisition campaigns, as well as for their assistance during the data collection activities and the setup of the scenarios. The first part of this work was supported by EMERITUS project, which was funded by the European Union's Horizon Europe research and innovation programme under Grant Agreement No 101073874.

REFERENCES

European Environment Agency (2024) «CLC+Backbone 2021 (raster 10 m), Europe, 3-yearly, Jun. 2024». European Environment Agency. Disponibile su: https://doi.org/10.2909/71FC9D1B-479F-4DA1-AA66-662A2FFF2CF7.

Jain, S. (2023) «Locality Induced Non-Universality for Abelian Symmetries». arXiv. Disponibile su: https://doi.org/10.48550/ARXIV.2306.05435.

Liu, S. *et al.* (2024) «Grounding DINO: Marrying DINO with Grounded Pre-Training for Open-Set Object Detection». arXiv. Disponibile su: https://doi.org/10.48550/arXiv.2303.05499.

Lüddecke, T. e Ecker, A.S. (2021) «Image Segmentation Using Text and Image Prompts». arXiv. Disponibile su: https://doi.org/10.48550/ARXIV.2112.10003.

Spiegler, P. *et al.* (2025) «TextSAM-EUS: Text Prompt Learning for SAM to Accurately Segment Pancreatic Tumor in Endoscopic Ultrasound». arXiv. Disponibile su: https://doi.org/10.48550/ARXIV.2507.18082.

This work is licensed under a Creative Commons Attribution-No Derivatives 4.0 International License.

Smart Earth Observation for a Sustainable Future

Edited by
Associazione Italiana di Telerilevamento (AIT)

Trends in Earth Observation is Directly Edited and published by AIT and it is aimed at hosting peer-review contributions that result as an extension of selected contributions to the biannual AIT Congresses. The Volume will therefore be published every two years.

This volume, organized in 5 thematic chapters, includes 38 contributions

Trends in Earth Observation is indexed by scopus and Web of Science

ISSN 2612-7911

ISBN 978-88-944687-3-1